

The Development of Dynamic Noise Perimetry

Rishi Rattan

Doctor of Philosophy

Cardiff School of Optometry and Vision Sciences

Cardiff University

2010

UMI Number: U585567

All rights reserved

INFORMATION TO ALL USERS

The quality of this reproduction is dependent upon the quality of the copy submitted.

In the unlikely event that the author did not send a complete manuscript and there are missing pages, these will be noted. Also, if material had to be removed, a note will indicate the deletion.



UMI U585567

Published by ProQuest LLC 2013. Copyright in the Dissertation held by the Author.
Microform Edition © ProQuest LLC.

All rights reserved. This work is protected against
unauthorized copying under Title 17, United States Code.



ProQuest LLC
789 East Eisenhower Parkway
P.O. Box 1346
Ann Arbor, MI 48106-1346

DECLARATION

This work has not previously been accepted in substance for any degree and is not concurrently submitted in candidature for any degree.

Signed.......... (Candidate)

Date..31-03-2010.....

STATEMENT 1

This thesis is being submitted in partial fulfilment of the requirements for the degree of PhD.

Signed.......... (Candidate)

Date..31-03-2010.....

STATEMENT 2

This thesis is the result of my own independent work/ investigation, except where otherwise stated. Other sources are acknowledged by explicit references.

Signed.......... (Candidate)

Date..31-03-2010.....

STATEMENT 3

I hereby give consent for my thesis, if accepted, to be available for photocopying and for inter-library loan, and for the title and summary to be made available to outside organisations.

Signed..... (Candidate)

Date.....

STATEMENT 4: Previously approved bar on access

I hereby give consent for my thesis, if accepted, to be available for photocopying and for inter-library loan **after expiry of a bar on access previously approved by the Graduate Development Committee.**

Signed.......... (Candidate)

Date..31-03-2010.....

Acknowledgements

First and foremost, I would like to express my sincere thanks to Professor John Wild, for his continued support, encouragement and guidance.

I am grateful to Professor Jyrki Rovamo for his teachings concerning visual noise and to Dr Gavin Powell for the development of the software for Dynamic Noise Perimetry. I would also like to extend my thanks to the staff and research student colleagues at the Cardiff School of Optometry and Vision Sciences for their support throughout my PhD Studentship. I am indebted to the individuals that participated in each study, and am grateful for their time, their enthusiasm and their generous commitment to each study.

I would like to express my love and gratitude to my wife Shilpi. Without her patience and support, this thesis would not have been completed. I would like to give special thanks to my mother and to my sisters for their unconditional love and support.

I am grateful to my Uncle and good friend, the late Professor AB Sharma, for his inspiration and encouragement throughout my life.

Finally, I dedicate this thesis to my father Ramesh who taught me, from a young age, to aspire to a good education.

Cardiff University

The Development of Dynamic Noise Perimetry

Rishi Rattan

Doctor of Philosophy

2010

This thesis describes the development of Dynamic Noise Perimetry (DNP), a novel method based on the equivalent noise input technique. The method, specifically targeted to an early stage of OAG, used a 0.5 cycle per degree sine-wave grating presented at 8Hz in conjunction with an external noise mask that was optimised for the stimulus. Equivalent noise and sampling efficiency were determined at various locations within the visual field to identify a stage of the disease that was analogous to ganglion cell shrinkage, a stage which is believed to precede conventional methods of detection.

A pilot study initially determined whether the spatial parameters of the mask, in terms of noise check size, were dependent on the spatial and temporal parameters of the grating stimulus. The results showed that the maximal dimensions of each check, i.e. the critical check size, were correlated with the drift frequency of the stimulus. In a second and preliminary study, the variation in the critical check size with grating spatial and temporal frequency was investigated as a function of eccentricity. Critical noise check size, in terms of noise checks per cycle, decreased with increasing spatial frequency and drift frequency of the stimulus, and with eccentric viewing. These results were used to optimise the critical parameters for the noise mask.

Temporal contrast sensitivity, equivalent noise and sampling efficiency were determined at various locations in the visual field, in 20 normal individuals and in 10 individuals with OAG. Temporal contrast sensitivity was reduced, and equivalent noise levels were elevated in early OAG, when compared with normal individuals. Derivative measures of sampling efficiency and equivalent noise declined with glaucomatous field loss. DNP was able to identify individuals with OAG, at locations which exhibited abnormal Pattern Deviation values and/ or abnormal retinal nerve fibre layer thickness. DNP clearly warrants further development.

1 OPEN ANGLE GLAUCOMA.....	1
1.1 CLASSIFICATION OF GLAUCOMA	1
1.1.1 <i>Open angle glaucoma (OAG)</i>	2
1.1.2 <i>Closed angle glaucoma (CAG)</i>	2
1.2 PREVALENCE	3
1.3 NEURAL TISSUES OF THE RETINA	5
1.3.1 <i>Retinal ganglion cells</i>	5
1.3.2 <i>The retinal nerve fibre layer</i>	6
1.3.3 <i>The retinal vasculature</i>	7
1.3.4 <i>The optic nerve head</i>	8
1.3.5 <i>The neuroretinal rim and the optic cup</i>	8
1.3.6 <i>The lamina cribrosa (LC)</i>	9
1.3.7 <i>Pathways to the visual cortex</i>	10
1.4 RISK FACTORS FOR OAG	11
1.4.1 <i>Raised intraocular pressure</i>	12
1.4.2 <i>Age</i>	12
1.4.3 <i>Family history</i>	13
1.4.4 <i>Ethnicity</i>	14
1.5 CLINICAL AETIOLOGY OF OAG.....	15
1.5.1 <i>Mechanical damage theory</i>	15
1.5.2 <i>Vascular damage theory</i>	17
1.5.3 <i>Oxidative stress</i>	19
1.5.4 <i>Apoptosis in OAG</i>	20
1.5.5 <i>Normal tension glaucoma</i>	22
1.5.6 <i>Selective loss theory</i>	24
1.6 CONVENTIONAL METHODS FOR THE DETECTION OF OAG.....	28
1.6.1 <i>Evaluation of the ONH in OAG</i>	28
1.6.2 <i>Standard Automated perimetry (SAP)</i>	29
1.7 DIGITAL IMAGING	31
1.7.1 <i>Confocal scanning laser topography</i>	31

1.7.2	<i>Optical Coherence Tomography</i>	32
1.7.3	<i>Scanning laser polarimetry</i>	34
1.8	VISUAL ELECTROPHYSIOLOGY	35
1.9	NEW METHODS OF PERIMETRY.....	37
1.9.1	<i>Short Wavelength Automated Perimetry</i>	38
1.9.2	<i>High-pass resolution perimetry</i>	39
1.9.3	<i>Critical Flicker Frequency</i>	40
1.9.4	<i>Temporal Modulation Perimetry</i>	40
1.9.5	<i>Motion perimetry</i>	41
1.9.6	<i>Frequency Doubling Technology</i>	42
1.10	TIME TO DETECTION	44
1.10.1	<i>The relationship between RGC density and visual function</i>	44
1.10.2	<i>Cell shrinkage hypothesis</i>	45
1.10.3	<i>Neuroprotection</i>	46
2	INTRODUCTION TO VISUAL NOISE.....	48
2.1	THE CONTRAST SENSITIVITY FUNCTION.....	48
2.1.1	<i>Causes of contrast sensitivity reduction</i>	48
2.2	THE MEASUREMENT OF CONTRAST THRESHOLDS.....	50
2.3	MEDIATORS OF CONTRAST SENSITIVITY	52
2.3.1	<i>Internal noise</i>	53
2.3.2	<i>Sampling efficiency</i>	53
2.4	EXTERNAL VISUAL NOISE	54
2.5	NOISE SPECTRAL DENSITY	56
2.5.1	<i>The signal to noise ratio</i>	60
2.6	THE EQUIVALENT INPUT NOISE TECHNIQUE	61
2.7	CLINICAL STUDIES OF SAMPLING EFFICIENCY AND INTERNAL NOISE.....	65
3	RATIONALE AND SUMMARY OF THESIS.....	68
3.1	THE EARLY DETECTION OF OAG	68
3.1.1	<i>Structural measures of OAG</i>	68

3.1.2	<i>Functional measures of OAG</i>	69
3.1.3	<i>The use of pathway-specific stimuli</i>	69
3.2	THE DEVELOPMENT OF PSYCHOPHYSICAL STIMULI.....	71
3.2.1	<i>Spatial contrast sensitivity</i>	72
3.2.2	<i>Temporal contrast sensitivity (TCS)</i>	73
3.3	A NOVEL APPROACH TO TEMPORAL CONTRAST SENSITIVITY TESTING.....	73
3.3.1	<i>Internal noise</i>	74
3.3.2	<i>Sampling efficiency</i>	74
3.3.3	<i>The equivalent noise paradigm</i>	74
3.3.4	<i>Psychophysical characteristics of the external noise image</i>	75
3.3.5	<i>Clinical application of the equivalent noise paradigm</i>	76
3.4	AIMS OF THE RESEARCH.....	79
3.5	THE OUTCOME OF EACH STUDY.....	81
3.5.1	<i>Aim 1: Development of the hardware and software</i>	81
3.5.2	<i>Aim 2: The relationship between drifting gratings and dynamic noise</i>	82
3.5.3	<i>Aim 3: Spatio-temporal relationships between gratings and dynamic noise</i>	83
3.5.4	<i>Aim 4: Between examination improvement in performance in normal individuals and in individuals with OAG</i>	85
3.5.5	<i>Aim 5: Derivation of $MC N_0$, $MC N_e$, N_{eq} and SE at visit 3 in normal individuals</i>	85
3.5.6	<i>Aim 6: Age-dependency at visit 3 of $MC N_0$, $MC N_e$, N_{eq} and SE</i>	86
3.5.7	<i>Aim 7: Derivation of TCS, N_{eq} and SE in OAG</i>	86
3.6	FURTHER DEVELOPMENT OF DNP.....	87
3.7	STUDY LOGISTICS.....	88
4	DEVELOPMENT OF THE HARDWARE AND SOFTWARE.....	92
4.1	CALIBRATION OF THE CRT DISPLAY MONITOR.....	92
4.1.1	<i>Calibration of CRT display used within the pilot study</i>	92
4.1.2	<i>Calibration of display used for the preliminary spatio-temporal noise study</i>	101
4.2	DEVELOPMENT OF SOFTWARE FOR THE NEW SET UP OF HARDWARE.....	107
4.2.1	<i>The use of random dither</i>	107
4.2.2	<i>Development of the threshold algorithm</i>	108

4.2.3 Development of the operator interface	112
5 THE SPATIAL LIMITS OF THE DYNAMIC NOISE MASK.....	115
5.1 SPATIAL LIMITATIONS OF WHITE PIXELATED NOISE	116
5.2 AIM: PILOT STUDY OF THE SPATIAL LIMITS OF DYNAMIC NOISE.....	117
5.3 METHODS	118
5.3.1 Stimuli.....	118
5.4 RESULTS.....	120
5.5 DISCUSSION.....	123
5.6 AIM: PRELIMINARY STUDY OF THE SPATIAL LIMITS OF DYNAMIC NOISE	125
5.7 METHODS	125
5.7.1 Stimuli.....	125
5.7.2 Subjects.....	126
5.7.3 Procedure.....	126
5.8 RESULTS.....	127
5.9 DISCUSSION.....	138
6 CLINICAL APPLICATION OF DYNAMIC NOISE PERIMETRY	142
6.1 COHORT.....	143
6.1.1 Normal individuals.....	143
6.1.2 Individuals with OAG	144
6.2 METHODS	146
6.2.1 Stimuli.....	146
6.2.2 Procedure.....	148
6.3 ANALYSIS	150
6.3.1 Calculation of sampling efficiency (SE) and equivalent noise (N_{eq})	150
6.3.2 Derivatives of DNP measures	152
6.3.3 Analysis of the results from the normal individuals.....	153
6.3.4 Analysis of the results from individuals with OAG	154
6.4 RESULTS: THE ABSOLUTE LEARNING EFFECT FOR THE NORMAL INDIVIDUALS	154

6.4.1 The learning effect for the normal individuals for Michelson contrast in the absence of noise ($MC N_0$)	154
6.4.2 The learning effect for the normal individuals for Michelson contrast in the presence of noise ($MC N_e$)	155
6.4.3 The learning effect for the normal individuals for equivalent noise (N_{eq})	155
6.4.4 The learning effect for the normal individuals for sampling efficiency (SE)	156
6.5 RESULTS: THE PROPORTIONATE LEARNING EFFECT FOR THE NORMAL INDIVIDUALS	173
6.5.1 The learning effect between visit 1 and 2 for the normal individuals for Michelson contrast in the absence of noise ($MC N_0$)	173
6.5.2 The learning effect between visit 2 and 3 for the normal individuals for Michelson contrast in the absence of noise ($MC N_0$)	174
6.5.3 The learning effect between visit 1 and 2 for the normal individuals for Michelson contrast in the presence of noise ($MC N_e$)	174
6.5.4 The learning effect between visit 2 and 3 for the normal individuals for Michelson contrast in the presence of noise ($MC N_e$)	175
6.5.5 The learning effect between visit 1 and 2 for the normal individuals for equivalent noise (N_{eq})	184
6.5.6 The learning effect between visit 2 and 3 for the normal individuals for equivalent noise (N_{eq})	184
6.5.7 The learning effect between visit 1 and 2 for the normal individuals for sampling efficiency (SE)	185
6.5.8 The learning effect between visit 2 and 3 for the normal individuals for sampling efficiency (SE)	185
6.6 RESULTS: THE ABSOLUTE LEARNING EFFECT FOR INDIVIDUALS WITH OAG	195
6.6.1 The learning effect for Michelson contrast in the absence of noise ($MC N_0$)	195
6.6.2 The learning effect for Michelson contrast in the presence of noise ($MC N_e$)	196
6.6.3 The learning effect for equivalent noise (N_{eq})	196
6.6.4 The learning effect for sampling efficiency (SE)	197
6.7 RESULTS: THE PROPORTIONATE LEARNING EFFECT FOR INDIVIDUALS WITH OAG	214
6.7.1 The learning effect between visit 1 and 2 for Michelson contrast in the absence of noise ($MC N_0$)	214

6.7.2 The learning effect between visit 2 and 3 for Michelson contrast in the absence of noise ($MC N_0$)	214
6.7.3 The learning effect between visit 1 and 2 for Michelson contrast in the presence of noise ($MC N_e$)	215
6.7.4 The learning effect between visit 2 and 3 for Michelson contrast in the presence of noise ($MC N_e$)	215
6.7.5 The learning effect between visit 1 and 2 for equivalent noise (N_{eq})	216
6.7.6 The learning effect between visit 2 and 3 for equivalent noise (N_{eq})	217
6.7.7 The learning effect between visit 1 and 2 for sampling efficiency (SE)	217
6.7.8 The learning effect between visit 2 and 3 for sampling efficiency (SE)	218
6.8 RESULTS: CHARACTERISTICS OF THE DNP MEASURES FOR NORMAL INDIVIDUALS AT THE THIRD VISIT	235
6.8.1 Michelson contrast of normal individuals in the absence of noise ($MC N_0$)	235
6.8.2 Michelson contrast of normal individuals in the presence of noise ($MC N_e$)	235
6.8.3 Equivalent noise (N_{eq}) of normal individuals	236
6.8.4 Sampling efficiency (SE) of normal individuals	236
6.8.5 Coefficient of variation for detection and discrimination data	237
6.9 RESULTS: CHARACTERISTICS OF THE AGE-DEPENDENCY OF THE DNP MEASURES FOR NORMAL INDIVIDUALS AT THE THIRD VISIT	240
6.9.1 Age-dependency of Michelson contrast thresholds in the absence of the noise mask ($MC N_0$)	240
6.9.2 Age-dependency of Michelson contrast thresholds in the presence of the noise mask ($MC N_e$)	240
6.9.3 Age-dependency of equivalent noise (N_{eq})	241
6.9.4 Age-dependency of sampling efficiency (SE)	241
6.9.5 Relative age-dependency for detection and discrimination data	241
6.10 RESULTS: DNP OUTCOMES FOR INDIVIDUALS WITH OAG	253
6.10.1 Distribution of DNP measures for the detection task at the superior temporal quadrant for individuals with OAG and for normal individuals	253
6.10.2 Distribution of DNP measures for the detection task at the superior nasal quadrant for individuals with OAG and for normal individuals	260

6.10.3 Distribution of DNP measures for the detection task at the inferior nasal quadrant for individuals with OAG and for normal individuals	267
6.10.4 Distribution of DNP measures for the detection task at the inferior temporal quadrant for individuals with OAG and for normal individuals	274
6.10.5 Distribution of DNP measures for the discrimination task at the superior temporal quadrant for individuals with OAG and for normal individuals	281
6.10.6 Distribution of DNP measures for the discrimination task at the superior nasal quadrant for individuals with OAG and for normal individuals	288
6.10.7 Distribution of DNP measures for the discrimination task at the inferior nasal quadrant for individuals with OAG and for normal individuals	295
6.10.8 Distribution of DNP measures for the discrimination task at the inferior temporal quadrant for individuals with OAG and for normal individuals	302
6.11 DISCUSSION	317
6.11.1 The potential for the learning effect.....	317
6.11.2 $MC N_0$, $MC N_e$, N_{eq} and SE of the normal eye.....	318
6.11.3 Age-dependency in terms of $MC N_0$, $MC N_e$, N_{eq} and SE	321
6.11.4 Determination of $MC N_0$, $MC N_e$, N_{eq} , SE, Log_{10} Ratio and SDI in OAG	322
6.12 CONCLUSIONS.....	325
7 GENERAL CONCLUSIONS AND PROPOSALS FOR FUTURE WORK	326
7.1 REVIEW OF FINDINGS	327
7.1.1 The spatial limits of the dynamic noise mask.....	327
7.1.2 Clinical application of Dynamic Noise Perimetry	327
7.2 PROPOSALS FOR FUTURE WORK	328
REFERENCES	331
APPENDIX	374
SUMMARY OF PATENTS PENDING.....	374
PATENT FILED UNDER THE PATENT COOPERATION TREATY (PCT)	375
ABSTRACT FOR ARVO.....	376

List of acronyms

CAG	Closed angle glaucoma
CCT	Central corneal thickness
CRT	Cathode Ray Tube
CSF	Contrast sensitivity function
DNP	Dynamic Noise Perimetry
E_{th}	Energy threshold
FDT	Frequency Doubling Technology Perimetry
G-H	Garway Heath et al (2000)
H	Harwerth et al (2007)
HPRP	High pass resolution perimetry
HRT	Heidelberg Retinal Tomography
IN	Inferior nasally
IOP	Intraocular pressure
IT	Inferior temporally
K	Koniocellular
LC	Lamina cribrosa

LGN	Lateral geniculate nucleus
M	Magnocellular
MC	Michelson contrast
MC N_0	Michelson contrast in the absence of noise
MC N_e	Michelson contrast in the presence of noise
MRA	Moorfields Regression Analysis
mVEP	Multifocal visual evoked potentials
N_e	Noise spectral density
N_{eq}	Equivalent noise
N_i	Internal noise
NRR	Neuroretinal rim
OAG	Open angle glaucoma
OCT	Ocular coherence tomography
OHT	Ocular hypertension
ONH	Optic nerve head
P	Parvocellular
PD	Pattern Deviation

PD _{Ab}	Abnormal pattern deviation value
PD _N	Normal pattern deviation value
PERG	Pattern electroretinogram
RGC	Retinal ganglion cell
RNFL	Retinal nerve fibre layer
RNFL _{Ab}	Abnormal retinal nerve fibre layer thickness
RNFL _N	Normal retinal nerve fibre layer thickness
SAP	Standard automated perimetry
SD	Standard Deviation
SDI	Signal detection index
SE	Sampling efficiency
SF	Spatial frequency
SLO	Scanning laser ophthalmoscopy
SLP	Scanning laser polarimetry
SN	Superior nasally
SNR	Signal-to-noise ratio
ST	Superior temporally

SWAP	Short wavelength automated perimetry
TCS	Temporal contrast sensitivity
TD	Total deviation
TF	Temporal frequency
TMP	Temporal modulation perimetry
VEP	Visual evoked potentials

1 Open angle glaucoma

Glaucoma is a leading cause of blindness and, by 2020, will affect approximately 80 million people worldwide (Quigley, 1996; Quigley and Broman, 2006). It is a multifactorial disease involving progressive damage to the optic nerve head (ONH) with subsequent visual field loss (Quigley and Green, 1979; Quigley and Addicks, 1981; Quigley et al., 1988; Harwerth et al., 2004). As a consequence of the field loss, the impact on an individual's quality of life increases with increasing severity of the disease (Gupta et al., 2005; Evans et al., 2009; Mills et al., 2009) with the concomitant increase in public resource utilisation (Traverso et al., 2005).

The purpose of this thesis was to develop a novel perimetric technique for the detection of glaucoma, which could identify functional damage prior to that of existing methods. The Candidate designed, developed and tested the technique for the purposes of this thesis. Software was developed with the assistance of Dr Gavin Powell, a software programmer working for Cardiff University.

1.1 Classification of glaucoma

Glaucoma is either primary or secondary in nature. Primary glaucomas are the direct result of complex disease processes (John, 2005). The precise mechanism of damage is not fully understood. Secondary glaucomas occur as a result either of ocular trauma or of existing disorder/ disease such as cataract or uveal melanoma. The primary and secondary

glaucomas are further classified in terms of an anatomical feature, the anterior chamber angle. The angle refers to the junction of the cornea and iris through which the aqueous humour, is able to drain out of the eye through the trabecular meshwork in order to maintain a healthy hydrostatic pressure. The pressure within the eye is referred to as intraocular pressure (IOP), and it may be within or without the normal range in the primary and secondary glaucomas. An elevated IOP, corrected for central corneal thickness (CCT) in the otherwise normal eye, above 21 mmHg, is referred to as ocular hypertension (OHT).

1.1.1 Open angle glaucoma (OAG)

OAG is characterised by an open anterior chamber angle. Aqueous is able to drain freely through the trabecular meshwork without any form of obstruction. The disease is initially asymptomatic and may be associated with an elevated IOP, although between one third and one half of individuals have normal IOPs. These individuals are considered to have normal tension glaucoma (NTG). The mean normal pressure corrected for the effect of CCT, is considered to be 16 mmHg with an upper limit of 21 mmHg (Sommer et al., 1991b; Bonomi et al., 1998; Gordon et al., 2002; Zeitz et al., 2004). OAG is generally bilateral although the disease is not necessarily symmetrical. Progression from normal visual vision to blindness occurs over several decades, although progression is faster where the OAG is associated with an elevated IOP (Heijl et al., 2009).

1.1.2 Closed angle glaucoma (CAG)

When the flow of aqueous is partially or fully obstructed, the angle is referred to as closed (Varma et al., 2006). Closed-angle glaucoma is more likely when the anterior chamber angle is narrow, which is more common in hypermetropic eyes and in Chinese individuals

(Seider et al., 2009). The obstruction of aqueous drainage elevates IOP to dangerous levels, causing direct injury to the ONH. Angle closure can occur suddenly (termed acute-onset) or more gradually (termed sub-acute); both modes are sight-threatening and require urgent medical intervention. Certain individuals may be anatomically pre-disposed to narrow anterior chamber angles and are susceptible to closure when the pupil widens in low levels of illumination. CAG is generally treated with pre-emptive surgical intervention for eyes considered at risk of angle-closure (Saunders, 1990; Reibaldi and Uva, 1992; Nolan et al., 2007); however, this method may not be best suited to acute angle closure glaucoma (Chen et al., 2009).

The breadth of the topic of open angle glaucoma is such that only an overview can be given within this thesis, particularly given the context, namely, the development of a novel technique of perimetry.

1.2 Prevalence

Of the 80 million people who will suffer with glaucoma by 2020, 74% of these will have the open angle form (Quigley and Broman, 2006). It is believed that half of all those affected with OAG are unaware that they have the disease (Tielsch et al., 1991), and of those individuals that present with the disease, the severity is linked to the extent of socio-economic deprivation (Ng et al., 2010).

African-Americans exhibit a significantly higher prevalence of OAG compared to Caucasians. The prevalence amongst African-Americans is 1.23% in those aged 40 to 49

years and 11.26% in those aged 80 years or older. Caucasian Americans exhibit a prevalence of 0.92% in those aged 40 to 49 years and 2.16% in those aged 80 years or older (Tielsch et al., 1991). The prevalence is higher for Hispanic-American (Varma et al., 2004) and Asian populations (Quigley and Broman, 2006) than for Caucasians. In Latin-America, the prevalence is approximately 20% between 80 and 90 years of age. The Chinese exhibit a prevalence of around 17% by this age compared to European Caucasians with approximately 8% (Quigley and Broman, 2006; Ekstrom, 2008). Despite the increased prevalence, African- and Hispanic-Americans both have a lower level of awareness of the condition, when compared with the level of awareness amongst Caucasians (Gasch et al., 2000).

Closed-angle glaucoma (CAG) is more prevalent amongst people of Chinese origin and amongst the Eskimo populations of Canada, Alaska and Greenland (Quigley, 1996). Greater longevity accounts for the higher prevalence in women, amongst these populations for both OAG and CAG; women account for 55.4% of OAG and for 69.5% of CAG (Quigley and Broman, 2006; Seider et al., 2009). The Chinese and individuals of South East Asian origin are approximately three times more likely to suffer from CAG than from OAG (Quigley, 1996). Globally, only 24% of primary glaucomas are of the closed angle-form. However, the number of individuals with CAG who are blind according to the World Health Organisation (WHO) definition of blindness i.e. $<3/60$ is identical to the number with OAG due to the increased morbidity of the latter (Quigley and Broman, 2006).

1.3 Neural tissues of the retina

The retina is comprised of three layers of cells. Several layers of neurons are interconnected by synapses made between axons and dendrites of each cell layer. Photoreceptor cells known as rods and cones are directly receptive to light and are located at the outer retina adjacent to the retinal pigment epithelium (RPE). The RPE contains melanin which helps to absorb excess light that enters through the pupil. There are approximately 130 million photoreceptors distributed across the retina. Approximately 7 million cones populate the macula which is the central area of the retina specialised for the interpretation of detail and colour (De Monasterio and Gouras, 1975; Saeed et al., 2006). At the fovea centralis of the macular, the ratio of rods to cones is 2:1, beyond the macula the ratio increases to 30:1 due to the steep fall in cone density with increasing retinal eccentricity (Curcio et al., 1990). The prevalence of rods increases with eccentricity and enables visual function at low light levels (De Monasterio and Gouras, 1975). A review is that of Saeed et al., (2006).

1.3.1 Retinal ganglion cells

There are approximately 1.5 million retinal ganglion cells within the retina. The cells are highly concentrated at the central retina, forming several layers at the macula, and are more sparsely arranged in the periphery. At the fovea, individual cones converge onto individual ganglion cells i.e. the ratio is 1:1. This low convergence preserves high spatial resolution at later stages of visual processing. At the peripheral retina, there is a high level of convergence, with as many as one hundred and fifty photoreceptors converging on a single retinal ganglion cell (RGC) (Curcio and Allen, 1990; Curcio et al., 1990; Rodieck, 1998). There are four known types of RGC within the human retina; midget, parasol,

bistratified and bplexiform (Watanabe and Rodieck, 1989; Dacey and Lee, 1994; Martin et al., 1997). The midget and parasol cells are the most prevalent (Watanabe and Rodieck, 1989; Curcio et al., 1990; Dacey and Petersen, 1992; Kolb et al., 1992; Rodieck, 1998; De Lima Silveira, 2004).

The midget cell has a small dendritic field, a small cell body and a thin axon. Midget cells comprise approximately 70% of the RGC population and are concentrated at the fovea. Parasol cells comprise approximately 10% of the RGC population, and have large dendritic fields, large cell bodies and thick axons. Parasol cells are more prevalent in the peripheral retina, although both midget and parasol cell axon diameters increase with increase retinal eccentricity (Watanabe and Rodieck, 1989; Curcio and Allen, 1990; Yamada et al., 1996; Weber et al., 1998; De Lima Silveira, 2004; Weber and Harman, 2005). Midget cells are connected to the photoreceptors via midget bipolar cells, whereas parasol cells are connected via diffuse bipolar cells (Kolb et al., 1992). The bplexiform cell is the exception, having direct connections with photoreceptors (Mariani, 1982)]. The bistratified cell has a small cell body and a thin axon, with a dendritic field of a similar size to the parasol cell (Martin et al., 1997; Rodieck, 1998).

1.3.2 The retinal nerve fibre layer

The retinal nerve fibre layer (RNFL) is made up of bundles of retinal ganglion cells and their axons that are grouped together in a characteristic distribution (Van Buren, 1963; Stone and Johnston, 1981; Quigley et al., 1989; Blumenthal and Weinreb, 2001). There are approximately 1.5 million RGCs, although the accuracy of various tissue analysis methods are limited by post-mortem cell shrinkage and physiological variability between individuals (Curcio and Allen, 1990).

RGC axons which originate from peripheral retinal areas are more superficial within the RNFL. All nerve fibres traverse the retina at the ONH, the structure that channels each RGC via the lamina cribrosa (LC) of the ONH and onwards to the lateral geniculate nucleus (LGN). The ONH is situated at approximately 15° in the nasal hemi-field of the retina and has a characteristic vertical oval shape measuring approximately 7° by 5°. The ONH is responsible for the characteristic blind spot in the temporal aspect of the visual field. Nerve fibres which extend from the macula to the temporal ONH form the papillomacular bundle. Nerve fibres from other parts of the retina arch around the papillomacular bundle to reach the ONH (Minckler, 1980; Ogden, 1983; Quigley et al., 1989). Fibres originating from the peripheral retina are known to have thicker cell axons (Quigley et al., 1988) whereas thinner nerve fibres tend to originate from areas adjacent to the macula. Nerve fibre bundles become increasingly dense as they approach the ONH, as they are joined by fibres from other retinal locations (Ogden, 1984).

1.3.3 The retinal vasculature

The central retinal artery, the main arterial blood supply to the retina, emerges from the upper nasal quadrant of the ONH and is situated nasally to the main venous drainage vessel, the central retinal vein (Jonas and Fernandez, 1994). The vessels branch into characteristic vascular arcades that follow the distribution of the RNFL. As they branch into smaller capillaries, there is a monotonic decrease in vessel diameter with increasing distance from the ONH (Mitchell et al., 1997). Arterioles have widest diameters at the inferior-temporal ONH margin; the diameters become successively thinner at the superior-temporal, superior-nasal and finally the inferior-nasal ONH margin. The venules follow a similar pattern (Jonas and Hayreh, 1999).

1.3.4 The optic nerve head

The nerve fibre layer becomes thinner with increasing distance from the ONH (Radius, 1980; Weinreb et al., 1995; Varma et al., 1996). The inferior region of the ONH, referred to as the inferior pole, has the highest density of nerve fibres, many of which have small diameters (Sanchez et al., 1986). Beyond infancy, ONH size is independent of age (Jonas et al., 1989b; Rudnicka et al., 2001). Males have a larger ONH than females (Ramrattan et al., 1999). Axial length is the strongest predictor of ONH size (Rudnicka et al., 2001), indicating that size is influenced by refractive error. Highly myopic eyes (beyond -8.00 dioptres) are characterised by increased axial length and increased ONH size (Jonas et al., 1988a).

1.3.5 The neuroretinal rim and the optic cup

The neuroretinal rim (NRR) and the optic cup are anatomical features of the ONH. The NRR is formed by the retinal nerve fibres, which coalesce within the ONH. NRR area may (Budde et al., 2000; Zangwill et al., 2004b) or may not (Jonas et al., 1989b; Jonas et al., 1992; Jonas et al., 2004b) increase with ONH size. In African American populations, ONH is inversely associated with NRR area (Varma et al., 1994).

The various segments of the NRR correspond with specific regions of the RNFL. The superior and inferior quadrants of the rim correspond with nerve fibres arriving from the superior and inferior retinal nerve fibre bundles, respectively. The nasal rim corresponds with axons from the nasal nerve fibre layer and the temporal rim corresponds with the papillomacular bundle. Axons originating in the extreme periphery of the retina will lie

more closely to the ONH margin. The shape of the rim is unaffected by the size of the ONH (Garway-Heath and Hitchings, 1998; Jonas and Budde, 2000).

The optic cup is characterised by the absence of retinal nerve fibres. Optic cup size increases with ONH size (Jonas et al., 1989a). Cup size does not vary with race (Zangwill et al., 2004c; Girkin et al., 2005).

1.3.6 The lamina cribrosa (LC)

Axons from the RNFL traverse the LC, a perforated structure of connective tissue. Most axons pass directly through the LC according to the distribution of the nerve fibre bundle; however, some fibres are more randomly arranged within the laminar pores (Morgan et al., 1998). A collagen fibrillar network forms the LC and associated septal plates. These structures are at the anterior part of the ONH and arise from the scleral collagen fibrils that form thick bundles of collagen in lamina plates. There are over ten plates stacked together, creating pore channels which secure the nerve fibre bundles within bundles of collagen and glial tissue. The septal plates are formed by thick bundles of collagen that are radially and obliquely arranged. The plates have many oval and round compartments due to the branching and regional irregularity in the shape of the myelinated nerve fibre bundle (Morgan-Davies et al., 2004).

The superior and inferior quadrants of the LC are characterised by a thinner septum and larger pores containing thicker bundles of nerve fibres (Quigley and Addicks, 1981). The structure of the LC is thicker in the nasal quadrant than in the temporal quadrant due to a higher proportion of connective tissue within the nasal LC (Radius and Bade, 1981). Nerve

fibre density also varies across the LC. The highest density of nerve fibres is concentrated in the inferior-temporal sector of the optic nerve (Mansoori et al., 2010).

The LC has a characteristic U-shaped configuration in which the central region is bowed posteriorly when compared to the periphery (Quigley et al., 1983). The central area of the LC has elastic properties which determine its shape under mechanical stress. Acute elevation of IOP increases cup depth and causes reversible bowing of the LC (Azua-Blanco et al., 1998). The relative flexibility of the LC varies between healthy individuals (Levy et al., 1981), and the flexibility is thought to relate to the proportion of elastic connective tissue present within the LC. Relative proportions of connective tissue do not vary according to race; however, the number of pores and the overall size of the LC does vary according to racial background (Dandona et al., 1990; Jonas et al., 2004a; Morgan-Davies et al., 2004).

1.3.7 Pathways to the visual cortex

RGCs project from the retina, via the ONH to a specific layer of the LGN. Midget cells project to the parvocellular (P) layer of the LGN and parasol cells project to the magnocellular (M) layer of the LGN. As such, midget and parasol cells are referred to as P and M cells, respectively. P and M geniculocortical pathways continue via distinct layers of the LGN and extend to the primary visual cortex in the occipital lobe (Perry et al., 1984; Shapley, 1990).

The M and P pathways are considered functionally distinct (Maunsell et al., 1990). The P pathway mediates fine spatial acuity, colour vision, high spatial frequencies and low temporal frequencies. The pathway terminates in the cortical area known as V4, an area

related to colour vision processing (Livingstone and Hubel, 1988; Merigan and Katz, 1990; Merigan et al., 1991b). The M pathway mediates the detection of low spatial frequencies and high temporal frequencies. The pathway is primarily responsible for motion perception, terminating in the Middle Temporal (MT) visual area of the brain. The area MT is responsible for motion processing (Derrington and Lennie, 1984; Newsome et al., 1985; Schiller, 1986; De Yoe and Van Essen, 1988; Lennie et al., 1990; Chapman et al., 2004).

A third geniculocortical pathway is known to connect the bistratified retinal ganglion cells to the LGN and the visual cortex. The pathway is a secondary mediator of colour vision, specifically blue-yellow opponent mechanisms, and projects to the interlaminar koniocellular layers of the LGN. The pathway has ganglion cell inputs that are predominately in the macula region of the retina (Martin et al., 1997; Szmajda et al., 2008) and is thought to terminate in the supragranular layers of the visual cortex (Livingstone and Hubel, 1988; Dacey and Lee, 1994; Dacey, 1999).

1.4 Risk factors for OAG

Primary risk factors for OAG are elevated IOP, reduced CCT, age greater than 50 years, a positive family history of the disease in a first degree relative and Afro-Caribbean descent (Gordon et al., 2002). Secondary risk factors include migraine headache, peripheral vasospasm. Tertiary risk factors include cardiovascular disease, systemic hypertension and diabetes.

1.4.1 Raised intraocular pressure

Longitudinal studies indicate that raised IOP is an important risk factor for the development of OAG (Sommer et al., 1991a; Tuulonen and Airaksinen, 1991; Quigley et al., 1994a; Gordon et al., 2002; Nemesure et al., 2007; Francis et al., 2008). Individuals with OHT have developed OAG within a follow-up period of 10 years (Tuulonen and Airaksinen, 1991). The prevalence of glaucoma increases as a function of elevated IOP, and the development of OAG is associated with both increased IOP and age (Gordon et al., 2002; Kass et al., 2002; Lee et al., 2003).

1.4.2 Age

There is a greater prevalence of blindness in the elderly population (Faubert, 2002). Although increasing age is acknowledged as a risk factor for OAG (Jonas et al., 2004b), gradual age-related alterations in the physiology and anatomy of the eye will increase an individual's susceptibility to develop OAG (Gordon et al., 2002).

With increasing age, the number of RGCs decreases at an average rate of 4000 fibres per year and diffuse thinning occurs around the ONH (Jonas et al., 1989a; Jonas and Dichtl, 1996; Baleanu et al., 2009; Sung et al., 2009a). RGCs with thinner axons exhibit increased susceptibility to the ageing process (Jonas et al., 1992). It is speculated that the NRR area decreases with increasing age (Garway-Heath et al., 1997); however, some studies find no such relationship between the two variables (Moya et al., 1999; Ramrattan et al., 1999).

The age-related alterations in various non-collagenous components of the LC result in reduced flexibility of laminar tissue. Elastin content in the LC increased when comparing

newborn human tissue to elderly human tissue, whereas total sulphated glycosaminoglycans and lipid content decreased (Albon et al., 2000a; Albon et al., 2000b; Jonas et al., 2004a). Therefore, the LC loses significant flexibility with age. Following the removal of a mechanical pressure source, the elderly LC is less able to regain its original shape. The loss in flexibility of the lamina plates suggests that fluctuations of IOP cause increased stress on RNFL axons at the site of the ONH (Quigley et al., 1991; Albon et al., 2000a; Albon et al., 2000b).

Blood flow to the retrobulbar ONH is reduced with age (Groh et al., 1996). A decrease in retinal and choroidal perfusion occurs at a rate of 8% per decade. The NRR has decreased perfusion at a rate of 8% per decade at the nasal rim and 4% per decade at the temporal rim. These findings are based on Doppler-Flowmeter measurements (Dolman et al., 1980). Reduced perfusion may relate to increased resistance within the vascular bed of the ONH, caused by increased density of capillaries and reduced blood vessel diameter. The vascular changes are thought to relate to altered auto-regulative mechanisms, rather than structural thinning of the RNFL (Pournaras et al., 2004; Boehm et al., 2005).

Alterations in the morphology of the trabecular meshwork occur with age. The pore size of the trabecular meshwork decreases with age, decreasing aqueous outflow and causing a slight increase in IOP over time (Saccà et al., 1998). Raised IOP will subsequently affect tissues that are already more susceptible to injury as a result of the ageing process.

1.4.3 Family history

A positive family history refers to an individual with a first-degree relative with OAG (i.e. a sibling or parent), and indicates a predisposing risk of developing the disease (Leske et

al., 2001; Klein et al., 2004; Coleman and Miglior, 2008). The proportion of individuals with OAG that have a first-degree relative with the condition is approximately one third (Vernon, 1991; Leske et al., 2001), although estimates indicate that up to 60% of individuals have familial OAG (Green et al., 2007). A positive family history increases the risk of developing OAG by three-fold, and family history is considered as significant a risk factor as age (Weih et al., 2001a). As a risk factor, family history may be linked with familial IOP levels (Weih et al., 2001a, b; Klein et al., 2004). The risk associated with a positive family history has been shown to extend to individuals with OHT, where approximately 40% of individuals with OHT have a positive family history of OAG (Zangwill et al., 2004c).

1.4.4 Ethnicity

African-American ethnicity is a risk factor for OAG (Gordon et al., 2002). The reasons for increased risk in this population are unclear although it is postulated that a larger horizontal and vertical cup-to-disc ratio is a contributing factor (Gordon et al., 2002). The Baltimore Eye Survey found that African-Americans have larger ONH areas, larger cup areas and larger cup-to-disc areas than their Caucasian counterparts (Varma et al., 1994). Some authors argue that increased ONH area is a poor risk factor for OAG and for NTG (Quigley et al., 1999). The ONH topography of African-Americans exhibits a deeper maximum cup depth than that of Caucasian-Americans (Girkin et al., 2005). African-Caribbeans in a Canadian urban population showed increased risk factors for development of OAG, including higher levels of IOP and thinner CCT (Fansi et al., 2009). African-Americans have significantly thinner central corneas (521.0 μ m) than Caucasians (550.4 μ m); Japanese individuals have thinner central corneas (531.7 μ m) than Chinese (555.6 μ m), Filipino (550.6) and Hispanic individuals (548.1 μ m) (Aghaian et al., 2004).

Older individuals, individuals with OAG and those suspected to exhibit OAG had thinner central corneas than healthy adults. Individuals with reduced CCT exhibit more progressive visual field loss and increased vertical and horizontal cup-to-disc ratios than those with a CCT in the normal range (Herndon et al., 2004; Kim and Chen, 2004). It is suggested that OAG suspects have a thicker CCT when compared with normal individuals (Brandt et al., 2001). However, in those with OAG, a thicker CCT is associated with less severe field loss (Sullivan-Mee et al., 2006; Lin et al., 2009).

1.5 Clinical aetiology of OAG

The precise aetiology of glaucomatous damage is still unknown (Agarwal et al., 2009; Caprioli and Zeyen, 2009). Clinical and experimental studies have shown that IOP-related damage occurs at the level of the ONH (Radius, 1987; Quigley et al., 1991; Burgoyne et al., 2005; Weber et al., 2008).

1.5.1 Mechanical damage theory

OAG is characterised by mechanical damage to the ONH due to the impact of raised IOP (Radius and Bade, 1981; Quigley et al., 1983). Glaucomatous ONH damage is characterised by ‘cupping’, a pathological increase in the size and depth of the optic cup (Jonas and Budde, 2000; Jonas et al., 2004a). Glaucomatous cupping corresponds with a thinning of the NRR. This thinning is a direct manifestation of nerve fibre loss, which may appear focally or concentrically as the cup size increases (Quigley and Addicks, 1981; Burgoyne et al., 2005). Diffuse patterns of NRR loss are believed to be more common than

focal loss (Emdadi et al., 1998; Garway-Heath and Hitchings, 1998), although patterns of loss become less clear with advancing disease (Jonas and Budde, 2000).

ONH cupping and posterior bowing of the ONH occurs with transient experimental IOP elevation. The early phase of this cupping is reversed when IOP is reduced to normal levels (Pederson and Gaasterland, 1984). Imaging techniques have shown an increase in NRR area following the therapeutic reduction of IOP in OAG and OHT (Tan and Hitchings, 2004). Other imaging studies have shown that the variation in cup floor topography is reduced in OAG, especially in the superior and inferior regions of the floor of the cup (Morgan-Davies et al., 2004). Post-mortem histological studies of the human ONH have revealed a propensity for focal glaucomatous damage at the superior and inferior poles of the ONH (Quigley and Addicks, 1981; Quigley et al., 1982). Neuronal death at the LGN occurs as a result of retrograde degeneration (Yucel et al., 2001; Yucel et al., 2003).

Compression of the LC is associated with morphological alterations of the optic cup. Moderate IOP elevation in primates causes a compression of the laminar sheets and a backward-bowing of the LC (Quigley et al., 1983; Azuara-Blanco et al., 1998). The laminar sheets collapse due to a pressure differential across the LC caused by raised IOP and a gradual decrease in pressure within the LC. At an advanced stage of OAG, there is distension of the LC pores, associated with a loss of supportive connective tissue (Miller and Quigley, 1988). Although a larger ONH may favour a more pronounced bowing of the LC (Jonas et al., 1999), ONH size, itself, is not believed to relate to risk of OAG (Jonas et al., 1991; Caprioli, 1992). The elasticity of the LC is decreased in OAG; however, the physiological process of ageing is also likely to impair LC elasticity (Azuara-Blanco et al., 1998; Morgan-Davies et al., 2004). The rearrangement of the extracellular matrix may

occur due to the migration of astrocytes in response to elevated IOP (Morgan, 2000). In laser-induced primate OAG, posterior to the LC, a partial loss of axonal myelin has been observed together with diffuse axon loss (Radius and Pederson, 1984).

The RNFL is affected by the mechanical pressure of raised IOP (King et al., 2000). Progressive injury to RNFL axons is compounded by impaired axoplasmic transport of neurotrophic factors (Hayreh et al., 1979). Elevated IOP causes extracellular fluid to permeate axonal membranes, creating passive intracellular fluid flow. The increased intracellular fluid levels are thought to dilute the adenosine triphosphate (ATP) concentration and subsequently disrupt axonal transport of neurotrophic factors (Band et al., 2009). Brain-derived neurotrophic factors are required for the development and survival of axons and the interruption induces an inflammatory response that ends in RG C death (Levin and Gordon, 2002).

The mechanical forces exerted by raised IOP are known to impact the autoregulation processes of the retinal vasculature (Robinson et al., 1986). Retinal stretching affects the integrity of the blood retinal barrier and results in leakage of vaso-dilating factors into the retina (Moore et al., 2008; Leske, 2009). A subsequent disruption of autoregulation has been identified due to the impairment of vasoconstriction agents (Buckley et al., 2002). The sensitivity and reactivity of retinal vessels is reduced following transient IOP elevation.

1.5.2 Vascular damage theory

Raised IOP is not the sole cause of glaucomatous damage. Decreased ocular blood flow is known to be an equally important predictor of retinal ganglion cell loss (Satilmis et al.,

2003). Blood flow within the choroid and anterior ONH is supplied by the posterior ciliary vessels. Ocular blood flow is negatively correlated with IOP for individuals with OAG who exhibit moderate to severe glaucomatous damage (Hitchings, 1991). Vascular abnormality is indicated by the increased variance in mean para-papillary blood flow for individuals with OAG when compared with normal individuals (Deokule et al., 2009).

Central retinal vein occlusion, branch retinal vein occlusion and ONH haemorrhage (at the level of the nerve fibre layer) are also associated with OAG (Sonnsjo and Krakau, 1993; Beaumont and Kang, 2002; Fingeret et al., 2005). Haemorrhages at the ONH are considered to be a risk factor for OAG (Jonas and Hayreh, 1999; Soares et al., 2004; Grieshaber et al., 2006) and are associated with progressive visual field loss (Prata et al., 2009). Chronic increase in vascular flow resistance may also impair neural tissue function (Sonnsjo and Krakau, 1993; Garhofer et al., 2004; Riva et al., 2004; Visontai et al., 2005).

Retrobulbar circulation is compromised in OAG (Rankin et al., 1996; Broadway et al., 1999; Liu et al., 1999). Individuals with OHT exhibit a reduced blood supply to the retina (Trew and Smith, 1991; Emre et al., 2004; Pournaras et al., 2004). Blood flow parameters are generally reduced in OAG and OHT (Hafez et al., 2003). The vascular damage theory and its role in the pathophysiology of OAG is supported by the increased prevalence of conditions such as coronary heart disease, systemic hypertension and migraine in individuals with OAG (Fuchsjager-Mayrl et al., 2004).

Vascular impairment is increasingly likely with age (Grodrum et al., 2002). There is an increased prevalence of retrobulbar circulatory abnormalities in the senile sclerotic ONH (Nicolela et al., 1996), and reduced blood flow in the LC and neuroretinal rim (Embleton

et al., 2002). Age-related decline of retrobulbar blood circulation is comparable to the type of retrobulbar circulatory dysfunction that occurs in OAG (Harris et al., 1994; Harris et al., 2000).

1.5.3 Oxidative stress

Neuronal metabolism is dependent upon the regulation of intracellular ion concentrations and the permeability of cellular membranes. When metabolic functions are impaired, there is an increase in intracellular concentrations of cellular oxidants and free radicals (Izzotti et al., 2009). This causes enhanced permeability of cell membranes and is referred to as oxidative stress. Cellular oxidants such as nitric oxide (NO) are known to be produced in response to raised IOP, as a result of the activation of astrocytes (Hernandez, 2000; Morgan, 2000). Increased intracellular concentrations of nitric oxide (NO) can lead to continuous calcium ion (Ca^{2+}) influx, which has a role in initiating a process of cell death called apoptosis (Weinreb and Levin, 1999). Large concentrations of NO ions encourage apoptosis within cultured ganglion cells of the rat (Morgan et al., 1999; Moreno et al., 2004; Sacca and Izzotti, 2008).

Oxidative stress is normally regulated by enzymes that catalyse the conversion of superoxide radicals to hydrogen peroxide. However, this activity is upregulated in neurones that are cultured under hydrostatic pressure (Samdani et al., 1997a; Samdani et al., 1997b). Studies modelling OAG in rat exhibit a significant decline in the antioxidant mechanism following a lengthy period of raised IOP (Moreno et al., 2004). Superoxide radicals also elevate lipofuscin production, the accumulation of which promotes increased oxidative stress and cellular apoptosis (Brunk and Terman, 2002; Ghanem et al., 2010).

Oxidative stress has a role in other mechanisms of damage. As discussed, the ONH is particularly susceptible to an impaired blood supply in OAG (Harris et al., 1994; Embleton et al., 2002; Satilmis et al., 2003). Increased oxidative stress can also result from re-perfusion of blood supply following a period of ischaemia (Osbourne et al., 2004).

1.5.4 Apoptosis in OAG

Cell death in OAG is believed to occur via apoptosis (Quigley et al., 1994b; Garcia-Valenzuela et al., 1995). A comprehensive review of apoptosis is that of Elmore (2007). Apoptosis is a genetically controlled process of cell death which occurs in a number of optic nerve diseases. It is also a physiological process that occurs as part of normal retinal development (Ilshner and Waring, 1992; Jacobson and McCarthy, 2002), in which defective or redundant cells are destroyed to improve tissue function in the mature retina. Individual cells undergo a process of shrinkage before eventually breaking down into vesicles known as apoptic bodies (Nickells, 1999). The components of the dying cell are then absorbed by surrounding cells or macrophages. The entire process occurs without an inflammatory response within the host tissue (Wyllie et al., 1980; Weber et al., 1998; Yucel et al., 2001; Elmore, 2007). This process is considered to involve a stage of cell shrinkage, which is believed to precede eventual cell death (Morgan et al., 2000; Weber et al., 2000; Yucel et al., 2001; Morgan, 2002; Guo et al., 2005).

Although the activation of apoptosis is thought to occur in response to a range of stimuli, neuronal death has been attributed to a loss of neurotrophic support (Oppenheim, 1991) and over-exposure to amino acids such as glutamate (Lipton and Rosenberg, 1994). These factors are known to play a role in the aetiology of OAG (Nickells, 1999). Brain-derived neurotrophic factor is critical for cell survival (Johnson et al., 1986; Levin and Gordon,

2002) and its interruption is known to occur as a result of IOP elevation (Hayreh et al., 1979). The upregulation of glutamate receptors creates a cascade that raises intracellular calcium ions, one of the oxidative free radicals to promote apoptosis (Weinreb and Levin, 1999). Glutamate levels are elevated in the vitreous of individuals with OAG and in monkeys with experimentally induced OAG (Dreyer et al., 1996; Bunting et al., 2009).

In contrast to the process of shrinkage and vesicular disposal that occurs with apoptosis, an alternative mechanism of cell death, called necrosis, involves cytoplasmic swelling and the rapid degradation of cell organelles (Jacobson and McCarthy, 2002). DNA defragmentation occurs and there is eventual disruption of tissue homeostasis, resulting in an immune-response. Necrosis has been linked to acute injury to the ONH (Bien et al., 1999), and is thought to occur when a rapid response to tissue injury is required. Both processes can occur simultaneously within the same tissue. The stimulation of glutamate receptors is known to trigger either an apoptotic or a necrotic response (Vorwerk et al., 1999a). Following experimental damage to the visual cortex of the adult rat, both apoptosis and necrosis have been identified at the level of the LGN (Kalil and Fedynyshyn, 1998) and both processes also occurred following pressure-induced ischaemia of the ONH (Buchi, 1992). In cases of rapid cell death, where apoptotic vesicles cannot be easily disposed by surrounding tissue, some cells will undergo necrosis (Wyllie, 1992). When both types of cell death occur, each appears to follow a different time course, in which neurons that die soon after insult will do so via necrosis and those neurons that die at a later stage will do so by apoptosis (Weber et al., 2000).

1.5.5 Normal tension glaucoma

As was discussed earlier, up to 50% of those suffering from OAG have 'normal' IOP levels, defined as within the range of 11 mmHg to 21 mmHg (Sommer et al., 1991b; Bonomi et al., 1998; Gordon et al., 2002; Kass et al., 2002). The pathophysiology of normal-tension glaucoma (NTG) is likely to differ from the structural alterations associated with elevated IOP (Araie et al., 1994; Duijm et al., 1997; Yamazaki and Drance, 1997; Hayreh, 2001).

NTG has been linked to ischaemic disorders of the vascular system which are thought to be associated with migraine and vasospasm (Phelps and Corbett, 1985; Gasser and Flammer, 1987). Vessel density and diameter is altered at a late stage NTG (Spraul et al., 2002). Disorders of the vascular system may occur independently of IOP as blood flow parameters are equally affected in high tension OAG and NTG (Logan et al., 2004). High tension OAG and NTG exhibit lower blood velocity, blood flow and blood volume parameters when compared with normal individuals (Harris et al., 2000; Sekeroglu et al., 2009). Vascular dysfunction may precede structural damage in individuals with high tension and NTG (Logan et al., 2004) although structural thinning of the RNFL has been identified in association with reduced retrobulbar blood flow velocities for individuals with OAG (Harris et al., 1994; Harris et al., 2000; Januleviciene et al., 2008; Moore et al., 2008).

The significance of ocular haemodynamics and perfusion pressure in OAG has been extensively reviewed (Hayreh, 2001; Leske, 2009). The blood supply to the ONH is proportional to the perfusion pressure, a factor dependent on mean arterial blood pressure (BP) and IOP. BP is comparatively more important than IOP in affecting perfusion

pressure. For IOP alone, a much greater increase would be required to affect ONH blood flow in a healthy individual. Resistance to blood flow is inversely proportional to the rate of flow. An auto-regulatory mechanism increases the resistance when perfusion pressure is low (by increasing vascular tone) to maintain a constant rate of blood flow to the ONH. However in the case of defective autoregulation (where a constant rate of blood flow is not regulated), even IOP values within the normal range (e.g. as with NTG) may reduce blood flow to the ONH by affecting perfusion pressure (Hayreh, 2001; Gherghel et al., 2004).

Defective retrobulbar blood flow velocities have been identified in NTG in the absence of structural alterations to retinal vessels (Plange et al., 2003a; Plange et al., 2003b). Anomalies of retrobulbar blood flow identified in NTG are not found in high tension OAG further indicating that raised IOP is not a prerequisite for vascular dysregulation (Yamazaki and Drance, 1997). Individuals with NTG have slower choroidal haemodynamics when compared with groups with OHT and high tension OAG (Duijm et al., 1997).

Autoregulation is reduced with age in diabetes mellitus, in arterial hypertension, in arterial hypotension, in hypercholesterolemia and with regional endothelial disorders (Hayreh et al., 1986; Hayreh et al., 1991; Haefliger et al., 1994; Hayreh et al., 1994). Vascular dysregulation in both OAG and NTG can be associated with systemic factors (Emre et al., 2004) given that increased systemic vascular resistance is exhibited by individuals with NTG (Harris et al., 1994; Pournaras et al., 2004; Stalmans et al., 2008). Auto-immune disorders have also been postulated as a cause of glaucomatous neuropathy (Wax et al., 1994; Sigal, 1999; Joachim et al., 2009).

Progressive visual field loss in NTG occurs in the absence of elevated IOP (Araie et al., 1994). Individuals with NTG exhibit more visual field loss in the inferior hemi-field than individuals with high tension OAG, suggesting different mechanisms of damage (Zeiter et al., 1992). Patterns of retinal nerve fibre loss (which may or may not correspond to visual field defects) are also known to differ between NTG and high tension OAG (Matsuno et al., 2001; Matsumoto et al., 2003).

Although NTG is believed to follow a mechanism of damage that is distinct from high tension OAG, individuals with NTG exhibit a lower CCT when compared with individuals with either OHT or OAG (Gunvant et al., 2008).

1.5.6 Selective loss theory

Histological and psychophysical studies provide evidence for preferential loss of large diameter RGCs in early stage OAG (Quigley et al., 1987; Glovinsky et al., 1991b; Glovinsky et al., 1993; Anderson and O'Brien, 1997). However, these findings have been challenged (Vickers et al., 1995; Vickers et al., 1997; Morgan et al., 2000; Ansari et al., 2002b).

Histological studies using laser photocoagulation have concluded that magnocellular RGCs may be preferentially damaged in the early stages of glaucoma (Quigley et al., 1987; Quigley et al., 1988; Glovinsky et al., 1991a; Anderson and O'Brien, 1997). At the fovea, preferential damage of larger fibres was shown to correlate with the degree of nerve fibre loss (Glovinsky et al., 1993). At the mid-peripheral retina, selective loss was most apparent at a stage of 50% overall cell loss (Glovinsky et al., 1991a). Magnocellular fibres at the LGN are also preferentially affected in chronic IOP elevation in monkey, but not in

acute IOP elevation (Dandona et al., 1991). A post-mortem analysis of glaucomatous human eyes also found that the larger nerve fibres (thought to be magnocellular fibres) were lost more extensively than smaller nerve fibres (Quigley et al., 1988). Selective magnocellular loss has also been observed at the level of the LGN (Chaturvedi et al., 1993).

One possible explanation for the selective loss theory is that magnocellular cells may encounter early dysfunction due an inherent reduced redundancy, owing to their small populations (Johnson, 1994). It has also been suggested that magnocellular cells are more susceptible to damage due to regional vulnerability at the LC of the ONH (Quigley et al., 1988). The superior and inferior poles of the ONH are generally traversed by larger diameter fibres extending to the peripheral retina, and these areas of the nerve correlate with the first site of glaucomatous damage (Quigley and Addicks, 1981; Quigley et al., 1982). This finding is consistent with the view that a preferential mechanism of loss is more likely to occur amongst peripheral nerve fibres, rather than peri-foveal nerve fibres, since peripheral regions of the retina contain a greater proportion of large-diameter nerve fibres (Quigley et al., 1987; Quigley et al., 1989). Preferential loss of superior ONH axons occurs in the experimental mouse model (Mabuchi et al., 2004). However, given that the LC is absent in the mouse ONH, this may relate to the anatomical position of the central artery and central vein.

The selective loss theory of retinal ganglion cell loss in OAG is contradicted by the distribution of loss across both parvocellular and magnocellular pathways at the level of the retinal ganglion cells, suggesting a non-preferential mechanism of loss in monkey OAG (Morgan et al., 2000). This finding is consistent with histological studies using

cytochrome oxidase biochemistry as a measure of metabolic activity in each pathway, which indicate non-preferential loss at the level of the LGN, (Crawford et al., 2000; Yucel et al., 2000; Yucel et al., 2003), and the visual cortex (Crawford et al., 2001; Harwerth et al., 2002).

Psychophysical investigation of individuals with OAG has involved the comparative assessment of parvocellular and magnocellular function. For example, assessment of the magnocellular pathway is based on its role in motion processing (Newsome et al., 1985; Newsome and Pare, 1988; Merigan et al., 1991a) and the segregation of parvocellular and magnocellular contributions to the area MT (Maunsell et al., 1990). It should be noted that psychophysical testing aimed at a specific pathway may not activate that pathway alone, as the pathways are not always functionally distinct (Logothetis et al., 1990). Resolution acuity for phase-reversed sinusoidal gratings is impaired in individuals with OAG and OHT, than the resolution acuity of stationary gratings, when compared to normal individuals (Anderson and O'Brien, 1997). Given that the stationary gratings are more specific to the parvocellular pathway and that temporally modulated gratings are more sensitive to the magnocellular pathway (Derrington and Lennie, 1984), this finding supports the view that preferential loss of magnocellular pathway occurs for individuals with OAG and OHT.

Psychophysical studies have conflicted with the selective loss theory (Morgan, 1994; Ansari et al., 2002b; McKendrick et al., 2004). Individuals with OAG have reduced sensitivity to both magno- and parvo-orientated stimuli, suggesting that both pathways are equally affected in OAG. Functional deficits of both pathways are also indicated by studies

using automated perimetry and electrophysiology (Graham et al., 1996; Yucel et al., 2003; Harwerth et al., 2004).

Chromatic stimuli are thought to be mediated primarily by the parvocellular pathway (Livingstone and Hubel, 1988), yet studies show that red-green opponent pathways are affected in OAG (Greenstein et al., 1996; Porciatti et al., 1997; Takeuchi et al., 2003), suggesting that both pathways are involved in glaucomatous loss. The koniocellular pathway (Martin et al., 1997) is known to mediate blue-yellow opponent mechanisms (Dacey and Petersen, 1992; Dacey and Lee, 1994), and this pathway is affected in early stages of functional glaucomatous damage (Johnson et al., 1993a, b).

The hypothesis that glaucomatous cell damage is specific to cell size and type is based on histological analysis of cell size distributions (Quigley et al., 1989; Glovinsky et al., 1991a). However, the classification of cell type according to size should be considered in the context of morphological cell changes in OAG. A number of studies have identified ganglion cell shrinkage in the primate model of glaucoma (Weber et al., 1998; Morgan et al., 2000; Yucel et al., 2001; Weber and Harman, 2005). Shrinkage of ganglion cells as part of a postulated mechanism of cell death may account for increased prevalence of small-diameter RGCs in histological studies of OAG (Yablonski and Asamoto, 1993; Morgan, 1994; Morgan et al., 2000; Ansari et al., 2002a; Morgan, 2002). Therefore, an absence of large-diameter RGCs can be misinterpreted as evidence for preferential loss.

1.6 Conventional methods for the detection of OAG

1.6.1 Evaluation of the ONH in OAG

Optic cup size relative to the size of the ONH in terms of NRR thickness is a primary indicator of glaucomatous damage. Increased cup size occurs as the NRR recedes, and is characteristic of individuals with OAG (Pederson and Anderson, 1980; Fingeret et al., 2005). The ONH is usually examined following dilation of the pupil, either by slit lamp biomicroscopy or by digital photography. Stereo-imaging permits a magnified and three-dimensional evaluation of the ONH (Tielsch et al., 1988; Varma et al., 1992; Girkin et al., 2004). The gold standard, however, is digital stereo imaging (DSI). This technique enables a floating cursor in three-dimensional space which facilitates the accurate delineation of Elschmig's Rim and, thereby, the accurate rendition of the planimetric description of the ONH characteristics. DSI exhibits improved sensitivity for the detection of OAG over other imaging techniques (Morgan et al., 2005). The technique can also be adapted to include stereo flicker chronoscopy for the identification of change in the appearance of the ONH over time. Flicker chronoscopy is highly sensitive and highly specific for distinguishing normal individuals from individuals with OAG (Barry et al., 2000; Morgan et al., 2005). The identification of the abnormal ONH is also confounded by normal variations in ONH morphology and, given that between-clinician agreement is an accepted source of variability, the differentiation of subtle abnormalities can be particularly difficult in the early stages of OAG.

1.6.2 Standard Automated perimetry (SAP)

Threshold perimetry determines the differential light threshold at the given locations within the visual field i.e. the minimum stimulus luminance necessary to evoke a 'seen' response by the observer. The output at each stimulus location is expressed as the reciprocal of the threshold in terms of sensitivity.

The current gold standard for visual field assessment is the Humphrey Visual Field Analyzer II (HFA) (Carl Zeiss Meditec, Dublin, CA). The instrument uses a Goldmann III stimulus which has an area of 4mm^2 and subtends a visual angle of 0.471° . The background luminance of the HFA is 10cdm^{-2} and the maximum stimulus luminance is 3183cdm^{-2} . The decibel (dB) is the unit of sensitivity for which 0.1 log units is equal to 1 dB. A high decibel value indicates high sensitivity (Anderson and Patella, 1999).

Threshold perimetry of the central field is usually based on one of two stimulus grids: 24-2 or 30-2, which examine the visual field out to 21° and 27° , respectively. An inter-stimulus separation of 6° is used, with stimuli located 3° on either side of the horizontal and vertical meridians. The inter-stimulus distance allows the instrument to detect a scotoma with a diameter of 8.4° with 100% probability. However, the probability of detection falls to 79% for a scotoma that measures 6° in diameter (Fankhauser and Bebié, 1979). The instrument may fail to detect small glaucomatous defects or the physiological blind spot due to the resolution limit of the technique (Heijl, 1993).

The standard algorithms for estimating threshold are the SITA (Swedish Interactive Threshold Algorithm) Standard and FAST algorithms, which are analogous to the older Full Threshold and FASTPAC algorithms, respectively. The SITA standard algorithm

utilises a 4-dB step size and the SITA Fast algorithm a 4dB step size. The SITA algorithms optimise the thresholding strategy by utilising two likelihood functions for each stimulus location. The likelihood functions are based upon the responses of normal individuals and individuals with OAG (Bengtsson et al., 1998; Wild et al., 1999). As the observer responds to the various stimuli the shape of the response function at each stimulus location will change with increasing numbers of responses (Bengtsson and Heijl, 1998). The threshold estimate is determined from the height of the function at the given location (Wild et al., 1999). Thresholds are adjusted following the end of the examination to reflect all responses given by the observer. Final threshold is based upon a frequency-of-seeing curve at a 50% probability (Bengtsson and Heijl, 1998; Bengtsson et al., 1998).

Sensitivity can be represented in terms of the Total Deviation (TD) and the Pattern Deviation (PD) maps. The TD map exhibits the difference between the measured sensitivity at the given location and the corresponding age-corrected normal value. The PD map is based upon a comparable difference in sensitivity; however, it is corrected for abnormalities in the height of the visual field using the general height adjustment (Asman et al., 2004a) which is defined as the 7th highest positive/ least negative deviation of the 56 locations (15th percentile) corresponding to the Program 24-2 grid (Anderson and Patella, 1999). The TD and the PD probability maps express the respective deviations in terms of probability values relative to the distribution of the deviations in the normal population. The Deviation maps allow the clinician to distinguish generalised visual field loss from localised visual field loss.

Glaucomatous visual field loss typically presents as a paracentral defect and/ or a defect in the nasal extremities of the central field which does not cross the horizontal mid-line

(Werner and Drance, 1977). The field loss increases in depth and then encroaches into the immediate surrounding regions of the visual field, eventually becoming an arcuate and then a hemifield defect. The field loss in one hemifield is usually in advance of that in the other hemifield and the field loss in one eye is usually in advance of that of the other eye (Werner and Drance, 1977).

Given the characteristic appearance of visual field loss in OAG, additional techniques such as the Glaucoma Hemifield Test (GHT) have been developed as an aid to identify visual field loss (Asman and Heijl, 1992). The GHT classifies the likelihood of glaucomatous visual field loss by comparing the number and probability level of the PD map above and below the horizontal midline.

1.7 Digital imaging

1.7.1 Confocal scanning laser topography

Confocal scanning laser ophthalmoscopy obtains a number of high resolution two-dimensional sectioned images of the ONH and its surrounding tissue. These sections are accumulated to form a three-dimensional topographical image of the ONH called the reflectance image which is a pixelated map derived from the reflectance of the features of the ONH and the peripapillary region. Lighter areas represent greater reflectance, e.g. the optic cup, and darker areas indicate least reflectance (Burgoyne, 2004; Girkin et al., 2005; Zangwill et al., 2005). The Heidelberg Retinal Tomograph (HRT III) (Heidelberg Engineering GmbH, Dossenheim, Germany) is the ‘gold standard’ for confocal scanning

laser tomography of the ONH. The HRT has achieved high sensitivity and specificity for the detection of OAG compared with techniques of structural imaging (Bathija et al., 1998; Artes and Chauhan, 2005; Burgansky-Eliash et al., 2007; Mowatt et al., 2008; Moreno-Montanes et al., 2009).

The utility of the technique was initially confounded by the variability in the ONH size and the physiological distribution of the RNFL amongst normal individuals (Kono et al., 1999; Artes and Chauhan, 2005; Burgansky-Eliash et al., 2007). The diagnostic accuracy of scanning laser tomography for OAG is dependent upon ONH size and the stage of OAG. The sensitivity and specificity of HRT is improved with a linear discriminant function known as the Moorfields Regression Analysis (MRA) (Burgansky-Eliash et al., 2007; Hewitt et al., 2009) which utilizes prior knowledge of the NRR and ONH size to statistically normalises these two dimensions (Jonas et al., 1988b; Foster et al., 2002; Ford et al., 2003). The MRA Report illustrates the NRR area relative to the expected range for a normal population (Garway-Heath et al., 2000b; Girkin et al., 2005; Strouthidis et al., 2009) The diagnostic performance is less satisfactory for ONH diameters greater than 3.1mm (Hoesl et al., 2009). Techniques for evaluating progression of the ONH derived by the HRT exhibit only moderate correlation with functional loss measured by SAP (Hudson et al., 2007; Strouthidis et al., 2010).

1.7.2 Optical Coherence Tomography

Optical Coherence Tomography (OCT) measures RNFL thickness by obtaining cross-sectional images of the peripapillary retina, created by analysing the intensity of laser echoes reflected from the retinal tissue (Hougaard et al., 2007; Leite et al., 2010). Optical reflectance creates a resulting profile of tissue depth which is referred to as an A-Scan. The

single cross-sectional A-Scans are gathered linearly across the tissues to form a single cross sectional image, referred to as a B-Scan. The resolution and scan quality of the image is based on the number of A-Scans and the acquisition speed of the instrument. Parallel B Scans are used to create a three-dimensional image of the ONH.

Early OCT technologies were referred to as time domain OCT (TD-OCT) which enabled an in-vivo resolution of 10 μ m (Huang et al., 1991; Fercher et al., 1993). Modern OCT technologies, based upon spectral domain OCT (SD-OCT) are referred to as high speed and/ or high resolution and possess an image acquisition speed which is 60- to 110-times faster than TD-OCT. An axial resolution of 5 to 7 μ m is achieved in the current commercially available devices but up to 2 to 3 μ m has been achieved in the research setting (Park et al., 2009; Mansoori et al., 2010). SD-OCT is able to acquire a B-Scan which contains 2048 A-Scans at an acquisition rate of 55,000 A-Scans per second (Wojtkowski et al., 2005; Wollstein et al., 2005).

The ONH, macular and peripapillary tissue are scanned for measurement of RNFL thickness. The Stratus OCT (Carl Zeiss Meditec, Inc, Dublin, Ca) has shown clinical utility for assessment of macular RNFL defects (Ip et al., 2002; Degenring et al., 2004; Ko et al., 2004). As can be expected, peripapillary RNFL measurements are more sensitive than macular thickness for the detection of OAG (Williams et al., 2002; Greenfield et al., 2003; Guedes et al., 2003; Wollstein et al., 2004; Mori et al., 2010). Measurement of RNFL thickness exhibits good test-retest reliability (Funaki et al., 2002; Budenz et al., 2005; Sehi et al., 2007) and the technique is a more sensitive tool for the detection of OAG when compared with HRT III (Leung et al., 2009).

Good agreement is present between visual field loss and RNFL thickness determined by OCT (Williams et al., 2002; Medeiros et al., 2005; Park et al., 2009). RNFL thickness measurements exhibit good concordance between fellow eyes of individuals with OAG (Bertuzzi et al., 2009). The Stratus OCT, a TD-OCT used in this thesis, also exhibits good agreement between structural and functional deficits in OAG (Budenz et al., 2005; Harwerth et al., 2007; Hougaard et al., 2007). The Stratus OCT software provides normal limits for each of two RNFL scanning protocols. The first is based upon three regular resolution scans (FAST RNFL thickness) and the second is based upon a single high resolution scan (RNFL thickness). Diagnostic sensitivities for the FAST RNFL thickness and RNFL thickness protocols are 72% and 77% respectively, with specificities of $\geq 95\%$ for each protocol or 73% and 81% for the RNFL thickness protocol (Moreno-Montanes et al., 2009). The moderately high sensitivities indicate that there is further room for development of RNFL thickness measurement (Hougaard et al., 2007). OCT scan quality deteriorates in the presence of media opacities (Burgoyne, 2004). The diagnostic power of the Stratus OCT for OAG varies even within the range of scan quality deemed as acceptable by the manufacturer (Sung et al., 2009b). The stage of OAG also influences the diagnostic capability of SD-OCT (Leite et al., 2010).

1.7.3 Scanning laser polarimetry

Scanning laser polarimetry (SLP) measures RNFL thickness by assessing the retardation of polarised light scatter, based on birefringence at the RNFL (Zangwill et al., 2004a). The extent of retardation provides a measure of RNFL thickness (Weinreb et al., 1990). When compared with other imaging techniques, SLP exhibits limited sensitivity in discriminating between normal individuals and individuals with OAG (Zangwill et al., 2001). The GDx VCC (variable corneal compensation; Carl Zeiss Meditec, Dublin, CA) has shown greater

accuracy in discriminating between normal individuals and those with OAG (Greenfield et al., 2002; Weinreb et al., 2003; Reus and Lemij, 2004a; Tannenbaum et al., 2004) and has detected RNFL thinning in OAG in the absence of perimetric field loss (Reus and Lemij, 2004b). The discrimination capability of the GDx VCC for OAG is independent of scan quality within the range recommended as acceptable by the manufacturer i.e. a Quality Score ≥ 8 (Sung et al., 2009b).

Limitations of SLP include atypical birefringence patterns (ABP) in older individuals (Bagga et al., 2005), unreliable imaging of large areas of peripapillary atrophy and limited effectiveness for individuals with nystagmus (Burgoyne, 2004). ABP create artefacts in RNFL images and are thought to be caused by an insufficient signal-to-noise ratio (Bagga et al., 2005). The Enhanced Corneal Compensation (ECC; GDx-ECC, Carl Zeiss Meditec) has been developed to address this issue. Associations between RNFL thickness and visual field loss for individuals with OAG are stronger with the ECC technology when compared with the VCC technology (Bowd et al., 2007).

1.8 Visual Electrophysiology

Unlike automated perimetry, electrophysiology techniques are not dependent on the subjective responses of the individual. The pattern electroretinogram (PERG) (Neoh et al., 1994; Maddess et al., 2000; Bayer and Erb, 2002; North et al., 2009) and multifocal visual evoked potential (mVEP) (Graham et al., 1999; Korth et al., 2000; Punjabi et al., 2008) are two methods that have been used for the detection of OAG.

The visual evoked potential (VEP) measures electrical signals produced in the visual cortex, whilst an individual views a specific stimulus. The stimulus may be a flash or a pattern (Graham et al., 1999; Bach, 2001; Graham et al., 2005). Luminance and wavelength may vary for a flash, whilst size and contrast may vary for a pattern. Foveal activity is largely represented due to cortical magnification factors and the responses of central retinal fibres. A localised stimulus is presented to elicit local responses within the central visual field; a method referred to as Multifocal VEP (mVEP) (Graham et al., 1999; Graham et al., 2005; Punjabi et al., 2008). VEP response amplitudes are reduced in individuals with OAG, when compared with normal individuals (Schmeisser and Smith, 1989; Korth et al., 2000; Hood et al., 2005; Balachandran et al., 2006). For individuals with OAG, studies indicate that mVEP is consistent with measures of SAP (Balachandran et al., 2006), and structural measures of RNFL thickness with the HRT (Punjabi et al., 2008).

The electroretinogram (ERG) is another technique for the assessment of retinal function. The technique provides a record of the summed electrical activity from the various layers of the retina. The response to a patterned stimulus produces the Pattern ERG (PERG). Studies show that PERG responses are altered in individuals with OAG (Wanger and Persson, 1983; Papst et al., 1984; Porciatti and von Berger, 1984; Bowd et al., 2009a), and in OHT (Porciatti et al., 1987; Bach and Speidel-Fiaux, 1989; North et al., 2009). PERG recordings have comparable sensitivity to SAP (Bach, 2001) and other functional methods for the detection of OAG (Graham et al., 1996; Maddess et al., 2000). PERG abnormalities in OAG precede conventional visual field loss (Hood et al., 2005; Ventura et al., 2005). However, in distinguishing normal individuals from individuals with OAG, the sensitivity and specificity of PERG is less than that of SAP (Bowd et al., 2009b). A measurement

paradigm for OAG detection called PERGLA (Lace Elettronica, Pisa, Italy) exhibits sensitivity and specificity values of 76% and 59% respectively, for classifying normal individuals and individuals with OAG. In comparison, SAP exhibits sensitivity and specificity values of 83% and 77%, respectively (Bowd et al., 2009b). Although electrophysiological sensitivity losses have been identified in both OAG and OHT, findings are not always consistent with structural measures of RNFL thickness (North et al., 2009; Sehi et al., 2009).

1.9 New methods of perimetry

SAP stimulates several types of RGCs within the retina. Therefore, the method is likely to have reduced sensitivity to early RGC loss due to considerable overlap in the receptive fields of the different types of RGCs (Delgado et al., 2002). The major classes of RGCs are known to be responsive to different types of stimuli. The parasol cells of the magnocellular pathway are known to play a pivotal role in motion perception, favouring low spatial and high temporal resolution (Ogden, 1984). As is discussed in Sections 1.3.7 and 3.1.3, the midget cells of the parvocellular pathway play a role in colour perception, favouring high spatial and low temporal resolution. Midget cells are far more prevalent than parasol cells, particularly at the central region of the retina (Dacey and Petersen, 1992). Bistratified ganglion cells contribute to the koniocellular pathway and are believed to play a role in short wavelength colour perception in the visual field (Dacey and Lee, 1994).

Novel psychophysical stimuli have been developed to isolate specific RGC populations within the visual pathway (Kelly, 1981a; Heron et al., 1987; Sample et al., 1988; Johnson

and Samuels, 1997). By using the characteristics of magnocellular, parvocellular and koniocellular pathways, a variety of stimuli have been developed in an effort to detect early signs of OAG. The pathway-specific stimuli are designed to preferentially activate each respective cell type. This is contrary to SAP, in which a broad-spectrum stimulus is used to assess visual function. Novel perimetry techniques use chromatic, spatio-temporal stimuli.

1.9.1 Short Wavelength Automated Perimetry

Short-Wavelength Automated Perimetry (SWAP) was developed for assessing the short-wavelength sensitive mechanism that is compromised in several forms of ocular disease including diabetic macular oedema (Hudson et al., 2003) OAG (Wild, 2001; Hudson et al., 2003; Sample et al., 2006b; Boel et al., 2008; Fogagnolo et al., 2008) and some neuro-ophthalmic disorders (Wild, 2001). OAG is associated with deficits in the red-green (Karwatsky et al., 2004) but more so in the blue-yellow spectrum (Drance et al., 1981; Adams et al., 1982; Sample and Weinreb, 1990; Johnson et al., 1993a; Greenstein et al., 1996; Castelo-Branco et al., 2004) i.e. the koniocellular pathway of the visual system (Casagrande et al., 2007). SWAP stimulates the koniocellular pathway generally with a narrow-band blue Goldmann V stimulus (peak sensitivity at 440nm) on a broad-band yellow background with luminance of 100cdm^{-2} . The yellow background adapts the long- and medium-wavelength sensitive pathways and saturates the rod response, so that the stimuli are primarily detected by the short-wavelength receptors (Wild, 2001; Ruppertsberg et al., 2003; Szmajda et al., 2008).

SWAP exhibits higher between-individual variability than SAP, indicating that the reference limits for normality are wider for SWAP than for SAP. Thus, greater deviations

from the normal value at any given location will be required for SWAP than for SAP to indicate abnormality (Wild et al., 1995; Blumenthal et al., 2000). Indeed, the current algorithm for SITA SWAP exhibits wider reference intervals than either SITA Standard or SITA FAST (Bengtsson and Heijl, 2006b; Bengtsson and Heijl, 2006a). The within-test variability i.e. the short-term fluctuation (Wild et al., 1995; Hutchings et al., 2001), and the between-test variability, i.e. the long term fluctuation (Hutchings et al., 2001) are both greater for SWAP than for SAP. The latter indicates that the apparent deterioration in the visual field, between examinations, must be greater for SWAP than for SAP to achieve statistical significance. In addition, SWAP exhibits a profound and residual learning effect for those individuals experienced in SAP. Therefore, apparent field loss from initial examinations may relate to inexperience rather than functional damage and the preliminary results should be interpreted with caution (Wild et al., 2006).

SWAP exhibits an age-related decline which is more pronounced than that of SAP (Wild et al., 1998). The decline can be attributed to a gradual loss of clarity in the media and/ or increasing light scatter arising from cataract (Wild, 2001).

1.9.2 High-pass resolution perimetry

High-pass resolution perimetry (HPRP) is believed to selectively target the parvocellular pathway (Frisen, 1992). The method involves ring-shaped stimuli that are presented on a photopic background at different locations within the visual field (Frisen, 1989; Wall et al., 2004b; Sample et al., 2006b). The stimulus ring has a bright core with a luminance of 25cdm^{-2} and is surrounded by dark borders with a luminance of 15cdm^{-2} . The ring is high-pass filtered to removed low spatial frequency information (Delgado et al., 2002). In a longitudinal study, HPRP detected glaucomatous progression at a median of 12 months

earlier than SAP, in individuals with early to moderate OAG (Chauhan et al., 1999). HPRP exhibits moderate agreement with Frequency Doubling Technology (FDT) and SWAP, for the detection of OAG, however the method is generally less sensitive than FDT (Sample et al., 2006b). The clinical utility of HPRP is limited by the fact that it cannot be standardised across different instruments (Chauhan et al., 1999) and the test is unable to delineate a small scotoma, or the location of the blind spot due to the large angle subtended by the target ring (Birt et al., 1998).

1.9.3 Critical Flicker Frequency

Critical Flicker Frequency (CFF) is a measure of the highest temporal frequency at which a stimulus of fixed contrast is detected as flickering. Flicker perimetry is considered more sensitive than SAP, for the detection of OAG (Lachenmayr et al., 1989; Lachenmayr and Gleissner, 1992) and is considered to be more immune to the effects of image degradation arising from optical defocus and light scatter arising from cataract (Lachenmayr and Gleissner, 1992; Matsumoto et al., 1997; Anderson et al., 2009). CFF is elevated in individuals with OHT and OAG, when compared with normal individuals (Tyler, 1981). It is hypothesised that this elevation is due to a selective loss of RGCs that mediate high temporal frequencies (Holopigian et al., 1990).

1.9.4 Temporal Modulation Perimetry

Temporal Modulation Perimetry (TMP) is a measure of contrast thresholds for grating stimuli, modulated at fixed temporal frequencies. TMP declines with age (Casson et al., 1993; Willis and Anderson, 2000). TMP discriminates individuals with OAG from normal

individuals (Yoshiyama and Johnson, 1997) and is considered to be more effective than SAP (Hot et al., 2008).

1.9.5 Motion perimetry

Motion is a visual function that is mediated by the magnocellular stream (Ogden, 1984). There are a number of methods for assessing motion, several of which use random dot stimuli (Burgess and Barlow, 1983; Wall and Ketoff, 1995; Barton et al., 1996). In this method, an individual is asked to distinguish the coherent motion of a group of dots from the random motion of a background pattern of dots. The measured response of the individual is the motion threshold, which is the minimum percentage of dots correctly judged to be moving in a particular direction against the noisy background (Joffe et al., 1997). MAP stimuli are thought to reduce the presence of cues relating to form and position in the judgement of displacement and direction. Stimulus form and position are likely to elicit responses from parvocellular systems (Nakayama and Tyler, 1981). Individuals with OAG exhibit motion deficits when assessed with random-dot stimuli (Trick et al., 1995; Bosworth et al., 1997; Joffe et al., 1997; Bosworth et al., 1998) and are less able to localise motion stimuli (Silverman et al., 1990; Bullimore et al., 1993; Wall and Ketoff, 1995). However, MAP is moderately sensitive (Silverman et al., 1990; Wall and Ketoff, 1995; Bosworth et al., 1997) and poorly specific (Joffe et al., 1997) for the detection of OAG relative to other novel forms of perimetry (Sample et al., 2000; Delgado et al., 2002; Monhart, 2007). MAP exhibits less between-test variability than SAP (Wall et al., 2009).

1.9.6 Frequency Doubling Technology

FDT is based on the phenomenon of the 'frequency doubling illusion' (Kelly, 1966; Kelly, 1981a). When a grating of low spatial frequency, usually less than 1 cycle per degree, undergoes high temporal counter-phase reversal greater than 15Hz, its perceived spatial frequency appears to double. Visual thresholds can be assessed by increasing the temporal frequency of the flicker, or by maintaining the temporal frequency and reducing the contrast (Spry et al., 2001). The frequency doubling illusion can be detected beyond the limits of conventional flicker thresholds (Kelly, 1966) and is thought to activate a non-linear subset of magnocellular cells called M_y cells (Kelly, 1981a; Maddess and Henry, 1992; Maddess et al., 1998). These cells comprise only 15% - 25% of the M-cell population i.e. only 1.5% - 2.5% of the total RGC population. M_y cells are thought to be responsive to high temporal frequency and low spatial frequency patterns. If the frequency doubling illusion activates a very sparse population of the M-cells, early damage in OAG may be more easily detected due to a reduced redundancy within the M_y system (Johnson, 1994; Alward, 2000).

For threshold measurements with FDT, there is speculation as to whether the observer perceives the spatial structure of the stimulus, or only an amorphous flicker (Hogg and Anderson, 2009). Several studies indicate that no spatial structure is apparent at threshold (Richards and Felton, 1973; Maddess and Henry, 1992), yet others suggest the contrary (Anderson and Johnson, 2002; McKendrick et al., 2003). FDT perimetry requires the observer to respond to any stimulus that flickers or shimmers or contains gratings (Anderson and Johnson, 2003), yet a response to a grating stimulus, as measured with orientation-thresholds, results in a 0.1 log unit threshold difference, when compared with a response to flicker (Quaid et al., 2005). Therefore, thresholds based on 'form' (i.e. the

grating) may be a cause of unexpected threshold elevation in normals (Flood and Flanagan, 1998). Some studies find no difference between orientation thresholds and detection thresholds of frequency-doubled stimuli (Vallam and Metha, 2007; Hogg and Anderson, 2009) and suggest that differences in thresholds may result from inappropriate psychophysical methodology. Detection and orientation-thresholds of frequency-doubled stimuli are considered identical with hard-edged or Gaussian-windowed targets (Hogg and Anderson, 2009).

Individuals with OHT and ‘early-stage’ OAG exhibit reduced contrast sensitivity to the frequency-doubled illusion when compared with normal individuals (Sponsel et al., 1998; Maddess et al., 1999; Cello et al., 2000). FDT shows greater sensitivity and specificity than SAP in differentiating individuals with OAG from normal individuals (Racette et al., 2008) and when compared with other novel methods of perimetry (Sample et al., 2006a; Nomoto et al., 2009). However, the technique is only moderately specific (Medeiros et al., 2004) and the predictive capability of FDT has been questioned (Costa, 2004) particularly in terms of repeatability (Tafreshi et al., 2009).

The underlying rationale for using the frequency-doubled stimulus has been questioned (White et al., 2002). The frequency doubling illusion may be attributed to “a cortical loss of temporal phase discrimination”, rather than functionality of M_y cells. Therefore the rationale for the technology is the subject of continued debate (Hot et al., 2008).

1.10 Time to detection

Substantial RGC loss is known to occur prior to detection with conventional SAP (Quigley et al., 1982; Quigley et al., 1989). Studies indicate a curvilinear relationship between RGC loss and sensitivity loss by SAP. However, sensitivity loss (in terms of dB) for SAP is not present for up to 60% of RGC loss (Harwerth et al., 1999). This finding suggests that there are substantial reserves within the RGC population which can maintain functional sensitivity to broad-spectrum stimuli, despite extensive structural damage (Garway-Heath et al., 2000a; Harwerth et al., 2002). The relationship between structure and function in OAG improves when retinal eccentricity is considered as an input parameter (Harwerth et al., 2004). A structure-function relationship has not yet been proven for early stage OAG. To assess the efficacy of any new detection tool, early OAG is the most important stage of the condition to model (Anderson, 2006).

1.10.1 The relationship between RGC density and visual function

The degree of sensitivity at any given location of the visual field should be proportional to the number of RGCs at the corresponding location for any level of structural damage (Quigley et al., 1989; Kerrigan-Baumrind et al., 2000; Harwerth et al., 2002; Harwerth et al., 2004). In moderate OAG, RNFL thickness is inversely related to sensitivity (Harwerth et al., 2004; Harwerth and Quigley, 2006). This relationship does not hold for early OAG, in which a decline in RNFL thickness precedes sensitivity loss (Sommer et al., 1991a; Bowd et al., 2000; Matsumoto et al., 2003; Wollstein et al., 2005; Bagga et al., 2006). In late-stage OAG, sensitivity loss can occur in the absence of any further reduction in RNFL thickness (Wollstein et al., 2005).

An improved structure-function relationship for SAP is present in the monkey model of OAG (Harwerth et al., 2004; Harwerth et al., 2007). It has been hypothesised that SAP exhibits reduced sensitivity to early RGC loss when compared with structural measures, due to the greater magnitude of the between-individual variability for SAP compared with that for structural measures such as OCT. The coefficient of variation (CV) for TD-OCT is half that derived by SAP, suggesting that OCT is more likely to interpret subtle deficits as outside of the normal distribution of RNFL thickness (Harwerth et al., 2007).

1.10.2 Cell shrinkage hypothesis

Histological studies of the morphology of normal and glaucomatous eyes in the primate model of OAG indicate reductions in both the dendritic field and the cell soma size for both parasol and the midget RGCs (Weber et al., 1998; Weber and Harman, 2005). Further evidence of cell shrinkage exists in both the magnocellular and parvocellular layers of the LGN (Weber et al., 2000; Yucel et al., 2001). Studies involving retrograde labelling of primate RGCs with horseradish peroxidase found similar reductions in cell soma size and concluded that cell shrinkage occurs as an intermediary stage, prior to ganglion cell death, in the primate model of OAG (Morgan et al., 2000; Weber and Harman, 2005).

If 'sick' RGCs undergo cell shrinkage during a cascade of events analogous to apoptosis, they may subsequently be mistaken as part of the remaining midget cell count. Cell counts that are based upon size may erroneously elevate the apparent prevalence of midget cells in the glaucomatous retina, thereby inferring a preferential magnocellular loss (Morgan et al., 2000; Morgan, 2002). The selective loss hypothesis seems less plausible in this regard. In the absence of selective loss of the M-pathway, psychophysical tests that target magnocellular or koniocellular function may prove to be more sensitive for the detection

of OAG due to the reduced redundancy of their relatively sparse cell populations (Johnson, 1994). However, neither a selective loss nor a reduced redundancy is a necessary prerequisite for psychophysical testing of these pathways. Regardless of these hypotheses, a narrow-band stimulus which targets a particular subset of ganglion cells is likely to be a more sensitive detection tool than a broad-spectrum stimulus which activates the majority of retinal ganglion cells.

1.10.3 Neuroprotection

OAG initiates a sequence of RGC degeneration and re-modelling, comparable to physiological processes such as apoptosis. It is unclear whether the apoptotic process can be reversed at an intermediary stage. Improved RGC function has been reported in studies where elevated IOP in OAG was reduced to normal levels (Ventura and Porciatti, 2005). This finding suggests that there may be a window of opportunity for neuroprotective therapies. RGCs cannot be regenerated after cell death, but 'sick' cells may respond to neuroprotective agents.

Agents that are directed to the retina may be able to block apoptotic pathways and prevent cell death (Nickells, 1999; Osborne et al., 1999; Osborne et al., 2004) or reduce the likelihood of secondary degeneration of neurons (Vorwerk et al., 1999b; Hatwick, 2001). One possible method involves the regulation of increased intracellular glutamate levels through the use of glial-derived neurotrophic factors (Naskar et al., 2000; Saragovi et al., 2009). Raised levels of intracellular calcium cause cell death via the activation of several enzymes (Stys and Lesiuk, 1996; Garthwaite et al., 1999). Therefore inhibitors of these enzymes may help to protect ganglion cells. An auto-protective mechanism known to involve gamma-aminobutyric acid (GABA) and adenosine has been reported in studies of

the rat optic nerve. The inhibition of agents that remove either GABA or adenosine, via the use of uptake inhibitors, increase the post-insult survival of axons (Fern et al., 1994; Fern et al., 1995). For the assessment of these agents and their clinical utility, a method is needed for the detection of OAG at a stage of the disease in which the prevailing pathology involves cell shrinkage, rather than cell death.

There is a pressing need to develop a tool that is more effective for the detection of the early stages of glaucomatous damage, both from an imaging perspective and a functional perspective. This thesis is predicated upon the hypothesis that an intermediary stage of RGC dysfunction, which involves RGC shrinkage, may correspond to changes in the levels of internal neural noise and the sampling efficiency of the visual system. Using narrow-band stimuli that are embedded in two-dimensional spatio-temporal noise, this thesis describes the development of a tool to identify a reversible stage of OAG.

2 Introduction to visual noise

2.1 The contrast sensitivity function

The human contrast sensitivity function (CSF) illustrates the sensitivity of the eye to a range of spatial frequencies. The CSF at high spatial frequencies is attenuated by the optics of the eye (Smith and Ratcliff, 2009) and by factors such as pupil size, retinal illuminance and optical defocus (Campbell and Green, 1965; Deely et al., 1991; Radhakrishnan and Pardhan, 2006). The attenuation in the CSF at low spatial frequencies is attributed to the effects of lateral inhibition (Schade, 1956; Rovamo et al., 1993b; Ghosh et al., 2006). The attenuation is dampened (seen as a flattening of the lower end of the CS function) when the number of grating cycles is kept constant and the spatial frequency is reduced (Savoy and McCann, 1975; Kukkonen, 1994). The CSF has been extensively reviewed in the literature (Pardhan, 2004; Smith and Ratcliff, 2009).

2.1.1 Causes of contrast sensitivity reduction

The contrast sensitivity decline with age can be attributed to both neural and optical factors (Pardhan, 2004; Gardiner et al., 2006; Lord, 2006; Falkenberg and Bex, 2007). A linear decline of contrast sensitivity occurs for the medium to high spatial frequencies (Derefeldt et al., 1979; Ross et al., 1985; Pardhan, 2004). Glare reduces contrast sensitivity at the higher spatial frequencies indicating that the attenuation is optical in nature (Paulsson and Sjostrand, 1980; McKendrick et al., 2007), and is influenced by the ageing of the crystalline lens and senile miosis (Wright and Drasdo, 1985; Pardhan et al., 1993). Lenticular opacities can also reduce contrast sensitivity at low spatial frequencies (Elliott et al., 1989; Pesudovs et al., 2004). One study suggests that senile miosis is not a

contributor to the age-related contrast sensitivity loss (Sloane et al., 1988). There is strong evidence of a neural basis for the decline in contrast sensitivity (Thayaparan et al., 2007; Powers, 2009). Neural loss affects the CSF at lower spatial frequencies (Hyvärinen et al., 1983a, b; Falkenberg and Bex, 2007).

Contrast sensitivity is impaired in OAG (Arden and Jacobson, 1978; Anderson and O'Brien, 1997; McKendrick et al., 2004; McKendrick et al., 2007) both at low (McKendrick et al., 2007; Hot et al., 2008) and high spatial frequencies (Chauhan et al., 1999; Ansari et al., 2002a, b). Other conditions such as cortical lesions (Bodis-Wollner, 1972; Bodis-Wollner and Diamond, 1976; Hayes and Merigan, 2007), amblyopia (Hess and Howell, 1977; Hood and Morrison, 2002; Zele et al., 2007) and cataract (Arundale, 1978; Elliott et al., 1989; Datta et al., 2008) also exhibit attenuation of the CSF. In clinical practice, contrast sensitivity is commonly either measured with the Vistech Contrast Sensitivity Test System (Ginsburg, 1984; Pesudovs et al., 2004) or the Pelli-Robson Chart (Powers, 2009). These methods are reviewed by Powers (2009).

The use of temporally modulated sine-wave gratings in contrast sensitivity testing is aimed at stimulating the magnocellular stream of the visual pathway (McKendrick et al., 2003; McKendrick et al., 2004; Medeiros et al., 2004; Anderson, 2006). Temporal contrast sensitivity (TCS) declines with age (Falkenberg and Bex, 2007; Hot et al., 2008) and is abnormal in OAG (Falcao-Reis et al., 1990; Yoshiyama and Johnson, 1997; McKendrick et al., 2007; Hot et al., 2008; Tafreshi et al., 2009).

2.2 The measurement of contrast thresholds

The probability of seeing a grating stimulus can be considered in terms of the psychometric function, given in Figure 2.1. The ordinate describes the relative frequency of 'seen' responses and the abscissa describes the relative intensity or contrast of the presented stimulus. Threshold is defined in terms of the probability that the stimulus is seen (Wetherill and Levitt, 1965) and is usually taken either as the 50% or the 75% probability.

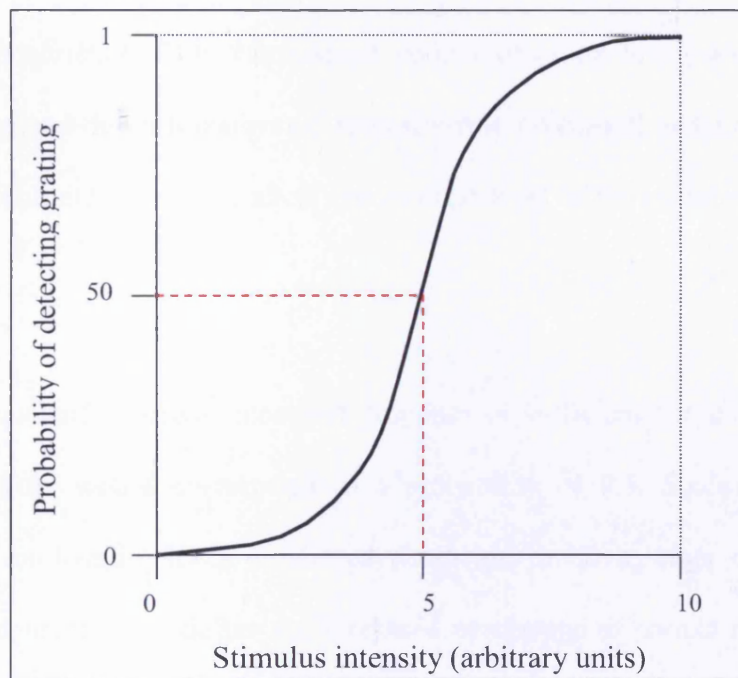


Figure 2.1 A schematic diagram of the psychometric function, which indicates a 0.5 probability of seeing the grating, corresponding to a threshold value of 5 units (indicated by the dotted line).

Experiments for contrast threshold determination often rely upon a two-alternative forced choice method in which an individual must choose between two images to decide which contains the stimulus. Following the decision input, another set of images are presented at a different contrast level. If the individual chooses correctly, the contrast is lowered for the

subsequent presentation and if the individual chooses incorrectly, the contrast is raised. This continuous sequence allows threshold to be determined according to the pre-defined probability designated to the threshold. This is referred to as the up-and-down rule which is based upon a sequential technique for estimating threshold where the final value may be considered to be the average of the contrast levels of the displayed stimuli (Dixon and Mood, 1948). This method was later adapted to the staircase method (Cornsweet, 1962). At infra-threshold levels, the individual is required to guess, at which point a correct response is simply a matter of chance. At this probability level, the individual would continue through much of the threshold determination without seeing the stimulus with any degree of confidence. This can impact upon motivation levels and attentiveness. Therefore, the up-and-down transformed response rule (Wetherill and Levitt, 1965) was developed, in which each response alters the contrast level of the stimulus until threshold is reached.

If a single correct and a single incorrect response is sufficient for this task then the designated threshold would correspond to a probability of 0.5. Since threshold must correspond to a probability level on the psychometric function, other combinations of responses were considered to define the threshold percentage of correct responses. If the number of incorrect responses required to increase contrast remained stable at 1, then the number of correct responses, 'n', required to lower the contrast level defined the probability of seeing the grating x, where $x^n = 0.50$. Threshold within the psychometric function was therefore considered dependent on the value of n such that:

$$x = 0.5^{1/n} \tag{4.2}$$

Where 'x' is the probability of seeing the grating and 'n' is the number of correct responses required to lower the contrast level.

Within the context of a two interval forced choice task, if n was greater than 1, this would ensure that the probability of seeing the grating was not just a matter of chance. Therefore 'n' values of 2 and 3 corresponded to probabilities of 0.71 and 0.79 respectively (Wetherill and Levitt, 1965).

2.3 Mediators of contrast sensitivity

As mentioned in the Section 2.1, contrast sensitivity attenuation in ocular disease can occur both with neural and optical factors which each limit perception (McKendrick et al., 2007; Zele et al., 2007; Datta et al., 2008). The nature of abnormality, whether it is primarily neural or optical, cannot be interpreted from conventional testing of contrast sensitivity. Thus, the detection of subtle disease in conditions such as OAG is often indistinguishable from physiological age-related sensitivity loss (Pardhan et al., 1996; Pelli and Farell, 1999; Pardhan, 2004). This is especially true in the case of increased light scatter arising from cataract, which frequently masks underlying neural dysfunction, and indicates the need for a more complex method of assessing the visual system which would clearly differentiate the optical from the neural component. Such an approach would provide a more robust link between visual function and ocular physiology (Pardhan, 2004; Odom et al., 2006).

Visual sensitivity can be considered as a product of two factors; equivalent noise and sampling efficiency (Legge et al., 1987; Pelli, 1990) which can be measured by assessing contrast sensitivity on a background of visual noise (Pelli and Farell, 1999; Pardhan, 2004; Falkenberg and Bex, 2007). Equivalent noise is a measure of internal neural noise or

random firing of ganglion cells and of optical factors such as increased light scatter due to lens opacity (Kersten et al., 1988; Pardhan et al., 1993; Pardhan, 2004). Sampling efficiency is a measure of neural function at the level of the retinal ganglion cell (RGC) and beyond (Pardhan, 2004; Hayes and Merigan, 2007).

2.3.1 Internal noise

Internal noise describes all physiological activity that occurs in the absence of an external stimulus at any stage of the visual pathway and is characterised by continual random variations in the activity of neurons that carry visual information along the visual pathway (Pelli et al., 2004; Falkenberg and Bex, 2007). Cells that fire spontaneously, without stimulation, generate internal neural noise within the visual system. In the 19th Century it was first described by Gustav Fechner as the ‘Augenschwartz’ of the eye. Seminal work has explored the impact of internal noise on stimulus detection performance (Barlow, 1956, 1957). Although internal noise occurs at any level in the visual pathway, for the purposes of vision research it is often considered to be a single source of noise within the visual system. One example at the retinal level would be the spontaneous reaction of rhodopsin that occurs in the absence of light within the cone photoreceptors (Levi et al., 2005). Therefore, if an external stimulus is to be perceived, its signal energy must be sufficient to evoke a visual response that exceeds the level of internal noise (Pelli, 1990; Pelli and Farell, 1999; Levi et al., 2005).

2.3.2 Sampling efficiency

The second mediator of visual sensitivity is known as sampling efficiency or calculation efficiency. It is based on an observer’s ability to accurately interpret the available signal

information (Legge et al., 1987; Pelli and Farell, 1999; Hayes and Merigan, 2007). Sampling efficiency indicates how a ‘real-life’ observer’s ability to detect a stimulus compares with that of a hypothetical ‘ideal’ observer. In addition to internal noise, detection performance is limited by sub-optimal sampling efficiency (Burgess and Barlow, 1983; Hayes and Merigan, 2007; McAnany and Alexander, 2009). Sub-optimal sampling efficiency is attributed to differences between stimulus and receptive field properties i.e. incomplete spatial or temporal summation or non-optimal decision strategies (Legge et al., 1987; Pardhan et al., 1996; Falkenberg and Bex, 2007). By definition, an ‘ideal’ observer is able to precisely interpret stimulus information and achieve optimal sampling efficiency (Abbey and Eckstein, 2006). It follows that both internal noise and sampling efficiency define the limits of visual sensitivity.

2.4 External visual noise

The measurement of sampling efficiency is carried out in the presence of an externally added visual noise stimulus. This external noise source is not inherent to the stimulus, but is usually superimposed upon the stimulus to eliminate the uncertainty of other parameters (Pelli, 1990; Pardhan, 2004; Odom et al., 2006). External visual noise elevates the detection threshold, compared to the threshold in the absence of noise and is therefore a measurable limit to detection. Such a property is a requirement for accurate measures of equivalent noise and sampling efficiency (Yates et al., 1998; Falkenberg and Bex, 2007).

Contrast thresholds in the presence of externally added noise are therefore limited by two factors; the external and the internal visual noise sources. The extent to which the stimulus

is 'masked' can be investigated by adding external visual noise to the given stimulus. When external visual noise image is used to reduce the visibility of an underlying stimulus, the noise image is referred to as a mask. The addition of external noise is required to estimate the amount of internal noise in the visual system, a measure referred to as equivalent noise (Pelli and Farell, 1999; Pardhan, 2004; McAnany and Alexander, 2009). Therefore, the term equivalent noise is considered analogous to the internal noise of the visual system.

External noise can vary both spatially and temporally. Depending upon the task, two types of noise patterns are generally used. When the stimulus comprises a sine-wave grating, it can be masked by another sine-wave grating that varies from the stimulus in spatial or temporal terms (Jamar and Koenderink, 1985; Matsuura et al., 2008). This noise image effectively masks the underlying stimulus. A more common type of noise mask resembles a checkerboard pattern that varies randomly in terms of luminance, both temporally and spatially (Kukkonen et al., 2002; Rovamo et al., 2003; Hayes and Merigan, 2007). Such a noise mask may vary in one or two spatial dimensions. When produced on a computer monitor, the two dimensional image comprises discrete 'packets' of luminance. These are usually screen pixels that are assigned random luminance levels, from one pixel to the next. An example of static pixel noise that is purely spatial, with no temporal component, is presented in Figure 2.2.

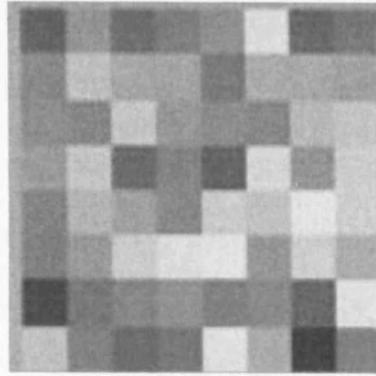


Figure 2.2 An example of a static two-dimensional noise mask. Note that the pixels vary randomly in luminance across the image and that each pixel has a finite size that can be considered to be an individual check.

The external noise image can also be varied temporally such that the luminance of each pixel or check will fluctuate over time and space. This type of noise is referred to as spatio-temporal or dynamic noise (Radhakrishnan and Pardhan, 2006; McAnany and Alexander, 2009).

2.5 Noise Spectral Density

The parameters of a noise mask may be quantified in terms of contrast and check size; or, if the mask is dynamic, in terms of check duration. The contrast of a noise mask is not dependent on the maxima and minima luminance values, as is the case with a sine-wave grating. Therefore, contrast is not expressed in terms of Michelson units (Michelson, 1927) as this does not account for the distribution of luminance over space. When all of the luminance values within a noise mask are distributed randomly around a mean, it is referred to as a Gaussian noise mask, and it is the spread of the values that provide the best estimate of the contrast of the image (Kukkonen et al., 1993; Hayes and Merigan, 2007; McAnany and Alexander, 2009). This latter contrast measure is referred to as the root

mean square (rms) contrast. The squares of each of the local contrasts are averaged across the area of the stimulus thereby accounting for its relative size. The square-root of the average contrast provides the rms contrast of the mask (Kukkonen, 1994). The strength of an external noise mask is referred to as the noise spectral density. The spectral density of two-dimensional pixel noise (N_e) is the product of the noise check area (A) and the root mean square contrast of the noise (C_{rms}) squared.

$$N_e = A \times C_{rms}^2 \quad (2.1)$$

Therefore, the strength of a static noise mask is altered by varying the pixel size, the contrast of the noise, or both (Kukkonen, 1994). As was previously stated, the check luminance of a spatio-temporal mask varies over space and time. This latter element, the duration of the noise check, is the length of time that an individual noise check remains at a particular luminance level. The spectral density of dynamic noise is defined as:

$$N_e = A \times C_{rms}^2 \times t_{check} \quad (2.2)$$

Where A is the area of the noise check, C_{rms} is the root mean square contrast of the noise image and t_{check} is the duration of noise check luminance.

Increasing any one of these variables will increase the theoretical noise spectral density and, hence, the strength of the noise mask (Kukkonen et al., 1999; Kukkonen et al., 2002).

In practical terms, there are limits to the application of an external noise mask. The parameters that define noise spectral density may only be increased up to a point, beyond which the mask becomes ineffective at reducing the visibility of an underlying stimulus; e.g., if the noise check size becomes too large, the stimulus will become more visible through each noise check. The same is true if check duration lasts too long. An external noise image has a limited bandwidth within which it can effectively mask a particular stimulus. The bandwidth of the noise mask is defined by the spatial and temporal parameters of the signal (Kukkonen, 1994; Rovamo et al., 2000; Rovamo et al., 2003). Increasing check size or duration in an effort to strengthen the mask has the practical consequence of reducing the bandwidth of the mask. An external noise mask that is capable of masking all the spatial and temporal frequencies of a stimulus is referred to as 'white' noise. White noise has a constant spectral density that describes its masking power. For the purposes of psychophysical research, an external noise mask is only described as 'white' when it falls within the same frequency range as the stimulus (Rovamo et al., 1992; Kukkonen, 1994; Kukkonen et al., 2002). Once the stimulus is known, the spatial and temporal parameters of the external noise mask may be experimentally determined to ensure two outcomes. Firstly, that the external noise mask is the limiting factor in determining signal detection threshold and therefore can be considered as 'white'. Secondly, with optimal spatial and temporal masking parameters, there is efficient use of the dynamic contrast range of a computer monitor.

Optimal mask parameters are determined by measuring signal detection thresholds in the presence of various noise masks. Evaluating the response function of the detection threshold against noise check size determines the optimal spatial parameter and evaluating against check durations will determine the optimal temporal parameter. Increasing both

spatial and temporal parameters, independently, will initially cause the detection threshold to rise and the practical noise power to increase, up to a critical point. At this critical point, the threshold reaches a maximum, beyond which, increasing either the check size or the check duration causes the threshold to fall (Nasanen et al., 1993; Kukkonen et al., 1995; Kukkonen et al., 2002). Even though the theoretical noise spectral density increases infinitely with check size and duration, the bandwidth of the external noise will no longer encompass the parameters of the stimulus and, henceforth, the stimulus becomes easier to see. The individual check size is too large and the underlying stimulus is visible within each check, creating a phenomenon known as the 'window effect' (Harmon and Julesz, 1973). Furthermore, when the check duration is too long, the check luminance stays constant for long enough to allow the stimulus to be sampled more easily, i.e. it becomes more visible (Kukkonen et al., 2002).

The rms contrast of Gaussian noise is the only parameter that will increase the effectiveness of the noise mask. However, for a computer generated noise mask, rms contrast is limited by the capabilities of the monitor and the graphics card. Given that the stimulus is shown in the presence of the external noise, the combination of stimulus and mask must utilise a limited range of grey levels, depending on the bit value of the hardware (Pelli and Zhang, 1991; Colombo and Derrington, 2001). In signal detection tasks, there is often a limited contrast range available for the noise mask. This provides further incentive for spatial and temporal noise parameters to be optimised, so that the resultant noise mask will require less rms contrast for it to be effective (Nasanen et al., 1993; Kukkonen, 1994; Kukkonen et al., 1995; Kukkonen et al., 2002).

2.5.1 The signal to noise ratio

The signal to noise ratio (SNR) (Nagaraja, 1964; Pelli, 1990; Odom et al., 2006) is a constant defined by the ratio of stimulus energy at threshold to noise spectral density. When a stimulus is embedded in an external noise mask, the energy required to see the stimulus at threshold increases in direct proportion to the noise spectral density (Pardhan, 2004; Pelli et al., 2004; McAnany and Alexander, 2009). A constant SNR is a requirement for estimating equivalent noise and sampling efficiency. When the SNR is constant, the external noise image is considered 'white'. Although the contrast of the noise mask can be increased, the extent of the increment is limited by the dynamic range of the monitor, especially when assessing the contrast thresholds of individuals with ocular disease. When the critical spatial and temporal parameters of a dynamic noise mask are exceeded, the signal will become increasingly visible, causing the SNR to fall.

Critical check size is measured in terms of checks per grating cycle, and as has been described in this Section, critical check size is influenced by the temporal and spatial parameters of the underlying stimulus. For low to medium spatial frequency gratings i.e. 1 to 4 cycles per degree, the critical check size is 4.2 checks per cycle (Kukkonen et al., 1995). However, for sine wave gratings of 64 cycles per degree, the critical check size falls to 2.6 checks per cycle. These findings indicate that critical check size is inversely related to the spatial parameters of the grating. Critical check duration, in terms of noise frames per flicker cycle, decreases with increasing flicker frequency from 8.3 at a flicker frequency of 1.25 Hz, to 1.6 at a flicker frequency of 20Hz (Kukkonen et al., 2002). Therefore, it can be inferred that critical check duration is inversely related to the temporal flicker frequency of the grating. The influence of temporally drifting gratings on the critical parameters of a noise mask has yet to be investigated.

2.6 The equivalent input noise technique

Measures of internal noise and sampling efficiency have been obtained by adopting proven psychophysical methods. The method is collectively referred to as the equivalent input noise technique and is described in seminal papers (Barlow, 1957; Mumford and Schelbe, 1968; Pelli, 1981; Burgess and Colborne, 1988) and is commonly used in studies of visual function (Pardhan, 2004; Falkenberg and Bex, 2007; Hayes and Merigan, 2007; McAnany and Alexander, 2009). To measure the noise within an amplifier, which can be considered analogous to the visual system, a series of calibrated noise levels are introduced at the input, whilst measuring the output noise level (Legge et al., 1987; Pelli, 1990). The output is a combination of the input (external) and the internal noise. The output noise versus the input noise describes the properties of the amplifier. The result is illustrated schematically in Figure 2.3.

In the example illustrated in Figure 2.3, at low levels of input or external noise, the internal noise of the amplifier dominates the output; hence the curve is initially flat. Throughout this stage, the external noise strength is insignificant compared to the internal noise of the system. Eventually, the external noise source exceeds the internal noise of the amplifier, after which, the output noise level rises to a sampling efficiency of 100%, suggesting a slope of 1. A ‘real-life’ observer always exhibits a sub-optimal sampling efficiency, indicating a slope steeper than 1. As the slope steepens, the sampling efficiency declines. Sampling efficiency, therefore, measures how well the ‘real-life’ observer interprets the stimulus with increasing noise (Simpson et al., 2003a; Simpson et al., 2003b; Karwatsy et al., 2006).

The equivalent noise input technique has been applied to the measurement of visual thresholds (Pelli et al., 2004; Odom et al., 2006; Hayes and Merigan, 2007). Stimulus contrast detection thresholds are measured in the presence of external noise to determine the equivalent noise and the sampling efficiency. The external noise level is plotted against the contrast energy threshold for the detection of an underlying stimulus. An example of the stimulus is a sine wave grating, shown in Figure 2.4. The paradigm is based upon the assumption that a single external noise source will dominate all internal noise i.e. the noise is considered to be 'white' and to be within its critical spatial and temporal limits. In the equivalent noise input technique, the strength of external noise is deliberately increased until it exceeds the amount of internal noise, thereby becoming the limiting factor in determining threshold.

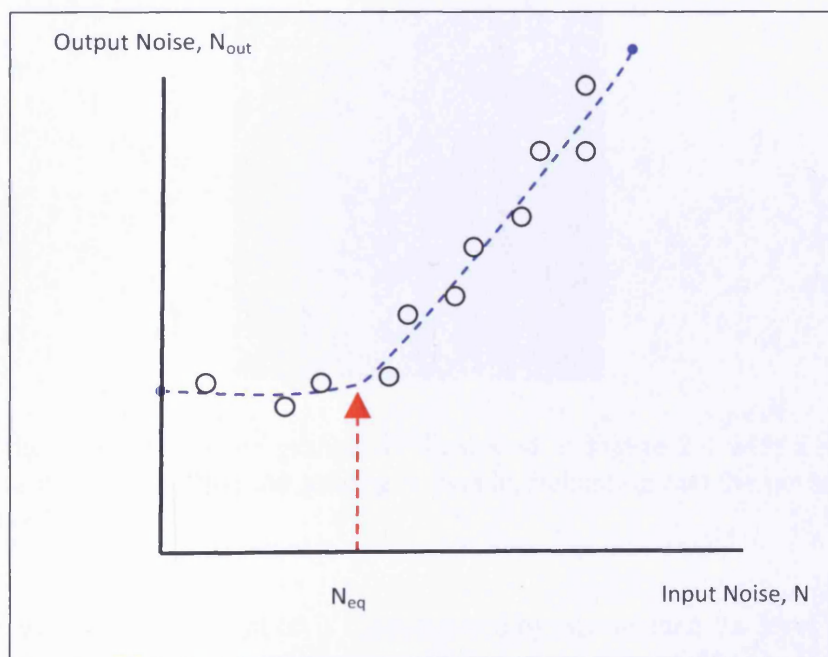


Figure 2.3 The properties of an amplifier, based upon the seminal methods of Mumford & Schelbe (1968). The output noise (N_{out}) is measured for a variety of levels of input noise (N_{eq}). The output follows a characteristic profile that can be used to evaluate the internal noise of the amplifier.

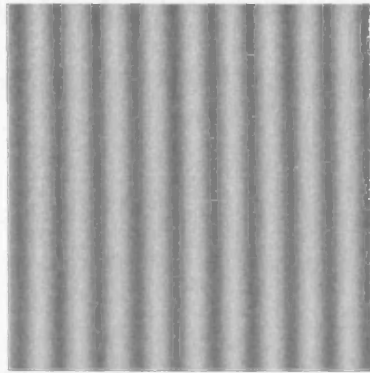


Figure 2.4 An example of a stimulus, a sine wave grating, that can be used within the equivalent input noise technique.

The visibility of the sine wave grating is reduced in the presence of the external noise mask. An example of the sine-wave grating in the presence of a noise mask is shown in Figure 2.5.

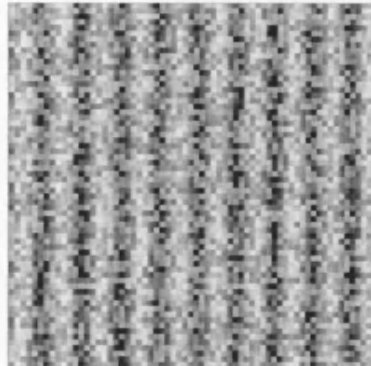


Figure 2.5 The same sine-wave grating as illustrated in Figure 2.4 with a superimposed external noise mask. Note that the grating is visible, indicating that the grating contrast is above threshold.

In summary, detection performance is characterised by two factors: the level of equivalent noise and the sampling efficiency with which the stimulus information is gathered and interpreted. It is important to note that the equivalent noise technique is dependent upon several assumptions:

1. The output noise (N_{out}) is proportional to the sum of the external (N) and equivalent noise (N_{eq}), where k is a constant.

$$N_{out} = k (N + N_{eq}) \quad (1.3)$$

2. The level of detection performance increases with the increase in contrast of the stimulus.
3. The equivalent noise level is considered to be contrast invariant such that it remains independent of the stimulus contrast.

Specifically, equivalent noise is assumed to be independent of external noise and stimulus contrast, thereby allowing the measurement of equivalent noise with two threshold measures at different levels of externally added noise (Pelli, 1990; Pelli and Farell, 1999; Odom et al., 2006). The advantage of the technique is in its ability to determine the basis for contrast sensitivity loss in ocular disease, which may be due to reduced sampling efficiency or elevated internal noise (Pardhan et al., 1993; Pelli and Farell, 1999; Pardhan, 2004). Knowing the underlying cause of sensitivity loss may, in turn, help to develop new detection techniques that show better sensitivity to ocular disease than conventional technologies.

2.7 Clinical studies of sampling efficiency and internal noise

The equivalent noise technique has been used to assess visual function in amblyopia (Levi and Klein, 2003; Pelli et al., 2004; Huang et al., 2007), cataract (Pardhan et al., 1993; Pardhan et al., 1996; Bennett et al., 1999) and OAG (Yates et al., 1998; Odom et al., 2006; Falkenberg and Bex, 2007).

Sampling efficiency is substantially reduced in amblyopia (Levi and Klein, 2003; Pelli et al., 2004) and equivalent noise is elevated when compared with normal controls (Levi and Klein, 2003; Pelli et al., 2004). Elevated noise levels have been attributed to optical, rather than to neural factors, as indicated by contrast sensitivity decline in cataract, when compared with age-matched normal individuals (Pardhan et al., 1993). These findings are consistent with investigations of optical defocus (Radhakrishnan and Pardhan, 2006) and studies of age-related contrast sensitivity decline (Bennett et al., 1999; Pardhan, 2004; Betts et al., 2007). However, the effect of ageing on equivalent noise levels remains unclear. Equivalent noise levels that were elevated with age have been attributed to neural as well as to optical sources (Betts et al., 2007). Ganglion cell noise is considered to be a neural contributor to the age-related decline in visual function (Pardhan, 2004). Although several studies indicate that equivalent noise levels increase with age (Bennett et al., 1999; Pardhan, 2004; Betts et al., 2007; Falkenberg and Bex, 2007), other studies have suggested that noise levels remain unchanged (Pardhan et al., 1996; Bennett et al., 1999). A neural component of contrast sensitivity loss may explain the decline of sampling efficiency with age (Bennett et al., 1999; Betts et al., 2007; Falkenberg and Bex, 2007).

Externally added noise has been used for the detection of OAG (Yates et al., 1998; Odom et al., 2006; Falkenberg and Bex, 2007). A study using radial optic flow stimuli indicates

that sampling efficiency was reduced in individuals with OAG when compared with age-matched individuals (Falkenberg and Bex, 2007). This finding was attributed to RGC loss across the visual field. However, equivalent noise levels were comparable with age-matched individuals suggesting that RGC activity is not elevated in OAG. The study also developed a model of complex motion processing using moderate spatial frequency sine wave gratings. A direction selective task resulted in reduced detection performance when motion inputs were deleted to simulate ganglion cell loss.

An external noise mask was superimposed on low spatial frequency sine wave gratings, and modulated at counter-phase flicker to assess contrast sensitivity in individuals with OAG patients and age-matched individuals (Yates et al., 1998). The mask exacerbated the difference in contrast threshold between the two groups compared with non-masked thresholds. This finding also suggests that sampling efficiency is impaired in OAG when compared to normal individuals. However, equivalent noise measures were not undertaken. Contrast thresholds for high contrast dot and short line segment stimuli have been measured in OAG and in normal individuals (Odom et al., 2006). An externally added noise mask did not help to differentiate between the two groups.

The existing studies of equivalent noise and sampling efficiency in OAG lack consistency in their findings for several reasons. The stage of OAG was either considered 'relatively advanced' (Falkenberg and Bex, 2007) or 'early' (Yates et al., 1998), or the pathophysiology of disease may have varied due to the inclusion of secondary glaucomas (Odom et al., 2006).

Measures of equivalent noise and sampling efficiency may provide new insights into OAG by characterising a phase of the disease which involves ganglion cell shrinkage (Morgan, 2002; Gupta and Yücel, 2007). The advantage of this method is based on the hypothesis that ganglion cell shrinkage precedes cell death. Therefore the stage of the disease may be amenable to neuroprotective therapies. The success of the equivalent noise technique, in identifying OAG at the 'shrinkage' stage of the disease will be dependent on the choice of stimulus used within the thresholding task and the use of an external noise mask that is optimally tuned to the underlying stimulus.

Given the role of the magnocellular pathway in the processing of motion (Lund et al., 1976; Maunsell and Van Essen, 1983; Mikami et al., 1986; Newsome et al., 1989; Maunsell et al., 1990; Born and Tootell, 1992; Tootell et al., 1995) and given the apparent damage to the magnocellular pathway in OAG (Quigley et al., 1988; Dandona et al., 1991; Glovinsky et al., 1991a; Chaturvedi et al., 1993; Glovinsky et al., 1993), a drifting low frequency grating may provide the most valuable insight into early glaucomatous damage. The parameters of a noise mask must be optimised prior to any clinical investigation for two main reasons. Firstly, the noise must be considered to be 'white' in the vicinity of the underlying stimulus so that it is the dominant source that limits threshold (Rovamo and Kukkonen, 1996; Kukkonen et al., 2002). Secondly, to ensure that the external noise mask is added to a grating stimulus, without exceeding the dynamic range of a computer monitor.

3 Rationale and summary of thesis

The work described in this thesis is a continuation of studies undertaken within the Clinical and Investigative Vision Sciences Group, Cardiff University, led by Professor John Wild. The project aimed to build upon, and bring together, two areas of study. Firstly, the psychophysical investigation of spatial and temporal visual processing and the use of visual noise stimuli (Kukkonen et al., 1999; Rovamo et al., 1999; Rovamo et al., 2001; Rovamo et al., 2003). Secondly, the development and refinement of novel methods for visual field examination (Asman et al., 2004b; Wild et al., 2006) and the relationship between structure and function in OAG (Morgan et al., 2005; Wild et al., 2005; Hudson et al., 2007).

3.1 The early detection of OAG

For the prevention of irreversible visual loss in OAG, there is a pressing need for the development of more sensitive and specific measures of structure and function which are able to identify the disease at the earliest possible stage.

3.1.1 Structural measures of OAG

The theoretical in vivo maximal resolution of current technologies for structural imaging is approximately $2\mu\text{m}$ (Wojtkowski et al., 2005). The parasol ganglion cells of the RNFL have an estimated mean axonal diameter of $1.97\mu\text{m}$ and the midsize ganglion cells have an estimated mean axonal diameter of $0.91\mu\text{m}$ (Watanabe and Rodieck, 1989; Peterson and Dacey, 1998; Weber et al., 2000; Weber et al., 2008), structural techniques may never

achieve the level of resolution necessary to detect, *in vivo*, the onset of cell shrinkage, a process which precedes retinal ganglion cell (RGC) death in OAG (Weber et al., 2000; Morgan, 2002; Gupta and Yücel, 2007). The intermediary stage of cell shrinkage may be amenable to neuroprotective therapies that can halt or reverse the process of cell death (Nickells, 1999; Osborne et al., 2004; Weber et al., 2008).

3.1.2 Functional measures of OAG

It is hypothesised that measures of visual function can be developed which detect *in vivo* cell shrinkage in OAG prior to cell death. The efficacy of current technologies that measure visual function is limited by several factors. Conventional measures such as standard automated perimetry (SAP) detect OAG only when up to 60% of retinal ganglion cells are irreversibly damaged (Quigley et al., 1982; Quigley et al., 1989; Harwerth et al., 1999; Kerrigan-Baumrind et al., 2000).

3.1.3 The use of pathway-specific stimuli

Although novel methods of perimetry, such as Frequency Doubling Technology Perimetry (FDT) and Short Wavelength Automated Perimetry (SWAP), are designed to be more sensitive than SAP to glaucomatous damage, they are limited by concerns such as specificity (Costa, 2004; Tafreshi et al., 2009), inter- and intra-test variability (Wild et al., 1995; Blumenthal et al., 2000; Boel et al., 2008) and the impact of age-related changes in the crystalline lens (Swanson et al., 2005; Anderson et al., 2009). FDT (Nomoto et al., 2009; Tafreshi et al., 2009) and Motion Automated Perimetry (MAP) (Wall et al., 1997; Delgado et al., 2002; Wall et al., 2009) have shown comparably better sensitivity for the

detection of OAG when compared with SAP, whilst specificity tends to be less favourable (Nomoto et al., 2009; Tafreshi et al., 2009).

Both FDT and MAP use stimuli that are thought to be mediated by the magnocellular stream of the visual pathway, due to its preference for achromatic, low spatial and high temporal resolution stimuli (Ogden, 1984; Callaway, 2005). In this way, the responses of other major processing streams are minimised. The parvocellular stream is only responsive to chromatic, high spatial and low temporal resolution stimuli (Maunsell et al., 1990; Callaway, 2005) and, the koniocellular stream, is a mediator of blue-yellow opponent mechanisms and is sensitive to short-wavelength stimuli (Dacey, 1999; Casagrande et al., 2007; Szmajda et al., 2008). These major streams can be targeted by pathway-specific stimuli in other novel methods of perimetry. The parvocellular stream is stimulated by high-pass resolution perimetry (Chauhan et al., 1999; Westcott et al., 2002; Wall et al., 2004a) and the koniocellular stream is stimulated by short-wavelength automated perimetry (Fogagnolo et al., 2008; Nomoto et al., 2009). It is postulated that more sensitive measures of visual function require the use of narrow-band stimuli that are specific to individual streams within the visual pathway.

The magnocellular pathway is thought to be selectively damaged in early OAG. Two possible explanations have been proposed. Firstly, the magnocellular pathway may suffer preferential loss in early OAG due to the increased susceptibility of the large diameter parasol ganglion cell axons (Quigley et al., 1987; Quigley et al., 1988; Glovinsky et al., 1991a). The large diameter cell axons are thought to traverse the LC of the ONH at a location that is particularly susceptible to mechanical damage resulting from IOP levels (Quigley and Addicks, 1981; Quigley et al., 1982; Quigley et al., 1988). Secondly, the

parasol cells of the magnocellular pathway comprise only 10% of the total population of retinal ganglion cells (Perry et al., 1984) suggesting a selective impairment of these cells, on the basis of reduced redundancy (Johnson, 1994), i.e. if all ganglion cells are affected by OAG, the magnocellular pathway will suffer a greater level of damage, in proportionate terms, owing to its smaller population of ganglion cells.

The mechanism for damage in OAG has been summarised in Chapter 1. There is ample evidence that the magnocellular and parvocellular pathways are equally affected in early OAG (Ansari et al., 2002b; McKendrick et al., 2004; Sample et al., 2006b; McKendrick et al., 2007). Such a finding refutes the preferential loss theory but is consistent with the reduced redundancy theory.

3.2 The development of psychophysical stimuli

The psychophysical investigation of visual processing is based upon the seminal role of sinusoidal grating stimuli, also known as sine wave gratings, for determining spatial contrast sensitivity (Campbell and Green, 1965). Human contrast sensitivity as a function of sine wave grating spatial frequency is characterised by the spatial contrast sensitivity function (CSF), a bell-shaped curve which peaks between 1 and 3 cycles per degree, depending upon the stimulus parameters (Arden, 1978). The CSF is attenuated at higher spatial frequencies by optical factors such as pupil size, retinal illuminance and optical defocus (Campbell and Green, 1965; Deely et al., 1991). The CSF is attenuated at lower spatial frequencies due to the effects of lateral inhibition (Schade, 1956; Rovamo et al.,

1993b). This topic has been reviewed in detail (Smith and Ratcliff, 2009) and has also been summarised in Chapter 2.

3.2.1 Spatial contrast sensitivity

As was discussed in Section 1 of Chapter 2, contrast sensitivity declines with age (Pardhan, 2004; Gardiner et al., 2006; Lord, 2006; Falkenberg and Bex, 2007). A linear decline occurs for medium to high spatial frequencies (Derefeldt et al., 1979; Ross et al., 1985; Pardhan, 2004). The low spatial frequencies are comparatively unaffected. These findings suggest that optical factors, such as ageing of the crystalline lens and senile miosis, are the primary causes of the age-related decline in spatial contrast sensitivity (Wright and Drasdo, 1985; Pardhan et al., 1993). However, there is also evidence of a neural basis for the contrast sensitivity decline with increasing age (Thayaparan et al., 2007; Powers, 2009). A detailed review is that of Powers (2009).

Contrast sensitivity is impaired for a range of ocular diseases, such as OAG (Arden and Jacobson, 1978; Anderson and O'Brien, 1997; McKendrick et al., 2007) and disorders such as amblyopia (Hess and Howell, 1977; Hood and Morrison, 2002; Zele et al., 2007) and cataract (Arundale, 1978; Elliott et al., 1989; Datta et al., 2008). Other conditions, such as cortical lesions, also result in contrast sensitivity loss (Bodis-Wollner, 1972; Bodis-Wollner and Diamond, 1976; Hayes and Merigan, 2007). Contrast sensitivity is commonly measured in clinical practice with the use of the Vistech Contrast Sensitivity Test System (Ginsburg, 1984; Pesudovs et al., 2004) the Pelli-Robson Chart (Elliott et al., 2007) and the CSV-1000 charts (Hiraoka et al., 2007). A review of current methods is that of Powers (2009).

3.2.2 Temporal contrast sensitivity (TCS)

Innovation in computer processing has increased the number of contrast sensitivity tests that utilise temporally modulated sine wave gratings. These tests measure temporal contrast sensitivity, a function which also declines with increasing age (Falkenberg and Bex, 2007; Hot et al., 2008) and which is impaired in OAG (Falcao-Reis et al., 1990; Yoshiyama and Johnson, 1997; McKendrick et al., 2007; Hot et al., 2008). FDT relies on TCS loss in OAG by using temporally modulated grating stimuli (Delgado et al., 2002; Sample et al., 2006b; Racette et al., 2008; Tafreshi et al., 2009).

3.3 A novel approach to temporal contrast sensitivity testing

The contrast sensitivity decline in ocular disease is due to both neural and optical sources that limit visual perception to stimuli (McKendrick et al., 2007; Zele et al., 2007; Datta et al., 2008). The nature of decline, whether it is primarily neural or optical, cannot be interpreted from conventional contrast sensitivity tests, alone, and therefore the detection of subtle disease in OAG is often indistinguishable from physiological age-related decline (Pardhan et al., 1996; Pelli and Farell, 1999; Pardhan, 2004). Therefore, the separation of optical and neural components is clinically desirable in age-related conditions such as glaucoma, where physiological changes of the crystalline lens can mask subtle underlying neural deficits.

3.3.1 Internal noise

Contrast sensitivity can be described in terms of its inverse which is known as threshold. This is the minimum contrast energy at which a stimulus can be detected. Visual thresholds are limited by a phenomenon seminally known as internal noise (N_i) (Barlow, 1956, 1957). The N_i of the visual system describes all physiological activity that occurs in the absence of an external stimulus, at any stage of the visual pathway. It was described in the 19th Century by Fechner as the response of the visual system to complete darkness (De Vries, 1943). Threshold is the minimal signal energy required to evoke a visual response in the presence of N_i . Therefore, elevated levels of N_i will result in relatively higher contrast thresholds.

3.3.2 Sampling efficiency

A second mediator of visual sensitivity is based upon an observer's ability to accurately interpret the available stimulus information. This factor is known as sampling efficiency (SE) (Legge et al., 1987; Pelli and Farell, 1999; Hayes and Merigan, 2007). SE is a measure of the observer's ability to detect a stimulus compared to that of a hypothetical 'ideal'. Therefore, reduced sampling efficiencies will result in relatively higher contrast thresholds (Legge et al., 1987; Pardhan et al., 1996; Falkenberg and Bex, 2007).

3.3.3 The equivalent noise paradigm

The measurement of N_i and SE is based upon a psychophysical technique known as the equivalent noise paradigm. It is described extensively within the literature (Legge et al., 1987; Pelli and Farell, 1999; Pardhan, 2004; McAnany and Alexander, 2009). The technique is based upon a detection task for determining contrast sensitivity for a given

stimulus. Temporally modulated sine wave gratings are commonly used (Karwatsy et al., 2006; McAnany and Alexander, 2009).

To estimate N_i and SE, an external source of noise is introduced within the contrast detection task. This external noise source, known as visual noise, can be a pixelated image made up of a series of square checks and characterised by random fluctuations in luminance over space and time (Radhakrishnan and Pardhan, 2006). The visibility of a sine wave grating is reduced when it is displayed in the presence of visual noise. If the noise image obscures the grating entirely, the grating is said to be masked by the external noise image.

Threshold is elevated in the presence of a noise mask as the grating is more difficult to detect. N_i , referred to as the equivalent noise (N_{eq}) of the visual system, and SE can be estimated from the MC threshold in the absence of noise ($MC N_0$) and the MC threshold in the presence of noise ($MC N_e$) (Legge et al., 1987; Pelli and Farell, 1999; Odom et al., 2006). The advantage of the equivalent noise technique is the ability to separate optical from neural contrast sensitivity loss (Pardhan et al., 1993; Pelli and Farell, 1999; Pardhan, 2004).

3.3.4 Psychophysical characteristics of the external noise image

The external noise image is defined in terms of its masking power i.e. its ability to mask the sine wave grating stimulus (Rovamo and Kukkonen, 1996; Kukkonen et al., 2002; Rovamo et al., 2003). The power of the noise mask is referred to as the noise spectral density. For a static mask, the spectral density is directly proportional to the size of the individual noise check and to the contrast of the mask (Kukkonen, 1994). Noise contrast is

measured in terms of the root mean square (rms), a value which describes the distribution of luminance across the image (Kukkonen et al., 1993). When the luminance of the noise checks is randomly modulated over time, the noise mask is referred to as a spatio-temporal, or dynamic, noise mask (Rovamo et al., 2000; McAnany and Alexander, 2009). In addition to check size and rms contrast, the spectral density of dynamic noise is proportional to the duration of each noise check. This parameter is the length of time that any particular check remains at one level of luminance (Kukkonen et al., 2002). Therefore, a high-spectral density dynamic noise mask will have relatively large checks, high rms contrast and a long check duration (Kukkonen et al., 1995; Kukkonen et al., 2002).

A noise mask can be made infinitely strong by increasing its check size and/ or contrast and/ or duration. However, the masking power of external noise has practical limits that are defined by the underlying stimulus. Comprehensive reviews are those of Kukkonen et al (1995), Kukkonen et al (2002) and Rovamo et al (2003). Noise check size and duration can be increased up to a critical point, beyond which the noise image becomes less effective at masking the grating. Noise contrast has no such critical point, although contrast is limited by the dynamic contrast range of the computer monitor (Kukkonen, 1994; Kukkonen et al., 2002). The equivalent noise paradigm must involve a noise mask with optimised spatial and temporal noise parameters to ensure that the noise mask is strong enough to reduce the visibility of the underlying grating.

3.3.5 Clinical application of the equivalent noise paradigm

SE is thought to be a measure of neural function across the visual pathway (Pardhan, 2004; Hayes and Merigan, 2007). N_i is thought to be a measure of neural noise or random firing

of RGCs and of optical factors such as increased light scatter due to lens opacities (Kersten et al., 1988; Pardhan et al., 1993; Pardhan, 2004).

It is hypothesised that RGC death in OAG is preceded by a stage of RGC shrinkage (Morgan, 2002; Gupta and Yücel, 2007). It is also hypothesised that this process may result in increased neural activity which would be manifested as N_{eq} measures that are above normal levels. The shrinkage stage of RGC death may also result in subtly impaired cell function, manifested as SE measures that are below normal levels. As the glaucomatous disease process develops further, shrinkage may become more wide spread and eventually result in RGC death. SE will continue to fall and to correlate with the extent of cell damage. RGC death will result in a loss of neural activity in locations of the retina which have suffered more advanced damage. The absence of neural activity in these locations would be indicated by N_{eq} measures that are below normal levels. Therefore, in locations of the retina where RGCs are undergoing shrinkage and are amongst other RGCs that are already dead, there will be a summation of both high and low levels of neural activity. These locations will be indicated by normal N_{eq} due to the summed response of all cells. Eventually, with extensive RGC death, N_{eq} levels will indicate an overall depression in neural activity, as the dead cells outweigh the response of the shrinking cells. In summary, it is hypothesised that early OAG (prior to RGC death) is characterised by high levels of N_{eq} , and reduced SE when compared with normal individuals. It is also hypothesised that as the disease progresses, SE will continue to fall, and N_{eq} will reach normative levels. In the late stage of the disease, it is hypothesised that both SE and N_{eq} will reach sub-normal levels. A schematic of the hypothesised relationship between N_{eq} level, SE and the stage of damage in OAG, is illustrated in Figure 3.1.

Studies indicate that OAG is associated with reduced SE, when compared with age-matched controls (Yates et al., 1998; Odom et al., 2006; Falkenberg and Bex, 2007). N_{eq} levels were comparable in control and OAG groups (Falkenberg and Bex, 2007) or were not measured (Yates et al., 1998; Odom et al., 2006). However, when N_{eq} was measured, it was measured in those where the stage of OAG was 'relatively advanced'. Therefore, a measure of N_{eq} would have reflected the summed response of absent and heightened neural activity.

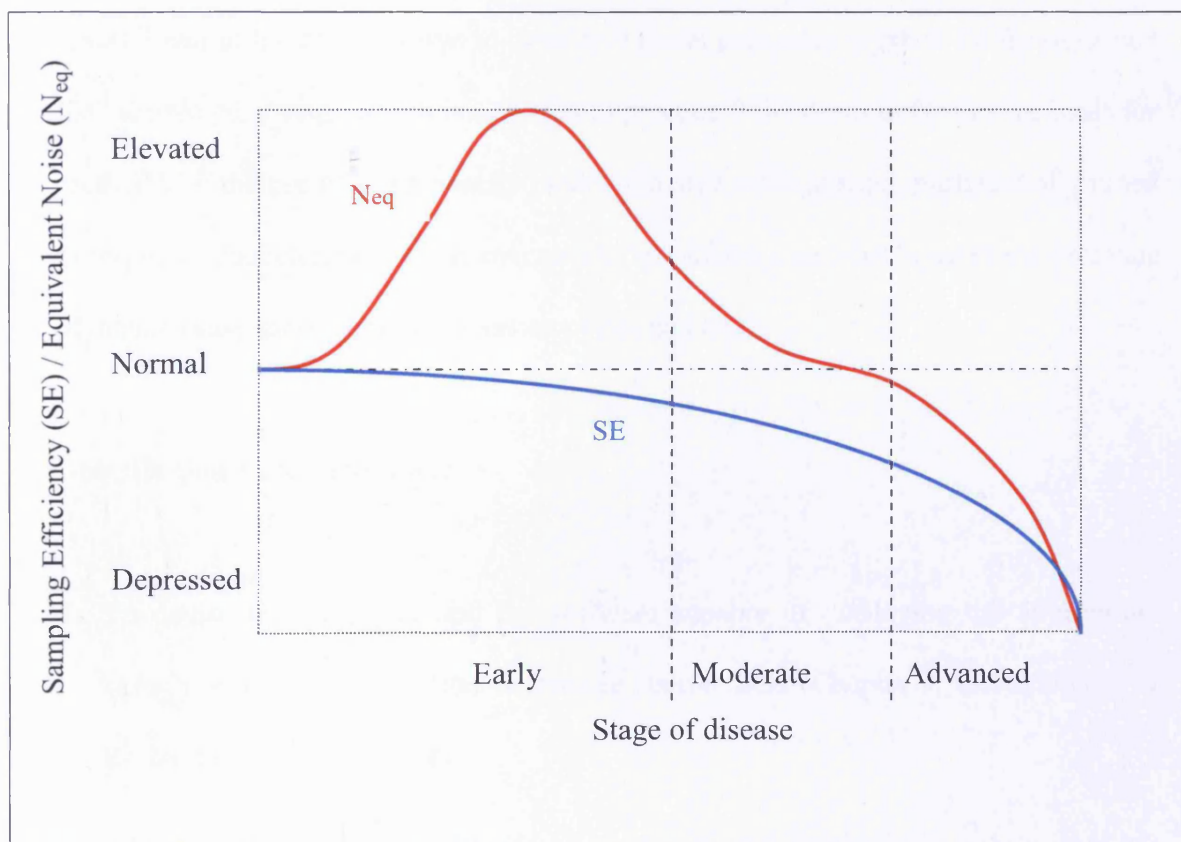


Figure 3.1 Schematic illustrating the hypothesised change in N_{eq} and SE with the progression of OAG. N_{eq} is raised in early OAG due to increased neural activity arising from RGC shrinkage. N_{eq} then declines to normative levels in moderate OAG due to the summed response of shrinking and dying RGCs. Thereafter N_{eq} falls as a result of depressed neural activity, due to RGC death. SE is at normative levels in early OAG, as the RGCs undergo shrinkage, but remain functional. Thereafter, SE falls in moderate and advanced stages of OAG due to continuing RGC death.

As has been discussed earlier in Section 3.1, an early stage of OAG will precede the detection capabilities of current structural and functional techniques. Existing studies measuring SE and N_{eq} have not identified OAG at a stage that precedes RGC death, a stage in which reduced SE should be accompanied by raised levels of N_{eq} .

3.4 Aims of the research

The overall aim of the research was to develop a novel perimetric method for the detection of RGC shrinkage, a stage which is believed to precede RGC death in OAG. The basis for the method was the use of a temporally modulated sine wave grating, preferentially tuned to the response characteristics of the magnocellular pathway, and displayed in the presence of a dynamic noise mask to elicit measures of N_{eq} and SE.

The specific aims were as follows:

1. To devise the hardware and the software capable of displaying the appropriate stimuli at any given location within the central field (Chapter 4, Development of the hardware and software).
2. To conduct a pilot study to determine the effects of a temporally modulated sine wave grating on the spatial limits of a dynamic noise mask in the normal eye (Chapter 5, The spatial limits of the dynamic noise mask).

3. To characterise, in the normal eye, the relationship between the spatial limits of a dynamic noise mask and the spatio-temporal parameters of the sine wave grating preferentially tuned to the response characteristics of the magnocellular pathway (Chapter 5, The spatial limits of the dynamic noise mask).
4. To determine any between-examination improvement (i.e. the learning effect), for a motion detection and a discrimination task, in MC N_0 , MC N_e , N_{eq} and SE over the course of several visits conducted over a short time period (once weekly for three weeks) (Chapter 6, Clinical Application of Dynamic Noise Perimetry Section 6.4).
5. To describe, in normal individuals and in individuals with OAG at visit 3, the characteristics of i) MC N_0 and MC N_e to the preferentially tuned stimulus presented at various locations in the central visual field, for both a motion detection task and a motion discrimination task; and ii) to calculate the corresponding N_{eq} and SE measures (Chapter 6, Clinical Application of Dynamic Noise Perimetry, Section 6.8).
6. To determine, in the normal eye, the age-dependency of MC N_0 , MC N_e , N_{eq} and SE derived at visit 3 for each motion task, separately. (Chapter 6, Clinical Application of Dynamic Noise Perimetry Section 6.9).
7. To determine the characteristics of MC N_0 , MC N_e , N_{eq} and SE, for each motion task for various levels of visual field loss in OAG. Secondly, to validate the measures of MC N_0 , MC N_e , N_{eq} and SE in OAG by comparing the findings with a

corresponding measurement of the RNFL thickness (Chapter 6, Clinical Application of Dynamic Noise Perimetry Section 6.10).

3.5 The outcome of each study

3.5.1 Aim 1: Development of the hardware and software

The pilot studies utilised existing hardware and software available within the School. The display monitor was calibrated according to the methods described in Chapter 4, Section 1. Thereafter, a new hardware set-up was required for the more expansive studies using dynamic noise stimuli. Software was written by Dr Gavin Powell and hardware was designed to enable testing at any location across the central visual field. A staircase algorithm was developed from seminal literature (Cornsweet, 1962; Wetherill and Levitt, 1965).

For each study, the monitor was calibrated to ensure the accuracy of the displayed luminance levels. The equivalent noise technique (Legge et al., 1987; Pelli and Farell, 1999) was adapted to determine estimates of N_{eq} and SE at any given location across the central visual field.

Two test methods were developed. The first was a motion detection task in which the observer was required to identify which of two consecutive images contained a sine wave grating. The second was a motion discrimination task in which the observer was required to assess the direction of motion of a sine wave grating within the given single presentation. In both paradigms, grating contrast was altered according to the pre-defined

algorithm to determine threshold. Software was written for each stage of the study, and a user-interface was developed to control the display monitor. The design and testing of the software is described in detail in Chapter 4, Section 2.

3.5.2 Aim 2: The relationship between drifting gratings and dynamic noise

The pilot study showed that for stationary gratings, critical noise check size increased from 3.5 to 3.8 checks per cycle for gratings with spatial frequencies of 1 and 8 cycles per degree (c/deg), respectively (Chapter 5). The findings are comparable with a critical check size of 4.2 checks per cycle for gratings of 1 to 4 c/deg found by Kukkonen et al. (1995), which falls to 2.6 checks per cycle for spatial frequencies up to 64 cycles (Kukkonen et al., 1995).

Critical check size for a noise mask in the presence of drifting gratings (16Hz) decreased from 2.4 to 2.0 checks per cycle for spatial frequencies of 1 and 8 c/deg. The critical noise check was inversely proportional to the temporal frequency of a drifting grating. Critical noise limits for drifting gratings have not been investigated in the literature. However, studies of flickering gratings indicate that critical noise check duration is reduced with increasing temporal flicker (Rovamo et al., 1996; Kukkonen et al., 2002). The findings of this pilot study were accepted for presentation in 2006 at the Annual Conference of the Association for Vision Research and Ophthalmology (ARVO) (Appendix).

3.5.3 Aim 3: Spatio-temporal relationships between gratings and dynamic noise

A preliminary study (Chapter 5) was required to validate findings and to characterise the relationship between drifting gratings of various spatial frequencies and the spatial limits of the dynamic noise mask. For sine wave gratings of 0.5c/deg, the critical check size decreased, in terms of checks per cycle, with increasing grating temporal frequency. The critical check size was larger for gratings that drifted at higher temporal frequencies when compared with the maximal check size for masking a slower grating. For a fixed spatial frequency, a drifting grating was more difficult to detect in the presence of a dynamic noise mask than a stationary grating. Increasing the grating drift rate would confound the ‘window effect’ which occurs when a grating becomes increasingly visible as noise check size increases. The check becomes analogous to a window through which the luminance profile of the grating becomes easier to see (Harmon and Julesz, 1973; Kukkonen et al., 2002). The perceived spatial frequency of the grating would change as its temporal frequency increases; which in turn alters the spatial cut-off of the noise mask. Seminal literature indicates that perceived spatial frequency changes when gratings are modulated at high temporal frequencies (Kelly, 1966, 1981b).

For sine wave gratings of 2.0 c/deg, the spatial cut-off of the noise mask was independent of temporal drift frequency. This finding was not consistent with that of the earlier pilot study in which stationary sine wave gratings of 1 and 8 c/deg were masked down from 3.6 and 3.5 checks per cycle to 2.4 and 2.0 checks per cycle, respectively, when drifted at 16Hz. However, for gratings drifting at 16 Hz, there is likely to be significantly more disruption to visual processing than would occur if drifting at 8Hz. For example, the frequency doubling illusion occurs at temporal frequencies beyond 16 Hz and thus may

account for the substantial impact on the critical spatial cut-off of the noise mask (Kelly, 1966; Kelly, 1981a).

For low spatial frequency drifting gratings, at 27° eccentricity in the superior nasal visual field, the critical check size of the noise mask was influenced by the temporal frequency of the underlying stimulus. Critical check size was lower in terms of checks per cycle at 27° compared with values determined for foveal viewing. At 8 Hz, the critical check size at 27° was 2.0 checks per cycle compared to 4.0 checks per cycle for foveal viewing. This difference can be explained by the decrease in retinal sampling density with increased retinal eccentricity (Rovamo and Virsu, 1979; Virsu and Rovamo, 1979; Melmoth et al., 2000).

A drifting sine wave grating, with a spatial frequency of 0.5 cycles per degree and a temporal frequency of 8 Hz was chosen for the clinical investigation of OAG. This stimulus was considered to preferentially activate the magnocellular stream (Willis and Anderson, 2000; Ansari et al., 2002b; Callaway, 2005) which is believed to be dysfunctional at an early stage of OAG (Johnson, 1994; McKendrick et al., 2007; Wall et al., 2009). The optimal parameters of the dynamic noise mask were determined for the grating stimulus to ensure that the maximal contrast range of the monitor was available for the measurement of N_{eq} and SE in OAG. Although noise check duration was known to impact the masking potency of dynamic noise, initial work indicated that increasing the duration above the rate of 30 frames per second tended to reduce contrast thresholds. This, in turn, indicated that the software was already operating at the temporal limits of the dynamic noise mask and that this aspect had been optimised.

3.5.4 Aim 4: Between examination improvement in performance in normal individuals and in individuals with OAG

In absolute terms, MC N_0 , MC N_e and SE improved over the course of the three visits for both the detection and the discrimination task in normal individuals and in individuals with OAG. N_{eq} remained broadly constant across the visits in normal individuals but worsened in individuals with OAG.

In proportionate terms, MC N_0 , MC N_e and SE improved between visit 1 and visit 2 for both the detection and discrimination tasks in normal individuals and continued to improve for the discrimination task from visit 2 to visit 3. For the individuals with OAG, the SE improved across the three visits.

The improvement in SE and the stability of N_{eq} is consistent with that of Gold et al., (1991) and is due to improved detection strategies rather than to reduced levels of neural activity.

3.5.5 Aim 5: Derivation of MC N_0 , MC N_e , N_{eq} and SE at visit 3 in normal individuals

In the normal eye, MC N_0 was maximal for foveal viewing and comparably lower at other locations. The inverse held true for MC N_e . The noise mask was considered to disrupt vision processing mechanisms with foveal viewing. N_{eq} levels in the normal individuals were consistent with other studies (Pardhan, 2004; Radhakrishnan and Pardhan, 2006). SE was also comparable with studies of motion detection and discrimination tasks (Simpson et

al., 2003a; Simpson et al., 2003b). This was true of both the motion detection and discrimination tasks.

3.5.6 Aim 6: Age-dependency at visit 3 of MC N_0 , MC N_e , N_{eq} and SE

An age-related decline was demonstrated for the measures of MC N_0 and MC N_e for both the detection and the discrimination tasks. N_{eq} increased with age which may, in part, be due to physiological changes within the crystalline lens which increase lens scatter and create uncertainty within the perceived image (Kersten et al., 1988; Pardhan et al., 1993). Increased neural firing may also be a significant contributor to raised N_{eq} levels (Pardhan, 2004; Betts et al., 2007; Falkenberg and Bex, 2007). SE declined with age, reflecting reduced RGC function. This is consistent with other studies (Pardhan et al., 1996; Falkenberg and Bex, 2007) and can be explained by physiological RGC loss with ageing (Kerrigan-Baumrind et al., 2000). Reduced SE and increased levels of N_{eq} were responsible for the decline of TCS with age.

3.5.7 Aim 7: Derivation of TCS, N_{eq} and SE in OAG

DNP was able to identify individuals with OAG that exhibited abnormal Pattern Deviation probability values (PD_{Ab}) and abnormal RNFL thickness ($OAG\ RNFL_{Ab}$) at the given locations, from an age-matched group of normal individuals. MC N_0 was most sensitive of all DNP measures, together with a derivative of N_{eq} and SE, referred to as the Signal Detection Index (SDI). These findings were true for both the detection and the discrimination tasks.

In some cases, N_{eq} identified individuals with OAG that did not demonstrate PD_{Ab} and/ or $RNFL_{Ab}$. However, N_{eq} did not always identify individuals with PD_{Ab} and/ or $RNFL_{Ab}$. This is consistent with the hypothesis (Section 3.4), which indicates that N_{eq} will rise to abnormal levels in early OAG and may appear normal in moderate to advanced OAG. SE did not consistently identify individuals with OAG. For individuals with PD_{Ab} and/ or $RNFL_{Ab}$, SE was often within the normal range. This finding was inconsistent with the hypothesis, which indicates that SE will decline with structural or functional decline. The lack of sensitivity of SE is likely to be explained in terms of the lack of optimisation of the noise mask for individuals with OAG.

3.6 Further development of DNP

The results indicate that a further study is warranted with a larger cohort of normal individuals and individuals with OAG to confirm the findings of the initial case series.

As mentioned previously, the dynamic noise mask was only moderately effective at distinguishing individuals with OAG $RNFL_{Ab}$ from age-matched normals. The measures of N_{eq} and SE were less sensitive than was originally hypothesised. As such, the parameters of the dynamic noise mask should be the subject of further study. An analysis of the harmonics within the noise mask may help to develop the concept beyond the current spatial and temporal approach. The mask should be developed specifically for use for individuals with OAG.

Although the detection and the discrimination task exhibited comparable sensitivity for the detection of OAG, the discrimination task only involved the need for a single stimulus presentation; therefore, thresholding time was half that of the detection task. A minimal examination is duration is critically important for perimetry. It is essential that the thresholding algorithm should be optimised along the lines of those currently used in clinical perimetry, which are based upon a Bayesian approach to estimation of thresholds, such as the PEST and ZEST algorithm (Anderson and Johnson, 2006).

3.7 Study logistics

The thesis commenced in 2004 under the supervision of Dr Outi Ukkonen with Professor John Wild as a secondary advisor. Considerable delays were encountered during the first year largely due to the problems associated with the development of the software necessary for generating the stimuli. The software engineering had been outsourced to an individual who had previously collaborated with Dr Ukkonen. At the end of the first year, Dr Ukkonen resigned her position as a Lecturer within the School. Consequently, Professor John Wild took over the position of supervisor. Shortly afterwards, the Candidate took six weeks leave of absence, to be married, and returned in the Autumn of 2005. Existing software within the School was used for the pilot study to investigate critical noise parameters with static and drifting sine wave gratings. The study was conducted with the support of Professor Jyrki Rovamo. At the end of 2005, the study was accepted for a poster presentation at the Annual Meeting of The Association for Research in Vision and Ophthalmology (ARVO). The introduction of a new software engineer, Dr Gavin Powell, facilitated the development of several new versions of software. The

development involved extensive collaboration between Dr Powell and the Candidate, which occurred over the following two years, and in which the Candidate designed the necessary parameters and the interface for all subsequent studies involving dynamic noise.

Before the clinical studies into OAG could begin, it became apparent that a more extensive study was necessary to determine the spatial limits of a dynamic noise mask. This preliminary study was considerably delayed by the development of new software which was designed to handle more complex stimuli. The previous hardware had been superseded and so it was also replaced. The new software was continually evaluated and modified over the first six months of 2006. There were several issues that hindered progress. Most notably, the calibration of the monitor proved to be a particularly time consuming process. A proven method for measuring the output of the monitor was followed in an effort to linearise the contrast response. However, the technique indicated that the monitor output was not linear. An alternative method was eventually developed by the Candidate by determining the optimal display characteristics of the monitor. The output was considerably improved, although not linear. Therefore a polynomial function was developed and programmed into the software, which finally solved the issue.

As a consequence, the study to determine the spatial limits of a dynamic noise mask began in late 2006 and was completed in early 2007. The findings provided the necessary parameters for the clinical investigation of OAG. The clinical investigation of OAG was significantly delayed by further software development issues. The method used for the assessment of individuals with OAG required considerably more programming than was originally anticipated. The extra programming related to a need for a motion

discrimination method, and more extensive parameters for the control of noise contrast and stimulus location.

In early 2006, it became apparent that the methods being developed for the investigation of OAG could have commercial application. After meetings with Cardiff University Research and Commercial Division, it was concluded that the method should be filed as a patent. Subsequently, the method was identified by Venture Capital firm Biofusion as a commercially viable opportunity for technology transfer to the private sector. This precipitated an initial patent filing in the UK. To date, patents have been filed to protect the methods described in this thesis in approximately 12 countries or regions, including the European Union and the United States (Appendix).

In the Summer of 2006, i.e. two years into the work for the thesis, the author decided to apply for a two-year full time Masters Degree in Business and Administration (MBA) to be undertaken following the completion of his PhD. By the summer of 2006, noise check studies were progressing well and the clinical investigation of OAG was shortly due to begin. Therefore, in the Summer of 2006, the author began the process of applying to business school with the aim of commencing in the Autumn of 2007.

Individuals with OAG were recruited from the Cardiff Eye Unit at The University Hospital of Wales and normal controls were recruited from Eye Clinic at Cardiff School of Optometry and Vision Sciences. The clinical investigation of OAG eventually began in the Spring of 2007 and was completed at the end of August 2007.

In early 2007, the Candidate was offered a place at the London Business School beginning in September of that year. Although Professor Wild had reservations about the timing of the course, the Candidate accepted the offer of a place as he felt that he would be able to complete all experimental work before commencing the MBA. He also expected to write-up his thesis during the first few months of the MBA programme.

At the beginning of September 2007, the Candidate began the Full-time MBA programme. Although he had expected to complete the writing-up of the thesis during the first few months of the MBA programme, it quickly became apparent that the work-load was far too intense and would not allow for the thesis to be written-up, simultaneously with MBA studies. Therefore, with the support of Professor Wild, the Candidate applied to Cardiff University for an extension of time, and was granted a two-year leave of absence to complete the MBA. Following a successful graduation from the MBA programme, and under the supervision of Professor Wild, the Candidate completed the write-up of this thesis.

Laboratory time was divided between software testing, monitor calibration, noise check studies and clinical studies into OAG. Total experimental time exceeded 500 hours, of which data collection was approximately 300 hours. Monitor calibration time was divided into the measurement of luminance steps for each of the colour guns, analysis of output, correction of software, measurement of the contrast response, and analysis and further correction of software.

4 Development of the hardware and software

4.1 Calibration of the CRT display monitor

CRT monitors are popular in perceptual research as their output is generally stable to within approximately 1%. Thus a level that is similar to human perceptual thresholds (Olds et al., 1999). There is a non-linear relationship between the voltage generated by the electron gun of a CRT monitor and the measured luminance output of the graphics card (Travis, 1991). The non-linearity can create visual perceptual anomalies to a given stimulus. To overcome the non-linearity, the CRT monitor can be calibrated. The voltage generated by the CRT is measured in terms of screen luminance. The relationship between the voltage and screen luminance is known as a gamma function and the function can be used to calibrate the output of the display (Stanislaw and Olzak, 1990; Colombo and Derrington, 2001).

The properties of any given monitor will vary with time and so periodic calibration is necessary. Stimuli that are presented on the monitor correspond to reference values within pre-defined colour 'look-up' tables within the graphics card. Calibration is designed to characterise the relationship between the values in the 'look up' tables and the measured output (Brainard, 1989).

4.1.1 Calibration of CRT display used within the pilot study

A initial investigative pilot study was performed using a high resolution cathode ray tube (CRT) monitor and a VGA (Texas Instruments, TIGA) graphics board driven by a Research Machines PC model computer and a Sony Multiscan 17seII 17" monitor (frame

rate 60Hz, resolution 640 x 480 pixels). The pixel size was 0.47mm x 0.47mm and the average luminance was 50cdm⁻².

The luminance response of the Sony Multiscan 17seII monitor was separately measured for each of the three individual colour guns using a Minolta Luminance Meter LS-110 for a monitor contrast of 80% and a monitor brightness of 90%. These latter settings had previously been used for other psychophysical research within the School. The luminance was measured, in candelas per square metre, at the geometric centre of the screen, which corresponded to a foveal stimulus presentation. The photometer was set to measure in 'slow' mode so that transient fluctuations at the level of the drive voltage could be averaged. The colour co-ordinates (CIE, 1932) of each gun output of the CRT were also recorded to ensure that the colours remained stable over varying luminance values. The graphics card generated luminance values that spanned the index range of each colour gun from 0 to 255 in steps of 15. The graphics card was instructed to generate the given luminance value using software developed previously within the School by Dr Jarmo Hallikainen. The software presented the output of each individual colour gun in discreet intervals of luminance over the entire index range. The screen luminance generated at each given index value was again measured at the centre of the screen..

A linear luminance output was necessary for the middle section of the index range as this section is responsible for generating luminance levels for low contrast stimuli. To investigate the settings that achieved linearity over the widest possible index range, the luminance response was separately recorded for each gun over a range of monitor brightness and contrast settings. Luminance measurements were undertaken after a 30 minute warm up of the monitor. Five measurements were recorded for each index step of

each gun and the median luminance value at each step was plotted against the given index level. The luminance of each colour gun increased exponentially when plotted in linear co-ordinates. An example of the function given by the red gun is shown in Figure 4.1. In order to find the region of the response function that could be considered linear, the data were plotted in logarithmic co-ordinates and a least-squares line was fitted to the data. The logarithmic plot of the data for the red gun contained in Figure 4.1 is shown in Figure 4.2.

A linear fit was applied to this relationship to verify continued linearity over the corresponding measured index range. The goodness of fit for each colour gun was defined in terms of the Coefficient of Determination (R^2) and was set at 0.9999.

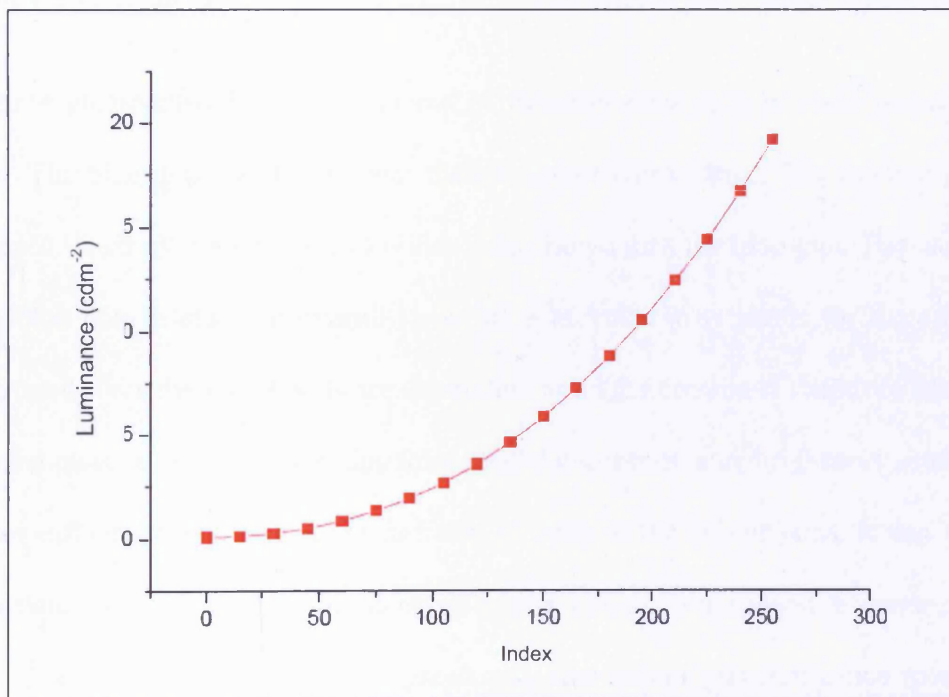


Figure 4.1 The measured luminance (\log_{10}) response output for the red gun within the CRT monitor.

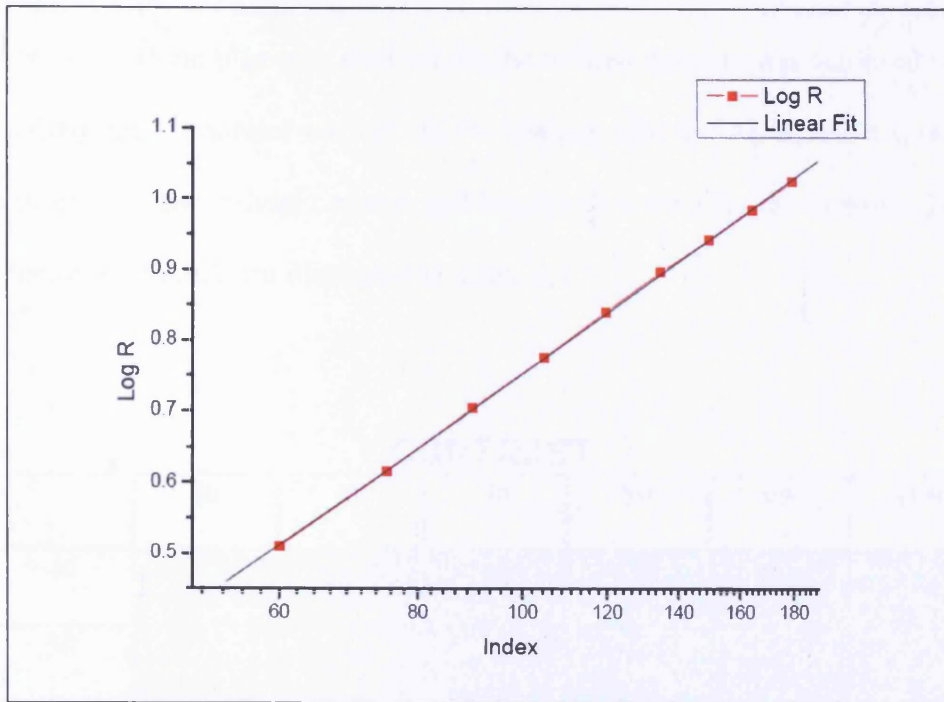


Figure 4.2 The \log_{10} of the luminance response function for the red gun for the data shown in Figure 4.1.

The three guns showed varying extents of linearity over each of their respective index ranges. The blue gun was linear over the narrowest index range. The red and green guns were each linear over a similar but wider index range than the blue gun. The narrow range of the blue gun limited the overall range of achievable grey levels for the stimulus and background since the grey levels are dependent upon the combined output of the red, green and blue guns. It also became apparent that the contrast and brightness settings of the monitor influenced the luminance function of each of the colour guns. It was considered appropriate to measure the output of only one colour gun against a range of monitor settings, given that each set of red, green and blue colour gun luminance measurements would have taken between 4 and 6 hours to collect. The blue gun was selected to determine the optimal monitor contrast and brightness settings. The blue gun possessed the narrowest linear index range of all three colour guns and, therefore, dictated the linear index range of the combined red green and blue gun output.



The index range of the blue gun, over which the desired linearity was achieved, varied for each combination of monitor contrast and brightness settings. An iterative approach was used to determine the optimal contrast and brightness setting for the monitor. The results of this iterative approach are illustrated in Table 4.1.

		CONTRAST					
		50	60	70	80	90	100
BRIGHTNESS	40				30-255		75-180
	50				30-255	30-255	40-210
	60				30-255	60-255	45-255
	70	90-255	75-255	60-255	60-255	60-255	
	80				75-255		60-255
	90				105-255		90-255
	100				105-240		105-255

Table 4.1 The linear index range for different contrast and brightness settings. Each index range corresponds to an R^2 value of 0.9999. The monitor characteristics were optimal for the blue gun at a contrast value of 80% and a brightness value of 60%.

Examples of curves describing the luminance output of the blue gun with specific contrast and brightness settings are shown in Figures 4.3 and 4.4. Each curve indicates the percentage contrast and brightness level of the monitor with the prefix 'C' and 'B', respectively. The greatest index range which had the highest R^2 value (between 30 and 255 index values) was achieved at a contrast level of 80% and brightness levels between 40% and 60% (Figure 4.3). The narrowest index range occurred at the 80% contrast and 100% brightness setting (Figure 4.4).

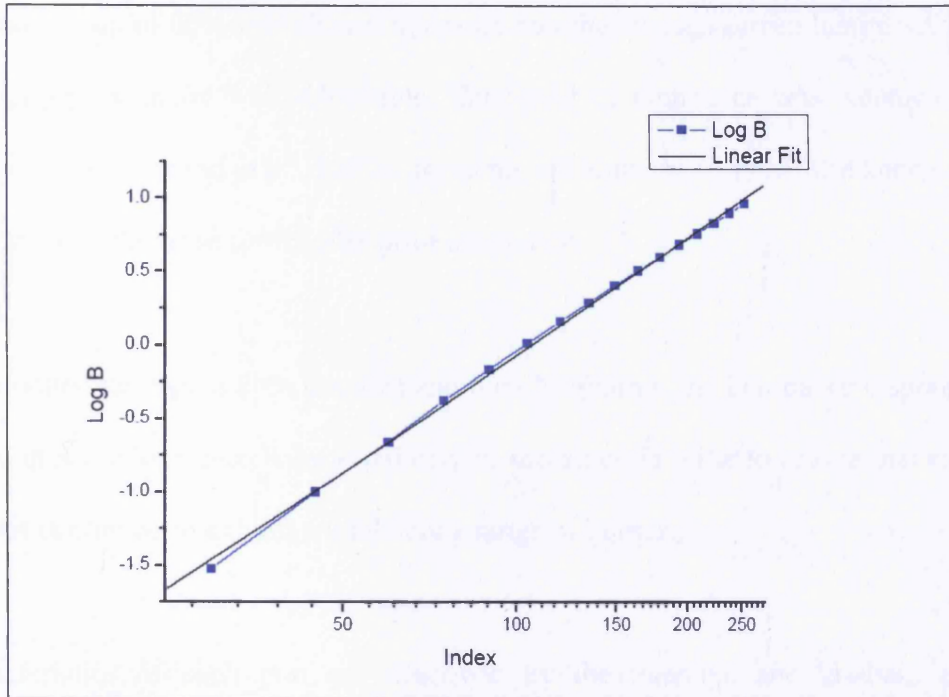


Figure 4.3 \log_{10} of the measured luminance for the blue gun plotted against \log_{10} of the given index for the 80% contrast and 40% brightness settings.

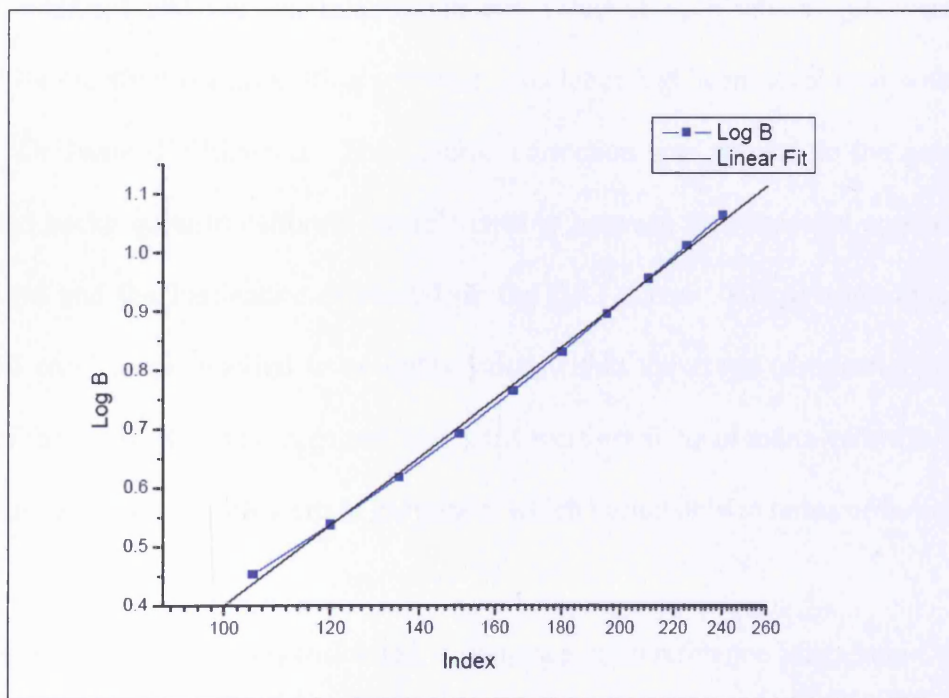


Figure 4.4 The \log_{10} of the measured luminance for the blue gun plotted against the \log_{10} of the given index at 80% contrast and 100% brightness of the display.

A brightness setting of 60% was chosen to ensure that the average screen luminance of 50 candelas per square metre was achievable. This level of luminance was commensurate with other studies (Rovamo et al., 1993b; Rovamo and Kukkonen, 1996; Kukkonen et al., 2002) and avoided the need for lengthy prior adaptation.

With the monitor settings at 80% contrast and 60% brightness, the luminance responses of the red and green colour guns were separately re-measured in order to ensure that each of the two guns continued to exhibit a wide index range of linearity.

The characteristics of each gun are described by the intercept and gradient of the corresponding linear function of the luminance output. The gradient is known as the gamma value and it is used to linearise the output of the given colour gun. The gamma value, the intercept and the maximal luminance value of each colour gun were then referenced by the stimulus generating software. The latter had been developed within the School by Dr Jarmo Hallikainen. The gamma correction was applied to the generated stimulus and background to calibrate the relationship between the requested output of the graphics card and the luminance displayed on the CRT screen. The average luminance value of 50 cdm^{-2} corresponded to an index value within the range of linearity. For the purposes of the study, the red, green and blue guns were set at equal index values such that the background and all stimuli were in greyscale, which varied only in terms of luminance.

To confirm that the monitor was calibrated, a sequence of 10 reference Michelson Contrast (MC) levels was generated by the Hallikainen software for a 10cm by 10cm stimulus situated at the centre of the screen and surrounded by an equiluminant background. The software presented the minimum luminance followed by the maximum luminance for each

reference contrast level. The screen luminances at each level of contrast were measured and the corresponding Michelson Contrast was calculated.

A photometer was setup to measure the luminance of the square only. The first contrast level was 0.512 and levels were halved at each step until a MC level of 0.001 was reached. The higher contrast values tended to be presented most accurately, as the large difference between the maximum and minimum luminance levels tended to offset the relative error. For this reason, a median value of three measurements for each luminance level was used between contrasts of 0.512 and 0.128. Whereas moderate contrasts in the range of 0.064 to 0.008, the median of five measurements was used. For low contrast levels between 0.004 and 0.001, the median was based upon nine measurements. At these low contrast levels, the maximum and minimal luminance values were particularly close together (to the order of 0.1 candelas per square metre); therefore, even minor variability in the output of the display resulted in large relative errors.

The median luminance values were used to calculate a series of MC values defined as the 'measured MC'. These corresponded with the series of 'requested MC' levels generated by the graphics card. The \log_{10} of the measured MC was plotted against the \log_{10} of the requested MC. A logarithmic transformation was used to assess the linearity of the combined colour gun output, essentially the result of the calibration process. The contrast response curve, following the calibration process, is shown in Figure 4.5. A linear fit was applied to the data using the function $Y = m \cdot X$ to ensure an intercept of zero. Where 'Y' represented the measured MC, 'X' represented the requested MC, and 'm' represented the gradient of the slope. The linear fit exhibited an R^2 value greater than 0.9999.

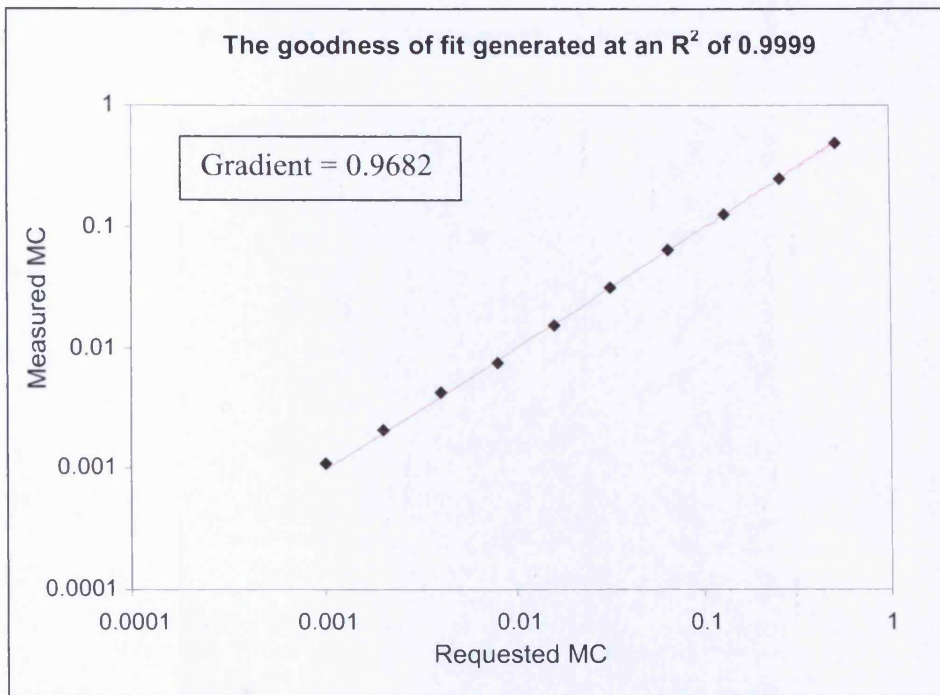


Figure 4.5 The contrast response of the graphics board following gamma correction.

The high R^2 value indicated that the monitor was calibrated. At the desired magnitude of the R^2 value, the discrepancy between the measured and the requested MC represented a -3% deviation at 0.512 and +10% deviation at 0.001. A summary of the relative error at each MC step is shown in Table 4.2.

Any deviation from an optimal goodness of fit, or a gradient below 0.95, would have required a further stage within the calibration process. When the output of the combined colour guns was non-linear, a 3rd order polynomial function was applied to the MC output to determine the relationship between the measured and requested MC. This equation was used to correct the output of the graphics card. Thereafter, the measurement of ten MC levels was repeated to ensure linearity.

Requested MC	Measured MC	Relative error
0.512	0.4945	-3%
0.256	0.2490	-3%
0.128	0.1255	-2%
0.064	0.0642	0%
0.032	0.0307	-4%
0.016	0.0154	-4%
0.008	0.0073	-9%
0.004	0.0042	5%
0.002	0.0021	5%
0.001	0.0011	10%

Table 4.2 The measured MC output of the graphics card following calibration. Relative error increases at lower contrast levels due to minor fluctuations in measured luminance.

4.1.2 Calibration of display used for the preliminary spatio-temporal noise study

A second study was devised to characterise the interactions between spatio-temporal noise and drifting gratings. The study was performed using a new set of equipment that enabled better computing power and a larger screen size. New hardware comprised a high resolution cathode ray tube (CRT) monitor (Mitsubishi Diamond Pro, frame rate 70Hz, resolution 1024 x 768 pixels) and a high specification graphics board. The Pixel size was 0.47mm x 0.47mm and the average luminance was 50.0 cdm^{-2} . A head support and chin rest was utilised to maintain a fixed viewing distance. A separate numerical keypad was

installed to enable the subjects to respond to the computer. The software was developed by Dr. Gavin Powell and the hardware was arranged as shown in Figure 4.6.



Figure 4.6 Configuration of the new hardware which comprised a high resolution cathode ray tube (CRT) monitor (Mitsubishi Diamond Pro, frame rate 70Hz, resolution 1024 x 768 pixels) and a high specification graphics board, a head support and chin rest and a separate numerical keypad. The CRT monitor is controlled by an operator using the adjacent computer (Research Machines) which has a keyboard, mouse and LCD monitor.

Luminance measurements were taken for the three individual colour guns using the Minolta Luminance Meter LS-110. These were used to determine gamma values as described in Section 4.4. Thereafter, the contrast response of the curve was measured to verify the calibration. It was apparent that the output of the monitor was not corrected by the calibration procedure. An example of the contrast response curve after the first calibration procedure is shown in Figure 4.7.

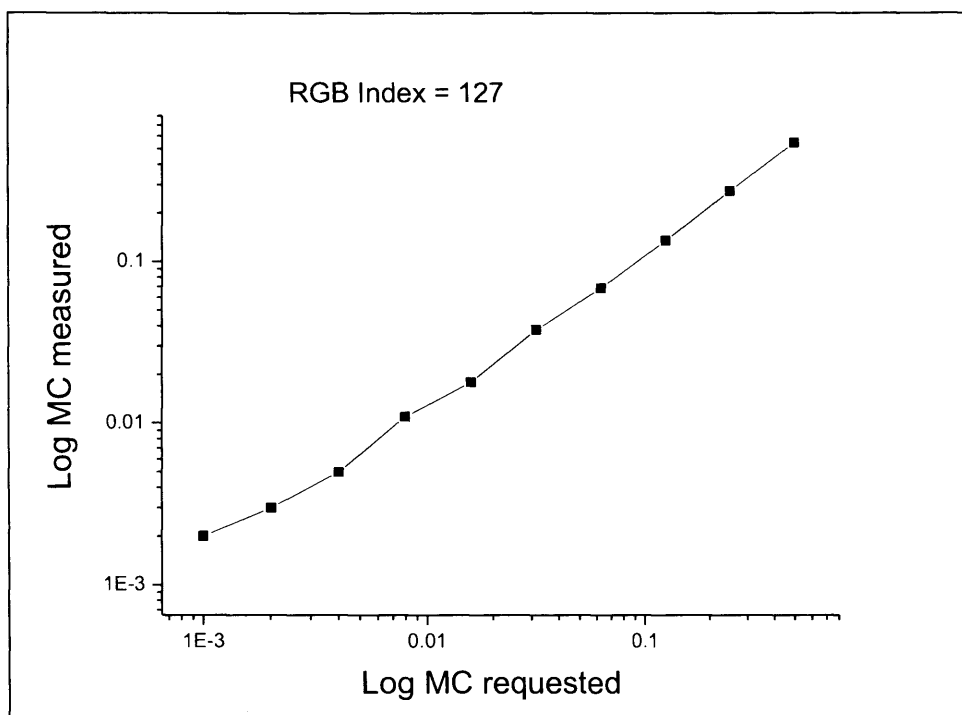


Figure 4.7 Contrast response curve following preliminary calibration. The measured contrast deviates below 0.01 Michelson units.

Background luminance was set so that the red, green and blue colour guns each had index values of 127. Equal index values were required to create an equiluminant calibration stimulus. Further investigation indicated that the contrast response became more accurate when colour gun index values equalled 95. However, the response did not meet the accuracy required for detection thresholds at low contrast levels. The contrast response curve at an index level of 95, is shown in Figure 4.8.

To overcome non-linear contract response at the lower end of the scale, a polynomial fitting equation was applied to the response function (Pelli and Zhang, 1991).

$$Y = 5.27295E-4 + 0.67913X + 0.04237X^2 \quad (4.4)$$

Where 'Y' is the \log_{10} of the measured MC and 'X' is the \log_{10} of the requested MC.

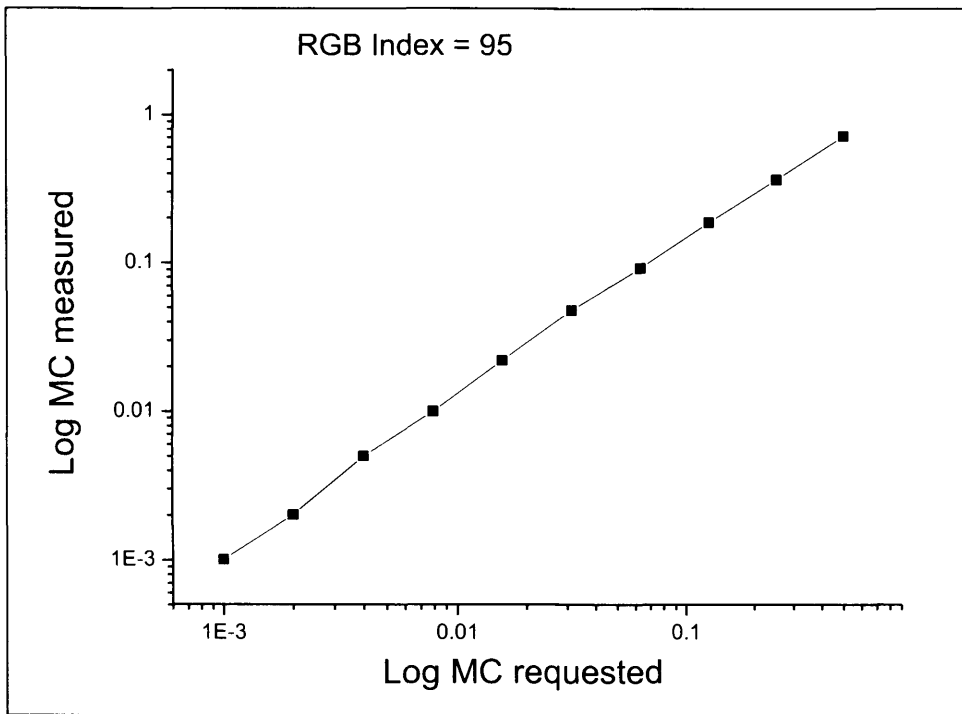


Figure 4.8 Contrast response curve following an adjustment of the red, green and blue (RGB) index level. The measured contrast fluctuates below 0.02 Michelson units.

The polynomial equation defined the output characteristics of the graphics card. The effect of the polynomial correction, on the contrast response curve, is shown in Figure 4.8. The polynomial equation was incorporated into the software. The resulting contrast response function is shown in Figure 4.9. The linear fit line demonstrated that the required level of accuracy was achieved and the corresponding R^2 value was greater than 0.9999.

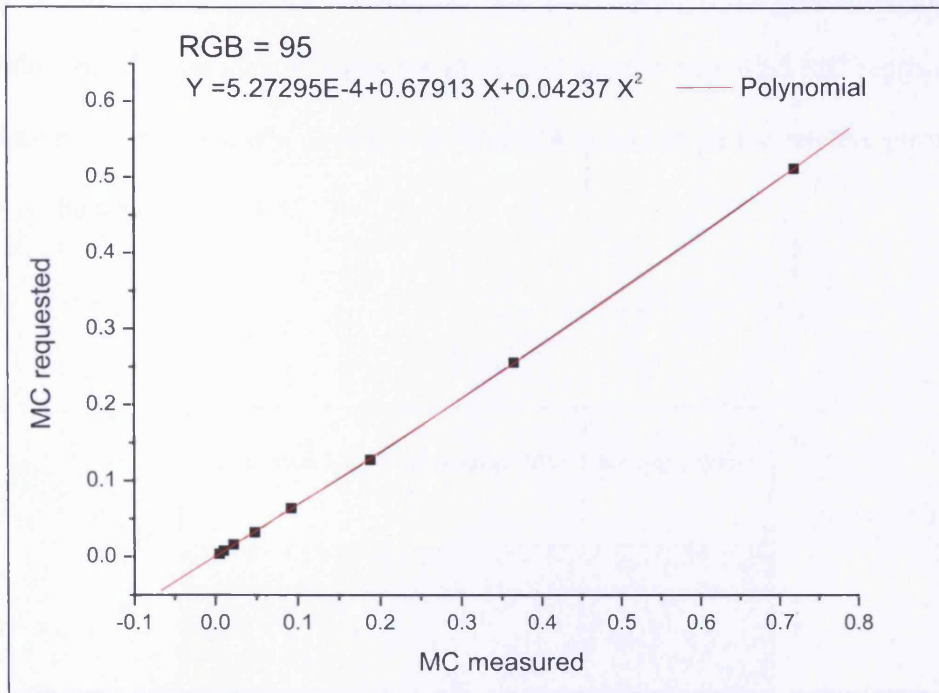


Figure 4.9 Polynomial fitting of the contrast response curve used to define the output characteristics of the graphics card.

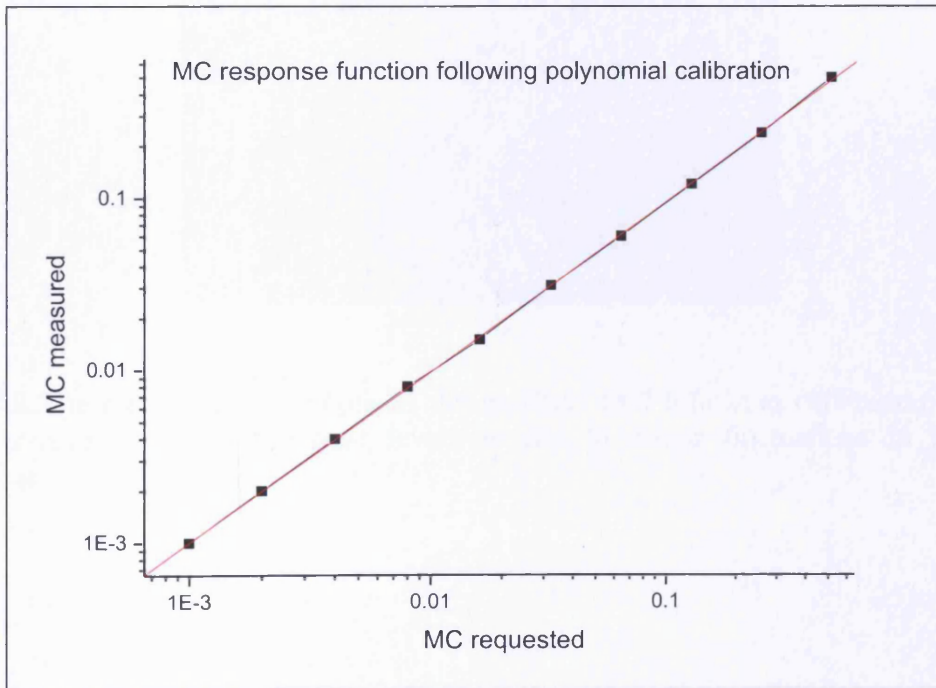


Figure 4.10 Final contrast response curve demonstrating successful calibration and accurate signal output.

The high R^2 value indicated that the monitor was calibrated. At the desired magnitude of the R^2 value, the discrepancy between the measured and the requested MC represented a -2% deviation at 0.512 and 0% deviation at 0.001. A summary of the relative error at each MC step is shown in Table 4.3.

Requested MC	Measured MC	Relative error
0.512	0.502	-2%
0.256	0.239	-7%
0.128	0.120	-6%
0.064	0.060	6%
0.032	0.031	-3%
0.016	0.015	-6%
0.008	0.008	0%
0.004	0.004	0%
0.002	0.002	0%
0.001	0.001	0%

Table 4.3 The measured MC output of the graphics card following calibration. Relative error increases at higher contrast levels is due to minor fluctuations in measured luminance.

4.2 Development of software for the new set up of hardware

4.2.1 The use of random dither

The graphics board produced an achromatic signal of 256 grey levels, corresponding to 8 bits. Thus, the luminance level of each pixel varied in relative luminance over a range from 0 to 255. Therefore, the achievable contrast range of the monitor extended from 1 $\{(255-0) / (255+0)\}$ to 0.0039 $\{(128-127) / (128+127)\}$ at the midpoint of the index range. However, each interval within the index range was insufficient for the measurement of detection thresholds over the proposed range of spatial frequencies. At low to medium spatial frequencies, a sine wave grating requires a greater range of grey levels to display the changes in luminance across the grating. The number of available grey levels was therefore increased using a method known as periodic dithering (Kukkonen, 1994).

A CRT display produces an achromatic 8 bit signal by combining the three separate colour gun signals. However, at low to medium spatial frequencies with moderate to high contrast levels, the analogue signal produces step, rather than continuous, changes in grey levels across a sine wave grating; this is called quantisation error. The limits of an 8 bit system translate into quantisation steps that are large enough to be seen, especially for high contrast gratings, which require a greater number of grey levels to bridge the gap between the maximum and minimum contrast levels. The quantisation error can be reduced to imperceptible levels by introducing low-strength noise (Aumala, 1996; Iannelli et al., 2006; Krause, 2006). A random dithering algorithm ensures that the limited number of grey levels does not give rise to visible steps in the variation in luminance level. The dither has the effect of smoothing contrast edges without degrading the entire image (Petri, 1996). If the size and contrast of the dither signal is kept small enough, the number of

grey levels is increased without causing any masking effects. The subsequent grating appears to have a smooth transition in the greyscale as the dither cannot be resolved by the optical capabilities of the human eye (Nasanen, 1989; Kukkonen, 1994).

A periodic dither signal was added to the 8 bit output of the graphics card. The amplitude of the dither was equal to one quantisation step i.e. one level of 256 values. An algorithm assigned a random number between -0.5 and 0.5 and added this to the required luminance at all locations within the grating. This value was then rounded to the nearest integer. The method is explained by equation 4.1 below:

$$\text{Ch:} = \text{round} (\text{Ipp} + ((\text{random} (999)/1000.0) - 0.5)) \quad (4.1)$$

Where Ch: is based on the term “character”, which indicates the new pixel luminance value with the added dither and ‘Ipp’ is the luminance value at one pixel within the grating.

The ensuing luminance profile resulting from the dithering will closely match the desired luminance necessary for a smooth grating, giving the appearance of more grey levels than can actually be created by the graphics card. This pseudo-extended range of grey levels enables the signal to exceed the 8 bit capability of the graphics board. These discrete additions of luminance are averaged by the visual system and result in a more linear quantisation of the grating. The dithering technique has been used throughout the thesis.

4.2.2 Development of the threshold algorithm

For this thesis, it was necessary to devise an algorithm for the determination of threshold with and without the noise mask. Such an algorithm required consideration of the starting

contrast level, the magnitude of the contrast change between responses and the end point of the sequence. The starting contrast was required to be as close as possible to the expected threshold and the magnitude of the contrast change was required to reflect the logarithmic sensitivity of the eye. For these reasons, logarithmic steps were considered most appropriate. The length of the sequence had to balance the increasing accuracy of the threshold estimate against the length of the sequence and the total length of the examination (Cornsweet, 1962).

The staircase algorithm was developed, based on the up-and-down transformed response rule (Wetherill & Levitt, 1965). As was discussed in Chapter 2, Section 2, the length of thresholding sequence was dependent on the number of correct responses, referred to as 'n', required to reduce the contrast of the grating. The initial pilot study showed that measuring thresholds when three correct responses were required to reduce grating contrast ($n = 3$, probability of seeing of 79%), still caused anxiety amongst individuals. Individuals often complained that they did not 'see' the grating for much of the examination. Increasing the value of n resulted in more awareness at threshold and greater levels of motivation. However, these benefits were partially offset by a longer staircase procedure. Four correct responses ($n = 4$) corresponded to a probability of 0.84 and this was used to define threshold for the purposes of the preliminary experiments. This rationale was supported by other research (Rovamo et al., 1993a; Kukkonen et al., 1995; Rovamo et al., 1996; Kukkonen et al., 2002).

Only one incorrect response was required to increase grating contrast and steps of $0.1 \log_{10}$ units were chosen on the basis of comparable experiments (Rovamo et al., 1992; Rovamo et al., 1993c). The starting contrast of the algorithm was at least $0.5 \log_{10}$ units above

threshold levels determined in pilot experiments. Subsequently, the grating was clearly supra-threshold at the start of all experiments.

During a 'starting phase' of the staircase, a single correct answer reduced the level of contrast. This modification was made to allow a rapid succession to threshold levels (Cornsweet, 1962). During this starting phase, the first incorrect response did not alter contrast (i.e. it was effectively ignored). However, a second incorrect response raised the contrast of the grating. The contrast level which elicited the second incorrect response was considered as the first 'reversal' of the staircase. Subsequently, a 'secondary phase' of the staircase was initiated, which required a sequence of four correct responses for a reduction in contrast. Each subsequent reversal corresponded with a directional change in the staircase, i.e. from a descending trend (consecutive decreases in contrast) to an upward trend (an increase in contrast level) and vice versa. Consecutive reversal points were usually supra and sub-threshold and it is these contrast levels that were used to determine the final threshold value.

Although a greater the number of reversals would lead to a more accurate final threshold (Cornsweet, 1962; Wetherill and Levitt, 1965), in practice the number of reversals needed to be balanced with the time taken to reach threshold. Comparable experiments indicated that six to eight reversals were acceptable for determining threshold (Kukkonen et al., 1995). The staircase algorithm allowed only the last six reversals of the staircase to determine threshold. The first two reversal values were ignored as they may have been biased by a run of accurate guesses, since the probability of seeing the grating was at first 50% and only thereafter adjusted to 84%. Figure 4.8 shows an example of a staircase procedure that determined threshold.

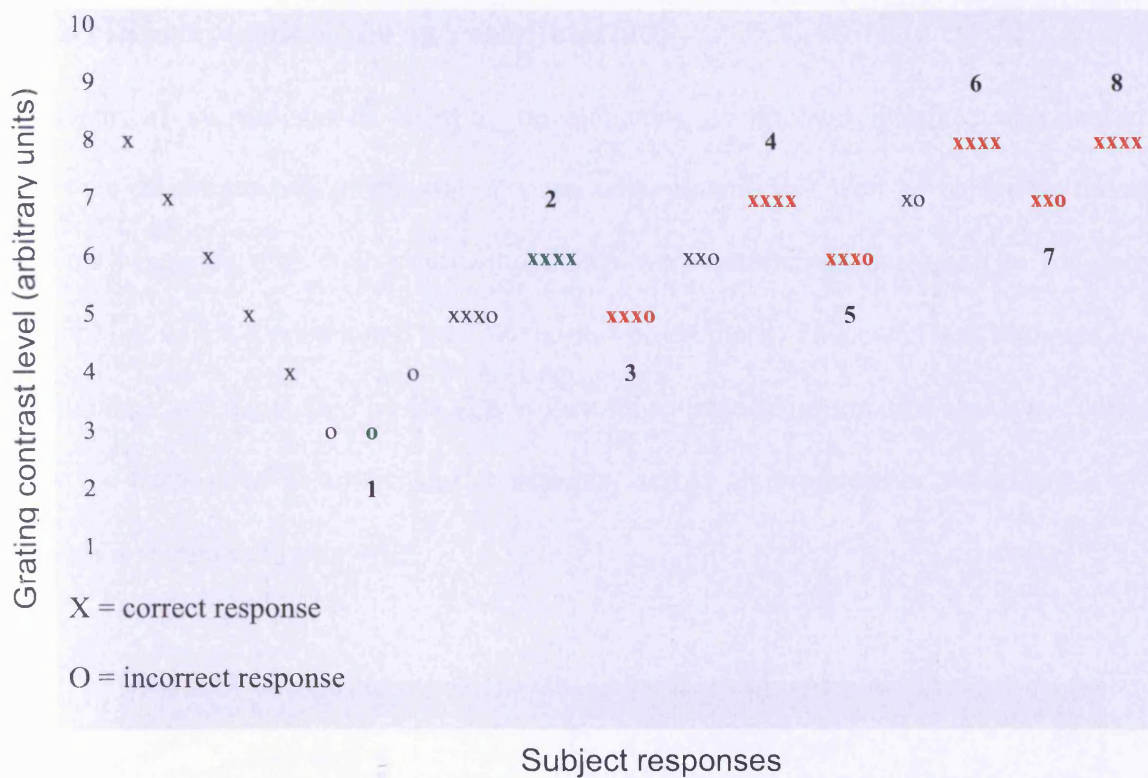


Figure 4.11 An example of the staircase algorithm where 8 reversals determine the length of the staircase, and the final six reversals are used to calculate threshold.

The threshold value was defined as the geometric mean of the final six reversals, of a sequence containing eight reversal points. Collection of data reduced the likelihood of results being skewed by observer error. A single threshold value was never taken as a final measure. The final threshold was based on the median of at least three separate staircase procedures. The median was considered more accurate than the mean as it was less susceptible to outliers. With the exception of the pre-defined algorithm of the pilot study, this threshold algorithm was used for all subsequent studies within the thesis.

4.2.3 Development of the operator interface

As part of the process of software development, an operator interface was needed to control the parameters of the stimulus and noise images that were presented on the main display monitor. For each study, thresholds were determined according to pre-defined variables, which were entered into a windows-based menu. This menu was designed by the Candidate and developed by Dr Gavin Powell, to include information that was controlled for the purpose of accuracy and consistency across all experiments. An example of the menu is shown in Figure 4.12.

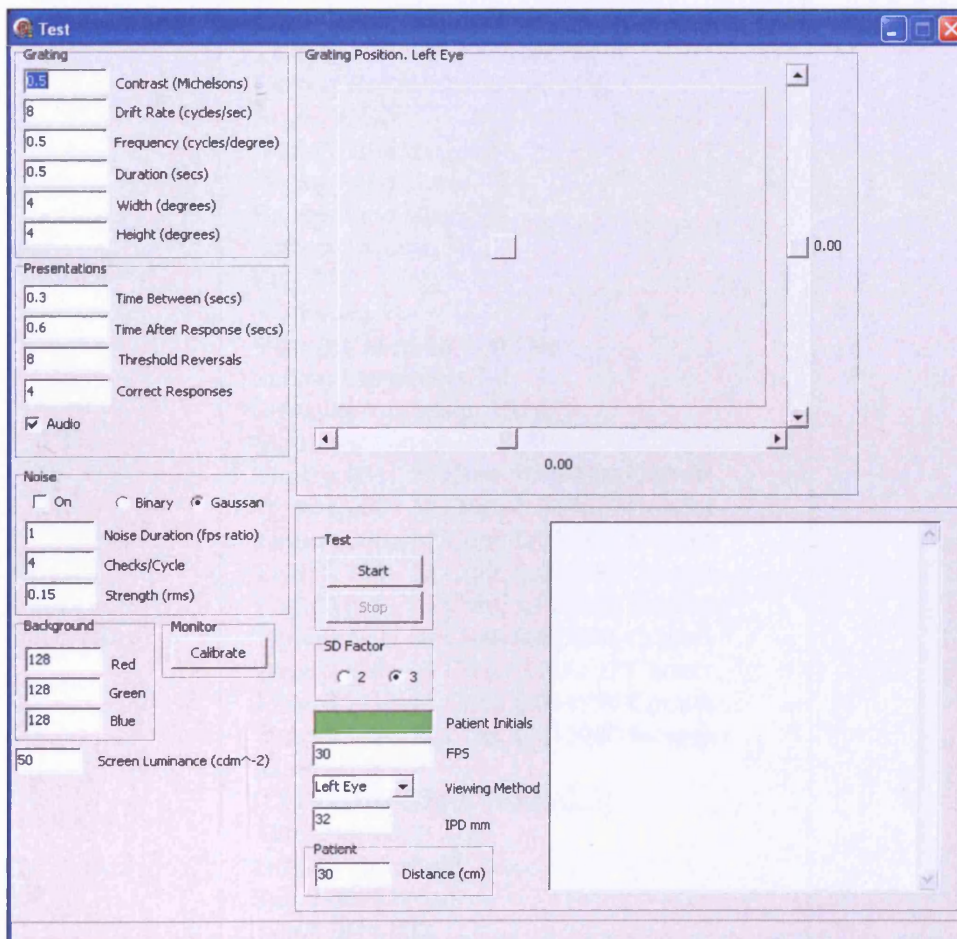


Figure 4.12 The operator interface menu, used to control stimulus and noise parameters throughout the preliminary study of dynamic noise and the clinical study of OAG.

In addition to stimulus and noise controls, the menu also had inputs for monitor luminance, stimulus onset and duration and participant data. At the end of each thresholding sequence, all inputs were extracted into log files to ensure that an accurate record of each participant threshold was retained. The log files were text summaries that recorded the entire threshold sequence, and an extract of one file is shown in Figure 4.12.

```
[INITIALS] [DATE] [TIME]
Contrast 0.06
Drift Rate 8
Frequency 0.5
Duration 0.5
Grating Width 4
Grating Height 4
Time Between Presentations 0.6
Time After Presentations 0.3
Threshold Reversals Required 8
Correct Responses Required 4
Audio is ON
Background Red 128
Background Green 128
Background Blue 128
PatientDistance 30
FPS 30
SD Factor 2
Viewing Method Left Eye
Screen Luminance 50
Stimulus x position 10.02
Stimulus y position -8.00
Time:0.031. M Cont: 0.060000 Correct
Time:0.000. M Cont: 0.047619 Correct
Time:0.000. M Cont: 0.037793 Correct
Time:0.001. M Cont: 0.029994 Correct
Time:0.000. M Cont: 0.023805 Incorrect
Time:0.127. M Cont: 0.023805 Correct
Time:0.000. M Cont: 0.018893 Correct
Time:0.218. M Cont: 0.014994 Correct
Time:0.333. M Cont: 0.011900 Incorrect
Reversal 1
[CONTINUED REVERSALS]
Threshold: 0.012763
GOOD Threshold
SD: 0.003318
Time: 0:44.032
```

Figure 4.13 An extract of one log file from the testing phase of development, used to record all parameter inputs and the sequence of the thresholding algorithm. These files ensured an accurate record of each measurement.

The software and hardware were continually tested until the calibration, threshold algorithm and interface were considered optimal. Thereafter, the preliminary study of dynamic noise was initiated.

5 The spatial limits of the dynamic noise mask

As has been discussed earlier (Chapters 2 and 3), the internal noise levels of the visual system can be estimated by measuring the contrast detection thresholds of a sine wave grating in the presence of an external noise mask (Legge et al., 1987). This method requires a noise source that is external to the visual system. A quantifiable source of external noise can be created using an array of pixels in which a two-dimensional pattern of noise checks follows random variations in luminance in the spatial domain (Pelli, 1981; Pelli, 1990). An analogue of internal noise can be achieved by random temporal variation of noise check luminance which produces spatio-temporal, or dynamic, noise. The resulting dynamic noise can be quantified spatially and temporally, and in terms of luminance, by the size of the individual noise checks, the temporal modulation of the checks, and by the differing levels of contrast, respectively.

Detection thresholds of a two-dimensional sine wave grating can be measured in terms of contrast and/ or stimulus energy. Detection thresholds are elevated in the presence of a strong two-dimensional external noise mask (Burgess et al., 1981; Pelli, 1981; Legge et al., 1987; Pelli, 1990). The noise mask only elevates detection thresholds beyond a certain noise spectral density. Beyond this density, the ratio of threshold stimulus energy to noise spectral density is a constant, known as the signal-to-noise ratio (SNR) (Pelli, 1981; Pelli, 1990). As the spectral density of the mask increases, stimulus energy at threshold also increases, maintaining a constant SNR (Nagaraja, 1964; Pelli, 1981; Luntinen et al., 1995). The strength of a noise mask, spectral density, is defined by several parameters; the root mean square (rms) contrast, the size of the noise check and, in the case of dynamic noise, the duration of the noise check (Legge et al., 1987). An external noise mask can be made

more effective by increasing the size of the noise check, and/ or by increasing the temporal duration of the noise check luminance, and/ or by increasing the rms contrast of the noise image.

To ensure that the noise mask is the limiting factor in grating detection (i.e. the cause of reduced visibility), unmasked contrast detection thresholds need to be elevated by a factor of at least three, when measured in the presence of the noise mask (Kukkonen, 1994; Pelli and Farell, 1999). This three-fold elevation ensures that the internal noise of the visual system accounts for only 25% of the stimulus energy level, thereby, ensuring that the external noise source is the dominant cause of threshold elevation. A two-fold elevation ensures that 50% of the threshold is determined by internal noise, i.e. the internal and external noise account for equal degradation of the stimulus (Kukkonen, 1994).

5.1 Spatial limitations of white pixelated noise

The external noise that effectively masks an underlying stimulus is frequently termed ‘white’ noise. Theoretically, ‘white’ noise has a constant spectral density for all stimulus spatial frequencies. However, noise can only be considered to be ‘white’ within a limited spatial and temporal bandwidth, and so the parameters for which this is possible must be determined experimentally. Within the given bandwidth, the external noise mask is considered to be effective. The effective parameters of spatio-temporal noise are directly related to the spatial frequency of the underlying sine wave grating (Carter and Henning, 1971; Stromeyer and Julesz, 1972; Pelli, 1981).

5.2 Aim: Pilot study of the spatial limits of dynamic noise

Clinical investigations of the visual system require a high strength noise mask which is not always achievable using a Cathode Ray Tube (CRT) monitor. In the case of the noise checks, the rms contrast is limited by the capabilities of the monitor and the graphics card, especially when the noise checks are superimposed upon a high contrast grating. The dynamic contrast range of the display is limited by a specific number of grey levels, ranging from white to black. The 'colour' of specific checks cannot exceed a certain level of grey, which will appear as an absolute level of black. For example, when the noise mask is superimposed onto a sine wave grating, the resultant colour of each check within the image will be the sum of the noise check colour and the corresponding regions of the underlying grating. If a dark check is superimposed onto a dark segment of the grating, the resultant check will exceed the contrast limits of the display and will be presented in a random colour.

The relationship between the spatial parameters of the noise mask and the spatial parameters of the underlying sine wave grating has been investigated with respect to stationary gratings and flickering sine wave gratings (Kukkonen et al., 1995; Rovamo et al., 1996). However, the effect of a noise mask on drifting gratings is unknown, particularly with respect to the critical size of the noise check. It was considered necessary to conduct a pilot study into the spatial limits of a noise check in the presence of a drifting grating.

The purpose of the study, therefore, was to determine the spatial limits of noise check size, when masking spatially and temporally modulated gratings, and to compare the outcome relative to that of a stationary grating.

5.3 Methods

Contrast detection tasks were designed to determine the detection threshold in the presence and in the absence of a spatio-temporal noise mask.

5.3.1 Stimuli

The stimuli consisted of a square patch of vertically presented sine wave gratings with sharply bordered edges. The gratings were presented at the centre of the display screen. The average luminance of the gratings was identical to the average luminance of the surround. Given that further studies were planned for the investigation of OAG, a grating temporal frequency of 16Hz was chosen for this study based on previous psychophysical (Willis and Anderson, 2000; Ansari et al., 2002b) and histological studies of magnocellular stream damage in OAG (Wilson, 1985; Pasternak and Leinen, 1986; Merigan and Maunsell, 1990).

The examination was undertaken in the absence of external illumination to maintain a constant screen luminance and to avoid reflections from the screen surface (Krantz, 2000). The size of the stimulus remained constant at 4° by 4° and the perceived spatial frequency was altered by changing the viewing distance from 29cm to 229cm. The given distance was maintained as near as was possible by a chinrest and the resulting spatial frequencies were 1 and 8 cycles per degree. The duration and the contrast of the noise were both kept constant. Therefore, the theoretical noise spectral density was considered proportional to the check size. To ensure that each noise check changed in luminance at a rate which disrupted the underlying grating, noise duration was kept equal to 30 frames per second to match the frame rate of the software. Noise rms contrast was varied between 0.2 and 0.3

depending upon the stimulus since stationary stimuli were more difficult to mask than temporally modulated stimuli. The choice of noise contrast does not affect the spatial limits of the noise check, however, as the value is dependent on the signal to noise ratio (SNR) which is independent of the noise contrast.

A two-interval forced choice task was used to determine threshold. The two stimulus presentations, each lasting 500ms, were separated by 600ms and the individual was required to choose the presentation that contained the grating by pressing either number '1' or number '2' on a conventional keyboard. Succeeding pairs of stimuli were presented 250ms after the previous response. An auditory cue was used to alert the individual to the imminent presentation of the stimulus. A different auditory signal was used to indicate a correct response and provided positive feedback.

The study utilised a twenty seven year old normal individual who was highly experienced in psychophysical experiments. The individual underwent a comprehensive ophthalmic examination involving refraction, visual acuities, intraocular pressure, anterior segment examination, slit lamp biomicroscopy of the ONH and fundus, and threshold perimetry of the central field. The individual had a distance visual acuity of 6/5 in both eyes and healthy ONHs and fundi. Intraocular pressures were normal. There was a negative family history for OAG. The individual wore the full distance refraction for the threshold measurements, and the contralateral eye was occluded. Three threshold measurements were obtained for the stationary grating and three were obtained for the drifting grating. The results for each modality were expressed as the median. The order of measurements between the stationary and the drifting gratings was randomised.

For both stationary and drifting sine wave gratings, contrast detection thresholds increased in proportion to the spectral density of the pixelated noise mask such that the signal-to-noise-ratio (SNR) was constant. However, contrast thresholds eventually declined when the dimensions of the noise check size exceeded a critical size. At this point, the gratings became gradually more visible indicating that the noise was no longer effective as a mask.

5.4 Results

The stationary gratings of 1 and 8 cycles per degree were successfully masked, down to 3.6 and 3.5 noise checks per cycle, respectively. The stationary gratings of 1 and 8 cycles per degree are shown in Figures 5.1 and 5.2 respectively. Contrast detection thresholds were plotted as \log_{10} Michelson units (MC) against \log_{10} noise check size (in checks per cycle). The drifting gratings of 1 and 8 cycles per degree were successfully masked, down to 2.4 and 2.0 checks per cycle, respectively. It should be noted that all thresholds were measured in the presence of a noise mask, and that not all Figures are drawn to the same scale. The drifting gratings of 1 and 8 cycles per degree are shown in Figures 5.3 and 5.4 respectively. Critical noise check values were determined from the intersection between the ascending and descending least square lines. Noise check size and therefore noise spectral density declined along the abscissa. As such, the negative slope in each Figure corresponded to the region in which the SNR was constant and the noise mask was considered 'white'. The positive slope in each Figure corresponded to the region in which the SNR declined, as the grating became gradually more visible from beneath the noise mask. A minimum of two data points were sufficient for either slope, provided they indicated a deviation from a constant SNR.

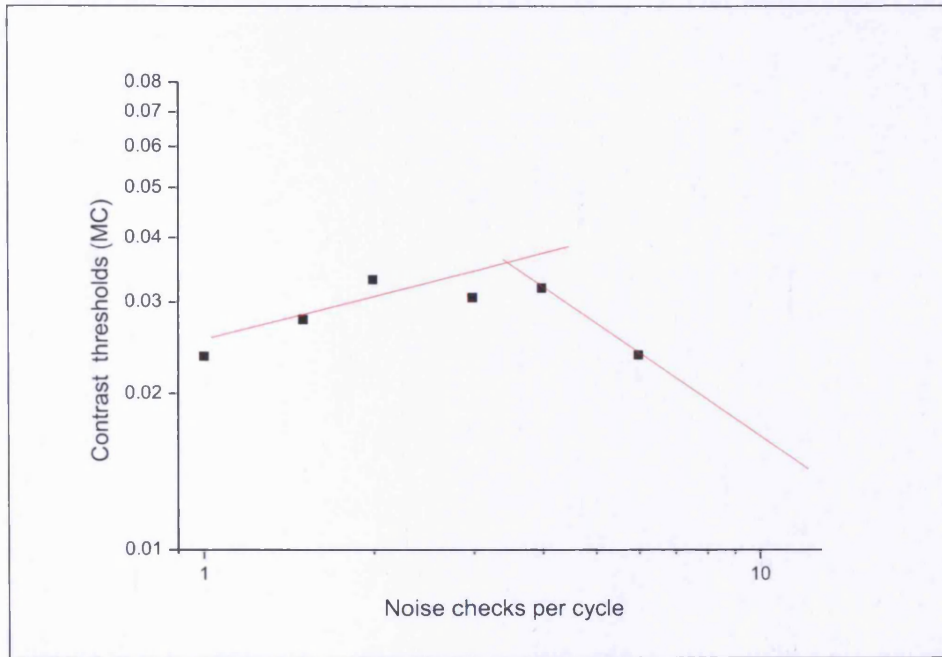


Figure 5.1 Log₁₀ of the Michelson Contrast threshold for the stationary sine wave grating of 1 cycle per degree against the size of the noise check (expressed as the number of noise checks per grating cycle).

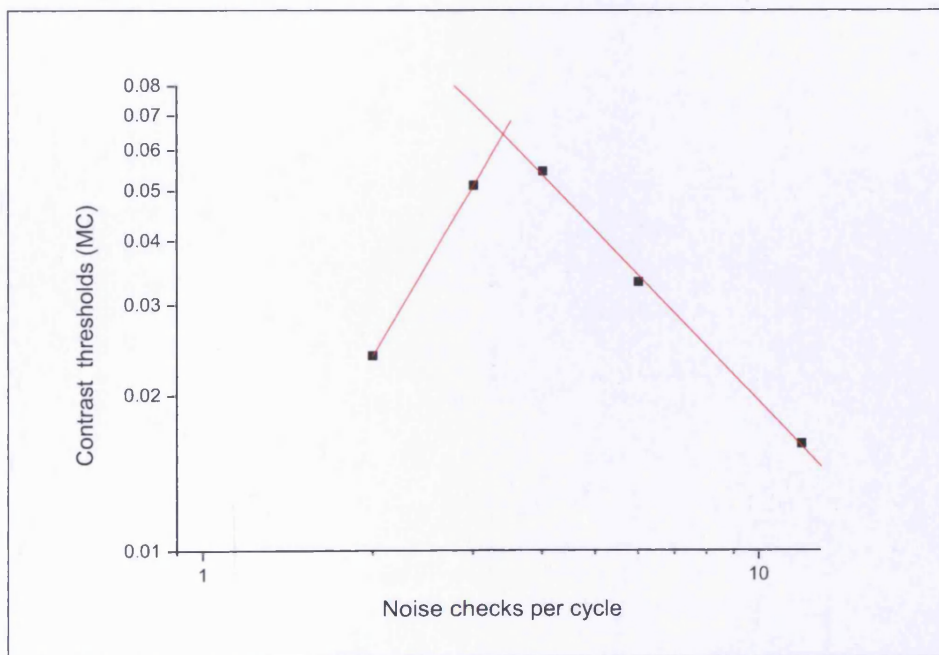


Figure 5.2 Log₁₀ of the Michelson Contrast threshold for the stationary sine wave grating of 8 cycles per degree presented against the size of the noise check (expressed as the number of noise checks per grating cycle).

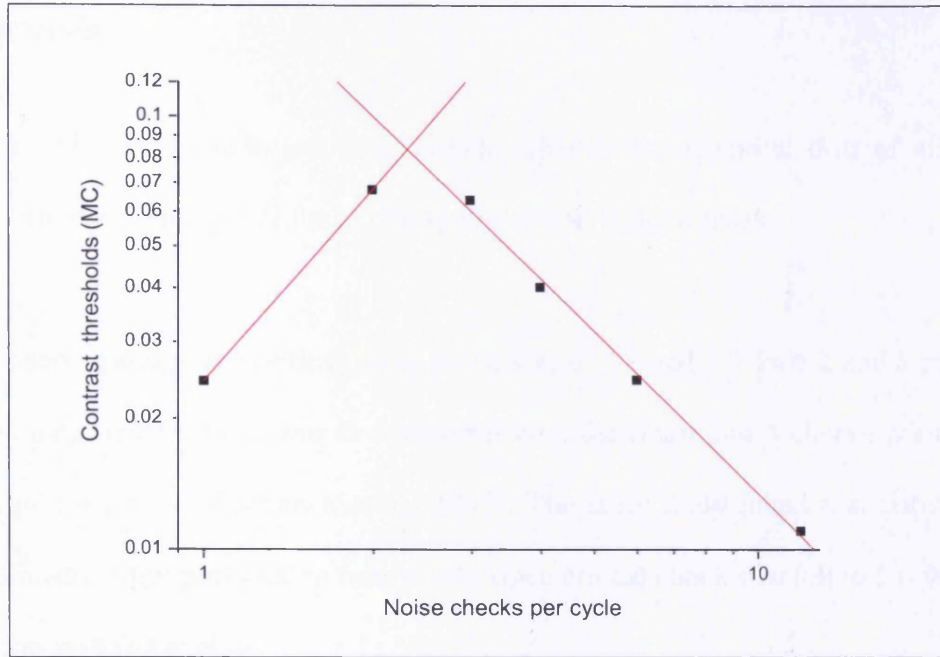


Figure 5.3 Log_{10} of the Michelson Contrast threshold for the drifting sine wave gratings (16 Hz) of 1 cycle per degree presented against the size of the noise check (expressed as the number of noise checks per grating cycle). Note the scaling of the ordinate is different to that in Figure 5.2.

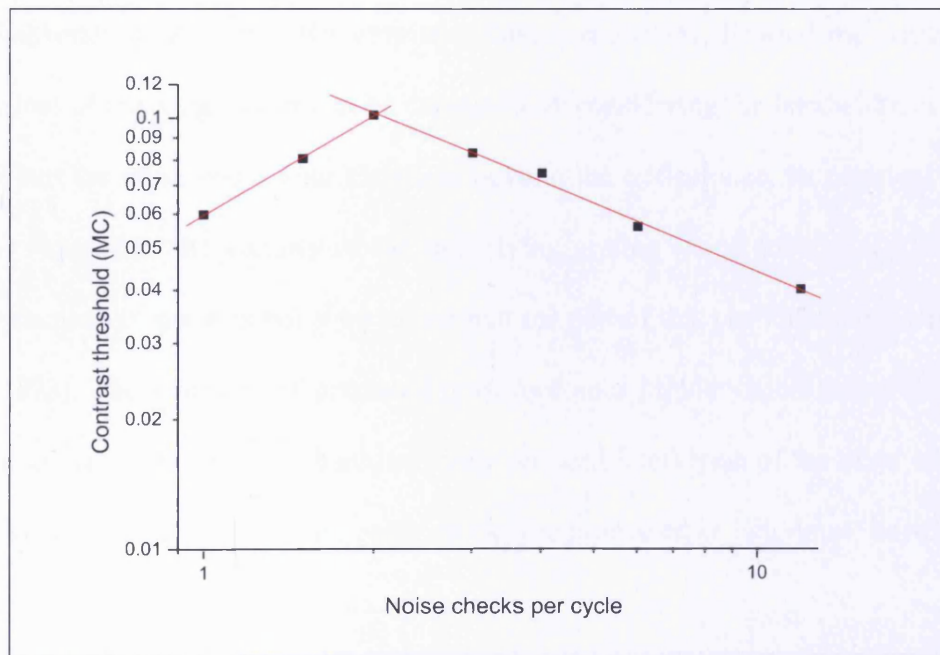


Figure 5.4 Log_{10} of the Michelson Contrast threshold for the drifting sine wave gratings (16 Hz) of 8 cycles per degree presented against the size of the noise check (expressed as the number of noise checks per grating cycle). Note the scaling of the ordinate is different to that in Figure 5.2.

5.5 Discussion

This pilot study was conducted to determine whether the temporal drift of sine wave gratings influenced the spatial limits of a spatio-temporal noise mask.

For stationary gratings, the critical noise check size of 3.6 and 3.5 for a 1 and 8 cycles per degree grating, respectively, was in agreement with the finding of 4 checks per cycle for gratings of 1-4 cycles (Kukkonen et al., 1995). The latter study found that critical check size was inversely proportional to bandwidth, since critical check size fell to 2.6 for spatial frequencies up to 64 cycles.

The present study, the masking effect of external spatio-temporal noise increased with the size of the noise check, in agreement with studies of external pixelated noise (Kukkonen, 1994; Kukkonen et al., 1995; Rovamo and Kukkonen, 1996). Beyond the critical check size, the loss of masking power can be explained by considering the bandwidth of external noise. When the noise check size increases beyond the critical size, its practical masking power is reduced in the vicinity of the underlying grating (Kukkonen et al., 1995). The ‘block structure’ of noise is believed to account for part of this phenomenon (Harmon and Julesz, 1973). The structure of pixelated noise becomes highly visible when check sizes are large and masking power is lost due to the reduced interaction of the pixel edges with the underlying grating. Instead, the noise checks are processed as ‘windows’ beyond which the grating becomes gradually more visible.

Since the findings of this pilot study were comparable to the findings of others (Kukkonen et al., 1995; Kukkonen et al., 2002) in the case of stationary gratings, it was reasonable to draw conclusions from the findings associated with drifting gratings. Critical check size

for the masking of the drifting grating decreased from 2.4 to 2.0 for respective spatial frequencies of 1 and 8 cycles per degree, modulated at 16Hz. These findings suggest that the critical noise check size is proportional to the temporal frequency of a drifting grating. The relative difference between the two critical values also suggests an inverse relationship with spatial frequency. In fact, this inverse relationship was more prominent in the case of drifting gratings, since there was a 0.4 difference in critical check per cycle values, compared with a 0.1 difference noted with the stationary gratings. It is possible that the bandwidth of spatio-temporal noise narrows more rapidly with increasing grating spatial frequency when the gratings are temporally modulated, given that critical noise check duration is reduced with increasing temporal flicker rate (Rovamo et al., 1996; Kukkonen et al., 2002).

In summary, the spatial cut-off for a two-dimensional, spatio-temporal mask is dependent upon the temporal parameters of the stimulus. The critical numbers of checks per cycle that mimic 'white' noise are lower for drifting gratings than for stationary gratings. This pilot study justified further investigation of the relationship between critical noise check size and grating drift frequency. Given that these were the findings of a pilot study, a further preliminary study was developed to validate these findings. The preliminary study investigated how critical check size varied with various grating spatial and temporal frequencies, and with retinal eccentricity.

5.6 Aim: Preliminary study of the spatial limits of dynamic noise

This study was developed to characterise the relationship between the spatial limits of a dynamic noise mask and the spatio-temporal parameters of a sine wave grating stimulus. The influence of stimulus eccentricity was considered given that glaucomatous functional damage manifests as visual field loss (Quigley and Addicks, 1981; Quigley et al., 1982; Quigley et al., 1989).

5.7 Methods

The study was undertaken using the apparatus described in Chapter 4, Section 4.1.2. Stimuli were generated using software developed by Dr Gavin Powell and the threshold algorithm was identical to that described in Chapter 4, Section 4.2.2.

5.7.1 Stimuli

The stimuli consisted of a square patch of vertical sine wave gratings with sharply attenuated edges (see Chapter 2, Figure 2.4). The gratings were presented, foveally, (at the centre of the CRT display screen) and in the superior nasal visual field at (-27, +4) in right eye format. The average luminance of the gratings matched the average luminance of the surround. The room had no source of illumination apart from the display. The size of the stimulus remained constant at 4° by 4° and the viewing distance was kept constant at 30cm. Distances were maintained by a chin and headrest.

Contrast detection thresholds were measured for a range of temporally drifting (0, 2 and 8 Hz) sine wave gratings. A maximum temporal frequency of 8 Hz was chosen to ensure that temporal modulation remained visible in the peripheral visual field. Grating spatial frequencies were 0.5 and 2.0 cycles per degree at the fovea, and 0.5 cycles per degree at the nasal periphery.

5.7.2 Subjects

Four individuals from 22 to 28 years were recruited: MD, JS, RR and CH. All individuals were highly experienced in visual psychophysical experiments. The individuals underwent a comprehensive ophthalmic examination involving refraction, visual acuities, intraocular pressure, anterior segment examination, slit lamp biomicroscopy of the ONH and fundus, and threshold perimetry of the central field. All individuals had corrected distance visual acuities of 6/5 in both eyes and healthy ONHs and fundi. Intraocular pressures were normal. There was a negative family history for OAG.

5.7.3 Procedure

Each subject was fully corrected with the distance prescription and the dominant eye was used. The contralateral eye was occluded. Results were based upon the median of three threshold measurements and the order of measurements between the stationary and the drifting gratings was randomised. The threshold at the fovea was derived from all four subjects, whilst that of the periphery was derived from three subjects.

Contrast thresholds were measured with and without spatio-temporal noise and the noise-masked gratings were determined for a range of noise check sizes. Noise masked

peripheral contrast thresholds could not be determined for sine wave gratings of 2.0 cycles per degree as this spatial frequency was difficult to resolve when masked with external noise, therefore the masked threshold contrast level exceeded the limits of the display. Noise duration and noise contrast were both kept constant for each type of grating stimulus. Therefore, the theoretical noise spectral density of noise was considered proportional to the check size. The noise duration was kept equal to 30 frames per second, matching the frame rate of the software. The noise rms contrast was set at 0.275 which was sufficiently high to mask the gratings at most check sizes, whilst allowing enough dynamic range for the underlying stimulus to be presented at supra threshold levels. The median of three separate thresholds was taken to indicate the final result for each subject. The median is preferred over the mean, as it reduces the impact of outliers. The order of measurements was randomised for all subjects.

5.8 Results

As with the pilot study, contrast thresholds initially increased in proportion to increasing noise strength. As the theoretical masking power of external noise continued to increase with check size, the practical limits were exceeded and the SNR began to fall.

Low spatial frequency sine wave gratings of 0.5 cycles per degree, drifting at 8.0, 2.0 and 0.5 Hz are shown in Figures 5.5, 5.6 and 5.7, respectively. Low spatial frequency gratings drifting at 8.0 Hz were masked down to 4.0 checks per cycle (Figure 5.5). Low spatial frequency gratings drifting at 2.0 Hz were masked down to 4.4 checks per cycle (Figure 5.6). Low spatial frequency gratings drifting at 0.5 Hz were masked down to 5.6, noise checks per cycle (Figure 5.7).

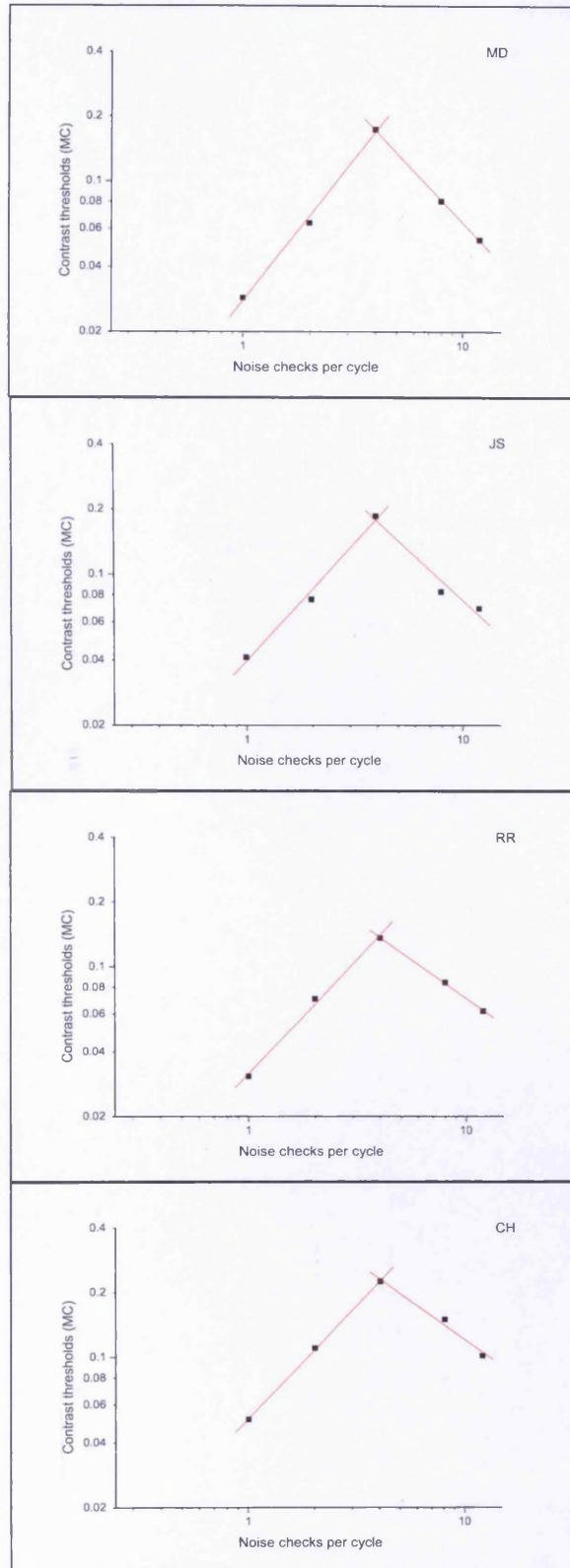


Figure 5.5 Log_{10} of the MC threshold for the drifting sine wave gratings (8 Hz) of 0.5 cycles per degree presented against the size of the noise check (expressed as the number of noise checks per grating cycle). Subject initials are indicated as MD, JS, RR and CH.

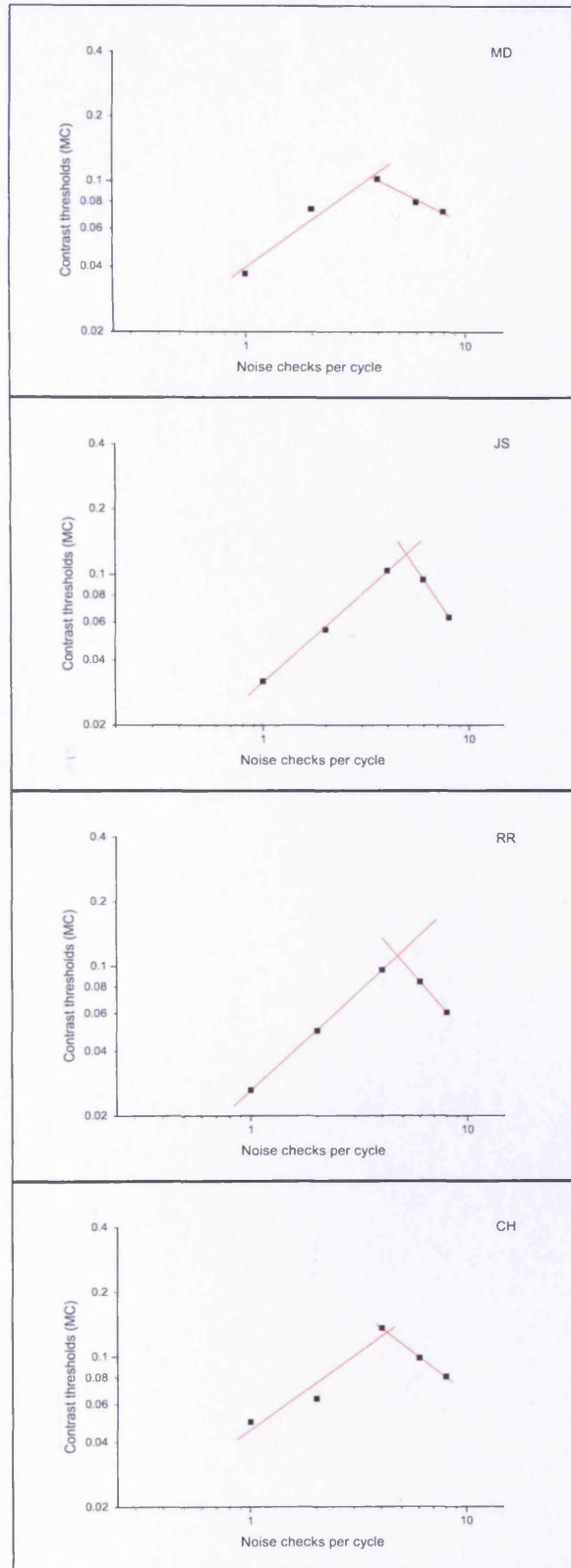


Figure 5.6 Log_{10} of the MC threshold for the drifting sine wave gratings (2 Hz) of 0.5 cycles per degree presented against the size of the noise check (expressed as the number of noise checks per grating cycle). Subject initials are indicated as MD, JS, RR and CH.

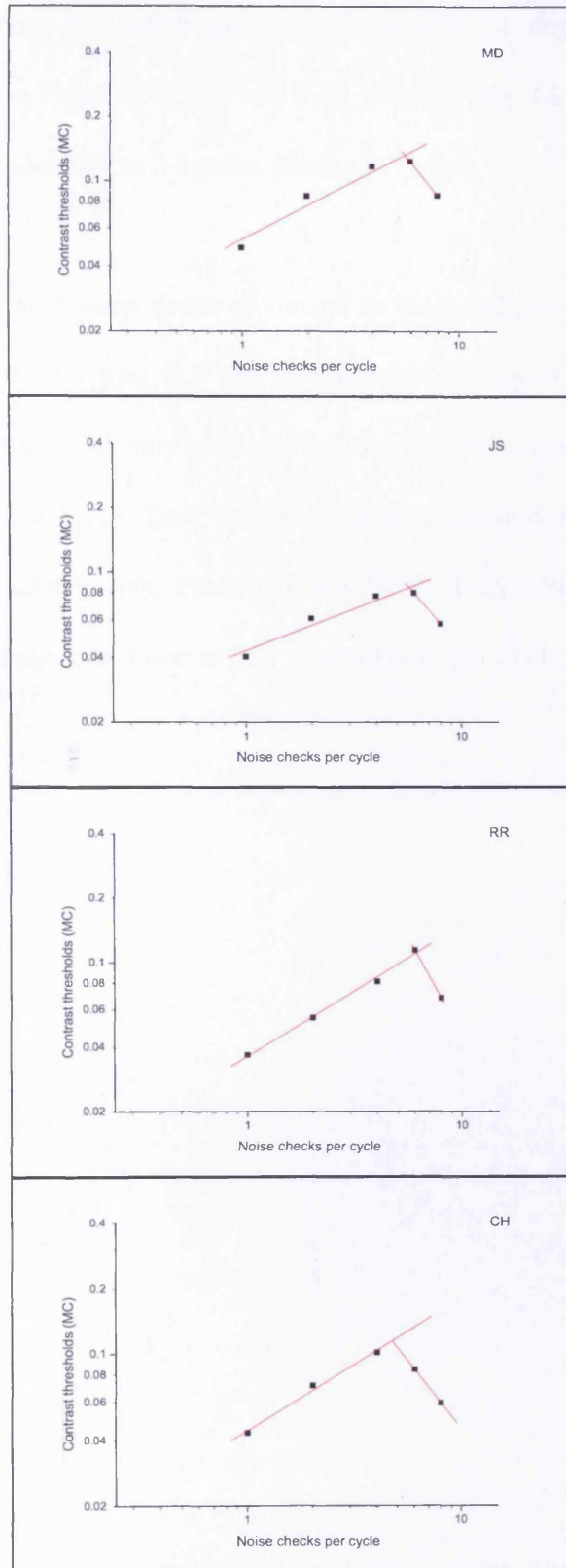


Figure 5.7 Log_{10} of the MC threshold for the drifting sine wave gratings (0.5 Hz) of 0.5 cycles per degree presented against the size of the noise check (expressed as the number of noise checks per grating cycle). Subject initials are indicated as MD, JS, RR and CH.

Medium spatial frequency sine wave gratings of 2.0 cycles per degree, drifting at 8.0, 2.0 and 0.5 Hz are shown in Figures 5.8, 5.9 and 5.10, respectively. Medium spatial frequency gratings were all masked down to 2.0 noise checks per cycle.

Low spatial frequency sine wave gratings viewed at the nasal periphery, of 0.5 cycles per degree, drifting at 8.0, 2.0 and 0.5 Hz, are shown in Figures 5.11, 5.12 and 5.13, respectively. Low spatial frequency gratings drifting at 8.0 Hz were masked down to 2.0 checks per cycle (Figure 5.11). Low spatial frequency gratings drifting at 2.0 Hz were masked down to 2.8 checks per cycle (Figure 5.12). Low spatial frequency gratings drifting at 0.5 Hz were masked down to 2.9, noise checks per cycle (Figure 5.13)

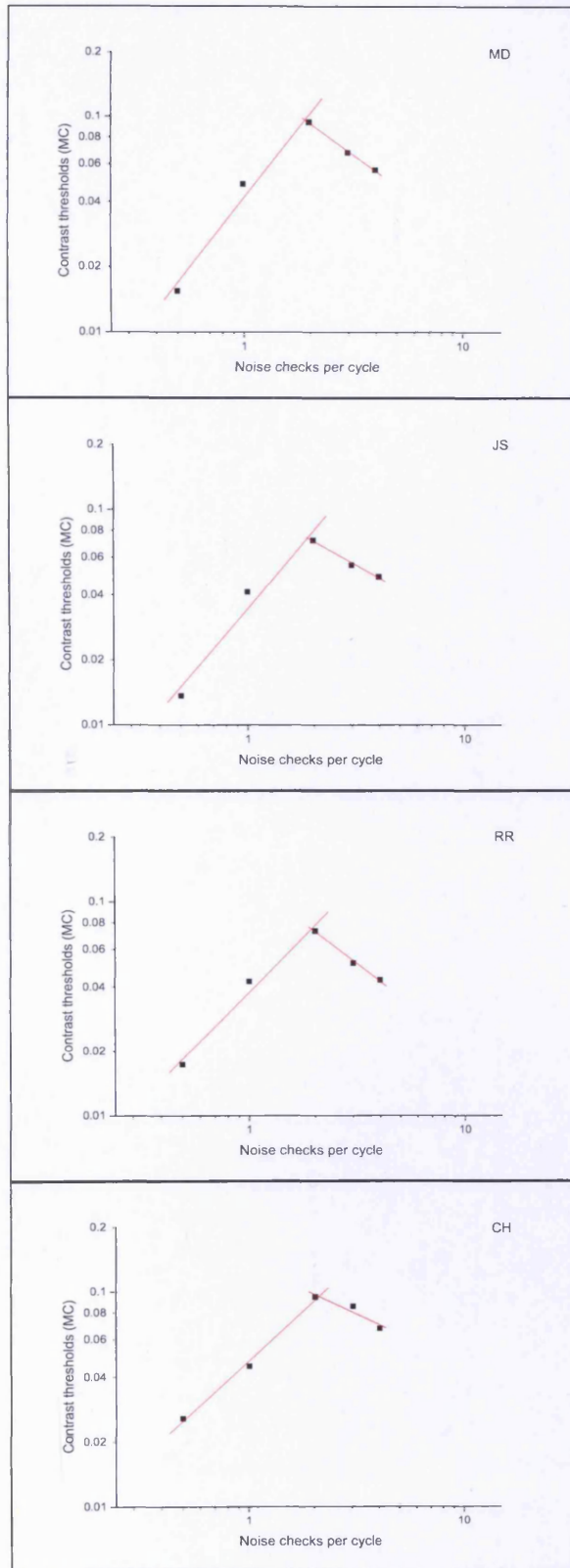


Figure 5.8 Log_{10} of the MC threshold for the drifting sine wave gratings (8 Hz) of 2.0 cycles per degree presented against the size of the noise check (expressed as the number of noise checks per grating cycle). Note the scaling of the ordinate is different to that in Figure 5.7. Subject initials are indicated as MD, JS, RR and CH.

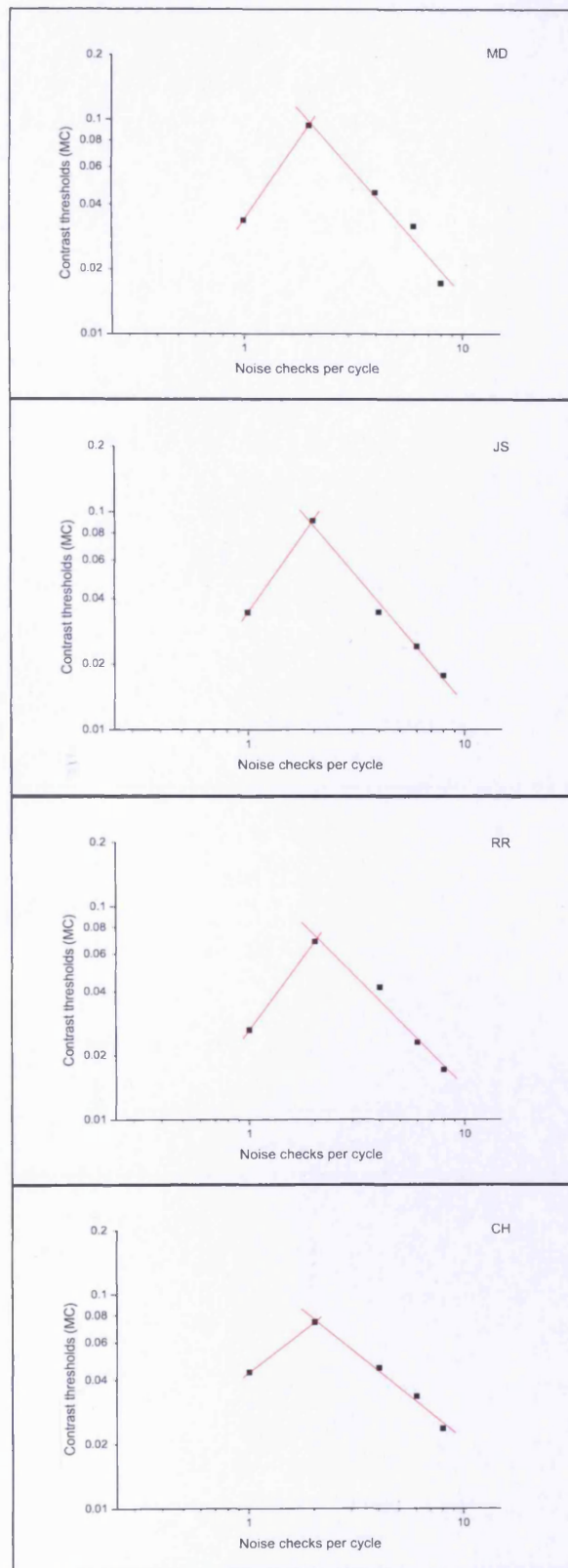


Figure 5.9 Log₁₀ of the MC threshold for the drifting sine wave gratings (2 Hz) of 2.0 cycles per degree presented against the size of the noise check (expressed as the number of noise checks per grating cycle). Note the scaling of the ordinate is different to that in Figure 5.7. Subject initials are indicated as MD, JS, RR and CH.

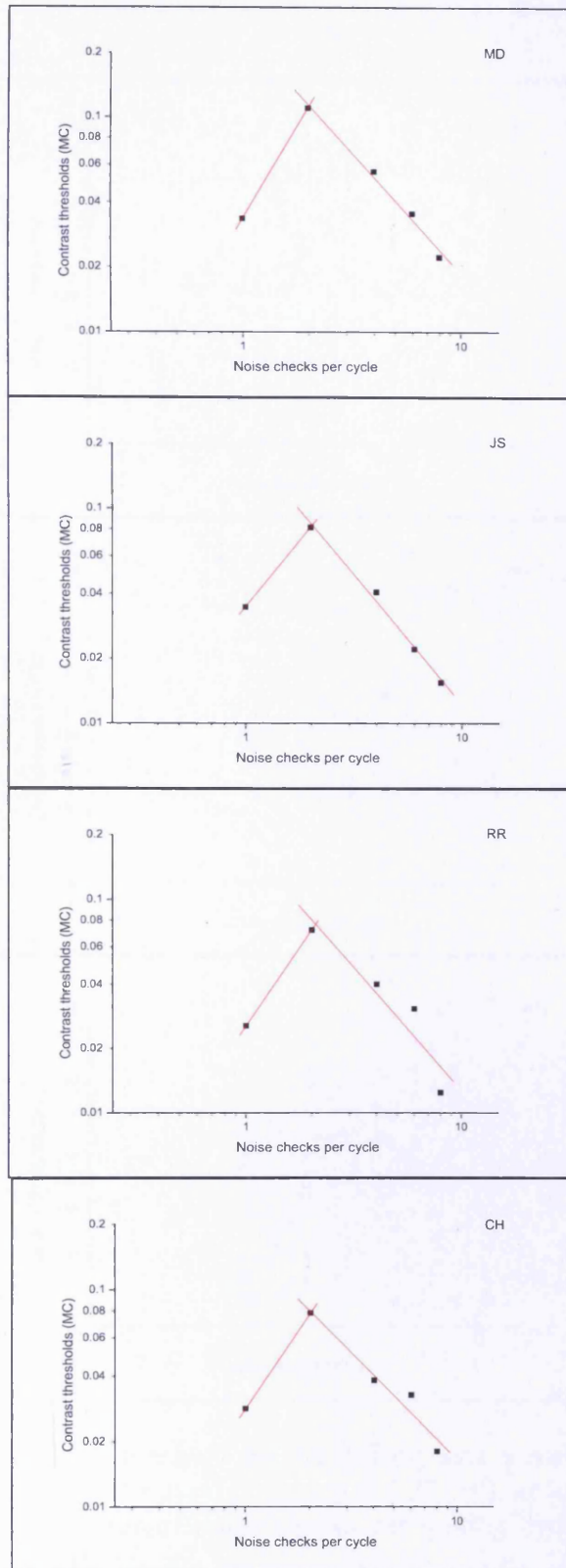


Figure 5.10 Log_{10} of the MC threshold for the drifting sine wave gratings (0.5 Hz) of 2.0 cycles per degree presented against the size of the noise check (expressed as the number of noise checks per grating cycle). Subject initials are indicated as MD, JS, RR and CH.

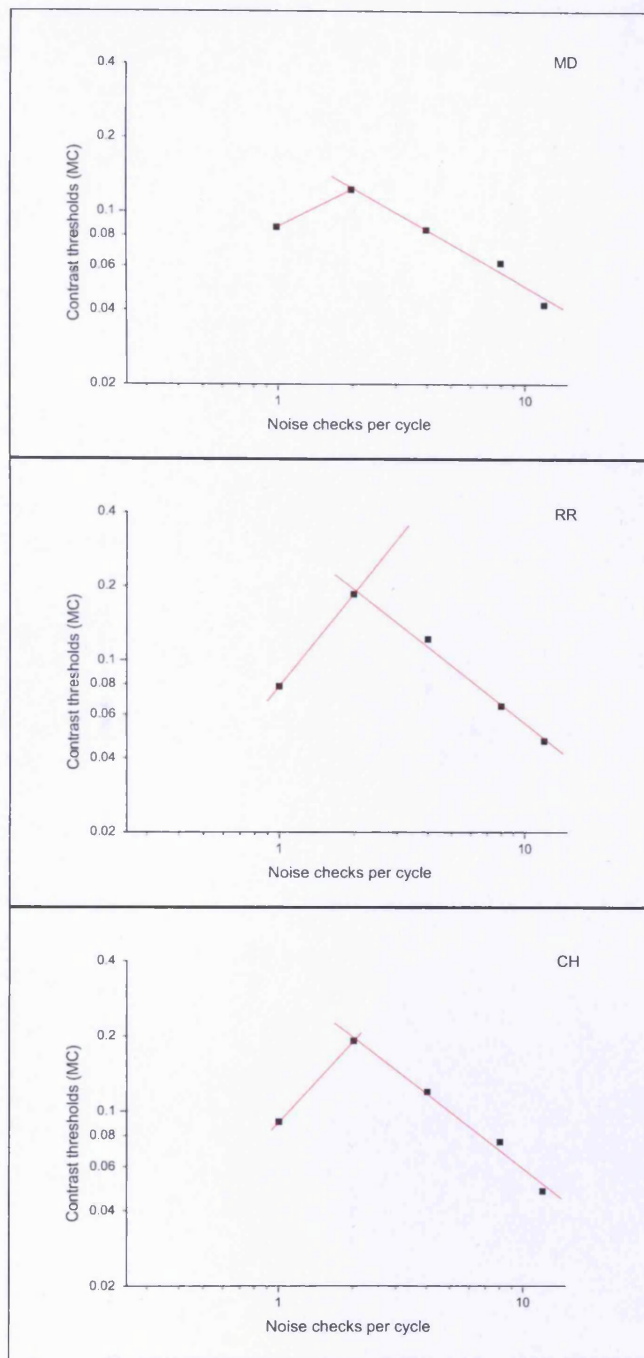


Figure 5.11 Log_{10} of the MC threshold for the drifting sine wave gratings (8 Hz) of 0.5 cycles per degree presented in the nasal periphery at (-27, +4), against the size of the noise check (expressed as the number of noise checks per grating cycle). Subject initials are indicated as MD, RR and CH.

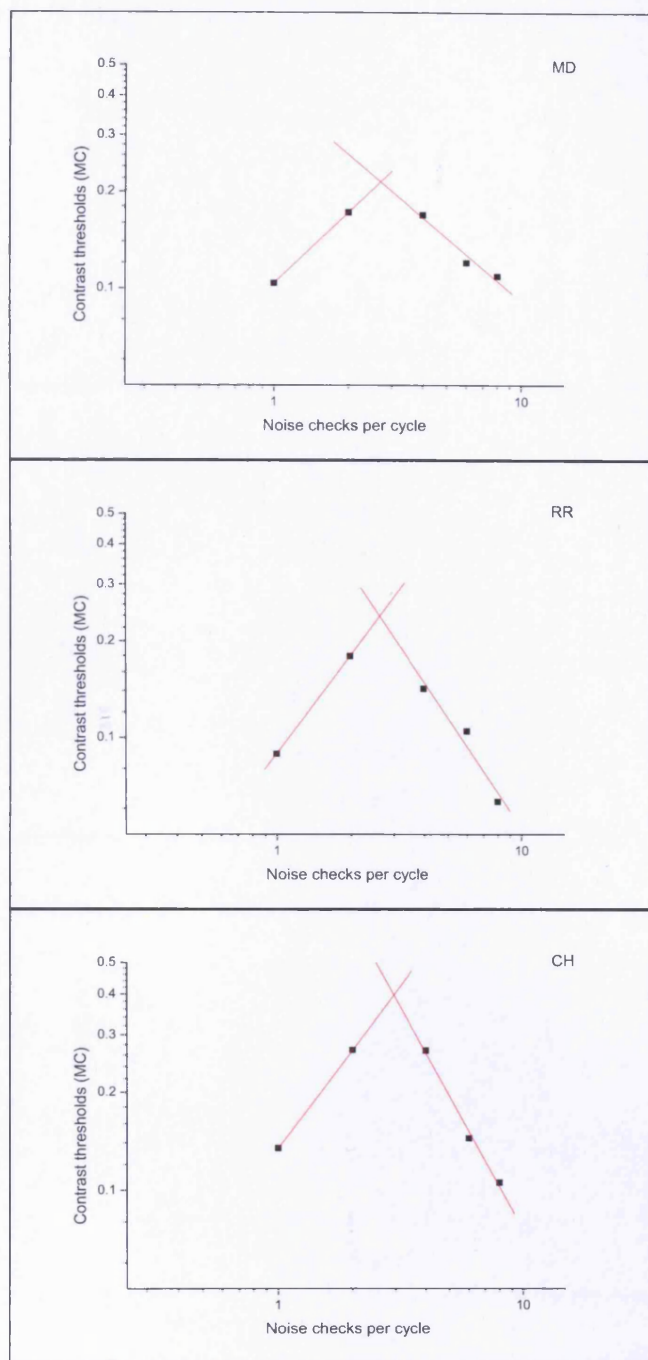


Figure 5.12 Log_{10} of the MC threshold for the drifting sine wave gratings (2 Hz) of 0.5 cycles per degree presented in the nasal periphery at (-27, +4), against the size of the noise check (expressed as the number of noise checks per grating cycle). Subject initials are indicated as MD, RR and CH.

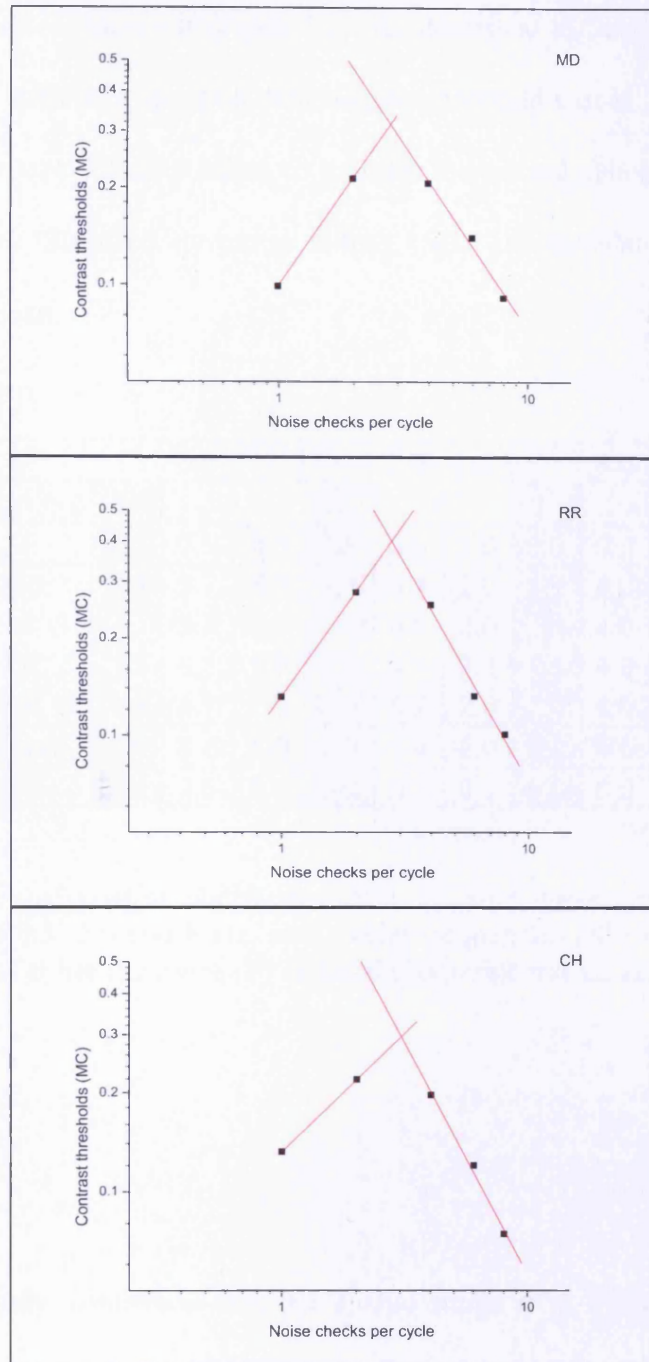


Figure 5.13 Log_{10} of the MC threshold for the drifting sine wave gratings (0.5 Hz) of 0.5 cycles per degree presented in the nasal periphery at (-27, +4), against the size of the noise check (expressed as the number of noise checks per grating cycle). Subject initials are indicated as MD, RR and CH.

A summary of results is shown in Table 5.1. As described in Section 5.7.3, the critical check size for each subject is based on their median threshold values. Thereafter, the mean of all critical check size values is taken to indicate the critical check size for each set of stimulus parameters. Standard deviation values (SD) are calculated as a measure of variance from the mean.

TF	0.5			2.0			8.0		
Location	N	F		N	F		N	F	
SF	0.5	0.5	2.0	0.5	0.5	2.0	0.5	0.5	2.0
MD	2.8	5.7	1.9	2.7	3.7	2.0	2.0	4.0	2.0
JS	-	5.7	2.0	-	4.9	2.0	-	4.0	1.9
RR	2.8	6.1	1.9	2.6	4.7	2.1	2.0	4.0	2.1
CH	3.0	4.7	2.0	3.0	4.2	2.0	2.0	4.0	2.1
Mean	2.9	5.6	2.0	2.8	4.4	2.0	2.0	4.0	2.0
SD	0.1	0.6	0.1	0.2	0.5	0.1	0.0	0.0	0.1

Table 5.1 Summary of critical check size data for sine wave gratings with temporal frequencies (TF) of 0.5, 2.0 and 8 Hz, and spatial frequencies (SF) of 0.5 and 2.0 cycles per degree located at either the fovea (F) or nasal (N) peripheral visual field.

5.9 Discussion

The preliminary study confirmed that the spatial limits of a dynamic noise mask are dependent on the temporal parameters of the underlying stimulus. For a sine wave of 0.5 cycles per degree, the critical check size (in terms of checks per cycle) decreased with increasing grating temporal frequency. The result was consistent between low spatial frequency gratings presented at the fovea and low spatial frequency gratings presented at the nasal location of the visual field. For sine wave gratings of 2.0 cycles per degree, the critical check size was unaffected by increasing grating temporal frequency. However,

critical check size fell when the grating stimulus was viewed eccentrically, for both grating spatial frequencies of 0.5 and 2.0 cycles per degree.

The spatial limits of a dynamic noise mask are influenced by a reduction in noise spectral density in the vicinity of the spatial frequency of the grating (Kukkonen et al., 1995). For drifting sine wave gratings, it is reasonable to conclude that increasing the temporal frequency (i.e. the grating drift rate) will confound the 'window effect' which usually occurs when individual noise checks become large enough to see the underlying stimulus (Harmon and Julesz, 1973). Why are drifting gratings more difficult to resolve when masked by spatio-temporal noise? The perceived spatial frequency of the grating can change as its temporal frequency increases; this will in turn alter the spatial cut-off of the noise mask. Perceived spatial frequency is known to change when gratings are drifted at certain temporal frequencies. An example of this is the frequency doubling illusion, in which a low spatial frequency sine wave grating appears to have doubled in spatial frequency, when modulated at moderate to high temporal frequencies (Kelly, 1966, 1981b). The illusion does not extend to moderate spatial frequency sine waves, which may explain why critical check size was unaffected by temporal frequency when masking gratings of 2.0 cycles per degree. Seminal work by Kelly (1966) indicates that this subjective phenomenon occurs over a limited range of spatial frequencies. In the latter study, the phenomenon only extended up to 2.0 cycles per degree when the grating was modulated at temporal frequencies that exceed 18 Hz, which is far higher than the 8 Hz within this study.

It should be noted that the results of the pilot study (Section 5.4) contradict the suggestion that higher spatial frequency gratings are unaffected by temporal drift. Results of the pilot

study show that a stationary sine wave grating of 8 cycles per degree was masked down from 3.5 to 2.0 checks per cycle, when drifted at 16Hz. For reasons explained, this cannot be attributed to the frequency doubling illusion. It is more practical to conclude that grating resolution was impaired due to the temporal drift rate of 16 Hz, when compared with the temporal drift of 8 Hz that was used in the current study. It is reasonable to conclude that significantly more disruption to visual processing occurs at a temporal frequency of 16 Hz, when compared with 8Hz.

The critical check size was smaller at the periphery than corresponding values at the fovea. At 8 Hz, the critical check size at the periphery was 2.0 checks per cycle versus 4.0 checks per cycle at the fovea. In simpler terms, larger checks were capable of masking the same grating stimulus at the periphery, when compared with the fovea. The difference is likely to be explained by sine wave grating resolution at the periphery, in the absence of M-scaling (Rovamo et al., 1992). A decrease in sampling density of retinal ganglion cells is known to occur with increased retinal eccentricity (Rovamo and Virsu, 1979; Virsu and Rovamo, 1979). For the spatial resolution of sine wave gratings, increasing eccentricity is similar to the effect of increasing viewing distance (Rovamo et al., 1992). It follows that a sine wave grating which appears to be further away will be perceived to have a higher spatial frequency. This phenomenon may explain why the critical check size values for a 0.5 cycle per degree grating at the nasal periphery, are comparable to critical values for a 2.0 cycles per degree sine wave grating at the fovea; the 0.5 cycle per degree grating may be 'perceived' as a 2.0 cycles per degree grating.

The temporal parameters of a stimulus are known to affect the spatial limits of a dynamic noise mask (Rovamo et al., 1996; Rovamo et al., 2000; Kukkonen et al., 2002). Although

duration was known to impact the masking potency of dynamic noise, it was found that increasing check duration above the current rate of 30 frames per second, reduced contrast thresholds. This indicated that the software was already operating at the temporal limits of the noise mask and that this aspect of the mask was optimised.

Clearly, the pilot and preliminary studies indicate that the optimal parameters of a spatio-temporal noise mask are directly related to the temporal parameters of an underlying stimulus. The results of these studies can be used to define the parameters of an effective noise mask for a range of temporally modulated sine wave gratings. An optimised noise mask enables a CRT monitor to be used for further clinical studies without exceeding the dynamic range of the display. This is particularly important for the clinical investigation of OAG.

6 Clinical application of Dynamic Noise Perimetry

It was shown in Chapter 4 that TCS measures were elicited from four normal individuals, at the foveal location and in the nasal peripheral field at -24° , 3° , to determine the optimal characteristics of the dynamic noise mask. Clearly, however, there was a pressing need to investigate the feasibility of DNP (i.e. the measure of Michelson contrast thresholds in the absence of noise ($MC N_0$) and in the presence of noise ($MC N_e$); and equivalent noise (N_{eq}) and Sampling efficiency (SE) in normal individuals, with no previous experience of psychophysics, with particular reference to the presence of a learning effect, the effect of age and to the establishment of confidence limits for normality. In addition there was a similar need to undertake an identical investigation, in parallel, on a cohort of individuals with varying degrees of OAG.

The specific aims of the two studies were:

1. To determine the presence of any learning effect on the motion detection and motion discrimination paradigms in a group of normal individuals and in a group of individuals with OAG.
2. To determine the effect of age on the motion detection and motion discrimination paradigms in the same group of normal individuals.
3. To establish appropriate confidence intervals for normality for the motion detection and motion discrimination paradigms.

4. To validate DNP in individuals with OAG for both the motion detection and motion discrimination paradigms, in comparison with standard automated perimetry and with RNFL thickness as measured by OCT.

6.1 Cohort

6.1.1 Normal individuals

Twenty consecutively presenting normal individuals ranging in age from 51 to 84 years (mean age 64.25 years, SD 9.61) were recruited from those attending the Eye Clinic at the Cardiff School of Optometry and Vision Sciences. All individuals underwent comprehensive ophthalmic examination including ophthalmic history, refraction, determination of visual acuity, threshold perimetry of the central field, tonometry, anterior segment examination and slit lamp biomicroscopy of the ONH and fundus following dilation with 1% Tropicamide. Seven additional younger normal individuals were recruited at a later stage to increase the range of the age group. The age of these additional normal individuals ranged from 15 to 29 years (mean age 25.29 years, SD 4.86).

Exclusion criteria for all individuals were the presence of ocular disorder and/ or disease; diabetes; a positive family history of OAG; any systemic medication known to affect the visual field; visual acuity of worse than 6/9 in each eye; intraocular pressures, un-corrected for the effect of central corneal thickness, greater than 21mmHg; and a crystalline lens appearance not greater than nuclear colour (NC) 2.0, nuclear opalescence (NO) 2.0, cortical (C) 1.0, or posterior subcapsular (P) 1.0 according to the Lens Opacity Classification System (LOCS) III (Chylack et al., 1993).

6.1.2 Individuals with OAG

Ten individuals with OAG were recruited from the Cardiff Eye Unit at the University Hospital of Wales, Cardiff. The cohort deliberately comprised 7 individuals with early stage OAG and three individuals with advanced OAG. The latter were used to ensure that DNP was capable of identifying locations of obvious damage. The age range of the individuals with OAG ranged from 51 to 79 years, (mean age 61.04 years, SD 10.04). All individuals exhibited an ONH characteristic of OAG (including increase in cup size, increase in cup to disc ratio, disc asymmetry, changes in the LC, loss of NRR, pallor, evidence of peripapillary atrophy, vessel changes or disc margin haemorrhage). All patients were under the care of Mr James Morgan, Consultant Ophthalmologist and were being treated with ocular hypotensive medication. The characteristics of the individuals with OAG are described in Table 6.1. OCT and SAP was conducted by the Candidate and ONH images were acquired by Mr James Morgan.

Exclusion criteria were similar to those for the normal individuals, i.e. an ocular disorder and/ or disease, other than OAG; diabetes; any systemic medication known to affect the visual field; visual acuity of worse than 6/9 in each eye; and a crystalline lens appearance not greater than nuclear colour (NC) 2.0, nuclear opalescence (NO) 2.0, cortical (C) 1.0, or posterior subcapsular (P) 1.0 according to the Lens Opacity Classification System (LOCS) III (Chylack et al., 1993).

Ethical approval for the study was obtained from the South East Wales Research and Ethics Committee. Individuals gave written informed consent prior to taking part in the study.

Case #	ONH	Pattern deviation	OCT RNFL	OCT segment analysis
1 LE				
2 LE				
3 RE				
4 LE				
5 RE				
6 RE				
7 LE				
8 LE				
9 LE				
10 RE				

Table 6.1 The optic nerve head, the Pattern Deviation probability map, the RNFL Thickness Chart and the Sector and Quadrant Averages for the ten individuals with OAG.

6.2 Methods

The hardware and software was broadly comparable to those used in Chapter 5. However, several modifications were made for the purposes of the clinical studies. The software was upgraded to enable a motion discrimination paradigm. The previous studies had involved a two-presentation motion detection task for threshold determination in which the individual indicated whether the stimulus was present in the first or second image. The discrimination paradigm allowed a response to be measured on the basis of one presentation, thereby reducing examination duration by approximately 50%. For the clinical studies of normal individuals and of individuals with OAG, both the motion detection and the motion discrimination paradigm were used. The hardware was correspondingly modified to allow individuals to respond to the motion discrimination task. This required the assignment of two response buttons from the numerical keypad configured for individual responses.

6.2.1 Stimuli

Stimuli were comparable to previous studies (Chapter 5) and comprised a square patch (4° by 4°) of vertically orientated sine wave gratings. The edges of the patch had sharply bordered edges. For the purpose of the clinical studies, the square patch was located on a grid comparable to that of SAP. The stimulus grid is shown in Figure 6.1. Stimuli were offset from the vertical and horizontal meridians by 4° and 2° , respectively, in order to reduce the impact of eye movements on the threshold at stimuli adjacent to each mid-line. The grid included a foveal stimulus and enabled the presentation of stimuli out to 30° horizontally and 24° vertically.

The average luminance of the gratings was 50cd/m^2 , which was identical to the average luminance of the surround. The grating spatial frequency was fixed at 0.5 cycles per degree and the grating drift rate was 8Hz. The noise check size was 4 checks per grating cycle. The temporal frequency of the noise mask was determined by the maximal frame rate of the monitor, at 30 frames per second. The description of the validation of the optimal check size and duration is given in Chapter 5.

Stimuli were presented at five specific locations within the visual field (0, 0), (+10, +8), (+10, -8), (-10, +8) and (-10, -8), representing the fovea and each of the four quadrants of the visual field, respectively (Figure 6.1).

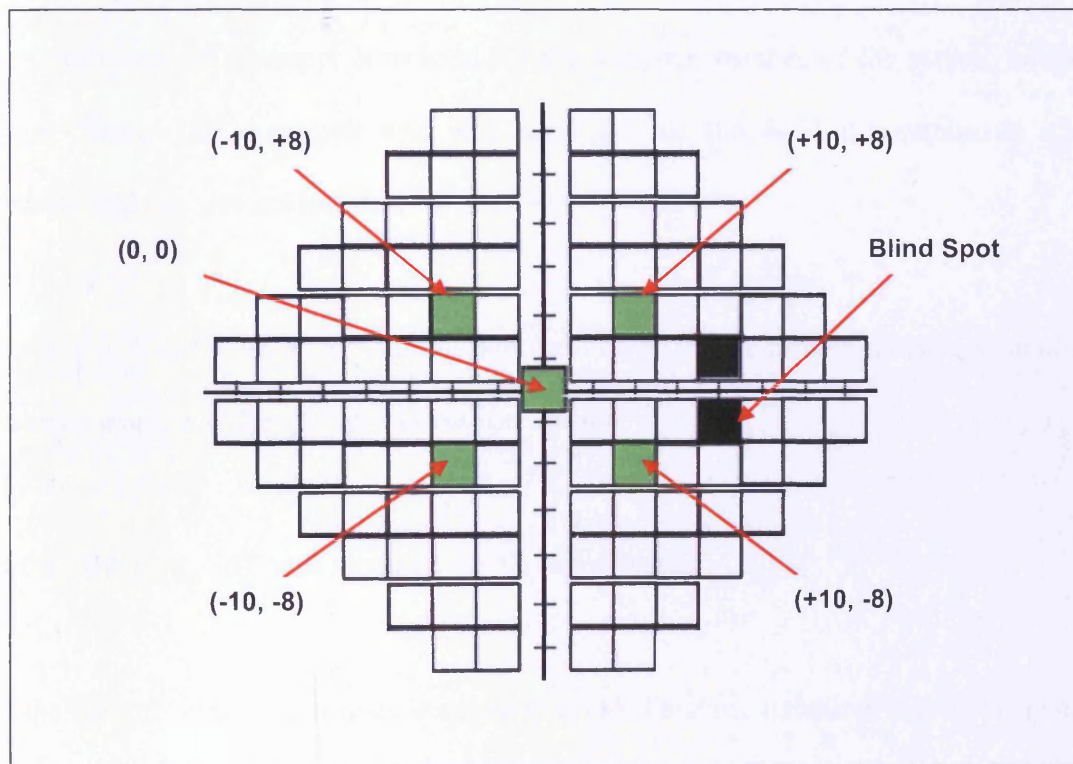


Figure 6.1 The stimulus grid for DNP, in right eye format. The stimuli are offset by 4° from either side of the vertical meridian and by 2° from either side of the horizontal meridian. Stimulus locations extend out to 30° eccentrically along the horizontal meridian and to 24° eccentrically along the vertical meridian. The five stimulus locations used in the clinical studies are indicated. The locations involving to the blind spot are highlighted in black.

6.2.2 Procedure

At the first visit, all individuals underwent a preliminary examination as described in Section 6.1.1. Threshold perimetry was undertaken using the SITA Standard algorithm and Program 24-2 of the Humphrey Field Analyzer 750 (Carl Zeiss Meditec, Dublin, CA, USA).

At the second visit, individuals completed a familiarisation session with DNP using the motion detection paradigm. Contrast thresholds were elicited for all stimulus locations in the absence of noise (MC N_0) and in the presence of noise (MC N_e). The order of stimulus locations was randomised for all threshold measurements as was the order of noise and no noise. Thus, a total of ten thresholds were measured. Individuals wore a near correction for the threshold measurements optimised for the viewing distance of the screen, which was set at 30cm. The dominant eye was used for all threshold measurements and the contralateral eye was occluded.

At visits 3, 4 and 5, each individual underwent DNP for the motion detection paradigm in the same manner as for the familiarisation session.

At the sixth visit, SAP was repeated for all individuals.

At the seventh visit, individuals completed a familiarisation session with DNP using the motion discrimination paradigm. Contrast thresholds were elicited for all stimulus locations in the absence of noise (MC N_0) and in the presence of noise (MC N_e). The order of stimulus locations was randomised for all threshold measurements as was the order of noise and no noise. Thus, a total of ten thresholds were measured.

At visits 8, 9 and 10, each individual underwent DNP for the motion discrimination paradigm in the same manner as for the corresponding familiarisation session.

At the last visit, visit eleven, RNFL thickness was determined using the Stratus OCT (Carl Zeiss Meditec, Dublin, CA, USA), using the 3.4 scan diameter RNFL at a resolution of 512 scans with software version 4.0.7. For all individuals, signal strength was greater than or equal to seven.

Each of the 11 visits was separated by a minimum of one week and a maximum of two weeks (mean 10.3 days, SD 1.9).

In summary, each individual underwent a total of 11 visits. The eight DNP visits each lasted approximately one hour.

One normal individual, aged 15 years, failed to complete the discrimination task. One individual with OAG, aged 69 years, failed to complete the discrimination task.

The between-examination individual variation in performance (i.e. the learning effect) for MC N_0 , MC N_e , N_{eq} and SE was separately determined for the motion detection and the motion discrimination task for each stimulus location, for each of the three consecutive visits, in the normal individuals and in the individuals with OAG. The learning effect was considered in absolute terms across the three visits and in proportionate terms from visit 1 to visit 2, and from visit 2 to visit 3.

6.3 Analysis

The visual field print-outs (both from the individuals with OAG and from the normal individuals) were assessed by an expert reader, Professor John Wild, to ensure quality control of the outcome and to confirm repeatable abnormality. For each set of visual field print-outs, the identity and diagnosis of the individual was masked to the reader.

6.3.1 Calculation of sampling efficiency (SE) and equivalent noise (N_{eq})

SE and N_{eq} are derivatives of the MC values in the absence of noise (MC N_0) and the MC values in the presence of noise (MC N_e) and are obtained by the following mathematical steps. Firstly, MC N_0 and MC N_e were transformed into signal energy (E_{th}), using equation 6.1. E_{th} is a comprehensive measure of the stimulus at threshold, based on its size, rms contrast, spatial frequency, temporal frequency and the duration for which it is visible. As was described in Chapter 2, Section 2.5, the rms contrast of a stimulus is a measure of local contrast levels across a stimulus relative to its area. The rms of the stimulus ($rms_{stimulus}$) can be derived from its MC at threshold.

$$\text{Signal energy, } E_{th} = (rms_{stimulus})^2 * L^2 * T \quad (6.1)$$

Where L = side length of a square stimulus (degrees)

And T = stimulus duration (seconds)

Given the pre-defined parameters of the stimulus, which included the dimensions of 4° by 4°, and the stimulus duration of 500ms (Chapter 5, Section 5.3.1), the equation can be simplified as follows:

$$\begin{aligned}
\text{Signal energy, } E_{\text{th}} &= (MC/\sqrt{2})^2 * 4^2 * 0.5 \\
&= (MC^2 / 2) * 16 * 0.5 \\
&= 4 * MC^2
\end{aligned}$$

Given that contrast sensitivity is measured in the absence of a noise mask (N_0) and in the presence of a noise mask (N_e), two signal energy values are derived with the DNP method.

The second mathematical step involves the calculation of the strength of the noise mask which is referred to as noise spectral density (N_e). As was discussed in Chapter 2, Section 2.5, N_e is calculated as follows:

$$\text{Noise spectral density, } N_e = (\text{rms}_{\text{noise}})^2 * p^2 * t \quad (6.2)$$

Where p = noise check side length (degrees)

And t = noise check duration (seconds)

Given the pre-defined parameters of the noise mask, including a check side length of 0.5° and check duration of $1/30$ seconds (Chapter 5, Section 5.3.1), the equation can be simplified as follows:

$$\begin{aligned}
\text{Noise spectral density, } N_e &= 0.2^2 * 0.50^2 * 1/30 \\
&= 3.33 \times 10^{-4}
\end{aligned}$$

Where check side length is based on 4 checks per grating cycle as determined in Chapter 5.

The final step in the derivations of SE and N_{eq} utilises the calculated values of signal energies in the absence of noise, $E_{th} N_0$, and in the presence of noise, $E_{th} N_e$, and the noise spectral density N_e :

$$SE = d' * N_e / (E_{th} N_e - E_{th} N_0) \quad (6.3)$$

Where $d' = 2$ and is based upon the threshold algorithm described in Chapter 4, Section 4.22

$$N_{eq} = E_{th} N_0 * (N_e / ((E_{th} N_e - E_{th} N_0))) \quad (6.4)$$

6.3.2 Derivatives of DNP measures

To improve the detection capabilities of MC N_0 , MC N_e , N_{eq} and SE, two independent derivatives are proposed. Firstly, the ratio of the Log_{10} of MC N_e and the Log_{10} of MC N_0 , termed the Log_{10} MC Ratio (Log_{10} Ratio). Secondly, another derivative which is based on the ratio of SE to N_{eq} , termed the Signal Detection Index (SDI). Both derivatives can be summarised as follows:

$$\text{Log}_{10} \text{ Ratio} = \text{Log}_{10} \text{ MC } N_e / \text{Log}_{10} \text{ MC } N_0 \quad (6.5)$$

$$\text{SDI} = SE / N_{eq} \quad (6.6)$$

Data from the current study was used to calculate Log_{10} Ratio and SDI for individuals with OAG and normal individuals, at each location for the detection and the discrimination task. Data were then plotted against the corresponding Pattern Deviation p-value for the given location. The derivatives of Log_{10} MC Ratio and SDI were not used to represent data within

the learning and age studies, as they are proposed only to improve the detection capabilities of DNP in OAG.

6.3.3 Analysis of the results from the normal individuals

For investigation of the learning effect, absolute performance across the three visits is illustrated using Box and Whiskers plots, in which the box indicates the 25th and 75th quartiles of the data set, with a central line indicating the median value. The Whiskers represent the 5th and 95th percentiles of the data, and the crosses at the extremes of the data represent the 1st and 99th percentiles. The small square within the box represents the group mean.

For the investigation of the effects of age, on each of the four main DNP outcomes (MC N_0 , MC N_e , N_{eq} and SE), four individuals from the older group of normal individuals (age range 51 to 84 years) were randomly selected and excluded from the analysis in order to balance the number of individuals between the older and younger age groups. Given that the investigation of learning was also considered as a function of age, these individuals were also excluded from the analysis of the learning effect. As was mentioned in Section 6.2.2, one normal individual failed to complete the discrimination task. Therefore, a total of 23 normal individuals are represented in the analysis for the detection method and a total of 22 normal individuals are represented in the analysis for the discrimination method.

All twenty normal individuals from the older group were included for the determination of the confidence limits for normality, necessary for the validation of the DNP technique in OAG. The younger group of normal individuals were not included in this analysis.

6.3.4 Analysis of the results from individuals with OAG

For the investigation of OAG, measures of MC N_0 , MC N_e , N_{eq} , SE, Log_{10} Ratio and SDI for all individuals were each separately plotted against the magnitude of the Pattern Deviation probability level, derived as a function of RNFL thickness at the given stimulus location (Garway-Heath et al., 2000b; Harwerth et al., 2007). The topographical correspondence between RNFL thickness and visual field location was considered in terms of that proposed by Garway-Heath et al. (2000) and by Harwerth et al. (2007).

6.4 RESULTS: The absolute learning effect for the normal individuals

The outcome of the between-visit variation in performance for MC N_0 , MC N_e , N_{eq} and SE for each of the five stimulus locations, foveal viewing, superior-temporally (ST), superior-nasally (SN), inferior-temporally (IT) and inferior-nasally (IN), is given in Tables 6.2, 6.4, 6.6 and 6.8 for the detection task and in Tables 6.3, 6.5, 6.7 and 6.9 for the discrimination task. The results are also graphically illustrated in terms of Box and Whiskers plots (Figures 6.2 to 6.9). For each location, a clinically meaningful change was defined as greater than 10% of lowest absolute measure.

6.4.1 The learning effect for the normal individuals for Michelson contrast in the absence of noise (MC N_0)

The distribution of MC N_0 across each of the five locations for the detection task is shown in Table 6.2 and Figure 6.2. The median of the distribution of the within-individual difference between visits 1 and 3 declined at the ST, IN and IT locations by clinically

meaningful amounts. The remaining two locations each exhibited clinically identical values across the visits.

The corresponding distribution of $MC N_0$ across each of the five locations for the discrimination task is shown in Table 6.3 and Figure 6.3. The median of the distribution of the within-individual difference between visits 1 and 3 declined for foveal viewing and at the ST, SN and IT locations by clinically meaningful amounts.

6.4.2 The learning effect for the normal individuals for Michelson contrast in the presence of noise ($MC N_e$)

The distribution of $MC N_e$ across each of the five locations for the detection task is shown in Table 6.4 and Figure 6.4. The median of the distribution of the within-individual difference between visits 1 and 3 declined at all locations by clinically meaningful amounts.

The corresponding distribution of $MC N_e$ across each of the five locations for the discrimination task is shown in Table 6.5 and Figure 6.5. The median of the distribution of the within-individual difference between visits 1 and 3 declined for foveal viewing and at the ST, SN and IT locations by clinically meaningful amounts.

6.4.3 The learning effect for the normal individuals for equivalent noise (N_{eq})

The distribution of N_{eq} across each of the five locations for the detection task is shown in Table 6.6 and Figure 6.6. The median of the distribution of the within-individual difference between visits 1 and 3 declined at the ST and IT locations by clinically meaningful amounts.

The corresponding distribution of N_{eq} across each of the five locations for the discrimination task is shown in Table 6.7 and Figure 6.7. The median of the distribution of the within-individual difference between visits 1 and 3 exhibited clinically identical values for all locations across the visits.

6.4.4 The learning effect for the normal individuals for sampling efficiency (SE)

The distribution of SE across each of the five locations for the detection task is shown in Table 6.8 and Figure 6.8. The median of the distribution of the within-individual difference between visits 1 and 3 increased at all locations by clinically meaningful amounts.

The corresponding distribution of SE across each of the five locations for the discrimination task is shown in Table 6.9 and Figure 6.9. The median of the distribution of the within-individual difference between visits 1 and 3 increased for foveal viewing and at the ST, SN and IT locations by clinically meaningful amounts.

Improvement in performance

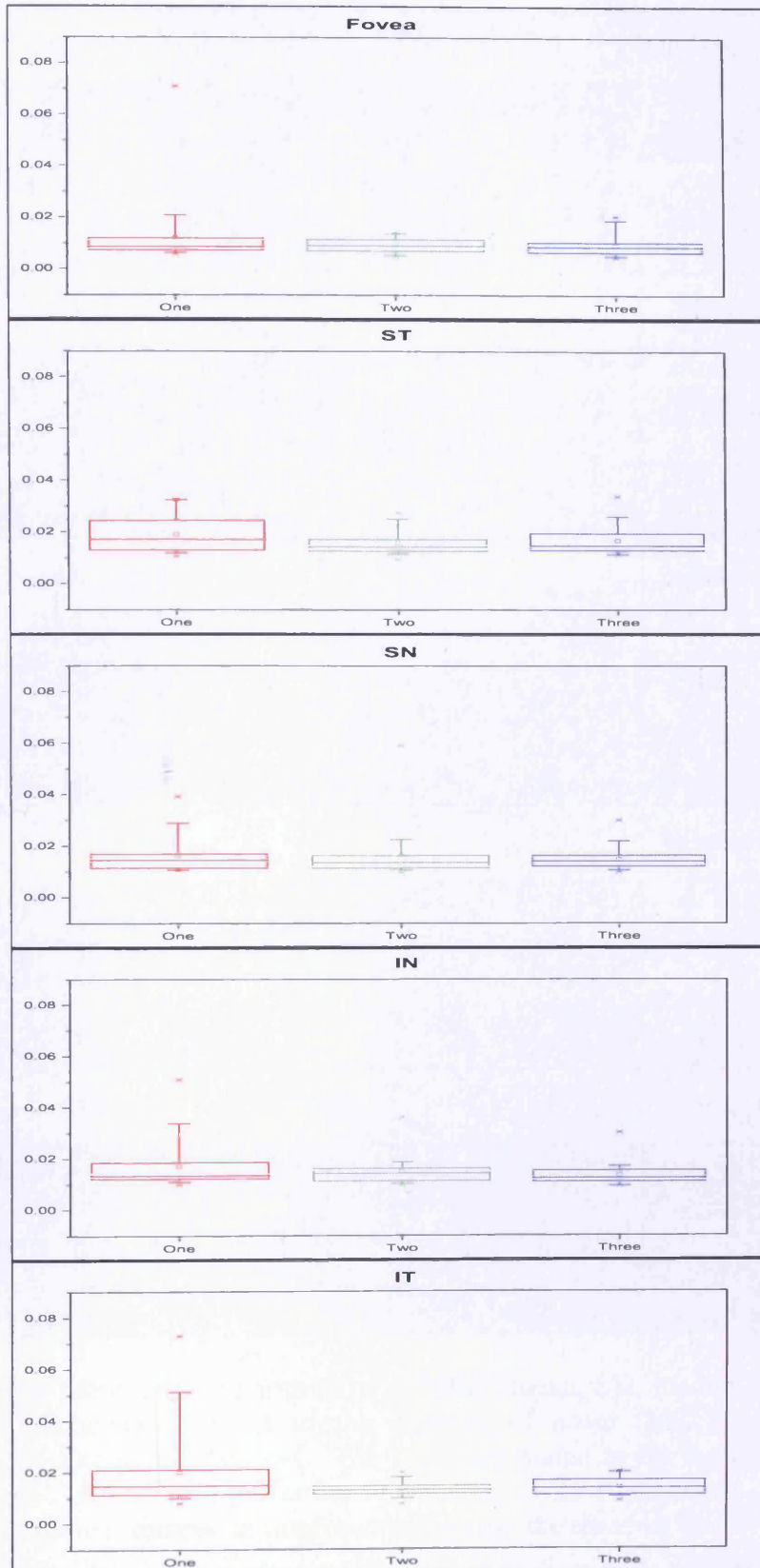


Figure 6.2 Motion detection: Box and Whiskers plot of the distribution of Michelson contrast thresholds (ordinate) in the absence of the noise mask ($MC N_0$) for all 23 normal individuals as a function of visits (abscissa).

Fovea	Visit			Improvement
	One	Two	Three	
Mean	0.012120	0.009116	0.009249	-0.002870
SD	0.013274	0.002591	0.003868	0.012566
Median	0.008470	0.008965	0.008622	-0.000216
25th percentile	0.007242	0.007134	0.006548	-0.001268
75th percentile	0.011822	0.011026	0.010125	0.001038
ST	Visit			Improvement
	One	Two	Three	
Mean	0.018936	0.015607	0.016655	-0.002281
SD	0.006831	0.004576	0.005490	0.005681
Median	0.017017	0.014143	0.014613	-0.001524
25th percentile	0.013035	0.012916	0.012818	-0.005560
75th percentile	0.023198	0.016857	0.018636	0.001652
SN	Visit			Improvement
	One	Two	Three	
Mean	0.017148	0.014868	0.013481	-0.001485
SD	0.009354	0.005256	0.004248	0.005111
Median	0.013447	0.014230	0.012385	-0.000254
25th percentile	0.012329	0.011746	0.011223	-0.001664
75th percentile	0.017619	0.016170	0.014713	0.000974
IN	Visit			Improvement
	One	Two	Three	
Mean	0.017148	0.014868	0.013481	-0.003667
SD	0.009354	0.005256	0.004248	0.006808
Median	0.013447	0.014230	0.012385	-0.001625
25th percentile	0.012329	0.011746	0.011223	-0.003010
75th percentile	0.017619	0.016170	0.014713	0.000229
IT	Visit			Improvement
	One	Two	Three	
Mean	0.020017	0.013118	0.013586	-0.006431
SD	0.015460	0.002631	0.003135	0.014623
Median	0.014805	0.012931	0.013364	-0.001008
25th percentile	0.011395	0.011379	0.011108	-0.007087
75th percentile	0.020139	0.014337	0.015662	0.001008

Table 6.2 Motion detection: The summary statistics, mean, SD, median and interquartile range for the Michelson contrast in the absence of noise (MC N_0) for 23 normal individuals at the five given locations. The summary statistics for the distribution of the within-individual difference in performance between visits 1 and 3 are given in column five. A negative value indicates an improvement across the three visits.

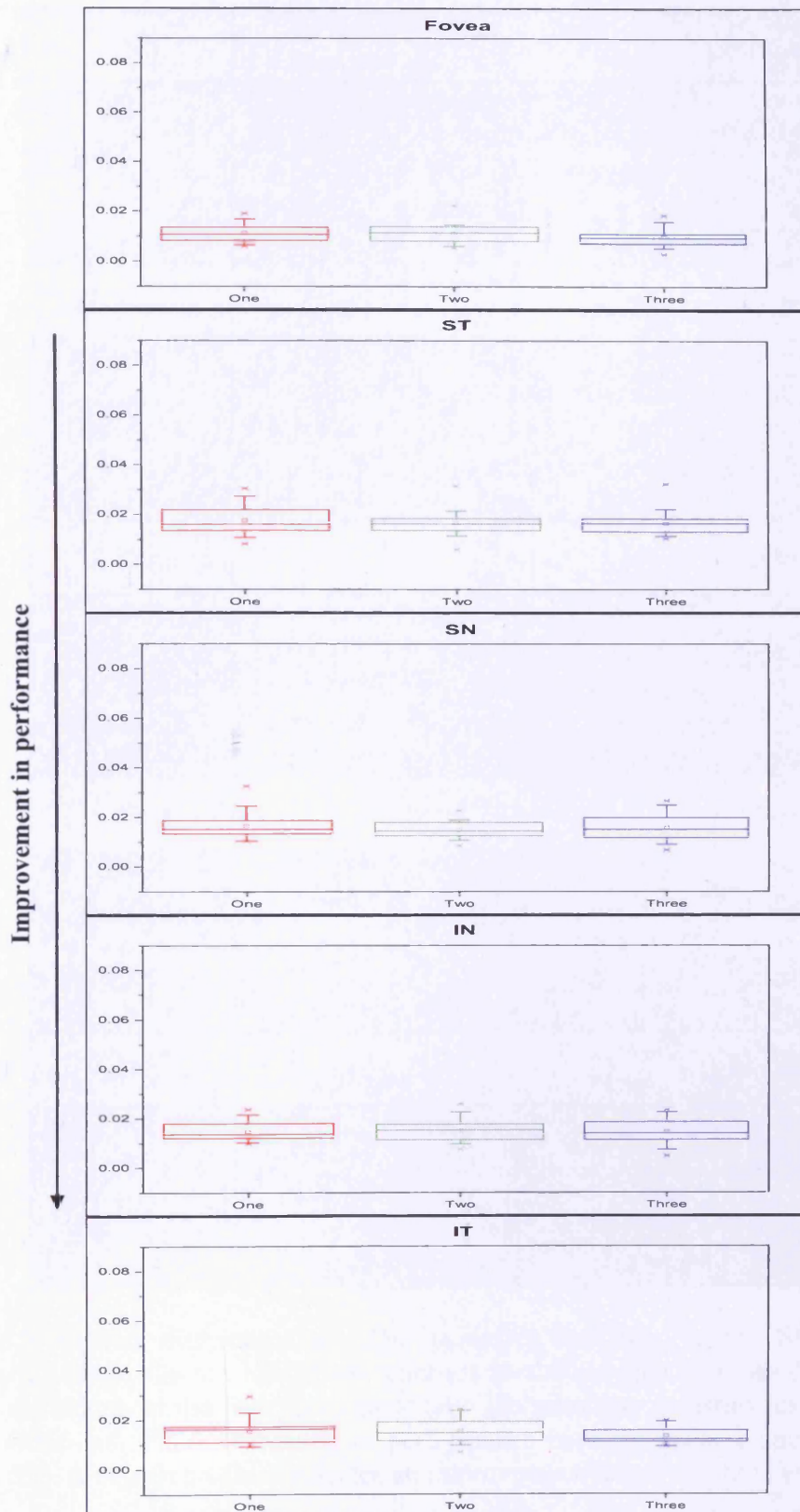


Figure 6.3 Motion discrimination: Box and Whiskers plot of the distribution of Michelson contrast thresholds (ordinate) in the absence of the noise mask ($MC N_0$) for all 22 normal individuals as a function of visits (abscissa).

Fovea	Visit			Improvement
	One	Two	Three	
Mean	0.011216	0.011107	0.010000	-0.001216
SD	0.003285	0.003850	0.003723	0.003127
Median	0.010608	0.011409	0.009396	-0.001438
25th percentile	0.008886	0.008348	0.007512	-0.002556
75th percentile	0.013233	0.013653	0.010908	0.000431
ST	Visit			Improvement
	One	Two	Three	
Mean	0.017483	0.016290	0.016436	-0.001048
SD	0.005827	0.004752	0.004689	0.005319
Median	0.015968	0.016151	0.016353	-0.001577
25th percentile	0.013639	0.013802	0.013363	-0.003399
75th percentile	0.021474	0.018090	0.017817	0.002499
SN	Visit			Improvement
	One	Two	Three	
Mean	0.014614	0.015070	0.014568	-0.000627
SD	0.003911	0.004530	0.004887	0.005673
Median	0.013708	0.015354	0.014051	-0.001370
25th percentile	0.012193	0.011668	0.012130	-0.004291
75th percentile	0.016615	0.017489	0.017847	0.001973
IN	Visit			Improvement
	One	Two	Three	
Mean	0.014614	0.015070	0.014568	-0.000047
SD	0.003911	0.004530	0.004887	0.004011
Median	0.013708	0.015354	0.014051	0.000516
25th percentile	0.012193	0.011668	0.012130	-0.001803
75th percentile	0.016615	0.017489	0.017847	0.002081
IT	Visit			Improvement
	One	Two	Three	
Mean	0.015266	0.015268	0.013319	-0.001947
SD	0.005007	0.004585	0.003261	0.005108
Median	0.016151	0.014613	0.011929	-0.001921
25th percentile	0.011223	0.011547	0.011079	-0.005354
75th percentile	0.016987	0.018251	0.015534	0.000118

Table 6.3 Motion discrimination: The summary statistics, mean, SD, median and interquartile range for the Michelson contrast in the absence of noise (MC N_0) for 22 normal individuals at the five given locations. The summary statistics for the distribution of the within-individual difference in performance between visits 1 and 3 are given in column five. A negative value indicates an improvement across the three visits.

Improvement in performance

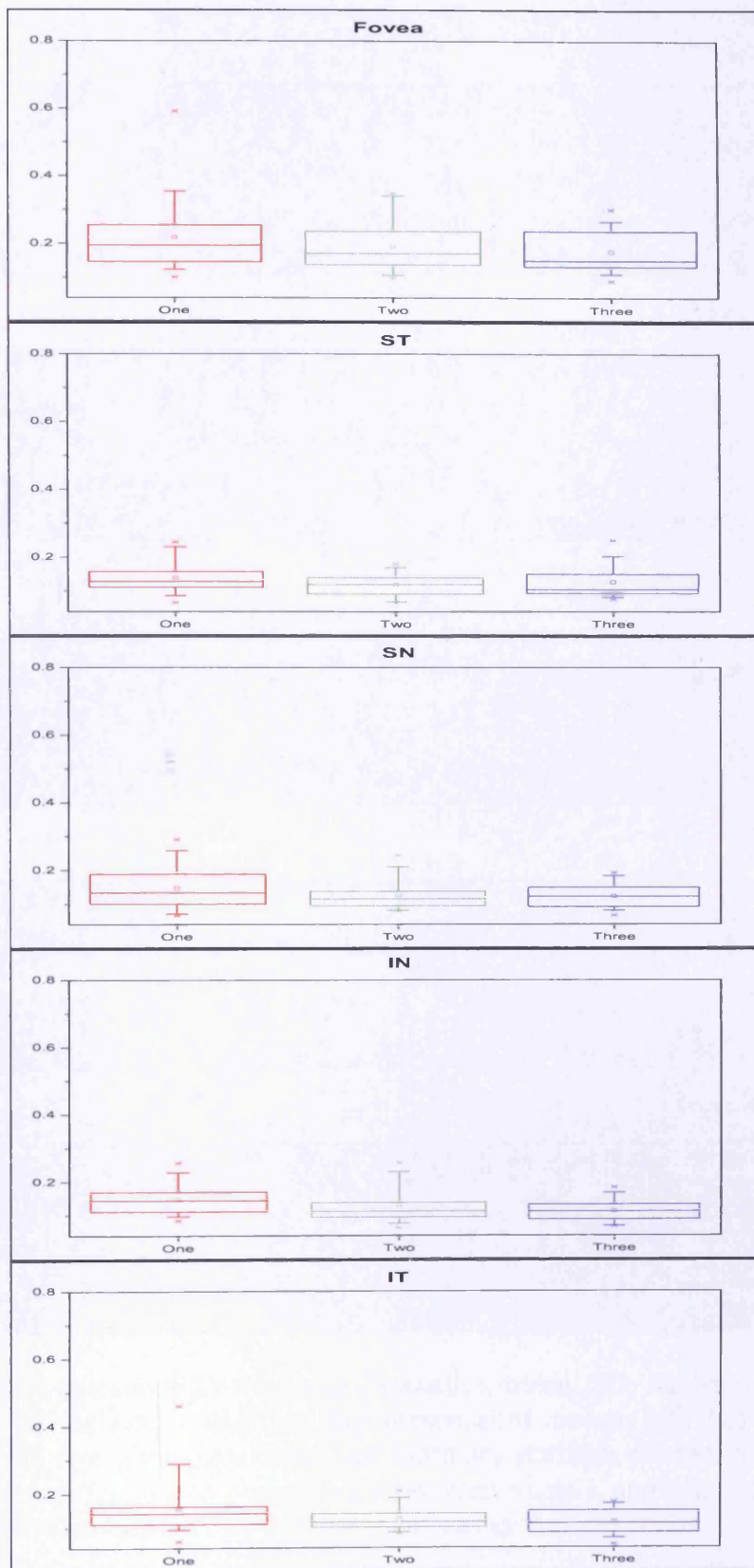


Figure 6.4 Motion detection: Box and Whiskers plot of the distribution of Michelson contrast thresholds (ordinate) in the presence of the noise mask (MC Ne) for all 23 normal individuals as a function of visits (abscissa). Note the marked difference in the scaling of the ordinate compared to Figure 6.3.

Fovea	Visit			Improvement
	One	Two	Three	
Mean	0.217182	0.191250	0.176778	-0.040403
SD	0.104014	0.075100	0.060088	0.084445
Median	0.192740	0.170262	0.149203	-0.017118
25th percentile	0.149321	0.137003	0.134092	-0.074468
75th percentile	0.252004	0.229987	0.225432	-0.000962
ST	Visit			Improvement
	One	Two	Three	
Mean	0.137222	0.117972	0.125676	-0.011546
SD	0.044298	0.029640	0.044675	0.052410
Median	0.126750	0.118415	0.104480	-0.020808
25th percentile	0.110084	0.097867	0.093482	-0.042932
75th percentile	0.155310	0.137995	0.147038	0.015377
SN	Visit			Improvement
	One	Two	Three	
Mean	0.147071	0.131499	0.112670	-0.024367
SD	0.041629	0.052578	0.032574	0.055898
Median	0.144875	0.112249	0.111540	-0.024779
25th percentile	0.115238	0.099541	0.088096	-0.060830
75th percentile	0.169164	0.138258	0.128915	0.023146
IN	Visit			Improvement
	One	Two	Three	
Mean	0.147071	0.131499	0.112670	-0.034402
SD	0.041629	0.052578	0.032574	0.030563
Median	0.144875	0.112249	0.111540	-0.042208
25th percentile	0.115238	0.099541	0.088096	-0.048537
75th percentile	0.169164	0.138258	0.128915	-0.016852
IT	Visit			Improvement
	One	Two	Three	
Mean	0.155767	0.124629	0.114530	-0.041236
SD	0.080258	0.034956	0.035902	0.065748
Median	0.141434	0.114978	0.110648	-0.026153
25th percentile	0.111632	0.100594	0.087592	-0.049800
75th percentile	0.160082	0.138722	0.146592	-0.006023

Table 6.4 Motion detection: The summary statistics, mean, SD, median and interquartile range for the Michelson contrast in the presence of noise (MC N_e) for 23 normal individuals at the five given locations. The summary statistics for the distribution of the within-individual difference in performance between visits 1 and 3 are given in column five. A negative value indicates an improvement across the three visits.

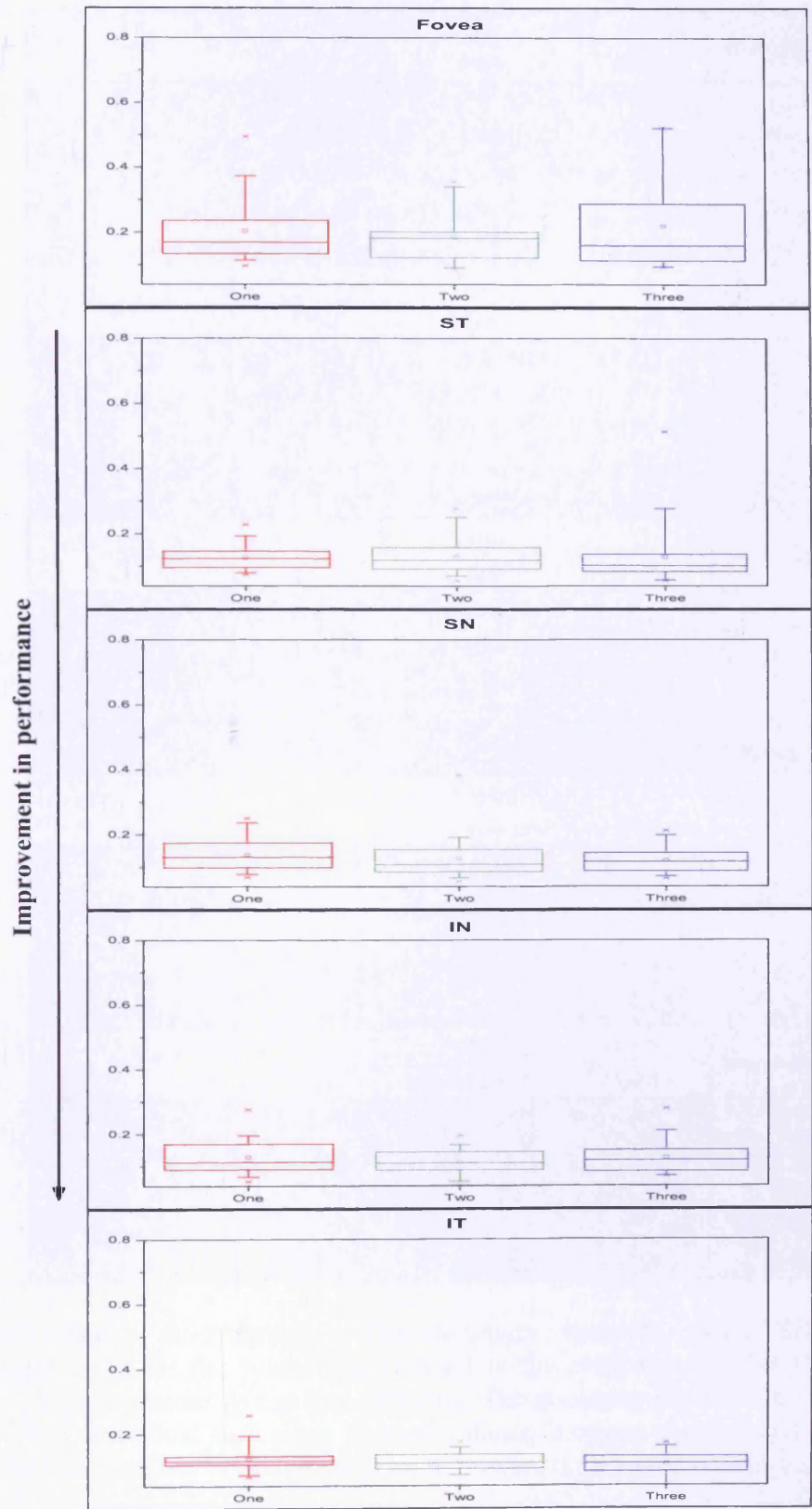


Figure 6.5 Motion discrimination: Box and Whiskers plot of the distribution of Michelson contrast thresholds (ordinate) in the presence of the noise mask ($MC N_e$) for all 22 normal individuals as a function of visits (abscissa).

Fovea	Visit			Improvement
	One	Two	Three	
Mean	0.203561	0.184085	0.219729	0.016167
SD	0.094717	0.074819	0.137167	0.107307
Median	0.168196	0.181866	0.158995	-0.016533
25th percentile	0.138254	0.125855	0.112812	-0.056611
75th percentile	0.234363	0.197810	0.285497	0.061347
ST	Visit			Improvement
	One	Two	Three	
Mean	0.125090	0.131788	0.128664	0.003573
SD	0.037415	0.058147	0.098330	0.072727
Median	0.121855	0.117708	0.101750	-0.011602
25th percentile	0.098418	0.092263	0.083556	-0.024901
75th percentile	0.143467	0.149584	0.129364	0.002355
SN	Visit			Improvement
	One	Two	Three	
Mean	0.128928	0.112929	0.125651	-0.017115
SD	0.052793	0.038412	0.049740	0.036231
Median	0.113143	0.110648	0.118601	-0.012548
25th percentile	0.094393	0.090170	0.088170	-0.033344
75th percentile	0.160268	0.141701	0.144148	0.003438
IN	Visit			Improvement
	One	Two	Three	
Mean	0.128928	0.112929	0.125651	-0.003277
SD	0.052793	0.038412	0.049740	0.040101
Median	0.113143	0.110648	0.118601	0.002711
25th percentile	0.094393	0.090170	0.088170	-0.017111
75th percentile	0.160268	0.141701	0.144148	0.022216
IT	Visit			Improvement
	One	Two	Three	
Mean	0.121879	0.109500	0.105807	-0.016072
SD	0.039446	0.034007	0.038725	0.048860
Median	0.114978	0.108811	0.107208	-0.020998
25th percentile	0.104834	0.092336	0.088805	-0.036421
75th percentile	0.130225	0.135082	0.126396	0.022317

Table 6.5 Motion discrimination: The summary statistics, mean, SD, median and interquartile range for the Michelson contrast in the presence of noise (MC N_e) for 22 normal individuals at the five given locations. The summary statistics for the distribution of the within-individual difference in performance between visits 1 and 3 are given in column five. A negative value indicates an improvement across the three visits.

Improvement in performance

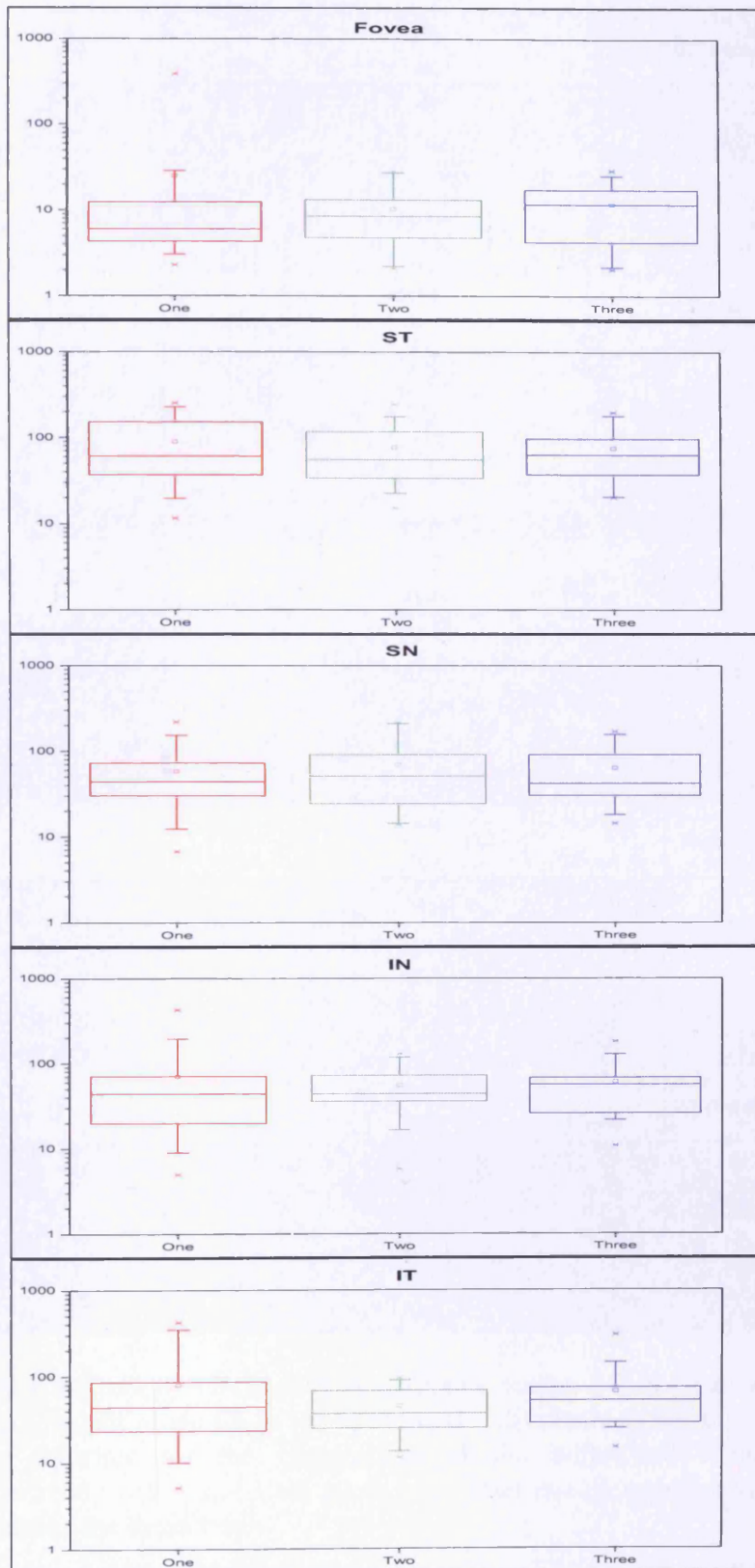


Figure 6.6 Motion detection: Box and Whiskers plot of the distribution of equivalent noise ($10^{-7} \text{ deg}^2 \text{ sec}^{-1}$) (ordinate) for all 23 normal individuals as a function of visits (abscissa). Note the marked difference in the scaling of the ordinate compared to Figure 6.5.

Fovea	Visit			Improvement
	One	Two	Three	
Mean	24.99	10.31	11.73	-13.26
SD	79.62	7.46	7.99	80.14
Median	5.96	8.42	11.73	2.68
25th percentile	4.29	4.95	4.28	-3.74
75th percentile	11.51	13.04	16.59	8.80
ST	Visit			Improvement
	One	Two	Three	
Mean	88.19	77.04	75.05	-13.14
SD	70.78	58.30	48.76	60.88
Median	59.98	54.93	62.43	14.25
25th percentile	37.54	33.90	39.49	-42.08
75th percentile	138.34	114.41	96.26	23.35
SN	Visit			Improvement
	One	Two	Three	
Mean	69.92	55.68	60.77	6.07
SD	92.23	32.13	41.60	51.52
Median	44.02	43.93	56.24	3.19
25th percentile	21.73	38.25	28.43	-22.83
75th percentile	67.46	71.70	67.91	25.27
IN	Visit			Improvement
	One	Two	Three	
Mean	69.92	55.68	60.77	-9.16
SD	92.23	32.13	41.60	75.95
Median	44.02	43.93	56.24	5.91
25th percentile	21.73	38.25	28.43	-15.37
75th percentile	67.46	71.70	67.91	26.34
IT	Visit			Improvement
	One	Two	Three	
Mean	79.67	44.75	65.84	-13.83
SD	102.34	23.98	61.21	115.67
Median	43.96	36.93	51.66	10.35
25th percentile	23.77	25.57	28.43	-13.69
75th percentile	78.79	63.71	71.05	20.71

Table 6.6 Motion detection: The summary statistics, mean, SD, median and interquartile range for the equivalent noise (N_{eq}) for 23 normal individuals at the five given locations. The summary statistics for the distribution of the within-individual difference in performance between visits 1 and 3 are given in column five. A negative value indicates an improvement across the three visits.

Improvement in performance

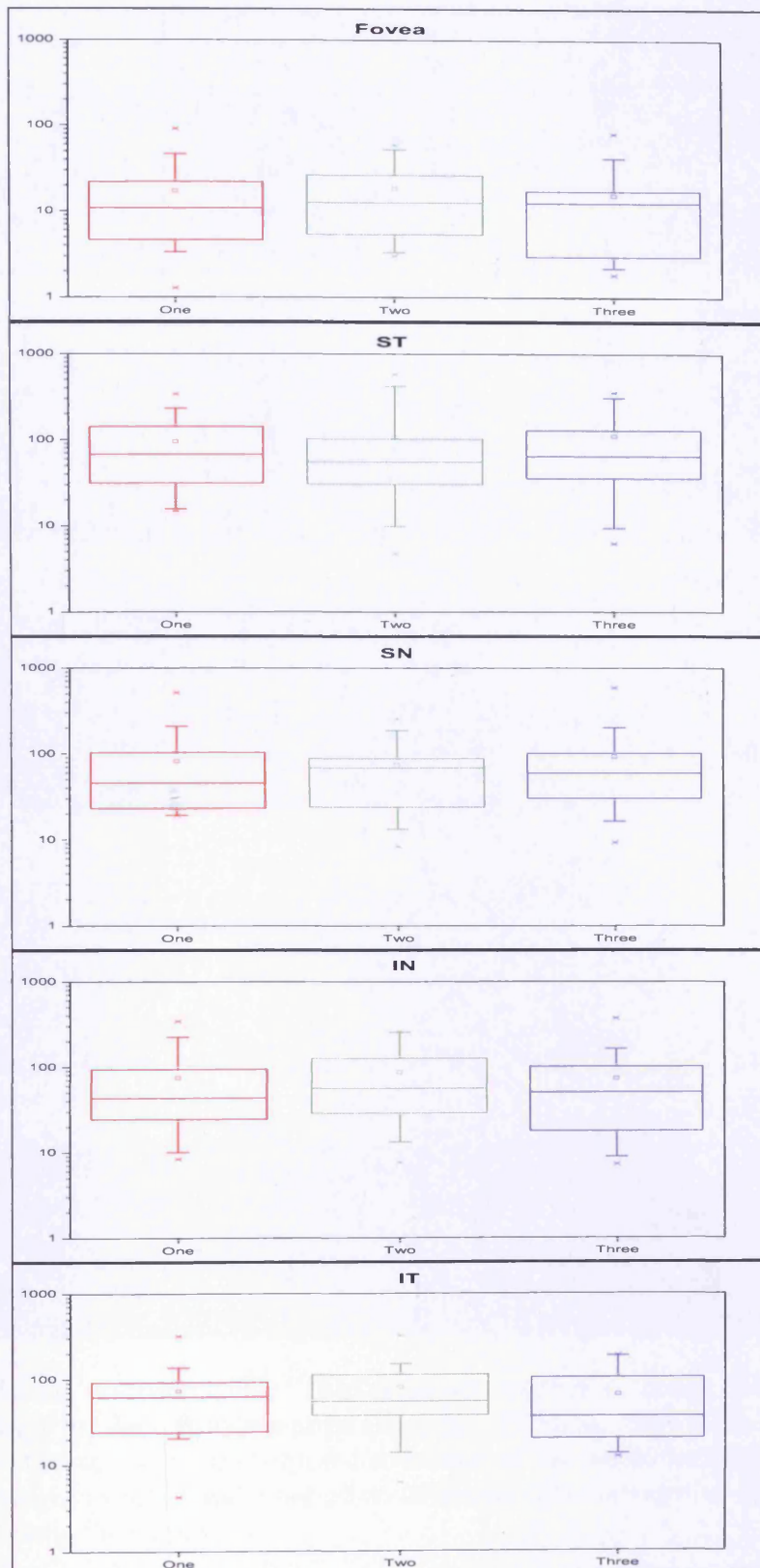


Figure 6.7 Motion discrimination: Box and Whiskers plot of the distribution of equivalent noise ($10^{-7} \text{ deg}^2 \text{ sec}^{-1}$) (ordinate) for all 22 normal individuals as a function of visits (abscissa).

Fovea	Visit			Improvement
	One	Two	Three	
Mean	17.24	18.30	15.49	-1.75
SD	19.56	16.76	17.41	25.09
Median	10.73	12.62	12.53	1.80
25th percentile	6.22	5.41	3.49	-4.87
75th percentile	19.79	25.21	17.04	6.95
ST	Visit			Improvement
	One	Two	Three	
Mean	94.54	106.17	111.15	16.61
SD	83.78	141.34	104.33	68.27
Median	66.62	55.15	63.92	-2.69
25th percentile	36.42	32.98	38.14	-17.73
75th percentile	137.33	98.59	124.91	31.51
SN	Visit			Improvement
	One	Two	Three	
Mean	74.88	87.20	73.97	10.47
SD	79.55	76.33	80.12	146.31
Median	43.52	56.45	50.54	-2.43
25th percentile	26.50	30.24	22.78	-36.36
75th percentile	88.63	122.17	97.07	42.53
IN	Visit			Improvement
	One	Two	Three	
Mean	74.88	87.20	73.97	-0.91
SD	79.55	76.33	80.12	66.63
Median	43.52	56.45	50.54	-2.71
25th percentile	26.50	30.24	22.78	-20.51
75th percentile	88.63	122.17	97.07	14.69
IT	Visit			Improvement
	One	Two	Three	
Mean	72.99	80.31	65.42	-7.57
SD	64.61	67.06	59.29	58.66
Median	62.20	55.18	36.68	-4.07
25th percentile	31.40	38.90	22.08	-38.01
75th percentile	90.59	107.99	93.22	17.69

Table 6.7 Motion discrimination: The summary statistics, mean, SD, median and interquartile range for the equivalent noise (N_{eq}) for 22 normal individuals at the five given locations. The summary statistics for the distribution of the within-individual difference in performance between visits 1 and 3 are given in column five. A negative value indicates an improvement across the three visits.

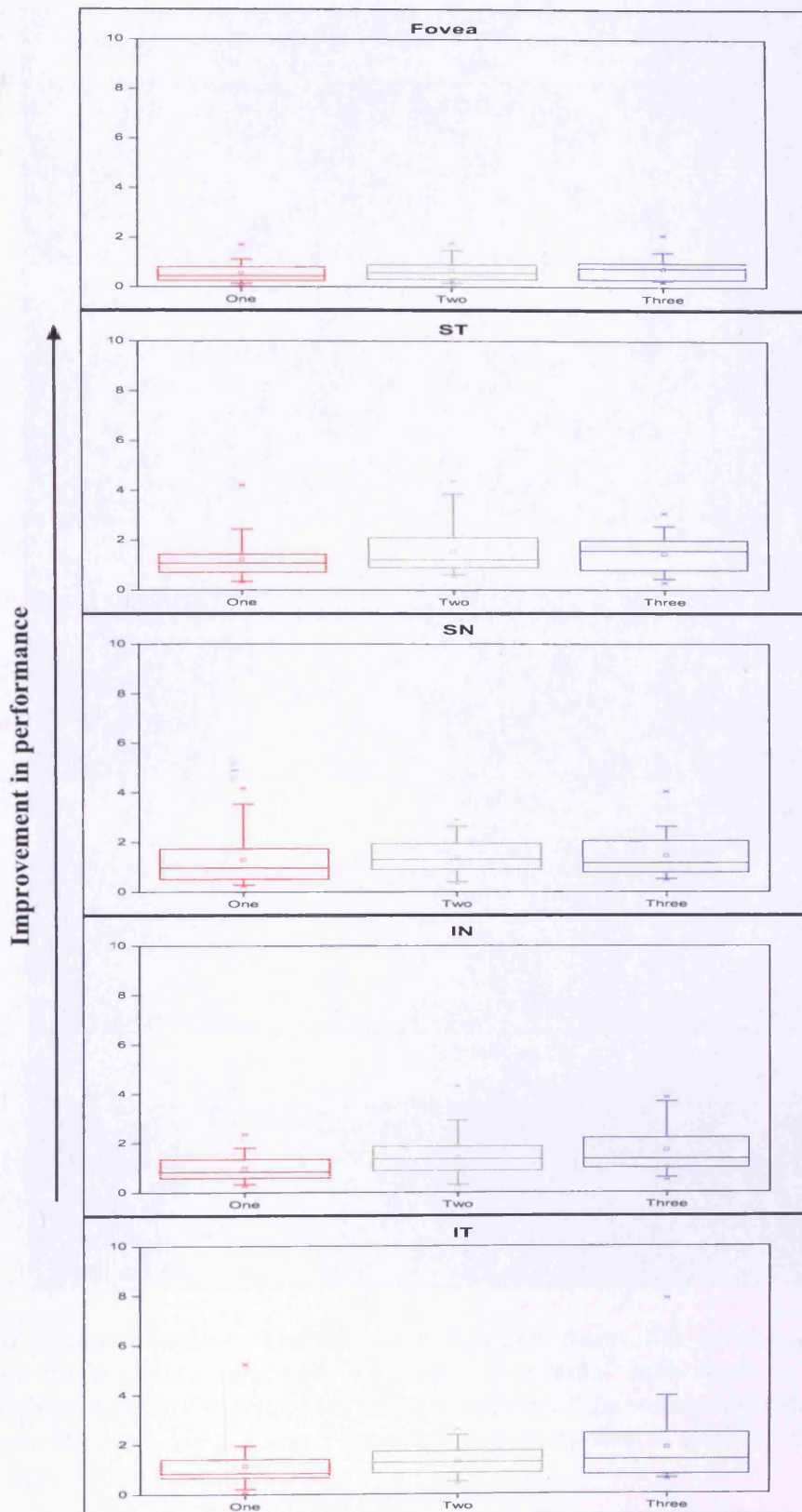


Figure 6.8 Motion detection: Box and Whiskers plot of the distribution of sampling efficiency (%) (ordinate) for all 23 normal individuals as a function of visits (abscissa). Note the marked difference in the scaling of the ordinate compared to Figure 6.7.

Fovea	Visit			Improvement
	One	Two	Three	
Mean	0.55	0.66	0.73	0.18
SD	0.40	0.44	0.47	0.37
Median	0.45	0.58	0.75	0.20
25th percentile	0.26	0.32	0.33	-0.01
75th percentile	0.75	0.89	0.93	0.39
ST	Visit			Improvement
	One	Two	Three	
Mean	1.21	1.53	1.43	0.22
SD	0.85	1.00	0.77	0.83
Median	1.06	1.20	1.55	0.49
25th percentile	0.70	0.88	0.79	-0.38
75th percentile	1.41	1.81	1.94	0.67
SN	Visit			Improvement
	One	Two	Three	
Mean	0.97	1.41	1.71	0.16
SD	0.51	0.94	1.01	0.97
Median	0.84	1.35	1.35	0.25
25th percentile	0.59	0.88	1.04	-0.38
75th percentile	1.28	1.72	2.19	0.81
IN	Visit			Improvement
	One	Two	Three	
Mean	0.97	1.41	1.71	0.74
SD	0.51	0.94	1.01	0.93
Median	0.84	1.35	1.35	0.41
25th percentile	0.59	0.88	1.04	0.21
75th percentile	1.28	1.72	2.19	0.81
IT	Visit			Improvement
	One	Two	Three	
Mean	1.12	1.32	1.84	0.72
SD	1.02	0.62	1.59	1.59
Median	0.84	1.27	1.37	0.51
25th percentile	0.67	0.87	0.78	0.12
75th percentile	1.36	1.68	2.23	1.03

Table 6.8 Motion detection: The summary statistics, mean, SD, median and interquartile range for the sampling efficiency (SE) for 23 normal individuals at the five given locations. The summary statistics for the distribution of the within-individual difference in performance between visits 1 and 3 are given in column five. A positive value indicates an improvement across the three visits.

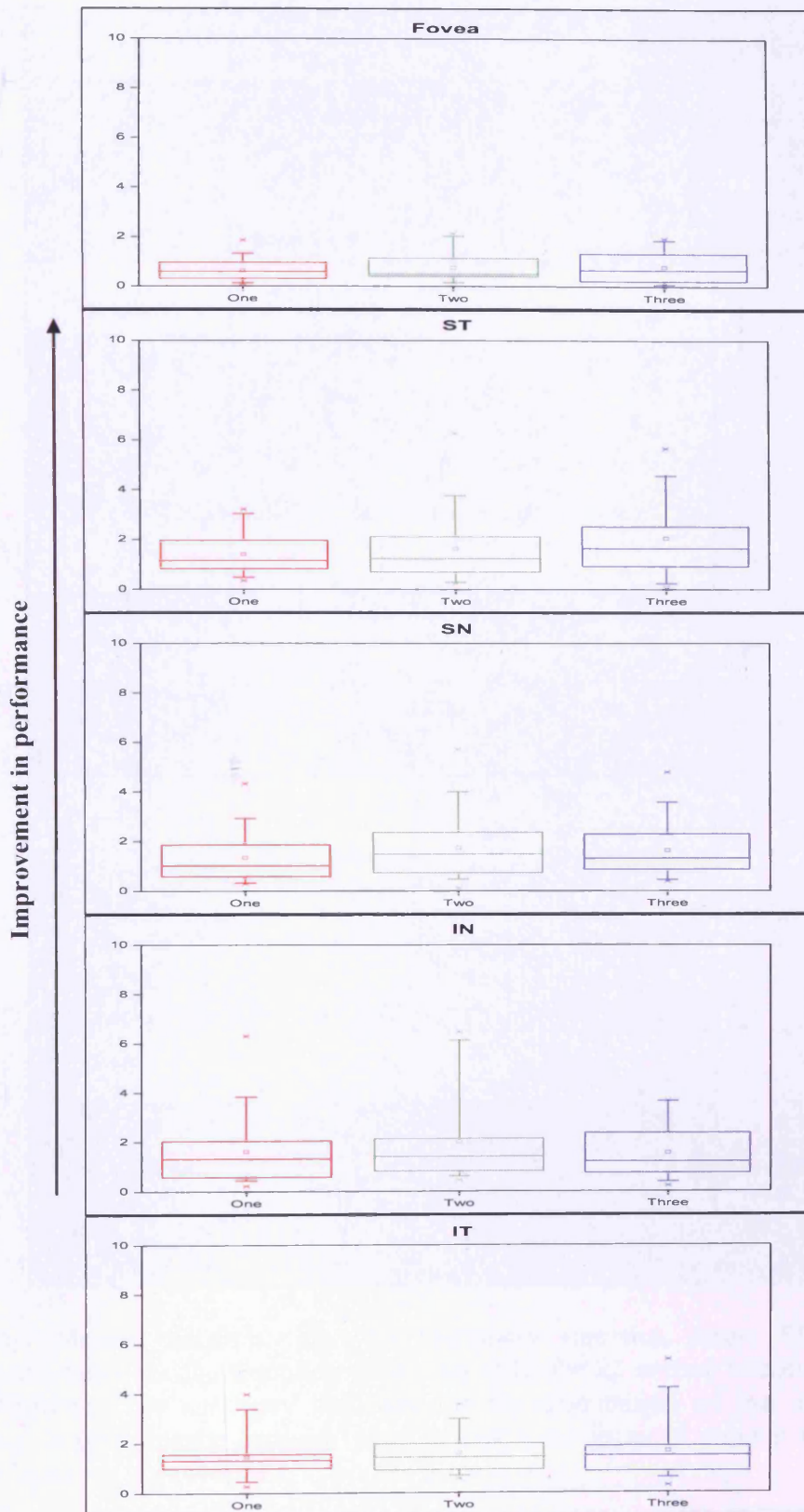


Figure 6.9 Motion discrimination: Box and Whiskers plot of the distribution of sampling efficiency (%) (ordinate) for all 22 normal individuals as a function of visits (abscissa).

Fovea	Visit			Improvement
	One	Two	Three	
Mean	0.63	0.76	0.80	0.17
SD	0.44	0.57	0.65	0.60
Median	0.59	0.51	0.66	0.04
25th percentile	0.31	0.43	0.21	-0.16
75th percentile	0.89	1.06	1.32	0.60
ST	Visit			Improvement
	One	Two	Three	
Mean	1.39	1.61	2.04	0.66
SD	0.78	1.38	1.50	1.02
Median	1.13	1.22	1.63	0.36
25th percentile	0.82	0.76	1.02	-0.07
75th percentile	1.80	2.02	2.50	0.90
SN	Visit			Improvement
	One	Two	Three	
Mean	1.61	2.00	1.55	0.30
SD	1.37	1.71	1.04	0.85
Median	1.32	1.42	1.21	0.23
25th percentile	0.66	0.85	0.82	-0.08
75th percentile	1.91	2.08	2.21	0.67
IN	Visit			Improvement
	One	Two	Three	
Mean	1.61	2.00	1.55	-0.06
SD	1.37	1.71	1.04	1.12
Median	1.32	1.42	1.21	-0.03
25th percentile	0.66	0.85	0.82	-0.52
75th percentile	1.91	2.08	2.21	0.46
IT	Visit			Improvement
	One	Two	Three	
Mean	1.46	1.60	1.65	0.20
SD	0.87	0.81	1.20	1.35
Median	1.31	1.42	1.47	0.23
25th percentile	1.00	0.92	0.93	-0.61
75th percentile	1.55	1.96	1.73	0.75

Table 6.9 Motion discrimination: The summary statistics, mean, SD, median and interquartile range for the sampling efficiency (SE) for 22 normal individuals at the five given locations. The summary statistics for the distribution of the within-individual difference in performance between visits 1 and 3 are given in column five. A positive value indicates an improvement across the three visits.

6.5 RESULTS: The proportionate learning effect for the normal individuals

The apparent between-individual differences in performance for each of the DNP measures, evident from the summary statistics in Tables 6.2 - 6.9 and the Box and Whiskers plots in Figures 6.2 – 6.9 necessitated a further analysis of the learning effect in proportionate terms.

6.5.1 The learning effect between visit 1 and 2 for the normal individuals for Michelson contrast in the absence of noise (MC N_0)

The proportionate improvement in MC N_0 across each of the five locations as a function of age for the detection task is shown in Figure 6.10. The between-individual differences in improvement ranged from approximately $\pm 75\%$. Of the 23 individuals, 11 individuals showed a positive improvement for foveal viewing, 19 at the ST location, 11 at the SN location, 13 at the IN location and 17 at the IT location.

The proportionate improvement in MC N_0 across each of the five locations as a function of age for the discrimination task is shown in Figure 6.11. The between-individual differences in improvement ranged from approximately -80% to $+50\%$. Of the 22 individuals, 12 individuals showed a positive improvement for foveal viewing, 13 at the ST location, 13 at the SN location, 13 at the IN location and 12 at the IT location.

6.5.2 The learning effect between visit 2 and 3 for the normal individuals for Michelson contrast in the absence of noise (MC N₀)

The proportionate improvement in MC N₀ across each of the five locations as a function of age for the detection task is shown in Figure 6.12. The between-individual differences in improvement ranged from approximately -80% to +50%. Of the 23 individuals, 12 individuals showed a positive improvement for foveal viewing, 9 at the ST location, 11 at the SN location, 17 at the IN location and 10 at the IT location.

The proportionate improvement in MC N₀ across each of the five locations as a function of age for the discrimination task is shown in Figure 6.13. The between-individual differences in improvement ranged from approximately to -/+85 %. Of the 22 individuals, 12 individuals showed a positive improvement for foveal viewing, 12 at the ST location, 10 at the SN location, 13 at the IN location and 16 at the IT location.

6.5.3 The learning effect between visit 1 and 2 for the normal individuals for Michelson contrast in the presence of noise (MC N_e)

The proportionate improvement in MC N_e across each of the five locations as a function of age for the detection task is shown in Figure 6.14. The between-individual differences in improvement ranged from approximately -80% to +70%. Of the 23 individuals, 15 individuals showed a positive improvement for foveal viewing, 14 at the ST location, 13 at the SN location, 16 at the IN location and 15 at the IT location.

The proportionate improvement in MC N_e across each of the five locations as a function of age for the discrimination task is shown in Figure 6.15. The between-individual

differences in improvement ranged from approximately to -60% to +90%. Of the 22 individuals, 17 individuals showed a positive improvement for foveal viewing, 12 at the ST location, 15 at the SN location, 15 at the IN location and 12 at the IT location.

6.5.4 The learning effect between visit 2 and 3 for the normal individuals for Michelson contrast in the presence of noise (MC N_e)

The proportionate improvement in MC N_e across each of the five locations as a function of age for the detection task is shown in Figure 6.16. The between-individual differences in improvement ranged from approximately +/- 60%. Of the 23 individuals, 13 individuals showed a positive improvement for foveal viewing, 9 at the ST location, 10 at the SN location, 17 at the IN location and 13 at the IT location.

The proportionate improvement in MC N_e across each of the five locations as a function of age for the discrimination task is shown in Figure 6.13. The between-individual differences in improvement ranged from approximately to -85 % to +75%. Of the 22 individuals, 12 individuals showed a positive improvement for foveal viewing, 17 at the ST location, 12 at the SN location, 8 at the IN location and 11 at the IT location.

Improvement in performance ↑

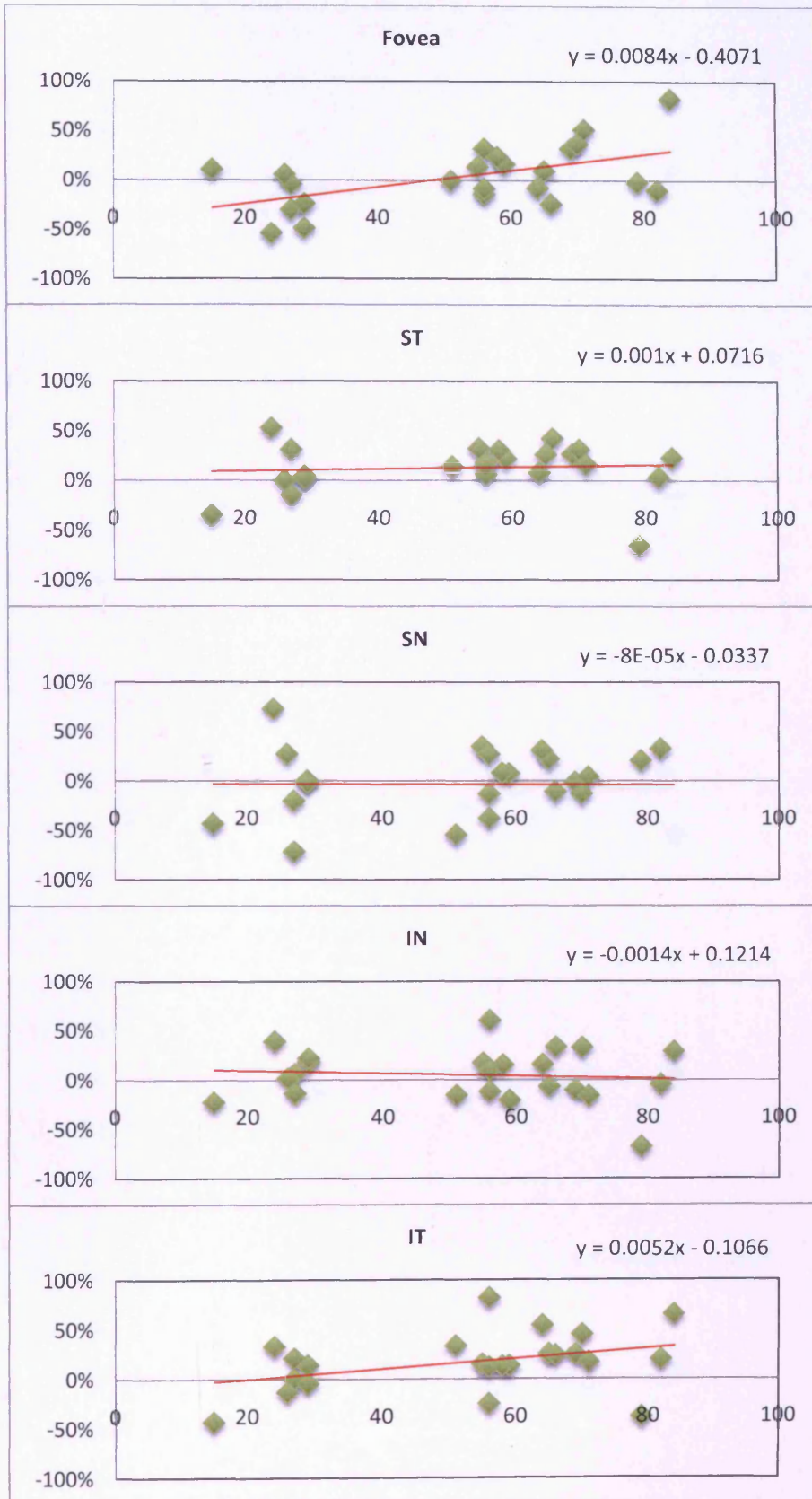


Figure 6.10 Motion detection: The proportionate improvement in performance (ordinate) from visit 1 to visit 2 for Michelson contrast thresholds in the absence of the noise mask ($MC N_0$) as a function of age (abscissa). A positive value indicates an improvement in performance.

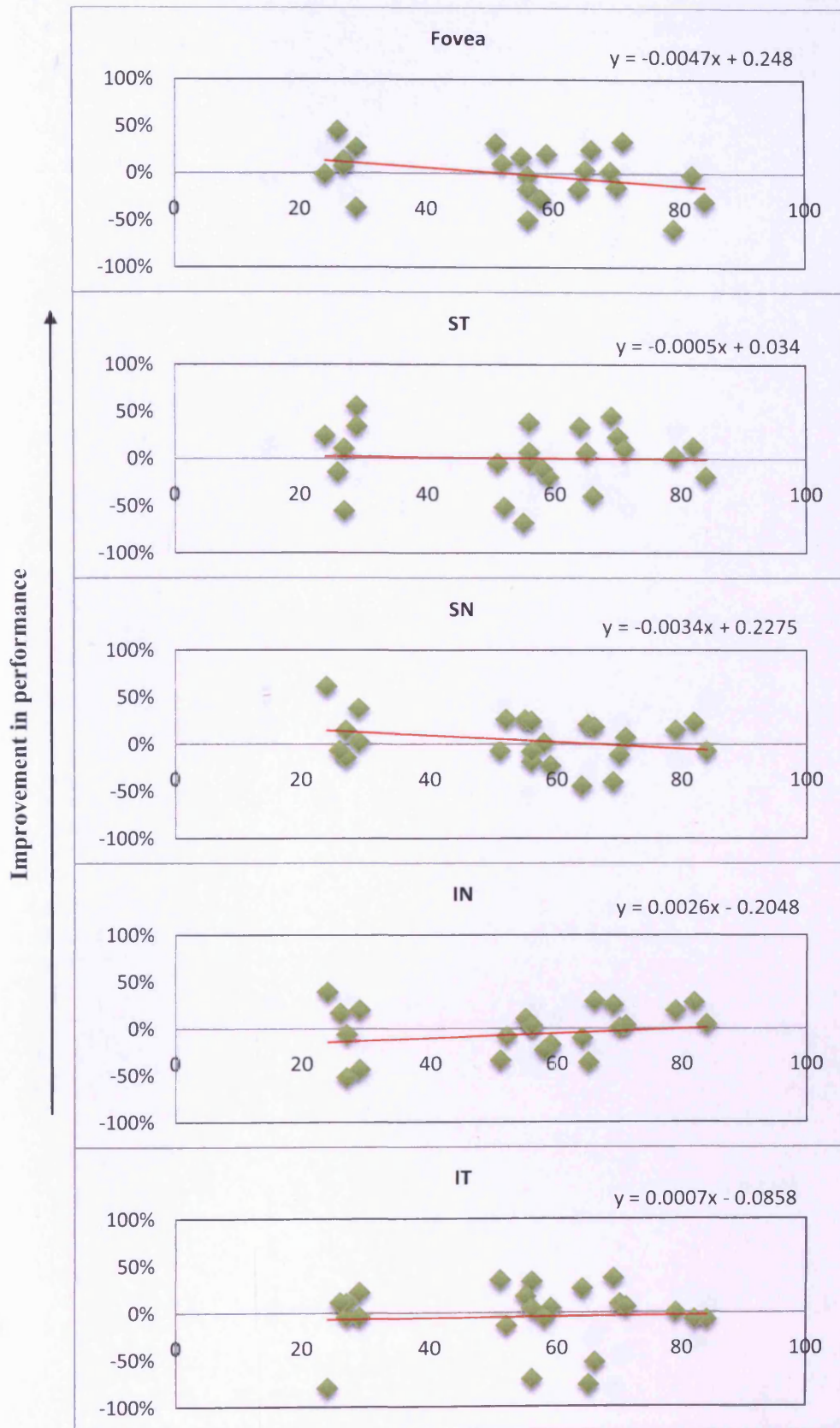


Figure 6.11 Motion discrimination: The proportionate improvement in performance (ordinate) from visit 1 to visit 2 for Michelson contrast thresholds in the absence of the noise mask (MC N_0) as a function of age (abscissa). A positive value indicates an improvement in performance.

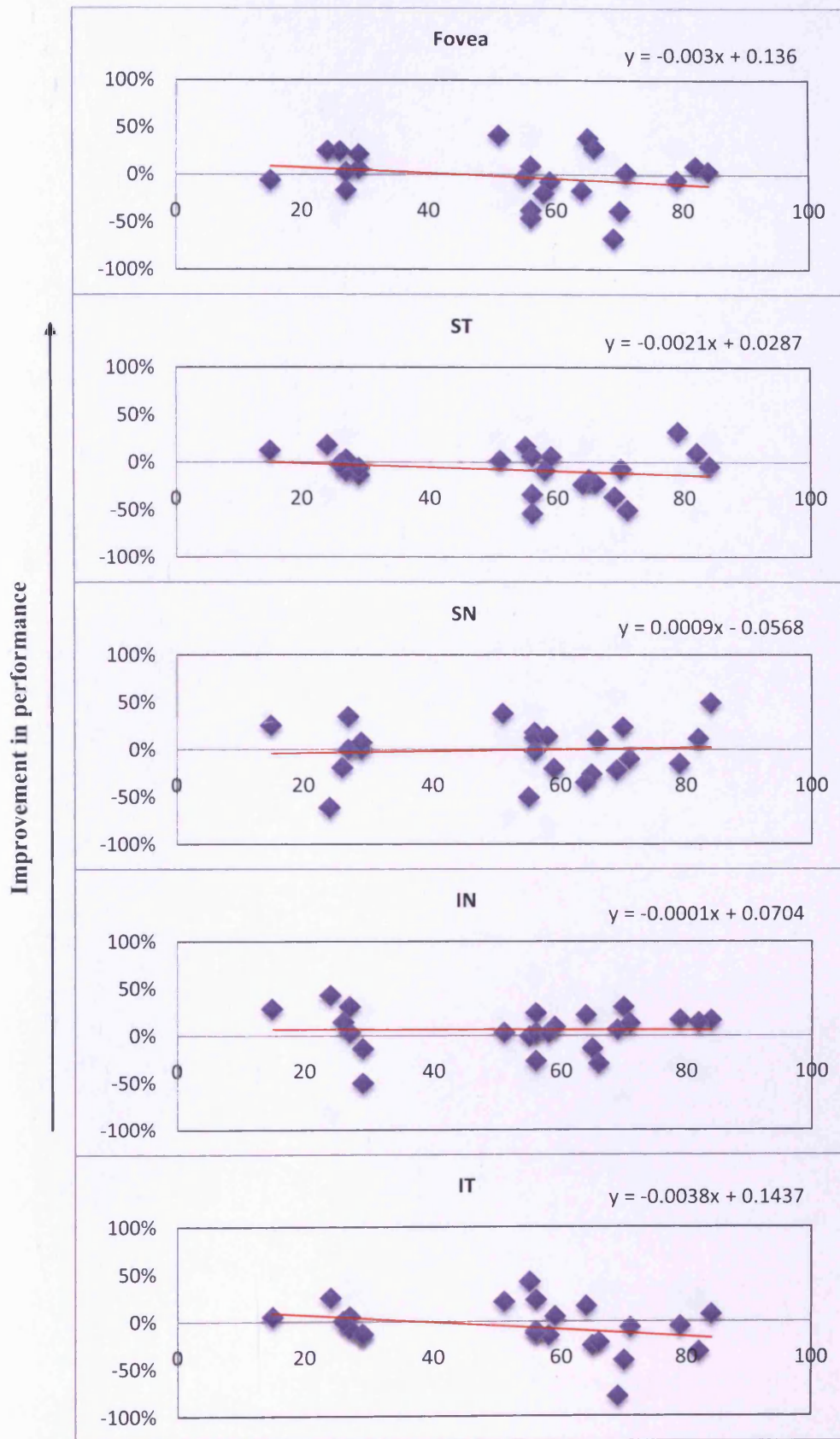


Figure 6.12 Motion detection: The proportionate improvement in performance (ordinate) from visit 2 to visit 3 for Michelson contrast thresholds in the absence of the noise mask ($MC N_0$) as a function of age (abscissa). A positive value indicates an improvement in performance.

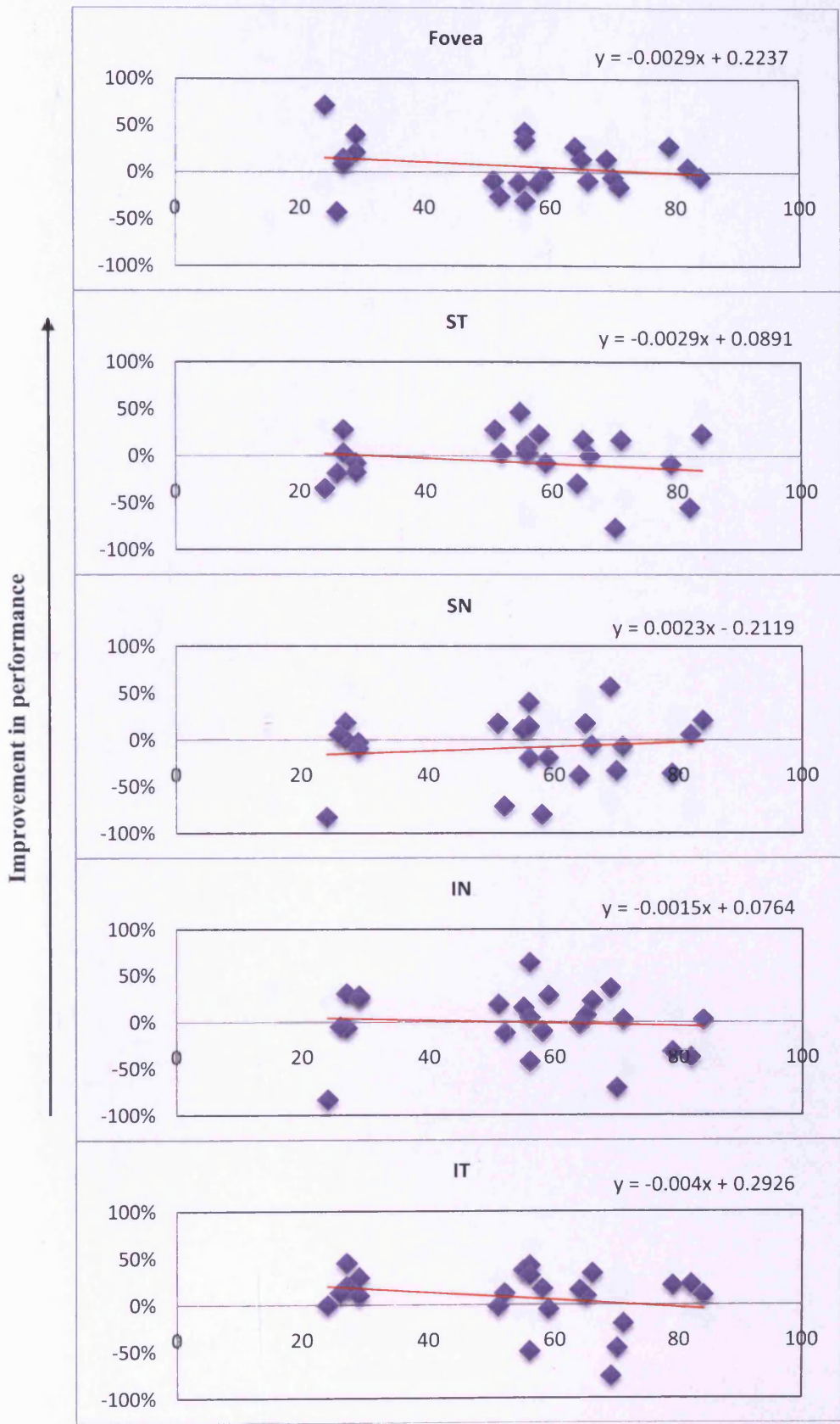


Figure 6.13 Motion discrimination: The proportionate improvement in performance (ordinate) from visit 2 to visit 3 for Michelson contrast thresholds in the absence of the noise mask ($MC N_0$) as a function of age (abscissa). A positive value indicates an improvement in performance.

Improvement in performance

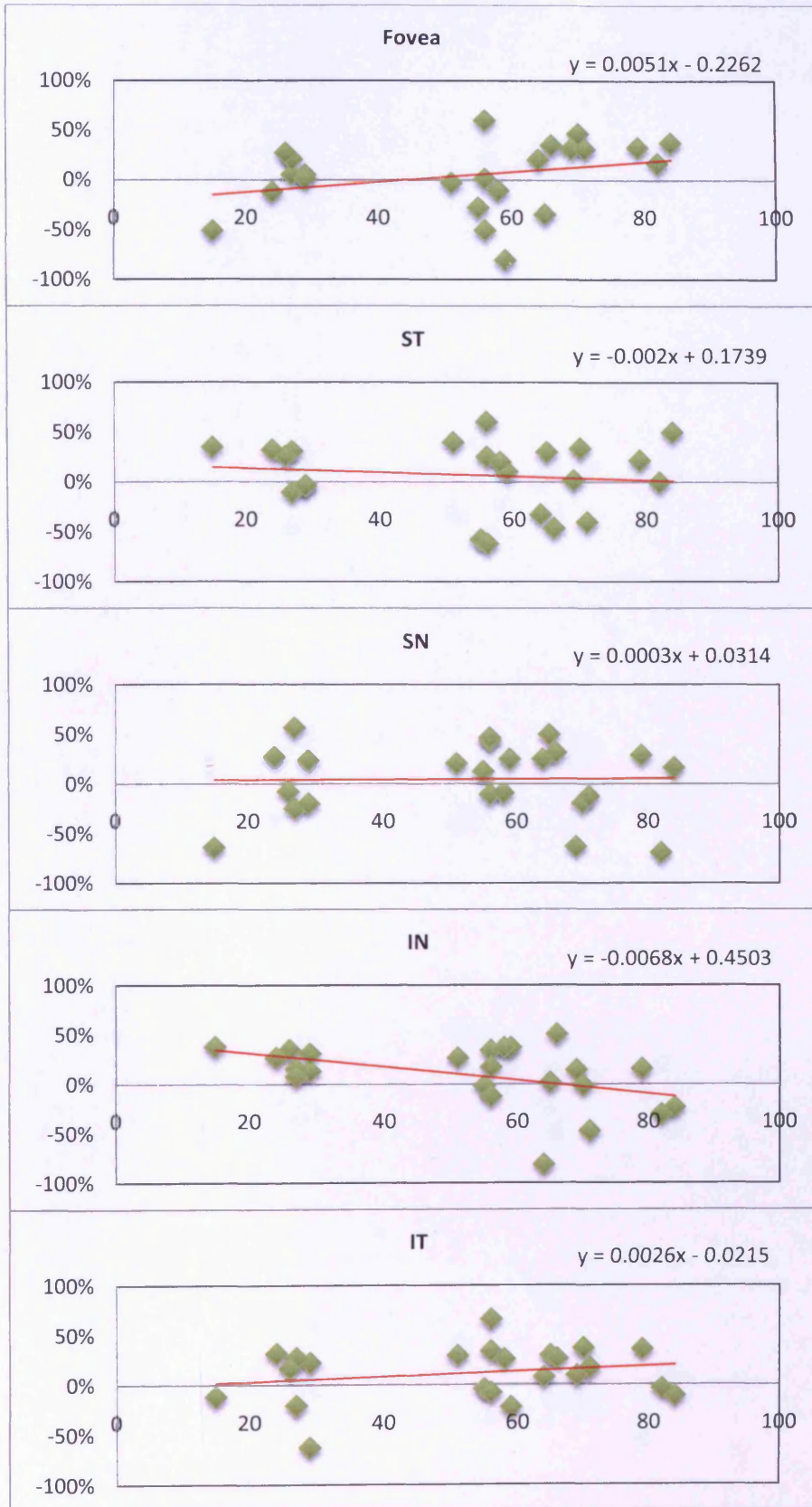


Figure 6.14 Motion detection: The proportionate improvement in performance (ordinate) from visit 1 to visit 2 for Michelson contrast thresholds in the presence of the noise mask ($MC N_c$) as a function of age (abscissa). A positive value indicates an improvement in performance.

Improvement in performance ↑

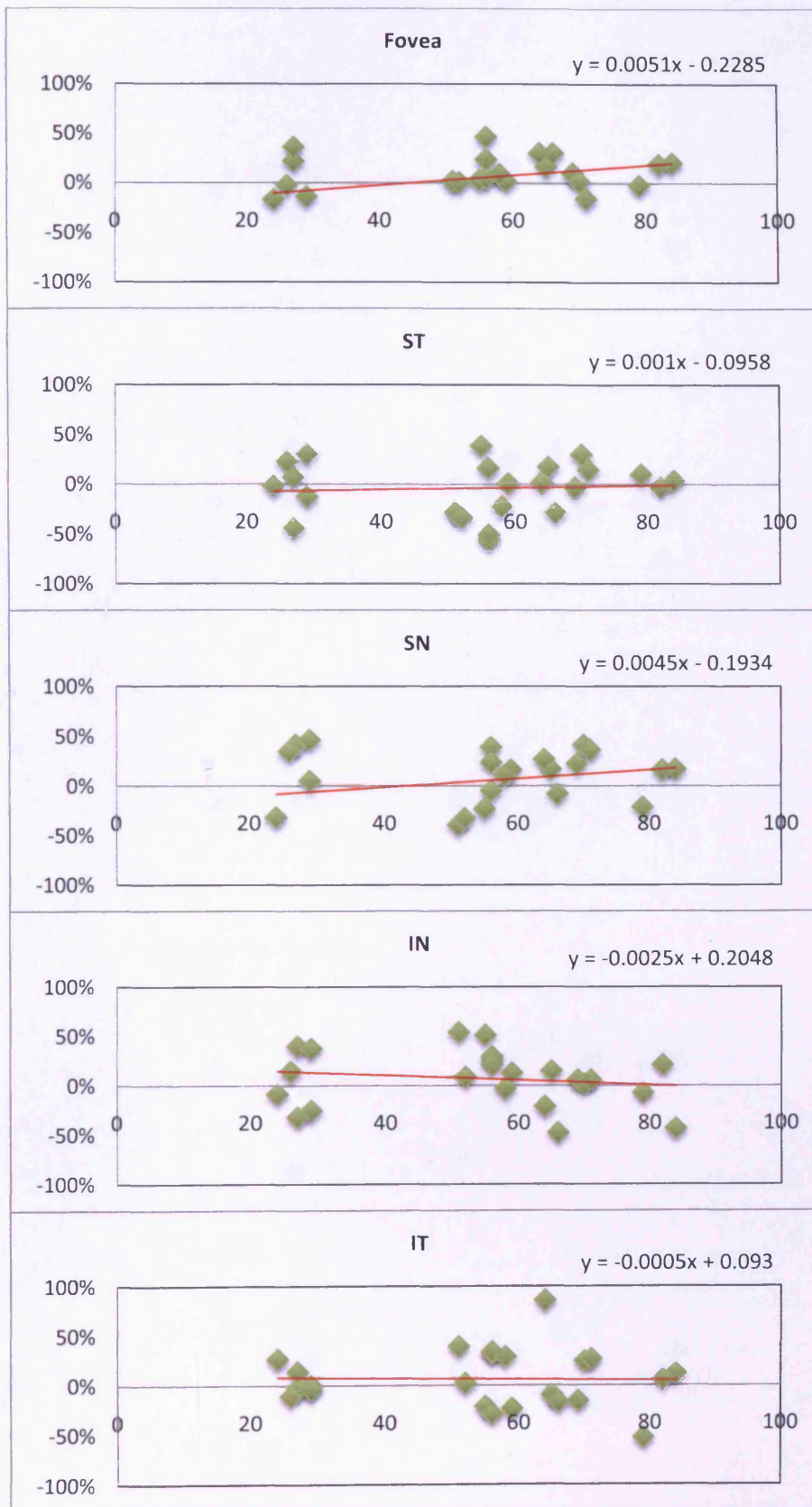


Figure 6.15 Motion discrimination: The proportionate improvement in performance (ordinate) from visit 1 to visit 2 for Michelson contrast thresholds in the presence of the noise mask ($MC N_e$) as a function of age (abscissa). A positive value indicates an improvement in performance.

Improvement in performance

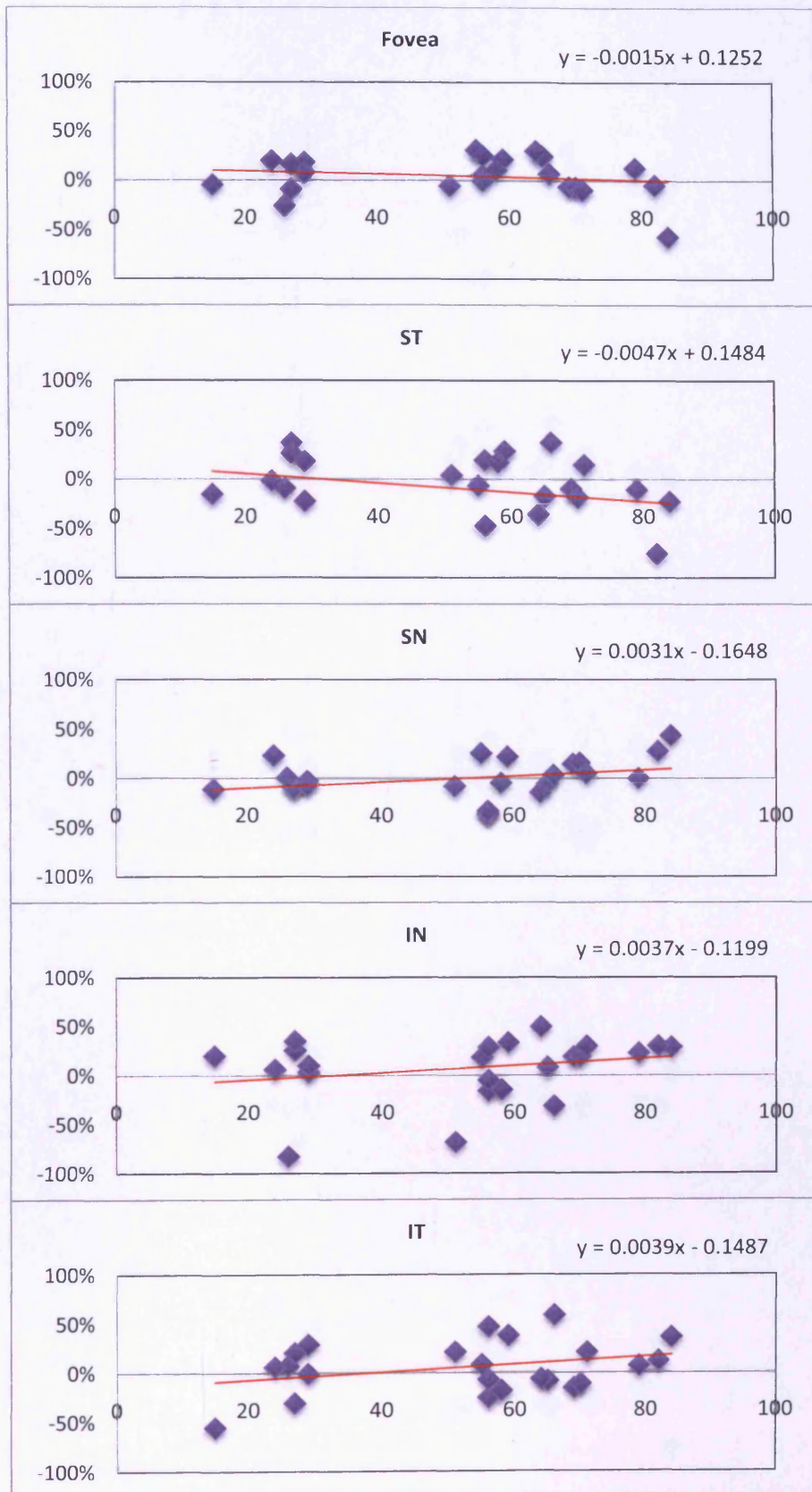


Figure 6.16 Motion detection: The proportionate improvement in performance (ordinate) from visit 2 to visit 3 for Michelson contrast thresholds in the presence of the noise mask ($MC N_e$) as a function of age (abscissa). A positive value indicates an improvement in performance.

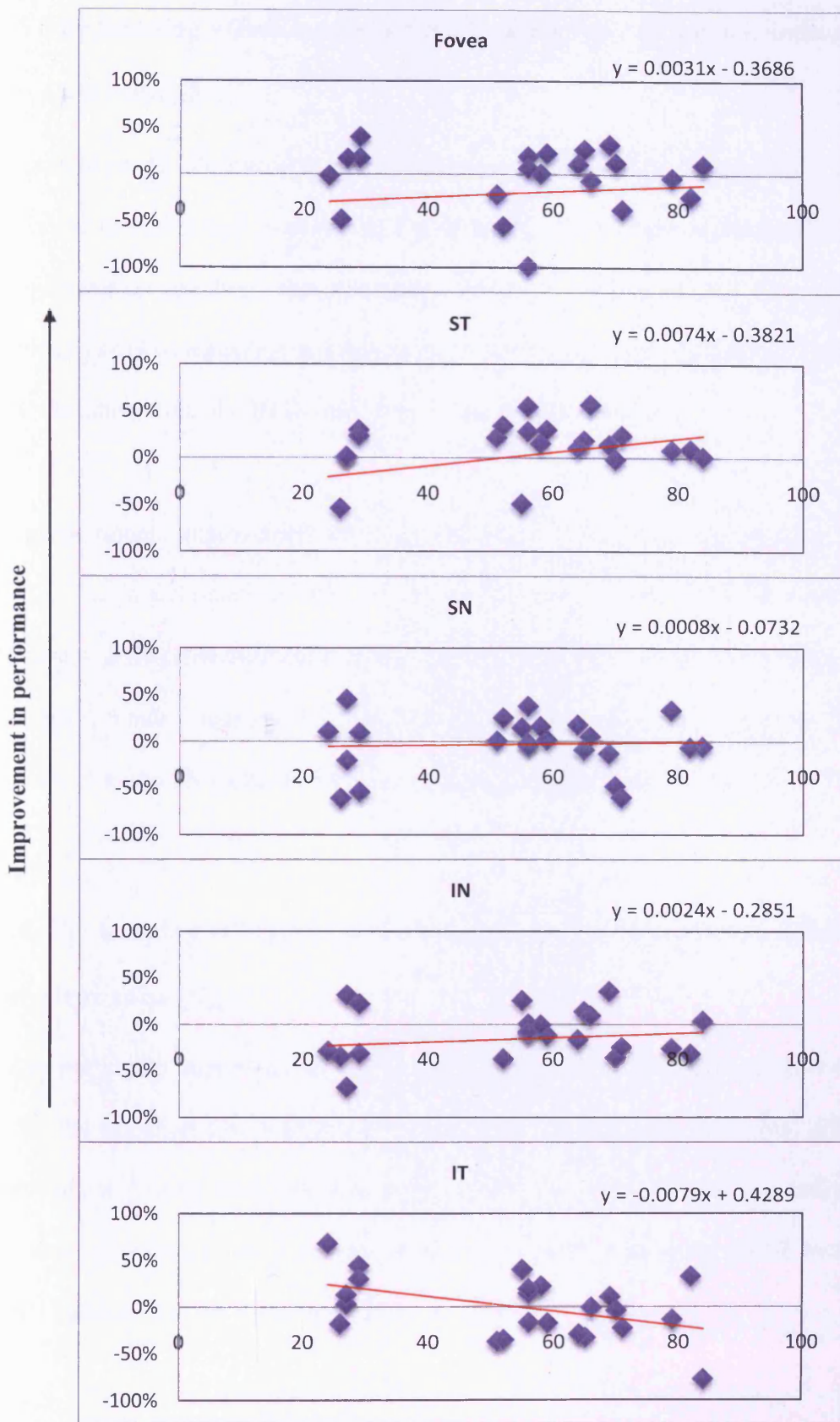


Figure 6.17 Motion discrimination: The proportionate improvement in performance (ordinate) from visit 2 to visit 3 for Michelson contrast thresholds in the presence of the noise mask ($MC N_e$) as a function of age (abscissa). A positive value indicates an improvement in performance.

6.5.5 The learning effect between visit 1 and 2 for the normal individuals for equivalent noise (N_{eq})

The proportionate improvement in N_{eq} across each of the five locations as a function of age for the detection task is shown in Figure 6.18. The between-individual differences in improvement ranged from approximately -700% to +100%. Of the 23 individuals, 10 individuals showed a positive improvement for foveal viewing, 13 at the ST location, 11 at the SN location, 10 at the IN location and 13 at the IT location.

The proportionate improvement in N_{eq} across each of the five locations as a function of age for the discrimination task is shown in Figure 6.19. The between-individual differences in improvement ranged from approximately to -600% to +100%. Of the 22 individuals, 8 individuals showed a positive improvement for foveal viewing, 11 at the ST location, 11 at the SN location, 8 at the IN location and 9 at the IT location.

6.5.6 The learning effect between visit 2 and 3 for the normal individuals for equivalent noise (N_{eq})

The proportionate improvement in N_{eq} across each of the five locations as a function of age for the detection task is shown in Figure 6.20. The between-individual differences in improvement ranged from approximately -800% to 100%. Of the 23 individuals, 10 individuals showed a positive improvement for foveal viewing, 12 at the ST location, 13 at the SN location, 9 at the IN location and 7 at the IT location.

The proportionate improvement in N_{eq} across each of the five locations as a function of age for the discrimination task is shown in Figure 6.21. The between-individual

differences in improvement ranged from approximately to -500 % to +100%. Of the 22 individuals, 14 individuals showed a positive improvement for foveal viewing, 10 at the ST location, 12 at the SN location, 13 at the IN location and 15 at the IT location.

6.5.7 The learning effect between visit 1 and 2 for the normal individuals for sampling efficiency (SE)

The proportionate improvement in SE across each of the five locations as a function of age for the detection task is shown in Figure 6.22. The between-individual differences in improvement ranged from approximately -100% to +700%. Of the 23 individuals, 15 individuals showed a positive improvement for foveal viewing, 14 at the ST location, 13 at the SN location, 16 at the IN location and 15 at the IT location.

The proportionate improvement in SE across each of the five locations as a function of age for the discrimination task is shown in Figure 6.23. The between-individual differences in improvement ranged from approximately to -100% to +400%. Of the 22 individuals, 17 individuals showed a positive improvement for foveal viewing, 12 at the ST location, 15 at the SN location, 15 at the IN location and 12 at the IT location.

6.5.8 The learning effect between visit 2 and 3 for the normal individuals for sampling efficiency (SE)

The proportionate improvement in SE across each of the five locations as a function of age for the detection task is shown in Figure 6.24. The between-individual differences in improvement ranged from approximately -50% to 500%. Of the 23 individuals, 13

individuals showed a positive improvement for foveal viewing, 9 at the ST location, 11 at the SN location, 17 at the IN location and 14 at the IT location.

The proportionate improvement in SE across each of the five locations as a function of age for the discrimination task is shown in Figure 6.22. The between-individual differences in improvement ranged from approximately to -100 % to +400%. Of the 22 individuals, the number of individuals showing a positive improvement were 12 for foveal viewing, 16 at the ST location, 12 at the SN location, 8 at the IN location and 10 at the IT location.

Improvement in performance

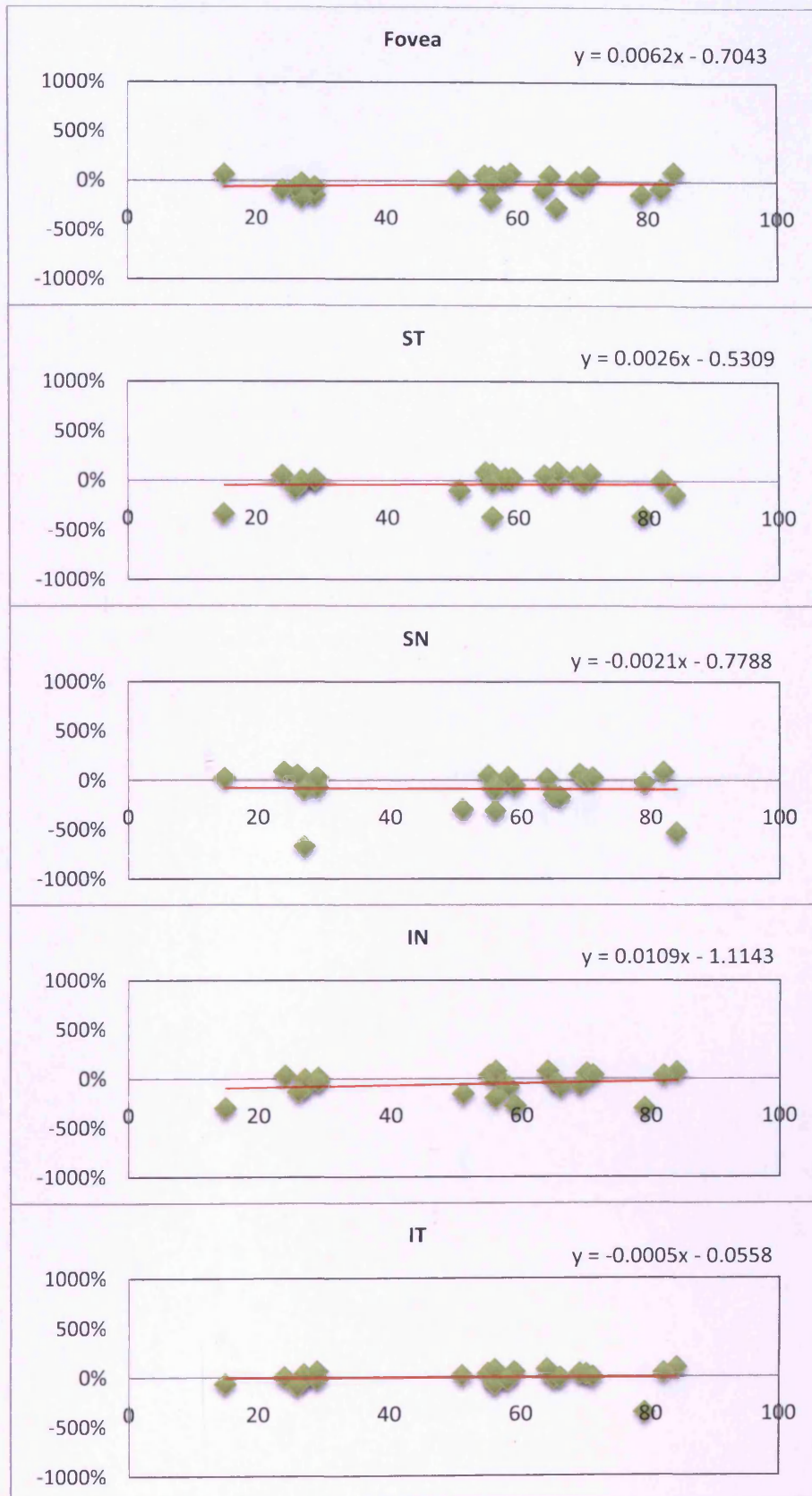


Figure 6.18 Motion detection: The proportionate improvement in performance (ordinate) from visit 1 to visit 2 in terms of equivalent noise (N_{eq}) as a function of age (abscissa). A positive value indicates an improvement in performance.

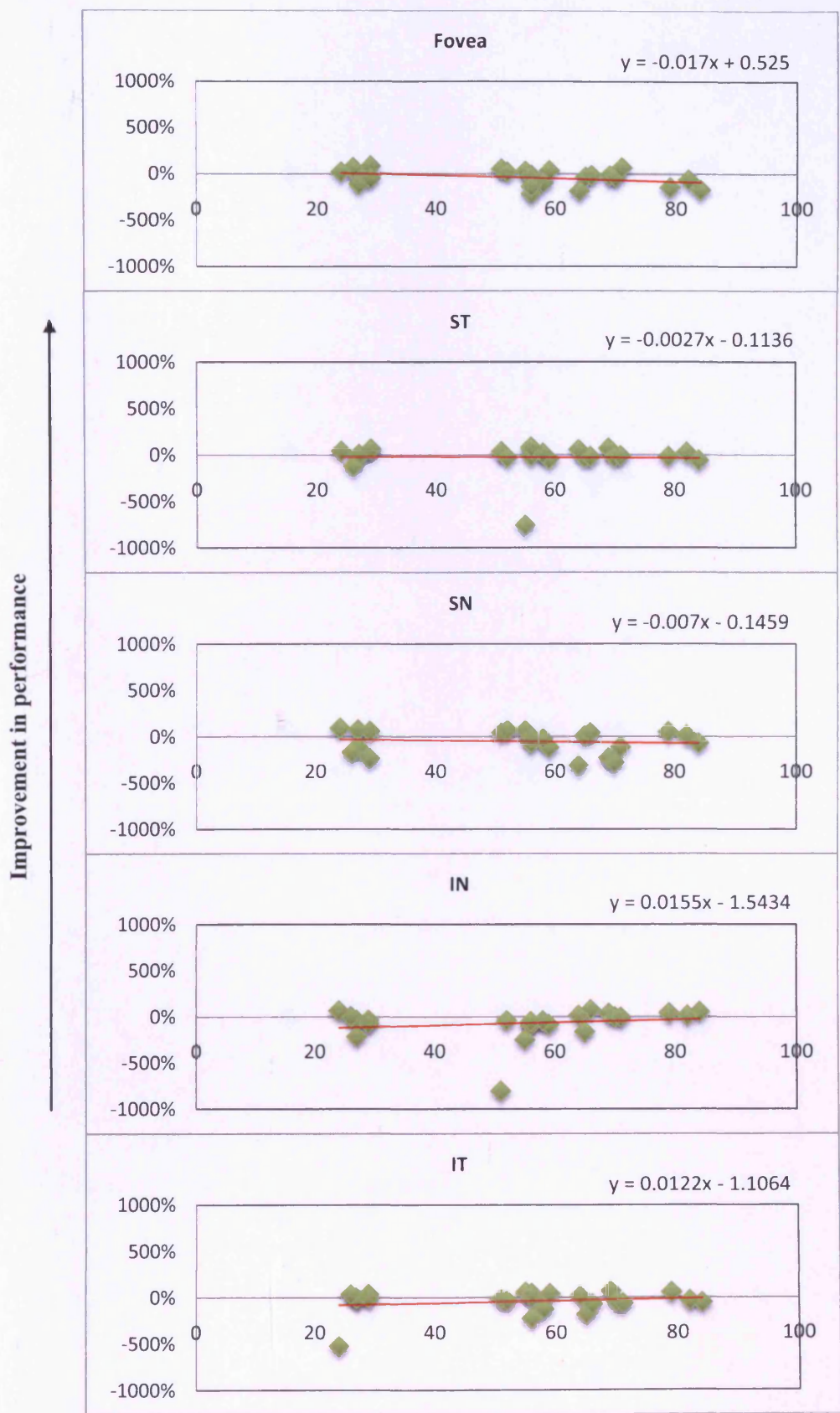


Figure 6.19 Motion discrimination: The proportionate improvement in performance (ordinate) from visit 1 to visit 2 in terms of equivalent noise (N_{eq}) as a function of age (abscissa). A positive value indicates an improvement in performance.

Improvement in performance ↑

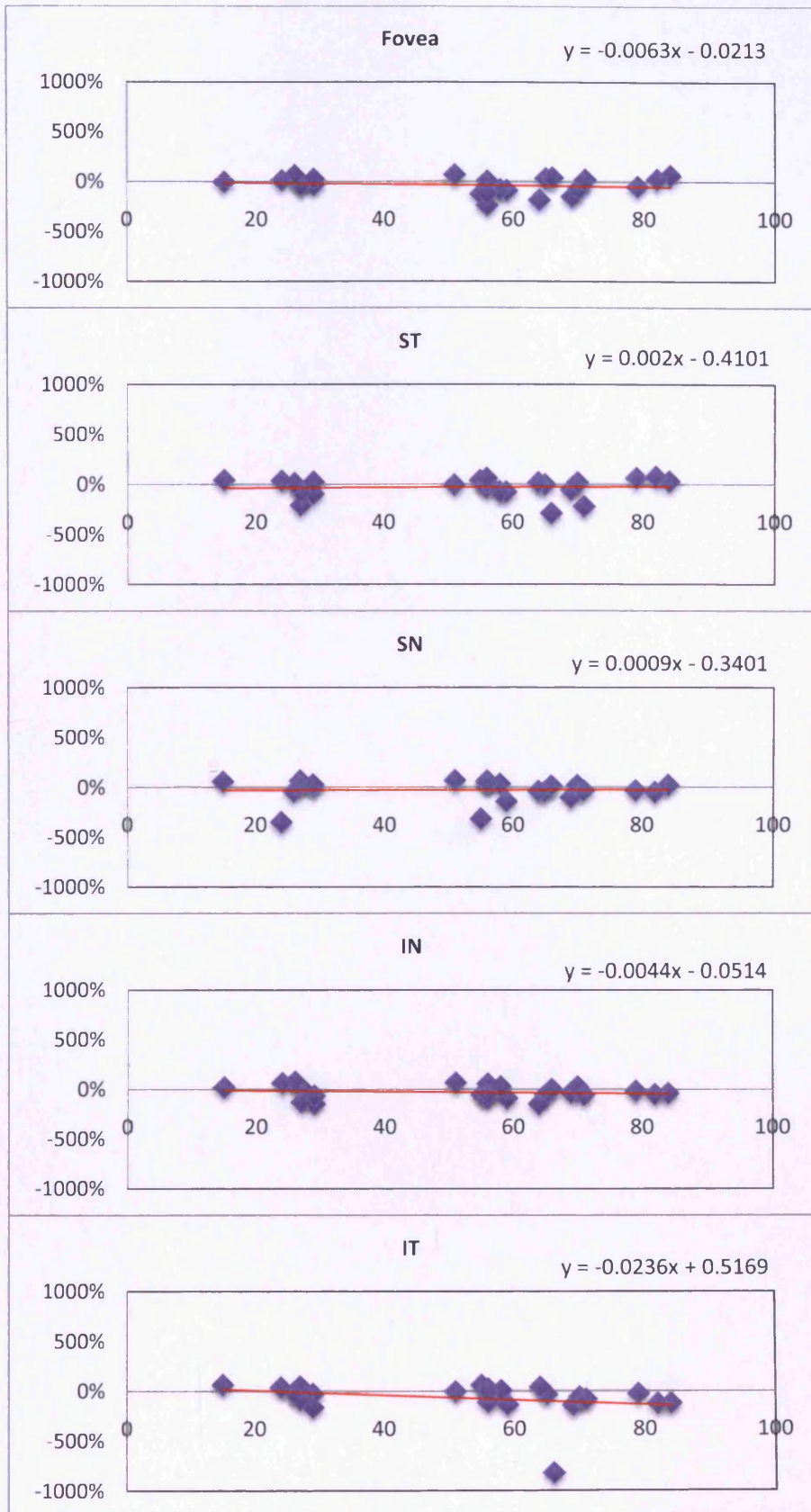


Figure 6.20 Motion detection: The proportionate improvement in performance (ordinate) from visit 2 to visit 3 in terms of equivalent noise (N_{eq}) as a function of age (abscissa). A positive value indicates an improvement in performance.

Improvement in performance

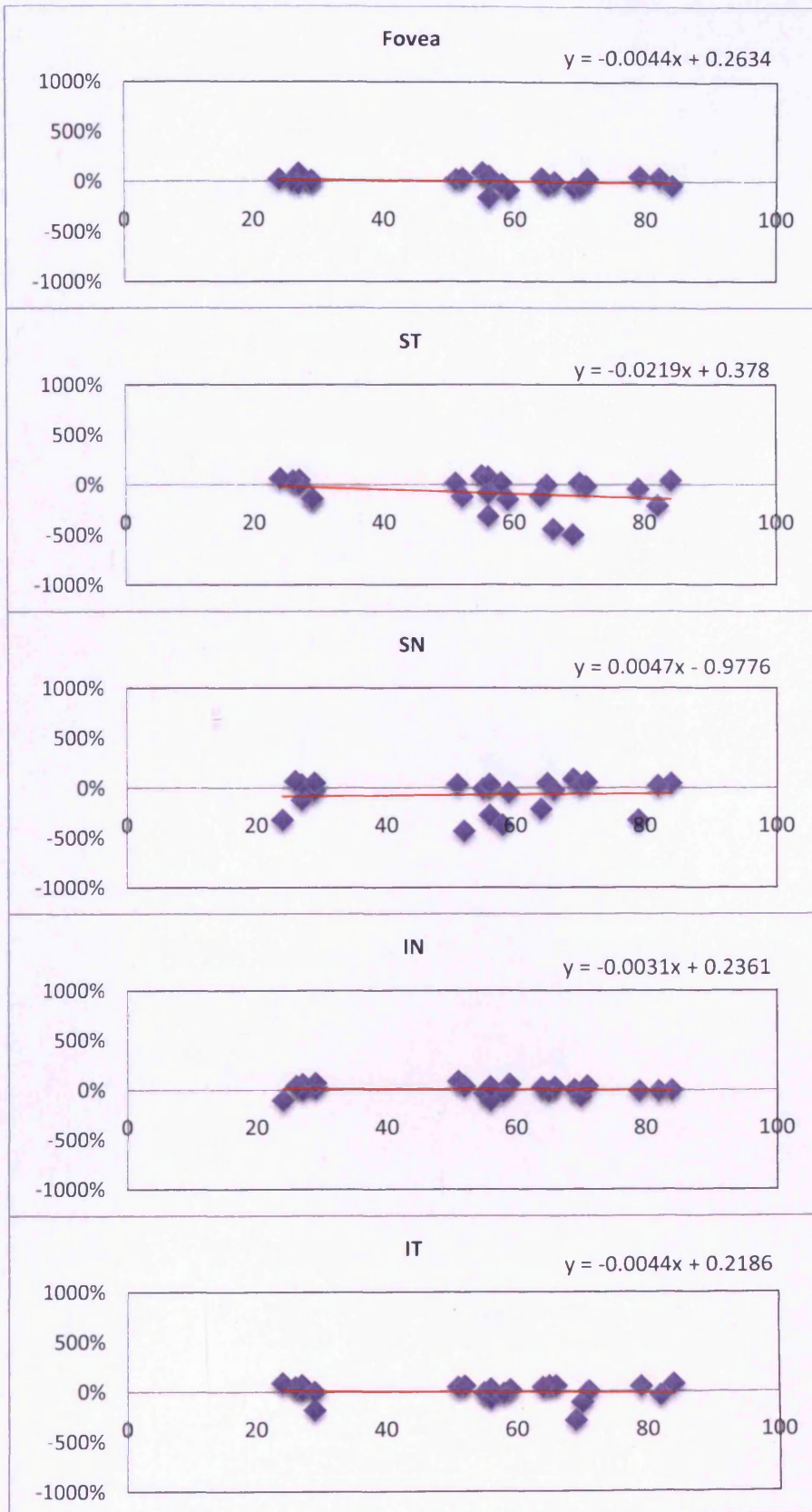


Figure 6.21 Motion discrimination: The proportionate improvement in performance (ordinate) from visit 2 to visit 3 in terms of equivalent noise (N_{eq}) as a function of age (abscissa). A positive value indicates an improvement in performance.

Improvement in performance ↑

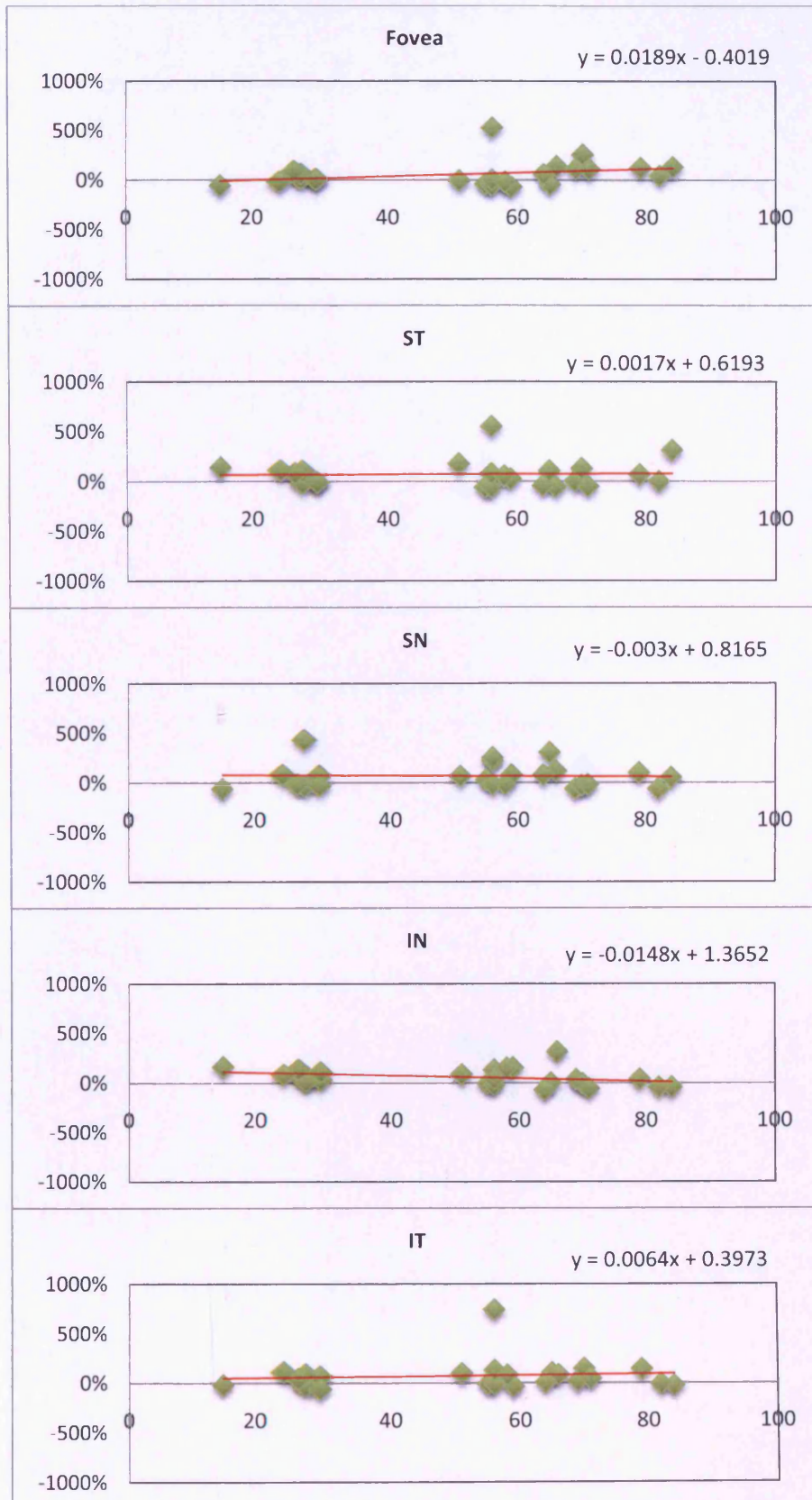


Figure 6.22 Motion detection: The proportionate improvement in performance (ordinate) from visit 1 to visit 2 in terms of sampling efficiency (SE) as a function of age (abscissa). A positive value indicates an improvement in performance.

Improvement in performance

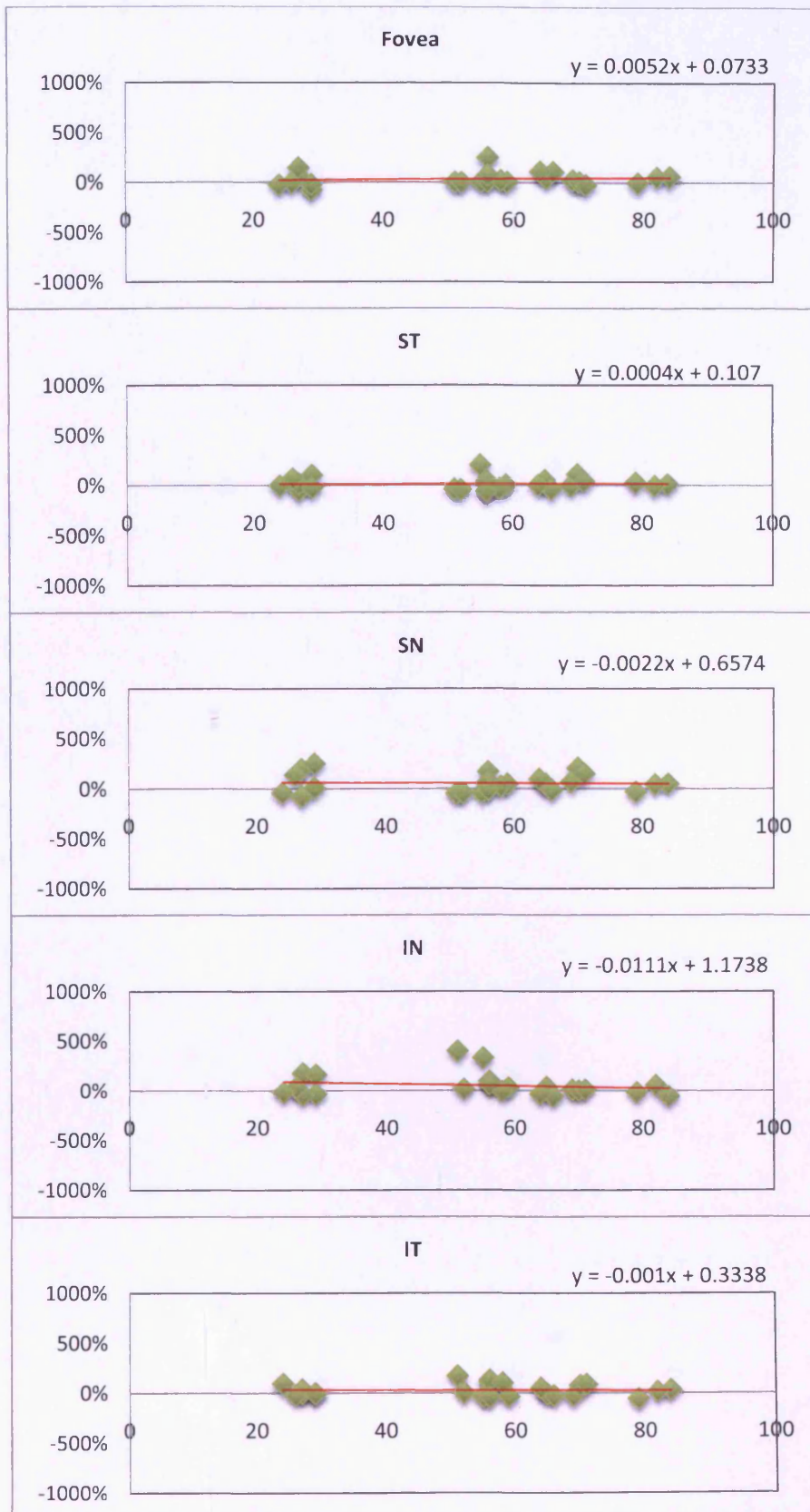


Figure 6.23 Motion discrimination: The proportionate improvement in performance (ordinate) from visit 1 to visit 2 in terms of sampling efficiency (SE) as a function of age (abscissa). A positive value indicates an improvement in performance.

Improvement in performance

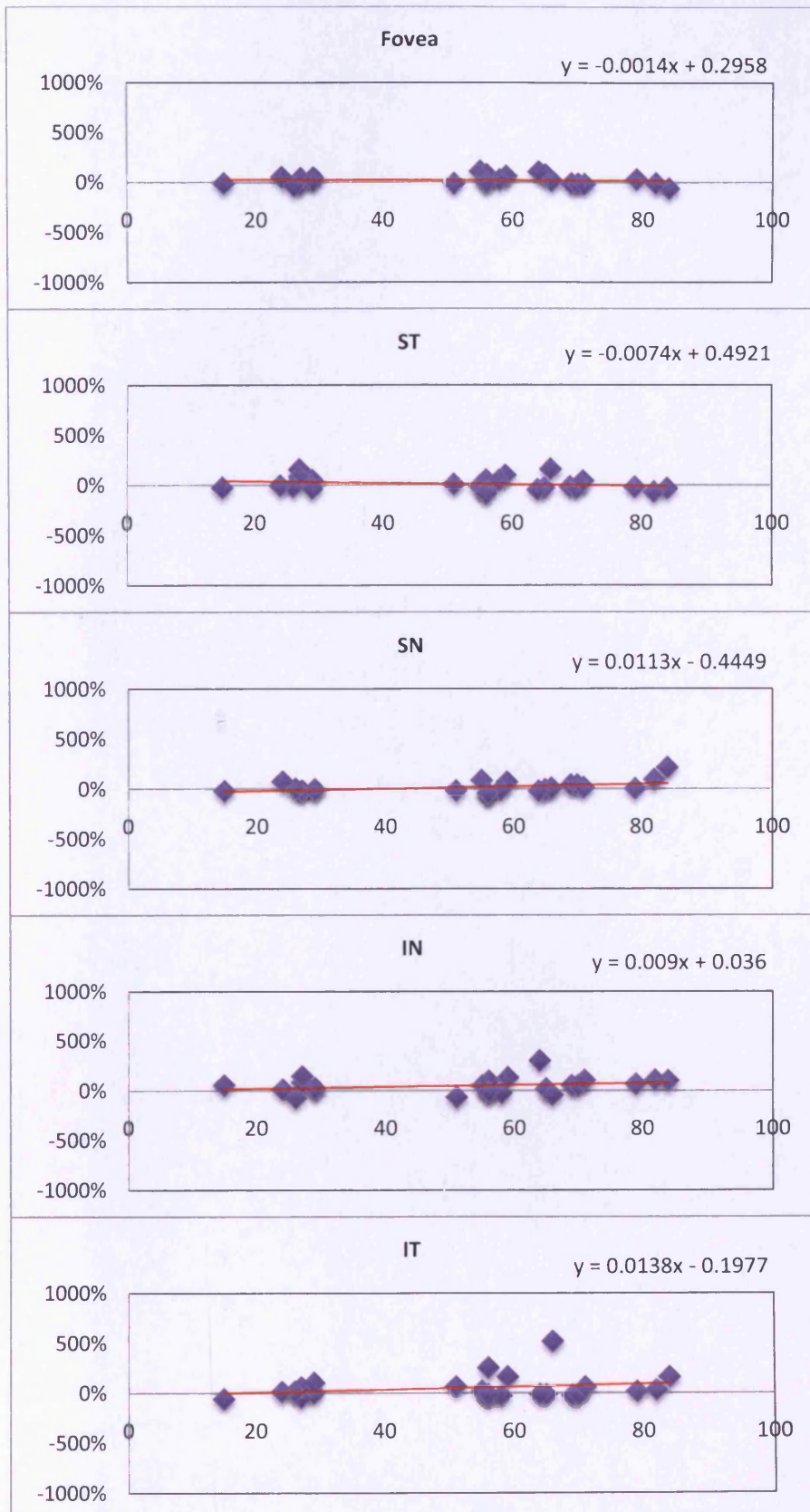


Figure 6.24 Motion detection: The proportionate improvement in performance (ordinate) from visit 2 to visit 3 in terms of sampling efficiency (SE) as a function of age (abscissa). A positive value indicates an improvement in performance.

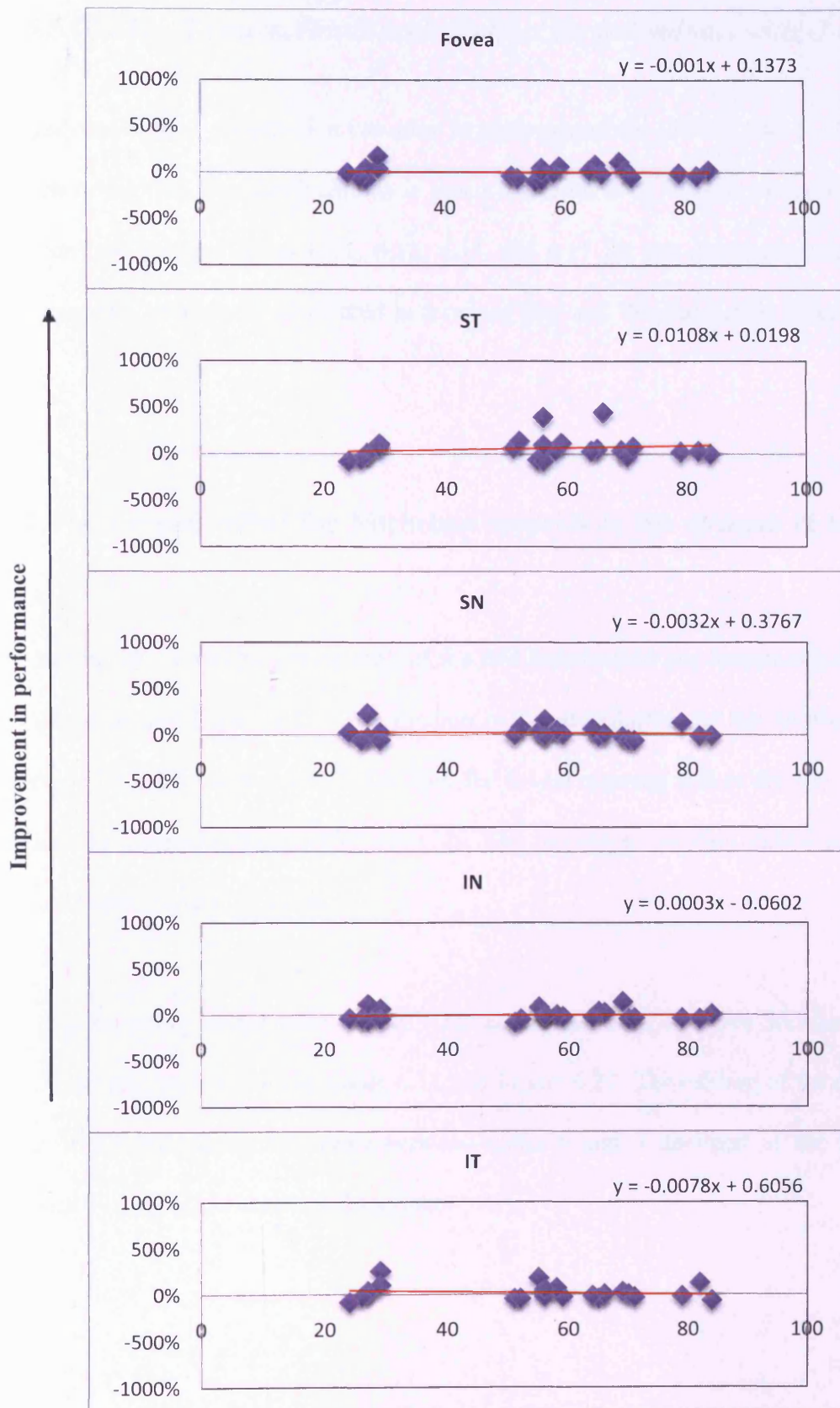


Figure 6.25 Motion discrimination: The proportionate improvement in performance (ordinate) from visit 2 to visit 3 in terms of sampling efficiency (SE) as a function of age (abscissa). A positive value indicates an improvement in performance.

6.6 RESULTS: The absolute learning effect for individuals with OAG

The outcome of the between-visit variation in performance for MC N_0 , MC N_e , N_{eq} and SE for each of the five stimulus locations is given in Tables 6.10, 6.12, 6.14 and 6.16 for the detection task and in Tables 6.11, 6.13, 6.15 and 6.17 for the discrimination task. The results are also graphically illustrated in terms of Box and Whiskers plots (Figures 6.29 to 6.33).

6.6.1 The learning effect for Michelson contrast in the absence of noise (MC N_0)

The distribution of MC N_0 across each of the five locations for the detection task is shown in Table 6.10 and Figure 6.26. The median of the distribution of the within-individual difference between visits 1 and 3 declined for foveal viewing and at the SN, IN and IT locations by clinically meaningful amounts. The remaining location exhibited clinically identical values across the visits.

The corresponding distribution of MC N_0 across each of the five locations for the discrimination task is shown in Table 6.11 and Figure 6.27. The median of the distribution of the within-individual difference between visits 1 and 3 declined at the ST and IT locations by a clinically meaningful amount.

6.6.2 The learning effect for Michelson contrast in the presence of noise (MC N_e)

The distribution of MC N_e across each of the five locations for the detection task is shown in Table 6.12 and Figure 6.28. The median of the distribution of the within-individual difference between visits 1 and 3 declined for foveal viewing and at the ST, IN and IT locations by clinically meaningful amounts.

The corresponding distribution of MC N_e across each of the five locations for the discrimination task is shown in Table 6.13 and Figure 6.29. The median of the distribution of the within-individual difference between visits 1 and 3 declined for foveal viewing and at the ST, SN and IT locations by a clinically meaningful amount.

6.6.3 The learning effect for equivalent noise (N_{eq})

The distribution of N_{eq} across each of the five locations for the detection task is shown in Table 6.14 and Figure 6.30. The median of the distribution of the within-individual difference between visits 1 and 3 declined at the ST, SN and IT locations by clinically meaningful amounts. At the remaining locations the median of the distribution of the within-individual difference between visits 1 and 3 increased by a clinically meaningful amount.

The corresponding distribution of N_{eq} across each of the five locations for the discrimination task is shown in Table 6.15 and Figure 6.31. The median of the distribution of the within-individual difference between visits 1 and 3 declined at increased at all locations by clinically meaningful amounts.

6.6.4 The learning effect for sampling efficiency (SE)

The distribution of SE across each of the five locations for the detection task is shown in Table 6.16 and Figure 6.32. The median of the distribution of the within-individual difference between visits 1 and 3 increased at all locations by clinically meaningful amounts.

The corresponding distribution of SE across each of the five locations for the discrimination task is shown in Table 6.17 and Figure 6.33. The median of the distribution of the within-individual difference between visits 1 and 3 increased for foveal viewing and at the ST, IN and IT locations by a clinically meaningful amount.

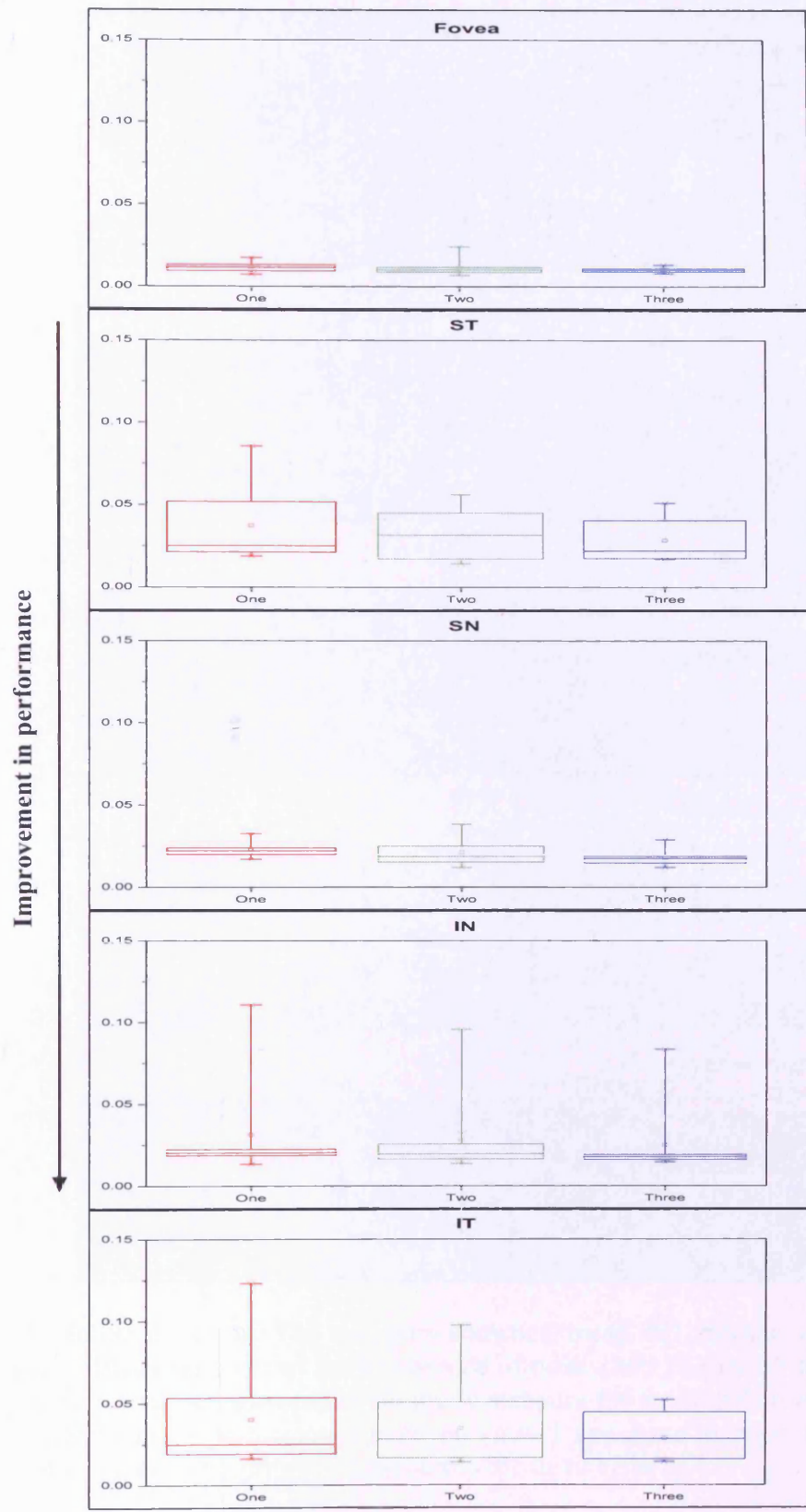


Figure 6.26 Motion detection: Box and Whiskers plot of the distribution of Michelson contrast thresholds (ordinate) in the absence of the noise mask ($MC N_0$) across a group of 10 individuals with OAG as a function of visits (abscissa).

Fovea	Visit			Improvement
	One	Two	Three	
Mean	0.011484	0.011351	0.010097	-0.001387
SD	0.003297	0.004934	0.001572	0.002745
Median	0.011220	0.010034	0.009820	-0.001830
25th percentile	0.009631	0.008744	0.009063	-0.003174
75th percentile	0.012819	0.011285	0.010672	-0.001457
ST	Visit			Improvement
	One	Two	Three	
Mean	0.037081	0.031567	0.028294	-0.008787
SD	0.022979	0.015883	0.013233	0.013819
Median	0.024953	0.031441	0.021904	-0.001554
25th percentile	0.021048	0.017017	0.017384	-0.013690
75th percentile	0.051738	0.044833	0.040385	-0.000801
SN	Visit			Improvement
	One	Two	Three	
Mean	0.022551	0.021028	0.017677	-0.004873
SD	0.004631	0.007933	0.004886	0.006278
Median	0.021904	0.018538	0.017418	-0.003592
25th percentile	0.019863	0.015172	0.014484	-0.005263
75th percentile	0.023672	0.024907	0.018538	-0.002445
IN	Visit			Improvement
	One	Two	Three	
Mean	0.031317	0.028407	0.024933	-0.006384
SD	0.030582	0.025640	0.022128	0.009117
Median	0.020350	0.019662	0.017787	-0.003974
25th percentile	0.018796	0.016471	0.016023	-0.004625
75th percentile	0.022412	0.025641	0.019117	-0.002099
IT	Visit			Improvement
	One	Two	Three	
Mean	0.040104	0.034591	0.028488	-0.011616
SD	0.031131	0.025734	0.013783	0.021446
Median	0.024871	0.028166	0.028108	-0.008078
25th percentile	0.020966	0.017145	0.016184	-0.009267
75th percentile	0.049115	0.041598	0.039570	-0.001415

Table 6.10 Motion detection: The summary statistics, mean, SD, median and interquartile range for the Michelson contrast in the absence of noise (MC N_0) for 10 individuals with OAG at the five given locations. The summary statistics for the distribution of the within-individual difference in performance between visits 1 and 3 are given in column five. A negative value indicates an improvement across the three visits.

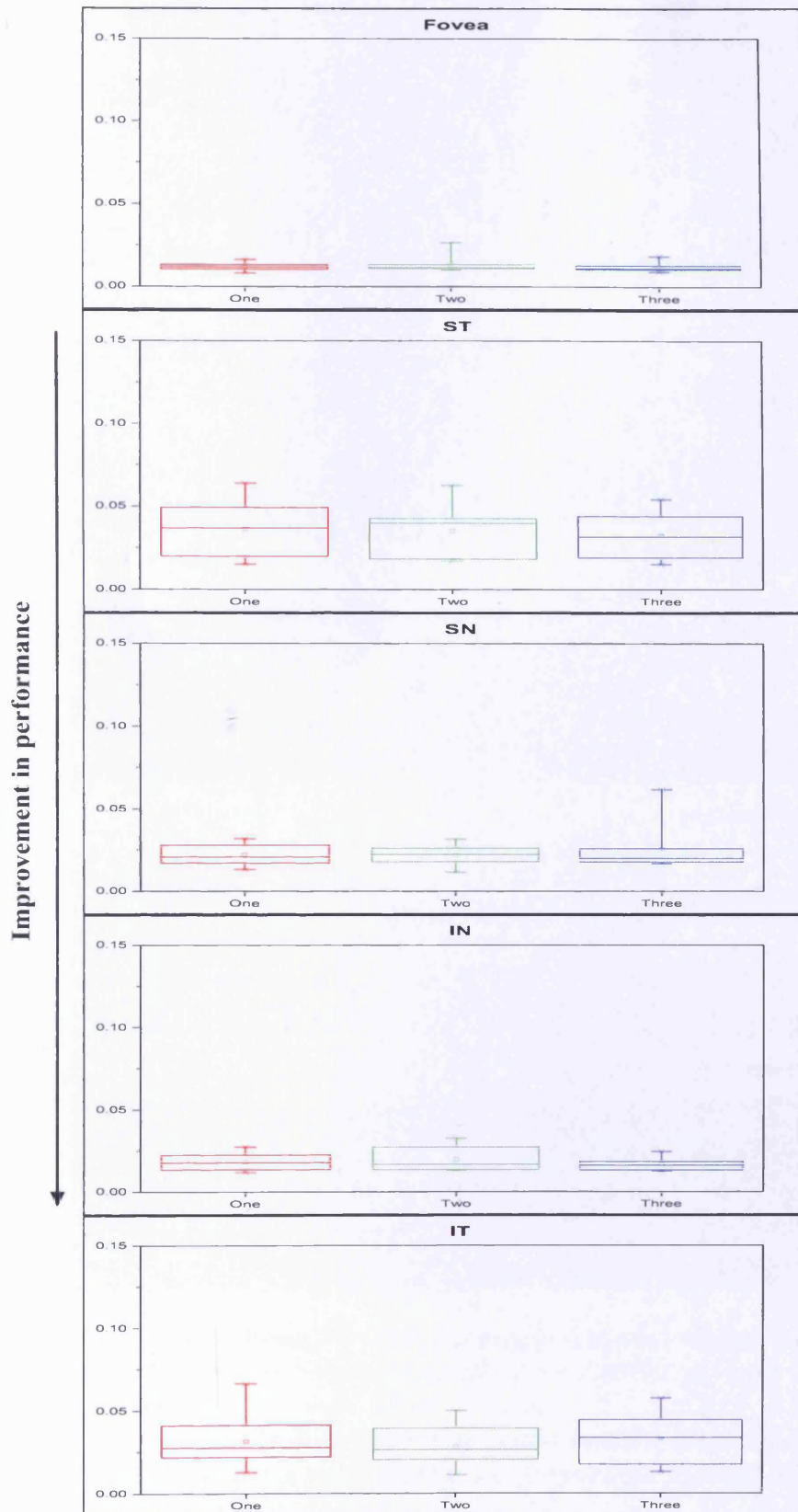


Figure 6.27 Motion discrimination: Box and Whiskers plot of the distribution of Michelson contrast thresholds (ordinate) in the absence of the noise mask ($MC N_0$) across a group of 9 individuals with OAG as a function of visits (abscissa).

Fovea	Visit			Improvement
	One	Two	Three	
Mean	0.011567	0.013060	0.011770	0.000203
SD	0.002657	0.005170	0.002833	0.001448
Median	0.011446	0.011188	0.010672	0.000000
25th percentile	0.010348	0.010606	0.010348	-0.000296
75th percentile	0.012818	0.013073	0.012522	0.000785
ST	Visit			Improvement
	One	Two	Three	
Mean	0.036099	0.034927	0.032157	-0.003941
SD	0.017549	0.016085	0.015320	0.007529
Median	0.036651	0.039530	0.031419	-0.001097
25th percentile	0.019962	0.018443	0.019765	-0.009644
75th percentile	0.047289	0.042259	0.043211	0.000457
SN	Visit			Improvement
	One	Two	Three	
Mean	0.021809	0.021702	0.025438	0.003630
SD	0.006650	0.006379	0.015011	0.016558
Median	0.020620	0.022093	0.019573	-0.000815
25th percentile	0.017553	0.018992	0.017737	-0.005549
75th percentile	0.026885	0.025300	0.025641	0.002764
IN	Visit			Improvement
	One	Two	Three	
Mean	0.018248	0.019845	0.016805	-0.001443
SD	0.005393	0.007421	0.004048	0.006236
Median	0.018106	0.016951	0.016151	-0.000433
25th percentile	0.014675	0.014758	0.013924	-0.005032
75th percentile	0.020421	0.023269	0.018179	0.000606
IT	Visit			Improvement
	One	Two	Three	
Mean	0.031355	0.027889	0.033066	0.001711
SD	0.014519	0.011853	0.015309	0.011491
Median	0.027599	0.026283	0.033399	0.001779
25th percentile	0.023227	0.020854	0.020534	-0.004898
75th percentile	0.035767	0.035966	0.042692	0.006506

Table 6.11 Motion discrimination: The summary statistics, mean, SD, median and interquartile range for the Michelson contrast in the absence of noise (MC N_0) for 9 individuals with OAG at the five given locations. The summary statistics for the distribution of the within-individual difference in performance between visits 1 and 3 are given in column five. A negative value indicates an improvement across the three visits.

Improvement in performance

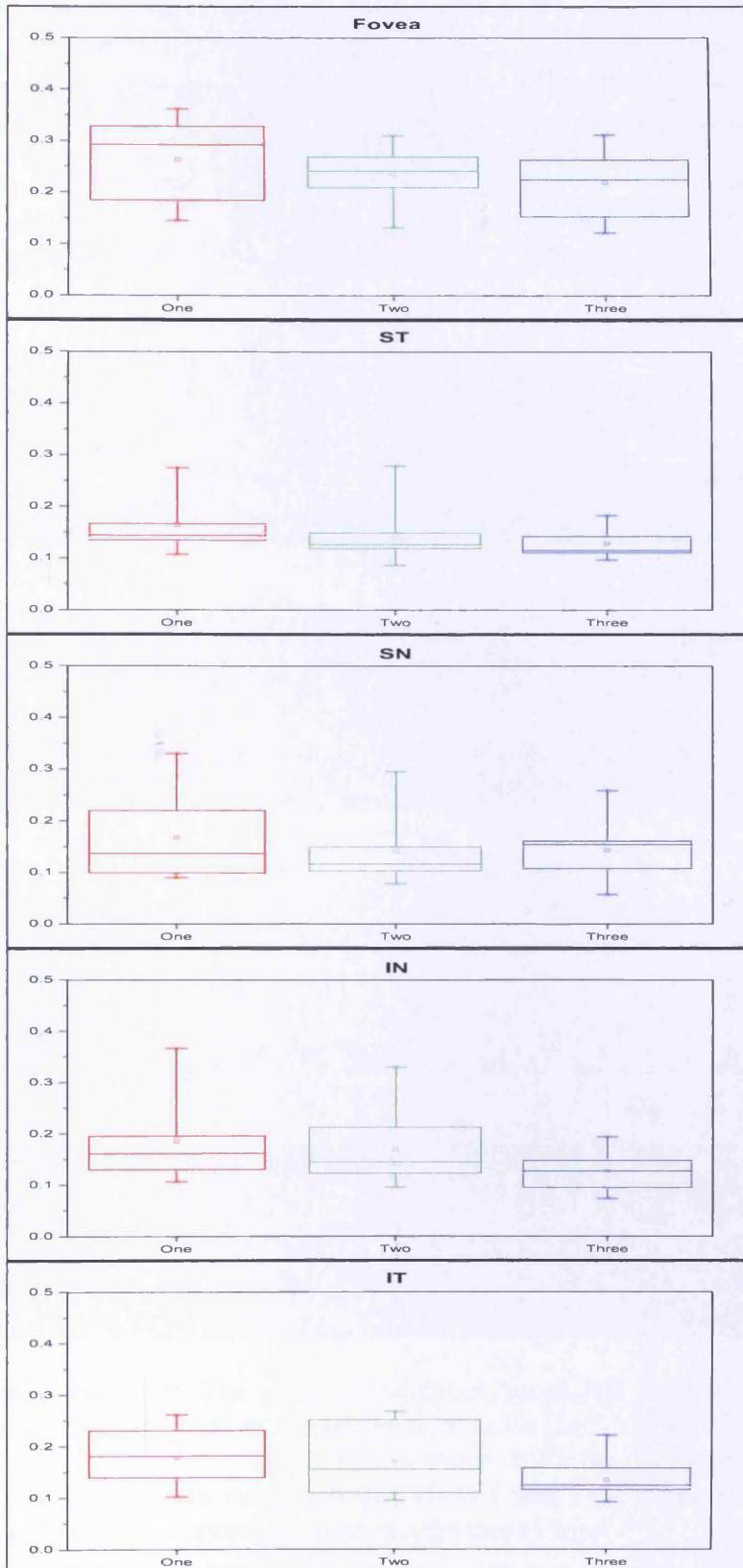


Figure 6.28 Motion detection: Box and Whiskers plot of the distribution of Michelson contrast thresholds (ordinate) in the presence of the noise mask ($MC N_e$) across a group of 10 individuals with OAG as a function of visits (abscissa).

Fovea	Visit			Improvement
	One	Two	Three	
Mean	0.263092	0.234795	0.219265	-0.043827
SD	0.076869	0.059889	0.068144	0.074261
Median	0.291508	0.241210	0.224788	-0.037680
25th percentile	0.195250	0.211266	0.159199	-0.084538
75th percentile	0.321137	0.267773	0.262759	-0.000394
ST	Visit			Improvement
	One	Two	Three	
Mean	0.163348	0.140545	0.127662	-0.035686
SD	0.051055	0.056166	0.026175	0.053743
Median	0.143227	0.126295	0.114978	-0.023913
25th percentile	0.133655	0.118415	0.110602	-0.031990
75th percentile	0.165872	0.148307	0.141959	-0.022824
SN	Visit			Improvement
	One	Two	Three	
Mean	0.167197	0.140644	0.142948	-0.024249
SD	0.084499	0.068660	0.058701	0.064175
Median	0.136014	0.116105	0.153537	-0.005363
25th percentile	0.098218	0.102659	0.107208	-0.065551
75th percentile	0.219088	0.149203	0.160287	0.010636
IN	Visit			Improvement
	One	Two	Three	
Mean	0.185158	0.169792	0.126968	-0.058190
SD	0.083133	0.072319	0.041599	0.076992
Median	0.161716	0.145138	0.127188	-0.032793
25th percentile	0.130553	0.123210	0.095584	-0.051223
75th percentile	0.195608	0.212754	0.148019	-0.027646
IT	Visit			Improvement
	One	Two	Three	
Mean	0.177672	0.170661	0.134046	-0.043626
SD	0.051828	0.067013	0.036207	0.041483
Median	0.181090	0.155244	0.123873	-0.028522
25th percentile	0.140261	0.113366	0.115396	-0.048222
75th percentile	0.216138	0.230989	0.149229	-0.022653

Table 6.12 Motion detection: The summary statistics, mean, SD, median and interquartile range for the Michelson contrast in the presence of noise (MC N_e) for 10 individuals with OAG at the five given locations. The summary statistics for the distribution of the within-individual difference in performance between visits 1 and 3 are given in column five. A negative value indicates an improvement across the three visits.

Improvement in performance

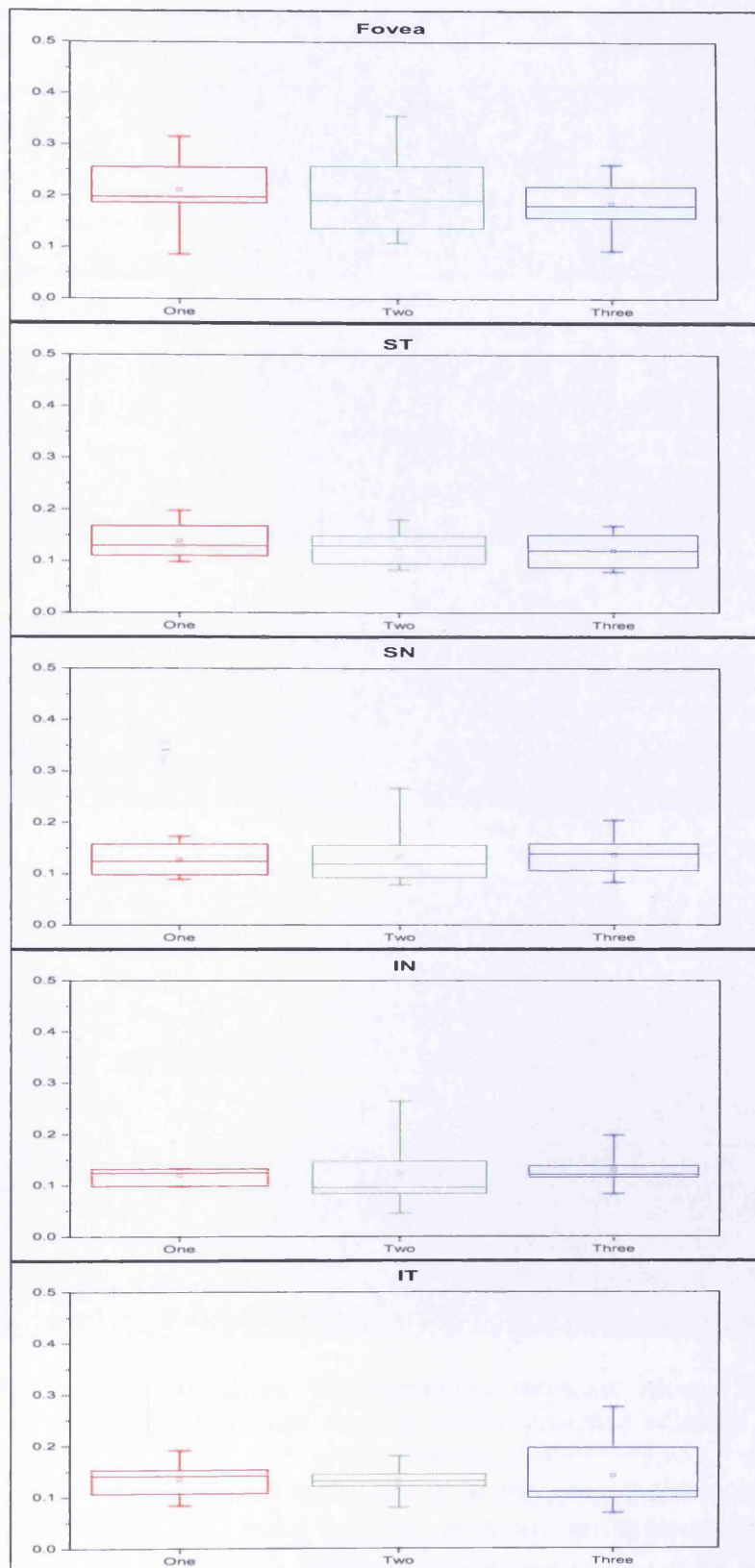


Figure 6.29 Motion discrimination: Box and Whiskers plot of the distribution of Michelson contrast thresholds (ordinate) in the presence of the noise mask ($MC N_e$) across a group of 9 individuals with OAG as a function of visits (abscissa).

Fovea	Visit			Improvement
	One	Two	Three	
Mean	0.212032	0.208460	0.185450	-0.026581
SD	0.070592	0.084999	0.053000	0.075852
Median	0.197410	0.191203	0.181090	-0.016944
25th percentile	0.186346	0.136719	0.157207	-0.047825
75th percentile	0.255141	0.257611	0.217967	-0.005560
ST	Visit			Improvement
	One	Two	Three	
Mean	0.138443	0.125808	0.119898	-0.018545
SD	0.036729	0.034038	0.034067	0.035398
Median	0.129337	0.128987	0.119449	-0.028603
25th percentile	0.111205	0.095827	0.088860	-0.036781
75th percentile	0.160209	0.144028	0.147448	0.007146
SN	Visit			Improvement
	One	Two	Three	
Mean	0.126898	0.134123	0.136005	0.009107
SD	0.032621	0.060460	0.038719	0.036708
Median	0.122864	0.118720	0.138102	0.020714
25th percentile	0.101974	0.095199	0.107345	-0.009652
75th percentile	0.150876	0.151176	0.153298	0.036968
IN	Visit			Improvement
	One	Two	Three	
Mean	0.119969	0.119689	0.129710	0.009741
SD	0.015244	0.070095	0.034823	0.043549
Median	0.124748	0.096241	0.121146	0.005003
25th percentile	0.110061	0.090011	0.118286	-0.011077
75th percentile	0.131676	0.126303	0.134625	0.011988
IT	Visit			Improvement
	One	Two	Three	
Mean	0.134846	0.131264	0.140132	0.005287
SD	0.030512	0.025627	0.063300	0.071417
Median	0.141197	0.130782	0.109520	-0.031957
25th percentile	0.115067	0.123583	0.100969	-0.045984
75th percentile	0.151487	0.140860	0.175136	0.034453

Table 6.13 Motion discrimination: The summary statistics, mean, SD, median and interquartile range for the Michelson contrast in the presence of noise (MC N_e) for 9 individuals with OAG at the five given locations. The summary statistics for the distribution of the within-individual difference in performance between visits 1 and 3 are given in column five. A negative value indicates an improvement across the three visits.

Improvement in performance ↓

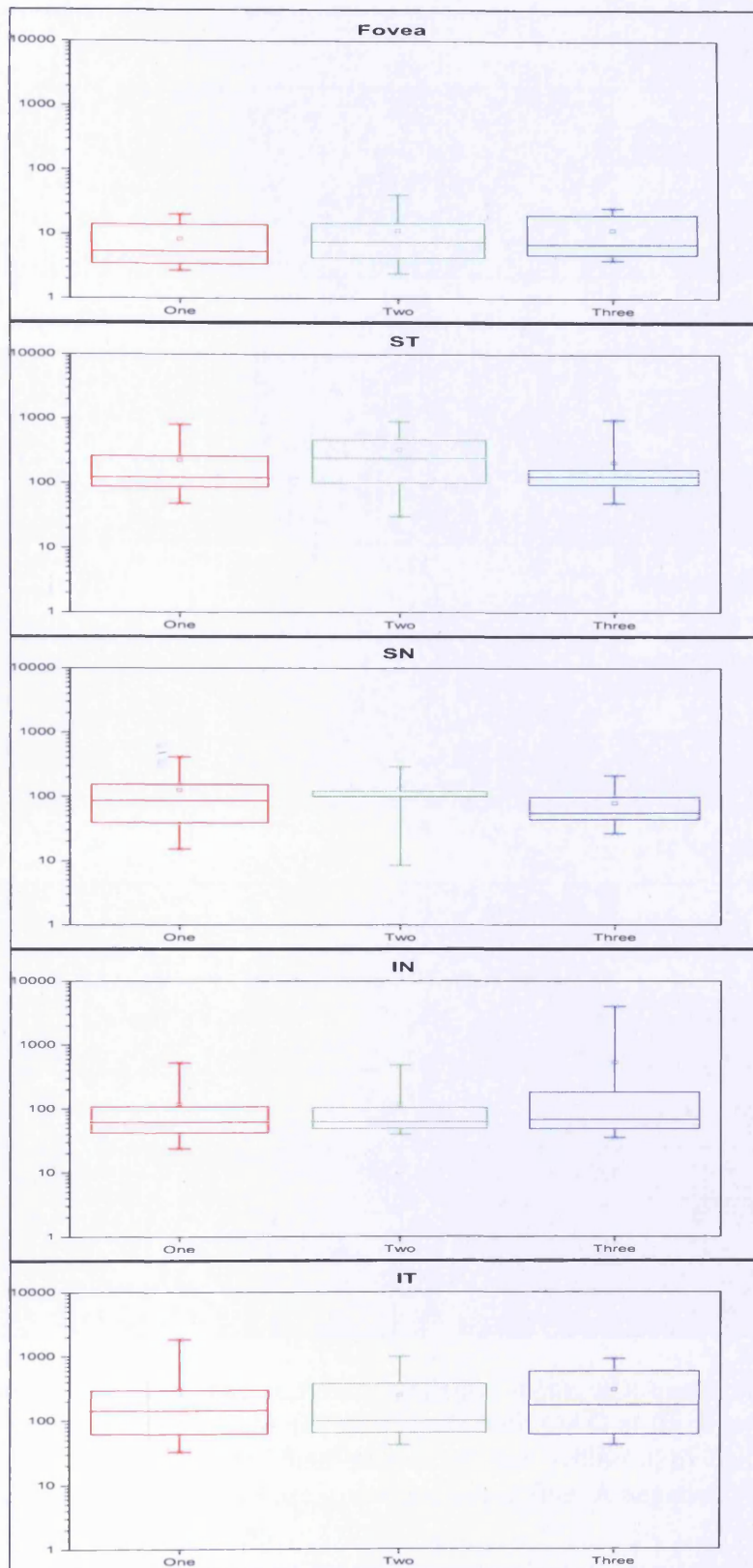


Figure 6.30 Motion detection: Box and Whiskers plot of the distribution of equivalent noise (ordinate) in the presence of the noise mask (N_{eq}) across a group of 10 individuals with OAG as a function of visits (abscissa).

Fovea	Visit			Improvement
	One	Two	Three	
Mean	8.29	11.38	11.58	3.29
SD	6.16	11.42	8.53	5.10
Median	5.34	7.49	6.94	3.22
25th percentile	3.56	4.75	4.76	0.86
75th percentile	12.74	13.33	19.28	5.57
ST	Visit			Improvement
	One	Two	Three	
Mean	222.81	330.58	208.73	-14.08
SD	236.18	297.85	282.79	312.58
Median	120.38	243.36	125.41	-35.13
25th percentile	85.70	99.88	94.16	-69.69
75th percentile	258.00	469.84	160.83	45.31
SN	Visit			Improvement
	One	Two	Three	
Mean	123.94	132.93	78.03	-45.91
SD	122.08	90.59	55.54	129.42
Median	85.38	101.44	55.08	-8.31
25th percentile	38.62	98.04	43.46	-63.74
75th percentile	150.94	120.58	96.83	11.41
IN	Visit			Improvement
	One	Two	Three	
Mean	117.35	119.12	528.05	410.70
SD	156.10	140.22	1285.97	1134.21
Median	62.03	62.37	67.37	24.87
25th percentile	42.48	49.13	48.84	0.00
75th percentile	107.22	103.65	182.11	74.89
IT	Visit			Improvement
	One	Two	Three	
Mean	305.63	242.81	294.33	-11.30
SD	509.54	285.45	295.76	552.54
Median	141.95	98.14	169.91	-13.15
25th percentile	74.23	65.72	62.34	-67.86
75th percentile	260.67	320.82	468.93	188.73

Table 6.14 Motion detection: The summary statistics, mean, SD, median and interquartile range for equivalent noise (N_{eq}) for 10 individuals with OAG at the five given locations. The summary statistics for the distribution of the within-individual difference in performance between visits 1 and 3 are given in column five. A negative value indicates an improvement across the three visits.

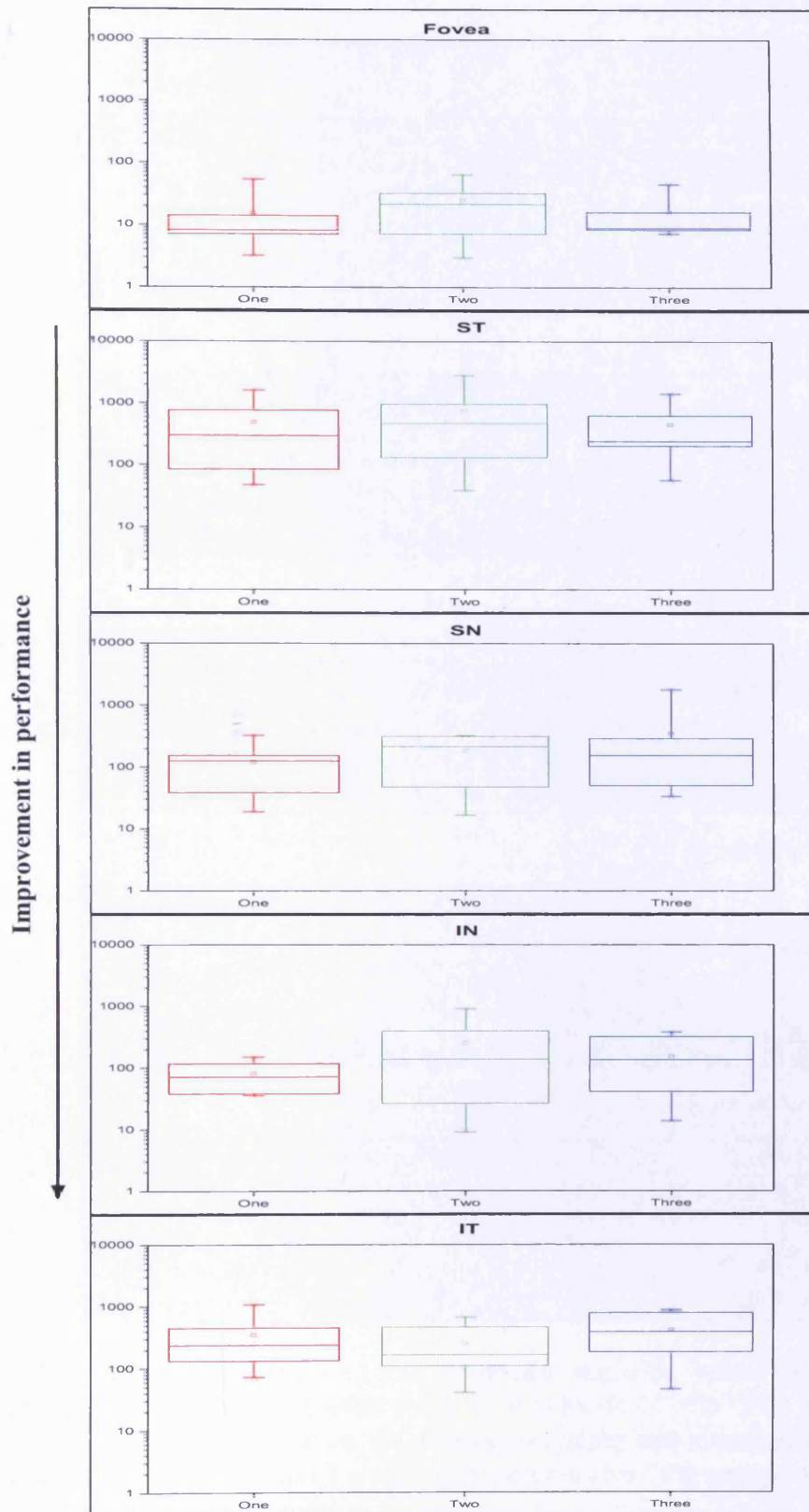


Figure 6.31 Motion discrimination: Box and Whiskers plot of the distribution of equivalent noise (ordinate) in the presence of the noise mask (N_{eq}) across a group of 9 individuals with OAG as a function of visits (abscissa).

Fovea	Visit			Improvement
	One	Two	Three	
Mean	15.52	25.16	16.32	0.79
SD	16.60	20.71	13.01	16.18
Median	8.08	21.62	8.92	2.06
25th percentile	7.02	7.10	8.36	0.70
75th percentile	14.08	32.48	16.14	4.53
ST	Visit			Improvement
	One	Two	Three	
Mean	491.86	749.02	454.48	-37.38
SD	568.06	913.08	458.20	216.24
Median	292.90	474.92	240.77	29.00
25th percentile	96.00	156.59	210.84	-206.40
75th percentile	584.06	933.96	537.57	147.92
SN	Visit			Improvement
	One	Two	Three	
Mean	121.07	185.44	349.19	228.12
SD	98.29	139.07	584.17	575.70
Median	124.29	213.27	154.91	12.57
25th percentile	37.94	47.93	52.17	-36.86
75th percentile	151.64	312.13	274.62	178.20
IN	Visit			Improvement
	One	Two	Three	
Mean	81.90	255.67	153.63	71.73
SD	43.28	314.48	142.67	125.02
Median	71.73	138.86	135.76	19.85
25th percentile	47.15	59.49	44.85	-9.77
75th percentile	110.08	309.73	228.83	145.74
IT	Visit			Improvement
	One	Two	Three	
Mean	350.93	248.27	413.47	62.53
SD	325.23	206.46	293.78	308.54
Median	237.87	165.48	385.21	103.51
25th percentile	158.80	121.78	209.83	-23.81
75th percentile	374.60	344.71	621.59	220.55

Table 6.15 Motion discrimination: The summary statistics, mean, SD, median and interquartile range for equivalent noise (N_{eq}) for 9 individuals with OAG at the five given locations. The summary statistics for the distribution of the within-individual difference in performance between visits 1 and 3 are given in column five. A negative value indicates an improvement across the three visits.

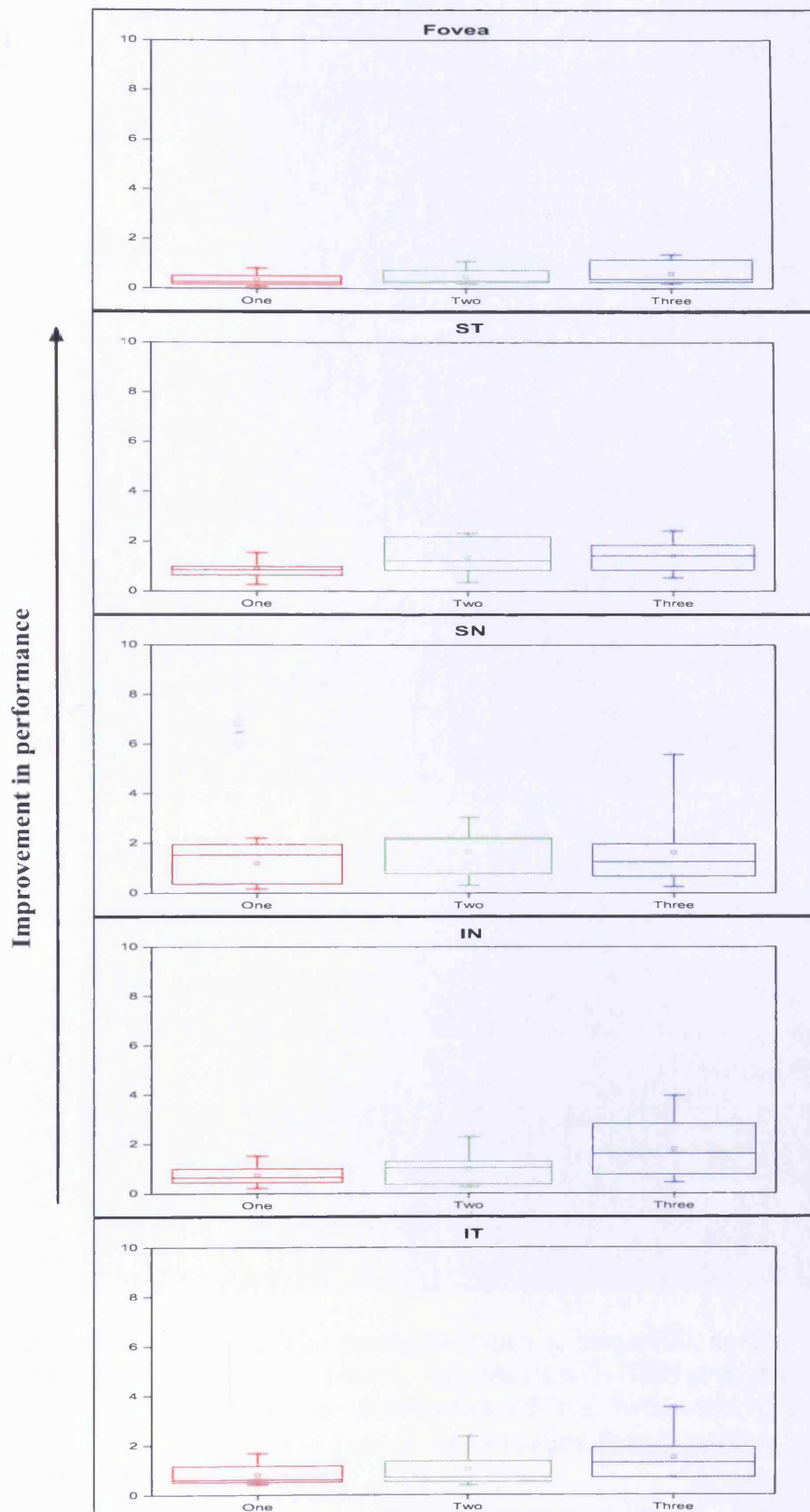


Figure 6.32 Motion detection: Box and Whiskers plot of the distribution of sampling efficiency (%) (ordinate) in the presence of the noise mask (SE) across a group of 10 individuals with OAG as a function of visits (abscissa).

Fovea	Visit			Improvement
	One	Two	Three	
Mean	0.34	0.48	0.59	0.25
SD	0.24	0.34	0.47	0.30
Median	0.25	0.30	0.37	0.18
25th percentile	0.16	0.23	0.26	0.01
75th percentile	0.47	0.68	0.99	0.51
ST	Visit			Improvement
	One	Two	Three	
Mean	0.86	1.35	1.40	0.54
SD	0.44	0.73	0.62	0.78
Median	0.83	1.22	1.41	0.46
25th percentile	0.63	0.82	0.84	0.21
75th percentile	0.97	2.18	1.84	0.56
SN	Visit			Improvement
	One	Two	Three	
Mean	1.17	1.66	1.61	0.44
SD	0.85	0.95	1.63	1.41
Median	1.51	2.15	1.24	0.12
25th percentile	0.35	0.77	0.67	-0.02
75th percentile	1.94	2.20	1.96	0.35
IN	Visit			Improvement
	One	Two	Three	
Mean	0.73	1.00	1.79	1.06
SD	0.43	0.65	1.29	1.13
Median	0.65	1.04	1.61	0.62
25th percentile	0.45	0.37	0.77	0.32
75th percentile	0.99	1.29	2.83	1.73
IT	Visit			Improvement
	One	Two	Three	
Mean	0.79	1.03	1.49	0.69
SD	0.40	0.63	0.87	0.84
Median	0.60	0.70	1.28	0.40
25th percentile	0.51	0.58	0.82	0.21
75th percentile	1.01	1.31	1.88	0.78

Table 6.16 Motion detection: The summary statistics, mean, SD, median and interquartile range for sampling efficiency (SE) for 10 individuals with OAG at the five given locations. The summary statistics for the distribution of the within-individual difference in performance between visits 1 and 3 are given in column five. A positive value indicates an improvement across the three visits.

Improvement in performance

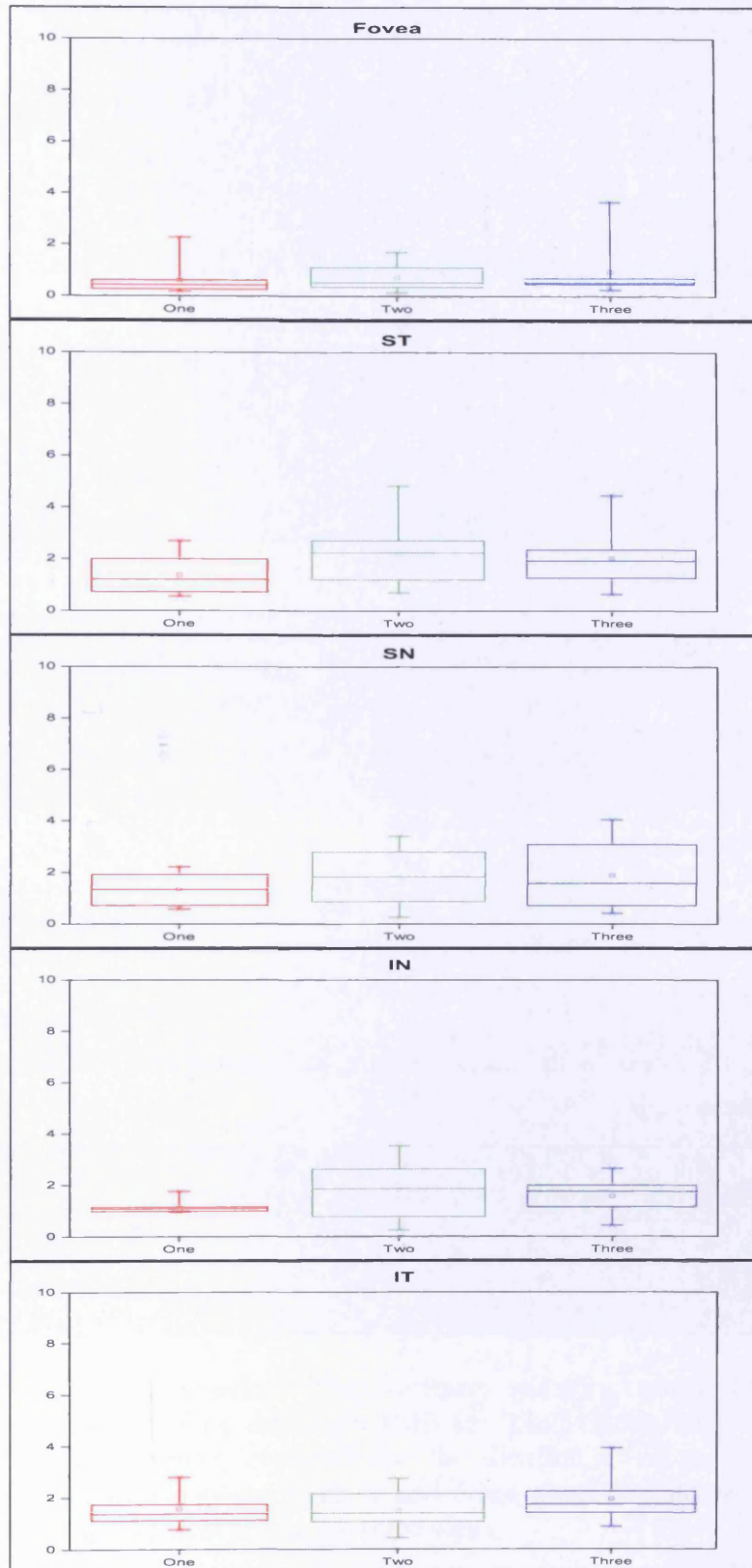


Figure 6.33 Motion discrimination: Box and Whiskers plot of the distribution of sampling efficiency (%) (ordinate) in the presence of the noise mask (SE) across a group of 9 individuals with OAG as a function of visits (abscissa).

Fovea	Visit			Improvement
	One	Two	Three	
Mean	0.59	0.72	0.93	0.34
SD	0.65	0.55	1.08	1.22
Median	0.43	0.51	0.51	0.09
25th percentile	0.26	0.34	0.46	0.06
75th percentile	0.60	1.10	0.68	0.34
ST	Visit			Improvement
	One	Two	Three	
Mean	1.37	2.21	2.02	0.64
SD	0.79	1.31	1.16	1.32
Median	1.19	2.23	1.92	0.27
25th percentile	0.72	1.27	1.27	-0.33
75th percentile	1.97	2.63	2.24	1.53
SN	Visit			Improvement
	One	Two	Three	
Mean	1.33	1.82	1.89	0.56
SD	0.67	1.14	1.40	1.24
Median	1.32	1.82	1.56	0.09
25th percentile	0.75	0.98	0.76	-0.17
75th percentile	1.77	2.66	2.71	0.50
IN	Visit			Improvement
	One	Two	Three	
Mean	1.15	4.11	1.57	0.42
SD	0.28	5.93	0.72	0.67
Median	1.08	2.42	1.76	0.22
25th percentile	1.00	1.32	1.16	0.18
75th percentile	1.12	3.08	1.92	0.77
IT	Visit			Improvement
	One	Two	Three	
Mean	1.56	1.48	1.94	0.39
SD	0.63	0.68	0.86	0.99
Median	1.37	1.39	1.73	0.37
25th percentile	1.16	1.06	1.44	-0.36
75th percentile	1.69	1.87	2.13	0.70

Table 6.17 Motion discrimination: The summary statistics, mean, SD, median and interquartile range for sampling efficiency (SE) for 9 individuals with OAG at the five given locations. The summary statistics for the distribution of the within-individual difference in performance between visits 1 and 3 are given in column five. A positive value indicates an improvement across the three visits.

6.7 RESULTS: The proportionate learning effect for individuals with OAG

6.7.1 The learning effect between visit 1 and 2 for Michelson contrast in the absence of noise (MC N₀)

The proportionate improvement in MC N₀ across each of the five locations as a function of age for the detection task is shown in Figure 6.34. The between-individual differences in improvement ranged from approximately -80% to +60%. Of the 10 individuals, 7 individuals showed a positive improvement for foveal viewing, 7 at the ST location, 5 at the SN location, 5 at the IN location and 8 at the IT location.

The proportionate improvement in MC N₀ across each of the five locations as a function of age for the discrimination task is shown in Figure 6.35. The between-individual differences in improvement ranged from approximately -80% to +50%. Of the 9 individuals, 3 individuals showed a positive improvement for foveal viewing, 5 at the ST location, 3 at the SN location, 3 at the IN location and 8 at the IT location.

6.7.2 The learning effect between visit 2 and 3 for Michelson contrast in the absence of noise (MC N₀)

The proportionate improvement in MC N₀ across each of the five locations as a function of age for the detection task is shown in Figure 6.36. The between-individual differences in improvement ranged from approximately -80% to +60%. Of the 10 individuals, 6 individuals showed a positive improvement for foveal viewing, 5 at the ST location, 7 at the SN location, 5 at the IN location and 7 at the IT location.

The proportionate improvement in $MC N_0$ across each of the five locations as a function of age for the discrimination task is shown in Figure 6.37. The between-individual differences in improvement ranged from approximately to -60% to +80%. Of the 9 individuals, 6 individuals showed a positive improvement for foveal viewing, 3 at the ST location, 3 at the SN location, 5 at the IN location and 2 at the IT location.

6.7.3 The learning effect between visit 1 and 2 for Michelson contrast in the presence of noise ($MC N_e$)

The proportionate improvement in $MC N_e$ across each of the five locations as a function of age for the detection task is shown in Figure 6.38. The between-individual differences in improvement ranged from approximately -100% to +70%. Of the 10 individuals, 6 individuals showed a positive improvement for foveal viewing, 7 at the ST location, 6 at the SN location, 6 at the IN location and 8 at the IT location.

The proportionate improvement in $MC N_e$ across each of the five locations as a function of age for the discrimination task is shown in Figure 6.39. The between-individual differences in improvement ranged from approximately to -70% to +70%. Of the 9 individuals, 4 individuals showed a positive improvement for foveal viewing, 4 at the ST location, 5 at the SN location, 5 at the IN location and 6 at the IT location.

6.7.4 The learning effect between visit 2 and 3 for Michelson contrast in the presence of noise ($MC N_e$)

The proportionate improvement in $MC N_e$ across each of the five locations as a function of age for the detection task is shown in Figure 6.40. The between-individual differences in

improvement ranged from approximately -70% to +70%. Of the 10 individuals, 7 individuals showed a positive improvement for foveal viewing, 4 at the ST location, 3 at the SN location, 6 at the IN location and 9 at the IT location.

The proportionate improvement in $MC N_e$ across each of the five locations as a function of age for the discrimination task is shown in Figure 6.41. The between-individual differences in improvement ranged from approximately to -70% to +80%. Of the 9 individuals, 4 individuals showed a positive improvement for foveal viewing, 5 at the ST location, 3 at the SN location, 3 at the IN location and 7 at the IT location.

6.7.5 The learning effect between visit 1 and 2 for equivalent noise (N_{eq})

The proportionate improvement in N_{eq} across each of the five locations as a function of age for the detection task is shown in Figure 6.42. The between-individual differences in improvement ranged from approximately -900% to +100%. Of the 10 individuals, 6 individuals showed a positive improvement for foveal viewing, 2 at the ST location, 4 at the SN location, 4 at the IN location and 8 at the IT location.

The proportionate improvement in N_{eq} across each of the five locations as a function of age for the discrimination task is shown in Figure 6.43. The between-individual differences in improvement ranged from approximately to -800% to +100%. Of the 9 individuals, 3 individuals showed a positive improvement for foveal viewing, 3 at the ST location, 5 at the SN location, 3 at the IN location and 8 at the IT location.

6.7.6 The learning effect between visit 2 and 3 for equivalent noise (N_{eq})

The proportionate improvement in N_{eq} across each of the five locations as a function of age for the detection task is shown in Figure 6.44. The between-individual differences in improvement ranged from approximately -700% to +100%. Of the 10 individuals, 5 individuals showed a positive improvement for foveal viewing, 6 at the ST location, 7 at the SN location, 3 at the IN location and 4 at the IT location.

The proportionate improvement in N_{eq} across each of the five locations as a function of age for the discrimination task is shown in Figure 6.45. The between-individual differences in improvement ranged from approximately to -500% to +100%. Of the 9 individuals, 5 individuals showed a positive improvement for foveal viewing, 5 at the ST location, 3 at the SN location, 3 at the IN location and 2 at the IT location.

6.7.7 The learning effect between visit 1 and 2 for sampling efficiency (SE)

The proportionate improvement in SE across each of the five locations as a function of age for the detection task is shown in Figure 6.46. The between-individual differences in improvement ranged from approximately -100% to +300%. Of the 10 individuals, 7 individuals showed a positive improvement for foveal viewing, 7 at the ST location, 8 at the SN location, 7 at the IN location and 7 at the IT location.

The proportionate improvement in SE across each of the five locations as a function of age for the discrimination task is shown in Figure 6.47. The between-individual differences in improvement ranged from approximately to -100% to +800%. Of the 9 individuals, 4

individuals showed a positive improvement for foveal viewing, 6 at the ST location, 5 at the SN location, 5 at the IN location and 6 at the IT location.

6.7.8 The learning effect between visit 2 and 3 for sampling efficiency (SE)

The proportionate improvement in SE across each of the five locations as a function of age for the detection task is shown in Figure 6.48. The between-individual differences in improvement ranged from approximately -100% to +1000%. Of the 10 individuals, 6 individuals showed a positive improvement for foveal viewing, 4 at the ST location, 3 at the SN location, 6 at the IN location and 10 at the IT location.

The proportionate improvement in SE across each of the five locations as a function of age for the discrimination task is shown in Figure 6.49. The between-individual differences in improvement ranged from approximately to -100% to +1000%. Of the 9 individuals, 5 individuals showed a positive improvement for foveal viewing, 3 at the ST location, 4 at the SN location, 4 at the IN location and 7 at the IT location.

Improvement in performance

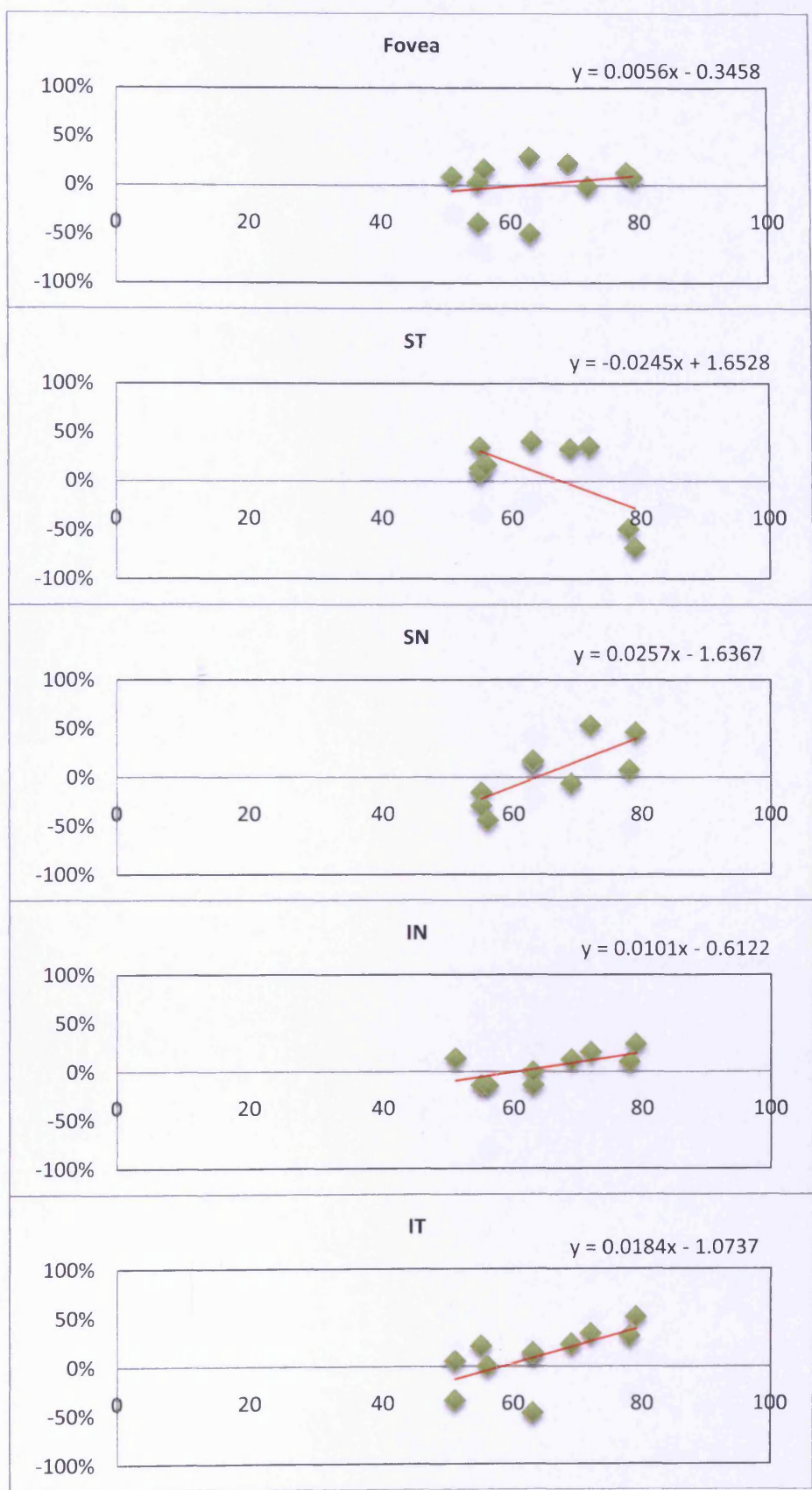


Figure 6.34 Motion detection: The proportionate improvement in performance (ordinate) from visit 1 to visit 2 in terms of Michelson contrast in the absence of the noise mask ($MC N_0$) as a function of age (abscissa). A positive value indicates an improvement in performance.

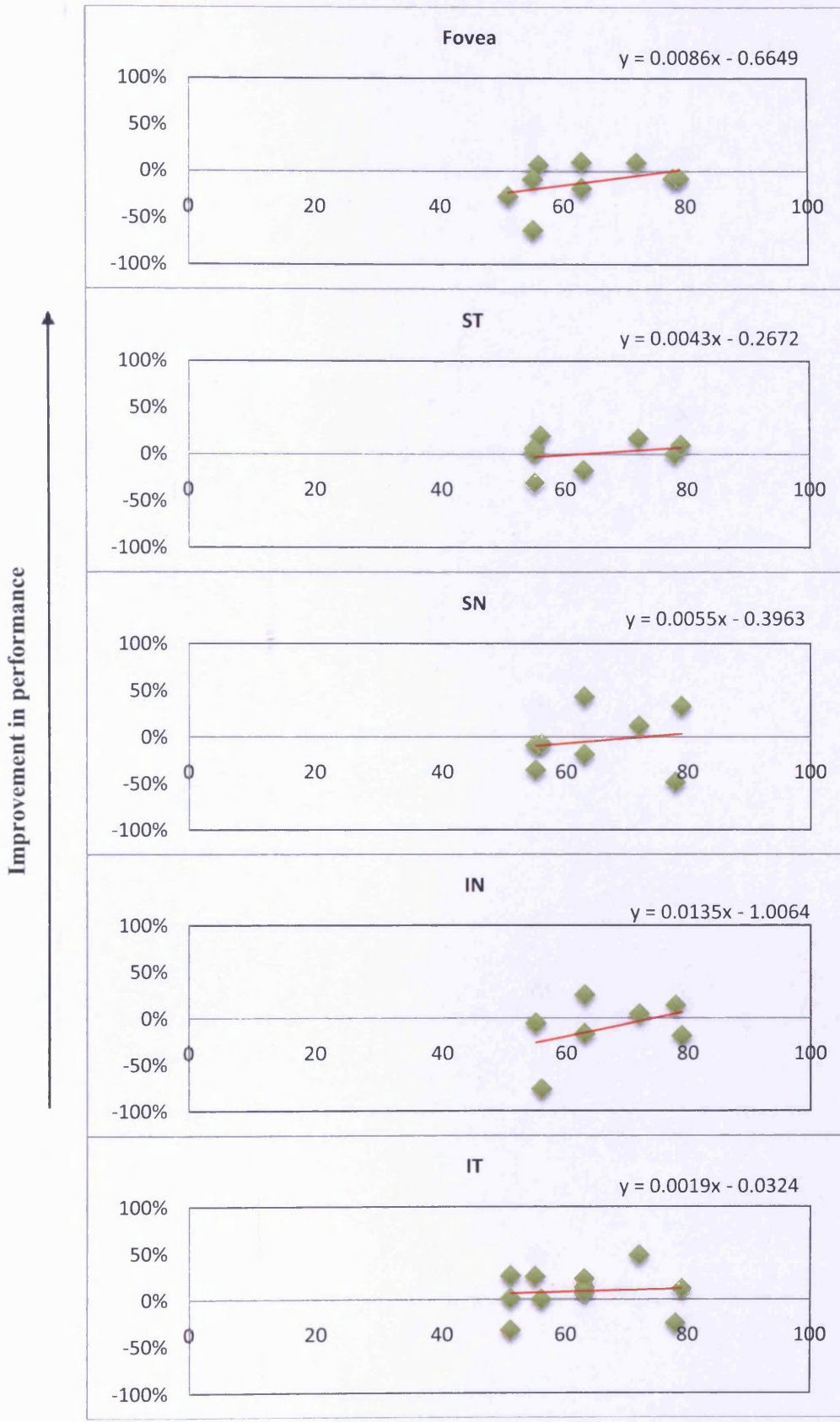


Figure 6.35 Motion discrimination: The proportionate improvement in performance (ordinate) from visit 1 to visit 2 in terms of Michelson contrast in the absence of the noise mask ($MC N_0$) as a function of age (abscissa). A positive value indicates an improvement in performance.

Improvement in performance

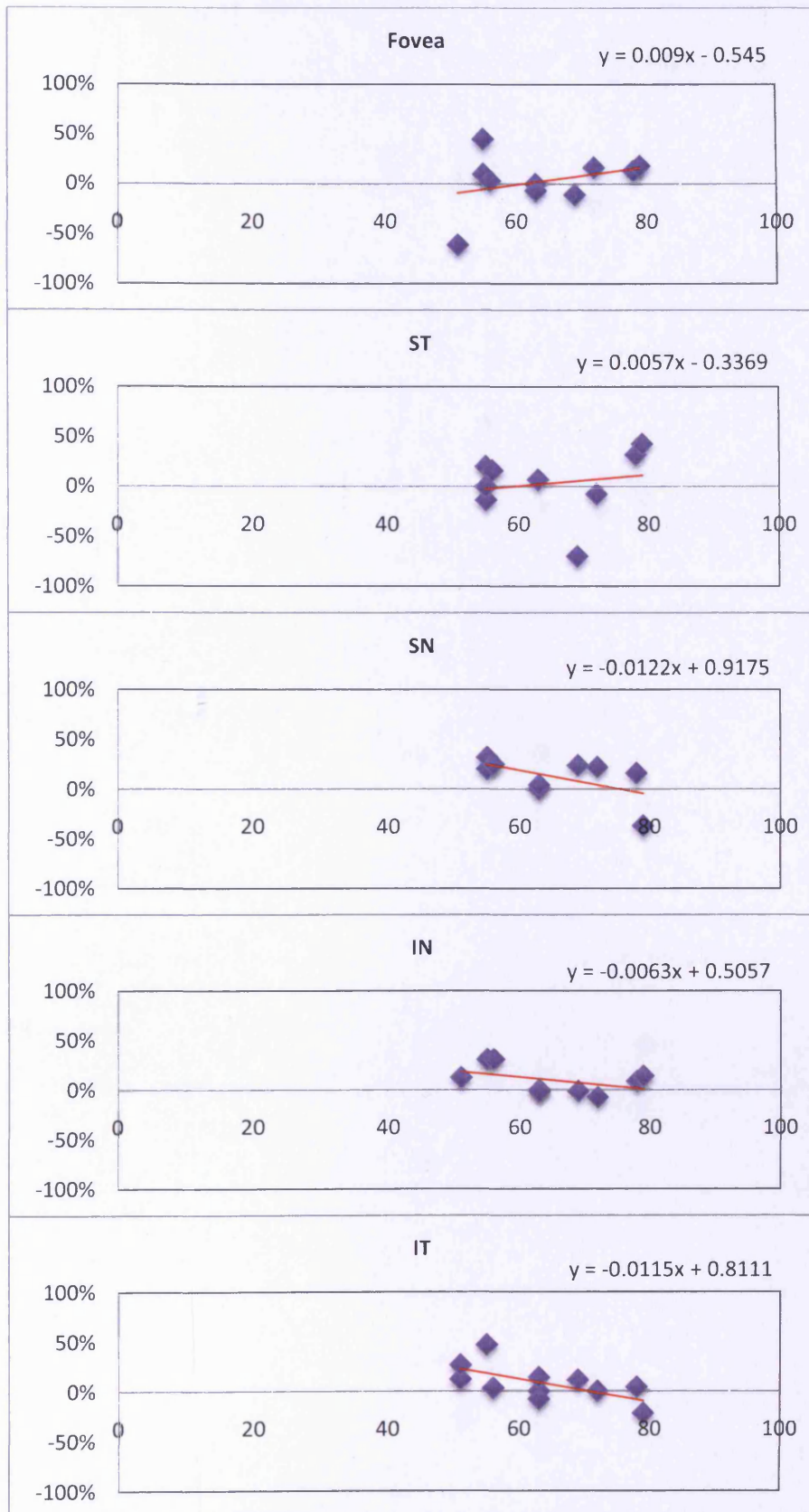


Figure 6.36 Motion detection: The proportionate improvement in performance (ordinate) from visit 2 to visit 3 in terms of Michelson contrast in the absence of the noise mask ($MC N_0$) as a function of age (abscissa). A positive value indicates an improvement in performance.

Improvement in performance

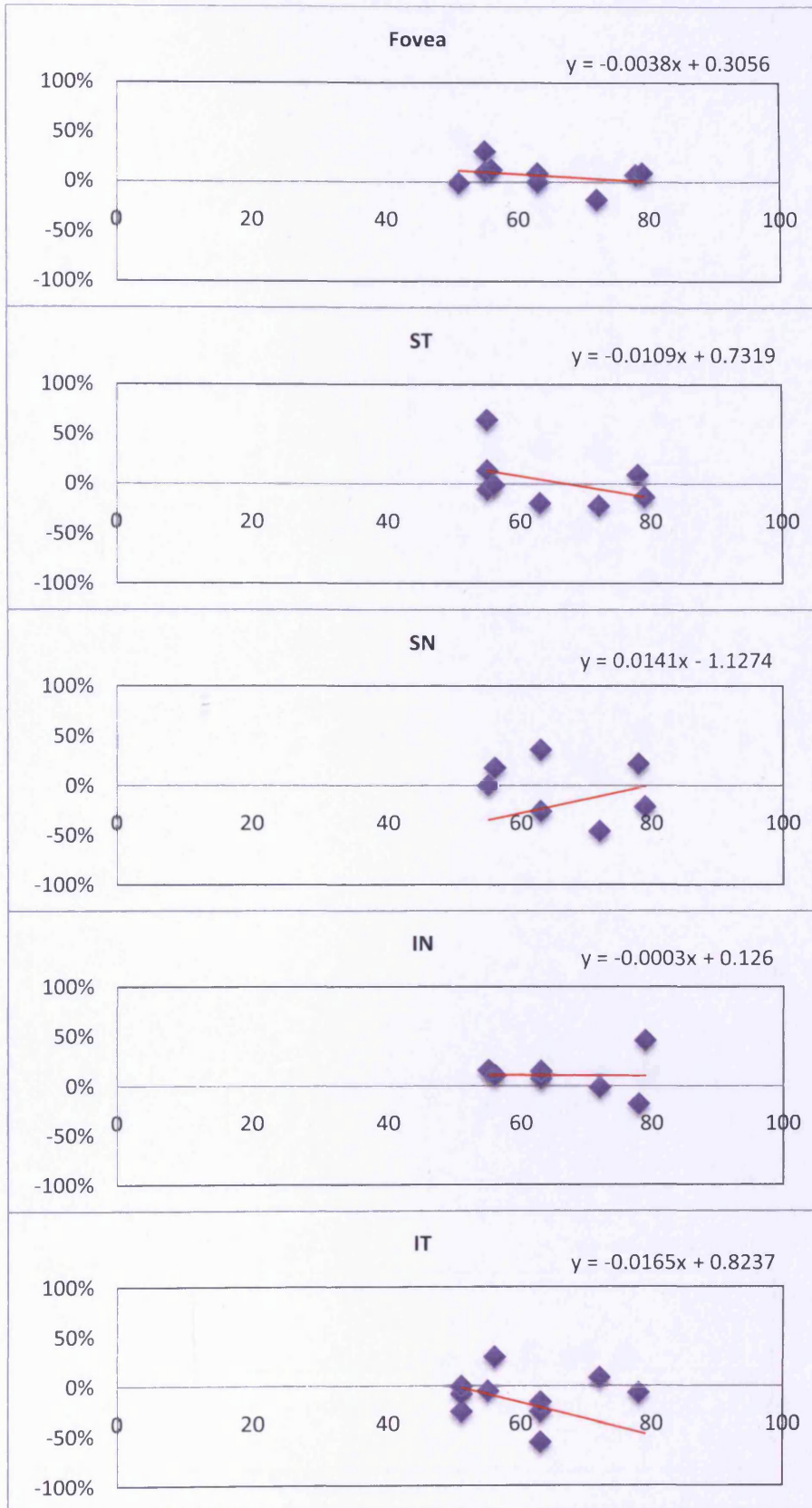


Figure 6.37 Motion discrimination: The proportionate improvement in performance (ordinate) from visit 2 to visit 3 in terms of Michelson contrast in the absence of the noise mask ($MC N_0$) as a function of age (abscissa). A positive value indicates an improvement in performance.

Improvement in performance

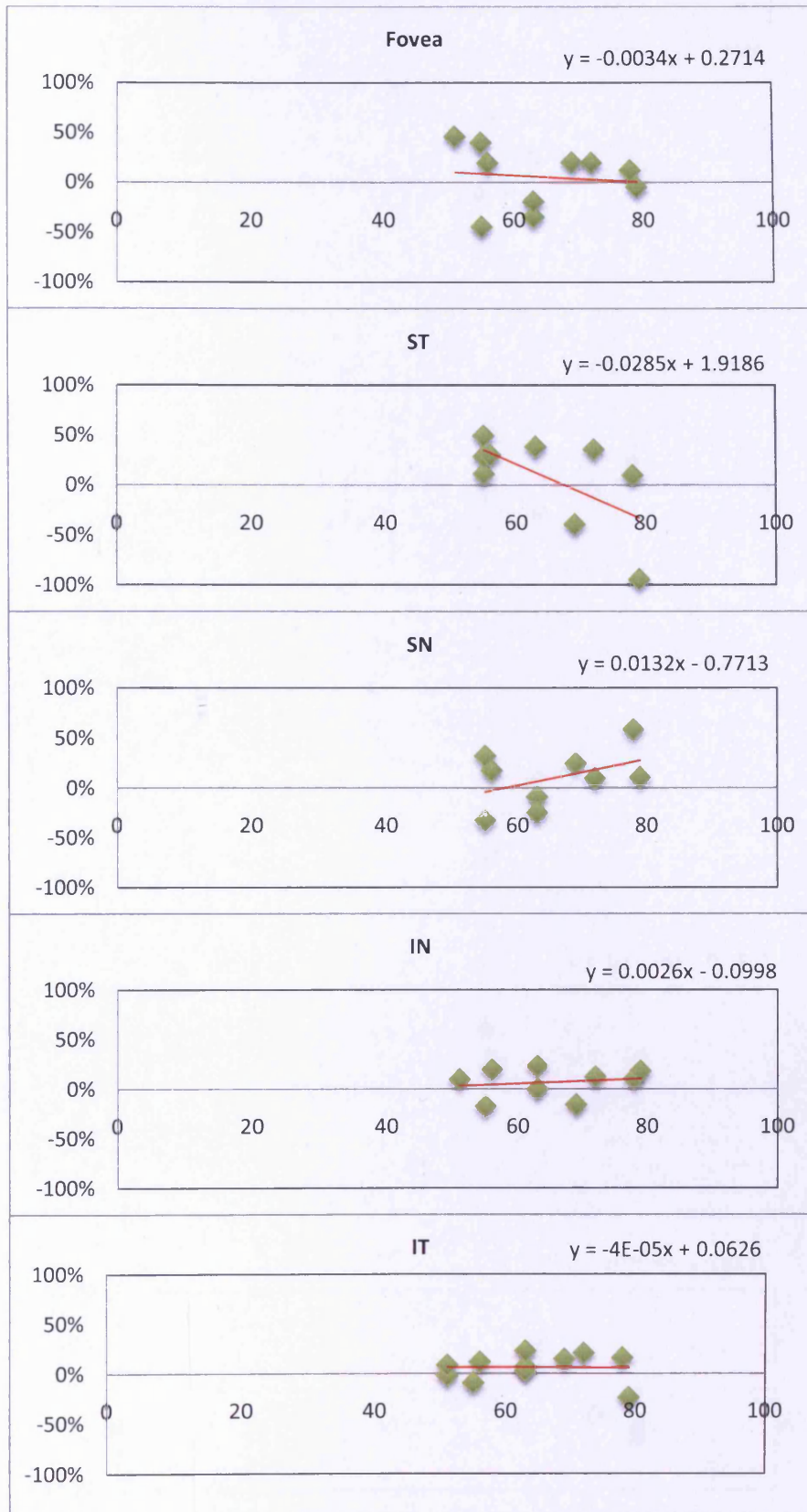


Figure 6.38 Motion detection: The proportionate improvement in performance (ordinate) from visit 1 to visit 2 in terms of Michelson contrast in the presence of the noise mask ($MC N_e$) as a function of age (abscissa). A positive value indicates an improvement in performance.

Improvement in performance

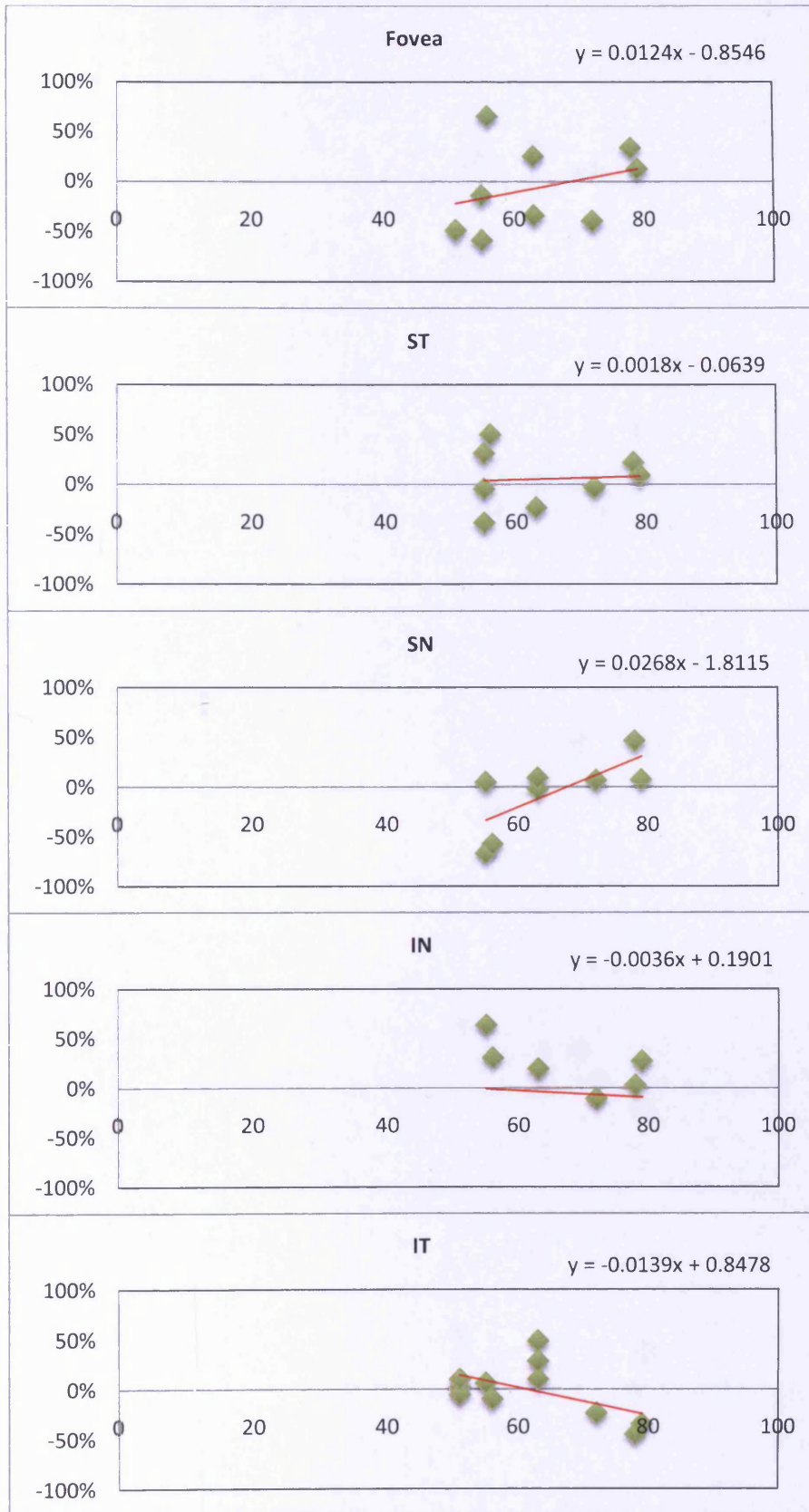


Figure 6.39 Motion discrimination: The proportionate improvement in performance (ordinate) from visit 1 to visit 2 in terms of Michelson contrast in the presence of the noise mask ($MC N_e$) as a function of age (abscissa). A positive value indicates an improvement in performance.

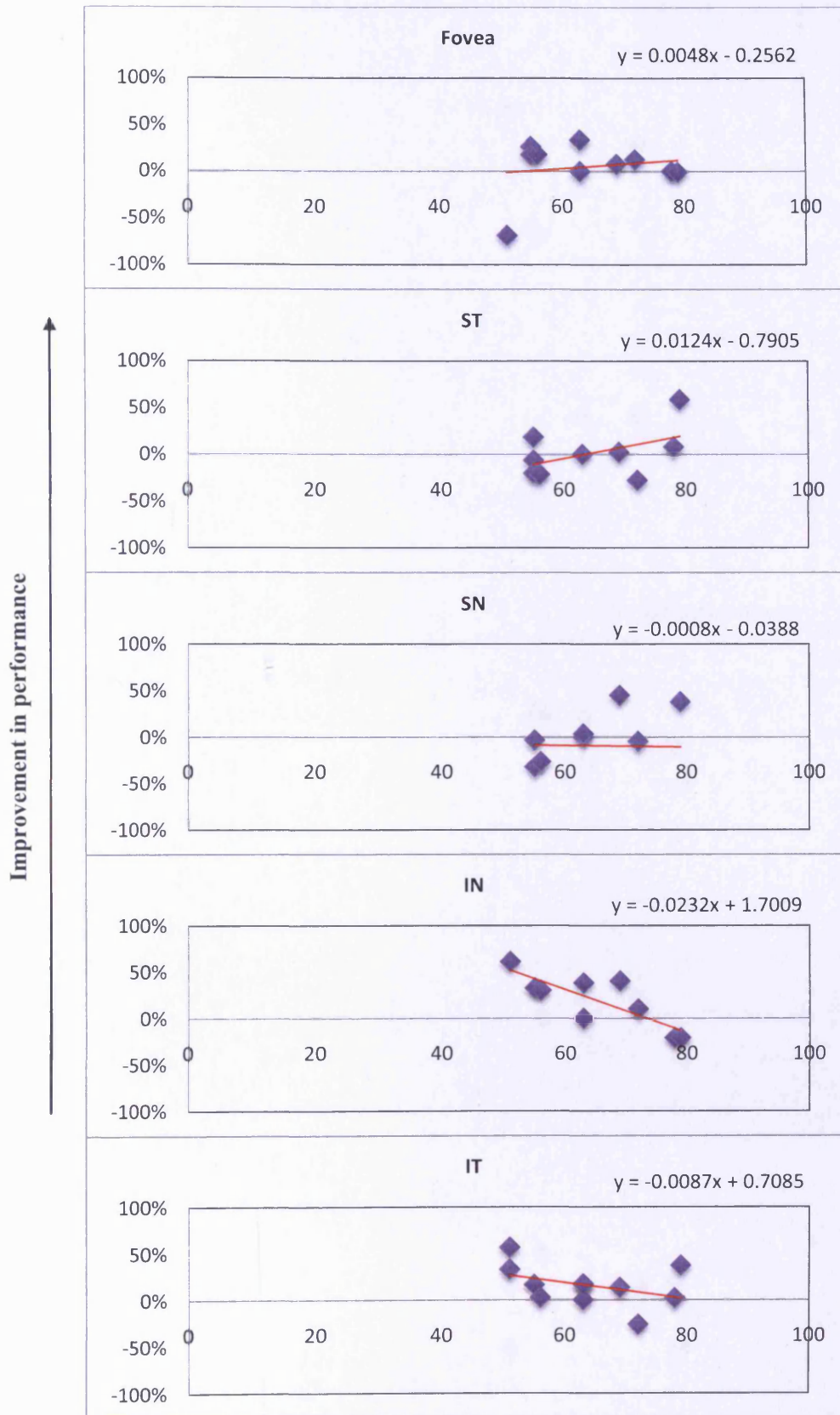


Figure 6.40 Motion detection: The proportionate improvement in performance (ordinate) from visit 2 to visit 3 in terms of Michelson contrast in the presence of the noise mask ($MC N_e$) as a function of age (abscissa). A positive value indicates an improvement in performance.

Improvement in performance ↑

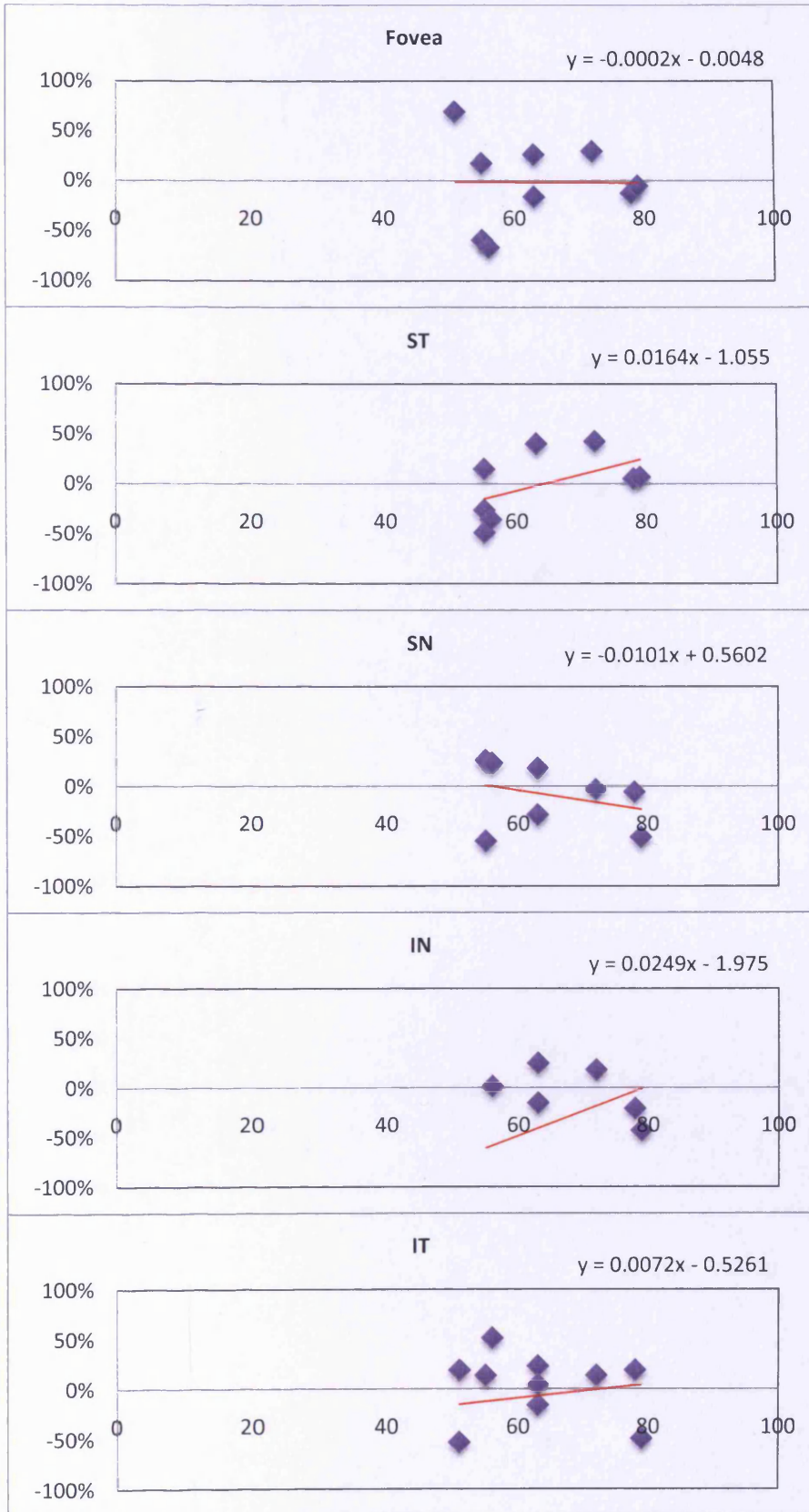


Figure 6.41 Motion discrimination: The proportionate improvement in performance (ordinate) from visit 2 to visit 3 in terms of Michelson contrast in the presence of the noise mask ($MC N_e$) as a function of age (abscissa). A positive value indicates an improvement in performance.

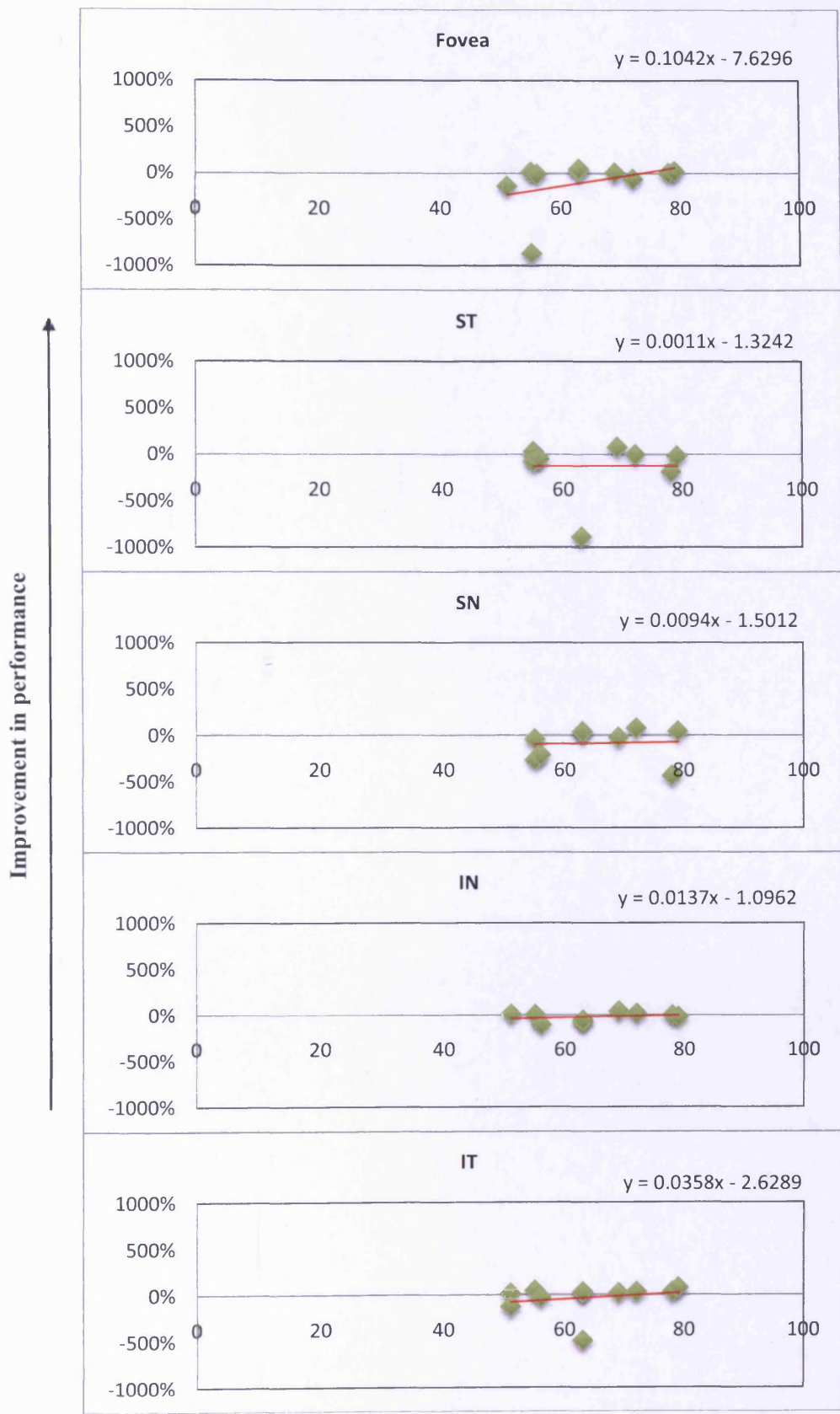


Figure 6.42 Motion detection: The proportionate improvement in performance (ordinate) from visit 1 to visit 2 in terms of equivalent noise (N_{eq}) as a function of age (abscissa). A positive value indicates an improvement in performance. Note the scaling of the ordinate is different to that of Figure 6.41.

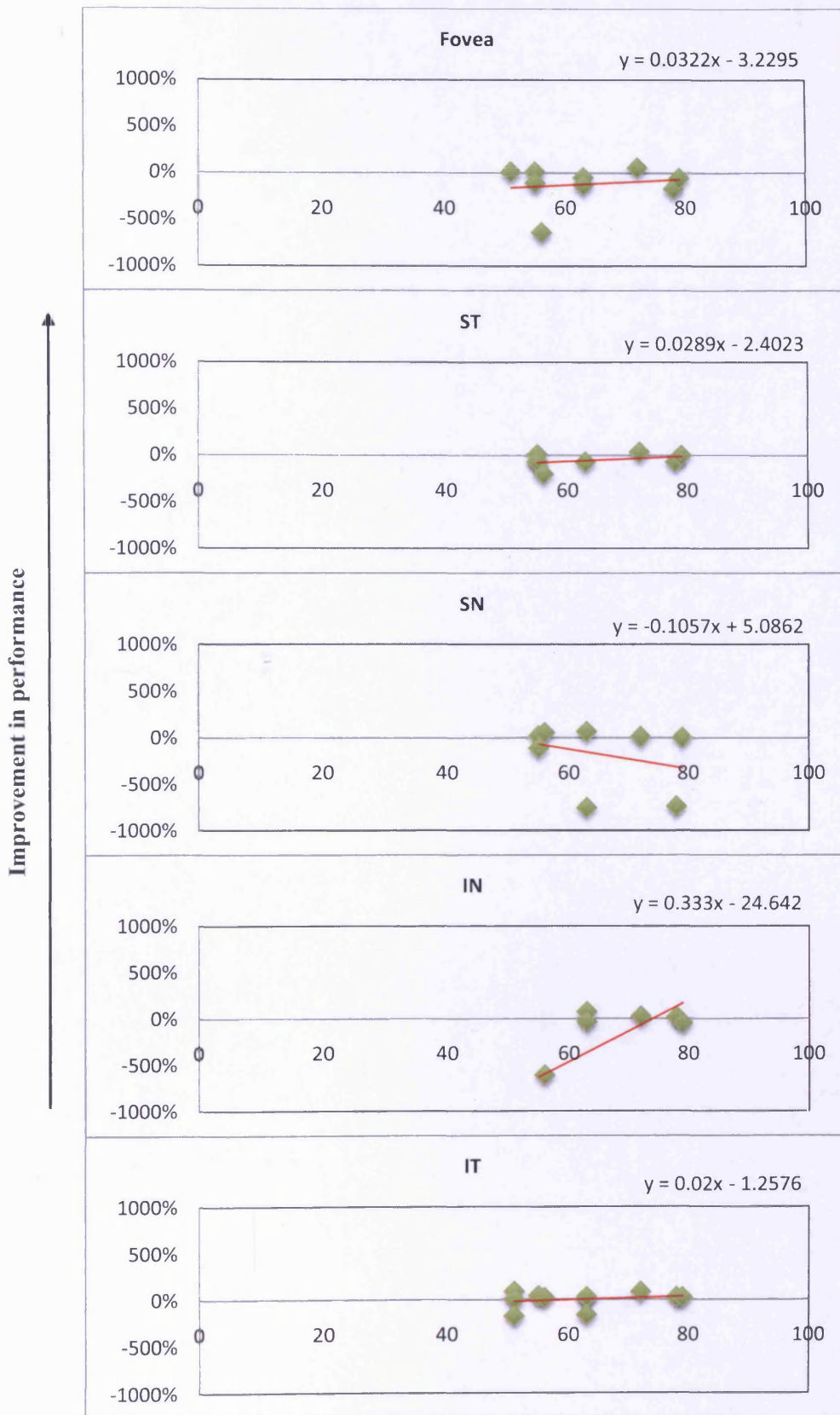


Figure 6.43 Motion discrimination: The proportionate improvement in performance (ordinate) from visit 1 to visit 2 in terms of equivalent noise (N_{eq}) as a function of age (abscissa). A positive value indicates an improvement in performance.

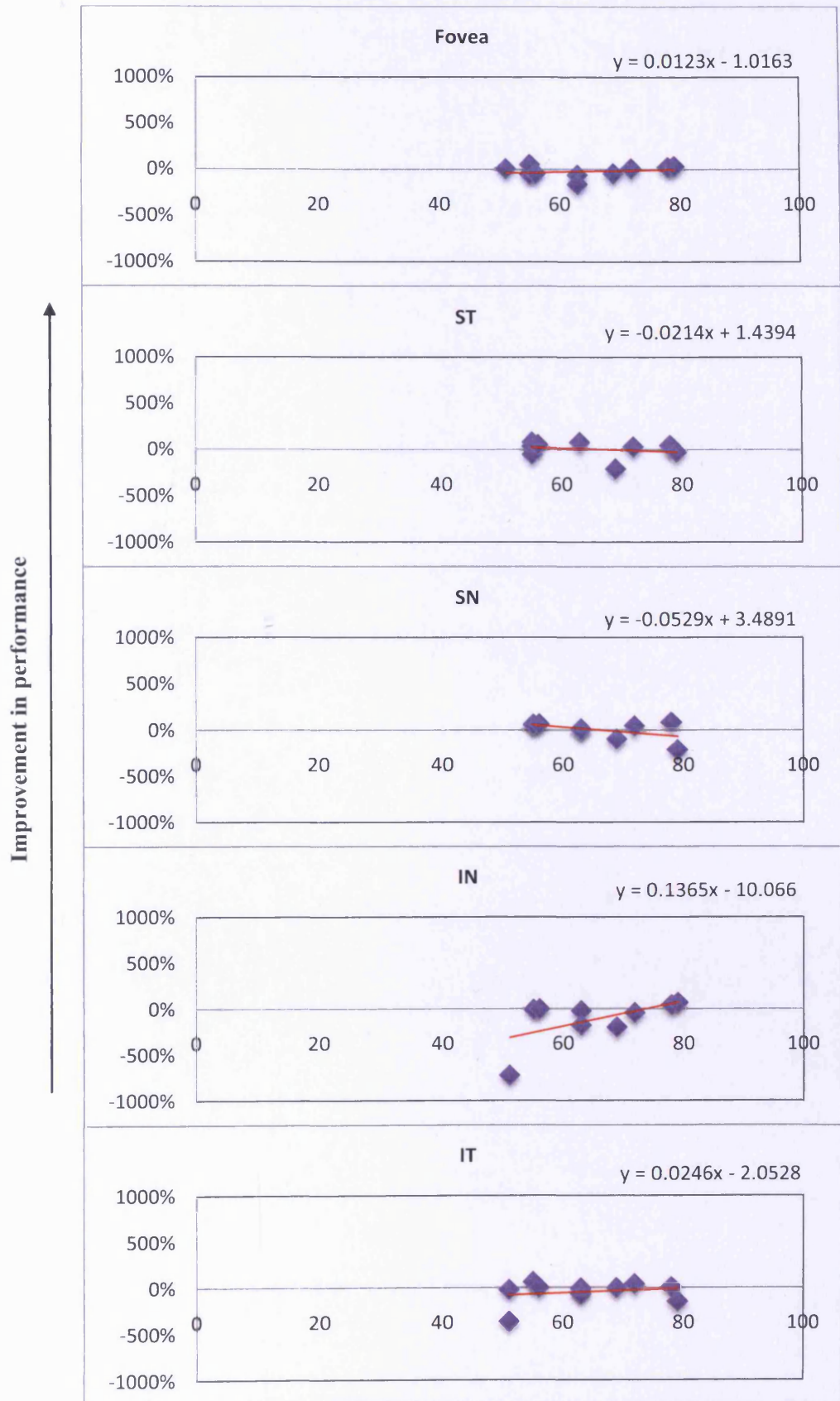


Figure 6.44 Motion detection: The proportionate improvement in performance (ordinate) from visit 2 to visit 3 in terms of equivalent noise (N_{eq}) as a function of age (abscissa). A positive value indicates an improvement in performance.

Improvement in performance

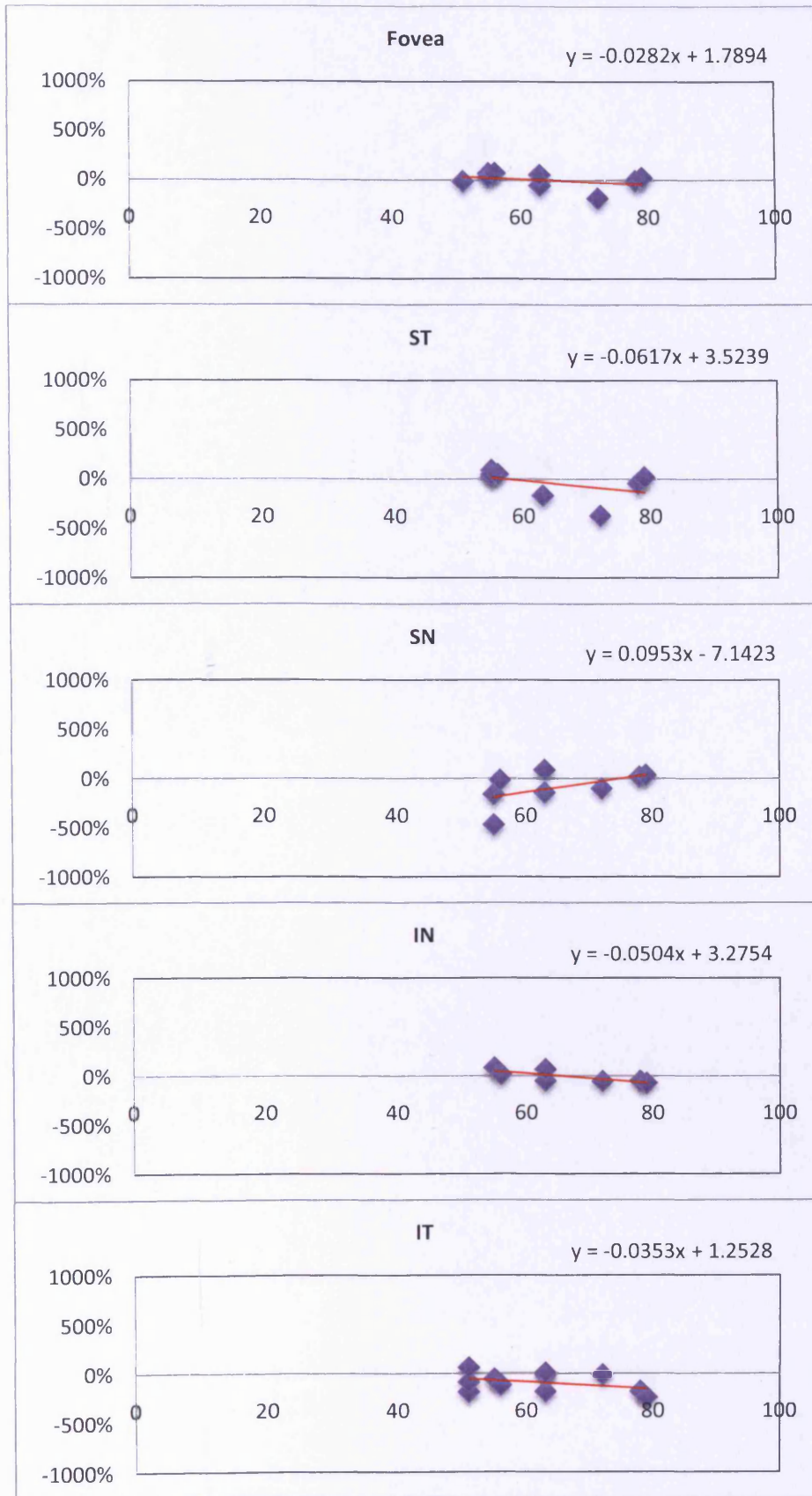


Figure 6.45 Motion discrimination: The proportionate improvement in performance (ordinate) from visit 2 to visit 3 in terms of equivalent noise (N_{eq}) as a function of age (abscissa). A positive value indicates an improvement in performance.

Improvement in performance ↑

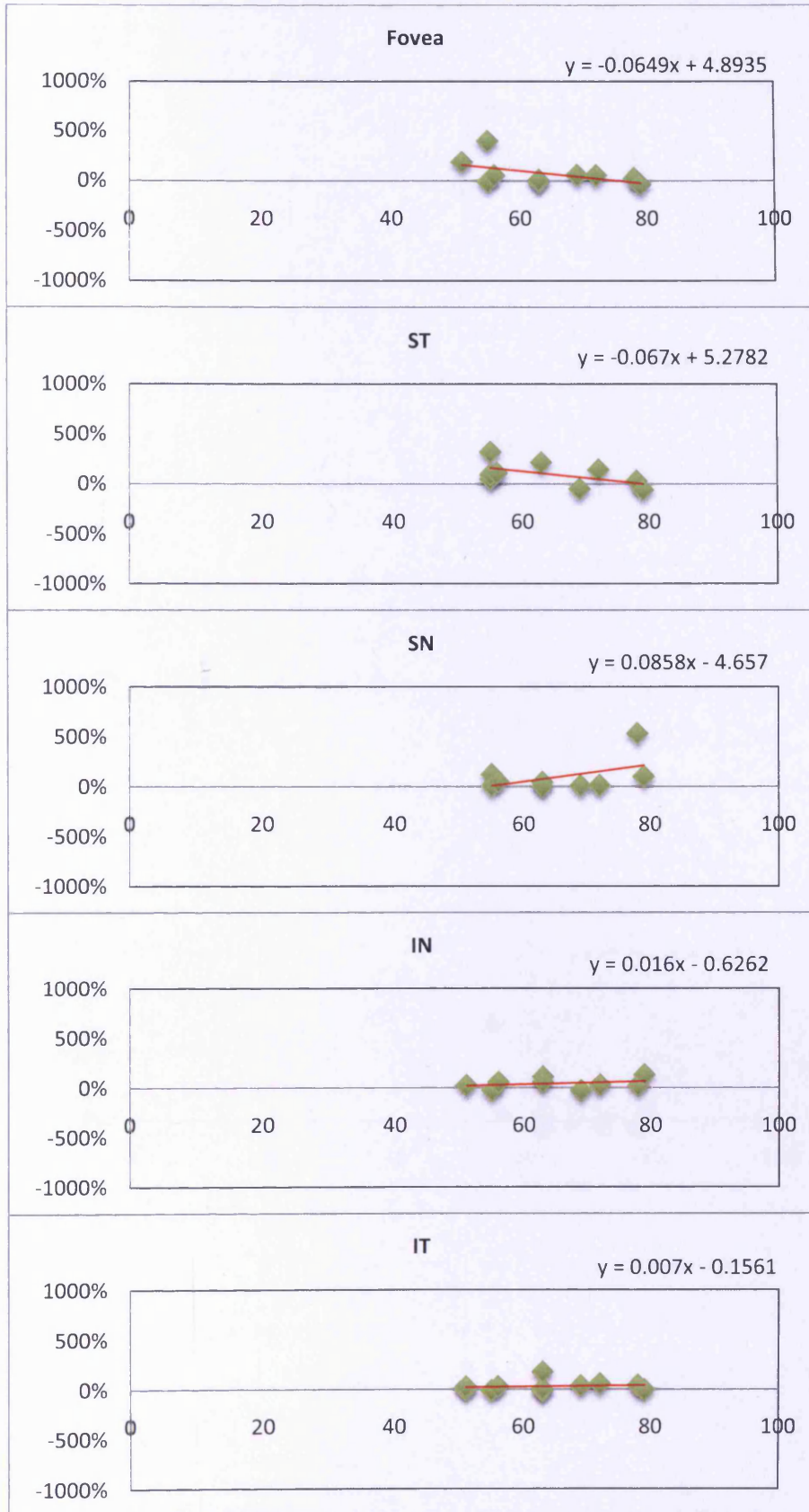


Figure 6.46 Motion detection: The proportionate improvement in performance (ordinate) from visit 1 to visit 2 in terms of sampling efficiency (SE) as a function of age (abscissa). A positive value indicates an improvement in performance.

Improvement in performance

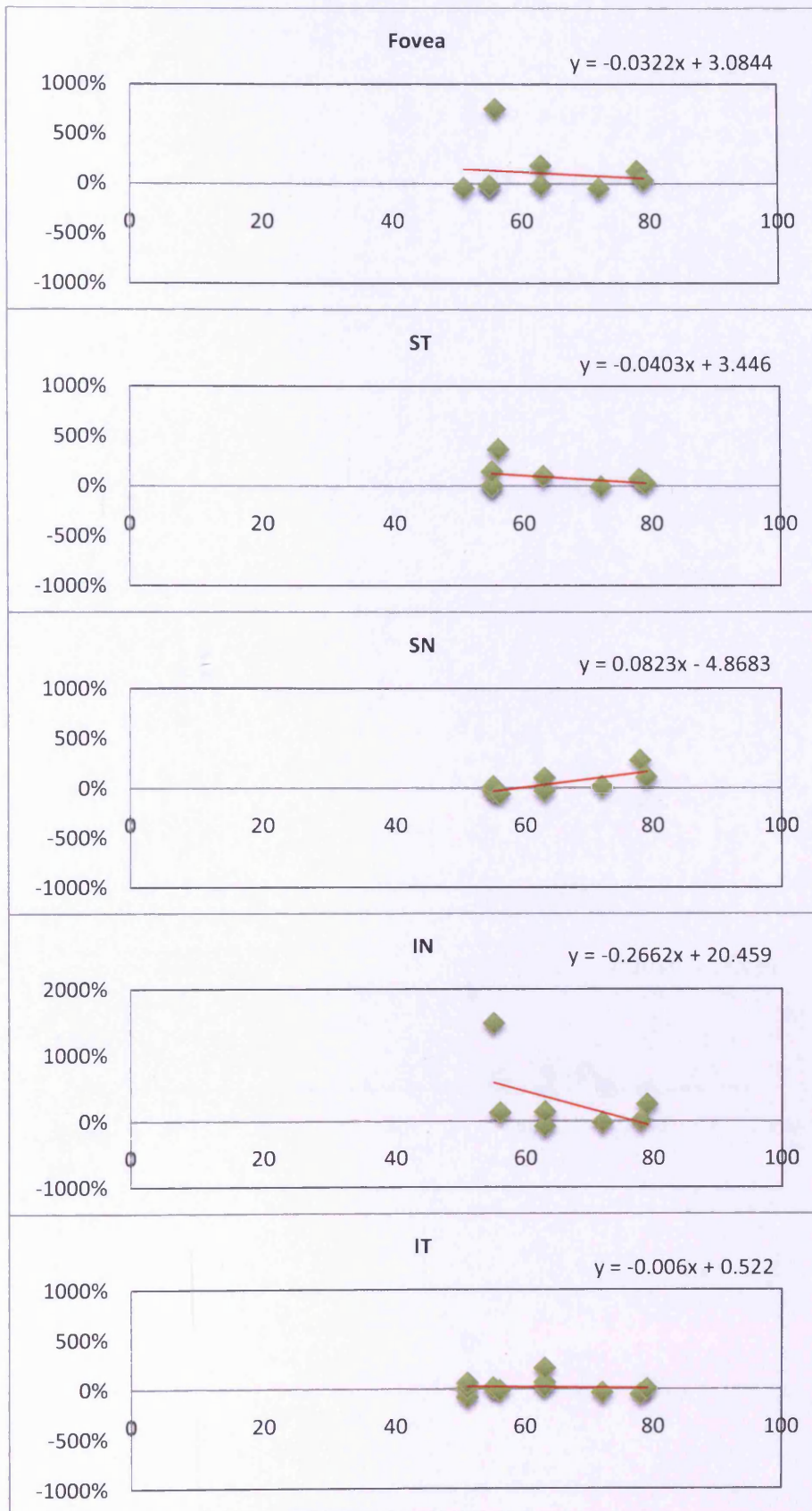


Figure 6.47 Motion discrimination: The proportionate improvement in performance (ordinate) from visit 1 to visit 2 in terms of sampling efficiency (SE) as a function of age (abscissa). A positive value indicates an improvement in performance.

Improvement in performance ↑

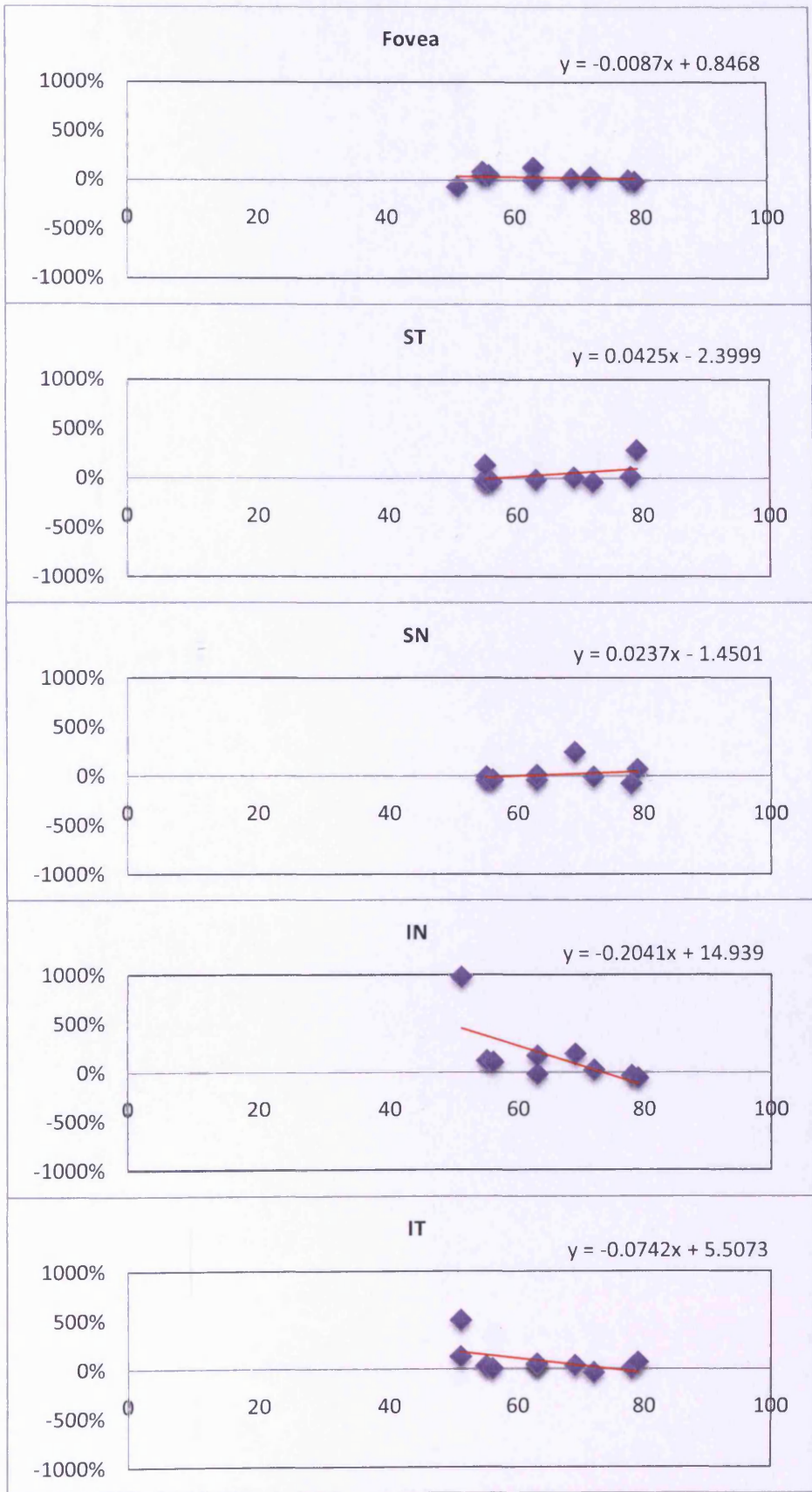


Figure 6.48 Motion detection: The proportionate improvement in performance (ordinate) from visit 2 to visit 3 in terms of sampling efficiency (SE) as a function of age (abscissa). A positive value indicates an improvement in performance.

Improvement in performance

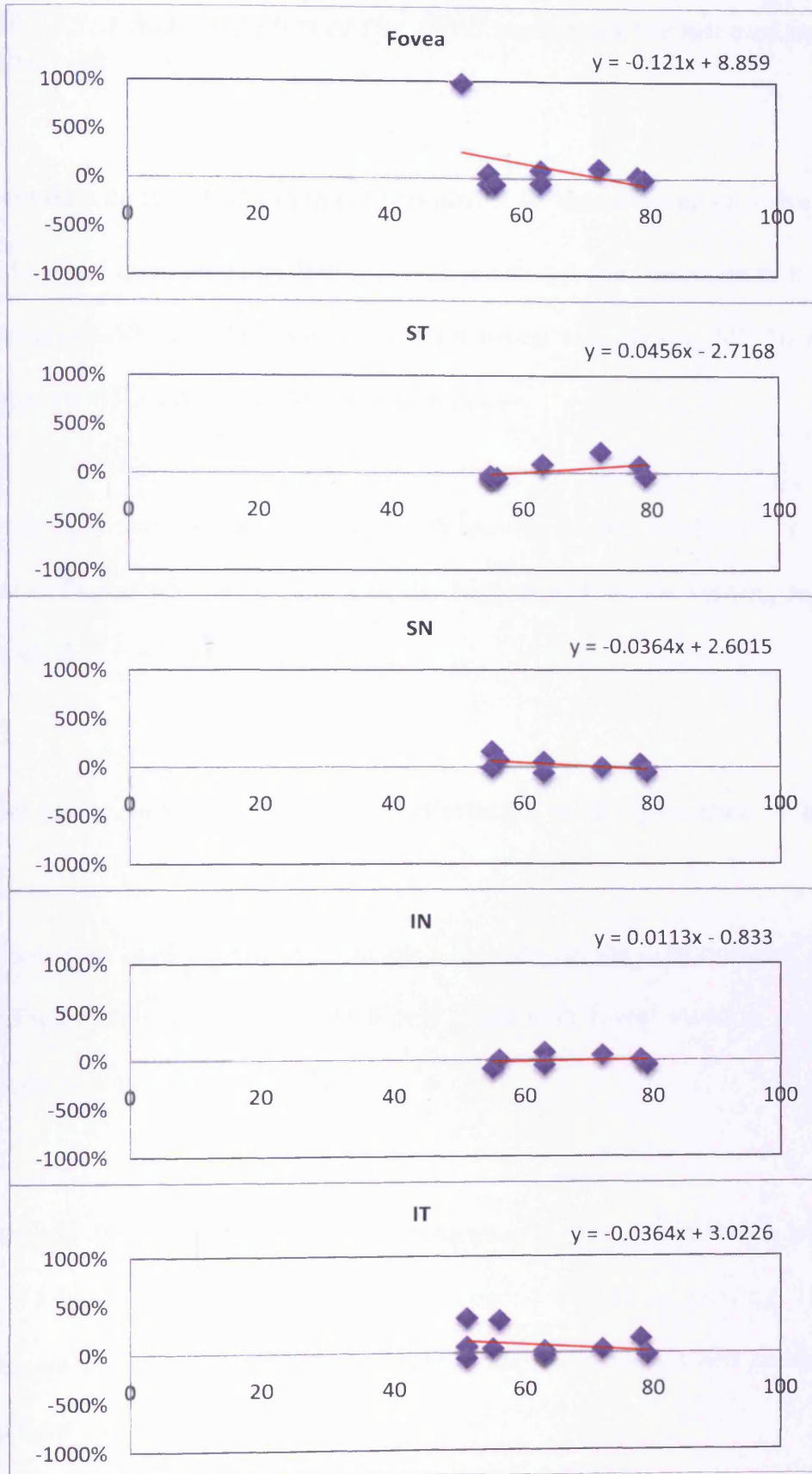


Figure 6.49 Motion discrimination: The proportionate improvement in performance (ordinate) from visit 2 to visit 3 in terms of sampling efficiency (SE) as a function of age (abscissa). A positive value indicates an improvement in performance.

6.8 RESULTS: Characteristics of the DNP measures for normal individuals at the third visit

6.8.1 Michelson contrast of normal individuals in the absence of noise (MC N_0)

The distribution of unmasked thresholds at each location for the detection task at visit 3 is shown in Figure 6.50 (top). TCS was highest for foveal viewing (i.e. MC N_0 was lowest) and lowest at the ST location (i.e. MC N_0 was highest).

The distribution of unmasked thresholds at each location for the discrimination task at visit 3 is shown in Figure 6.51 (top). TCS was also highest with foveal viewing and lowest at the ST location.

6.8.2 Michelson contrast of normal individuals in the presence of noise (MC N_e)

The distribution of masked thresholds at each location for the detection task at visit 3 is shown in Figure 6.50 (middle top). TCS was worst with foveal viewing, and better but similar for the four peripheral locations.

The distribution of masked thresholds at each location for the discrimination task at visit 3 is shown in Figure 6.51 (middle top). TCS was poorest with foveal viewing. The variance was highest at the foveal location and higher at the ST location when compared to the remaining three locations.

6.8.3 Equivalent noise (N_{eq}) of normal individuals

The distribution of N_{eq} values at each location for the discrimination task at visit 3 is shown in Figure 6.50 (middle bottom). N_{eq} was lowest with foveal viewing, when compared with the other locations. The ST location exhibited the highest N_{eq} level of all locations.

The distribution of N_{eq} values at each location for the discrimination task at visit 3 is shown in Figure 6.51 (middle bottom). The SD exceeded the mean with foveal viewing and at the SN and IN locations. The SD at the ST and IT locations were slightly less than the mean. These findings indicated the considerable variability in performance between individuals which, in turn, suggested that the use of equivalent noise would be of limited value for the identification of abnormality.

6.8.4 Sampling efficiency (SE) of normal individuals

The distribution of SE at each location for the detection task at visit 3 is shown in Figure 6.50 (bottom). SE was lowest with foveal viewing when compared with the other locations. The IT location exhibited the highest level of SE.

The distribution of SE at each location for the discrimination task at visit 3 is shown in Figure 6.51 (bottom). SE was lowest with foveal viewing when compared with the other locations. However, the ST location exhibited the highest SE of all locations, which contradicts the sensitivity profile exhibited for the detection task (Figure 6.50, bottom). The difference in regional variation between detection and discrimination is likely to be

related to the between-individual variability given that the highest SE values for both tasks also have the highest SDs.

6.8.5 Coefficient of variation for detection and discrimination data

In order to understand the SD in the context of the mean, the coefficient of variation (CV), defined as the ratio of the SD to the mean, was calculated for MC N₀, MC N_e, N_{eq} and SE at each location (Table 6.18). The CV for MC N₀ indicated that the IT location was less variable than foveal viewing for both the detection and the discrimination task. The CV for MC N_e with the detection task was comparable at all locations. However, for the discrimination task, the CV was significantly higher at the ST location and with foveal viewing compared with the remaining locations, and to the CVs for the detection task. In terms of N_{eq} and SE, CVs for both detection and discrimination were unacceptable in terms of variability. CVs exceeded 100% for N_{eq}, with the discrimination task.

MC N₀	Fovea	ST	SN	IN	IT
Detection	0.42	0.33	0.29	0.32	0.23
Discrimination	0.37	0.29	0.32	0.34	0.24
MC N_e	Fovea	ST	SN	IN	IT
Detection	0.34	0.36	0.28	0.29	0.31
Discrimination	0.62	0.76	0.32	0.40	0.37
N_{eq}	Fovea	ST	SN	IN	IT
Detection	0.68	0.65	0.71	0.68	0.93
Discrimination	1.12	0.94	1.29	1.08	0.91
SE	Fovea	ST	SN	IN	IT
Detection	0.64	0.54	0.60	0.59	0.86
Discrimination	0.82	0.73	0.69	0.67	0.73

Table 6.18 The coefficient of variation (%) for the group mean contrast thresholds in the absence of the noise mask (MC N₀), in the presence of the noise mask (MC N_e), for equivalent noise (N_{eq}) and for sampling efficiency (SE).

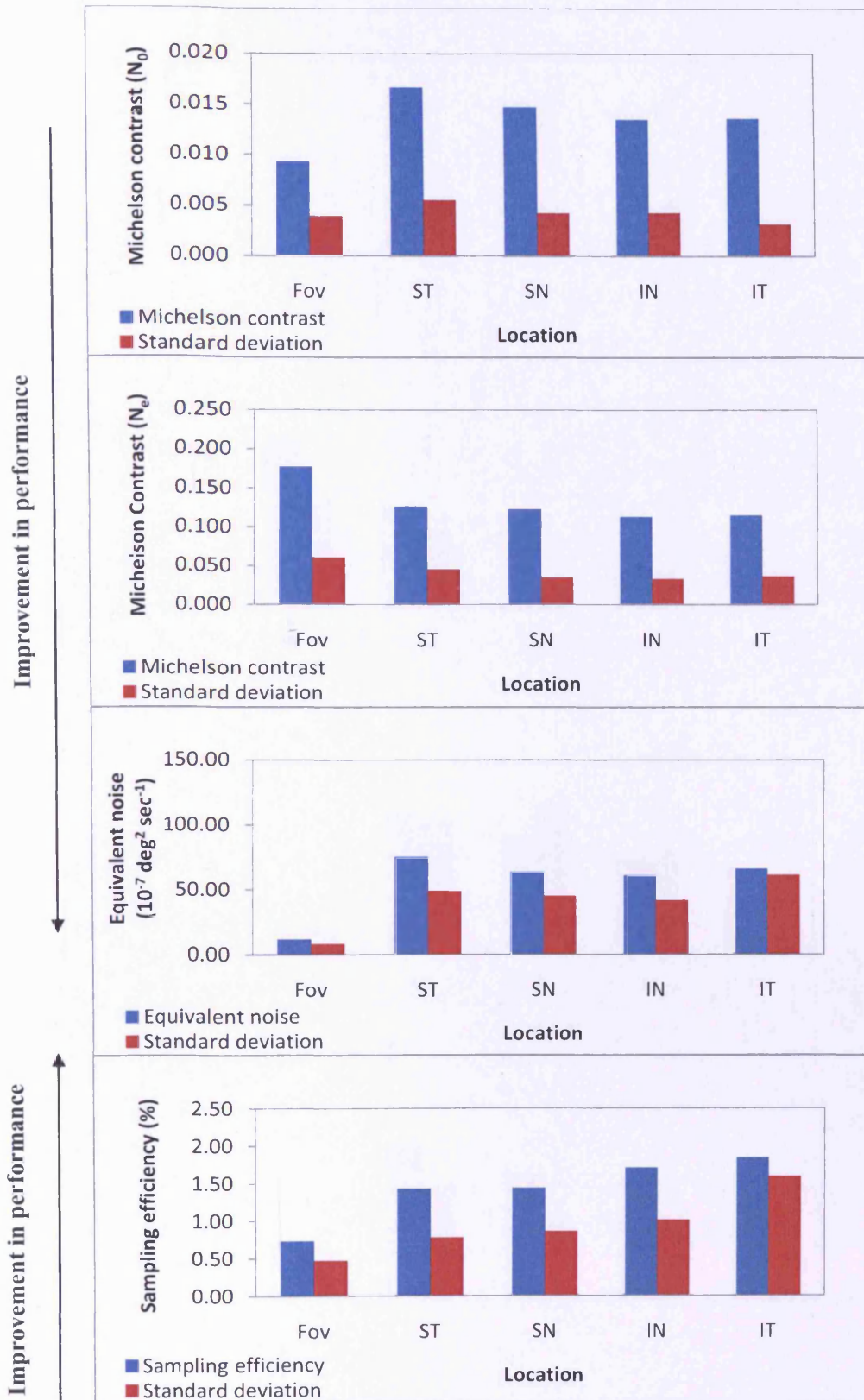


Figure 6.50 Motion detection task: Group Mean (SD) of contrast thresholds in the absence of noise (MC N_0), in the presence of noise (MC N_e), and in terms of equivalent noise (N_{eq}) and sampling efficiency (SE), for the 20 normal observers, derived at the third visit for each stimulus location. Note the difference in scaling for the ordinates.

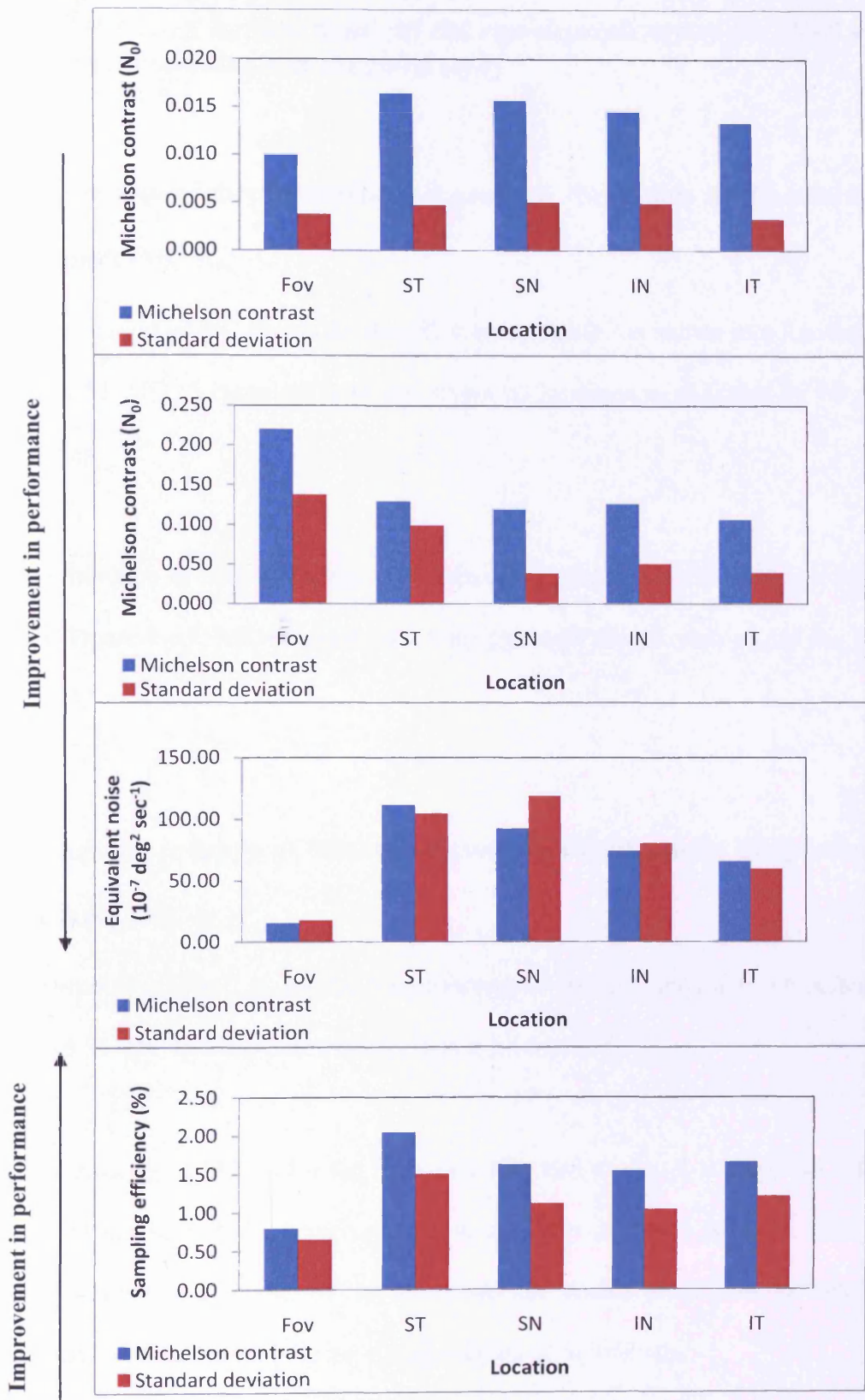


Figure 6.51 Motion discrimination task: Group Mean (SD) of contrast thresholds in the absence of noise ($MC N_0$), in the presence of noise ($MC N_e$), and in terms of equivalent noise (N_{eq}) and sampling efficiency (SE), for the 20 normal observers, derived at the third visit for each stimulus location. Note the difference in scaling for the ordinates.

6.9 RESULTS: Characteristics of the age-dependency of the DNP measures for normal individuals at the third visit

6.9.1 Age-dependency of Michelson contrast thresholds in the absence of the noise mask (MC N_0)

The distribution of MC N_0 for the detection task at visit 3 is shown as a function of age in Figure 6.52. MC N_0 increased with age across all locations as indicated by the gradient of the slope.

The distribution of MC N_0 for the discrimination task at visit 3 is shown as a function of age in Figure 6.53. MC N_0 increased with age with foveal viewing, at the ST and IT locations.

6.9.2 Age-dependency of Michelson contrast thresholds in the presence of the noise mask (MC N_e)

The distribution of MC N_e for the detection task at visit 3 is shown as a function of age in Figure 6.54. MC N_e increased with age across all locations.

The distribution of MC N_e for the discrimination task at visit 3 is shown as a function of age in Figure 6.55. MC N_e increased with age only at the IT location. However, with foveal viewing and at the ST location, the age-related trend was influenced by the magnitude of the variability in the younger group of individuals.

6.9.3 Age-dependency of equivalent noise (N_{eq})

The distribution of N_{eq} for the detection task at visit 3 is shown as a function of age in Figure 6.56. N_{eq} increased with age at the ST, SN and IT locations.

The distribution of N_{eq} for the discrimination task at visit 3 is shown as a function of age in Figure 6.57. N_{eq} increased with age at all locations.

6.9.4 Age-dependency of sampling efficiency (SE)

The distribution of SE for the detection task at visit 3 is shown as a function of age in Figure 6.58. SE declined with age at all locations.

The distribution of SE for the discrimination task at visit 3 is shown as a function of age in Figure 6.59. SE did not decline with age.

6.9.5 Relative age-dependency for detection and discrimination data

In order to understand the magnitude of the age-related slope in the context of the group mean threshold, the relative change per decade (%) was calculated for MC N_0 , MC N_e , N_{eq} and SE for the detection task at visit 3 (Table 6.19) and for the discrimination task (Table 6.20).

For the detection task, and in relative terms MC N_0 and MC N_e increased with age at all locations. N_{eq} increased with age at all locations except with foveal viewing. SE declined with age at all locations except the SN location (Table 6.19).

For the discrimination task, in relative terms MC N_0 increased with foveal viewing and at the ST location. MC N_e declined, indicating an improvement in performance with age at all locations except the IT location. However, this could be explained by the presence of outliers. N_{eq} increased with age at all locations. SE increased with age at all locations except the IT location (Table 6.20).

Improvement in performance ↓

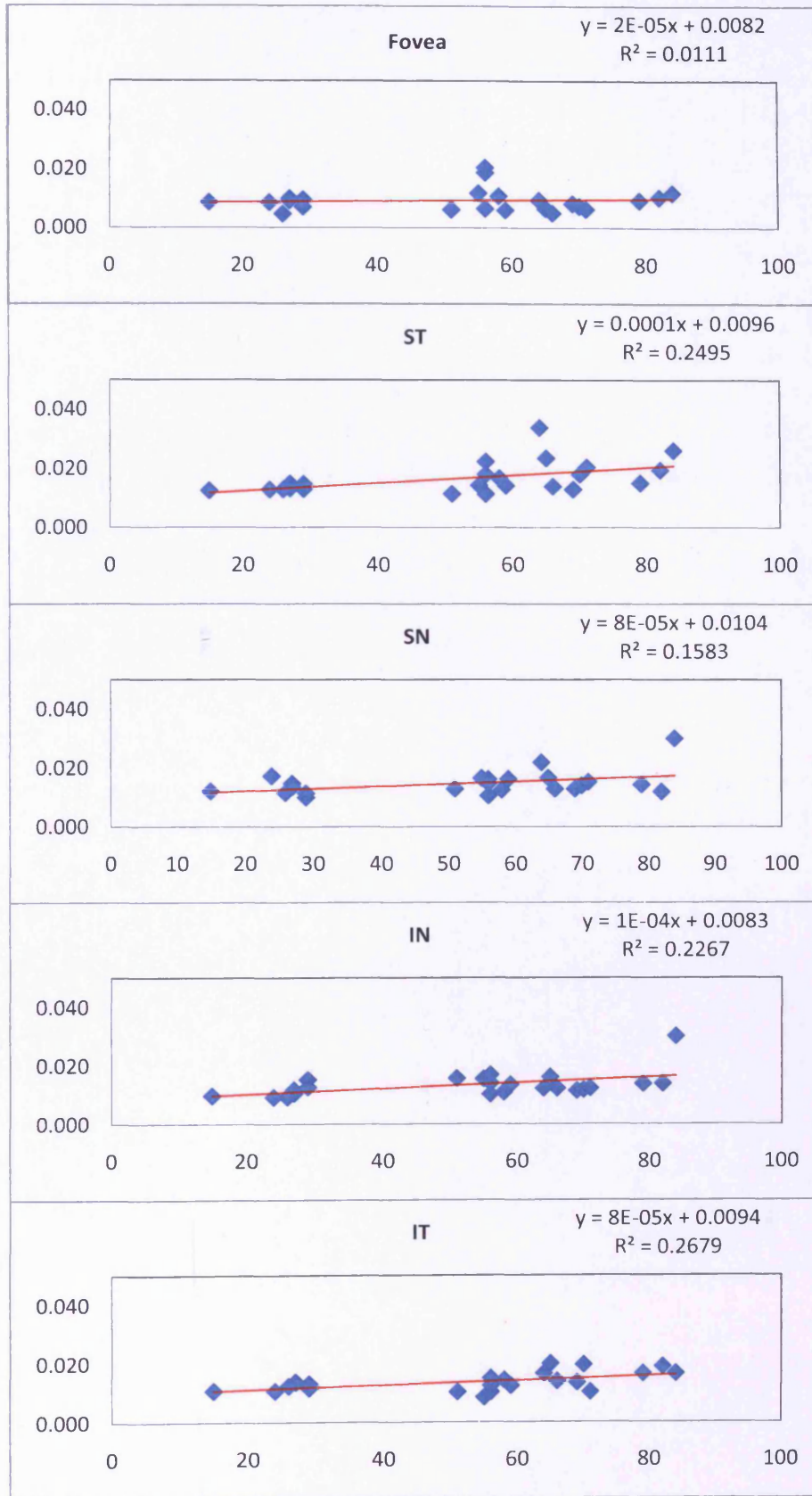


Figure 6.52 Motion detection: Distribution of Michelson Contrast thresholds in the absence of noise ($MC N_0$) (ordinate) within the normal eye as a function of age (abscissa).

Improvement in performance ↓

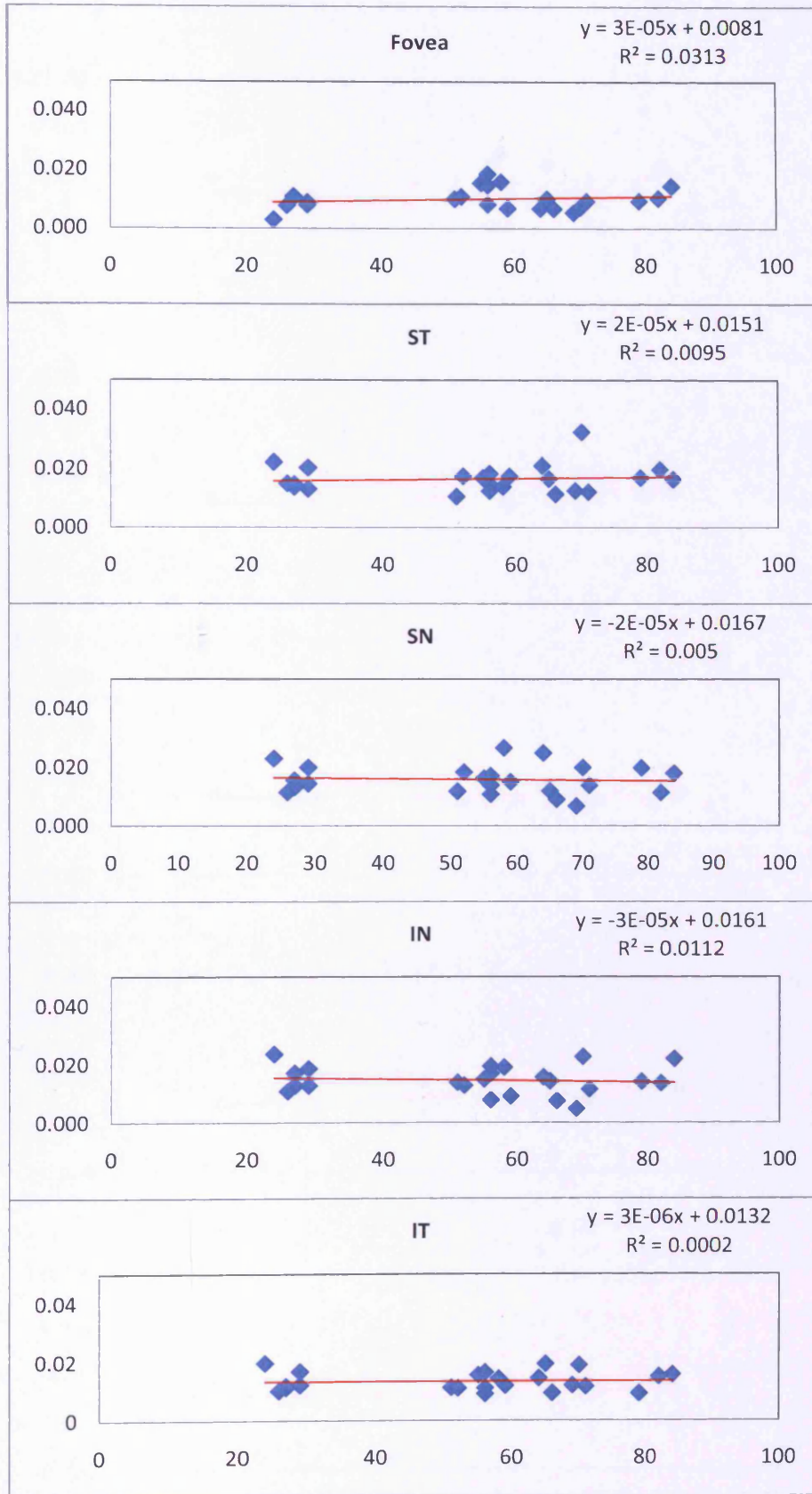


Figure 6.53 Motion discrimination: Distribution of Michelson Contrast thresholds in the absence of noise ($MC N_0$) (ordinate) within the normal eye as a function of age (abscissa).

Improvement in performance ↓

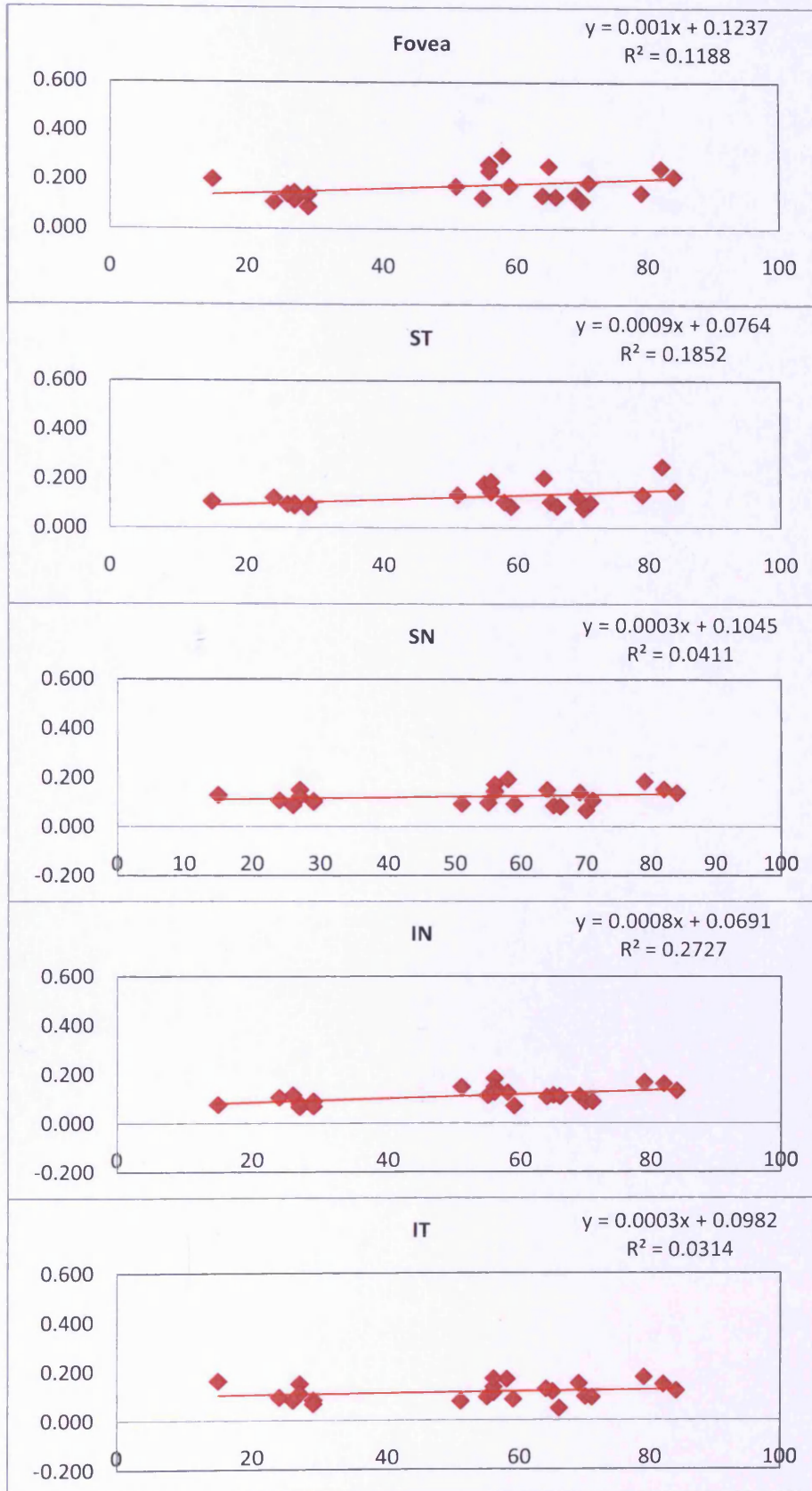


Figure 6.54 Motion detection: Distribution of Michelson Contrast thresholds in the presence of noise ($MC N_e$) (ordinate) within the normal eye as a function of age (abscissa).

Improvement in performance ↓

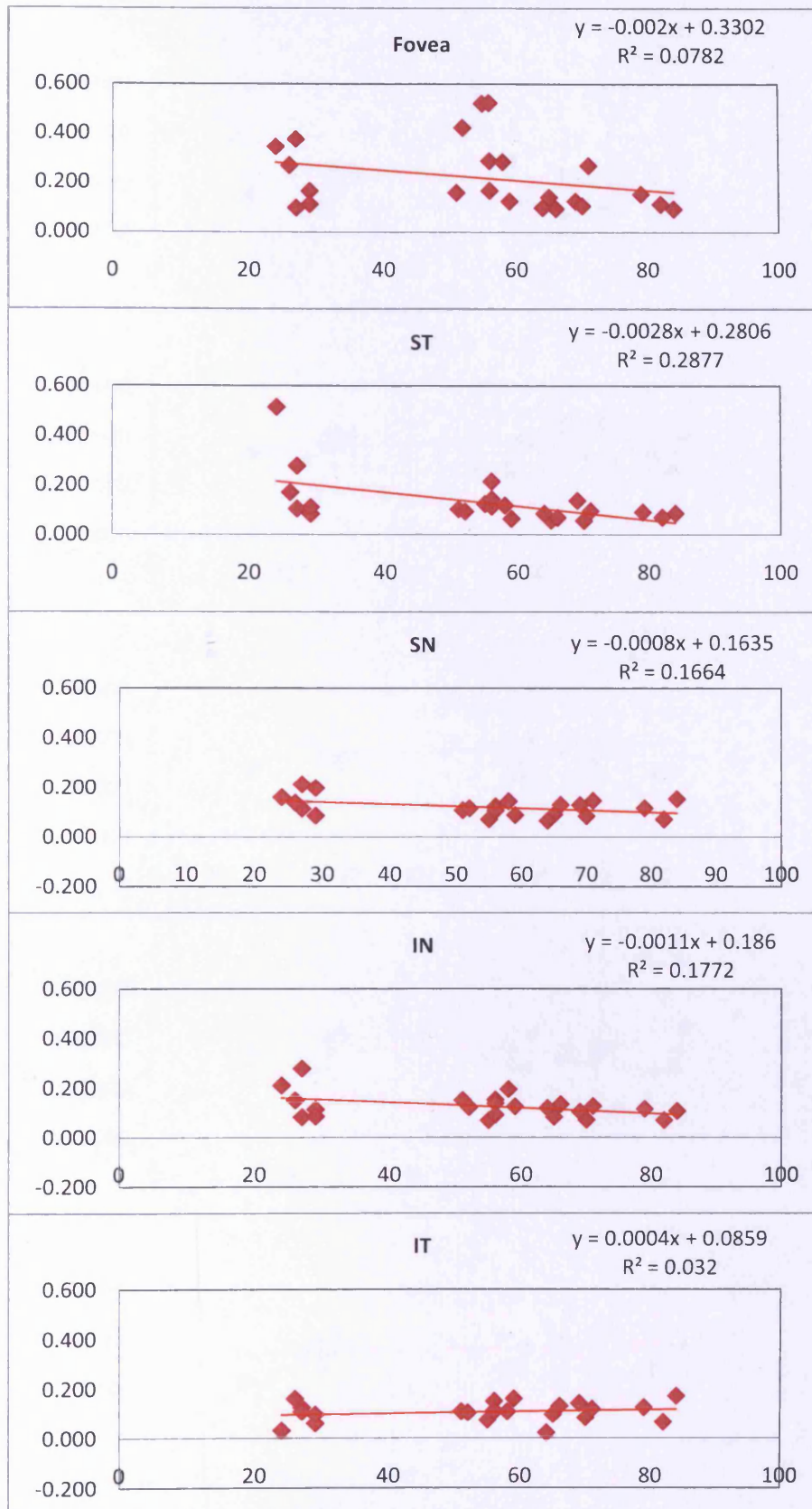


Figure 6.55 Motion discrimination: Distribution of Michelson Contrast thresholds in the presence of noise ($MC N_e$) (ordinate) within the normal eye as a function of age (abscissa).

Improvement in performance ↓

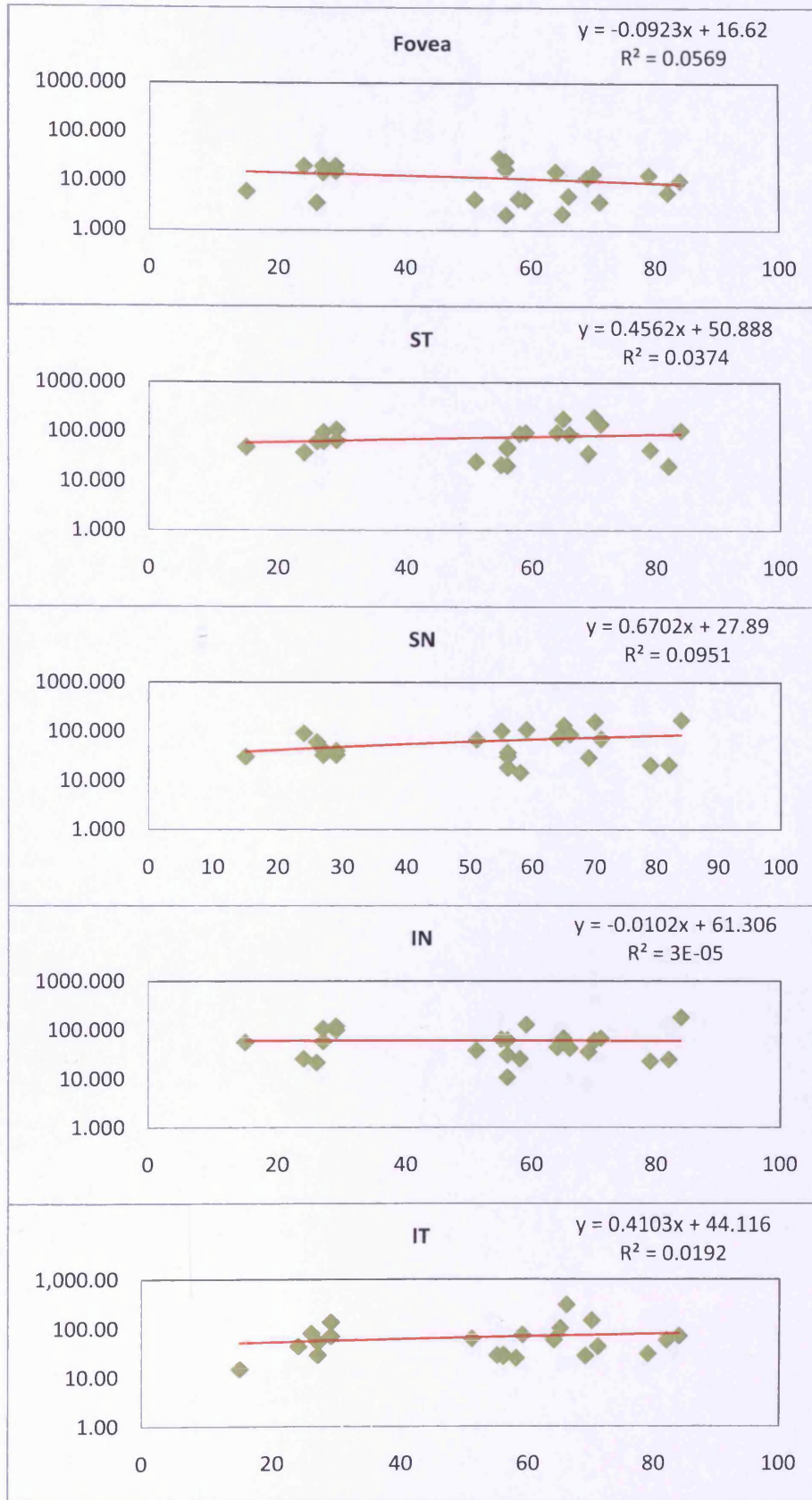


Figure 6.56 Motion detection: Distribution of equivalent noise (N_{eq}) (ordinate) within the normal eye as a function of age (abscissa).

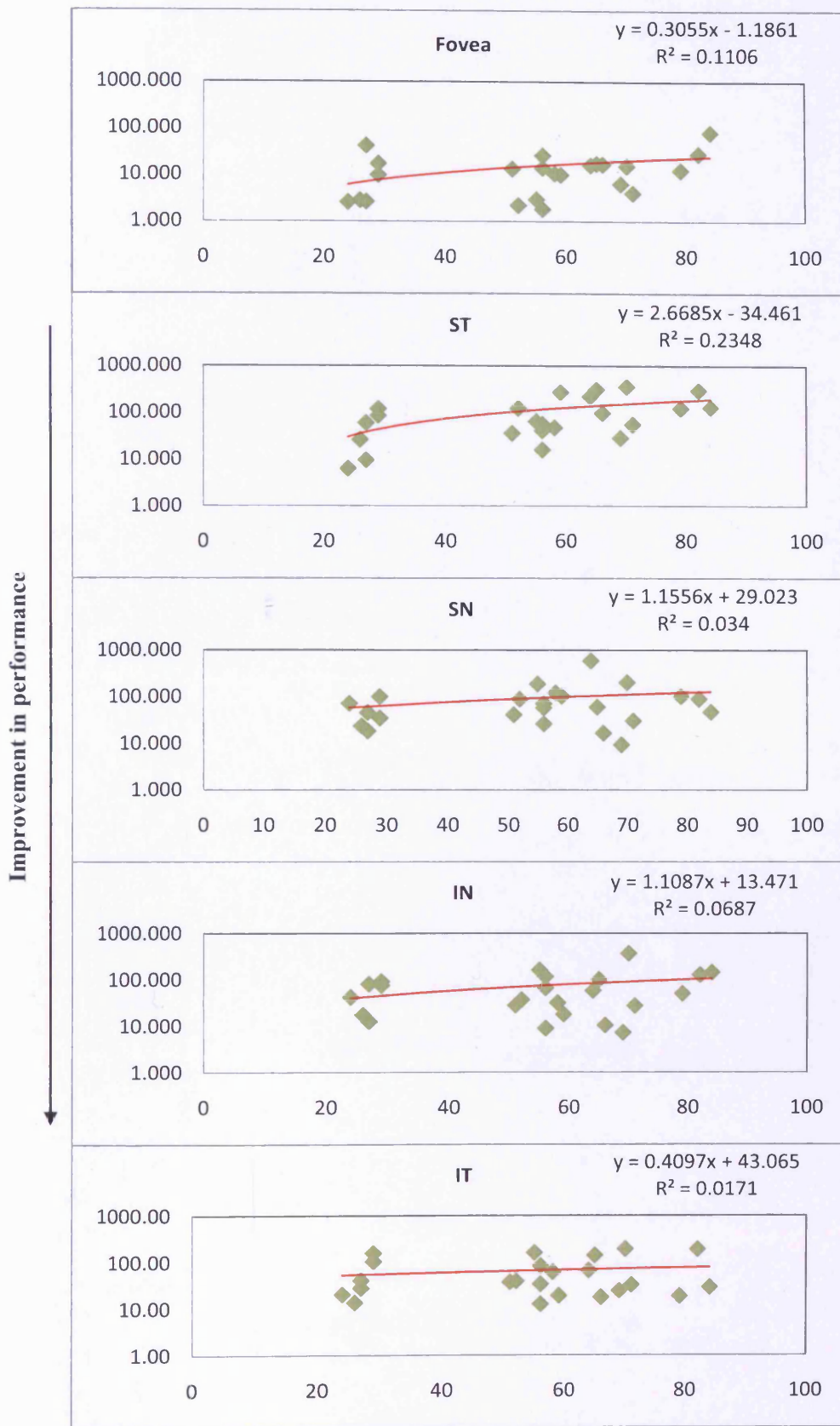


Figure 6.57 Motion discrimination: Distribution of equivalent noise (N_{eq}) (ordinate) within the normal eye as a function of age (abscissa).

Improvement in performance ↑

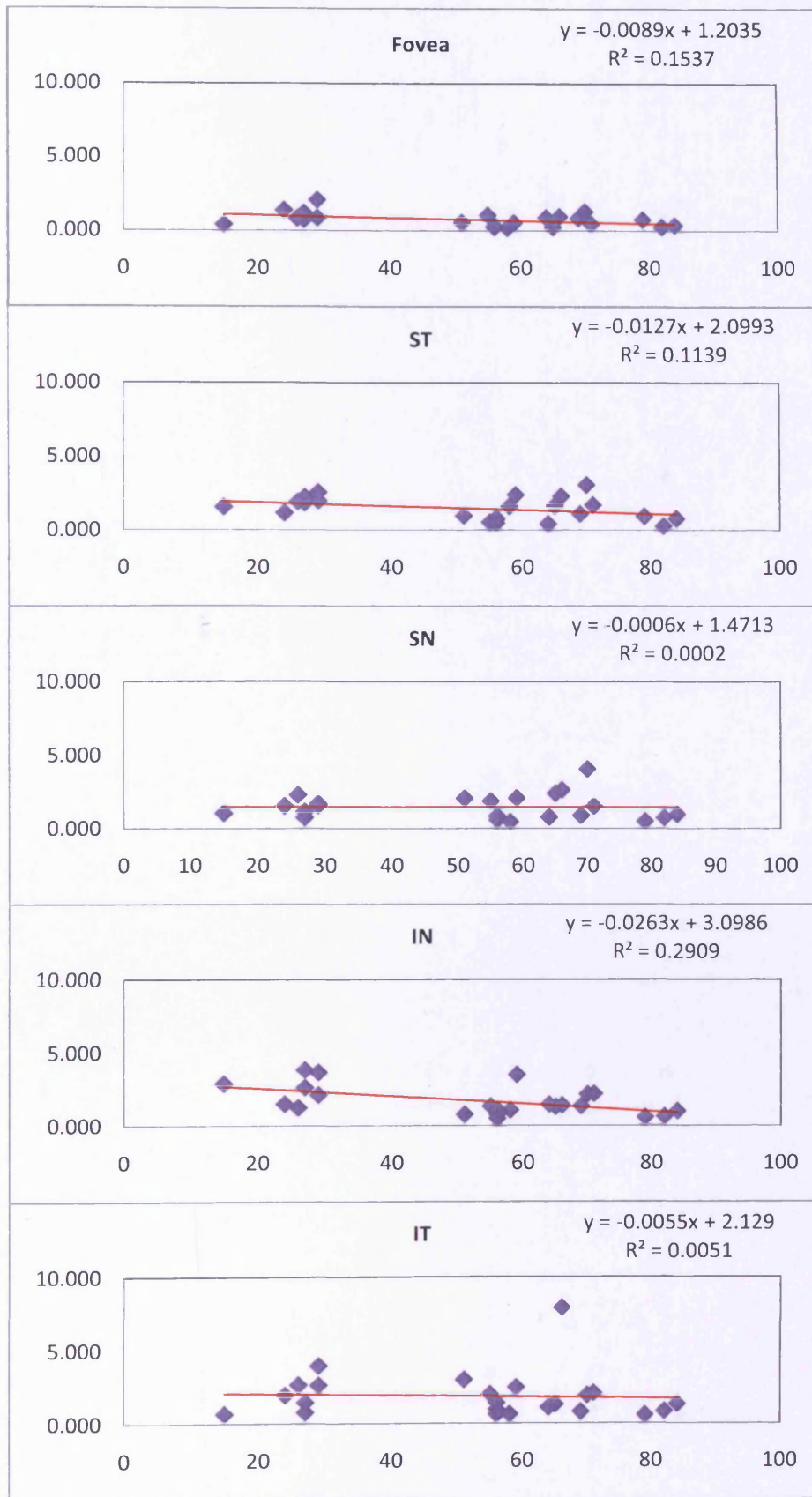


Figure 6.58 Motion detection: Distribution of sampling efficiency (SE) (%) (ordinate) within the normal eye as a function of age (abscissa).

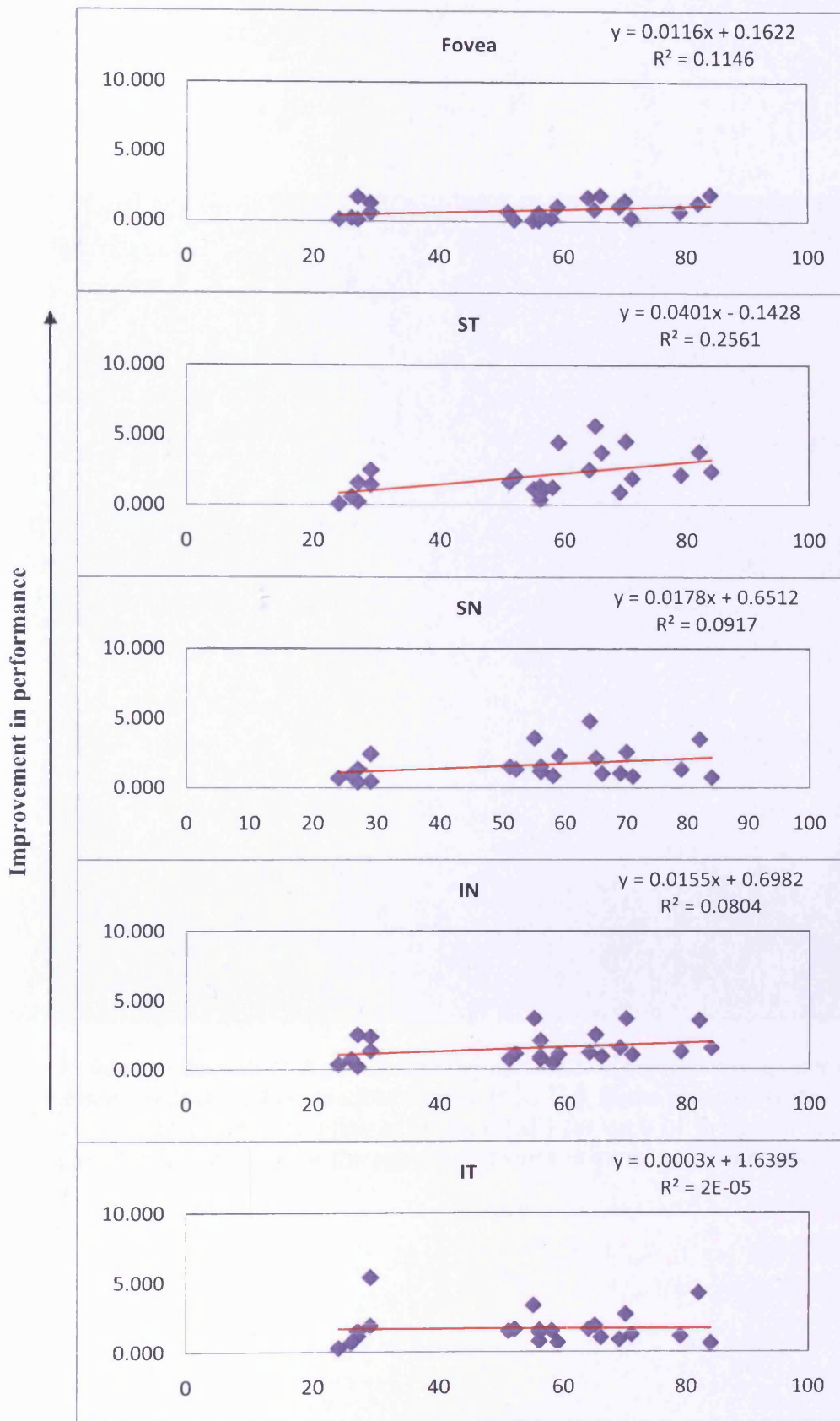


Figure 6.59 Motion discrimination: Distribution of sampling efficiency (SE) (%) (ordinate) within the normal eye as a function of age (abscissa).

MC N_0		Detection				
Location	Fovea	ST	SN	IN	IT	
Group mean	0.009249	0.016655	0.014705	0.013481	0.013586	
Age-related slope	0.000020	0.000100	0.000080	0.000100	0.000080	
Coefficient of Determination	0.01	0.25	0.16	0.23	0.27	
Relative change per decade	2%	6%	5%	7%	6%	
MC N_e						
Location	Fovea	ST	SN	IN	IT	
Group mean	0.176778	0.125676	0.122243	0.112670	0.114530	
Age-related slope	0.001000	0.000900	0.000300	0.000800	0.000300	
Coefficient of Determination	0.12	0.19	0.04	0.27	0.03	
Relative change per decade	6%	7%	2%	7%	3%	
N_{eq}						
Location	Fovea	ST	SN	IN	IT	
Group mean	11.73	75.05	63.38	60.77	65.84	
Age-related slope	-0.09	0.46	0.67	-0.01	0.41	
Coefficient of Determination	0.06	0.04	0.10	0.00	0.02	
Relative change per decade	-8%	6%	11%	0%	6%	
SE						
Location	Fovea	ST	SN	IN	IT	
Group mean	0.73	1.43	1.44	1.71	1.84	
Age-related slope	-0.01	-0.01	0.00	-0.03	-0.01	
Coefficient of Determination	0.15	0.11	0.00	0.29	0.01	
Relative change per decade	-12%	-9%	0%	-15%	-3%	

Table 6.19 Motion detection: Age-dependency in terms of relative change per decade (%) for Michelson Contrast in the absence of noise (MC N_0), in the presence of noise (MC N_e), equivalent noise (N_{eq}) and sampling efficiency (SE) for each of the given locations. The Coefficient of Determination for the age-related slope is given as an indication of between-individual variability.

MC N₀		Discrimination				
Location	Fovea	ST	SN	IN	IT	
Group mean	0.010000	0.016436	0.015683	0.014568	0.013319	
Age-related slope	0.000030	0.000020	-0.000020	-0.000030	0.000003	
Coefficient of Determination	0.03	0.01	0.01	0.01	0.00	
Relative change per decade	3%	1%	-1%	-2%	0%	
MC N_e						
Location	Fovea	ST	SN	IN	IT	
Group mean	0.219729	0.128664	0.119159	0.125651	0.105807	
Age-related slope	-0.002000	-0.002800	-0.000800	-0.001100	0.000400	
Coefficient of Determination	0.08	0.29	0.17	0.18	0.03	
Relative change per decade	-9%	-22%	-7%	-9%	4%	
N_{eq}						
Location	Fovea	ST	SN	IN	IT	
Group mean	15.49	111.15	92.08	73.97	65.42	
Age-related slope	0.31	2.67	1.16	1.11	0.41	
Coefficient of Determination	0.01	0.23	0.03	0.07	0.02	
Relative change per decade	20%	24%	13%	15%	6%	
SE						
Location	Fovea	ST	SN	IN	IT	
Group mean	0.80	2.04	1.62	1.55	1.65	
Age-related slope	0.01	0.04	0.02	0.02	0.00	
Coefficient of Determination	0.11	0.26	0.09	0.08	0.00	
Relative change per decade	15%	20%	11%	10%	0%	

Table 6.20 Motion discrimination: Age-dependency in terms of relative change per decade (%) for Michelson Contrast in the absence of noise (MC N₀), in the presence of noise (MC N_e), equivalent noise (N_{eq}) and sampling efficiency (SE) for each of the given locations. The Coefficient of Determination for the age-related slope is given as an indication of between-individual variability.

6.10 RESULTS: DNP outcomes for individuals with OAG

6.10.1 Distribution of DNP measures for the detection task at the superior temporal quadrant for individuals with OAG and for normal individuals

The 90th percentile of the distribution for the twenty normal individuals as a function of the Pattern Deviation probability level at the corresponding location (abscissa) is given in Figures 6.60 – 6.65 in terms of Michelson contrast thresholds in the absence of noise ($MC N_0$), in the presence of noise ($MC N_0$), equivalent noise (N_{eq}), sampling efficiency (SE), Log_{10} Ratio and the signal detection index (SDI) (ordinates). Of the ten individuals with OAG, six exhibited abnormality by Pattern Deviation probability analysis at the given stimulus location (described as PD_{Ab}) and, of these, two also exhibited abnormality in terms of RNFL thickness at the location (described as $PD_{Ab} RNFL_{Ab}$). The remaining four individuals exhibited a sensitivity within the normal range by Pattern Deviation probability analysis (described as PD_N) and, of these, two also exhibited abnormality in terms of RNFL thickness at the given location (described as $PD_N RNFL_{Ab}$).

Of the ten individuals with OAG, $MC N_0$ identified five individuals as abnormal: two with $PD_{Ab} RNFL_{Ab}$, one with $PD_N RNFL_N$, one with $PD_{Ab} RNFL_N$ and one with $PD_N RNFL_{Ab}$ (Figure 6.60). $MC N_e$ identified one individual with $PD_N RNFL_{Ab}$ as abnormal (Figure 6.61). N_{eq} identified two individuals as abnormal: one with $PD_{Ab} RNFL_N$ and one with $PD_{Ab} RNFL_{Ab}$ (Figure 6.62). SE identified none of the individuals as abnormal (Figure 6.63). Log_{10} Ratio identified three individuals as abnormal: one with $PD_{Ab} RNFL_N$, one with $PD_N RNFL_{Ab}$, and one with $PD_{Ab} RNFL_{Ab}$ (Figure 6.64). SDI identified four individuals as abnormal: two with $PD_{Ab} RNFL_{Ab}$, one with $PD_N RNFL_N$ and one with $PD_{Ab} RNFL_N$ (Figure 6.65). A summary of findings is shown in Table 6.21.

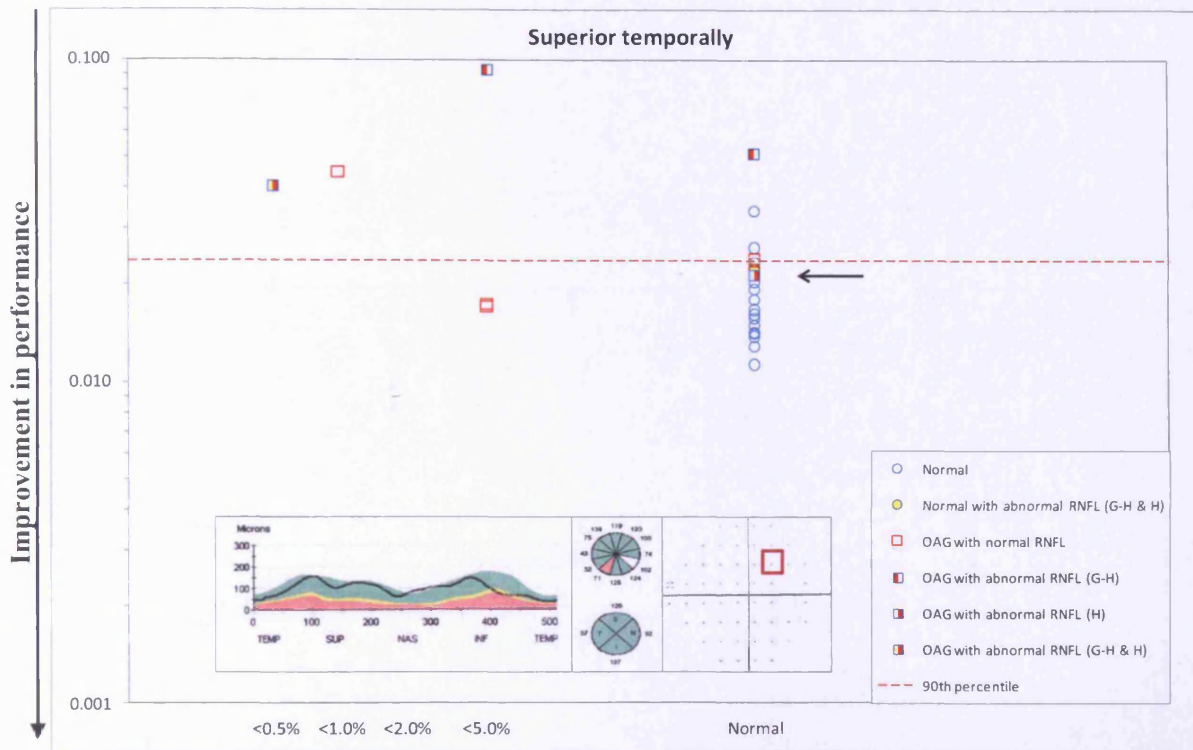


Figure 6.60 Motion detection: Michelson contrast thresholds in the absence of noise ($MC N_0$) for the stimuli in the superior temporal quadrant (ordinate) as a function of the Pattern Deviation probability level at the corresponding location (abscissa). The 90th percentile of the distribution of Michelson contrast thresholds amongst the 20 normal individuals is indicated by the red dotted line. Michelson contrast thresholds for these 20 individuals are indicated by the circles. Individuals with OAG are indicated by the squares. The percentile associated with the given RNFL thickness derived from the OCT printout at the given stimulus location is indicated by the colour (yellow <5%; red <1%) according to the topographical mapping of Garway-Heath et al (2000) (left half of the circle/ square indicated as G-H) or Harwerth et al (2007) (right half of the circle/ square indicated as H). The RNFL Thickness Chart (left), the Sector Averages (middle [top]), the Quadrant averages (Middle [bottom]) and the Pattern Deviation probability map (right) are given in the bottom panel for the individual exhibiting the contrast threshold indicated by the black arrow. The stimulus location for SAP corresponding to that for DNP is indicated by the red square.

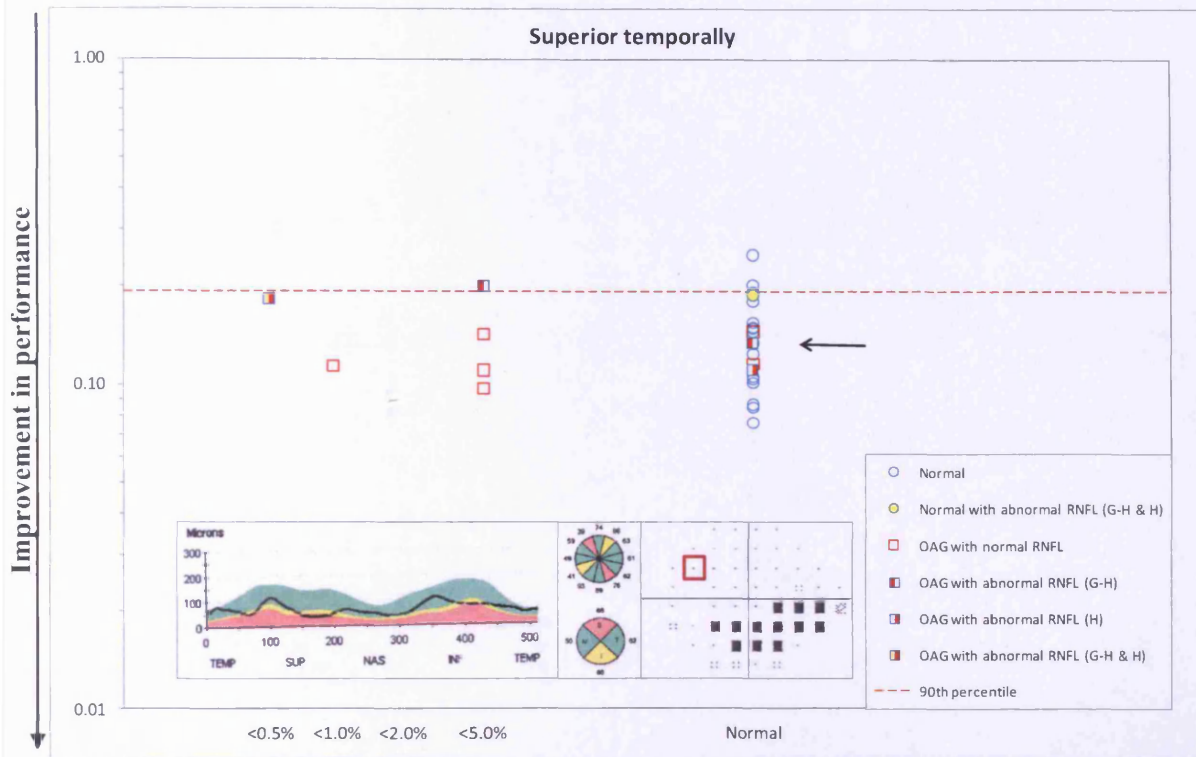


Figure 6.61 Motion detection: Michelson contrast thresholds in the presence of noise ($MC N_e$) for the stimuli in the superior temporal quadrant (ordinate) as a function of the Pattern Deviation probability level at the corresponding location (abscissa). The 90th percentile of the distribution of Michelson contrast thresholds amongst the 20 normal individuals is indicated by the red dotted line. Michelson contrast thresholds for these 20 individuals are indicated by the circles. Individuals with OAG are indicated by the squares. The percentile associated with the given RNFL thickness derived from the OCT printout at the given stimulus location is indicated by the colour (yellow <5%; red <1%) according to the topographical mapping of Garway-Heath et al (2000) (left half of the circle/ square indicated as G-H) or Harwerth et al (2007) (right half of the circle/ square indicated as H). The RNFL Thickness Chart (left), the Sector Averages (middle [top]), the Quadrant averages (Middle [bottom]) and the Pattern Deviation probability map (right) are given in the bottom panel for the individual exhibiting the contrast threshold indicated by the black arrow. The stimulus location for SAP corresponding to that for DNP is indicated by the red square.

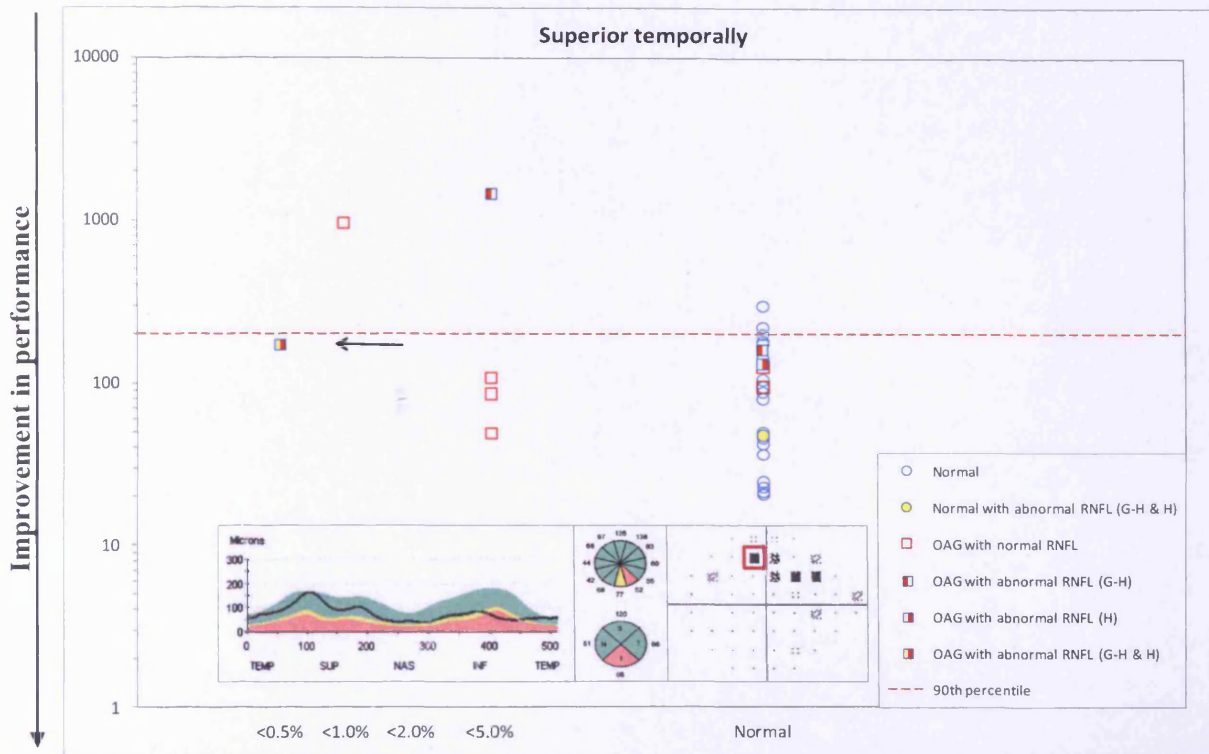


Figure 6.62 Motion detection: equivalent noise (N_{eq}) for the stimuli in the superior temporal quadrant (ordinate) as a function of the Pattern Deviation probability level at the corresponding location (abscissa). The 90th percentile of the distribution of equivalent noise amongst the 20 normal individuals is indicated by the red dotted line. Equivalent noise for these 20 individuals is indicated by the circles. Individuals with OAG are indicated by the squares. The percentile associated with the given RNFL thickness derived from the OCT printout at the given stimulus location is indicated by the colour (yellow <5%; red <1%) according to the topographical mapping of Garway-Heath et al (2000) (left half of the circle/ square indicated as G-H) or Harwerth et al (2007) (right half of the circle/ square indicated as H). The RNFL Thickness Chart (left), the Sector Averages (middle [top]), the Quadrant averages (Middle [bottom]) and the Pattern Deviation probability map (right) are given in the bottom panel for the individual exhibiting the contrast threshold indicated by the black arrow. The stimulus location for SAP corresponding to that for DNP is indicated by the red square.

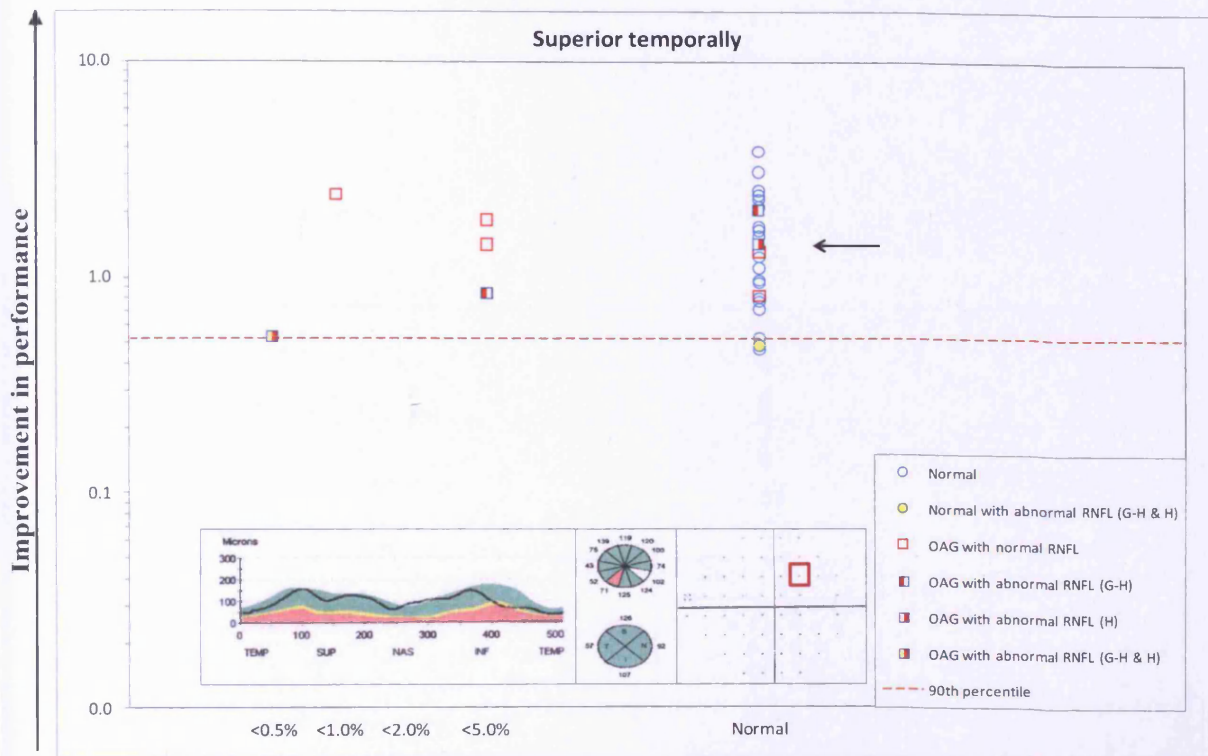


Figure 6.63 Motion detection: sampling efficiency (SE) for the stimuli in the superior temporal quadrant (ordinate) as a function of the Pattern Deviation probability level at the corresponding location (abscissa). The 90th percentile of the distribution of sampling efficiency amongst the 20 normal individuals is indicated by the red dotted line. Sampling efficiency for these 20 individuals is indicated by the circles. Individuals with OAG are indicated by the squares. The percentile associated with the given RNFL thickness derived from the OCT printout at the given stimulus location is indicated by the colour (yellow <5%; red <1%) according to the topographical mapping of Garway-Heath et al (2000) (left half of the circle/ square indicated as G-H) or Harwerth et al (2007) (right half of the circle/ square indicated as H). The RNFL Thickness Chart (left), the Sector Averages (middle [top]), the Quadrant averages (Middle [bottom]) and the Pattern Deviation probability map (right) are given in the bottom panel for the individual exhibiting the contrast threshold indicated by the black arrow. The stimulus location for SAP corresponding to that for DNP is indicated by the red square.

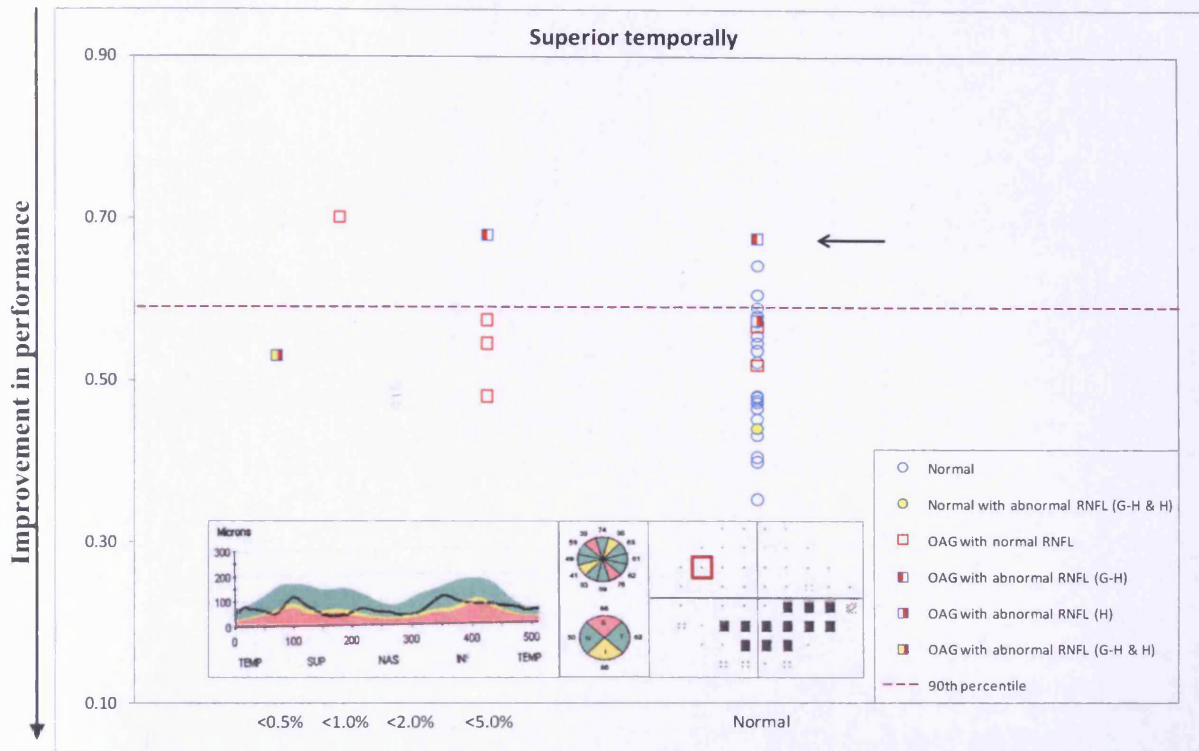


Figure 6.64 Motion detection: Log_{10} Ratio for the stimuli in the superior temporal quadrant (ordinate) as a function of the Pattern Deviation probability level at the corresponding location (abscissa). The 90th percentile of the distribution of the Log_{10} Ratio amongst the 20 normal individuals is indicated by the red dotted line. Log_{10} Ratio for these 20 individuals is indicated by the circles. Individuals with OAG are indicated by the squares. The percentile associated with the given RNFL thickness derived from the OCT printout at the given stimulus location is indicated by the colour (yellow <5%; red <1%) according to the topographical mapping of Garway-Heath et al (2000) (left half of the circle/ square indicated as G-H) or Harwerth et al (2007) (right half of the circle/ square indicated as H). The RNFL Thickness Chart (left), the Sector Averages (middle [top]), the Quadrant averages (Middle [bottom]) and the Pattern Deviation probability map (right) are given in the bottom panel for the individual exhibiting the contrast threshold indicated by the black arrow. The stimulus location for SAP corresponding to that for DNP is indicated by the red square.

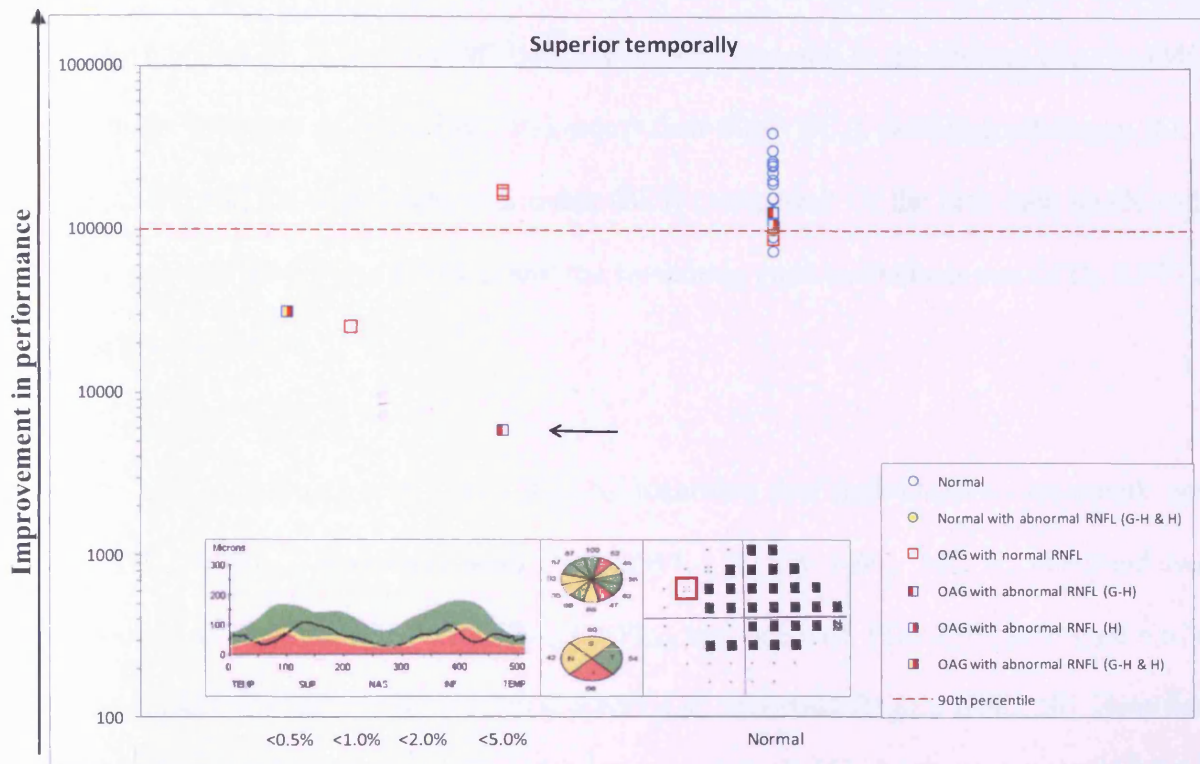


Figure 6.65 Motion detection: Signal detection index (SDI) for the stimuli in the superior temporal quadrant (ordinate) as a function of the Pattern Deviation probability level at the corresponding location (abscissa). The 90th percentile of the distribution of the Signal detection index amongst the 20 normal individuals is indicated by the red dotted line. Signal detection index for these 20 individuals is indicated by the circles. Individuals with OAG are indicated by the squares. The percentile associated with the given RNFL thickness derived from the OCT printout at the given stimulus location is indicated by the colour (yellow <5%; red <1%) according to the topographical mapping of Garway-Heath et al (2000) (left half of the circle/ square indicated as G-H) or Harwerth et al (2007) (right half of the circle/ square indicated as H). The RNFL Thickness Chart (left), the Sector Averages (middle [top]), the Quadrant averages (Middle [bottom]) and the Pattern Deviation probability map (right) are given in the bottom panel for the individual exhibiting the contrast threshold indicated by the black arrow. The stimulus location for SAP corresponding to that for DNP is indicated by the red square.

6.10.2 Distribution of DNP measures for the detection task at the superior nasal quadrant for individuals with OAG and for normal individuals

The 90th percentile of the distribution for the twenty normal individuals as a function of the Pattern Deviation probability level at the corresponding location (abscissa) is given in Figures 6.66 – 6.71, in terms of Michelson contrast thresholds in the absence of noise ($MC N_0$), in the presence of noise ($MC N_0$), equivalent noise (N_{eq}), sampling efficiency (SE), \log_{10} Ratio and the signal detection index (SDI) (ordinates). Of the nine individuals with OAG, one exhibited $PD_{Ab} RNFL_{Ab}$ and the remaining eight individuals were $PD_N RNFL_N$ at the given location.

Of the nine individuals with OAG, $MC N_0$ identified four individuals as abnormal: one with $PD_{Ab} RNFL_{Ab}$, and three with $PD_N RNFL_N$ (Figure 6.66). $MC N_e$ identified two individuals as abnormal: one with $PD_{Ab} RNFL_{Ab}$ and one with $PD_N RNFL_N$ (Figure 6.67). N_{eq} identified one individual with $PD_N RNFL_N$ as abnormal (Figure 6.68). SE identified two individuals as abnormal: one with $PD_{Ab} RNFL_{Ab}$ and one with $PD_N RNFL_N$ (Figure 6.69). \log_{10} Ratio identified one individual with $PD_N RNFL_N$ as abnormal (Figure 6.70). SDI identified one individual with $PD_{Ab} RNFL_{Ab}$ as abnormal (Figure 6.71). A summary of findings is shown in Table 6.22.

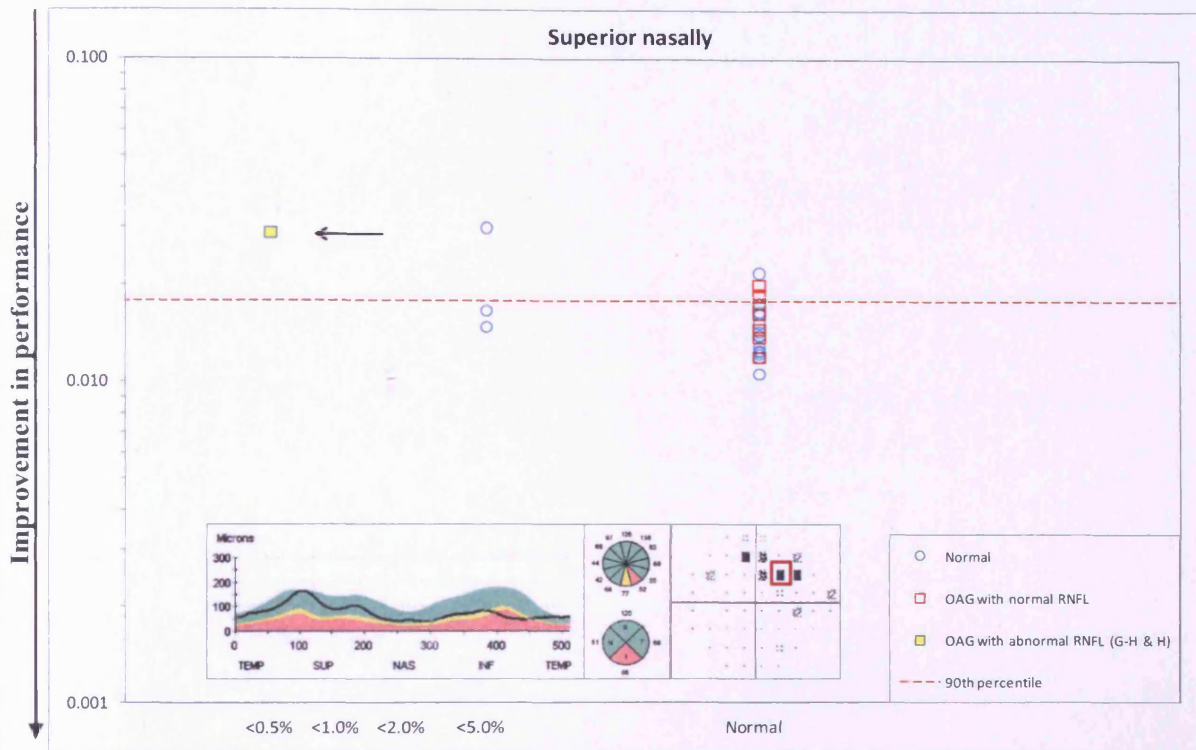


Figure 6.66 Motion detection: Michelson contrast thresholds in the absence of noise ($MC N_0$) for the stimuli in the superior nasal quadrant (ordinate) as a function of the Pattern Deviation probability level at the corresponding location (abscissa). The 90th percentile of the distribution of Michelson contrast thresholds amongst the 20 normal individuals is indicated by the red dotted line. Michelson contrast thresholds for these 20 individuals are indicated by the circles. Individuals with OAG are indicated by the squares. The percentile associated with the given RNFL thickness derived from the OCT printout at the given stimulus location is indicated by the colour (yellow <5%; red <1%) according to the topographical mapping of Garway-Heath et al (2000) (left half of the circle/ square indicated as G-H) or Harwerth et al (2007) (right half of the circle/ square indicated as H). The RNFL Thickness Chart (left), the Sector Averages (middle [top]), the Quadrant averages (Middle [bottom]) and the Pattern Deviation probability map (right) are given in the bottom panel for the individual exhibiting the contrast threshold indicated by the black arrow. The stimulus location for SAP corresponding to that for DNP is indicated by the red square.

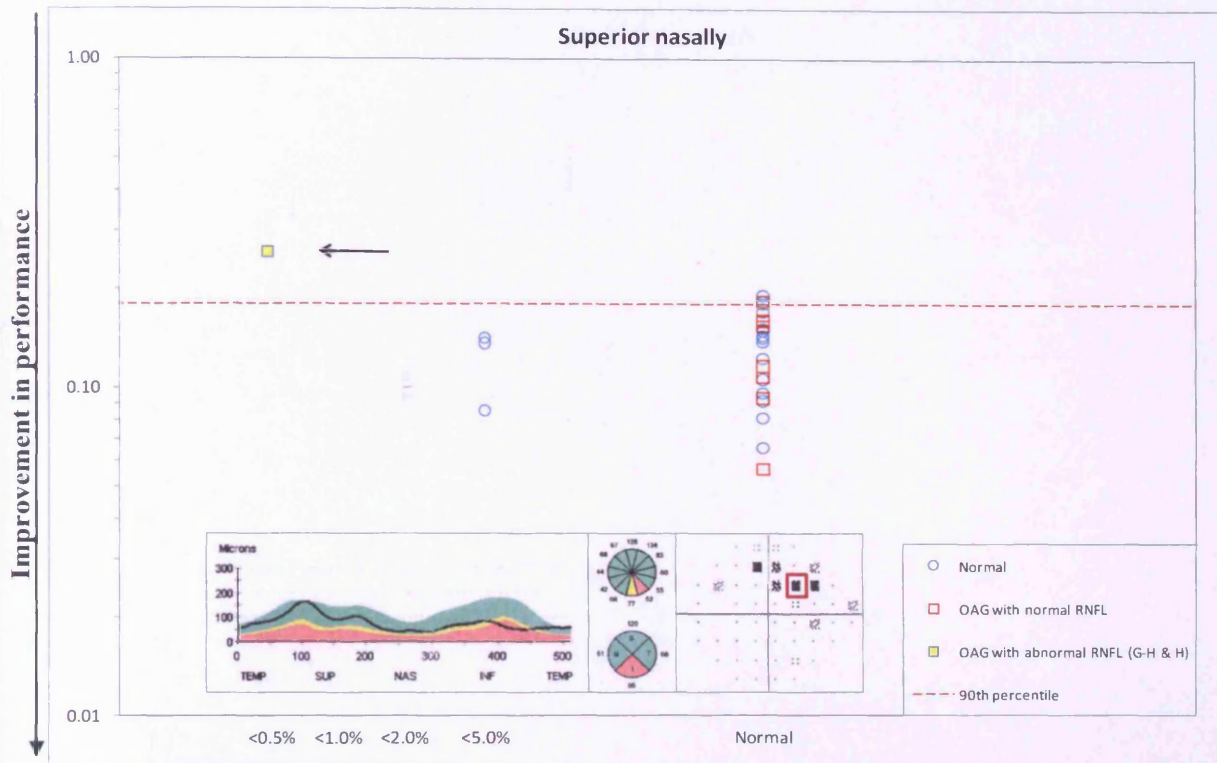


Figure 6.67 Motion detection: Michelson contrast thresholds in the presence of noise ($MC N_e$) for the stimuli in the superior nasal quadrant (ordinate) as a function of the Pattern Deviation probability level at the corresponding location (abscissa). The 90th percentile of the distribution of Michelson contrast thresholds amongst the 20 normal individuals is indicated by the red dotted line. Michelson contrast thresholds for these 20 individuals are indicated by the circles. Individuals with OAG are indicated by the squares. The percentile associated with the given RNFL thickness derived from the OCT printout at the given stimulus location is indicated by the colour (yellow <5%; red <1%) according to the topographical mapping of Garway-Heath et al (2000) (left half of the circle/ square indicated as G-H) or Harwerth et al (2007) (right half of the circle/ square indicated as H). The RNFL Thickness Chart (left), the Sector Averages (middle [top]), the Quadrant averages (Middle [bottom]) and the Pattern Deviation probability map (right) are given in the bottom panel for the individual exhibiting the contrast threshold indicated by the black arrow. The stimulus location for SAP corresponding to that for DNP is indicated by the red square.

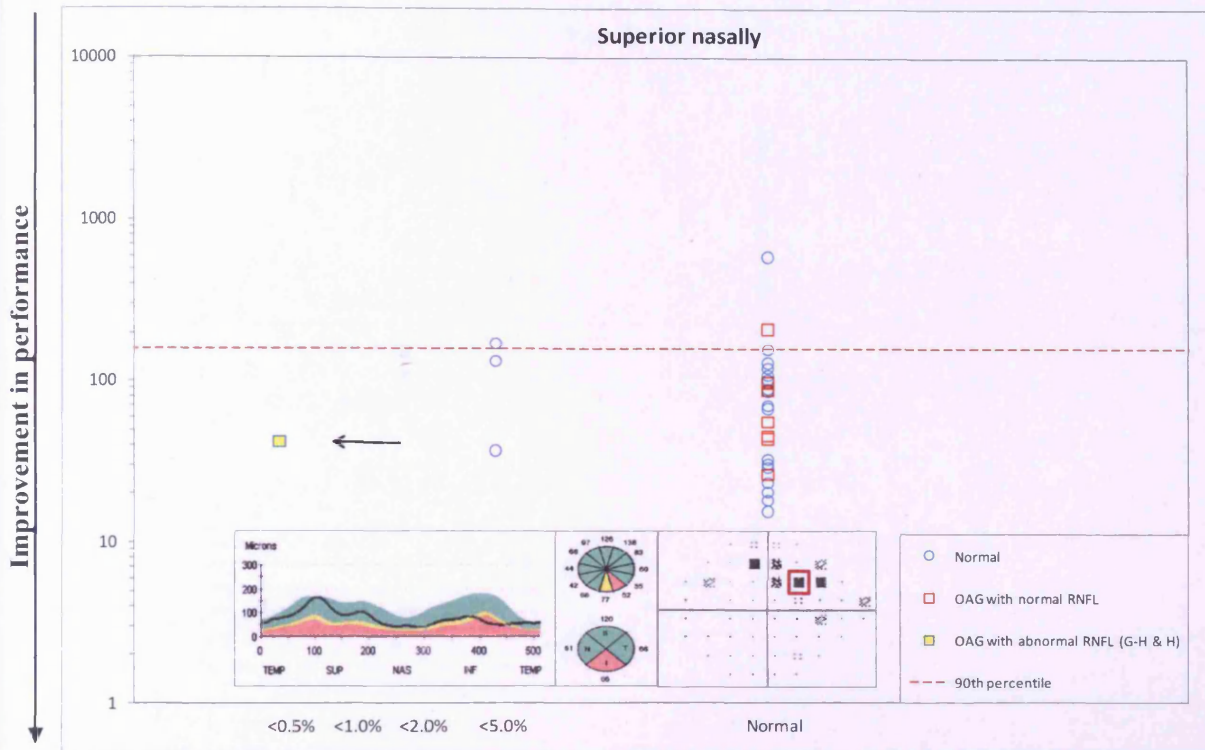


Figure 6.68 Motion detection: equivalent noise (N_{eq}) for the stimuli in the superior nasal quadrant (ordinate) as a function of the Pattern Deviation probability level at the corresponding location (abscissa). The 90th percentile of the distribution of equivalent noise amongst the 20 normal individuals is indicated by the red dotted line. Equivalent noise for these 20 individuals is indicated by the circles. Individuals with OAG are indicated by the squares. The percentile associated with the given RNFL thickness derived from the OCT printout at the given stimulus location is indicated by the colour (yellow <5%; red <1%) according to the topographical mapping of Garway-Heath et al (2000) (left half of the circle/ square indicated as G-H) or Harwerth et al (2007) (right half of the circle/ square indicated as H). The RNFL Thickness Chart (left), the Sector Averages (middle [top]), the Quadrant averages (Middle [bottom]) and the Pattern Deviation probability map (right) are given in the bottom panel for the individual exhibiting the contrast threshold indicated by the black arrow. The stimulus location for SAP corresponding to that for DNP is indicated by the red square.

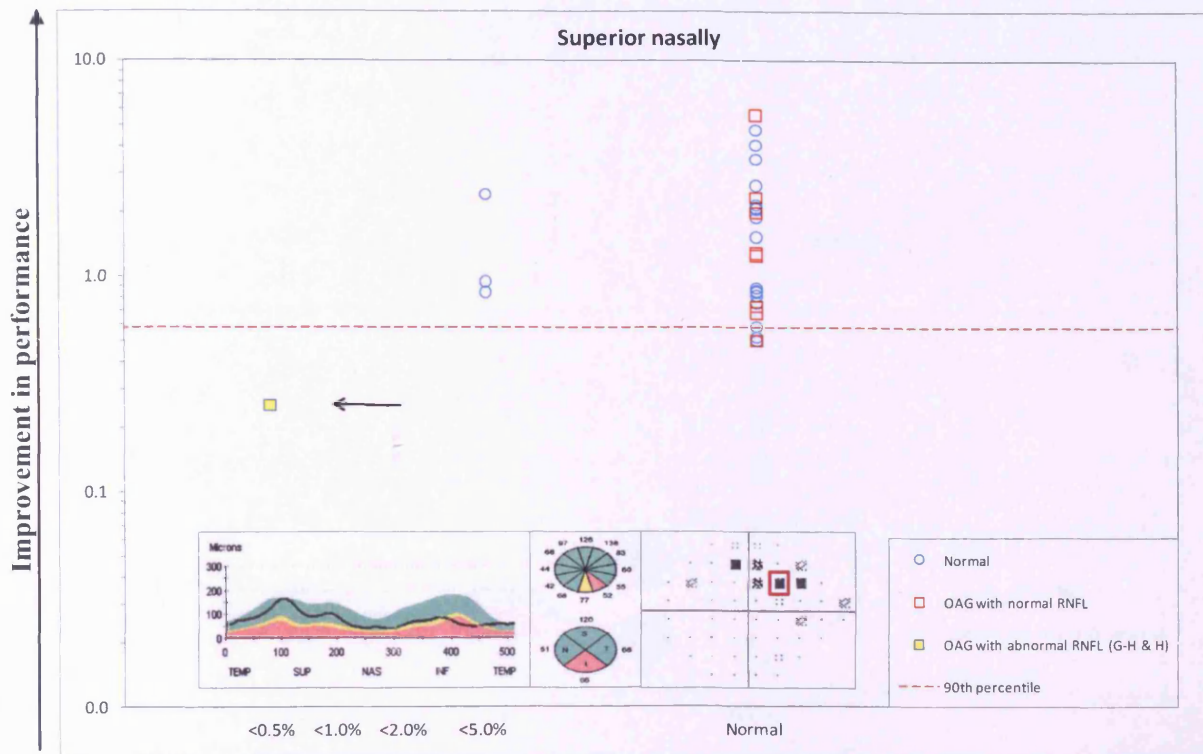


Figure 6.69 Motion detection: sampling efficiency (SE) for the stimuli in the superior nasal quadrant (ordinate) as a function of the Pattern Deviation probability level at the corresponding location (abscissa). The 90th percentile of the distribution of sampling efficiency amongst the 20 normal individuals is indicated by the red dotted line. Sampling efficiency for these 20 individuals is indicated by the circles. Individuals with OAG are indicated by the squares. The percentile associated with the given RNFL thickness derived from the OCT printout at the given stimulus location is indicated by the colour (yellow <5%; red <1%) according to the topographical mapping of Garway-Heath et al (2000) (left half of the circle/ square indicated as G-H) or Harwerth et al (2007) (right half of the circle/ square indicated as H). The RNFL Thickness Chart (left), the Sector Averages (middle [top]), the Quadrant averages (Middle [bottom]) and the Pattern Deviation probability map (right) are given in the bottom panel for the individual exhibiting the contrast threshold indicated by the black arrow. The stimulus location for SAP corresponding to that for DNP is indicated by the red square.

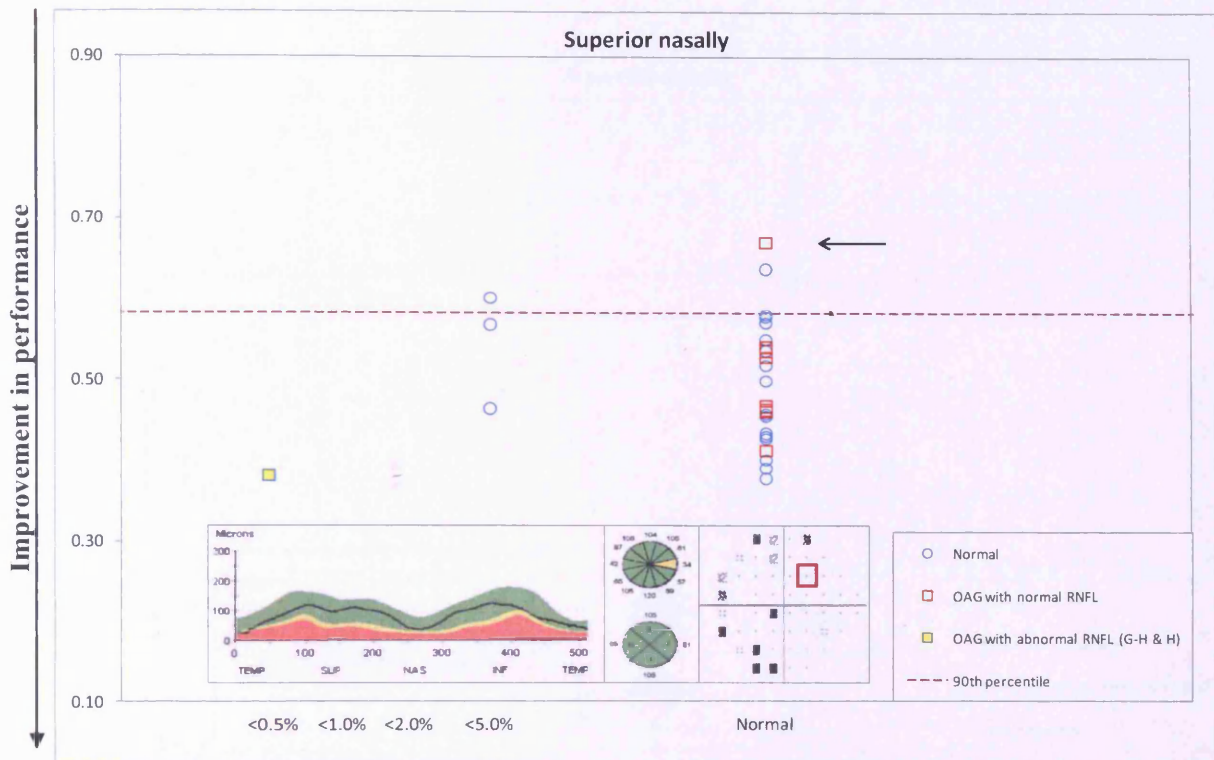


Figure 6.70 Motion detection: Log_{10} Ratio for the stimuli in the superior nasal quadrant (ordinate) as a function of the Pattern Deviation probability level at the corresponding location (abscissa). The 90th percentile of the distribution of the Log_{10} Ratio amongst the 20 normal individuals is indicated by the red dotted line. Log_{10} Ratio for these 20 individuals is indicated by the circles. Individuals with OAG are indicated by the squares. The percentile associated with the given RNFL thickness derived from the OCT printout at the given stimulus location is indicated by the colour (yellow <5%; red <1%) according to the topographical mapping of Garway-Heath et al (2000) (left half of the circle/ square indicated as G-H) or Harwerth et al (2007) (right half of the circle/ square indicated as H). The RNFL Thickness Chart (left), the Sector Averages (middle [top]), the Quadrant averages (Middle [bottom]) and the Pattern Deviation probability map (right) are given in the bottom panel for the individual exhibiting the contrast threshold indicated by the black arrow. The stimulus location for SAP corresponding to that for DNP is indicated by the red square.

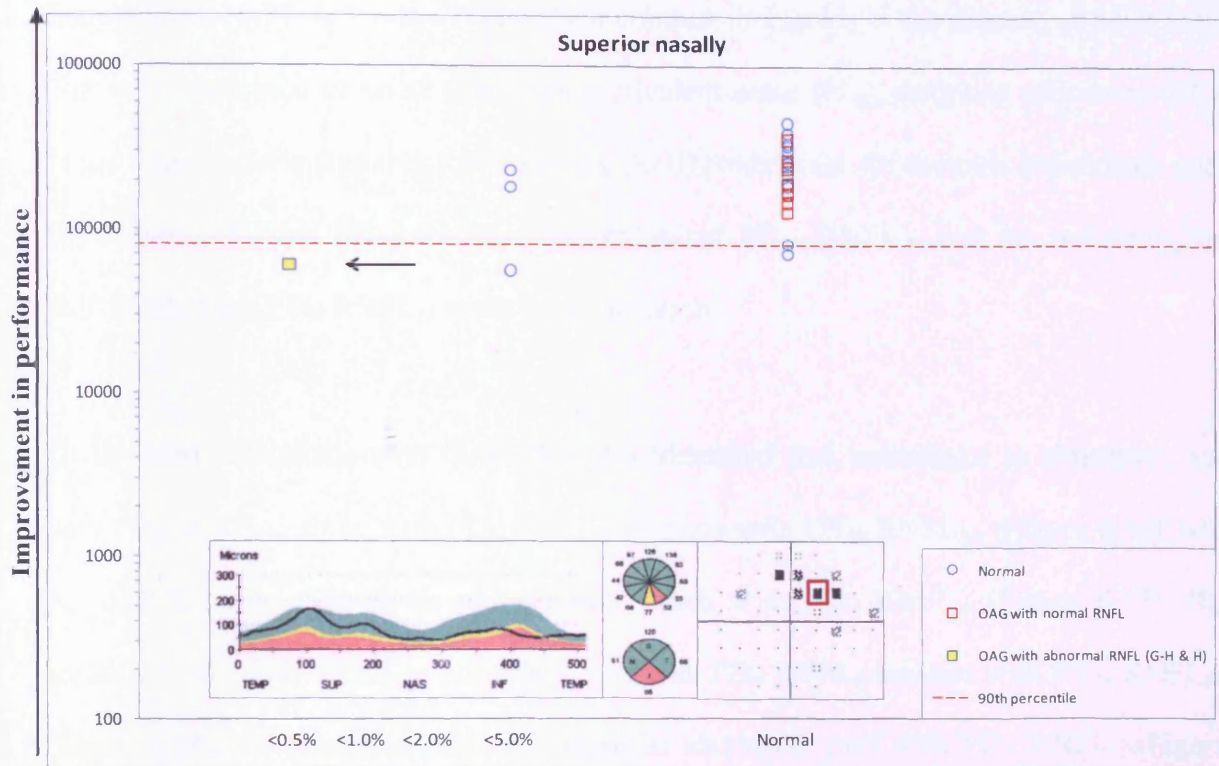


Figure 6.71 Motion detection: Signal detection index (SDI) for the stimuli in the superior nasal quadrant (ordinate) as a function of the Pattern Deviation probability level at the corresponding location (abscissa). The 90th percentile of the distribution of the Signal detection index amongst the 20 normal individuals is indicated by the red dotted line. Signal detection index for these 20 individuals is indicated by the circles. Individuals with OAG are indicated by the squares. The percentile associated with the given RNFL thickness derived from the OCT printout at the given stimulus location is indicated by the colour (yellow <5%; red <1%) according to the topographical mapping of Garway-Heath et al (2000) (left half of the circle/ square indicated as G-H) or Harwerth et al (2007) (right half of the circle/ square indicated as H). The RNFL Thickness Chart (left), the Sector Averages (middle [top]), the Quadrant averages (Middle [bottom]) and the Pattern Deviation probability map (right) are given in the bottom panel for the individual exhibiting the contrast threshold indicated by the black arrow. The stimulus location for SAP corresponding to that for DNP is indicated by the red square.

6.10.3 Distribution of DNP measures for the detection task at the inferior nasal quadrant for individuals with OAG and for normal individuals

The 90th percentile of the distribution for the twenty normal individuals as a function of the Pattern Deviation probability level at the corresponding location (abscissa) is given in Figures 6.72 – 6.77, in terms of Michelson contrast thresholds in the absence of noise ($MC N_0$), in the presence of noise ($MC N_0$), equivalent noise (N_{eq}), sampling efficiency (SE), \log_{10} Ratio and the signal detection index (SDI) (ordinates). Of the nine individuals with OAG, two exhibited $PD_{Ab} RNFL_N$, one exhibited $PD_{Ab} RNFL_{Ab}$ and the remaining six individuals were $PD_N RNFL_N$ at the given location.

Of the nine individuals with OAG, $MC N_0$ identified five individuals as abnormal: one with $PD_{Ab} RNFL_N$, three with $PD_N RNFL_N$ and one with $PD_{Ab} RNFL_{Ab}$ (Figure 6.72). $MC N_e$ identified two individuals as abnormal: each with $PD_N RNFL_N$ (Figure 6.73). N_{eq} identified three individuals as abnormal: two with $PD_N RNFL_N$ and one with $PD_{Ab} RNFL_{Ab}$ (Figure 6.74). SE identified two individuals as abnormal: each with $PD_N RNFL_N$ (Figure 6.75). \log_{10} Ratio identified three individuals as abnormal: two with $PD_N RNFL_N$ and one with $PD_{Ab} RNFL_{Ab}$ (Figure 6.76). SDI identified five individuals as abnormal: one with $PD_{Ab} RNFL_N$, three with $PD_N RNFL_N$ and one with $PD_{Ab} RNFL_{Ab}$ (Figure 6.77). A summary of findings is shown in Table 6.23.

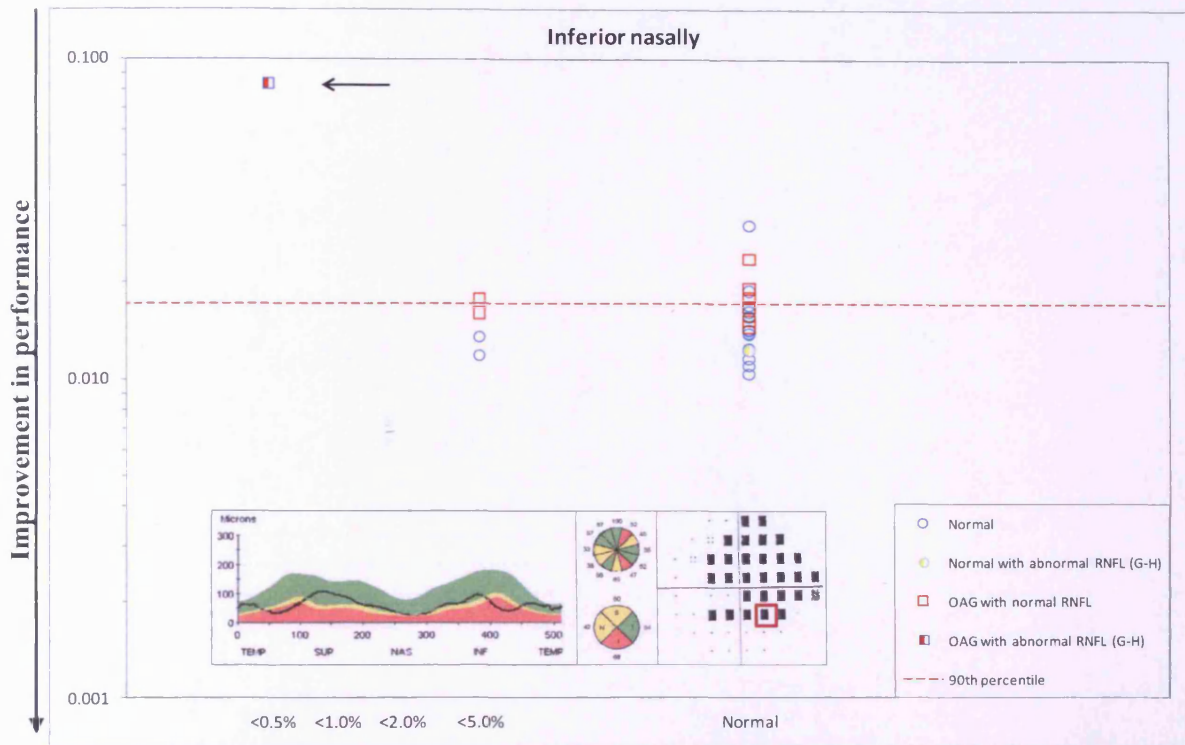


Figure 6.72 Motion detection: Michelson contrast thresholds in the absence of noise ($MC N_0$) for the stimuli in the inferior nasal quadrant (ordinate) as a function of the Pattern Deviation probability level at the corresponding location (abscissa). The 90th percentile of the distribution of Michelson contrast thresholds amongst the 20 normal individuals is indicated by the red dotted line. Michelson contrast thresholds for these 20 individuals are indicated by the circles. Individuals with OAG are indicated by the squares. The percentile associated with the given RNFL thickness derived from the OCT printout at the given stimulus location is indicated by the colour (yellow <5%; red <1%) according to the topographical mapping of Garway-Heath et al (2000) (left half of the circle/ square indicated as G-H) or Harwerth et al (2007) (right half of the circle/ square indicated as H). The RNFL Thickness Chart (left), the Sector Averages (middle [top]), the Quadrant averages (Middle [bottom]) and the Pattern Deviation probability map (right) are given in the bottom panel for the individual exhibiting the contrast threshold indicated by the black arrow. The stimulus location for SAP corresponding to that for DNP is indicated by the red square.

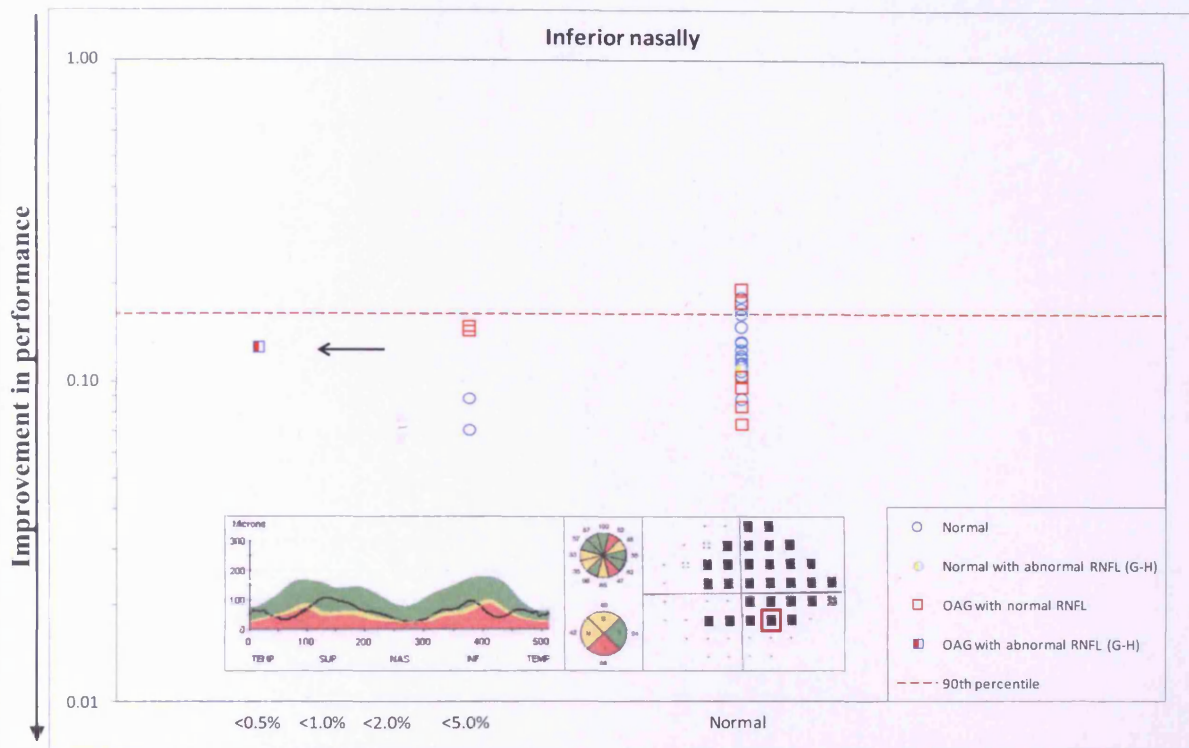


Figure 6.73 Motion detection: Michelson contrast thresholds in the presence of noise ($MC N_e$) for the stimuli in the inferior nasal quadrant (ordinate) as a function of the Pattern Deviation probability level at the corresponding location (abscissa). The 90th percentile of the distribution of Michelson contrast thresholds amongst the 20 normal individuals is indicated by the red dotted line. Michelson contrast thresholds for these 20 individuals are indicated by the circles. Individuals with OAG are indicated by the squares. The percentile associated with the given RNFL thickness derived from the OCT printout at the given stimulus location is indicated by the colour (yellow <5%; red <1%) according to the topographical mapping of Garway-Heath et al (2000) (left half of the circle/ square indicated as G-H) or Harwerth et al (2007) (right half of the circle/ square indicated as H). The RNFL Thickness Chart (left), the Sector Averages (middle [top]), the Quadrant averages (Middle [bottom]) and the Pattern Deviation probability map (right) are given in the bottom panel for the individual exhibiting the contrast threshold indicated by the black arrow. The stimulus location for SAP corresponding to that for DNP is indicated by the red square.

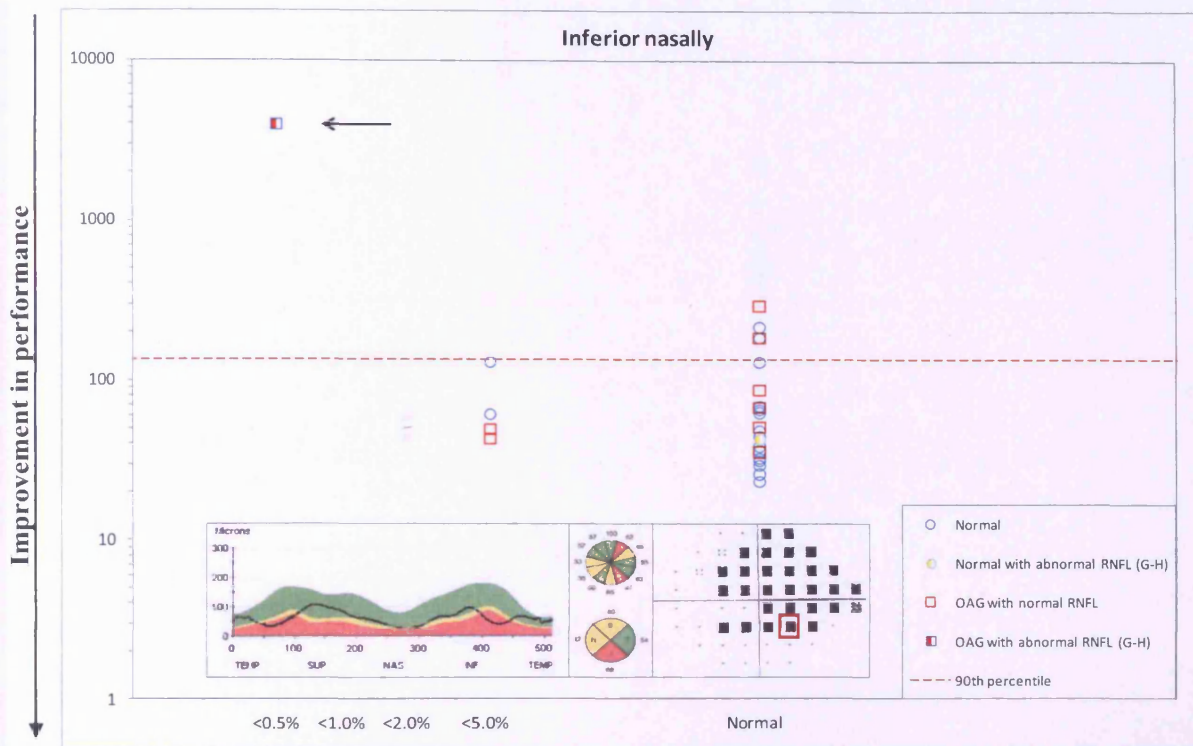


Figure 6.74 Motion detection: equivalent noise (N_{eq}) for the stimuli in the inferior nasal quadrant (ordinate) as a function of the Pattern Deviation probability level at the corresponding location (abscissa). The 90th percentile of the distribution of equivalent noise amongst the 20 normal individuals is indicated by the red dotted line. Equivalent noise for these 20 individuals is indicated by the circles. Individuals with OAG are indicated by the squares. The percentile associated with the given RNFL thickness derived from the OCT printout at the given stimulus location is indicated by the colour (yellow <5%; red <1%) according to the topographical mapping of Garway-Heath et al (2000) (left half of the circle/ square indicated as G-H) or Harwerth et al (2007) (right half of the circle/ square indicated as H). The RNFL Thickness Chart (left), the Sector Averages (middle [top]), the Quadrant averages (Middle [bottom]) and the Pattern Deviation probability map (right) are given in the bottom panel for the individual exhibiting the contrast threshold indicated by the black arrow. The stimulus location for SAP corresponding to that for DNP is indicated by the red square.

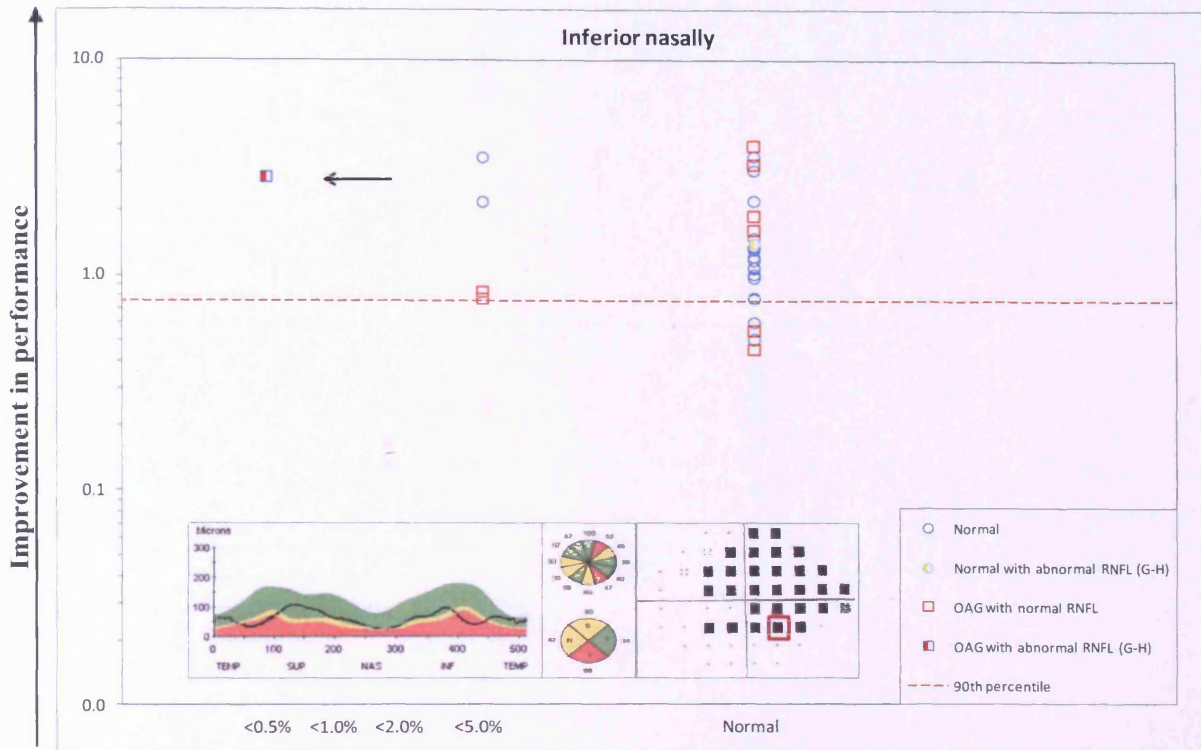


Figure 6.75 Motion detection: sampling efficiency (SE) for the stimuli in the inferior nasal quadrant (ordinate) as a function of the Pattern Deviation probability level at the corresponding location (abscissa). The 90th percentile of the distribution of sampling efficiency amongst the 20 normal individuals is indicated by the red dotted line. Sampling efficiency for these 20 individuals is indicated by the circles. Individuals with OAG are indicated by the squares. The percentile associated with the given RNFL thickness derived from the OCT printout at the given stimulus location is indicated by the colour (yellow <5%; red <1%) according to the topographical mapping of Garway-Heath et al (2000) (left half of the circle/ square indicated as G-H) or Harwerth et al (2007) (right half of the circle/ square indicated as H). The RNFL Thickness Chart (left), the Sector Averages (middle [top]), the Quadrant averages (Middle [bottom]) and the Pattern Deviation probability map (right) are given in the bottom panel for the individual exhibiting the contrast threshold indicated by the black arrow. The stimulus location for SAP corresponding to that for DNP is indicated by the red square.

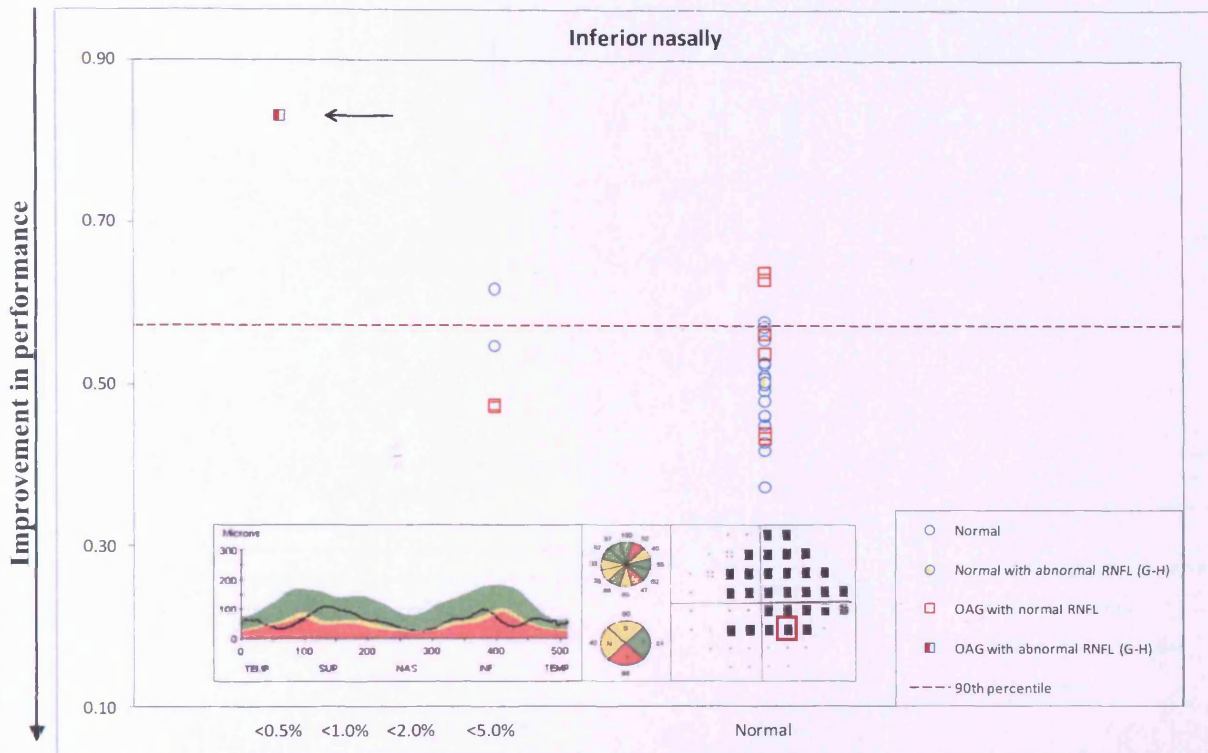


Figure 6.76 Motion detection: Log_{10} Ratio for the stimuli in the inferior nasal quadrant (ordinate) as a function of the Pattern Deviation probability level at the corresponding location (abscissa). The 90th percentile of the distribution of the Log_{10} Ratio amongst the 20 normal individuals is indicated by the red dotted line. Log_{10} Ratio for these 20 individuals is indicated by the circles. Individuals with OAG are indicated by the squares. The percentile associated with the given RNFL thickness derived from the OCT printout at the given stimulus location is indicated by the colour (yellow <math><5\%</math>; red <math><1\%</math>) according to the topographical mapping of Garway-Heath et al (2000) (left half of the circle/ square indicated as G-H) or Harwerth et al (2007) (right half of the circle/ square indicated as H). The RNFL Thickness Chart (left), the Sector Averages (middle [top]), the Quadrant averages (Middle [bottom]) and the Pattern Deviation probability map (right) are given in the bottom panel for the individual exhibiting the contrast threshold indicated by the black arrow. The stimulus location for SAP corresponding to that for DNP is indicated by the red square.

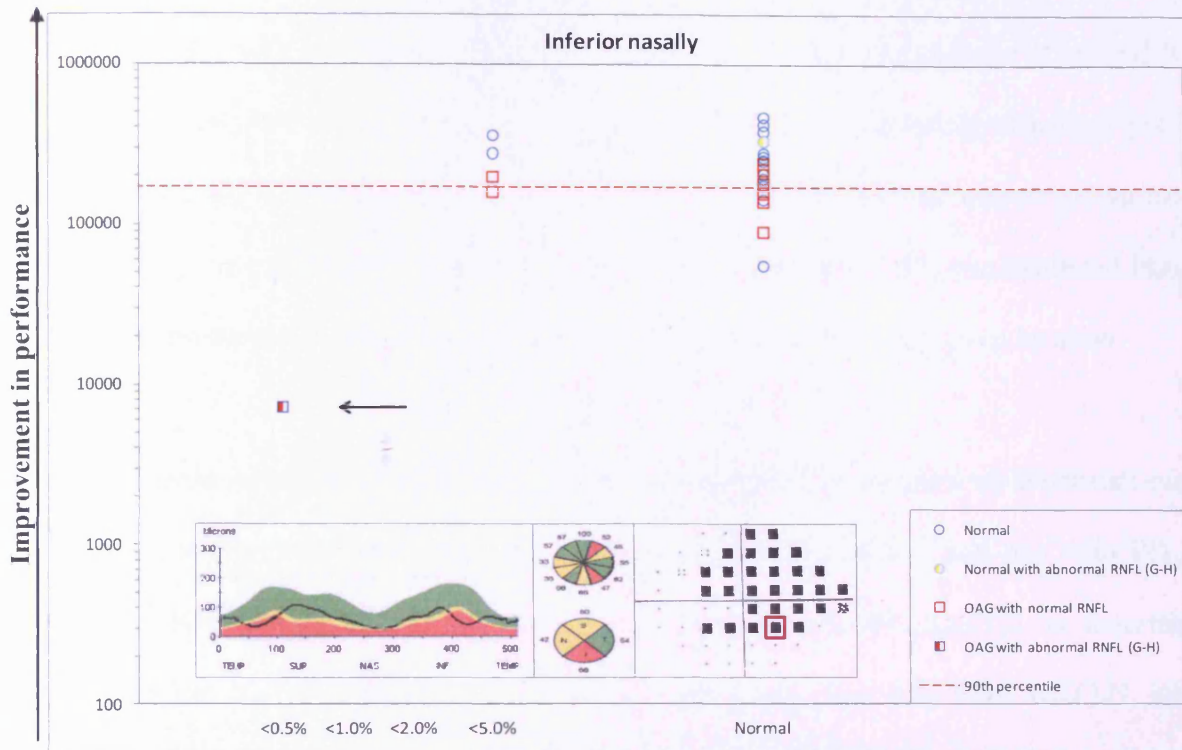


Figure 6.77 Motion detection: Signal detection index (SDI) for the stimuli in the inferior nasal quadrant (ordinate) as a function of the Pattern Deviation probability level at the corresponding location (abscissa). The 90th percentile of the distribution of the Signal detection index amongst the 20 normal individuals is indicated by the red dotted line. Signal detection index for these 20 individuals is indicated by the circles. Individuals with OAG are indicated by the squares. The percentile associated with the given RNFL thickness derived from the OCT printout at the given stimulus location is indicated by the colour (yellow <5%; red <1%) according to the topographical mapping of Garway-Heath et al (2000) (left half of the circle/ square indicated as G-H) or Harwerth et al (2007) (right half of the circle/ square indicated as H). The RNFL Thickness Chart (left), the Sector Averages (middle [top]), the Quadrant averages (Middle [bottom]) and the Pattern Deviation probability map (right) are given in the bottom panel for the individual exhibiting the contrast threshold indicated by the black arrow. The stimulus location for SAP corresponding to that for DNP is indicated by the red square.

6.10.4 Distribution of DNP measures for the detection task at the inferior temporal quadrant for individuals with OAG and for normal individuals

The 90th percentile of the distribution for the twenty normal individuals as a function of the Pattern Deviation probability level at the corresponding location (abscissa) is given in Figures 6.78 – 6.83, in terms of Michelson contrast thresholds in the absence of noise ($MC N_0$), in the presence of noise ($MC N_0$), equivalent noise (N_{eq}), sampling efficiency (SE), \log_{10} Ratio and the signal detection index (SDI) (ordinates). Of the eleven individuals with OAG, two exhibited $PD_{Ab} RNFL_N$, one exhibited $PD_N RNFL_{Ab}$, one exhibited $PD_{Ab} RNFL_{Ab}$ and the remaining seven individuals were $PD_N RNFL_N$ at the given location.

Of the eleven individuals with OAG, $MC N_0$ identified six individuals as abnormal: two with $PD_N RNFL_N$, two with $PD_{Ab} RNFL_N$, one with $PD_N RNFL_{Ab}$ and one with $PD_{Ab} RNFL_{Ab}$ (Figure 6.78). $MC N_e$ identified one individual with $PD_N RNFL_{Ab}$ as abnormal (Figure 6.79). N_{eq} identified five individuals as abnormal: two with $PD_{Ab} RNFL_N$, one with $PD_N RNFL_{Ab}$, one with $PD_N RNFL_N$ and one with $PD_{Ab} RNFL_{Ab}$ (Figure 6.80). SE identified three individuals as abnormal: each with $PD_N RNFL_N$ (Figure 6.81). \log_{10} Ratio identified three individuals as abnormal: one with $PD_{Ab} RNFL_N$, one with $PD_N RNFL_N$ and one with $PD_{Ab} RNFL_{Ab}$ (Figure 6.82). SDI identified six individuals as abnormal: three with $PD_N RNFL_N$, two with $PD_{Ab} RNFL_N$ and one with $PD_{Ab} RNFL_{Ab}$ (Figure 6.83). A summary of findings is shown in Table 6.24.

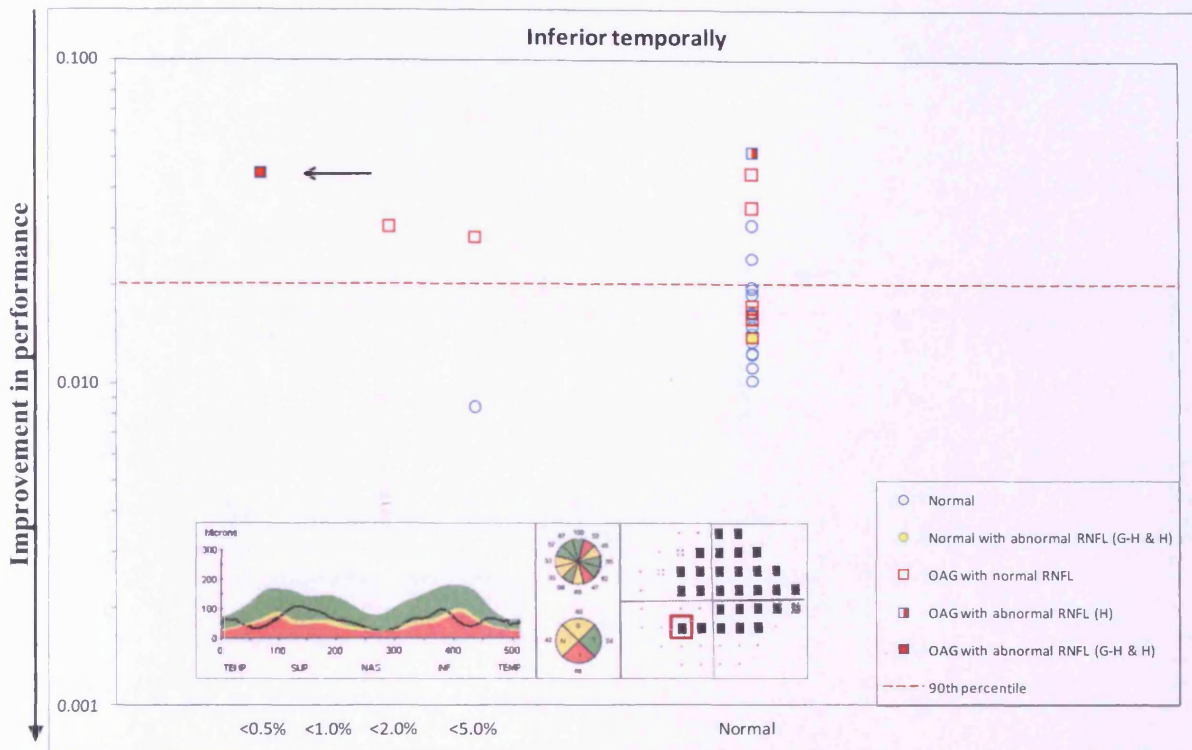


Figure 6.78 Motion detection: Michelson contrast thresholds in the absence of noise ($MC N_0$) for the stimuli in the inferior temporal quadrant (ordinate) as a function of the Pattern Deviation probability level at the corresponding location (abscissa). The 90th percentile of the distribution of Michelson contrast thresholds amongst the 20 normal individuals is indicated by the red dotted line. Michelson contrast thresholds for these 20 individuals are indicated by the circles. Individuals with OAG are indicated by the squares. The percentile associated with the given RNFL thickness derived from the OCT printout at the given stimulus location is indicated by the colour (yellow <5%; red <1%) according to the topographical mapping of Garway-Heath et al (2000) (left half of the circle/ square indicated as G-H) or Harwerth et al (2007) (right half of the circle/ square indicated as H). The RNFL Thickness Chart (left), the Sector Averages (middle [top]), the Quadrant averages (Middle [bottom]) and the Pattern Deviation probability map (right) are given in the bottom panel for the individual exhibiting the contrast threshold indicated by the black arrow. The stimulus location for SAP corresponding to that for DNP is indicated by the red square.

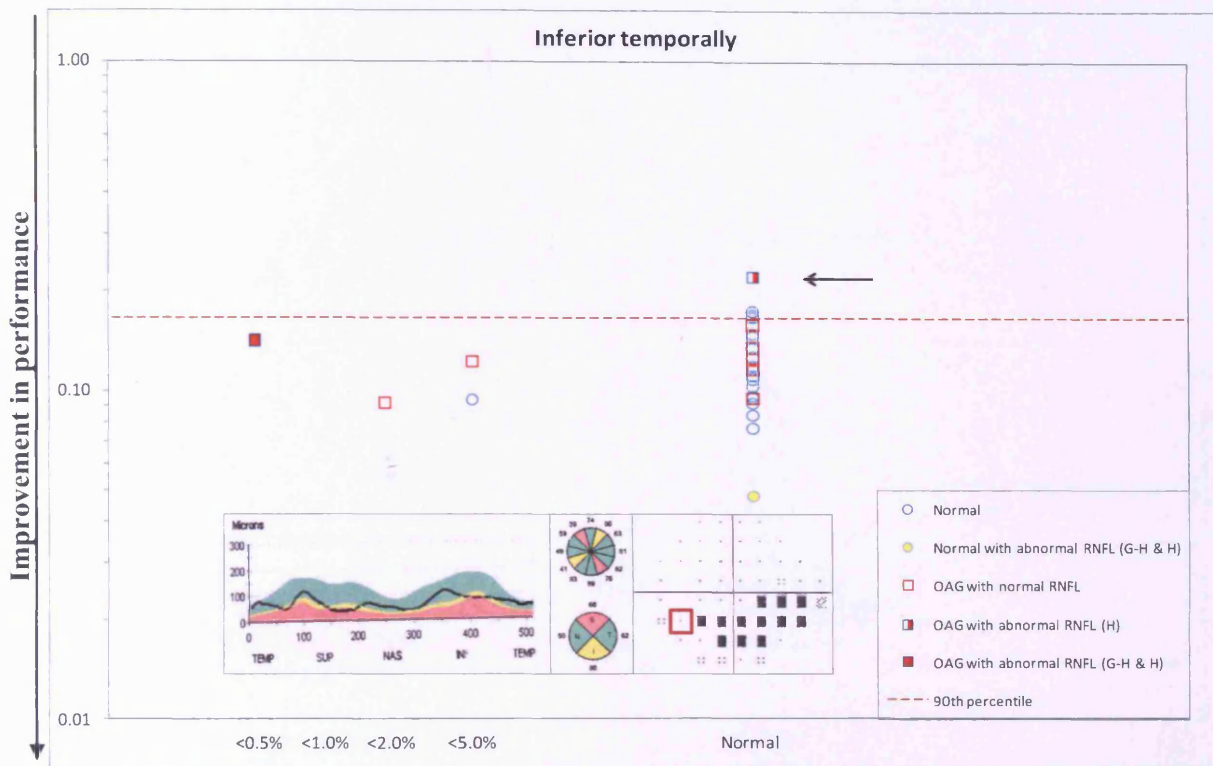


Figure 6.79 Motion detection: Michelson contrast thresholds in the presence of noise ($MC N_e$) for the stimuli in the inferior temporal quadrant (ordinate) as a function of the Pattern Deviation probability level at the corresponding location (abscissa). The 90th percentile of the distribution of Michelson contrast thresholds amongst the 20 normal individuals is indicated by the red dotted line. Michelson contrast thresholds for these 20 individuals are indicated by the circles. Individuals with OAG are indicated by the squares. The percentile associated with the given RNFL thickness derived from the OCT printout at the given stimulus location is indicated by the colour (yellow <5%; red <1%) according to the topographical mapping of Garway-Heath et al (2000) (left half of the circle/ square indicated as G-H) or Harwerth et al (2007) (right half of the circle/ square indicated as H). The RNFL Thickness Chart (left), the Sector Averages (middle [top]), the Quadrant averages (Middle [bottom]) and the Pattern Deviation probability map (right) are given in the bottom panel for the individual exhibiting the contrast threshold indicated by the black arrow. The stimulus location for SAP corresponding to that for DNP is indicated by the red square.

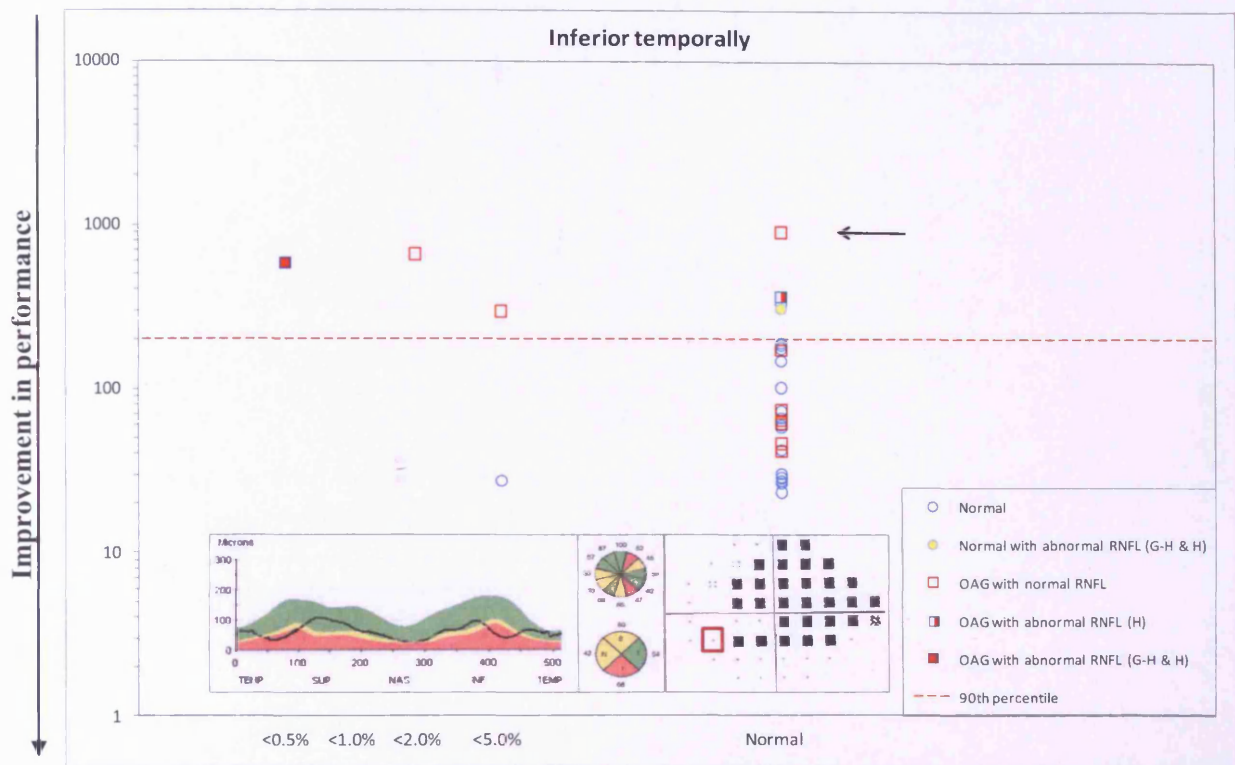


Figure 6.80 Motion detection: equivalent noise (N_{eq}) for the stimuli in the inferior temporal quadrant (ordinate) as a function of the Pattern Deviation probability level at the corresponding location (abscissa). The 90th percentile of the distribution of equivalent noise amongst the 20 normal individuals is indicated by the red dotted line. Equivalent noise for these 20 individuals is indicated by the circles. Individuals with OAG are indicated by the squares. The percentile associated with the given RNFL thickness derived from the OCT printout at the given stimulus location is indicated by the colour (yellow <5%; red <1%) according to the topographical mapping of Garway-Heath et al (2000) (left half of the circle/ square indicated as G-H) or Harwerth et al (2007) (right half of the circle/ square indicated as H). The RNFL Thickness Chart (left), the Sector Averages (middle [top]), the Quadrant averages (Middle [bottom]) and the Pattern Deviation probability map (right) are given in the bottom panel for the individual exhibiting the contrast threshold indicated by the black arrow. The stimulus location for SAP corresponding to that for DNP is indicated by the red square.

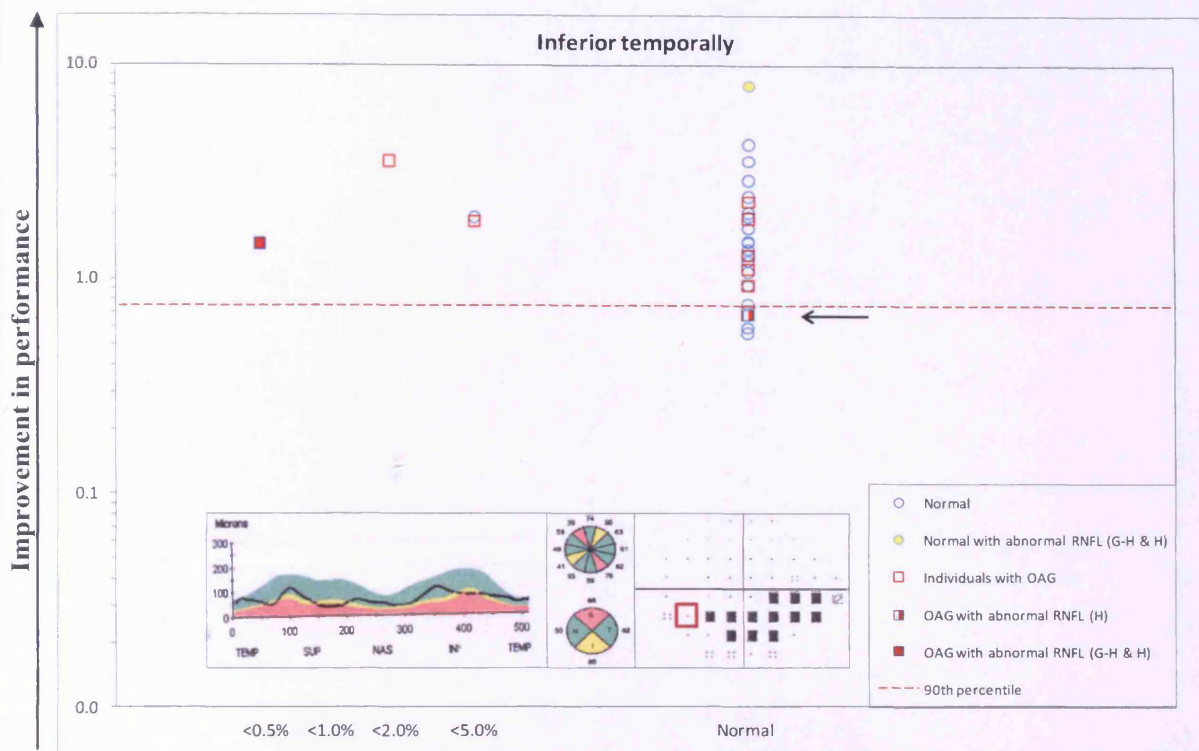


Figure 6.81 Motion detection: sampling efficiency (SE) for the stimuli in the inferior temporal quadrant (ordinate) as a function of the Pattern Deviation probability level at the corresponding location (abscissa). The 90th percentile of the distribution of sampling efficiency amongst the 20 normal individuals is indicated by the red dotted line. Sampling efficiency for these 20 individuals is indicated by the circles. Individuals with OAG are indicated by the squares. The percentile associated with the given RNFL thickness derived from the OCT printout at the given stimulus location is indicated by the colour (yellow <5%; red <1%) according to the topographical mapping of Garway-Heath et al (2000) (left half of the circle/ square indicated as G-H) or Harwerth et al (2007) (right half of the circle/ square indicated as H). The RNFL Thickness Chart (left), the Sector Averages (middle [top]), the Quadrant averages (Middle [bottom]) and the Pattern Deviation probability map (right) are given in the bottom panel for the individual exhibiting the contrast threshold indicated by the black arrow. The stimulus location for SAP corresponding to that for DNP is indicated by the red square.

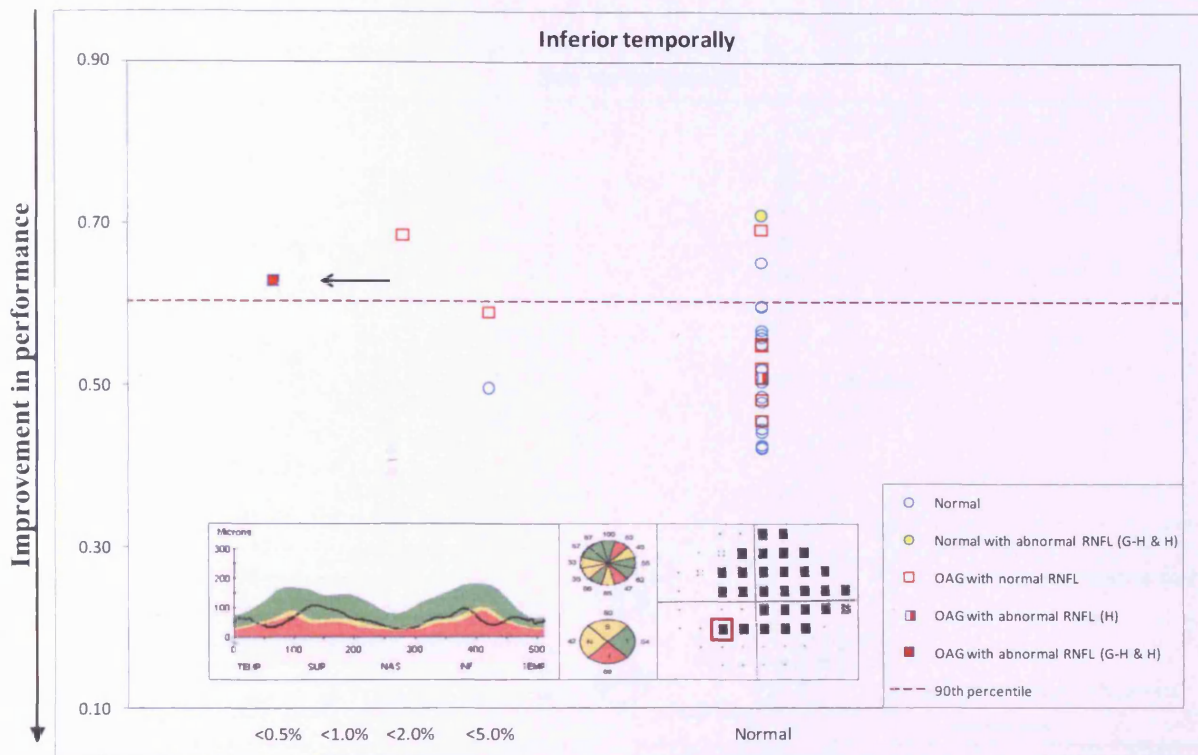


Figure 6.82 Motion detection: Log_{10} Ratio for the stimuli in the inferior temporal quadrant (ordinate) as a function of the Pattern Deviation probability level at the corresponding location (abscissa). The 90th percentile of the distribution of the Log_{10} Ratio amongst the 20 normal individuals is indicated by the red dotted line. Log_{10} Ratio for these 20 individuals is indicated by the circles. Individuals with OAG are indicated by the squares. The percentile associated with the given RNFL thickness derived from the OCT printout at the given stimulus location is indicated by the colour (yellow <5%; red <1%) according to the topographical mapping of Garway-Heath et al (2000) (left half of the circle/ square indicated as G-H) or Harwerth et al (2007) (right half of the circle/ square indicated as H). The RNFL Thickness Chart (left), the Sector Averages (middle [top]), the Quadrant averages (Middle [bottom]) and the Pattern Deviation probability map (right) are given in the bottom panel for the individual exhibiting the contrast threshold indicated by the black arrow. The stimulus location for SAP corresponding to that for DNP is indicated by the red square.

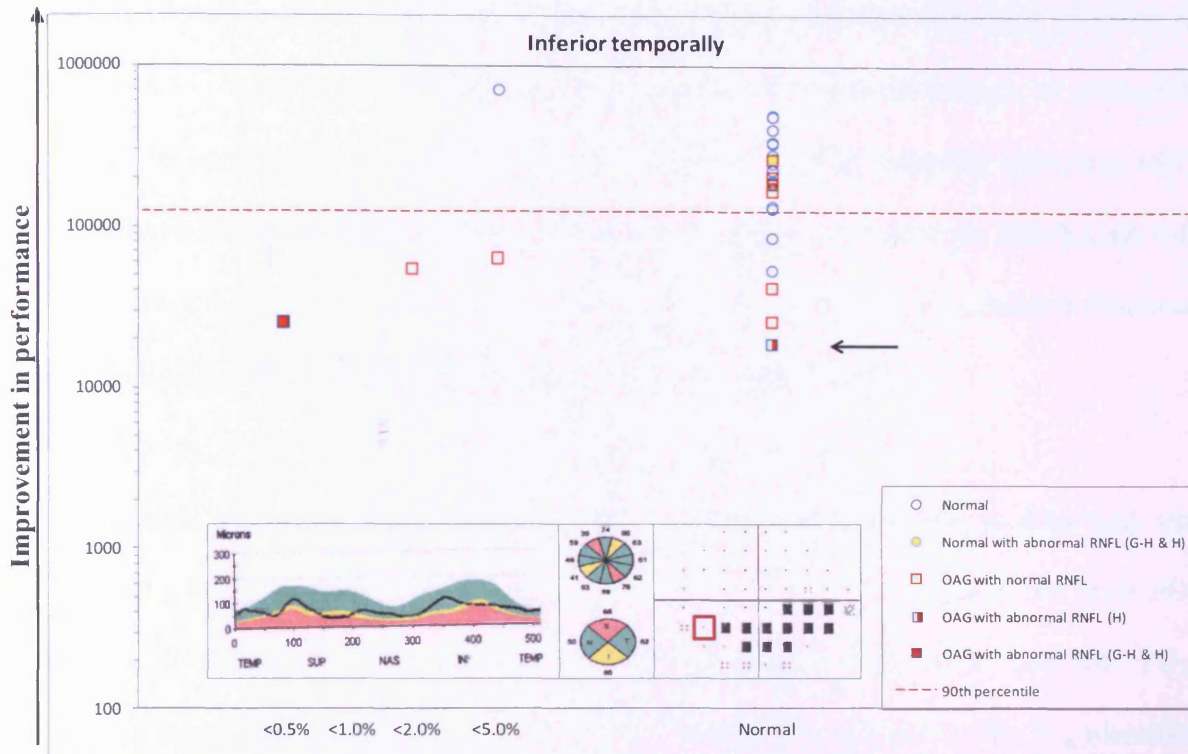


Figure 6.83 Motion detection: Signal detection index (SDI) for the stimuli in the inferior temporal quadrant (ordinate) as a function of the Pattern Deviation probability level at the corresponding location (abscissa). The 90th percentile of the distribution of the Signal detection index amongst the 20 normal individuals is indicated by the red dotted line. Signal detection index for these 20 individuals is indicated by the circles. Individuals with OAG are indicated by the squares. The percentile associated with the given RNFL thickness derived from the OCT printout at the given stimulus location is indicated by the colour (yellow <5%; red <1%) according to the topographical mapping of Garway-Heath et al (2000) (left half of the circle/ square indicated as G-H) or Harwerth et al (2007) (right half of the circle/ square indicated as H). The RNFL Thickness Chart (left), the Sector Averages (middle [top]), the Quadrant averages (Middle [bottom]) and the Pattern Deviation probability map (right) are given in the bottom panel for the individual exhibiting the contrast threshold indicated by the black arrow. The stimulus location for SAP corresponding to that for DNP is indicated by the red square.

6.10.5 Distribution of DNP measures for the discrimination task at the superior temporal quadrant for individuals with OAG and for normal individuals

The 90th percentile of the distribution for the twenty normal individuals as a function of the Pattern Deviation probability level at the corresponding location (abscissa) is given in Figures 6.84 – 6.89, in terms of Michelson contrast thresholds in the absence of noise ($MC N_0$), in the presence of noise ($MC N_e$), equivalent noise (N_{eq}), sampling efficiency (SE), \log_{10} Ratio and the signal detection index (SDI) (ordinates). Of the eight individuals with OAG, one exhibited $PD_{Ab} RNFL_{Ab}$, four exhibited $PD_{Ab} RNFL_N$, two exhibited described as $PD_N RNFL_{Ab}$ and one exhibited $PD_N RNFL_N$ at the given location.

Of the eight individuals with OAG, $MC N_0$ identified six individuals as abnormal: one with $PD_{Ab} RNFL_{Ab}$, three with $PD_{Ab} RNFL_N$, one with $PD_N RNFL_N$ and one with $PD_N RNFL_{Ab}$ (Figure 6.84). $MC N_e$ identified three individuals as abnormal: one with $PD_{Ab} RNFL_N$, one with $PD_N RNFL_N$ and one with $PD_N RNFL_{Ab}$ (Figure 6.85). N_{eq} identified three individuals as abnormal: one with $PD_{Ab} RNFL_{Ab}$, one with $PD_{Ab} RNFL_N$ and one with $PD_N RNFL_{Ab}$ (Figure 6.86). SE identified one individual with $PD_N RNFL_N$ as abnormal (Figure 6.87). \log_{10} Ratio identified one of the individuals as abnormal (Figure 6.88). SDI identified six individuals as abnormal: one with $PD_{Ab} RNFL_{Ab}$, three with $PD_{Ab} RNFL_N$, one with $PD_N RNFL_N$ and one with $PD_N RNFL_{Ab}$ (Figure 6.89). A summary of findings is shown in Table 6.25.

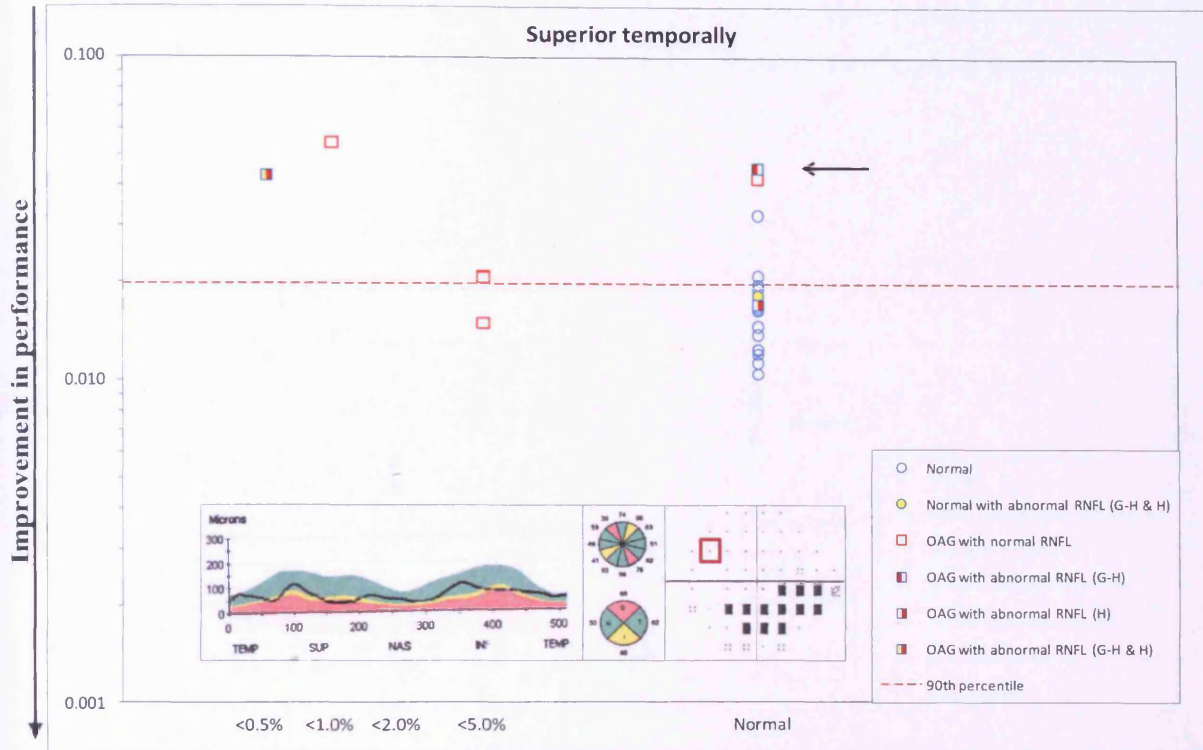


Figure 6.84 Motion discrimination: Michelson contrast thresholds in the absence of noise ($MC N_0$) for the stimuli in the superior temporal quadrant (ordinate) as a function of the Pattern Deviation probability level at the corresponding location (abscissa). The 90th percentile of the distribution of Michelson contrast thresholds amongst the 20 normal individuals is indicated by the red dotted line. Michelson contrast thresholds for these 20 individuals are indicated by the circles. Individuals with OAG are indicated by the squares. The percentile associated with the given RNFL thickness derived from the OCT printout at the given stimulus location is indicated by the colour (yellow <5%; red <1%) according to the topographical mapping of Garway-Heath et al (2000) (left half of the circle/ square indicated as G-H) or Harwerth et al (2007) (right half of the circle/ square indicated as H). The RNFL Thickness Chart (left), the Sector Averages (middle [top]), the Quadrant averages (Middle [bottom]) and the Pattern Deviation probability map (right) are given in the bottom panel for the individual exhibiting the contrast threshold indicated by the black arrow. The stimulus location for SAP corresponding to that for DNP is indicated by the red square.

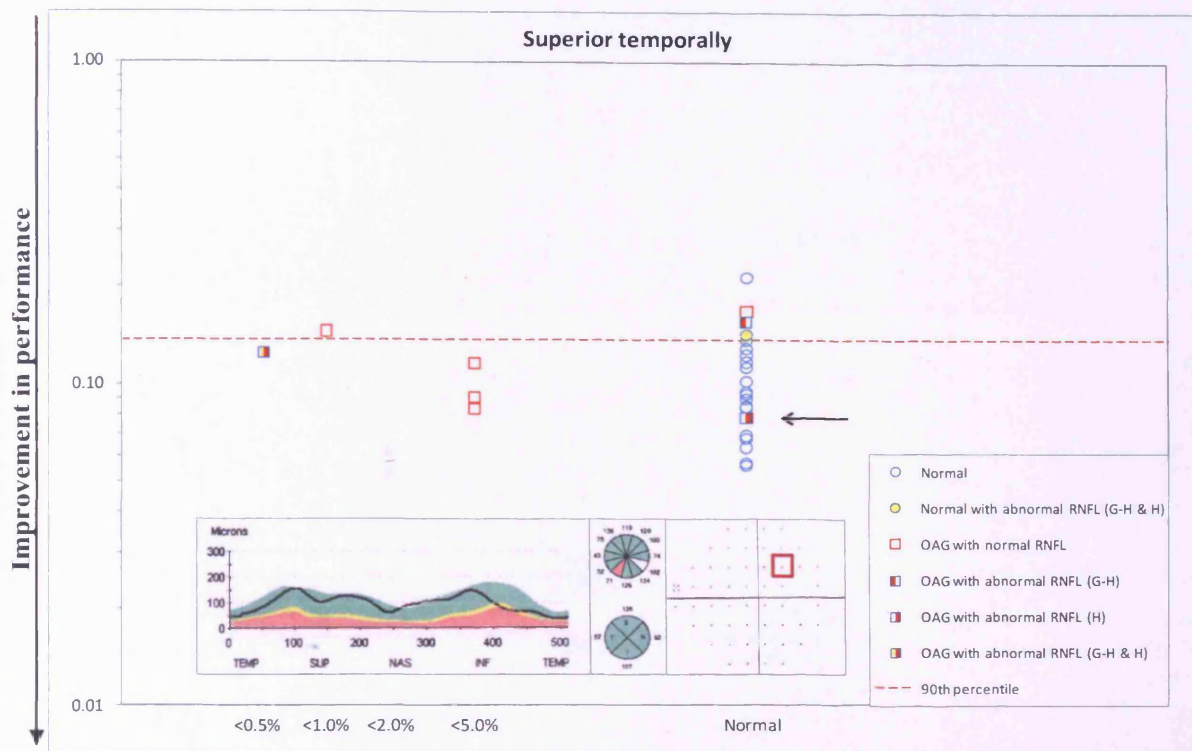


Figure 6.85 Motion discrimination: Michelson contrast thresholds in the presence of noise ($MC N_e$) for the stimuli in the superior temporal quadrant (ordinate) as a function of the Pattern Deviation probability level at the corresponding location (abscissa). The 90th percentile of the distribution of Michelson contrast thresholds amongst the 20 normal individuals is indicated by the red dotted line. Michelson contrast thresholds for these 20 individuals are indicated by the circles. Individuals with OAG are indicated by the squares. The percentile associated with the given RNFL thickness derived from the OCT printout at the given stimulus location is indicated by the colour (yellow <5%; red <1%) according to the topographical mapping of Garway-Heath et al (2000) (left half of the circle/ square indicated as G-H) or Harwerth et al (2007) (right half of the circle/ square indicated as H). The RNFL Thickness Chart (left), the Sector Averages (middle [top]), the Quadrant averages (Middle [bottom]) and the Pattern Deviation probability map (right) are given in the bottom panel for the individual exhibiting the contrast threshold indicated by the black arrow. The stimulus location for SAP corresponding to that for DNP is indicated by the red square.

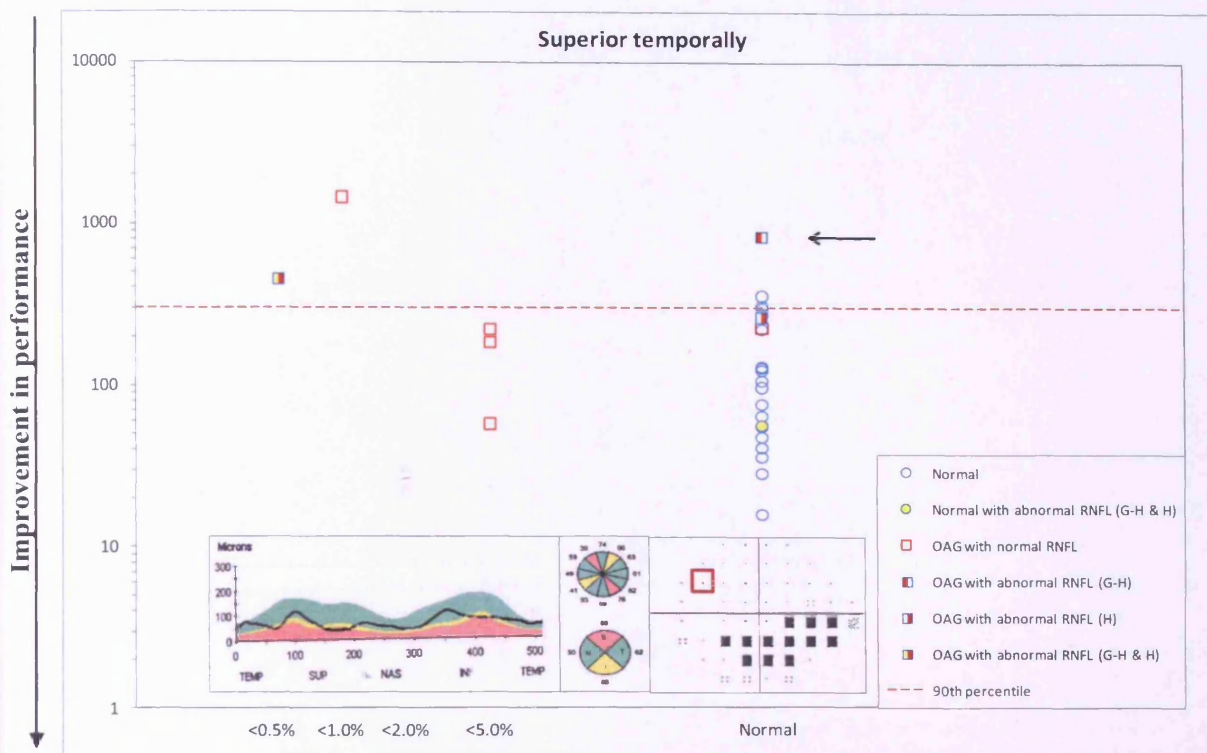


Figure 6.86 Motion discrimination: equivalent noise (N_{eq}) for the stimuli in the superior temporal quadrant (ordinate) as a function of the Pattern Deviation probability level at the corresponding location (abscissa). The 90th percentile of the distribution of equivalent noise amongst the 20 normal individuals is indicated by the red dotted line. Equivalent noise for these 20 individuals is indicated by the circles. Individuals with OAG are indicated by the squares. The percentile associated with the given RNFL thickness derived from the OCT printout at the given stimulus location is indicated by the colour (yellow <5%; red <1%) according to the topographical mapping of Garway-Heath et al (2000) (left half of the circle/ square indicated as G-H) or Harwerth et al (2007) (right half of the circle/ square indicated as H). The RNFL Thickness Chart (left), the Sector Averages (middle [top]), the Quadrant averages (Middle [bottom]) and the Pattern Deviation probability map (right) are given in the bottom panel for the individual exhibiting the contrast threshold indicated by the black arrow. The stimulus location for SAP corresponding to that for DNP is indicated by the red square.

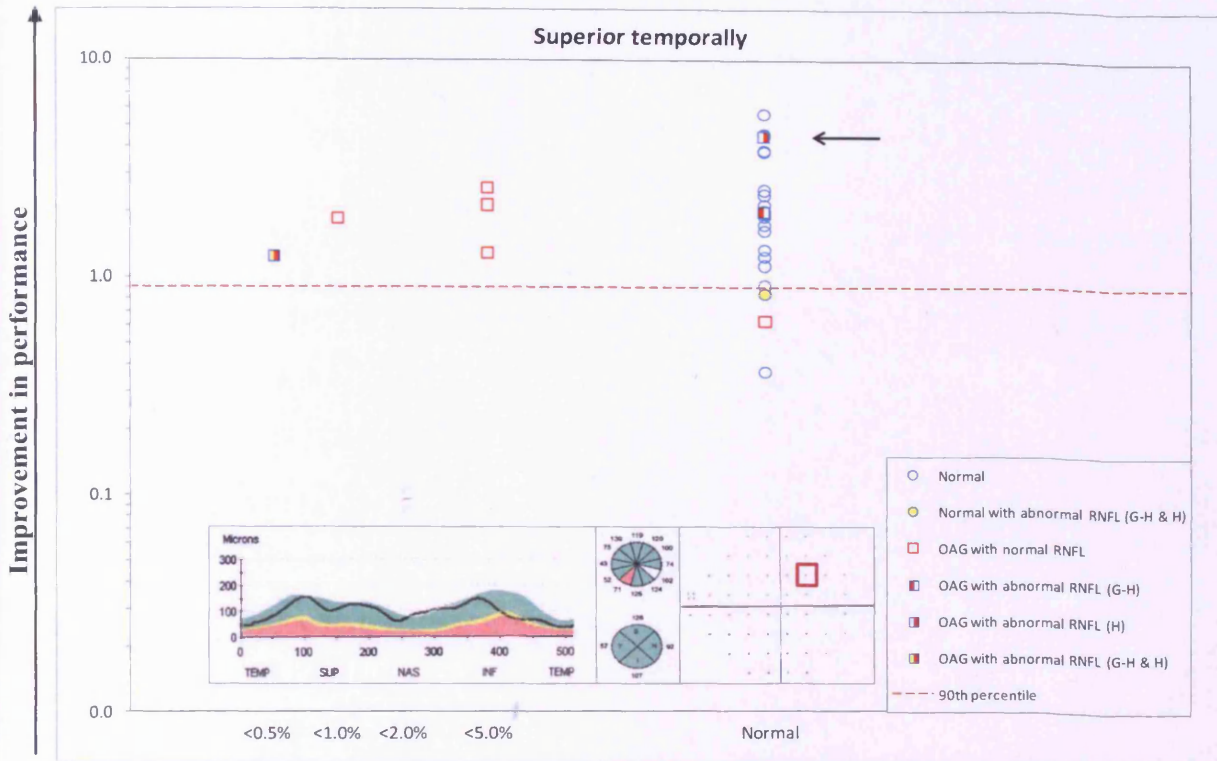


Figure 6.87 Motion discrimination: sampling efficiency (SE) for the stimuli in the superior temporal quadrant (ordinate) as a function of the Pattern Deviation probability level at the corresponding location (abscissa). The 90th percentile of the distribution of sampling efficiency amongst the 20 normal individuals is indicated by the red dotted line. Sampling efficiency for these 20 individuals is indicated by the circles. Individuals with OAG are indicated by the squares. The percentile associated with the given RNFL thickness derived from the OCT printout at the given stimulus location is indicated by the colour (yellow <math><5\%</math>; red <math><1\%</math>) according to the topographical mapping of Garway-Heath et al (2000) (left half of the circle/ square indicated as G-H) or Harwerth et al (2007) (right half of the circle/ square indicated as H). The RNFL Thickness Chart (left), the Sector Averages (middle [top]), the Quadrant averages (Middle [bottom]) and the Pattern Deviation probability map (right) are given in the bottom panel for the individual exhibiting the contrast threshold indicated by the black arrow. The stimulus location for SAP corresponding to that for DNP is indicated by the red square.

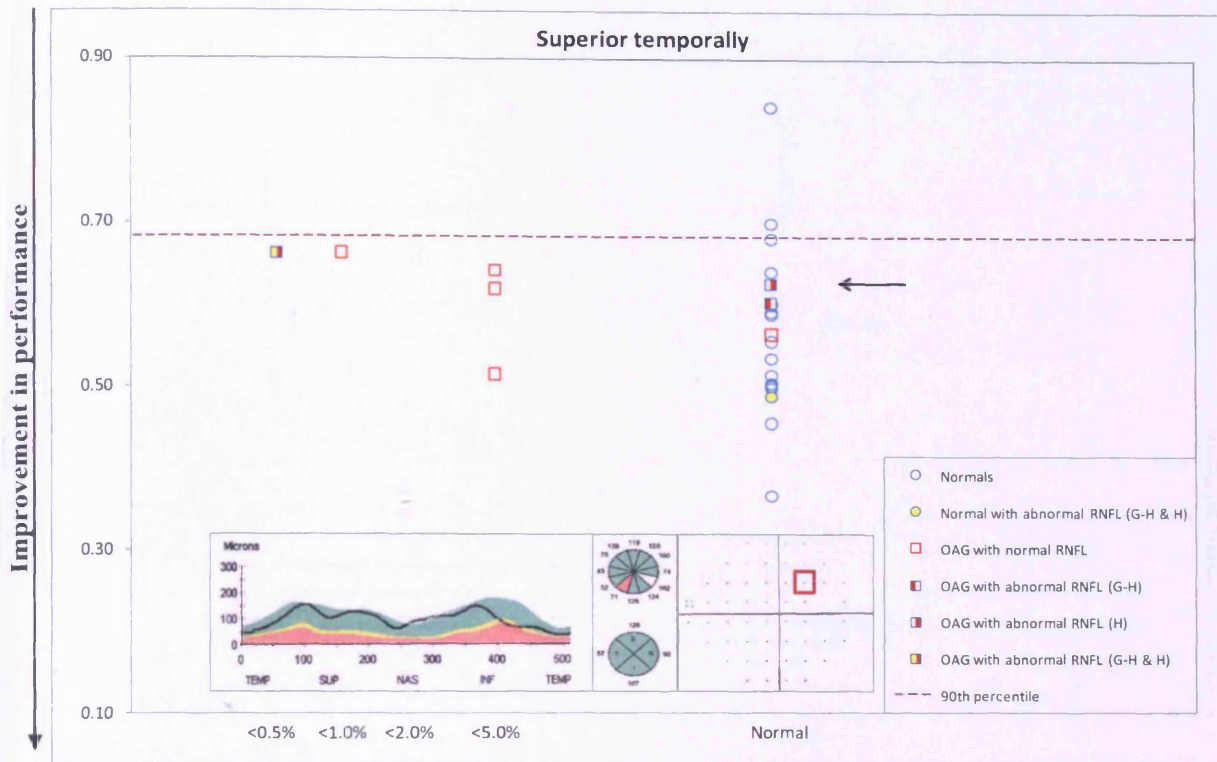


Figure 6.88 Motion discrimination: Log_{10} Ratio for the stimuli in the superior temporal quadrant (ordinate) as a function of the Pattern Deviation probability level at the corresponding location (abscissa). The 90th percentile of the distribution of the Log_{10} Ratio amongst the 20 normal individuals is indicated by the red dotted line. Log_{10} Ratio for these 20 individuals is indicated by the circles. Individuals with OAG are indicated by the squares. The percentile associated with the given RNFL thickness derived from the OCT printout at the given stimulus location is indicated by the colour (yellow <5%; red <1%) according to the topographical mapping of Garway-Heath et al (2000) (left half of the circle/ square indicated as G-H) or Harwerth et al (2007) (right half of the circle/ square indicated as H). The RNFL Thickness Chart (left), the Sector Averages (middle [top]), the Quadrant averages (Middle [bottom]) and the Pattern Deviation probability map (right) are given in the bottom panel for the individual exhibiting the contrast threshold indicated by the black arrow. The stimulus location for SAP corresponding to that for DNP is indicated by the red square.

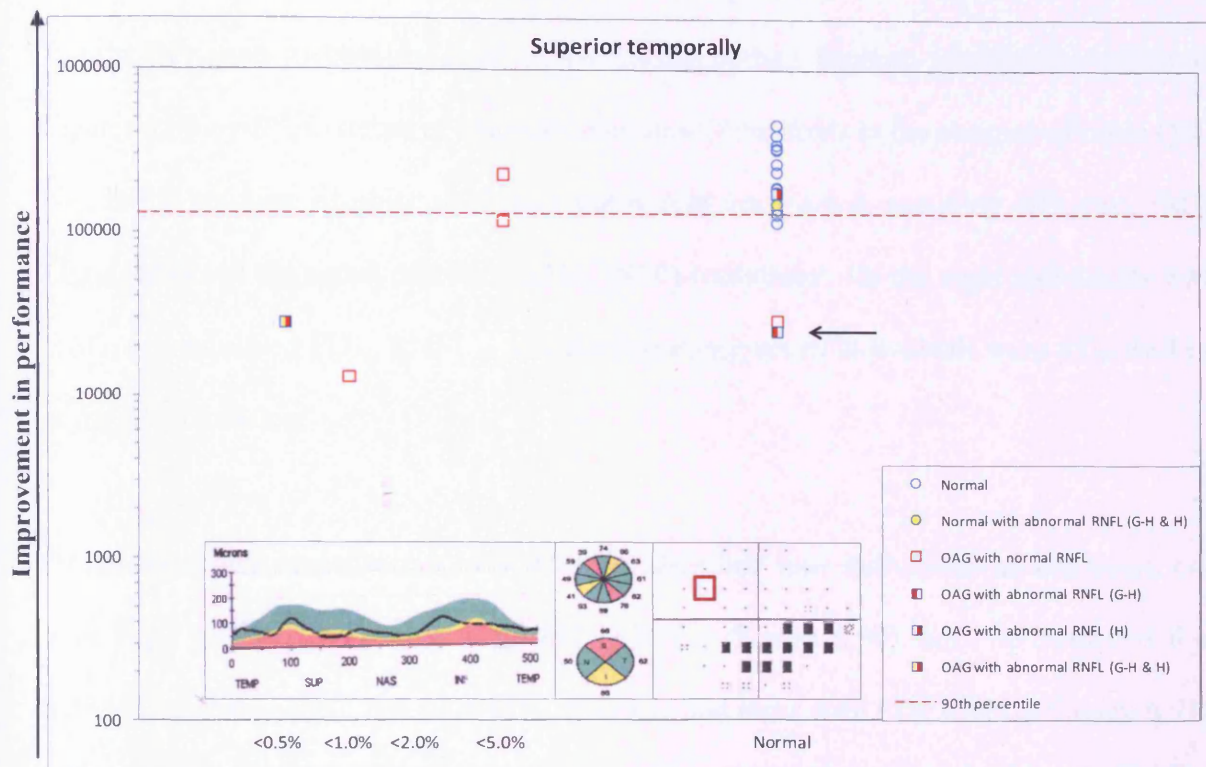


Figure 6.89 Motion discrimination: Signal detection index (SDI) for the stimuli in the superior temporal quadrant (ordinate) as a function of the Pattern Deviation probability level at the corresponding location (abscissa). The 90th percentile of the distribution of the Signal detection index amongst the 20 normal individuals is indicated by the red dotted line. Signal detection index for these 20 individuals is indicated by the circles. Individuals with OAG are indicated by the squares. The percentile associated with the given RNFL thickness derived from the OCT printout at the given stimulus location is indicated by the colour (yellow <5%; red <1%) according to the topographical mapping of Garway-Heath et al (2000) (left half of the circle/ square indicated as G-H) or Harwerth et al (2007) (right half of the circle/ square indicated as H). The RNFL Thickness Chart (left), the Sector Averages (middle [top]), the Quadrant averages (Middle [bottom]) and the Pattern Deviation probability map (right) are given in the bottom panel for the individual exhibiting the contrast threshold indicated by the black arrow. The stimulus location for SAP corresponding to that for DNP is indicated by the red square.

6.10.6 Distribution of DNP measures for the discrimination task at the superior nasal quadrant for individuals with OAG and for normal individuals

The 90th percentile of the distribution for the twenty normal individuals as a function of the Pattern Deviation probability level at the corresponding location (abscissa) is given in Figures 6.90 – 6.95, in terms of Michelson contrast thresholds in the absence of noise ($MC N_0$), in the presence of noise ($MC N_0$), equivalent noise (N_{eq}), sampling efficiency (SE), \log_{10} Ratio and the signal detection index (SDI) (ordinates). Of the eight individuals with OAG, one exhibited $PD_{Ab} RNFL_{Ab}$ and the remaining seven individuals were $PD_N RNFL_N$ at the given location.

Of the eight individuals with OAG, $MC N_0$ identified four individuals as abnormal: one with $PD_{Ab} RNFL_{Ab}$, and three with $PD_N RNFL_N$ (Figure 6.90). $MC N_e$ identified four individuals as abnormal: one with $PD_{Ab} RNFL_{Ab}$ and three with $PD_N RNFL_N$ (Figure 6.91). N_{eq} identified three individuals as abnormal: each with $PD_N RNFL_N$ (Figure 6.92). SE identified three individuals as abnormal: one with $PD_{Ab} RNFL_{Ab}$ and two with $PD_N RNFL_N$ (Figure 6.93). \log_{10} Ratio identified one individual with $PD_N RNFL_N$ as abnormal (Figure 6.94). SDI identified four individuals as abnormal: one with one with $PD_{Ab} RNFL_{Ab}$ and three with $PD_N RNFL_N$ (Figure 6.95). A summary of findings is shown in Table 6.26.

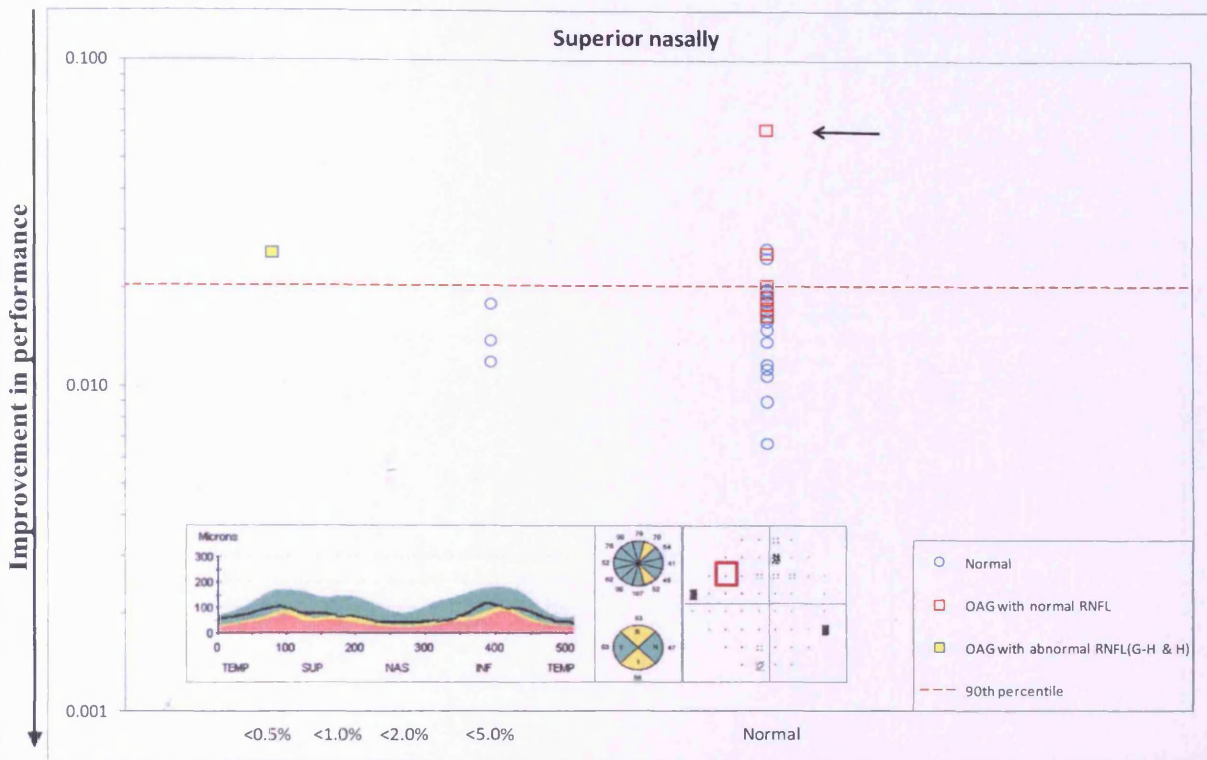


Figure 6.90 Motion discrimination : Michelson contrast thresholds in the absence of noise ($MC N_0$) for the stimuli in the superior nasal quadrant (ordinate) as a function of the Pattern Deviation probability level at the corresponding location (abscissa). The 90th percentile of the distribution of Michelson contrast thresholds amongst the 20 normal individuals is indicated by the red dotted line. Michelson contrast thresholds for these 20 individuals are indicated by the circles. Individuals with OAG are indicated by the squares. The percentile associated with the given RNFL thickness derived from the OCT printout at the given stimulus location is indicated by the colour (yellow <5%; red <1%) according to the topographical mapping of Garway-Heath et al (2000) (left half of the circle/ square indicated as G-H) or Harwerth et al (2007) (right half of the circle/ square indicated as H). The RNFL Thickness Chart (left), the Sector Averages (middle [top]), the Quadrant averages (Middle [bottom]) and the Pattern Deviation probability map (right) are given in the bottom panel for the individual exhibiting the contrast threshold indicated by the black arrow. The stimulus location for SAP corresponding to that for DNP is indicated by the red square.

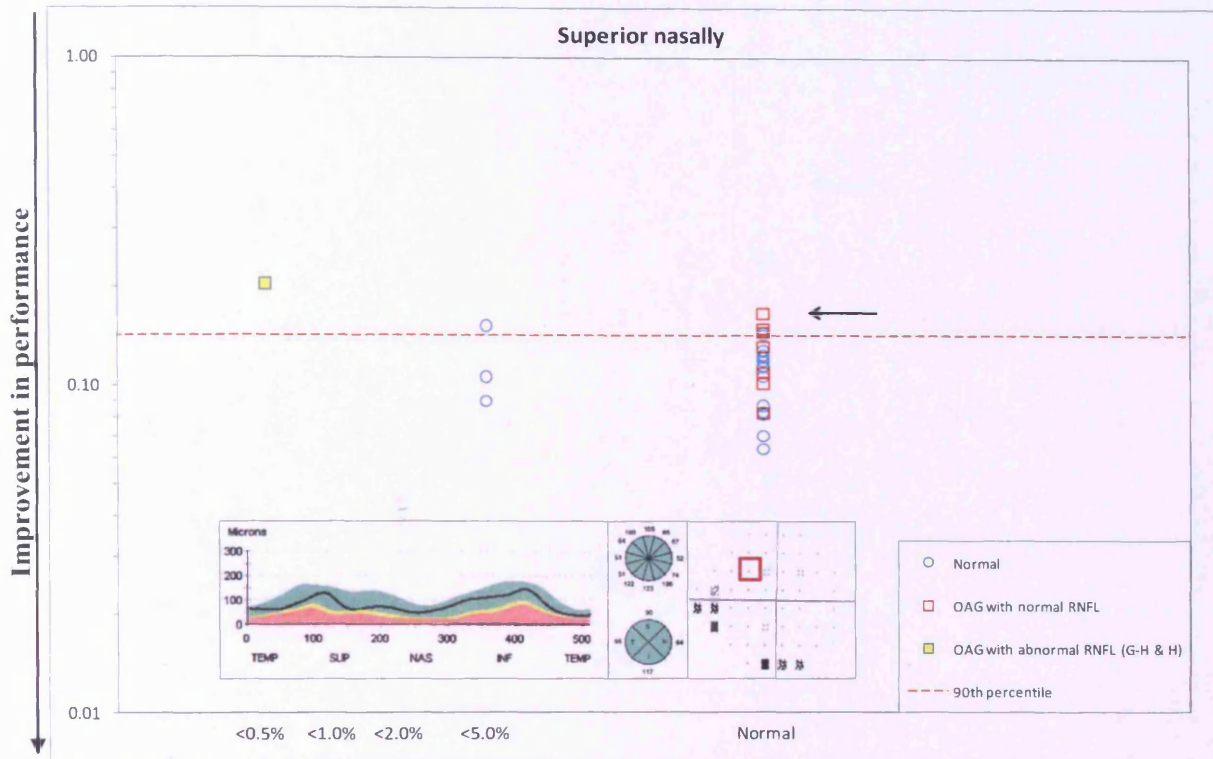


Figure 6.91 Motion discrimination: Michelson contrast thresholds in the presence of noise ($MC N_e$) for the stimuli in the superior nasal quadrant (ordinate) as a function of the Pattern Deviation probability level at the corresponding location (abscissa). The 90th percentile of the distribution of Michelson contrast thresholds amongst the 20 normal individuals is indicated by the red dotted line. Michelson contrast thresholds for these 20 individuals are indicated by the circles. Individuals with OAG are indicated by the squares. The percentile associated with the given RNFL thickness derived from the OCT printout at the given stimulus location is indicated by the colour (yellow <5%; red <1%) according to the topographical mapping of Garway-Heath et al (2000) (left half of the circle/ square indicated as G-H) or Harwerth et al (2007) (right half of the circle/ square indicated as H). The RNFL Thickness Chart (left), the Sector Averages (middle [top]), the Quadrant averages (Middle [bottom]) and the Pattern Deviation probability map (right) are given in the bottom panel for the individual exhibiting the contrast threshold indicated by the black arrow. The stimulus location for SAP corresponding to that for DNP is indicated by the red square.

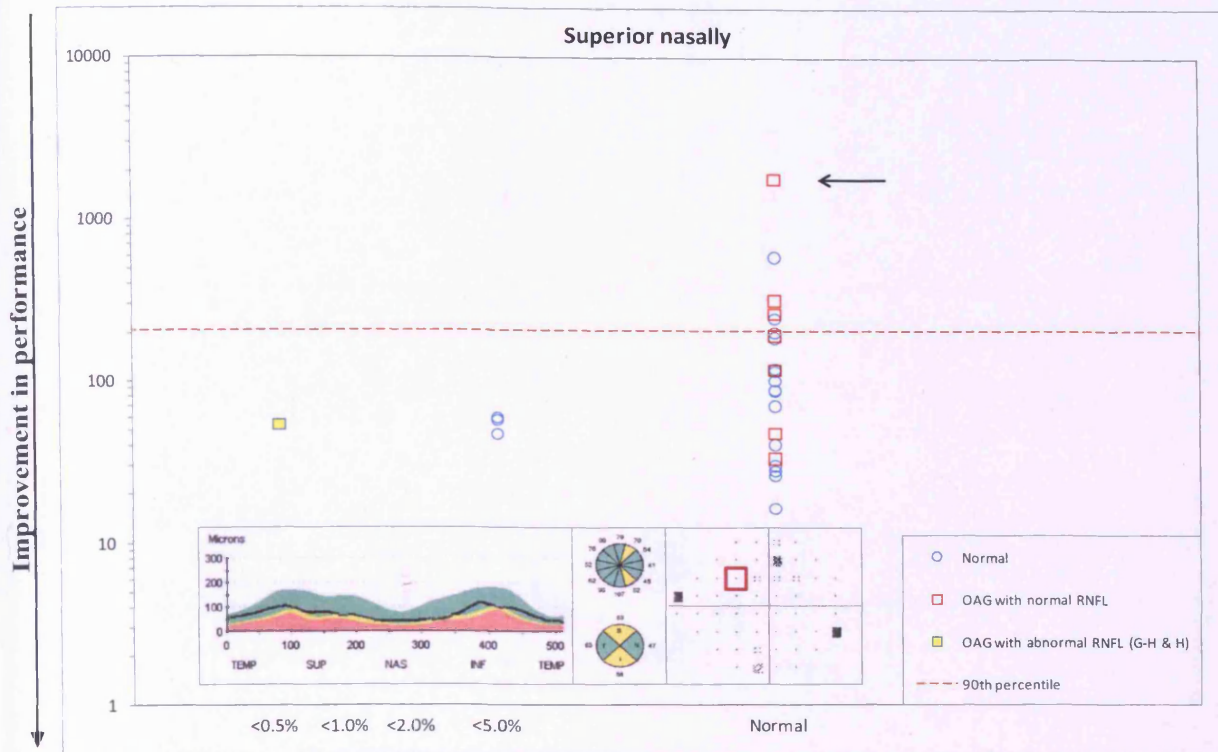


Figure 6.92 Motion discrimination: equivalent noise (N_{eq}) for the stimuli in the superior nasal quadrant (ordinate) as a function of the Pattern Deviation probability level at the corresponding location (abscissa). The 90th percentile of the distribution of equivalent noise amongst the 20 normal individuals is indicated by the red dotted line. Equivalent noise for these 20 individuals is indicated by the circles. Individuals with OAG are indicated by the squares. The percentile associated with the given RNFL thickness derived from the OCT printout at the given stimulus location is indicated by the colour (yellow <5%; red <1%) according to the topographical mapping of Garway-Heath et al (2000) (left half of the circle/ square indicated as G-H) or Harwerth et al (2007) (right half of the circle/ square indicated as H). The RNFL Thickness Chart (left), the Sector Averages (middle [top]), the Quadrant averages (Middle [bottom]) and the Pattern Deviation probability map (right) are given in the bottom panel for the individual exhibiting the contrast threshold indicated by the black arrow. The stimulus location for SAP corresponding to that for DNP is indicated by the red square.

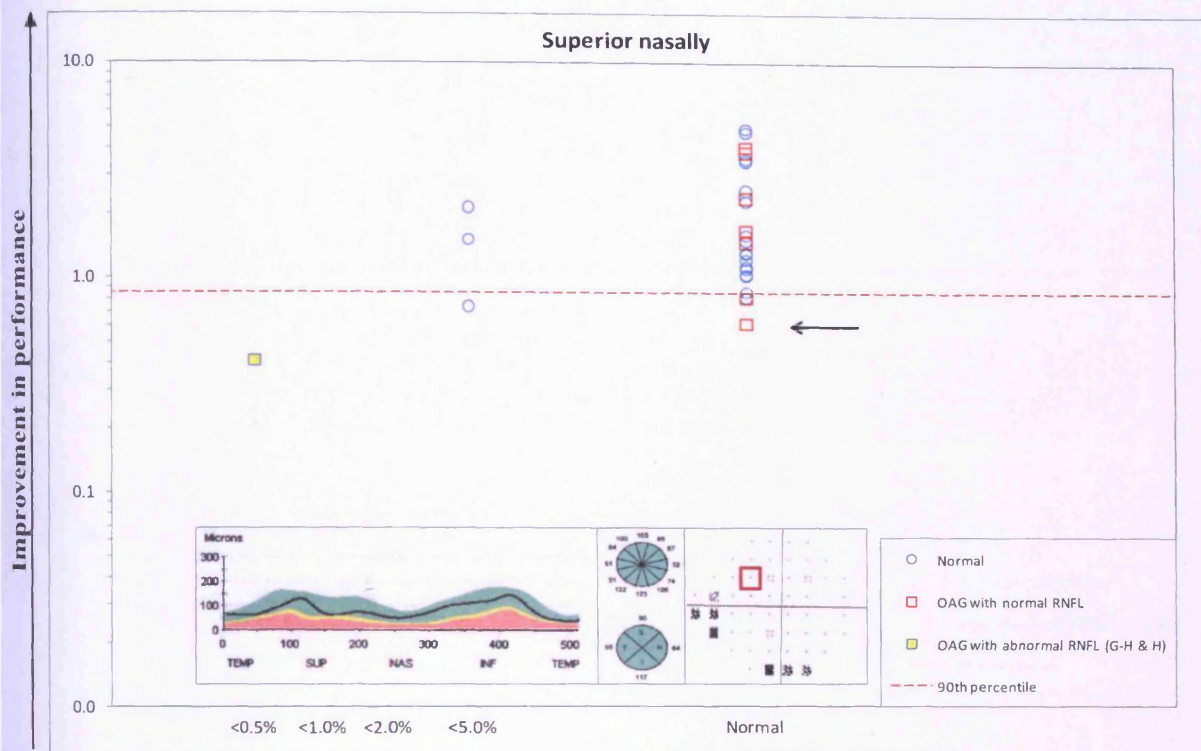


Figure 6.93 Motion discrimination: sampling efficiency (SE) for the stimuli in the superior nasal quadrant (ordinate) as a function of the Pattern Deviation probability level at the corresponding location (abscissa). The 90th percentile of the distribution of sampling efficiency amongst the 20 normal individuals is indicated by the red dotted line. Sampling efficiency for these 20 individuals is indicated by the circles. Individuals with OAG are indicated by the squares. The percentile associated with the given RNFL thickness derived from the OCT printout at the given stimulus location is indicated by the colour (yellow <5%; red <1%) according to the topographical mapping of Garway-Heath et al (2000) (left half of the circle/ square indicated as G-H) or Harwerth et al (2007) (right half of the circle/ square indicated as H). The RNFL Thickness Chart (left), the Sector Averages (middle [top]), the Quadrant averages (Middle [bottom]) and the Pattern Deviation probability map (right) are given in the bottom panel for the individual exhibiting the contrast threshold indicated by the black arrow. The stimulus location for SAP corresponding to that for DNP is indicated by the red square.

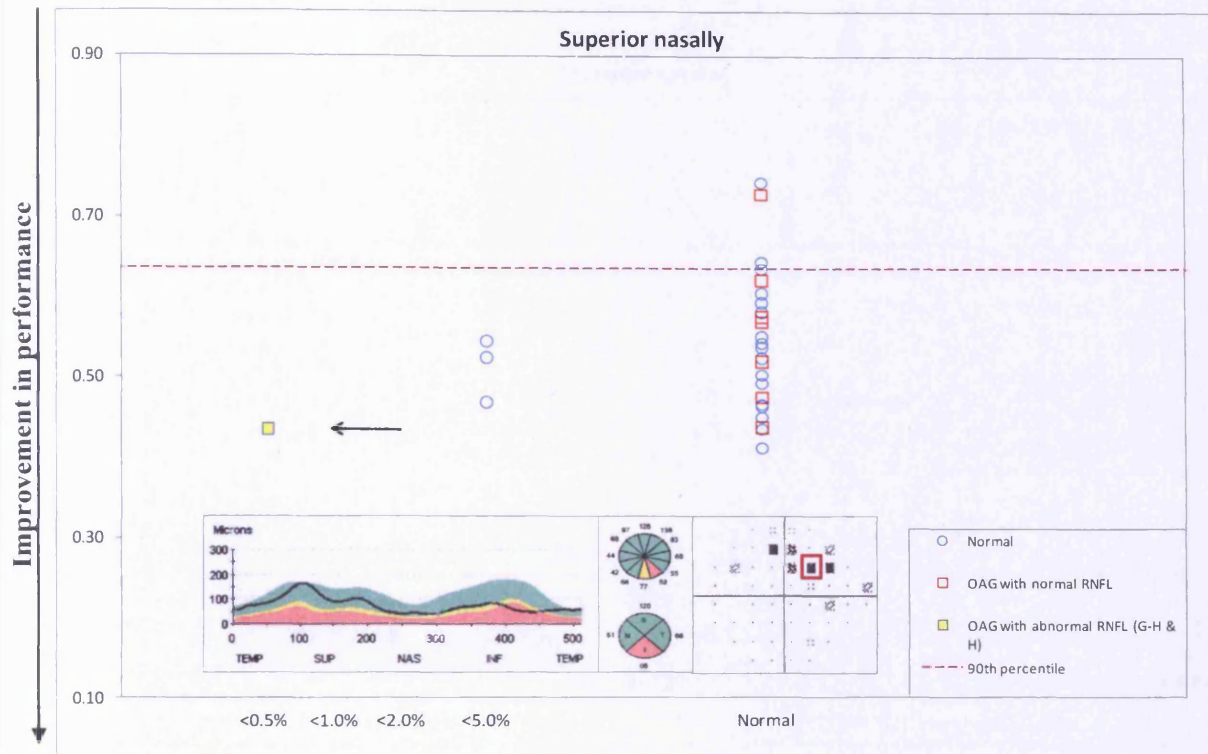


Figure 6.94 Motion discrimination: Log₁₀ Ratio for the stimuli in the superior nasal quadrant (ordinate) as a function of the Pattern Deviation probability level at the corresponding location (abscissa). The 90th percentile of the distribution of the Log₁₀ Ratio amongst the 20 normal individuals is indicated by the red dotted line. Log₁₀ Ratio for these 20 individuals is indicated by the circles. Individuals with OAG are indicated by the squares. The percentile associated with the given RNFL thickness derived from the OCT printout at the given stimulus location is indicated by the colour (yellow <math><5\%</math>; red <math><1\%</math>) according to the topographical mapping of Garway-Heath et al (2000) (left half of the circle/ square indicated as G-H) or Harwerth et al (2007) (right half of the circle/ square indicated as H). The RNFL Thickness Chart (left), the Sector Averages (middle [top]), the Quadrant averages (Middle [bottom]) and the Pattern Deviation probability map (right) are given in the bottom panel for the individual exhibiting the contrast threshold indicated by the black arrow. The stimulus location for SAP corresponding to that for DNP is indicated by the red square.

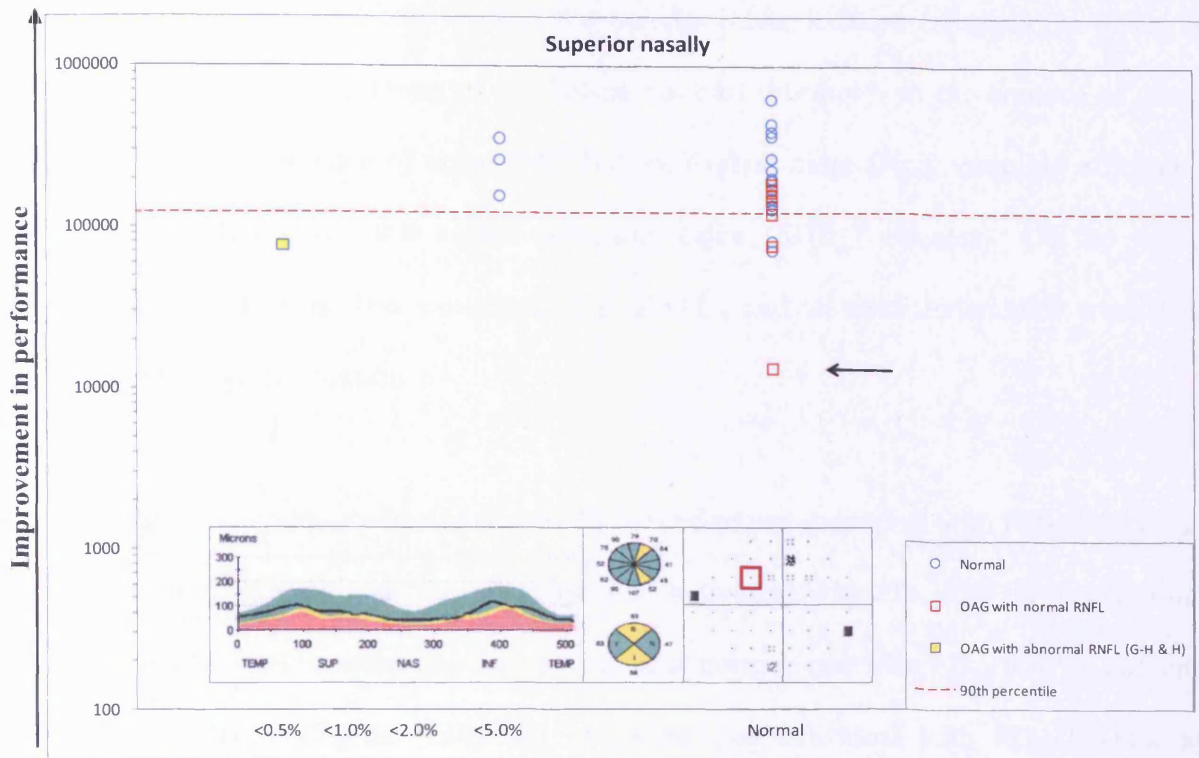


Figure 6.95 Motion discrimination: Signal detection index (SDI) for the stimuli in the superior nasal quadrant (ordinate) as a function of the Pattern Deviation probability level at the corresponding location (abscissa). The 90th percentile of the distribution of the Signal detection index amongst the 20 normal individuals is indicated by the red dotted line. Signal detection index for these 20 individuals is indicated by the circles. Individuals with OAG are indicated by the squares. The percentile associated with the given RNFL thickness derived from the OCT printout at the given stimulus location is indicated by the colour (yellow <5%; red <1%) according to the topographical mapping of Garway-Heath et al (2000) (left half of the circle/ square indicated as G-H) or Harwerth et al (2007) (right half of the circle/ square indicated as H). The RNFL Thickness Chart (left), the Sector Averages (middle [top]), the Quadrant averages (Middle [bottom]) and the Pattern Deviation probability map (right) are given in the bottom panel for the individual exhibiting the contrast threshold indicated by the black arrow. The stimulus location for SAP corresponding to that for DNP is indicated by the red square.

6.10.7 Distribution of DNP measures for the discrimination task at the inferior nasal quadrant for individuals with OAG and for normal individuals

The 90th percentile of the distribution for the twenty normal individuals as a function of the Pattern Deviation probability level at the corresponding location (abscissa) is given in Figures 6.96 – 6.101, in terms of Michelson contrast thresholds in the absence of noise ($MC N_0$), in the presence of noise ($MC N_e$), equivalent noise (N_{eq}), sampling efficiency (SE), \log_{10} Ratio and the signal detection index (SDI) (ordinates). Of the seven individuals with OAG, two exhibited $PD_{Ab} RNFL_N$ and all other individuals were $PD_N RNFL_N$ at the given location.

Of the seven individuals with OAG, $MC N_0$ identified one individual with $PD_{Ab} RNFL_N$ as abnormal (Figure 6.96). $MC N_e$ identified one individual with $PD_N RNFL_N$ as abnormal (Figure 6.97). N_{eq} identified two individuals as abnormal: one with $PD_{Ab} RNFL_N$ and one with $PD_N RNFL_N$ (Figure 6.98). SE identified one individual with $PD_N RNFL_N$ as abnormal (Figure 6.99). \log_{10} Ratio identified one individual with $PD_{Ab} RNFL_N$ as abnormal (Figure 6.100). SDI identified two individuals as abnormal: one with $PD_{Ab} RNFL_N$ and one with $PD_N RNFL_N$ (Figure 6.101). A summary of findings is shown in Table 6.27.

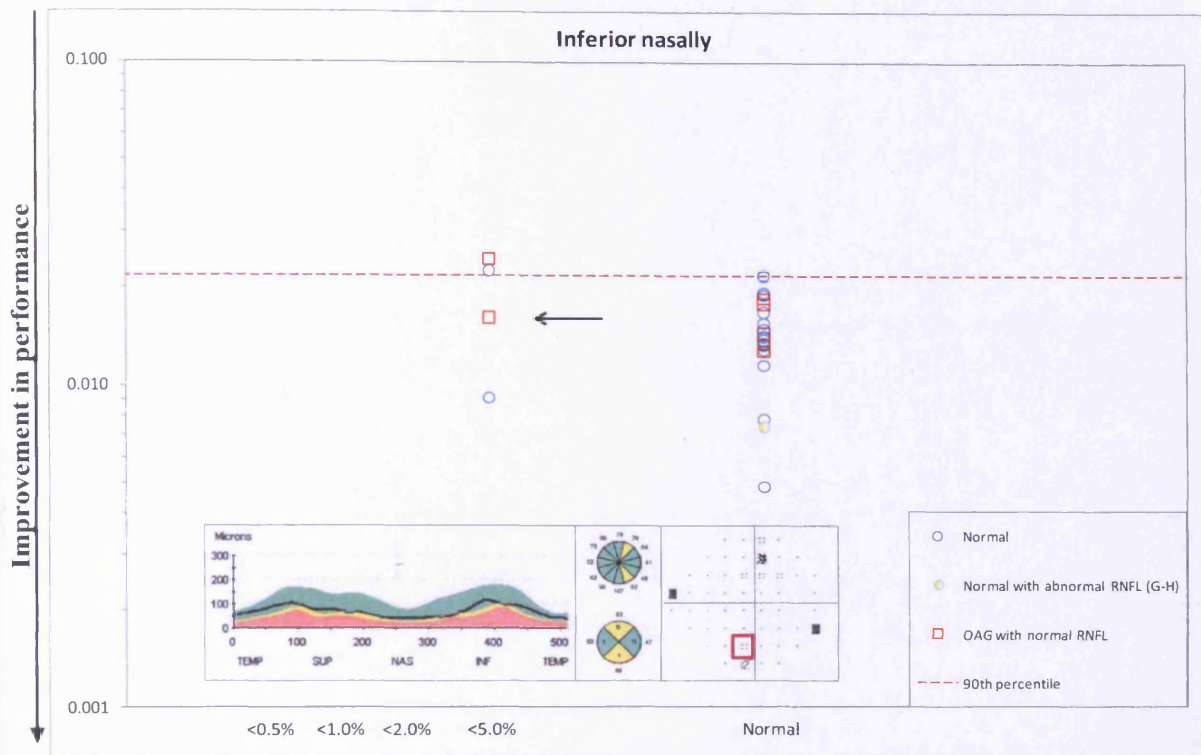


Figure 6.96 Motion discrimination: Michelson contrast thresholds in the absence of noise ($MC N_0$) for the stimuli in the inferior nasal quadrant (ordinate) as a function of the Pattern Deviation probability level at the corresponding location (abscissa). The 90th percentile of the distribution of Michelson contrast thresholds amongst the 20 normal individuals is indicated by the red dotted line. Michelson contrast thresholds for these 20 individuals are indicated by the circles. Individuals with OAG are indicated by the squares. The percentile associated with the given RNFL thickness derived from the OCT printout at the given stimulus location is indicated by the colour (yellow <5%; red <1%) according to the topographical mapping of Garway-Heath et al (2000) (left half of the circle/ square indicated as G-H) or Harwerth et al (2007) (right half of the circle/ square indicated as H). The RNFL Thickness Chart (left), the Sector Averages (middle [top]), the Quadrant averages (Middle [bottom]) and the Pattern Deviation probability map (right) are given in the bottom panel for the individual exhibiting the contrast threshold indicated by the black arrow. The stimulus location for SAP corresponding to that for DNP is indicated by the red square.

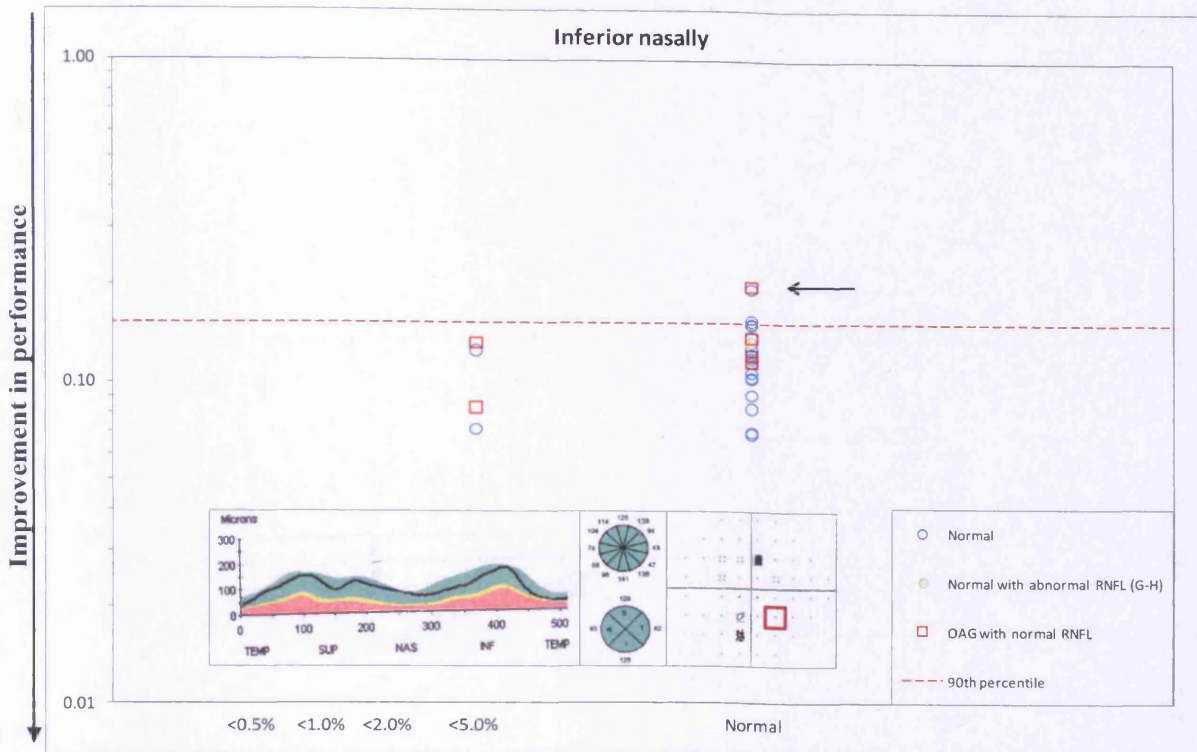


Figure 6.97 Motion discrimination: Michelson contrast thresholds in the presence of noise ($MC N_e$) for the stimuli in the inferior nasal quadrant (ordinate) as a function of the Pattern Deviation probability level at the corresponding location (abscissa). The 90th percentile of the distribution of Michelson contrast thresholds amongst the 20 normal individuals is indicated by the red dotted line. Michelson contrast thresholds for these 20 individuals are indicated by the circles. Individuals with OAG are indicated by the squares. The percentile associated with the given RNFL thickness derived from the OCT printout at the given stimulus location is indicated by the colour (yellow <5%; red <1%) according to the topographical mapping of Garway-Heath et al (2000) (left half of the circle/ square indicated as G-H) or Harwerth et al (2007) (right half of the circle/ square indicated as H). The RNFL Thickness Chart (left), the Sector Averages (middle [top]), the Quadrant averages (Middle [bottom]) and the Pattern Deviation probability map (right) are given in the bottom panel for the individual exhibiting the contrast threshold indicated by the black arrow. The stimulus location for SAP corresponding to that for DNP is indicated by the red square.

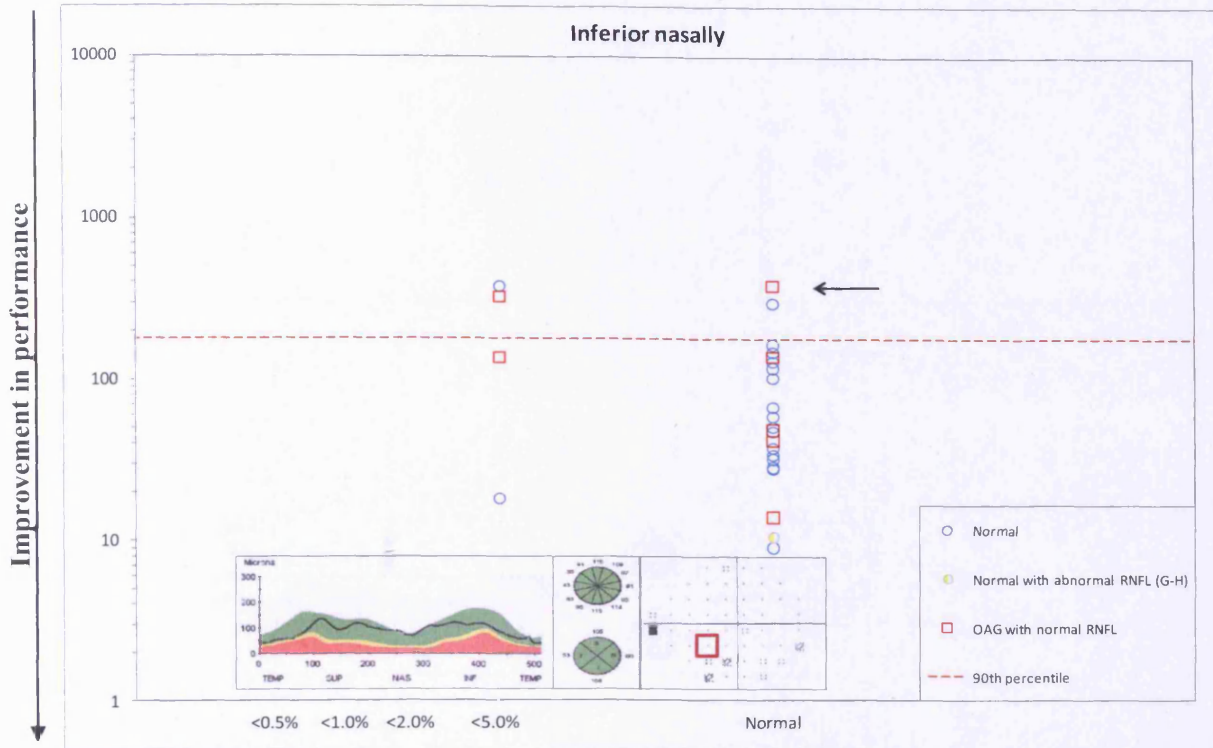


Figure 6.98 Motion discrimination: equivalent noise (N_{eq}) for the stimuli in the inferior nasal quadrant (ordinate) as a function of the Pattern Deviation probability level at the corresponding location (abscissa). The 90th percentile of the distribution of equivalent noise amongst the 20 normal individuals is indicated by the red dotted line. Equivalent noise for these 20 individuals is indicated by the circles. Individuals with OAG are indicated by the squares. The percentile associated with the given RNFL thickness derived from the OCT printout at the given stimulus location is indicated by the colour (yellow <5%; red <1%) according to the topographical mapping of Garway-Heath et al (2000) (left half of the circle/ square indicated as G-H) or Harwerth et al (2007) (right half of the circle/ square indicated as H). The RNFL Thickness Chart (left), the Sector Averages (middle [top]), the Quadrant averages (Middle [bottom]) and the Pattern Deviation probability map (right) are given in the bottom panel for the individual exhibiting the contrast threshold indicated by the black arrow. The stimulus location for SAP corresponding to that for DNP is indicated by the red square.

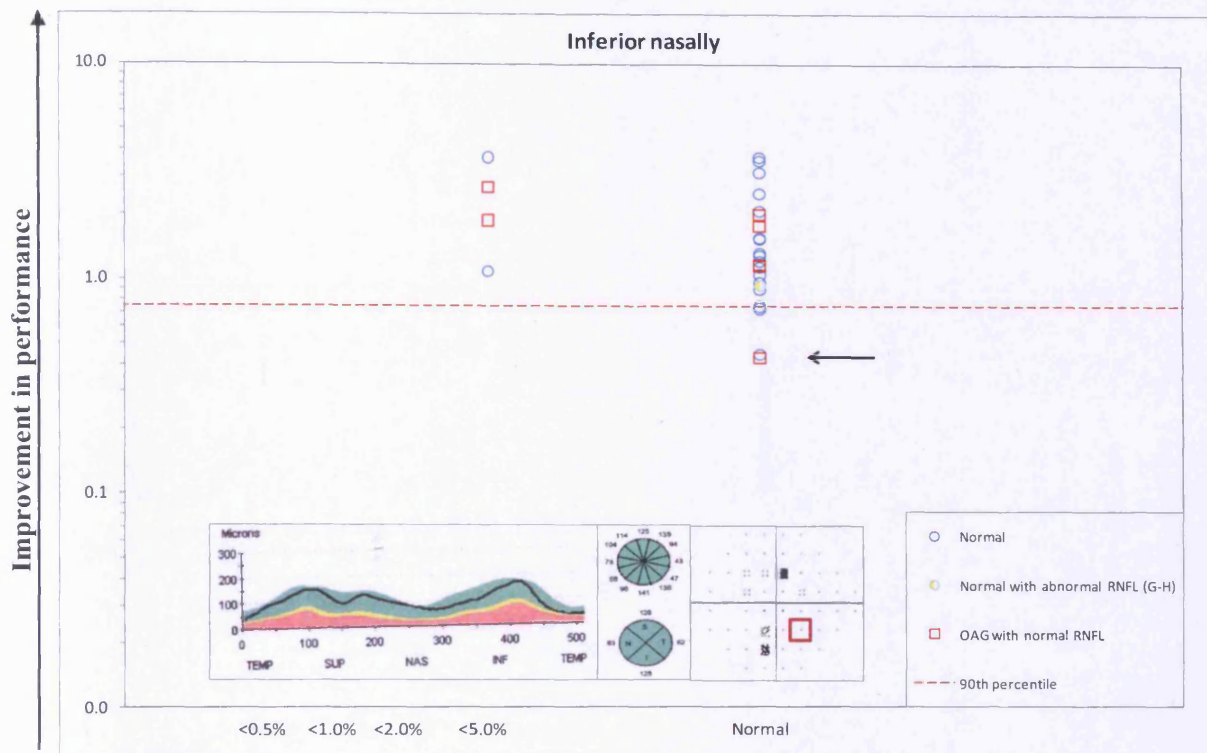


Figure 6.99 Motion discrimination: sampling efficiency (SE) for the stimuli in the inferior nasal quadrant (ordinate) as a function of the Pattern Deviation probability level at the corresponding location (abscissa). The 90th percentile of the distribution of sampling efficiency amongst the 20 normal individuals is indicated by the red dotted line. Sampling efficiency for these 20 individuals is indicated by the circles. Individuals with OAG are indicated by the squares. The percentile associated with the given RNFL thickness derived from the OCT printout at the given stimulus location is indicated by the colour (yellow <5%; red <1%) according to the topographical mapping of Garway-Heath et al (2000) (left half of the circle/ square indicated as G-H) or Harwerth et al (2007) (right half of the circle/ square indicated as H). The RNFL Thickness Chart (left), the Sector Averages (middle [top]), the Quadrant averages (Middle [bottom]) and the Pattern Deviation probability map (right) are given in the bottom panel for the individual exhibiting the contrast threshold indicated by the black arrow. The stimulus location for SAP corresponding to that for DNP is indicated by the red square.

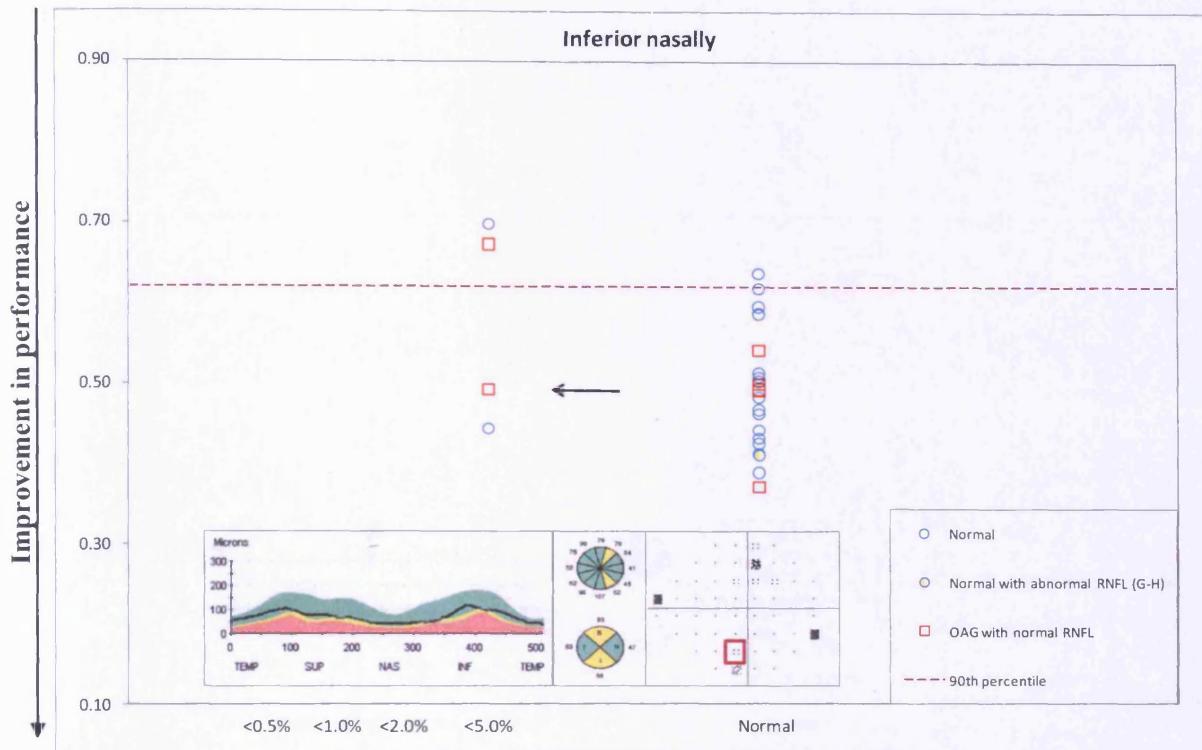


Figure 6.100 Motion discrimination: Log_{10} Ratio for the stimuli in the inferior nasal quadrant (ordinate) as a function of the Pattern Deviation probability level at the corresponding location (abscissa). The 90th percentile of the distribution of the Log_{10} Ratio amongst the 20 normal individuals is indicated by the red dotted line. Log_{10} Ratio for these 20 individuals is indicated by the circles. Individuals with OAG are indicated by the squares. The percentile associated with the given RNFL thickness derived from the OCT printout at the given stimulus location is indicated by the colour (yellow <5%; red <1%) according to the topographical mapping of Garway-Heath et al (2000) (left half of the circle/ square indicated as G-H) or Harwerth et al (2007) (right half of the circle/ square indicated as H). The RNFL Thickness Chart (left), the Sector Averages (middle [top]), the Quadrant averages (Middle [bottom]) and the Pattern Deviation probability map (right) are given in the bottom panel for the individual exhibiting the contrast threshold indicated by the black arrow. The stimulus location for SAP corresponding to that for DNP is indicated by the red square.

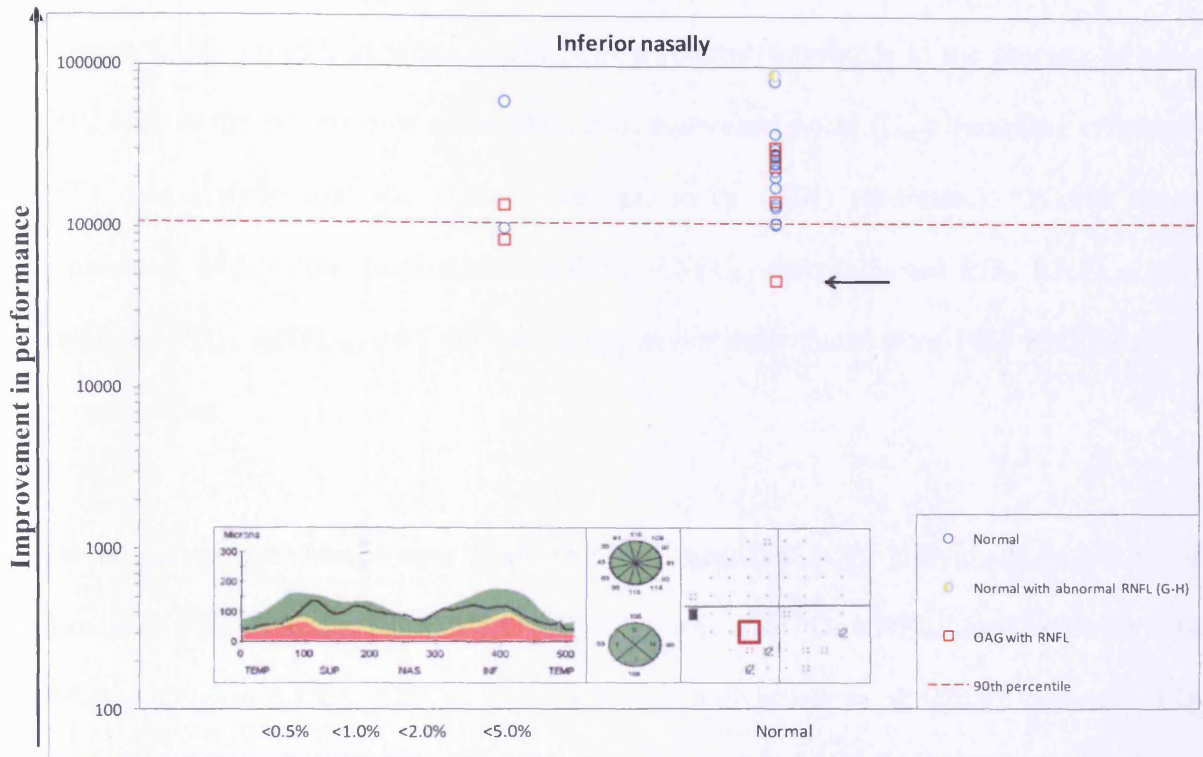


Figure 6.101 Motion discrimination: Signal detection index (SDI) for the stimuli in the inferior nasal quadrant (ordinate) as a function of the Pattern Deviation probability level at the corresponding location (abscissa). The 90th percentile of the distribution of the Signal detection index amongst the 20 normal individuals is indicated by the red dotted line. Signal detection index for these 20 individuals is indicated by the circles. Individuals with OAG are indicated by the squares. The percentile associated with the given RNFL thickness derived from the OCT printout at the given stimulus location is indicated by the colour (yellow <5%; red <1%) according to the topographical mapping of Garway-Heath et al (2000) (left half of the circle/ square indicated as G-H) or Harwerth et al (2007) (right half of the circle/ square indicated as H). The RNFL Thickness Chart (left), the Sector Averages (middle [top]), the Quadrant averages (Middle [bottom]) and the Pattern Deviation probability map (right) are given in the bottom panel for the individual exhibiting the contrast threshold indicated by the black arrow. The stimulus location for SAP corresponding to that for DNP is indicated by the red square.

6.10.8 Distribution of DNP measures for the discrimination task at the inferior temporal quadrant for individuals with OAG and for normal individuals

The 90th percentile of the distribution for the twenty normal individuals as a function of the Pattern Deviation probability level at the corresponding location (abscissa) is given in Figures 6.102 – 6.107, in terms of Michelson contrast thresholds in the absence of noise ($MC N_0$), in the presence of noise ($MC N_0$), equivalent noise (N_{eq}), sampling efficiency (SE), \log_{10} Ratio and the signal detection index (SDI) (ordinates). Of the eleven individuals with OAG, two exhibited $PD_{Ab} RNFL_N$, one exhibited $PD_N RNFL_{Ab}$, two exhibited $PD_{Ab} RNFL_{Ab}$ and the remaining seven individuals were $PD_N RNFL_N$ at the given location.

Of the eleven individuals with OAG, $MC N_0$ identified eight individuals as abnormal: three with $PD_N RNFL_N$, two with $PD_{Ab} RNFL_N$, one with $PD_N RNFL_{Ab}$ and two with $PD_{Ab} RNFL_{Ab}$ (Figure 6.102). $MC N_e$ identified four individuals as abnormal: two with $PD_N RNFL_N$, one with $PD_N RNFL_{Ab}$ and one with $PD_{Ab} RNFL_{Ab}$ (Figure 6.103). N_{eq} identified nine individuals as abnormal: four with $PD_N RNFL_N$, two with $PD_{Ab} RNFL_N$, one with $PD_N RNFL_{Ab}$ and two with $PD_{Ab} RNFL_{Ab}$ (Figure 6.104). SE identified none of the individuals as abnormal (Figure 6.105). \log_{10} Ratio identified five individuals as abnormal: two with $PD_N RNFL_N$, one with $PD_{Ab} RNFL_N$, one with $PD_N RNFL_{Ab}$ and one with $PD_{Ab} RNFL_{Ab}$ (Figure 6.106). SDI identified eight individuals as abnormal: three with $PD_N RNFL_N$, two with $PD_{Ab} RNFL_N$, one with $PD_N RNFL_{Ab}$ and two with $PD_{Ab} RNFL_{Ab}$ (Figure 6.107). A summary of findings is shown in Table 6.28.

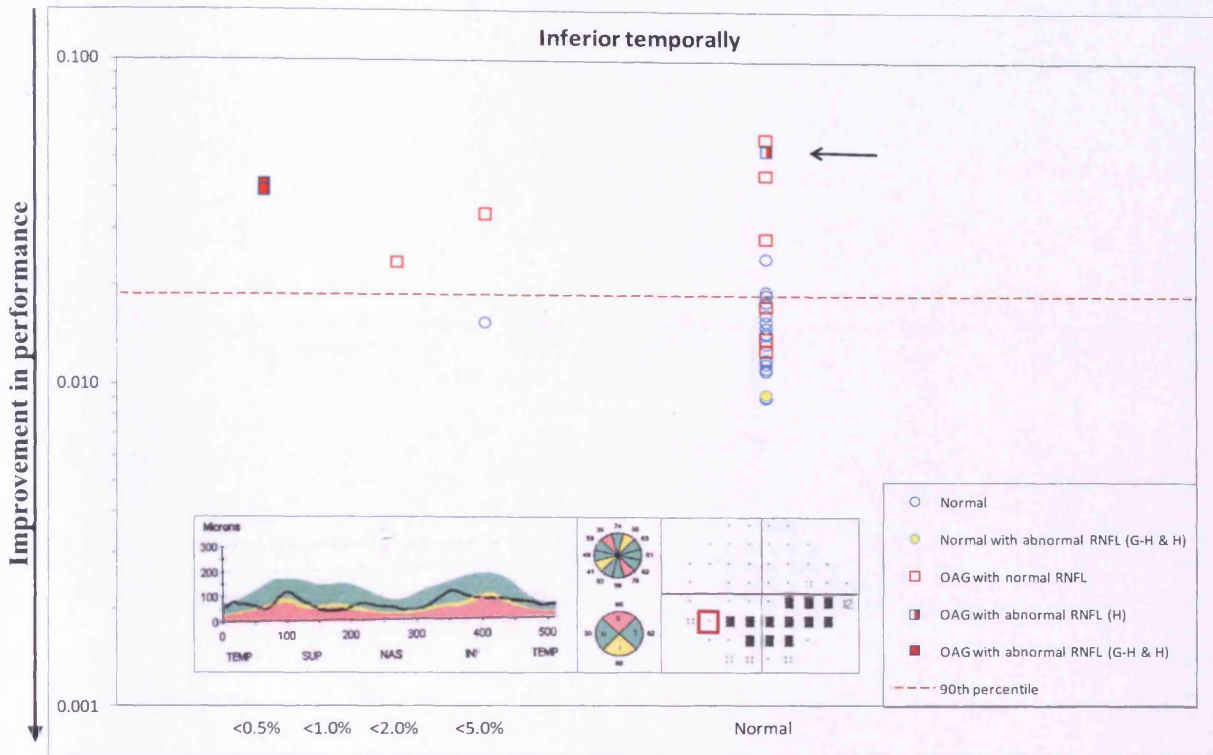


Figure 6.102 Motion discrimination: Michelson contrast thresholds in the absence of noise ($MC N_0$) for the stimuli in the inferior temporal quadrant (ordinate) as a function of the Pattern Deviation probability level at the corresponding location (abscissa). The 90th percentile of the distribution of Michelson contrast thresholds amongst the 20 normal individuals is indicated by the red dotted line. Michelson contrast thresholds for these 20 individuals are indicated by the circles. Individuals with OAG are indicated by the squares. The percentile associated with the given RNFL thickness derived from the OCT printout at the given stimulus location is indicated by the colour (yellow <5%; red <1%) according to the topographical mapping of Garway-Heath et al (2000) (left half of the circle/ square indicated as G-H) or Harwerth et al (2007) (right half of the circle/ square indicated as H). The RNFL Thickness Chart (left), the Sector Averages (middle [top]), the Quadrant averages (Middle [bottom]) and the Pattern Deviation probability map (right) are given in the bottom panel for the individual exhibiting the contrast threshold indicated by the black arrow. The stimulus location for SAP corresponding to that for DNP is indicated by the red square.

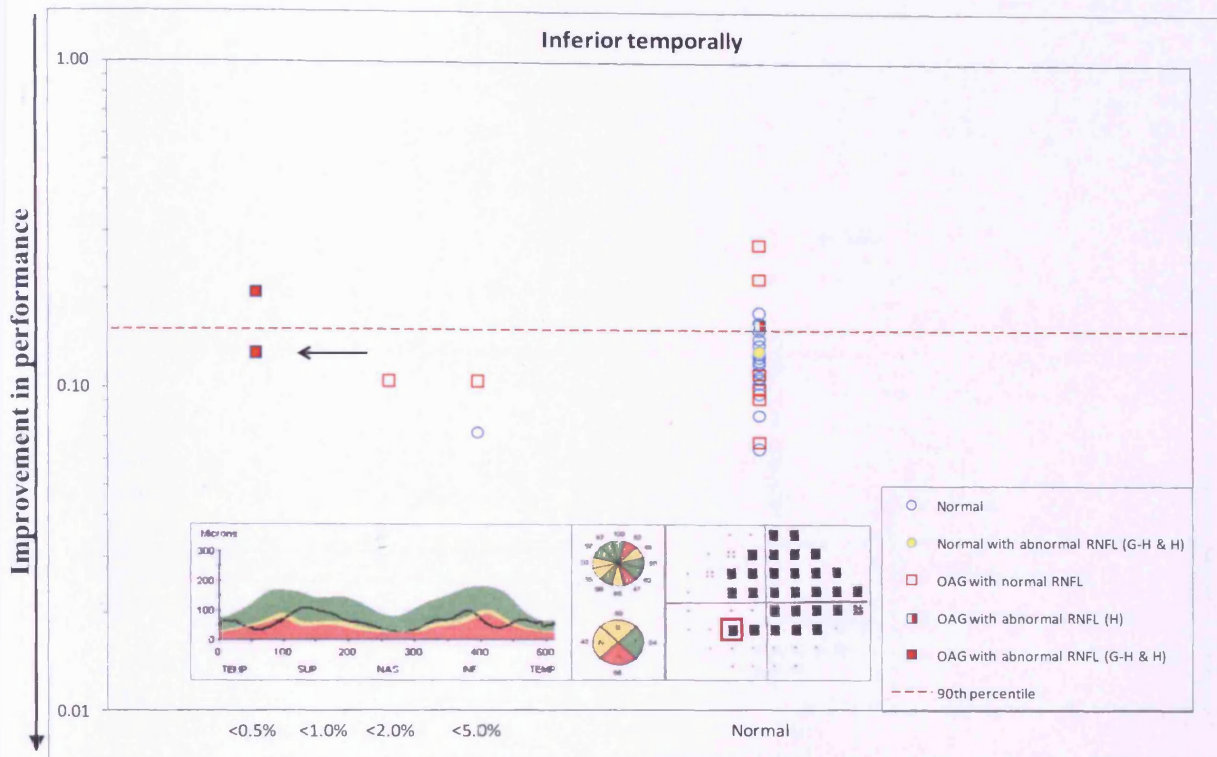


Figure 6.103 Motion discrimination: Michelson contrast thresholds in the presence of noise ($MC N_e$) for the stimuli in the inferior temporal quadrant (ordinate) as a function of the Pattern Deviation probability level at the corresponding location (abscissa). The 90th percentile of the distribution of Michelson contrast thresholds amongst the 20 normal individuals is indicated by the red dotted line. Michelson contrast thresholds for these 20 individuals are indicated by the circles. Individuals with OAG are indicated by the squares. The percentile associated with the given RNFL thickness derived from the OCT printout at the given stimulus location is indicated by the colour (yellow <5%; red <1%) according to the topographical mapping of Garway-Heath et al (2000) (left half of the circle/ square indicated as G-H) or Harwerth et al (2007) (right half of the circle/ square indicated as H). The RNFL Thickness Chart (left), the Sector Averages (middle [top]), the Quadrant averages (Middle [bottom]) and the Pattern Deviation probability map (right) are given in the bottom panel for the individual exhibiting the contrast threshold indicated by the black arrow. The stimulus location for SAP corresponding to that for DNP is indicated by the red square.

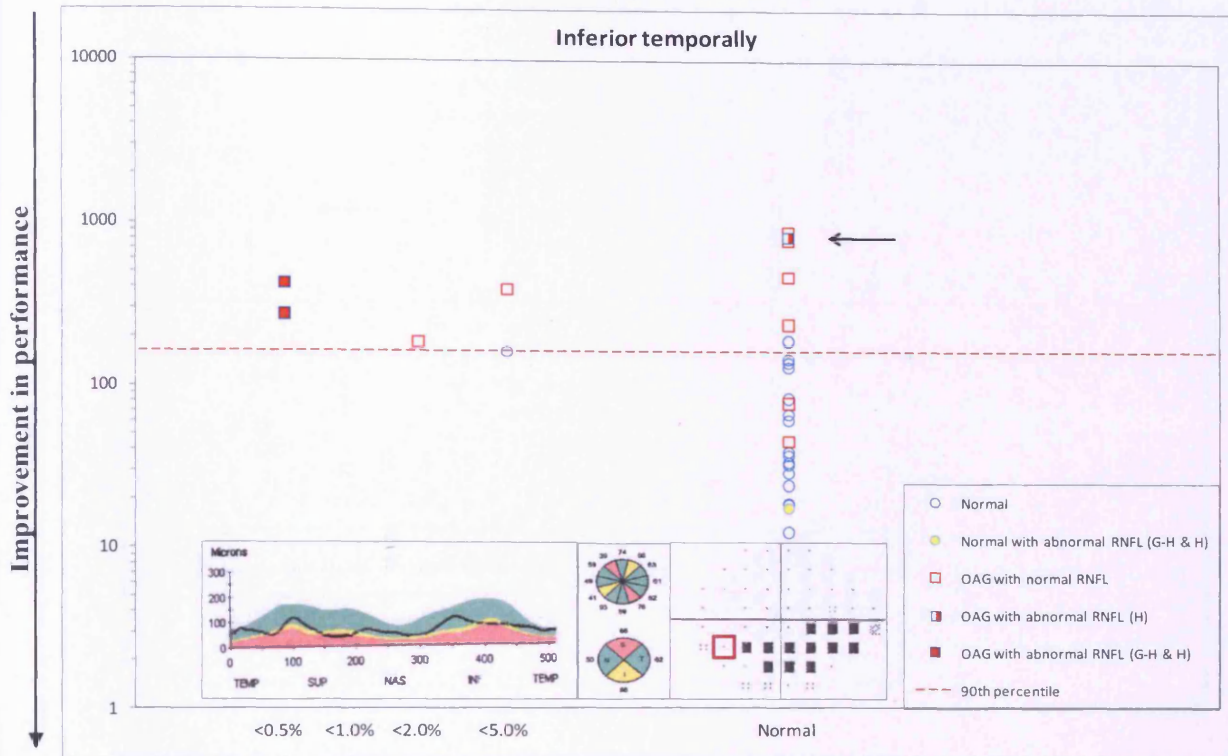


Figure 6.104 Motion discrimination: equivalent noise (N_{eq}) for the stimuli in the inferior temporal quadrant (ordinate) as a function of the Pattern Deviation probability level at the corresponding location (abscissa). The 90th percentile of the distribution of equivalent noise amongst the 20 normal individuals is indicated by the red dotted line. Equivalent noise for these 20 individuals is indicated by the circles. Individuals with OAG are indicated by the squares. The percentile associated with the given RNFL thickness derived from the OCT printout at the given stimulus location is indicated by the colour (yellow <5%; red <1%) according to the topographical mapping of Garway-Heath et al (2000) (left half of the circle/ square indicated as G-H) or Harwerth et al (2007) (right half of the circle/ square indicated as H). The RNFL Thickness Chart (left), the Sector Averages (middle [top]), the Quadrant averages (Middle [bottom]) and the Pattern Deviation probability map (right) are given in the bottom panel for the individual exhibiting the contrast threshold indicated by the black arrow. The stimulus location for SAP corresponding to that for DNP is indicated by the red square.

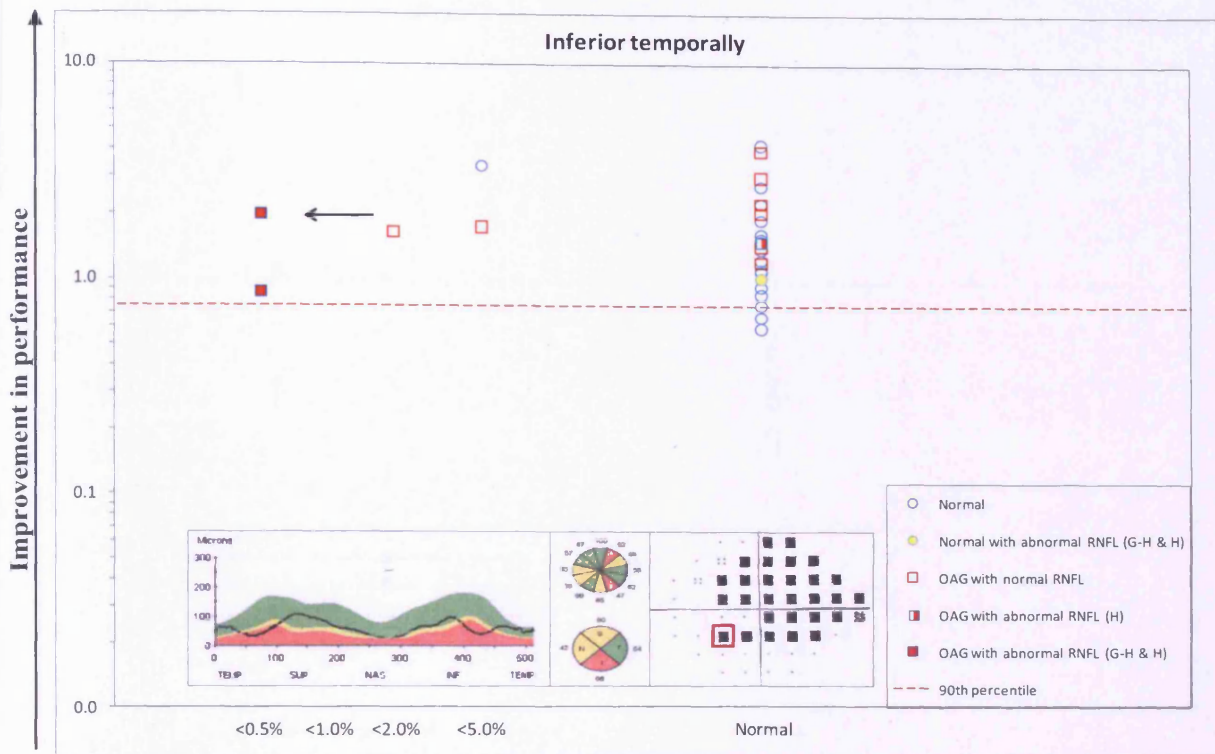


Figure 6.105 Motion discrimination: sampling efficiency (SE) for the stimuli in the inferior temporal quadrant (ordinate) as a function of the Pattern Deviation probability level at the corresponding location (abscissa). The 90th percentile of the distribution of sampling efficiency amongst the 20 normal individuals is indicated by the red dotted line. Sampling efficiency for these 20 individuals is indicated by the circles. Individuals with OAG are indicated by the squares. The percentile associated with the given RNFL thickness derived from the OCT printout at the given stimulus location is indicated by the colour (yellow <5%; red <1%) according to the topographical mapping of Garway-Heath et al (2000) (left half of the circle/ square indicated as G-H) or Harwerth et al (2007) (right half of the circle/ square indicated as H). The RNFL Thickness Chart (left), the Sector Averages (middle [top]), the Quadrant averages (Middle [bottom]) and the Pattern Deviation probability map (right) are given in the bottom panel for the individual exhibiting the contrast threshold indicated by the black arrow. The stimulus location for SAP corresponding to that for DNP is indicated by the red square.

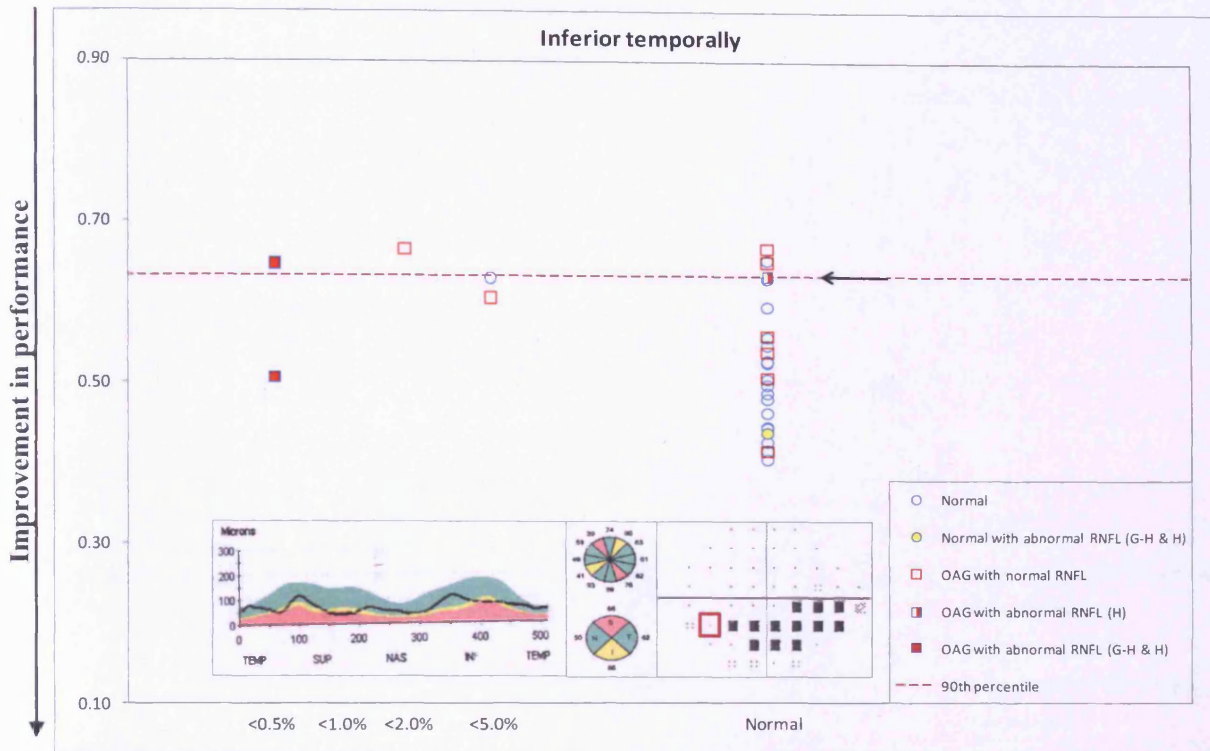


Figure 6.106 Motion discrimination: Log_{10} Ratio for the stimuli in the inferior temporal quadrant (ordinate) as a function of the Pattern Deviation probability level at the corresponding location (abscissa). The 90th percentile of the distribution of the Log_{10} Ratio amongst the 20 normal individuals is indicated by the red dotted line. Log_{10} Ratio for these 20 individuals is indicated by the circles. Individuals with OAG are indicated by the squares. The percentile associated with the given RNFL thickness derived from the OCT printout at the given stimulus location is indicated by the colour (yellow <5%; red <1%) according to the topographical mapping of Garway-Heath et al (2000) (left half of the circle/ square indicated as G-H) or Harwerth et al (2007) (right half of the circle/ square indicated as H). The RNFL Thickness Chart (left), the Sector Averages (middle [top]), the Quadrant averages (Middle [bottom]) and the Pattern Deviation probability map (right) are given in the bottom panel for the individual exhibiting the contrast threshold indicated by the black arrow. The stimulus location for SAP corresponding to that for DNP is indicated by the red square.

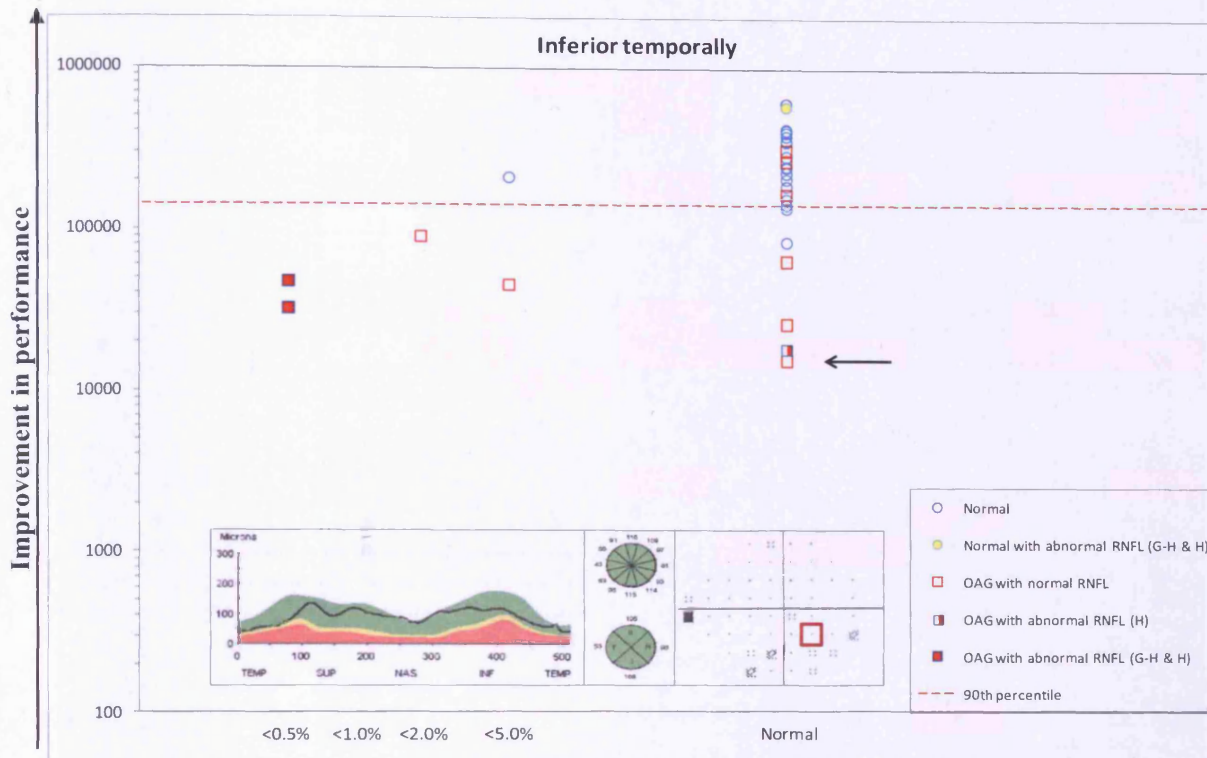


Figure 6.107 Motion discrimination: Signal detection index (SDI) for the stimuli in the inferior temporal quadrant (ordinate) as a function of the Pattern Deviation probability level at the corresponding location (abscissa). The 90th percentile of the distribution of the Signal detection index amongst the 20 normal individuals is indicated by the red dotted line. Signal detection index for these 20 individuals is indicated by the circles. Individuals with OAG are indicated by the squares. The percentile associated with the given RNFL thickness derived from the OCT printout at the given stimulus location is indicated by the colour (yellow <5%; red <1%) according to the topographical mapping of Garway-Heath et al (2000) (left half of the circle/ square indicated as G-H) or Harwerth et al (2007) (right half of the circle/ square indicated as H). The RNFL Thickness Chart (left), the Sector Averages (middle [top]), the Quadrant averages (Middle [bottom]) and the Pattern Deviation probability map (right) are given in the bottom panel for the individual exhibiting the contrast threshold indicated by the black arrow. The stimulus location for SAP corresponding to that for DNP is indicated by the red square.

Case	Location	Quadrant	Pattern Deviation	RNFL (G-H)	RNFL (H)	MC N ₀	MC N ₁	N _{eq}	SE	Log ₁₀ Ratio	SDI
1	(-6, 12)	ST	< 0.5%	< 5%	< 1%	< 10%	N	N	N	N	< 10%
2	(-10, 8)	ST	N	N	N	< 10%	N	N	N	N	< 10%
3	(10, 8)	ST	< 5%	N	N	N	N	N	N	N	N
3	(6, 12)	ST	< 1%	N	N	< 10%	N	< 10%	N	< 10%	< 10%
4	(-10, 8)	ST	< 5%	N	N	N	N	N	N	N	N
5	(10, 8)	ST	< 5%	N	N	N	N	N	N	N	N
6	(10, 8)	ST	N	N	N	N	N	N	N	N	N
8	(-14, 8)	ST	N	< 1%	N	< 10%	N	N	N	< 10%	N
9	(-14, 8)	ST	< 5%	< 1%	N	< 10%	< 10%	< 10%	N	< 10%	< 10%
10	(10, 12)	ST	N	N	< 1%	N	N	N	N	N	N
11	(-10, 8)	ST	N	N	N	N	N	N	N	N	N
12	(14, 8)	ST	N	N	N	N	N	N	N	N	N
13	(10, 8)	ST	N	N	N	< 10%	N	N	N	N	< 10%
14	(10, 8)	ST	N	N	N	N	N	N	< 10%	N	N
15	(-10, 8)	ST	N	N	N	N	< 10%	< 10%	N	N	N
16	(10, 8)	ST	N	N	N	N	N	N	N	N	N
17	(-10, 8)	ST	N	N	N	N	N	N	N	N	N
18	(10, 8)	ST	N	N	N	N	N	N	N	N	N
19	(-14, 8)	ST	N	N	N	N	N	N	N	N	N
20	(-10, 8)	ST	N	< 5%	< 5%	N	N	N	< 10%	N	N
21	(10, 8)	ST	N	N	N	N	N	N	N	N	N
22	(10, 8)	ST	N	N	N	N	N	N	N	N	N
23	(-10, 8)	ST	N	N	N	< 10%	< 10%	< 10%	N	N	N
24	(-10, 8)	ST	N	N	N	N	N	N	N	N	N
25	(10, 8)	ST	N	N	N	N	N	N	N	N	N
26	(10, 8)	ST	N	N	N	N	N	N	N	N	N
27	(-10, 8)	ST	N	N	N	N	N	N	N	N	N
28	(10, 8)	ST	N	N	N	N	N	N	N	N	N
29	(-10, 8)	ST	N	N	N	N	N	N	N	< 10%	N
30	(-10, 8)	ST	N	N	N	N	N	N	N	< 10%	< 10%

Table 6.21 Motion detection: Summary of results for individuals with OAG (case numbers 1 to 10) and normal individuals (case numbers 11 to 30) at the superior temporal location, showing Pattern Deviation in terms of p-values, RNFL thickness in terms of p-values and DNP values in terms of the 90th percentile. Normal Pattern Deviation and RNFL thickness values are indicated with the letter 'N'. Abnormal DNP values (< 10%) are highlighted in red.

Case	Location	Quadrant	Pattern Deviation	RNFL (G-H)	RNFL (H)	MC N ₀	MC N _s	N _{eq}	SE	Log ₁₀ Ratio	SDI
1	(10, 8)	SN	< 0.5%	< 5%	< 5%	< 10%	< 10%	N	< 10%	N	< 10%
2	(10, 8)	SN	N	N	N	N	N	< 10%	N	< 10%	N
3	(-10, 8)	SN	N	N	N	N	N	N	N	N	N
4	(10, 8)	SN	N	N	N	< 10%	N	N	N	N	N
5	(-10, 8)	SN	N	N	N	N	N	N	N	N	N
6	(-10, 8)	SN	N	N	N	N	< 10%	N	< 10%	N	N
7	(10, 8)	SN	N	N	N	N	N	N	N	N	N
8	(14, 8)	SN	N	N	N	< 10%	N	N	N	N	N
10	(-14, 8)	SN	N	N	N	< 10%	N	N	N	N	N
11	(10, 8)	SN	N	N	N	N	N	N	N	N	N
12	(-14, 8)	SN	N	N	N	N	N	N	N	N	N
13	(-10, 8)	SN	N	N	N	< 10%	N	< 10%	N	N	< 10%
14	(-10, 8)	SN	N	N	N	N	N	N	N	N	N
15	(10, 8)	SN	N	N	N	N	N	N	N	N	N
16	(-10, 8)	SN	N	N	N	N	N	N	N	N	N
17	(10, 8)	SN	N	N	N	N	< 10%	N	< 10%	N	N
18	(-10, 8)	SN	N	N	N	N	N	N	N	N	N
19	(14, 8)	SN	N	N	N	N	N	N	< 10%	N	N
20	(10, 8)	SN	N	N	N	N	N	N	N	N	N
21	(-10, 8)	SN	N	N	N	N	N	N	N	N	N
22	(-10, 8)	SN	N	N	N	N	N	N	N	N	N
23	(10, 8)	SN	N	N	N	< 10%	N	< 10%	N	N	N
24	(10, 8)	SN	N	N	N	N	< 10%	N	N	N	< 10%
25	(-10, 8)	SN	N	N	N	N	N	N	N	N	N
26	(-10, 8)	SN	N	N	N	N	N	N	N	N	N
27	(10, 8)	SN	N	N	N	N	N	N	N	N	N
28	(-10, 8)	SN	N	N	N	N	N	N	N	N	N
29	(10, 8)	SN	N	N	N	N	N	N	N	< 10%	N
30	(10, 8)	SN	N	N	N	N	N	N	N	< 10%	N

Table 6.22 Motion detection: Summary of results for individuals with OAG (case numbers 1 to 10) and normal individuals (case numbers 11 to 30) at the superior nasal location, showing Pattern Deviation in terms of p-values, RNFL thickness in terms of p-values and DNP values in terms of the 90th percentile. Normal Pattern Deviation and RNFL thickness values are indicated with the letter 'N'. Abnormal DNP values (< 10%) are highlighted in red.

Case	Location	Quadrant	Pattern Deviation	RNFL (G-H)	RNFL (H)	MC N ₀	MC N _e	N _{90q}	SE	Log ₁₀ Ratio	SDI
1	(10, -12)	IN	< 5%	N	N	< 10%	N	N	N	N	< 10%
2	(10, -8)	IN	N	N	N	N	N	< 10%	N	< 10%	N
3	(-6, -12)	IN	< 5%	N	N	N	N	N	N	N	N
4	(10, -8)	IN	N	N	N	N	N	N	N	N	N
5	(-10, -8)	IN	N	N	N	N	N	N	N	N	N
6	(-10, -8)	IN	N	N	N	< 10%	< 10%	N	< 10%	N	< 10%
7	(10, -8)	IN	N	N	N	< 10%	N	< 10%	N	< 10%	< 10%
9	(10, -8)	IN	< 0.5%	< 1%	N	< 10%	N	< 10%	N	< 10%	< 10%
10	(-10, -8)	IN	N	N	N	< 10%	< 10%	N	< 10%	N	< 10%
11	(10, -8)	IN	N	N	N	N	N	N	N	N	N
12	(-14, -8)	IN	N	N	N	N	N	N	N	N	N
13	(-10, -8)	IN	N	N	N	< 10%	N	< 10%	N	< 10%	< 10%
14	(-10, -8)	IN	N	N	N	N	N	N	N	N	N
15	(10, -8)	IN	N	N	N	N	N	N	N	N	N
16	(-10, -8)	IN	N	N	N	< 10%	N	< 10%	N	N	< 10%
17	(10, -8)	IN	N	N	N	N	< 10%	N	< 10%	N	N
18	(-10, -8)	IN	N	N	N	N	N	N	N	N	N
19	(14, -8)	IN	N	N	N	N	N	N	N	N	N
20	(10, -8)	IN	N	N	N	N	N	N	N	N	N
21	(-10, -8)	IN	N	N	N	N	< 10%	N	< 10%	N	N
22	(-10, -8)	IN	N	N	N	N	N	N	N	< 10%	N
23	(10, -8)	IN	N	N	N	N	N	N	N	N	N
24	(10, -8)	IN	N	N	N	N	N	N	N	N	N
25	(-10, -8)	IN	N	N	N	N	N	N	N	N	N
26	(-10, -8)	IN	N	N	N	N	N	N	N	N	N
27	(10, -8)	IN	N	< 5%	N	N	N	N	N	N	N
28	(-10, -8)	IN	N	N	N	N	N	N	N	N	N
29	(10, -8)	IN	N	N	N	N	N	N	N	N	N
30	(10, -8)	IN	N	N	N	N	N	N	N	N	N

Table 6.23 Motion detection: Summary of results for individuals with OAG (case numbers 1 to 10) and normal individuals (case numbers 11 to 30) at the inferior nasal location, showing Pattern Deviation in terms of p-values, RNFL thickness in terms of p-values and DNP values in terms of the 90th percentile. Normal Pattern Deviation and RNFL thickness values are indicated with the letter 'N'. Abnormal DNP values (< 10%) are highlighted in red.

Case	Location	Quadrant	Pattern Deviation	RNFL (G-H)	RNFL (H)	MC N ₀	MC N _s	N _{eq}	SE	Log ₁₀ Ratio	SDI
1	(-10, -8)	IT	N	N	N	N	N	N	< 10%	N	N
2	(-10, -8)	IT	N	N	N	N	N	N	N	N	N
4	(-10, -8)	IT	N	N	N	N	N	N	N	N	N
5	(10, -8)	IT	N	N	N	N	N	N	N	N	N
6	(10, -8)	IT	N	N	N	< 10%	N	N	< 10%	N	< 10%
7	(-10, -8)	IT	< 5%	N	N	< 10%	N	< 10%	N	N	< 10%
7	(-6, -12)	IT	< 2%	N	N	< 10%	N	< 10%	N	< 10%	< 10%
8	(-14, -8)	IT	N	N	< 1%	< 10%	< 10%	< 10%	< 10%	N	< 10%
9	(-14, -8)	IT	N	N	N	< 10%	N	< 10%	N	< 10%	< 10%
9	(-10, -8)	IT	< 0.5%	< 1%	< 1%	< 10%	N	< 10%	N	< 10%	< 10%
10	(10, -8)	IT	N	N	N	N	N	N	N	N	N
11	(-10, -8)	IT	N	N	N	N	N	N	N	N	N
12	(14, -8)	IT	N	N	N	< 10%	N	< 10%	N	< 10%	< 10%
13	(10, -8)	IT	N	N	N	N	N	N	N	N	N
14	(10, -8)	IT	N	N	N	N	N	N	N	N	N
15	(-10, -8)	IT	N	N	N	N	N	N	N	N	N
16	(10, -8)	IT	N	N	N	N	N	N	N	N	N
17	(-10, -8)	IT	N	N	N	N	< 10%	N	< 10%	N	N
18	(10, -8)	IT	N	N	N	N	N	N	N	N	N
19	(-14, -8)	IT	N	N	N	< 10%	N	N	N	N	< 10%
20	(-10, -8)	IT	N	N	N	N	< 10%	N	< 10%	N	N
21	(10, -8)	IT	N	N	N	N	N	N	N	N	N
22	(10, -8)	IT	N	N	N	N	N	N	N	N	N
23	(-10, -8)	IT	N	N	N	N	N	N	N	N	N
24	(-10, -8)	IT	N	N	N	N	N	N	N	N	N
25	(10, -8)	IT	N	N	N	N	N	N	N	N	N
26	(10, -8)	IT	N	N	N	N	N	N	N	N	N
27	(-10, -8)	IT	N	< 5%	< 5%	N	N	< 10%	N	< 10%	N
28	(10, -8)	IT	N	N	N	N	N	N	N	N	N
29	(-10, -8)	IT	N	N	N	N	N	N	N	N	N
30	(-10, -8)	IT	N	N	N	N	N	N	N	N	N

Table 6.24 Motion detection: Summary of results for individuals with OAG (case numbers 1 to 10) and normal individuals (case numbers 11 to 30) at the inferior temporal location, showing Pattern Deviation in terms of p-values, RNFL thickness in terms of p-values and DNP values in terms of the 90th percentile. Normal Pattern Deviation and RNFL thickness values are indicated with the letter 'N'. Abnormal DNP values (< 10%) are highlighted in red.

Case	Location	Quadrant	Pattern Deviation	RNFL (G-H)	RNFL (H)	MC N ₀	MC N ₁	N ₉₀	SE	Log ₁₀ Ratio	SDI
1	(-6, 12)	ST	< 0.5%	< 5%	< 1%	< 10%	N	< 10%	N	N	< 10%
3	(10, 8)	ST	< 5%	N	N	N	N	N	N	N	N
3	(6, 12)	ST	< 1%	N	N	< 10%	< 10%	< 10%	N	N	< 10%
4	(-10, 8)	ST	< 5%	N	N	< 10%	N	N	N	N	< 10%
5	(10, 8)	ST	< 5%	N	N	< 10%	N	N	N	N	< 10%
6	(10, 8)	ST	N	N	N	< 10%	< 10%	N	< 10%	N	< 10%
8	(-14, 8)	ST	N	< 1%	N	< 10%	< 10%	< 10%	N	N	< 10%
10	(10, 12)	ST	N	N	< 1%	N	N	N	N	N	N
11	(-10, 8)	ST	N	N	N	N	N	N	N	N	N
12	(14, 8)	ST	N	N	N	N	N	N	N	N	N
13	(10, 8)	ST	N	N	N	N	N	N	N	N	N
14	(10, 8)	ST	N	N	N	N	N	N	N	N	N
15	(-10, 8)	ST	N	N	N	N	N	N	N	N	N
16	(10, 8)	ST	N	N	N	N	N	N	N	N	N
17	(-10, 8)	ST	N	N	N	N	N	N	N	N	N
18	(10, 8)	ST	N	N	N	N	N	N	N	N	N
19	(-14, 8)	ST	N	N	N	N	N	N	N	N	N
20	(-10, 8)	ST	N	< 5%	< 5%	N	< 10%	N	< 10%	N	N
21	(10, 8)	ST	N	N	N	N	< 10%	N	< 10%	N	N
22	(10, 8)	ST	N	N	N	N	N	N	N	N	N
23	(-10, 8)	ST	N	N	N	< 10%	N	N	N	N	< 10%
24	(-10, 8)	ST	N	N	N	N	N	N	N	N	N
25	(10, 8)	ST	N	N	N	N	N	N	N	N	N
26	(10, 8)	ST	N	N	N	N	N	N	N	N	N
27	(-10, 8)	ST	N	N	N	N	N	N	N	N	N
28	(10, 8)	ST	N	N	N	N	N	N	N	N	N
29	(-10, 8)	ST	N	N	N	< 10%	N	< 10%	N	< 10%	< 10%
30	(-10, 8)	ST	N	N	N	N	N	< 10%	N	< 10%	N

Table 6.25 Motion discrimination: Summary of results for individuals with OAG (case numbers 1 to 10) and normal individuals (case numbers 11 to 30) at the superior temporal location, showing Pattern Deviation in terms of p-values, RNFL thickness in terms of p-values and DNP values in terms of the 90th percentile. Normal Pattern Deviation and RNFL thickness values are indicated with the letter 'N'. Abnormal DNP values (< 10%) are highlighted in red.

Case	Location	Quadrant	Pattern Deviation	RNFL (G-H)	RNFL (H)	MC N ₀	MC N _s	N _{eq}	SE	Log ₁₀ Ratio	SDI
1	(10, 8)	SN	< 0.5%	< 5%	< 5%	< 10%	< 10%	N	< 10%	N	< 10%
3	(-10, 8)	SN	N	N	N	< 10%	N	< 10%	N	< 10%	< 10%
4	(10, 8)	SN	N	N	N	N	N	N	N	N	N
5	(-10, 8)	SN	N	N	N	N	< 10%	N	< 10%	N	N
6	(-10, 8)	SN	N	N	N	< 10%	< 10%	N	N	N	< 10%
7	(10, 8)	SN	N	N	N	N	< 10%	N	< 10%	N	N
8	(14, 8)	SN	N	N	N	< 10%	N	< 10%	N	N	< 10%
10	(-14, 8)	SN	N	N	N	N	N	< 10%	N	N	N
11	(10, 8)	SN	N	N	N	N	< 10%	N	< 10%	N	N
12	(-14, 8)	SN	N	N	N	N	N	N	N	N	N
13	(-10, 8)	SN	N	N	N	N	< 10%	N	< 10%	N	N
14	(-10, 8)	SN	N	N	N	N	N	N	N	N	N
15	(10, 8)	SN	N	N	N	N	N	N	N	N	N
16	(-10, 8)	SN	N	N	N	N	N	< 10%	N	N	N
17	(10, 8)	SN	N	N	N	N	N	N	N	N	N
18	(-10, 8)	SN	N	N	N	N	N	N	N	N	N
19	(14, 8)	SN	N	N	N	N	N	N	N	N	N
20	(10, 8)	SN	N	N	N	N	N	N	N	N	N
21	(-10, 8)	SN	N	N	N	N	N	N	N	N	N
22	(-10, 8)	SN	N	N	N	N	N	N	N	N	N
23	(10, 8)	SN	N	N	N	< 10%	N	< 10%	N	< 10%	< 10%
24	(10, 8)	SN	N	N	N	< 10%	N	N	N	N	< 10%
25	(-10, 8)	SN	N	N	N	N	N	N	N	N	N
26	(-10, 8)	SN	N	N	N	N	N	N	N	< 10%	N
27	(10, 8)	SN	N	N	N	N	N	N	N	N	N
28	(-10, 8)	SN	N	N	N	N	N	N	N	N	N
29	(10, 8)	SN	N	N	N	N	N	N	N	N	N
30	(10, 8)	SN	N	N	N	N	N	N	N	N	N

Table 6.26 Motion discrimination: Summary of results for individuals with OAG (case numbers 1 to 10) and normal individuals (case numbers 11 to 30) at the superior nasal location, showing Pattern Deviation in terms of p-values, RNFL thickness in terms of p-values and DNP values in terms of the 90th percentile. Normal Pattern Deviation and RNFL thickness values are indicated with the letter 'N'. Abnormal DNP values (< 10%) are highlighted in red.

Case	Location	Quadrant	Pattern Deviation	RNFL (G-H)	RNFL (H)	MC N ₀	MC N _t	N _{eq}	SE	Log ₁₀ Ratio	SDI
1	(10, -12)	IN	< 5%	N	N	< 10%	N	< 10%	N	< 10%	< 10%
3	(-6, -12)	IN	< 5%	N	N	N	N	N	N	N	N
4	(10, -8)	IN	N	N	N	N	< 10%	N	< 10%	N	N
5	(-10, -8)	IN	N	N	N	N	N	N	N	N	N
6	(-10, -8)	IN	N	N	N	N	N	< 10%	N	N	< 10%
7	(10, -8)	IN	N	N	N	N	N	N	N	N	N
10	(-10, -8)	IN	N	N	N	N	N	N	N	N	N
11	(10, -8)	IN	N	N	N	N	N	N	N	N	N
12	(-14, -8)	IN	N	N	N	N	N	N	N	N	N
13	(-10, -8)	IN	N	N	N	< 10%	N	N	N	N	< 10%
14	(-10, -8)	IN	N	N	N	N	N	N	N	N	N
15	(10, -8)	IN	N	N	N	N	N	N	N	N	N
16	(-10, -8)	IN	N	N	N	N	N	< 10%	N	N	N
17	(10, -8)	IN	N	N	N	N	N	N	N	N	N
18	(-10, -8)	IN	N	N	N	N	N	N	N	N	N
19	(14, -8)	IN	N	N	N	N	< 10%	N	N	N	N
20	(10, -8)	IN	N	N	N	N	N	N	N	N	N
21	(-10, -8)	IN	N	N	N	N	N	N	< 10%	N	N
22	(-10, -8)	IN	N	N	N	N	N	N	N	N	N
23	(10, -8)	IN	N	N	N	N	N	N	N	N	N
24	(10, -8)	IN	N	N	N	N	< 10%	N	< 10%	N	N
25	(-10, -8)	IN	N	N	N	N	N	N	N	N	N
26	(-10, -8)	IN	N	N	N	N	N	N	N	< 10%	N
27	(10, -8)	IN	N	< 5%	N	N	N	N	N	N	N
28	(-10, -8)	IN	N	N	N	N	N	N	N	N	N
29	(10, -8)	IN	N	N	N	< 10%	N	< 10%	N	< 10%	< 10%
30	(10, -8)	IN	N	N	N	N	N	N	N	N	N

Table 6.27 Motion discrimination: Summary of results for individuals with OAG (case numbers 1 to 10) and normal individuals (case numbers 11 to 30) at the inferior nasal location, showing Pattern Deviation in terms of p-values, RNFL thickness in terms of p-values and DNP values in terms of the 90th percentile. Normal Pattern Deviation and RNFL thickness values are indicated with the letter 'N'. Abnormal DNP values (< 10%) are highlighted in red.

Case	Location	Quadrant	Pattern Deviation	RNFL (G-H)	RNFL (H)	MC N ₀	MC N ₁	N _{eq}	SE	Log ₁₀ Ratio	SDI
1	(-10, -8)	IT	N	N	N	N	N	< 10%	N	< 10%	N
4	(-10, -8)	IT	N	N	N	N	N	N	N	N	N
5	(10, -8)	IT	N	N	N	N	N	N	N	N	N
6	(10, -8)	IT	N	N	N	< 10%	< 10%	< 10%	N	N	< 10%
7	(-10, -8)	IT	< 5%	N	N	< 10%	N	< 10%	N	< 10%	< 10%
7	(-6, -12)	IT	< 2%	N	N	< 10%	N	< 10%	N	N	< 10%
8	(-14, -8)	IT	N	N	< 1%	< 10%	< 10%	< 10%	N	< 10%	< 10%
9	(-14, -8)	IT	N	N	N	< 10%	< 10%	< 10%	N	N	< 10%
9	(-10, -8)	IT	< 0.5%	< 1%	< 1%	< 10%	N	< 10%	N	< 10%	< 10%
9	(-6, -8)	IT	< 0.5%	< 1%	< 1%	< 10%	< 10%	< 10%	N	N	< 10%
10	(10, -8)	IT	N	N	N	< 10%	N	< 10%	N	< 10%	< 10%
11	(-10, -8)	IT	N	N	N	N	N	N	N	N	N
12	(14, -8)	IT	N	N	N	N	N	N	N	N	N
13	(10, -8)	IT	N	N	N	N	< 10%	N	< 10%	N	N
14	(10, -8)	IT	N	N	N	N	N	N	N	N	N
15	(-10, -8)	IT	N	N	N	N	N	< 10%	N	< 10%	N
16	(10, -8)	IT	N	N	N	N	N	N	N	N	N
17	(-10, -8)	IT	N	N	N	N	N	N	N	N	N
18	(10, -8)	IT	N	N	N	N	N	N	N	N	N
19	(-14, -8)	IT	N	N	N	< 10%	N	N	N	N	< 10%
20	(-10, -8)	IT	N	N	N	N	N	N	N	N	N
21	(10, -8)	IT	N	N	N	N	N	N	N	N	N
22	(10, -8)	IT	N	N	N	N	< 10%	N	< 10%	N	N
23	(-10, -8)	IT	N	N	N	N	N	N	N	< 10%	N
24	(-10, -8)	IT	N	N	N	N	N	N	N	N	N
25	(10, -8)	IT	N	N	N	N	N	N	N	N	N
26	(10, -8)	IT	N	N	N	N	N	N	N	N	N
27	(-10, -8)	IT	N	< 5%	< 5%	N	N	N	N	N	N
28	(10, -8)	IT	N	N	N	N	N	N	N	N	N
29	(-10, -8)	IT	N	N	N	N	N	< 10%	N	N	N
30	(-10, -8)	IT	N	N	N	< 10%	N	N	N	N	< 10%

Table 6.28 Motion discrimination: Summary of results for individuals with OAG (case numbers 1 to 10) and normal individuals (case numbers 11 to 30) at the inferior temporal location, showing Pattern Deviation in terms of p-values, RNFL thickness in terms of p-values and DNP values which are highlighted above the 90th percentile. Normal Pattern Deviation and RNFL thickness values are indicated with the letter 'N'.

6.11 Discussion

6.11.1 The potential for the learning effect

Normal individuals demonstrated a clinically meaningful learning effect, in absolute terms, across the visits for both the detection and the discrimination tasks for MC N_0 and for MC N_e . Between-individual variability tended to decline with subsequent visits for both tasks. The learning effect was also present in terms of proportionate change in threshold. For the detection task, the learning effect was greatest from visit 1 to visit 2, and was near zero between visit 2 and visit 3. This finding is comparable to existing studies of learning in SAP (Horani et al., 2002; Rossetti et al., 2006; Wild et al., 2006). For the discrimination task, the learning effect occurred between visit 1 and visit 2, and persisted, but lessened, between visit 2 and visit 3. The continued learning effect with the discrimination task is likely to arise from its comparative complexity compared to the motion detection task. The extent to which the learning effect would persist to a fourth visit is unknown. It should be noted that the discrimination task was conducted following the series of visits for the detection task and, despite this, exhibited a clinically meaningful learning effect.

N_{eq} did not demonstrate a clinically meaningful improvement in normal individuals across the three visits, either in absolute or in proportionate terms. SE improved from visit 1 to visit 2 with the detection task, and continued to improve from visit 2 to visit 3 with the discrimination task. Therefore, the learning effect can be explained by the improved ability of an individual to correctly interpret the available stimulus information. These findings are consistent with another study of perceptual learning, which found that internal noise levels were unchanged within a repeated discrimination task and improved performance was explained by increased efficiency (Gold et al., 1999). Therefore, the perimetric

learning effect, observed in a range of studies (Rossetti et al., 2006; Wild et al., 2006; Contestabile et al., 2007) can be attributed to improved detection strategies that enhance perceptual signal strength.

The learning effect for both the detection and discrimination tasks, in absolute terms, across the three visits for the individuals with OAG was present for MC N_0 , MC N_e and SE. However, the between-individual variability in performance was greater than that for the normal individuals. N_{eq} worsened over the three visits. The apparent worsening in N_{eq} is likely to be explained by the wider distribution of N_{eq} amongst the individuals with OAG, rather than the increasing levels of neural noise.

The learning effect for the detection task, in proportionate terms, was present for MC N_0 , MC N_e and SE across the three visits. The learning effect for the discrimination task, in proportionate terms was only present for SE, and persisted from visit 2 to visit 3. This outcome may be explained either by the variation within- and between-individuals in the functional damage at the respective stimulus locations or by the complexity of the task for those with OAG. The latter would suggest that further improvement would be obtained over subsequent visits.

6.11.2 MC N_0 , MC N_e , N_{eq} and SE of the normal eye

In the normal individuals, MC N_0 was lowest for foveal viewing and comparably lower at other locations. This was true for both the motion detection and the motion discrimination tasks. Therefore, foveal viewing exhibited greatest sensitivity to the stimulus. In the presence of noise, MC N_e was comparably worse with foveal viewing than at all other locations. This finding held for both the motion detection and the motion discrimination

tasks. It is postulated for two reasons that the dynamic noise mask disrupts visual processing with foveal viewing comparably more than at other stimulus locations. Firstly, the fovea is tuned to high spatial frequency stimuli, owing to low convergence of cones onto RGCs via bipolar cells (Dacey, 1993), and exhibits maximum cone density and an absence of vasculature (Curcio et al., 1990) resulting in high spatial resolution at later stages of visual processing (Curcio and Allen, 1990; Rodieck, 1998). Therefore, the spatial frequencies within the dynamic noise mask will impact visual perception of the stimulus. Secondly, as eccentricity increases from the fovea, retinal sampling density decreases (Rovamo and Virsu, 1979; Rovamo et al., 1992) and this decrease is thought to become the limiting factor in spatial resolution (Rossi and Roorda, 2009). Therefore, the higher spatial frequencies within the dynamic noise mask will be less perceptible than with foveal viewing.

Given the higher spatial resolution of the fovea, it is reasonable to question why this location performed comparably better than the peripheral locations for the detection and discrimination of the low spatial frequency stimulus, when presented in the absence of noise. The reason may be explained by the edge-effects associated with a square stimulus (Hogg and Anderson, 2009). At the fovea, low thresholds in the absence of the noise mask may be influenced by the perception of a high-spatial frequency stimulus edge, which becomes less apparent in the presence of the noise mask. Comparable studies have indicated that normal individuals would exhibit comparably lower sensitivity to a soft-edged stimulus e.g. with contrast at the stimulus edge attenuated with a cosine ramp. However, on-going studies in the School with the DNP stimulus suggest that this is not the case (Alshaghroud, 2010; Wild, 2010). Therefore, higher sensitivities at the fovea may be

explained by the high sampling density of the photoreceptor mosaic, which decreases with eccentricity (Green, 1970).

N_{eq} was lowest with foveal viewing, for both the motion detection and the motion discrimination tasks, when compared with peripheral locations. This finding indicates that the fovea exhibited the lowest level of baseline neural activity of all locations. The comparative reduction in N_{eq} can be explained by high sensitivity in terms of MC N_0 levels, which, as has been discussed, may have been influenced by the anatomical characteristics of the fovea (Curcio and Allen, 1990; Curcio et al., 1990). N_{eq} levels of the normal individuals were generally between 10 and $150^{10^{-7}} \text{ deg}^2 \text{ sec}^{-1}$ at the various locations of the visual field. These values are consistent with that of $9.9^{10^{-7}} \text{ deg}^2$ for foveal viewing using a static noise mask in normal individuals of a similar age range (Pardhan, 2004; Radhakrishnan and Pardhan, 2006).

SE was lowest at the fovea for both the motion detection and discrimination task. The comparative low level of SE can be explained by the performance of the fovea in terms of MC N_e , which, as has been discussed indicates that the fovea exhibited comparably greater disruption in visual processing due to the higher spatial frequencies within the noise mask. SE in the normal eye was generally between 1.2 and 2.5%, which is comparable to that of 1-2% for a drifting grating stimulus presented to normal individuals (Simpson et al., 2003a; Simpson et al., 2003b).

N_{eq} and SE measures exhibited comparatively greater between-individual variability than their respective input measures of MC N_0 and MC N_e . This increased variability is explained by the mathematical transformation which is used to calculate N_{eq} and SE (See

Section 6.2.2). The transformation magnifies the values at the extremes of the data range. For all measures, the discrimination task exhibited comparably greater between-individual variability than the detection task. The increase in the magnitude of between-individual variability may be explained by the comparative difficulty of the discrimination task with peripheral viewing (Green, 1983). Increased uncertainty with the discrimination task may explain comparably higher levels of N_{eq} when compared with the detection task (Mareschal et al., 2008). The judgement of direction is considered to be more difficult than the judgement of motion, alone, (Ball et al., 1983), and is particularly true for older individuals (Bennett et al., 2007). With the exception of the ST location, SE was comparable for the detection and the discrimination task. However, SE within a discrimination task will systematically decline at higher stimulus speeds (Simpson et al., 2003a) although this was not considered within the scope of this investigation.

6.11.3 Age-dependency in terms of MC N_0 , MC N_e , N_{eq} and SE

As would be expected, measures of MC N_0 and MC N_e increased with age. This finding is comparable to other studies of contrast sensitivity for sine wave gratings of low and high spatial frequencies (Arundale, 1978; Ross et al., 1985; Wright and Drasdo, 1985; Elliott et al., 1990; Willis and Anderson, 2000; McKendrick et al., 2007). SE decreased with increasing age for both the detection and the discrimination tasks. This finding is consistent with other studies (Pardhan et al., 1996; Bennett et al., 1999; Falkenberg and Bex, 2007) and can be explained by the physiological loss of RGCs with ageing (Bennett et al., 1999; Kerrigan-Baumrind et al., 2000) rather than the reduced retinal illumination arising from reduced pupil size and loss of transparency of the crystalline lens (Sloane et al., 1988). N_{eq} increased with age which may, in part, be due to the described changes

within the crystalline lens (Kersten et al., 1988; Pardhan et al., 1993) or increased neural firing (Pardhan, 2004; Betts et al., 2007; Falkenberg and Bex, 2007)

6.11.4 Determination of MC N_0 , MC N_e , N_{eq} , SE, Log_{10} Ratio and SDI in OAG

At the 90th percentile, DNP clearly identified individuals with OAG who exhibited both PD_{Ab} and/ or $RNFL_{Ab}$ for the detection and also for the discrimination tasks (Tables 6.21 - 6.28). The most sensitive measures were MC N_0 and the SDI.

For the detection task, MC N_0 and the SDI identified 11 and 10 stimulus locations as abnormal, respectively, out of a group total of 16 locations with PD_{Ab} and/ or $RNFL_{Ab}$. Of the remaining 5/ 6 stimulus locations, 4 exhibited a PD probability value at the 5% level and a normal RNFL thickness, one exhibited PD_N $RNFL_{Ab}$. In addition, MC N_0 and the SDI identified 11 and 9 locations, respectively which exhibited PD_N $RNFL_N$. It is possible that the latter could have arisen as a consequence of an incomplete learning effect.

For the discrimination task, MC N_0 and the SDI each identified 12 stimulus locations as abnormal, respectively, out of 15 locations with PD_{Ab} and/ or $RNFL_{Ab}$. Of the remaining 3 locations, 2 exhibited a PD probability value at the 5% level and a normal RNFL thickness, and one exhibited PD_N $RNFL_{Ab}$. In addition, MC N_0 and the SDI identified 7 and 8 locations, respectively, which exhibited PD_N $RNFL_N$. Again, it is possible that the latter outcome could have arisen as a consequence of an incomplete learning effect.

Given that the 90th percentile was used to define the confidence limits of DNP, two normal individuals would always exhibit apparent abnormality for each of the DNP outcome

measures. Three normal individuals exhibited stimulus locations which were apparently abnormal by three or more different DNP measures (Tables 6.21 – 6.28).

The effectiveness of the DNP stimulus in the absence of noise may be explained by its spatial and temporal parameters, designed to preferentially activate the M-pathway of the visual system (Merigan and Katz, 1990; Merigan et al., 1991a). The M-pathway is known to have a pivotal role in the perception of motion (Ogden, 1984; Callaway, 2005), a capability which is believed to be impaired in OAG (Falcao-Reis et al., 1990; Yoshiyama and Johnson, 1997; McKendrick et al., 2007; Hot et al., 2008). The limited effect of the dynamic noise mask was unexpected with respect to its ability to differentiate normal individuals from individuals with OAG given that external visual noise has previously differentiated normal individuals from individuals with OAG (Yates et al., 1998; Odom et al., 2006; Falkenberg and Bex, 2007).

There are several possible reasons to explain why measures of N_{eq} and SE were less sensitive than measures of MC N_0 . Firstly, as was explained within the hypothesis (Chapter 3, Section 3.3.5, and Figure 6.108 below), N_{eq} and SE levels are believed to correlate with a particular stage of damage in OAG. As such, N_{eq} will exceed normative levels only at a stage which is thought to precede RGC death, a stage which is believed to involve cell shrinkage. Beyond this stage N_{eq} is expected to decline to normative levels as RGC death becomes widespread. For the purposes of this study, a cohort of individuals with OAG was recruited with varying degrees of glaucomatous damage. Therefore, it is reasonable to expect that some locations with advanced structural and functional damage to the RNFL would exhibit normative levels of N_{eq} since the summed response of elevated N_{eq} due to dying/ shrinking cells and a sub-normal N_{eq} from dead cells may result in a

normal level of N_{eq} . This is comparable to the findings of another study (Falkenberg and Bex, 2007).

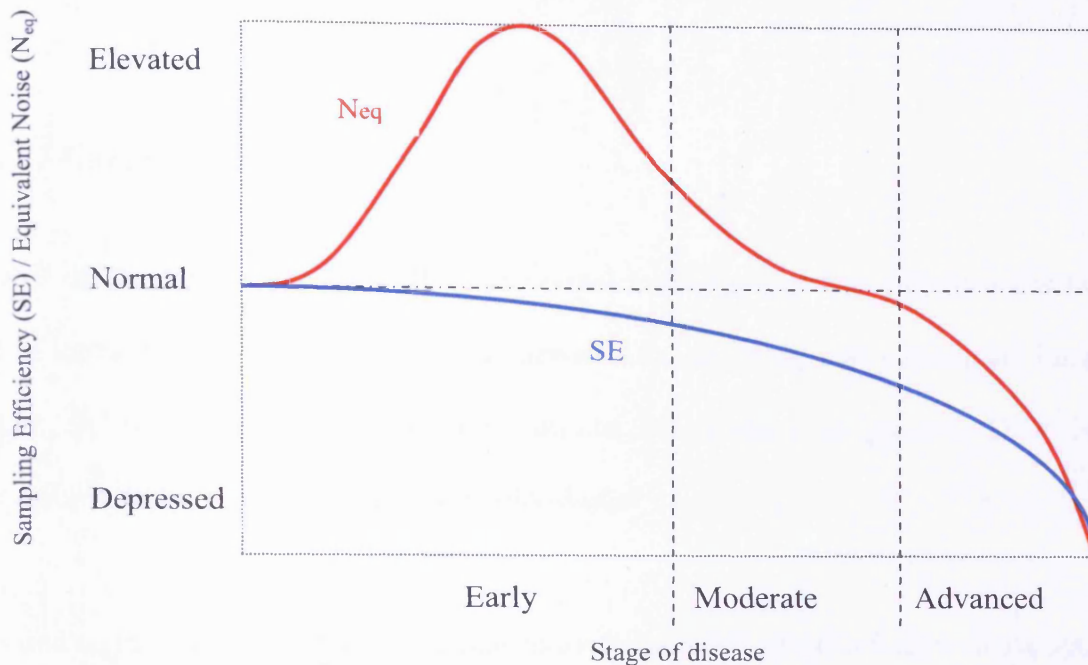


Figure 6.108 Duplicate of Figure 3.1, Chapter 3 repeated for the purposes of the Discussion. Schematic illustrating the hypothesised change in N_{eq} and SE with the progression of OAG. N_{eq} is raised in early OAG due to increased neural activity arising from RGC shrinkage. N_{eq} then declines to normative levels in moderate OAG due to the summed response of shrinking and dying RGCs. Thereafter N_{eq} falls as a result of depressed neural activity, due to RGC death. SE is at normative levels in early OAG, as the RGCs undergo shrinkage, but remain functional. Thereafter, SE falls in moderate and advanced stages of OAG due to continuing RGC death.

According to the cell shrinkage hypothesis (Chapter 3, Section 3), SE is expected to fall with increasing RGC death. In this study, individuals with PD_{Ab} and/or $RNFL_{Ab}$ continued to elicit normative SE at the given locations. As has been discussed, the noise mask was considered less effective for these individuals. Whilst the dynamic noise mask was developed to optimally mask the underlying stimulus, it was clearly not optimised for the assessment of individuals with OAG. Therefore, although the mask provided the necessary

thresholds to elicit N_{eq} and SE, it did not reduce perception to the DNP stimulus to the extent that would be clinically useful. This may explain the normative levels of SE in locations with functional and/ or structural damage.

6.12 Conclusions

DNP demonstrates a learning effect in normal individuals and in individuals with OAG. The learning effect is attributed to improved SE, indicating that individuals improve in their ability to utilise the available stimulus information. In general, DNP outcome measures decline with age in normal individuals.

Based on the 90th percentile for normal individuals, DNP identified individuals with OAG who exhibited PD_{Ab} and $RNFL_{Ab}$ for both the detection and the discrimination tasks.

The compelling finding of the study is that the DNP method is highly sensitive for the detection of OAG in individuals exhibiting PD_{Ab} and/ or $RNFL_{Ab}$. Clearly, individuals with OAG demonstrate abnormal levels of N_{eq} , particularly at locations with PD_N $RNFL_N$. This is commensurate with the shrinkage hypothesis. In addition, DNP identifies individuals with OAG that do not exhibit PD_{Ab} or $RNFL_{Ab}$. This latter outcome could have arisen due to an incomplete learning effect in some individuals with OAG and this aspect requires further investigation.

Overall, the results do not disprove the hypothesis that a detectable, intermediary stage of shrinkage will precede RGC death. DNP clearly warrants further development.

7 General conclusions and proposals for future work

This thesis was concerned with the development of a new method for assessing visual function, called Dynamic Noise Perimetry (DNP), based upon the measurement of contrast sensitivity to a temporally modulated sine wave grating, in the absence ($MC N_0$) and in the presence ($MC N_e$) of a dynamic noise mask. The technique permits the estimation of equivalent noise (N_{eq}) and sampling efficiency (SE) at locations within the visual field; information which may prove to be useful for identifying OAG prior to conventional methods of detection and at a stage in which the disease is characterised by RGC shrinkage.

The development of DNP was divided into two stages. Firstly, the parameters of the dynamic noise mask were optimised for the normal eye for use with a temporally modulated grating. An optimised mask ensured that the limited contrast range of the display would be sufficient for clinical studies. Secondly, a sine-wave grating, targeted at the magnocellular stream of the visual pathway, was used to assess the spatio-temporal contrast sensitivity in a group of normal individuals and in a group of individuals with OAG. The optimised noise mask was used to measure $MC N_0$, $MC N_e$, N_{eq} and SE, and to characterise the following: the presence of a learning effect for normal individuals and for individuals with OAG, the distribution of DNP measures for normal individuals, and to characterise the effects of age. Thereafter, DNP was used to identify individuals with OAG at the 90th percentile of the distribution of normal individuals. These findings were compared with the Pattern Deviation probability values of SAP and with RNFL thickness derived by OCT.

7.1 Review of findings

7.1.1 The spatial limits of the dynamic noise mask

The study designed to optimise the parameters of the dynamic noise mask showed that critical check size decreased in terms of checks per cycle with increasing temporal frequency of a drifting sine wave grating. This finding was attributed to the limits in spatial processing at high temporal frequencies which reduces grating visibility when masked with external noise. Eccentric viewing of low spatial frequency drifting gratings showed that the critical check size within a spatio-temporal noise mask was influenced by the temporal frequency of the underlying grating.

7.1.2 Clinical application of Dynamic Noise Perimetry

For both the detection and the discrimination tasks, DNP exhibited a learning effect in absolute and proportionate terms, based on measures of MC N_0 , MC N_e and SE. N_{eq} remained broadly constant over consecutive visits for the normal individuals. However, N_{eq} worsened in absolute terms over the course of consecutive visits in OAG. The DNP outcome measures of MC N_0 , MC N_e , N_{eq} and SE in the normal individuals generally worsened with age.

The overwhelming conclusion was that, at the 90th percentile, DNP identified individuals for OAG that exhibited abnormal Pattern Deviation probability (PD_{Ab}) using SAP and/ or abnormal RNFL thickness ($RNFL_{Ab}$), from a group of age-matched normal individuals with both the detection and the discrimination tasks. The most sensitive DNP measures

proved to be the Michelson contrast threshold in the absence of the noise mask ($MC N_0$) and a derivative of N_{eq} and SE called the signal detection index (SDI).

7.2 Proposals for future work

The results of the clinical study of individuals with OAG are sufficiently promising to warrant a more extensive study of normal individuals and individuals with OAG. Within the subsequent study, it will be important to determine test-retest variability.

A further study is needed to determine which motion task is more suitable as a clinical tool. Although the motion detection task exhibited less between-individual variability amongst normal individuals, the discrimination task only involved the need for a single stimulus presentation. As such, it reduced the time required to elicit a single threshold measure to half that of the detection task. The length of time required for any perimetric method is a major concern for the clinical application of psychophysical tests. Individuals are susceptible to fatigue when perimetric tests are lengthy or complex and the economic considerations associated with the chair time are also important. To reduce the likelihood of fatigue, further development of the algorithm should be prioritised as a means of speeding up the entire test, such as methods currently used in clinical perimetry e.g. PEST and ZEST algorithms (Anderson and Johnson, 2006).

The dynamic noise mask was less effective than expected in distinguishing individuals with OAG from normal individuals. Therefore, Michelson contrast in the presence of noise ($MC N_e$) and sampling efficiency (SE) were less sensitive to PD_{Ab} and $RNFL_{Ab}$ than other

DNP measures. Although the noise mask had been optimised for use with the DNP stimulus, it had not been specifically developed as a detection tool for OAG. For individuals with OAG, it is possible that the higher spatial frequencies within the noise mask confounded its ability to degrade the DNP stimulus. Given that the noise mask is a complex stimulus containing many frequencies, a Fourier analysis of the mask may help to interpret its characteristics. Once the characteristics of the mask are fully understood, further development of the DNP method should involve the development of a novel dynamic noise mask that is optimised for individuals with OAG.

The square grating stimulus used in clinical studies was designed to have a hard-edged stimulus window, which was comparable to other temporal contrast sensitivity tests such as Frequency Doubling Perimetry. There is some evidence to suggest that a hard-edged stimulus window can produce perceptual artefacts, and it is speculated that a Gaussian filtered edge is more likely to elicit higher thresholds, when compared with a hard-edged grating (Hogg and Anderson, 2009). Therefore a Gaussian-edged stimulus may be more appropriate for the further development of this method. Further studies should compare the influence of Gaussian-edged stimuli on sampling efficiency and equivalent noise levels, when compared with a hard-edged stimulus. However, on-going studies in this respect suggest that Gaussian stimuli are not more sensitive than hard-edged stimuli, for the detection of OAG (Alshaghroud, 2010; Wild, 2010).

Several other clinical applications of DNP should also be considered. For example, ARMD is a leading cause of blindness in the Western world. Early detection may permit individuals to adopt lifestyle changes (Sorensen and Kemp, 2010) or use nutritional supplements to delay the onset of this disease. This method can be adapted to a macular

test by changing grating parameters to higher spatial frequencies. DNP may also have a role in the detection of neurological diseases such as multiple sclerosis, which may exhibit subtle subclinical deficiencies of visual function, measurable with N_{eq} and/ or SE.

Finally, both grating and noise stimuli have been developed in greyscale, to elicit a response from largely achromatic regions of the visual pathway. As such, the clinical use of chromatic gratings and noise can also be considered for future work, to elicit responses from chromatic pathways e.g. koniocellular pathway, which are known to be affected in OAG.

References

Abbey C, and Eckstein M (2006) Classification images for detection, contrast discrimination, and identification tasks with a common ideal observer. *Journal of Vision* 6: 335-355.

Adams A, Rodic R, Husted R, and Stamper R (1982) Spectral sensitivity and color discrimination changes in glaucoma and glaucoma-suspect patients. *Investigative Ophthalmology and Visual Science* 23: 516-524.

Agarwal R, Gupta S K, Agarwal P, Saxena R, and Agrawal S S (2009) Current concepts in the pathophysiology of glaucoma. *Indian Journal of Ophthalmology* 57: 257-266.

Aghaian E, Choe J E, Lin S, and Stamper R L (2004) Central corneal thickness of Caucasians, Chinese, Hispanics, Filipinos, African Americans, and Japanese in a glaucoma clinic. *Ophthalmology* 111: 2211-2219.

Albon J, Karwatowski W S S, Easty D L, Sims T J, and Duance V C (2000a) Age related changes in the non-collagenous components of the extracellular matrix of the human lamina cribrosa. *British Journal of Ophthalmology* 84: 311-317.

Albon J, Purslow P P, Karwatowski W S S, and Easty D L (2000b) Age related compliance of the lamina cribrosa in human eyes. *British Journal of Ophthalmology* 84: 318-323.

Alshaghroud K (2010) Cardiff School of Optometry and Vision Sciences. *Personal communication*.

Alward W L M (2000) Frequency doubling technology perimetry for the detection of glaucomatous visual field loss. *American Journal of Ophthalmology* 129: 376-378.

Anderson A J, and Johnson C A (2002) Mechanisms isolated by frequency-doubling technology perimetry. *Investigative Ophthalmology and Visual Science* 43: 398-401.

Anderson A J, and Johnson C A (2003) Frequency-doubling technology perimetry. *Ophthalmology Clinics of North America* 16: 213-225.

Anderson A J, and Johnson C A (2006) Comparison of the ASA, MOBS, and ZEST threshold methods. *Vision Research* 46: 2403-2411.

Anderson D R, and Patella V (1999) *Automated static perimetry. 2nd Edition*. St. Louis: Mosby, Inc.

Anderson R S (2006) The psychophysics of glaucoma: Improving the structure/function relationship. *Progress in Retinal and Eye Research* 25: 79-97.

Anderson R S, and O'Brien C (1997) Psychophysical evidence for a selective loss of M ganglion cells in glaucoma. *Vision Research* 37: 1079-1083.

Anderson R S, Redmond T, McDowell D R, Breslin K, and Zlatkova M (2009) The robustness of various forms of perimetry to different levels of induced intraocular straylight. *Investigative Ophthalmology and Visual Science*: 4022-4028.

Ansari E A, Morgan J E, and Snowden R J (2002a) Glaucoma: squaring the psychophysics and neurobiology. *British Journal of Ophthalmology* 86: 823-826.

Ansari E A, Morgan J E, and Snowden R J (2002b) Psychophysical characterisation of early functional loss in glaucoma and ocular hypertension. *British Journal of Ophthalmology* 86: 1131-1135.

Araie M, Sekine M, Suzuki Y, and Koseki N (1994) Factors contributing to the progression of visual-field damage in eyes with normal-tension glaucoma. *Ophthalmology* 101: 1440-1444.

Arden G B (1978) The importance of measuring contrast sensitivity in cases of visual disturbance. *British Journal of Ophthalmology* 62: 198-209.

Arden G B, and Jacobson J J (1978) A simple grating test for contrast sensitivity: preliminary results indicate value in screening for glaucoma. *Investigative Ophthalmology and Visual Science* 17: 23-32.

Artes P H, and Chauhan B C (2005) Longitudinal changes in the visual field and optic disc in glaucoma. *Progress in Retinal and Eye Research* 24: 333-354.

Arundale K (1978) An investigation into the variation of human contrast sensitivity with age and ocular pathology. *British Journal of Ophthalmology* 62: 213-215.

Asman P, and Heijl A (1992) Glaucoma Hemifield Test: Automated Visual Field Evaluation. *Arch Ophthalmol* 110: 812-819.

Asman P, Wild J M, and Heijl A (2004a) Appearance of the pattern deviation map as a function of change in area of localized field loss. *Investigative Ophthalmology and Visual Science* 45: 3099-3106.

Asman P, Wild J M, and Heijl A (2004b) Appearance of the pattern deviation map as a function of change in area of localized field loss. *Investigative Ophthalmology and Visual Science* 45: 3099-3106.

Aumala O (1996) Turning interference and noise into improved resolution. *Measurement* 19: 41-48.

Azura-Blanco A, Harris A, Cantor L B, Abreu M M, and Weinland M (1998) Effects of short term increase of intraocular pressure on optic disc cupping. *British Journal of Ophthalmology* 82: 880-883.

Bach M (2001) Electrophysiological approaches for early detection of glaucoma. *European Journal of Ophthalmology* 11: S41-S49.

Bach M, and Speidel-Fiaux A (1989) Pattern electroretinogram in glaucoma and ocular hypertension. *Documenta Ophthalmologica* 73: 173-181.

Bagga H, Feuer W J, and Greenfield D S (2006) Detection of psychophysical and structural injury in eyes with glaucomatous optic neuropathy and normal standard automated perimetry. *Archives of Ophthalmology* 124: 169-176.

Bagga H, Greenfield D S, and Feuer W J (2005) Quantitative assessment of atypical birefringence images using scanning laser polarimetry with variable corneal compensation. *American Journal of Ophthalmology* 139: 437-446.

Balachandran C, Graham S, Klistorner A, and Goldberg I (2006) Comparison of objective diagnostic test in glaucoma: Heidelberg retinal tomograph and multifocal visual evoked potentials. *Journal of Glaucoma* 15: 110-116.

Baleanu D, Tornow R P, Horn F K, Laemmer R, Roessler C W, Juenemann A G, Kruse F E et al. (2009) Retinal Nerve Fiber Layer Thickness in Normals Measured by Spectral Domain OCT. *Journal of Glaucoma* 30: 30.

Ball K, Sekuler R, and Machamer J (1983) Detection and identification of moving targets. *Vision Research* 23: 229-238.

Band L R, Hall C L, Richardson G, Jensen O E, Siggers J H, and Foss A J (2009) Intracellular flow in optic nerve axons: A mechanism for cell death in glaucoma. *Investigative Ophthalmology and Visual Science* 50: 3750-3758.

Barlow H B (1956) Retinal noise and absolute threshold. *Journal of the Optical Society of America A - Optics Image Science and Vision* 46: 634-639.

Barlow H B (1957) Increment thresholds at low intensities considered as signal/noise discrimination. *Journal of Physiology* 136: 469-488.

Barry C, Eikelboom R, Kanagasingam Y, Jitsakia L, Morgan W, House P, and Cuypers M (2000) Comparison of optic disc image assessment methods when examining serial photographs for glaucomatous progression. *British Journal of Ophthalmology* 84: 28-30.

Barton J J S, Rizzo M, Nawrot M, and Simpson T (1996) Optical blur and the perception of global coherent motion in random dot cinematograms. *Vision Research* 36: 3051-3059.

Bathija R, Zangwill L, Berry C, Sample P A, and Weinreb R N (1998) Detection of early glaucomatous structural damage with confocal scanning laser tomography. *Journal of Glaucoma* 7: 121-127.

Bayer A U, and Erb C (2002) Short wavelength automated perimetry, frequency doubling technology perimetry, and pattern electroretinography for prediction of progressive glaucomatous standard visual field defects. *Ophthalmology* 109: 1009-1017.

Beaumont P E, and Kang H K (2002) Clinical characteristics of retinal venous occlusions occurring at different sites. *British Journal of Ophthalmology* 86: 572-580.

Bengtsson B, and Heijl A (1998) Evaluation of a new perimetric threshold strategy, SITA, in patients with manifest and suspect glaucoma. *Acta Ophthalmologica Scandinavica* 76: 268-272.

Bengtsson B, and Heijl A (2006a) Diagnostic sensitivity of fast blue-yellow and standard automated perimetry. *Ophthalmology* 113: 1092-1097.

Bengtsson B, and Heijl A (2006b) Diagnostic sensitivity of fast blue-yellow and standard automated perimetry in early glaucoma: a comparison between different test programs. *Ophthalmology* 113: 1092-1097.

Bengtsson B, Heijl A, and Olsson J (1998) Evaluation of a new threshold visual field strategy, SITA in normal subjects. *Acta Ophthalmologica Scandinavica* 76: 165-169.

Bennett P J, Sekuler A B, and Ozin L (1999) Effects of aging on calculation efficiency and equivalent noise. *Journal of the Optical Society of America A - Optics Image Science and Vision* 16: 654-668.

Bennett P J, Sekuler R, and Sekuler A B (2007) The effects of aging on motion detection and direction identification. *Vision Research* 47: 799-809.

Bertuzzi F, Hoffman D C, De Fonseca A M, Souza C, and Caprioli J (2009) Concordance of retinal nerve fiber layer defects between fellow eyes of glaucoma patients measured by optical coherence tomography. *American Journal of Ophthalmology* 148: 148-154.

Betts L R, Sekuler A B, and Bennett P J (2007) The effects of aging on orientation discrimination. *Vision Research* 47: 1769-1780.

Bien A, Seidenbecher C, Böckers T, Sabel B, and Kreutz M (1999) Apoptotic versus necrotic characteristics of retinal ganglion cell (RGC) death after partial optic nerve injury. *Journal of Neurotrauma* 16: 153-163.

Birt C M, Shin D H, McCarty B, Kim C, Lee D T, and Chung H S (1998) Comparison between high-pass resolution perimetry and differential light sensitivity perimetry in patients with glaucoma. *Journal of Glaucoma* 7: 111-116.

Blumenthal E Z, Sample P A, Zangwill L, Lee A C, Kono Y, and Weinreb R N (2000) Comparison of long-term variability for standard and short-wavelength automated perimetry in stable glaucoma patients. *American Journal of Ophthalmology* 129: 309-313.

Blumenthal E Z, and Weinreb R N (2001) Assessment of the retinal nerve fiber layer in clinical trials of glaucoma neuroprotection. *Survey of Ophthalmology* 45: S305-S312.

Bodis-Wollner I (1972) Visual acuity and contrast sensitivity in patients with cerebral lesions. *Science* 178: 769-771.

- Bodis-Wollner I, and Diamond S P (1976) The measurement of spatial contrast sensitivity in cases of blurred vision associated with cerebral lesions. *Brain* 99: 695-710.
- Boehm A G, Koeller A U, and Pillunat L E (2005) The effect of age on optic nerve head blood flow. *Investigative Ophthalmology and Visual Science* 46: 1291-1295.
- Boel B, Karl-Johan H, and Elisabet A (2008) Test-retest variability for standard automated perimetry and short-wavelength automated perimetry in diabetic patients. *Acta Ophthalmologica* 86: 170-176.
- Bonomi L, Marchini G, Marraffa M, Bernardi P, De Franco I, Perfetti S, Varotto A et al. (1998) Prevalence of glaucoma and intraocular pressure distribution in a defined population: The Egna-Neumarkt Study. *Ophthalmology* 105: 209-215.
- Born R T, and Tootell R B H (1992) Segregation of global and local motion processing in primate middle temporal visual area. *Nature* 357: 497-499.
- Bosworth C F, Sample P A, Gupta N, Bathija R, and Weinreb R N (1998) Motion automated perimetry identifies early glaucomatous field defects. *Archives of Ophthalmology* 116: 1153-1158.
- Bosworth C F, Sample P A, and Weinreb R N (1997) Perimetric motion thresholds are elevated in glaucoma suspects and glaucoma patients. *Vision Research* 37: 1989-1997.
- Bowd C, Tafreshi A, Vizzeri G, Zangwill L M, Sample P A, and Weinreb R N (2009a) Repeatability of pattern electroretinogram measurements using a new paradigm optimized for glaucoma detection. *Journal of Glaucoma* 18: 437-442.
- Bowd C, Tavares I M, Medeiros F A, Zangwill L M, Sample P A, and Weinreb R N (2007) Retinal nerve fiber layer thickness and visual sensitivity using scanning laser polarimetry with Variable and Enhanced Corneal Compensation. *Ophthalmology* 114: 1259-1265.
- Bowd C, Vizzeri G, Tafreshi A, Zangwill L M, Sample P A, and Weinreb R N (2009b) Diagnostic accuracy of pattern electroretinogram optimized for glaucoma detection. *Ophthalmology* 116: 437-443.
- Bowd C, Weinreb R N, Williams J M, and Zangwill L M (2000) The retinal nerve fiber layer thickness in ocular hypertensive, normal, and glaucomatous eyes with optical coherence tomography. *Archives of Ophthalmology* 118: 22-26.
- Brainard D H (1989) Calibration of a computer controlled color monitor. *Color Research AND Application* 14: 23-34.
- Brandt J D, Beiser J A, Kass M A, and Gordon M O (2001) Central corneal thickness in the ocular hypertension treatment study (OHTS). *Ophthalmology* 108: 1779-1788.
- Broadway D C, Nicoleta M T, and Drance S M (1999) Optic disc appearances in primary open angle glaucoma. *Survey of Ophthalmology* 43: S223-S243.

- Brunk U T, and Terman A (2002) Lipofuscin: Mechanisms of age-related accumulation and influence on visual function. *Free Radical Biology and Medicine* 33: 611-619.
- Buchi E (1992) Apoptotic versus necrotic characteristics of retinal ganglion cell (RGC) death after partial optic nerve injury. *Experimental Eye Research* 55: 605-613.
- Buckley C H, Hadoke P W F, and O'Brien C J (2002) Systemic vascular endothelial cell dysfunction in normal pressure glaucoma. *British Journal of Ophthalmology* 86: 227-232.
- Budde W M, Jonas J B, Martus P, and Grundler A E (2000) Influence of optic disc size on neuroretinal rim shape in healthy eyes. *Journal of Glaucoma* 9: 357-362.
- Budenz D L, Michael A, Chang R T, McSoley J, and Katz J (2005) Sensitivity and specificity of the StratusOCT for perimetric glaucoma. *Ophthalmology* 112: 3-9.
- Bullimore M, Wood J, and Swenson K (1993) Motion perception in glaucoma. *Investigative Ophthalmology and Visual Science* 34: 3526-3533.
- Bunting H, Still R, Williams D R, Gravenor M, and Austin M W (2009) Evaluation of plasma glutamate levels in normal tension glaucoma. *Ophthalmic Research* 43: 197-200.
- Burgansky-Eliash Z, Wollstein G, Bilonick R A, Ishikawa H, Kagemann L, and Schuman J S (2007) Glaucoma detection with the Heidelberg retina tomograph 3. *Ophthalmology* 114: 466-471.
- Burgess A E, and Barlow H B (1983) The precision of numerosity discrimination in arrays of random dots. *Vision Research* 23: 811-820.
- Burgess A E, and Colborne B (1988) Visual signal detection. IV. Observer inconsistency. *Journal of the Optical Society of America A - Optics Image Science and Vision* 5: 617-627.
- Burgess A E, Wagner R F, Jennings R J, and Barlow H B (1981) Efficiency of human visual signal discrimination. *Science* 214: 93-94.
- Burgoyne C F (2004) Image analysis of optic nerve disease. *Eye* 18: 1207-1213.
- Burgoyne C F, Crawford-Downs J, Bellezza A J, Francis-Suh J K, and Hart R T (2005) The optic nerve head as a biomechanical structure: A new paradigm for understanding the role of IOP-related stress and strain in the pathophysiology of glaucomatous optic nerve damage. *Progress in Retinal Eye Research* 24: 39-73.
- Callaway E M (2005) Structure and function of parallel pathways in the primate early visual system. *The Journal of Physiology* 566: 13-19.
- Campbell F W, and Green D G (1965) Optical and retinal factors affecting visual resolution. *Journal of Physiology* 181: 576-593.
- Caprioli J (1992) Discrimination between normal and glaucomatous eyes. *Investigative Ophthalmology and Visual Science* 33: 153-159.

- Caprioli J, and Zeyen T (2009) A critical discussion of the rates of progression and causes of optic nerve damage in glaucoma: International Glaucoma Think Tank II: July 25-26, 2008, Florence, Italy. *Journal of Glaucoma* 18: S1-21.
- Carter B E, and Henning G B (1971) The detection of gratings in narrow-band visual noise. *Journal of Physiology* 219: 355-365.
- Casagrande V A, Yazar F, Jones K D, and Ding Y (2007) The morphology of the koniocellular axon pathway in the macaque monkey. *Cerebral Cortex* 17: 2334-2345.
- Casson R J, Johnson C A, and Nelson-Quigg J (1993) Temporal modulation perimetry: The effects of aging and eccentricity on sensitivity in normals. *Investigative Ophthalmology and Visual Science* 34: 3096-3102.
- Castelo-Branco M, Faria P, Forjaz V, Kozak L R, and Azevedo H (2004) Simultaneous comparison of relative damage to chromatic pathways in ocular hypertension and glaucoma: Correlation with clinical measures. *Investigative Ophthalmology and Visual Science* 45: 499-505.
- Cello K E, Nelson-Quigg J M, and Johnson C A (2000) Frequency doubling technology perimetry for detection of glaucomatous visual field loss. *American Journal of Ophthalmology* 129: 314-322.
- Chapman C, Hoag R, and Giaschi D (2004) The effect of disrupting the human magnocellular pathway on global motion perception. *Vision Research* 44: 2551-2557.
- Chaturvedi N, Hedley-Whyte T, and Dreyer E B (1993) Lateral geniculate nucleus in glaucoma. *American Journal of Ophthalmology* 116: 182 - 188.
- Chauhan B C, House P H, McCormick T A, and LeBlanc R P (1999) Comparison of conventional and high-pass resolution perimetry in a prospective study of patients with glaucoma and healthy controls. *Archives of Ophthalmology* 117: 24-33.
- Chen Y H, Lu D W, Cheng J H, Chen J T, and Chen C L (2009) Trabeculectomy in patients With primary angle-closure glaucoma. *Journal of Glaucoma* 18: 679-683.
- Chylack L T, Jr., Wolfe J K, Singer D M, Leske M C, Bullimore M A, Bailey I L, Friend J et al. (1993) The Lens Opacities Classification System III. *Archives of Ophthalmology* 111: 831-836.
- CIE (1932) Commission internationale de l'Eclairage proceedings, 1931. Cambridge: Cambridge University Press.
- Coleman A L, and Miglior S (2008) Risk factors for glaucoma onset and progression. *Survey of Ophthalmology* 53 Suppl: S3-10.
- Colombo E, and Derrington A (2001) Visual calibration of CRT monitors. *Displays* 22: 87-95.

- Contestabile M, Perdicchi A, Amodeo S, Recupero V, and Recupero S (2007) The influence of learning effect on frequency doubling technology perimetry (Matrix). *Journal of Glaucoma* 16: 297-301.
- Cornsweet T N (1962) The staircase-method in psychophysics. *American Journal of Psychology* 75: 485-491.
- Costa V P (2004) Frequency doubling technology perimetry abnormalities as predictors of glaucomatous visual field loss. *American Journal of Ophthalmology* 138: 897-898.
- Crawford M L J, Harwerth R S, Smith E L, III, Shen F, and Carter-Dawson L (2000) Glaucoma in primates: Cytochrome oxidase reactivity in parvo- and magnocellular pathways. *Investigative Ophthalmology and Visual Science* 41: 1791-1802.
- Crawford M L J, Harwerth R S, Smith III E L, Mills S, and Ewing B (2001) Experimental glaucoma in primates: Changes in cytochrome oxidase blobs in V1 cortex. *Investigative Ophthalmology and Visual Science* 42: 358.
- Curcio C A, and Allen K A (1990) Topography of ganglion cells in human retina. *Journal of Comparative Neurology* 300: 5-25.
- Curcio C A, Sloan K R, Kalina R E, and Hendrickson A E (1990) Human photoreceptor topography. *Journal of Comparative Neurology* 292: 497-523.
- Dacey D, and Lee B (1994) The blue-on opponent pathway in primate retina originates from a distinct bistratified ganglion cell type. *Nature* 367: 731-735.
- Dacey D, and Petersen M (1992) Dendritic field size and morphology of midget and parasol ganglion cells of the human retina. *Proceedings of the National Academy of Sciences USA* 89: 9666-9670.
- Dacey D M (1993) The mosaic of midget ganglion cells in the human retina. *Journal of Neuroscience* 13: 5334-5355.
- Dacey D M (1999) Primate retina: cell types, circuits and color opponency. *Progress in Retinal and Eye Research* 18: 737-763.
- Dandona L, Hendrickson A, and Quigley H (1991) Selective effects of experimental glaucoma on axonal transport by retinal ganglion cells to the dorsal lateral geniculate nucleus. *Investigative Ophthalmology and Visual Science* 32: 1593-1599.
- Dandona L, Quigley H A, Brown A E, and Enger C (1990) Quantitative regional structure of the normal human lamina cribrosa. A racial comparison. *Archives of Ophthalmology* 108: 393-398.
- Datta S, Foss A J E, Grainge M J, Gregson R M, Zaman A, Masud T, Osborn F et al. (2008) The importance of acuity, stereopsis, and contrast sensitivity for health-related quality of life in elderly women with cataracts. *Investigative Ophthalmology and Visual Science* 49: 1-6.

- De Lima Silveira L C (2004) Comparative study of the primate retina. In: Kass, J H, and Collins, C E [eds.] *The primate visual system*. CRC Press, pp. 29-52.
- De Monasterio F, and Gouras P (1975) Functional properties of ganglion cells of the rhesus monkey retina. *Journal of Physiology* 251: 167-195.
- De Vries H L (1943) The quantum character of light and its bearing upon threshold of vision, the differential sensitivity and visual acuity of the eye. *Physica* 10: 553-564.
- De Yoe E A, and Van Essen D C (1988) Concurrent processing streams in monkey visual cortex. *Trends in Neuroscience* 11: 219-226.
- Deely R J, Drasdo N, and Charman W N (1991) A simple parametric model of the human ocular modulation transfer function. *Ophthalmic and Physiological Optics* 11: 91-93.
- Degenring R F, Aschmoneit I, Kampeter B, Budde W M, and Jonas J B (2004) Optical coherence tomography and confocal scanning laser tomography for assessment of macular edema. *American Journal of Ophthalmology* 138: 354-361.
- Delgado M F, Nguyen N T A, Cox T A, Singh K, Lee D A, Dueker D K, Fechtner R D et al. (2002) Automated perimetry - A report by the American Academy of Ophthalmology. *Ophthalmology* 109: 2362-2374.
- Deokule S, Vizzeri G, Boehm A, Bowd C, and Weinreb R N (2009) Association of visual field severity and parapapillary retinal blood flow in open-angle glaucoma. *Journal of Glaucoma* 24: 24.
- Derefeldt F, Lennerstrand G, and Lundh B (1979) Age variations in normal human contrast sensitivity. *Acta Ophthalmologica* 57: 679-690.
- Derrington A, and Lennie P (1984) Spatial and temporal contrast sensitivities of neurones in lateral geniculate nucleus of macaque. *Journal of Physiology* 357: 219-240.
- Dixon W J, and Mood A M (1948) A method for obtaining and analyzing sensitivity data. *Journal of the American Statistical Association* 43: 109-126.
- Dolman C L, McCormick A Q, and Drance S M (1980) Ageing of the optic nerve. *Archives of Ophthalmology* 98: 2053-2058.
- Drance S, Lakowski R, Schulzer M, and Douglas G (1981) Acquired color vision changes in glaucoma: use of 100-hue test and Pickford anomaloscope as predictors of glaucomatous field change. *Archives of Ophthalmology* 99: 829-831.
- Dreyer E, Zurakowski D, Schumer R, Podos S M, and Lipton S (1996) Elevated glutamate levels in the vitreous body of humans and monkeys with glaucoma. *Archives of Ophthalmology* 114: 299-305.
- Duijm H F, van den Berg T J, and Greve E L (1997) Choroidal haemodynamics in glaucoma. *British Journal of Ophthalmology* 81: 735-742.

Ekstrom C (2008) Incidence of open-angle glaucoma in central Sweden. *Acta Ophthalmologica* 86: 747-754.

Elliott D, Whitaker D, and MacVeigh D (1990) Neural contribution to spatiotemporal contrast sensitivity decline in healthy ageing eyes. *Vision Research* 30: 541-547.

Elliott D B, Gilchrist J, and Whitaker D (1989) Contrast sensitivity and glare sensitivity changes with three types of cataract morphology: are these techniques necessary in a clinical evaluation of cataract? *Ophthalmic and Physiological Optics* 9: 25-30.

Elliott D B, Sanderson K, and Conkey A (2007) The reliability of the Pelli-Robson contrast sensitivity chart. *Ophthalmic and Physiological Optics* 10: 21-24.

Elmore S (2007) Apoptosis: A review of programmed cell death. *Toxicologic Pathology* 35: 495-516.

Embleton S J, Hosking S L, Hilton E J R, and Cunliffe I A (2002) Effect of senescence on ocular blood flow in the retina, neuroretinal rim and lamina cribrosa, using scanning laser flow doppler flowmetry. *Eye* 16: 156-162.

Emdadi A, Zangwill L, Sample P, Kono Y, Anton A, and Weinreb R (1998) Patterns of optic disc damage in patients with early focal visual field loss. *American Journal of Ophthalmology* 126: 763-771.

Emre M, Orgul S, Gugleta K, and Flammer J (2004) Ocular blood flow alteration in glaucoma is related to systemic vascular dysregulation. *British Journal of Ophthalmology* 88: 662-666.

Evans K, Law S K, Walt J, Buchholz P, and Hansen J (2009) The quality of life impact of peripheral versus central vision loss with a focus on glaucoma versus age-related macular degeneration. *Clin Ophthalmol* 3: 433-445.

Falcao-Reis F, O'Donoghue E, Buceti R, Hitchings R A, and Arden G B (1990) Peripheral contrast sensitivity in glaucoma and ocular hypertension. *British Journal of Ophthalmology* 74: 712-716.

Falkenberg H K, and Bex P J (2007) Sources of motion-sensitivity loss in glaucoma. *Investigative Ophthalmology and Visual Science* 48: 2913-2921.

Fankhauser F, and Bebié H (1979) Threshold fluctuations, interpolations and spatial resolution in perimetry. In: Greve, E L [ed.] *Documenta Ophthalmologica Proceedings Series*. Vol. 19. The Hague: Junk Publishers, pp. 295-309.

Fansi A A, Papamatheakis D G, and Harasymowycz P J (2009) Racial variability of glaucoma risk factors between African Caribbeans and caucasians in a Canadian urban screening population. *Canadian Journal of Ophthalmology* 44: 576-581.

Faubert J (2002) Visual perception and ageing. *Canadian Journal of Experimental Psychology* 56: 164-176.

- Fercher A F, Hitzenberger C K, Drexler W, Kamp G, and Sattmann H (1993) In vivo optical coherence tomography. *American Journal of Ophthalmology* 116: 113-114.
- Fern R, Ransom B, and Waxman S (1995) Voltage-gated calcium channels in CNS white matter: Role in axonic injury. *Journal of Neurophysiology* 74: 369-377.
- Fern R, Waxman S, and Ransom B (1994) Modulation of anoxic injury in CNS white matter by adenosine and GABA. *Journal of Neurophysiology* 72: 2609-2616.
- Fingeret M, Flanagan J, Johnson C, Cavallerano A, Quinn C, Mann D, and Semes L (2005) Glaucoma without cupping. *Optometry* 76: 223-224; author reply 224-225.
- Flood T, and Flanagan J (1998) The influence of detection versus resolution threshold criteria in frequency doubling perimetry. *Optometry and Vision Science* 75: S31.
- Fogagnolo P, Rossetti L, Ranno S, Ferreras A, Orzalesi N, Nucci C, Cerulli L et al. (2008) Short-wavelength automated perimetry and frequency-doubling technology perimetry in glaucoma. *Progress in Brain Research* Volume 173: 101-124.
- Ford B A, Artes P H, McCormick T A, Nicolela M T, LeBlanc R P, and Chauhan B C (2003) Comparison of data analysis tools for detection of glaucoma with the Heidelberg Retina Tomograph. *Ophthalmology* 110: 1145-1150.
- Foster P J, Buhrmann R, Quigley H A, and Johnson G J (2002) The definition and classification of glaucoma in prevalence surveys. *British Journal of Ophthalmology* 86: 238-242.
- Francis B A, Varma R, Chopra V, Lai M Y, Shtir C, and Azen S P (2008) Intraocular pressure, central corneal thickness, and prevalence of open-angle glaucoma: the Los Angeles Latino Eye Study. *American Journal of Ophthalmology* 146: 741-746.
- Frisen L (1989) High pass resolution perimetry: A clinical review. *Documenta Ophthalmologica* 83: 1-25.
- Frisen L (1992) High-pass resolution perimetry: Evidence for parvocellular neural channel dependence. *Neuro-ophthalmology* 4: 257-264.
- Fuchsjager-Mayrl G, Wally B, Georgopoulos M, Rainer G, Kircher K, Buehl W, Amoako-Mensah T et al. (2004) Ocular blood flow and systemic blood pressure in patients with primary open-angle glaucoma and ocular hypertension. *Investigative Ophthalmology and Visual Science* 45: 834-839.
- Funaki S, Shirakashi M, Yaoeda K, Abe H, Kunimatsu S, Suzuki Y, Tomita G et al. (2002) Specificity and sensitivity of glaucoma detection in the Japanese population using scanning laser polarimetry. *British Journal of Ophthalmology* 86: 70-74.
- Garcia-Valenzuela E, Shareef S, Walsh J, and Sharma S (1995) Programmed cell death of retinal ganglion cells during experimental glaucoma. *Experimental Eye Research* 61: 33-44.

Gardiner S K, Johnson C A, and Spry P (2006) Normal age-related sensitivity loss for a variety of visual functions throughout the visual field. *Optometry and Vision Science* 83: 438-443.

Garhofer G, Zawinka C, Resch H, Huemer K H, Schmetterer L, and Dorner G T (2004) Response of retinal vessel diameters to flicker stimulation in patients with early open angle glaucoma. *Journal of Glaucoma* 13: 340-344.

Garthwaite G, Brown G, Batchelor A, Goodwin D, and Garthwaite J (1999) Mechanisms of ischaemic damage to central white matter axons: A quantitative histological analysis using the rat optic nerve. *Neuroscience* 94: 1219-1230.

Garway-Heath D F, Caprioli J, Fitzke F W, and Hitchings R A (2000a) Scaling the hill of vision: The physiological relationship between light sensitivity and ganglion cell numbers. *Investigative Ophthalmology and Visual Science* 41: 1774-1782.

Garway-Heath D F, and Hitchings R A (1998) Quantitative evaluation of the optic nerve head in glaucoma. *British Journal of Ophthalmology* 82: 352-361.

Garway-Heath D F, Poinoosawmy D, Fitzke F W, and Hitchings R A (2000b) Mapping the visual field to the optic disc in normal tension glaucoma eyes. *Ophthalmology* 107: 1809-1815.

Garway-Heath D F, Wollstein G, and Hitchings R A (1997) Ageing changes of the optic nerve head in relation to open angle glaucoma. *British Journal of Ophthalmology* 81: 840-845.

Gasch A T, Wang P, and Pasquale L R (2000) Determinants of glaucoma awareness in a general eye clinic. *Ophthalmology* 107: 303-308.

Gasser P, and Flammer J (1987) Influence of vasospasm on visual function. *Documenta Ophthalmologica* 66: 3-18.

Ghanem A A, Arafa L F, and El-Baz A (2010) Oxidative stress markers in patients with primary open-angle glaucoma. *Current Eye Research* 35: 295-301.

Gherghel D, Hosking S L, and Cunliffe I A (2004) Abnormal systemic and ocular vascular response to temperature provocation in primary open-angle glaucoma patients: A case for autonomic failure? *Investigative Ophthalmology and Visual Science* 45: 3546-3554.

Ghosh K, Sarkar S, and Bhaumik K (2006) A possible explanation of the low-level brightness–contrast illusions in the light of an extended classical receptive field model of retinal ganglion cells. *Biological Cybernetics* 94: 89-96.

Ginsburg A (1984) A new contrast sensitivity vision test chart. *American Journal of Optometry and Physiological Optics* 61: 403-407.

Girkin C A, McGwin G, Jr, Long C, DeLeon-Ortega J, Graf C M, and Everett A W (2004) Subjective and objective optic nerve assessment in African Americans and whites. *Investigative Ophthalmology and Visual Science* 45: 2272-2278.

Girkin C A, McGwin J, Gerald, Xie A, and Deleon-Ortega J (2005) Differences in optic disc topography between black and white normal subjects. *Ophthalmology* 112: 33-39.

Glovinsky Y, Quigley H, and Dunkelberger G (1991a) Retinal ganglion cell loss is size dependent in experimental glaucoma. *Investigative Ophthalmology and Visual Science* 32: 484-491.

Glovinsky Y, Quigley H A, Dandona L, Brown A E, and Dunkelberger G R (1991b) Large ganglion-cells are selectively damaged in experimental glaucoma. *Investigative Ophthalmology and Visual Science* 32: 1103-1103.

Glovinsky Y, Quigley H A, and Pease M (1993) Foveal ganglion cell loss is size dependent in experimental glaucoma. *Investigative Ophthalmology and Visual Science* 34: 395.

Gold J, Bennett P J, and Sekuler A B (1999) Signal but not noise changes with perceptual learning. *Nature* 402: 176-178.

Gordon M O, Beiser J A, Brandt J D, Heuer D K, Higginbotham E J, Johnson C A, Keltner J L et al. (2002) The Ocular Hypertension Treatment Study : Baseline factors that predict the onset of primary open-angle glaucoma. *Archives of Ophthalmology* 120: 714-720.

Graham S, Drance S, Chauhan B, Swindale N, Hnik P, Mikelberg F, and Douglas G (1996) Comparison of psychophysical and electrophysiological testing in early glaucoma. *Investigative Ophthalmology and Visual Science* 37: 2651-2662.

Graham S L, Klistorner A, Grigg J R, and Billson F A (1999) Objective perimetry in glaucoma: Recent advances with multifocal stimuli. *Survey of Ophthalmology* 43: S199-S209.

Graham S L, Klistorner A I, and Goldberg I (2005) Clinical application of objective perimetry using multifocal visual evoked potentials in glaucoma practice. *Archives of Ophthalmology* 123: 729-739.

Green C M, Kearns L S, Wu J, Barbour J M, Wilkinson R M, Ring M A, Craig J E et al. (2007) How significant is a family history of glaucoma? Experience from the Glaucoma Inheritance Study in Tasmania. *Clinical Experimental Ophthalmologica* 35: 793-799.

Green D G (1970) Regional variations in the visual acuity for interference fringes on the retina. *Journal of Physiology* 207: 351-356.

Green M (1983) Contrast detection and direction discrimination of drifting gratings. *Vision Research* 23: 281-289.

Greenfield D S, Bagga H, and Knighton R W (2003) Macular thickness changes in glaucomatous optic neuropathy detected using optical coherence tomography. *Archives of Ophthalmology* 121: 41-46.

Greenfield D S, Knighton R W, Feuer W J, Schiffman J C, Zangwill L, and Weinreb R N (2002) Correction for corneal polarization axis improves the discriminating power of scanning laser polarimetry. *American Journal of Ophthalmology* 134: 27-33.

Greenstein V C, Halevy D, Zaidi Q, Koenig K L, and Ritch R H (1996) Chromatic and luminance systems deficits in glaucoma. *Vision Research* 36: 621-629.

Grieshaber M C, Terhorst T, and Flammer J (2006) The pathogenesis of optic disc splinter haemorrhages: a new hypothesis. *Acta Ophthalmologica Scandinavica* 84: 62-68.

Grodrum K, Heijl A, and Bengtsson B (2002) Optic disc hemorrhages and generalized vascular disease. *Journal of Glaucoma* 11: 226-230.

Groh M J, Michelson G, Langhans M J, and Harazny J (1996) Influence of age on retinal and optic nerve head blood circulation. *Ophthalmology* 103: 529-534.

Guedes V, Schuman J S, Hertzmark E, Wollstein G, Correnti A, Mancini R, Lederer D et al. (2003) Optical coherence tomography measurement of macular and nerve fiber layer thickness in normal and glaucomatous human eyes. *Ophthalmology* 110: 177-189.

Gunvant P, Porsia L, Watkins R J, Bayliss-Brown H, and Broadway D C (2008) Relationships between central corneal thickness and optic disc topography in eyes with glaucoma, suspicion of glaucoma, or ocular hypertension. *Clinical Experimental Ophthalmologica* 2: 591-599.

Guo L, Moss S E, Alexander R A, Ali R R, Fitzke F W, and Cordeiro M F (2005) Retinal ganglion cell apoptosis in glaucoma is related to intraocular pressure and IOP-induced effects on extracellular matrix. *Investigative Ophthalmology and Visual Science* 46: 175-182.

Gupta N, and Yücel Y (2007) Glaucoma as a neurodegenerative disease. *Current Opinion in Ophthalmology* 18: 110-114.

Gupta V, Srinivasan G, Mei S S, Gazzard G, Sihota R, and Kapoor K S (2005) Utility values among glaucoma patients: an impact on the quality of life. *British Journal of Ophthalmology* 89: 1241-1244.

Haefliger I O, Meyer P, Flammer J, and Luscher T F (1994) The vascular endothelium as a regulator of the ocular circulation - a new concept in ophthalmology. *Survey of Ophthalmology* 39: 123-132.

Hafez A S, Bizzarro R L G, and Lesk M R (2003) Evaluation of optic nerve head and peripapillary retinal blood flow in glaucoma patients, ocular hypertensives, and normal subjects. *American Journal of Ophthalmology* 136: 1022-1031.

Harmon L D, and Julesz B (1973) Masking in visual recognition: Effects of two dimensional filtered noise. *Science* 180: 1194 - 1197.

Harris A, Harris M, Biller J, Garzozzi H, Zarfty D, Ciulla T A, and Martin B (2000) Aging affects the retrobulbar circulation differently in women and men *Archives of Ophthalmology* 118: 1076-1080.

Harris A, Sergott R C, Spaeth G L, Katz J L, Shoemaker J A, and Martin B J (1994) Color doppler analysis of ocular vessel blood velocity in normal-tension glaucoma. *American Journal of Ophthalmology* 118: 642-649.

Harwerth R S, Carter-Dawson L, Shen F, Smith E L, III, and Crawford M L J (1999) Ganglion cell losses underlying visual field defects from experimental glaucoma. *Investigative Ophthalmology and Visual Science* 40: 2242-2250.

Harwerth R S, Carter-Dawson L, Smith E L, III, Barnes G, Holt W F, and Crawford M L J (2004) Neural losses correlated with visual losses in clinical perimetry. *Investigative Ophthalmology and Visual Science* 45: 3152-3160.

Harwerth R S, Crawford M L J, Frishman L J, Viswanathan S, Smith E L, and Carter-Dawson L (2002) Visual field defects and neural losses from experimental glaucoma. *Progress in Retinal and Eye Research* 21: 91-125.

Harwerth R S, and Quigley H A (2006) Visual field defects and retinal ganglion cell losses in patients with glaucoma. *Archives of Ophthalmology* 124: 853-859.

Harwerth R S, Vilupuru A S, Rangaswamy N V, and Smith E L, III (2007) The relationship between nerve fiber layer and perimetry measurements. *Investigative Ophthalmology and Visual Science* 48: 763-773.

Hatwick A (2001) Beyond intraocular pressure: Neuroprotective strategies for future glaucoma therapy. *Optometry and Vision Science* 78: 85-94.

Hayes R D, and Merigan W H (2007) Mechanisms of sensitivity loss due to visual cortex lesions in humans and macaques. *Cerebral Cortex* 17: 1117-1128.

Hayreh S S (2001) Blood flow in the optic nerve head and factors that may influence it. *Progress in Retinal and Eye Research* 20: 595-624.

Hayreh S S, Bill A, and Sperber G O (1991) Metabolic effects of high intraocular-pressure in old arteriosclerotic monkeys. *Investigative Ophthalmology and Visual Science* 32: 810-810.

Hayreh S S, Bill A, and Sperber G O (1994) Effects of high intraocular-pressure on the glucose-metabolism in the retina and optic-nerve in old atherosclerotic monkeys. *Graefes Archive for Clinical and Experimental Ophthalmology* 232: 745-752.

Hayreh S S, March W, and Anderson D R (1979) Pathogenesis of block of rapid orthograde axonal transport by elevated intraocular pressure. *Experimental Eye Research* 28: 515-523.

Hayreh S S, Servais G E, and Viridi P S (1986) Fundus lesions in malignant hypertension. V. Hypertensive optic neuropathy. *Ophthalmology* 93: 74-87.

- Heijl A (1993) Perimetric point density and detection of glaucomatous visual field loss. *Acta Ophthalmologica* 71: 445-450.
- Heijl A, Bengtsson B, Hyman L, and Leske M C (2009) Natural history of open-angle glaucoma. *Ophthalmology* 116: 2271-2276.
- Hernandez M R (2000) The optic nerve head in glaucoma: Role of astrocytes in tissue remodelling. *Progress in Retinal Eye Research* 19: 297-321.
- Herndon L W, Weizer J S, and Stinnett S S (2004) Central corneal thickness as a risk factor for advanced glaucoma damage. *Archives of Ophthalmology* 122: 17-21.
- Heron G, Adams A, and Husted R (1987) Foveal and non-foveal measures of short wavelength sensitive pathways in glaucoma and ocular hypertension. *Ophthalmic and Physiological Optics* 7: 403-404.
- Hess R, and Howell E (1977) The threshold contrast sensitivity function in strabismic amblyopia; evidence for a two type classification. *Vision Research* 17: 1049-1056.
- Hewitt A W, Chappell A J, Straga T, Landers J, Mills R A, and Craig J E (2009) Sensitivity of confocal laser tomography versus optical coherence tomography in detecting advanced glaucoma. *Clinical Experimental Ophthalmologica* 37: 836-841; quiz 903-834.
- Hiraoka T, Okamoto C, Ishii Y, Kakita T, and Oshika T (2007) Contrast sensitivity function and ocular higher-order aberrations following overnight orthokeratology. *Investigative Ophthalmology and Visual Science* 48: 550-556.
- Hitchings R A (1991) The ocular pulse. *British Journal of Ophthalmology* 75: 65.
- Hoesl L M, Mardin C Y, Horn F K, Juenemann A G, and Laemmer R (2009) Influence of glaucomatous damage and optic disc size on glaucoma detection by scanning laser tomography. *Journal of Glaucoma* 18: 385-389.
- Hogg R E, and Anderson A J (2009) Appearance of the Frequency-Doubling stimulus at threshold. *Investigative Ophthalmology and Visual Science* 50: 1477-1482.
- Holopigian K, Seiple W, Mayron C, Koty R, and Lorenzo M (1990) Electrophysiological and psychophysical flicker sensitivity in patients with primary open-angle glaucoma and ocular hypertension. *Investigative Ophthalmology and Visual Science* 31: 1863-1868.
- Hood A S, and Morrison J D (2002) The dependence of binocular contrast sensitivities on binocular single vision in normal and amblyopic human subjects. *The Journal of Physiology* 540: 607-622.
- Hood D C, Xu L, Thienprasiddhi P, Greenstein V C, Odel J G, Grippo T M, Liebmann J M et al. (2005) The pattern electroretinogram in glaucoma patients with confirmed visual field deficits. *Investigative Ophthalmology and Visual Science* 46: 2411-2418.

- Horani A, Frenkel S, Yahalom C, Farber M D, Ticho U, and Blumenthal E Z (2002) The learning effect in visual field testing of healthy subjects using frequency doubling technology. *Journal of Glaucoma* 11: 511-516.
- Hot A, Dul M W, and Swanson W H (2008) Development and evaluation of a contrast sensitivity perimetry test for patients with glaucoma. *Investigative Ophthalmology and Visual Science* 49: 3049-3057.
- Hougaard J, Heijl A, and Bengtsson B (2007) Glaucoma detection by Stratus OCT. *Journal of Glaucoma* 16: 302-306.
- Huang C, Tao L, Zhou Y, and Lu Z-L (2007) Treated amblyopes remain deficient in spatial vision: A contrast sensitivity and external noise study. *Vision Research* 47: 22-34.
- Huang D, Swanson E A, Lin C P, Schuman J S, Stinson W G, Chang W, Hee M R et al. (1991) Optical coherence tomography. *Science* 254: 1178-1181.
- Hudson C, Flanagan J G, Turner G S, Chen H C, Young L B, and McLeod D (2003) Correlation of a scanning laser derived oedema index and visual function following grid laser treatment for diabetic macular oedema. *British Journal of Ophthalmology* 87: 455-461.
- Hudson C J W, Kim L S, Hancock S A, Cunliffe I A, and Wild J M (2007) Some dissociating factors in the analysis of structural and functional progressive damage in open-angle glaucoma. *British Journal of Ophthalmology* 91: 624-628.
- Hutchings N, Hosking S L, Wild J M, and Flanagan J G (2001) Long-term fluctuation in short-wavelength automated perimetry in glaucoma suspects and glaucoma patients. *Investigative Ophthalmology & Visual Science* 42: 2332-2337.
- Hyvärinen L, Laurinen P, and Rovamo J (1983a) Contrast sensitivity in evaluation of visual impairment due to diabetes. *Acta Ophthalmologica Scandinavica* 61: 94-101.
- Hyvärinen L, Laurinen P, and Rovamo J (1983b) Contrast sensitivity in evaluation of visual impairment due to macular degeneration and optic nerve lesions. *Acta Ophthalmologica Scandinavica* 61: 161-170.
- Iannelli L, Johansson K H, Jonsson U T, and Vasca F (2006) Averaging of nonsmooth systems using dither. *Automatica* 42: 669-676.
- Ilschner S, and Waring P (1992) Fragmentation of DNA in the retina of chicken embryos coincides with retinal ganglion cell death. *Biochemical and Biophysical Research Communications* 183: 1056-1061.
- Ip M S, Baker B J, Duker J S, Reichel E, Baumal C R, Gangnon R, and Puliafito C A (2002) Anatomical outcomes of surgery for idiopathic macular hole as determined by optical coherence tomography. *Archives of Ophthalmology* 120: 29-35.

Izzotti A, Sacca S C, Longobardi M, and Cartiglia C (2009) Sensitivity of ocular anterior chamber tissues to oxidative damage and its relevance to the pathogenesis of glaucoma. *Investigative Ophthalmology and Visual Science* 50: 5251-5258.

Jacobson M, and McCarthy N (2002) Preface. In: Jacobson, M, and McCarthy, N [eds.] *Apoptosis: The molecular biology of programmed cell death*. Oxford University Press, pp. vii-ix.

Jamar J H T, and Koenderink J J (1985) Contrast detection and detection of contrast modulation for noise gratings. *Vision Research* 25: 511-521.

Januleviciene I, Sliesoraityte I, Siesky B, and Harris A (2008) Diagnostic compatibility of structural and haemodynamic parameters in open-angle glaucoma patients. *Acta Ophthalmologica* 86: 552-557.

Joachim S C, Grus F H, Kraft D, White-Farrar K, Barnes G, Barbeck M, Ghanaati S et al. (2009) Complex antibody profile changes in an experimental autoimmune glaucoma animal model. *Investigative Ophthalmology and Visual Science* 50: 4734-4742.

Joffe K M, Raymond J E, and Chrichton A (1997) Motion coherence perimetry in glaucoma and suspected glaucoma. *Vision Research* 37: 955-964.

John S W M (2005) Mechanistic insights into glaucoma provided by experimental genetics - The Cogan lecture. *Investigative Ophthalmology and Visual Science* 46: 2650-2661.

Johnson C, and Samuels S (1997) Screening for glaucomatous visual field loss with frequency-doubling perimetry. *Investigative Ophthalmology and Visual Science* 38: 413-425.

Johnson C A (1994) Selective versus nonselective losses in glaucoma. *Journal of Glaucoma* 3: S32-S44.

Johnson C A, Adams A J, Casson E J, and Brandt J D (1993a) Blue-on-yellow perimetry can predict the development of glaucomatous visual field loss. *Archives of Ophthalmology* 111: 645-650.

Johnson C A, Adams A J, Casson E J, and Brandt J D (1993b) Progression of early glaucomatous visual field loss as detected by blue-on-yellow and standard white-on-white automated perimetry. *Archives of Ophthalmology* 111: 651-656.

Johnson J, Barde Y-A, Schwab M, and Thoenen H (1986) Brain-derived neurotrophic factor supports the survival of cultured rat retinal ganglion cells. *Journal of Neuroscience* 6: 3031-3038.

Jonas J B, Berenshtein E, and Holbach L (2004a) Lamina cribrosa thickness and spatial relationships between intraocular space and cerebrospinal fluid space in highly myopic eyes. *Investigative Ophthalmology and Visual Science* 45: 2660-2665.

Jonas J B, and Budde W M (2000) Diagnosis and pathogenesis of glaucomatous optic neuropathy: Morphological aspects. *Progress in Retinal Eye Research* 19: 1-40.

- Jonas J B, Budde W M, and Panda-Jonas S (1999) Ophthalmoscopic evaluation of the optic nerve head. *Survey of Ophthalmology* 43: 293-320.
- Jonas J B, and Dichtl A (1996) Evaluation of the retinal nerve fiber layer. *Survey of Ophthalmology* 40: 369-378.
- Jonas J B, and Fernandez M C (1994) Shape of the neuroretinal rim and position of the central retinal vessels in glaucoma. *British Journal of Ophthalmology* 78: 99-102.
- Jonas J B, Gusek G C, and Fernandez M C (1991) Correlation of the blind spot size to the area of the optic disc and peripapillary atrophy. *American Journal of Ophthalmology* 111: 559-565.
- Jonas J B, Gusek G C, Guggenmoos-Holzmann I, and Naumann G O H (1988a) Size of the optic nerve scleral canal and comparison with intravitreal determination of optic disc dimensions. *Graefe's Archive for Clinical and Experimental Ophthalmology* 226: 213-215.
- Jonas J B, Gusek G C, and Naumann G O H (1988b) Morphometric optic disc evaluation in normals and glaucoma. *Ophthalmic Research* 20: 76-76.
- Jonas J B, and Hayreh S S (1999) Optic disc morphology in experimental central retinal artery occlusion in rhesus monkeys. *American Journal of Ophthalmology* 127: 523-530.
- Jonas J B, Martus P, Horn F K, Junemann A, Korth M, and Budde W M (2004b) Predictive factors of the optic nerve head for development or progression of glaucomatous visual field loss. *Investigative Ophthalmology and Visual Science* 45: 2613-2618.
- Jonas J B, Nguyen N X, and Naumann G O H (1989a) Optic disc morphometry in simple optic nerve atrophy. *Acta Ophthalmologica* 67: 199-203.
- Jonas J B, Schmidt A M, Mullerbergh J A, Schlotzschardt U M, and Naumann G O H (1992) Human optic nerve fibre count and optic disc size. *Investigative Ophthalmology and Visual Science* 33: 2012-2018.
- Jonas J B, Zach F M, Gusek G C, and Naumann G O H (1989b) Pseudoglaucomatous physiological large cups. *American Journal of Ophthalmology* 107: 137-144.
- Kalil R, and Fedynyshyn J (1998) Axotomy induces two cytologically distinct types of cell death in the dorsal lateral geniculate nucleus (LGN) of the adult rat. *Society for Neuroscience* 24: 1303.
- Karwatsky P, Overbury O, and Faubert J (2004) Red-green chromatic mechanisms in normal aging and glaucomatous observers. *Investigative Ophthalmology & Visual Science* 45: 2861-2866.
- Karwatsky P, Bertone A, Overbury O, and Faubert J (2006) Defining the nature of motion perception deficits in glaucoma using simple and complex motion stimuli. *Optometry and Vision Science* 83: 466-472.

Kass M A, Heuer D K, Higginbotham E J, Johnson C A, Keltner J L, Miller J P, Parrish Ii R K et al. (2002) The Ocular Hypertension Treatment Study: A randomized trial determines that topical ocular hypotensive medication delays or prevents the onset of primary open-angle glaucoma. *Archives of Ophthalmology* 120: 701-713.

Kelly D (1981a) Nonlinear visual responses to flickering sinusoidal gratings. *Journal of the Optical Society of America A - Optics Image Science and Vision* 71: 1051-1055.

Kelly D H (1966) Frequency doubling in visual responses. *Journal of the Optical Society of America A - Optics Image Science and Vision* 56: 1628-1633.

Kelly D H (1981b) Disappearance of stabilized chromatic gratings. *Science* 214: 1257-1258.

Kerrigan-Baumrind L A, Quigley H A, Pease M E, Kerrigan D F, and Mitchell R S (2000) Number of ganglion cells in glaucoma eyes compared with threshold visual field tests in the same persons. *Investigative Ophthalmology and Visual Science* 41: 741-748.

Kersten D, Hess R, and Plant G (1988) Assessing contrast sensitivity behind cloudy media. *Clinical Vision Sciences* 2: 143-158.

Kim J W, and Chen P P (2004) Central corneal pachymetry and visual field progression in patients with open-angle glaucoma. *Ophthalmology* 111: 2126-2132.

King A, Bolton N, Aspinall P, and O'Brien C (2000) Measurement of peripapillary retinal nerve fibre layer volume in glaucoma. *American Journal of Ophthalmology* 129: 599-607.

Klein B E K, Klein R, and Lee K E (2004) Heritability of risk factors for primary open-angle glaucoma: The Beaver Dam Eye Study. *Investigative Ophthalmology and Visual Science* 45: 59-62.

Ko T H, Fujimoto J G, Duker J S, Paunescu L A, Drexler W, Baumal C R, Puliafito C A et al. (2004) Comparison of ultrahigh- and standard-resolution optical coherence tomography for imaging macular hole pathology and repair. *Ophthalmology* 111: 2033-2043.

Kolb H, Linberg K A, and Fisher S K (1992) Neurons of the human retina: A golgi study. *Journal of Comparative Neurology* 318: 147-187.

Kono Y, Jonas J B, Zangwill L, Berry C C, and Weinreb R N (1999) Agreement of measurement of parapapillary atrophy with confocal scanning laser ophthalmoscopy and planimetry of photographs. *Journal of Glaucoma* 8: 105-110.

Korth M, Kohl S, Martus P, and Sembritzki O (2000) Motion-evoked pattern visual evoked potentials in glaucoma. *Journal of Glaucoma* 9: 376-387.

Krantz J H (2000) Presidential Address: Tell me, what did you see? The stimulus on computers. *Behavior Research Methods, Instruments and Computers* 32: 221-229.

Krause L (2006) Effective quantization by averaging and dithering. *Measurement* 39: 681-694.

Kukkonen H, Rovamo J, Donner K, Tammikallio M, and Raninen A (2002) Noise frame duration, masking potency and whiteness of temporal noise. *Investigative Ophthalmology and Visual Science* 43: 3131-3135.

Kukkonen H, Rovamo J, and Melmoth D (1999) Spatial integration and effective spectral density of one-dimensional noise masks. *Vision Research* 39: 1775-1782.

Kukkonen H, Rovamo J, and Nasanen R (1995) Masking potency and whiteness of noise at various noise check sizes. *Investigative Ophthalmology and Visual Science* 36: 513-518.

Kukkonen H, Rovamo J, Tiippana K, and Nasanen R (1993) Michelson contrast, RMS contrast and energy of various spatial stimuli at threshold. *Vision Research* 33: 1431-1436.

Kukkonen H T (1994) Effects of pixel noise and stimulus structure on visual detection performance. PhD, Aston University.

Lachenmayr B, and Gleissner M (1992) Flicker perimetry versus resists retinal image degradation. *Investigative Ophthalmology and Visual Science* 33: 3539-3542.

Lachenmayr B, Rothbacher H, and Gleissner M (1989) Automated flicker perimetry versus quantitative static perimetry in early glaucoma. In: Heijl, A [ed.] *Perimetry Update 1988/1989*. Amsterdam: Kugler Publications, pp. 359-369.

Lee A, Mukesh B N, McCarty C A, and Taylor H R (2003) Risk factors associated with the incidence open-angle glaucoma: The visual impairment project. *Investigative Ophthalmology and Visual Science* 44: 3783-3789.

Legge G E, Kersten D, and Burgess A E (1987) Contrast discrimination in noise. *Journal of the Optical Society of America A - Optics Image Science and Vision* 4: 391-404.

Leite M T, Zangwill L M, Weinreb R N, Rao H L, Alencar L M, Sample P A, and Medeiros F A (2010) Effect of disease severity on the performance of Cirrus Spectral-Domain OCT for glaucoma diagnosis. *Investigative Ophthalmology and Visual Science* 2010: 24.

Lennie P, Trevarthen C, Van Essen D C, and Wassle H (1990) Parallel processing of visual information. In: Spillman, L, and Werner, S [eds.] *Visual perception: The neurological foundations*. San Diego: Academic Press Inc., pp. 103-128.

Leske M C (2009) Ocular perfusion pressure and glaucoma: clinical trial and epidemiologic findings. *Current Opinion in Ophthalmology* 20: 73-78.

Leske M C, Nemesure B, He Q, Wu S, Hejtmancik J F, and Hennis A (2001) Patterns of open-angle glaucoma in the Barbados Family Study. *Ophthalmology* 108: 1015-1022.

Leung C K, Ye C, Weinreb R N, Cheung C Y, Qiu Q, Liu S, Xu G et al. (2009) Retinal nerve fiber layer imaging with spectral-domain optical coherence tomography a study on diagnostic agreement with Heidelberg Retinal Tomograph. *Ophthalmology* 117: 267-274.

Levi D M, and Klein S A (2003) Noise provides some new signals about the spatial vision of amblyopes. *Journal of Neuroscience* 23: 2522-2526.

Levi D M, Klein S A, and Chen I (2005) What is the signal in noise? *Vision Research* 45: 1835-1846.

Levin L A, and Gordon L K (2002) Retinal ganglion cell disorders: Types and treatments. *Progress in Retinal Eye Research* 21: 465-484.

Levy N S, Crapps E E, and Bonney R C (1981) Displacement of the optic nerve head. Response to acute intraocular pressure elevation in primate eyes. *Archives of Ophthalmology* 99: 2166-2174.

Lin W, Aoyama Y, Kawase K, and Yamamoto T (2009) Relationship between central corneal thickness and visual field defect in open-angle glaucoma. *Japanese Journal of Ophthalmology* 53: 477-481.

Lipton S, and Rosenberg P (1994) Excitatory amino acids as a final common pathway for neurological disorders. *New England Journal of Medicine* 330: 613-622.

Liu C J, Chiou H-J, Chiang S-C, Chou J C, Chou Y-H, and Liu J-H (1999) Variations in ocular hemodynamics in patients with early and late glaucoma. *Acta Ophthalmologica Scandinavica* 77: 658-662.

Livingstone M, and Hubel D (1988) Segregation of form, color, movement, and depth: Anatomy, physiology and perception. *Science* 240: 740-749.

Logan J F J, Rankin S J A, and Jackson A J (2004) Retinal blood flow measurements and neuroretinal rim damage in glaucoma. *British Journal of Ophthalmology* 88: 1049-1054.

Logothetis N K, Schiller P H, Charles E R, and Hurlbert A C (1990) Perceptual deficits and the activity of the color-opponent and broad-band pathways at isoluminance. *Science* 247: 214-217.

Lord S (2006) Visual risk factors for falls in older people. *Age and Ageing* 35-S2: ii42-ii45.

Lund J S, Lund R D, Hendrickson A, Brunt A H, and Fuchs A (1976) The origin of efferent pathways from the primary visual cortex, area 17, in the macaque monkey as shown by retrograde transport of horseradish peroxidase. *Journal of Comparative Neurology* 164: 287-304.

Luntinen O, Rovamo J, and Näsänen R (1995) Modelling the increase of contrast sensitivity with grating area and exposure time. *Vision Research* 35: 2339-2346.

Mabuchi F, Aihara M, Mackey M R, Lindsey J D, and Weinreb R N (2004) Regional optic nerve damage in experimental mouse glaucoma. *Investigative Ophthalmology and Visual Science* 45: 4358-4358.

- Maddess T, Goldberg I, Dobinson J, Wine S, Welsh A H, and James A C (1999) Testing for glaucoma with the spatial frequency doubling illusion. *Vision Research* 39: 4258-4273.
- Maddess T, Hemmi J M, and James A C (1998) Evidence for spatial aliasing effects in the Y-like cells of the magnocellular visual pathway. *Vision Research* 38: 1843-1859.
- Maddess T, and Henry G H (1992) Performance of nonlinear visual units in ocular hypertension and glaucoma. *Clinical Vision Sciences* 7: 371-383.
- Maddess T, James A C, Goldberg I, Wine S, and Dobinson J (2000) Comparing a parallel PERG, automated perimetry, and frequency-doubling thresholds. *Investigative Ophthalmology and Visual Science* 41: 3827-3832.
- Mansoori T, Viswanath K, and Balakrishna N (2010) Correlation Between Peripapillary Retinal Nerve Fiber Layer Thickness and Optic Nerve Head Parameters Using Spectral Domain Optical Coherence Tomography. *Journal of Glaucoma* 2010: 22.
- Mareschal I, Bex P J, and Dakin S C (2008) Local motion processing limits fine direction discrimination in the periphery. *Vision Research* 48: 1719-1725.
- Mariani A P (1982) Biplexiform cells: Ganglion cells of the primate retina that contact photoreceptors. *Science* 216: 1134-1136.
- Martin P R, White A J R, Goodchild A K, Wilder H D, and Sefton A E (1997) Evidence that blue-on cells are part of the third geniculocortical pathway in primates. *European Journal of Neuroscience* 9: 1536 - 1541.
- Matsumoto C, Okuyama S, Iwagaki A, Otsuki T, and Otori T (1997) The influence of target blur on perimetric threshold values in automated light-sensitive perimetry and flicker perimetry. In: Wall, M, and Wild, J [eds.] *Perimetry Update 1996/1997*. Amsterdam: Kugler Publications, pp. 191-200.
- Matsumoto C, Shirato S, Haneda M, Yamashiro H, and Saito M (2003) Study of retinal nerve fibre layer thickness within normal hemivisual field in primary open-angle glaucoma and normal-tension glaucoma. *Japanese Journal of Ophthalmology* 47: 22-27.
- Matsuno K, Kurimoto Y, Umihira J, Hoya T, and N Y (2001) Comparative study of retinal nerve fiber layer loss in normal-tension glaucoma and chronic open-angle glaucoma. *Ophthalmologica* 215: 108-112.
- Matsuura K, Miura K, Taki M, Tabata H, Inaba N, Kawano K, and Miles F A (2008) Ocular following responses of monkeys to the competing motions of two sinusoidal gratings. *Neuroscience Research* 61: 56-69.
- Maunsell J, Nealey T, and DePriest D (1990) Magnocellular and parvocellular contributions to responses in the middle temporal visual area (MT) of the macaque monkey. *Journal of Neuroscience* 10: 3323-3334.

Maunsell J H R, and Van Essen D C (1983) Functional properties of neurons in the middle temporal visual area in the macaque monkey, I: selectivity for stimulus direction, speed and orientations. *Journal of Neurophysiology* 49: 1148-1167.

McAnany J J, and Alexander K R (2009) Contrast thresholds in additive luminance noise: Effect of noise temporal characteristics. *Vision Research* 49: 1389-1396.

McKendrick A M, Anderson A J, Johnson C A, and Fortune B (2003) Appearance of the frequency doubling stimulus in normal subjects and patients with glaucoma. *Investigative Ophthalmology and Visual Science* 44: 1111-1116.

McKendrick A M, Badcock D R, and Morgan W H (2004) Psychophysical measurement of neural adaptation abnormalities in magnocellular and parvocellular pathways in glaucoma. *Investigative Ophthalmology and Visual Science* 45: 1846-1853.

McKendrick A M, Sampson G P, Walland M J, and Badcock D R (2007) Contrast sensitivity changes due to glaucoma and normal aging: Low-spatial-frequency losses in both magnocellular and parvocellular pathways. *Investigative Ophthalmology and Visual Science* 48: 2115-2122.

Medeiros F A, Sample P A, and Weinreb R N (2004) Frequency Doubling Technology perimetry abnormalities as predictors of glaucomatous visual field loss. *American Journal of Ophthalmology* 137: 863-871.

Medeiros F A, Zangwill L M, Bowd C, Vessani R M, Susanna J, Remo, and Weinreb R N (2005) Evaluation of retinal nerve fiber layer, optic nerve head, and macular thickness measurements for glaucoma detection using optical coherence tomography. *American Journal of Ophthalmology* 139: 44-55.

Melmoth D R, Kukkonen H T, Makela P K, and Rovamo J M (2000) The Effect of Contrast and Size Scaling on Face Perception in Foveal and Extrafoveal Vision. *Investigative Ophthalmology and Visual Science* 41: 2811-2819.

Merigan W, Byrne C, and Maunsell J (1991a) Does primate motion perception depend on the magnocellular pathway? *Journal of Neuroscience* 11: 3422-3429.

Merigan W H, and Katz L M (1990) Spatial resolution across the macaque retina. *Vision Research* 30: 985-991.

Merigan W H, Katz L M, and Maunsell J H (1991b) The effects of parvocellular lateral geniculate lesions on the acuity and contrast sensitivity of macaque monkeys. *Journal of Neuroscience* 11: 994-1001.

Merigan W H, and Maunsell J H R (1990) Macaque vision after magnocellular lateral geniculate lesions. *Visual Neuroscience* 5: 347-352.

Michelson A (1927) *Studies in Optics*. University of Chicago Press.

Mikami A, Newsome W T, and Wurtz R H (1986) Motion selectivity in macaque visual cortex, I: mechanisms of direction and speed selectivity in extrastriate area MT. *Journal of Neurophysiology* 55: 1308-1327.

Miller K, and Quigley H A (1988) The clinical appearance of the lamina cribrosa as a function of the extent of glaucomatous nerve damage. *Ophthalmology* 95: 135-138.

Mills T, Law S K, Walt J, Buchholz P, and Hansen J (2009) Quality of life in glaucoma and three other chronic diseases: a systematic literature review. *Drugs Aging* 26: 933-950.

Minckler D S (1980) The organization of nerve fiber bundles in the primate optic nerve head. *Archives of Ophthalmology* 98: 1630-1636.

Mitchell P, Smith W, Chey T, and Henley P R (1997) Open-angle glaucoma and diabetes - The Blue Mountains Eye Study, Australia. *Ophthalmology* 104: 712-718.

Monhart M (2007) What are the options of psychophysical approaches in glaucoma? *Survey of Ophthalmology* 52: S127-S133.

Moore D, Harris A, Wudunn D, Kheradiya N, and Siesky B (2008) Dysfunctional regulation of ocular blood flow: A risk factor for glaucoma? *Clinical Ophthalmology* 2: 849-861.

Moreno-Montanes J, Anton A, Garcia N, Olmo N, Morilla A, and Fallon M (2009) Comparison of retinal nerve fiber layer thickness values using stratus optical coherence tomography and Heidelberg Retina Tomograph-III. *Journal of Glaucoma* 18: 528-534.

Moreno M C, Campanelli J, Sande P, Saenz D A, Sarmiento M I, and Rosenstein R E (2004) Retinal oxidative stress induced by high intraocular pressure. *Free Radical Biology and Medicine* 37: 803-812.

Morgan-Davies J, Taylor N, Hill A R, Aspinall P, O'Brien C J, and Azuara-Blanco A (2004) Three dimensional analysis of the lamina cribrosa in glaucoma. *British Journal of Ophthalmology* 88: 1299-1304.

Morgan J E (1994) Selective cell death in glaucoma: Does it really occur? *British Journal of Ophthalmology* 78: 875-880.

Morgan J E (2000) Optic nerve head structure in glaucoma: Astrocytes as mediators of axonal damage. *Eye* 14: 437-444.

Morgan J E (2002) Retinal ganglion cell shrinkage in glaucoma. *Journal of Glaucoma* 11: 365-370.

Morgan J E, Caprioli J, and Koscki Y (1999) Nitric oxide mediates exotoxic and anoxic damage in rat retinal ganglion cells co-cultured with astroglia. *Archives of Ophthalmology* 117: 1524-1529.

Morgan J E, Jeffery G, and Foss A J (1998) Axon deviation in the human lamina cribrosa. *British Journal of Ophthalmology* 82: 680-683.

Morgan J E, Sheen N J L, North R V, Goyal R, Morgan S, Ansari E, and Wild J M (2005) Discrimination of glaucomatous optic neuropathy by digital stereoscopic analysis. *Ophthalmology* 112: 855-862.

Morgan J E, Uchida H, and Caprioli J (2000) Retinal ganglion cell death in experimental glaucoma. *British Journal of Ophthalmology* 84: 303-310.

Mori S, Hangai M, Sakamoto A, and Yoshimura N (2010) Spectral-domain Optical Coherence Tomography Measurement of Macular Volume for Diagnosing Glaucoma. *J Glaucoma* 2010: 15.

Mowatt G, Burr J M, Cook J A, Siddiqui M A, Ramsay C, Fraser C, Azuara-Blanco A et al. (2008) Screening tests for detecting open-angle glaucoma: systematic review and meta-analysis. *Investigative Ophthalmology and Visual Science* 49: 5373-5385.

Moya F J, Brigatti L, and Caprioli J (1999) Effect of ageing on optic nerve appearance: A longitudinal study. *British Journal of Ophthalmology* 83: 567-572.

Mumford W W, and Schelbe E H (1968) *Noise performance factors in communication systems*. Dedham, MA.: Horizon House-Microwave Inc.

Nagaraja N S (1964) Effect of luminance noise on contrast thresholds. *Journal of the Optical Society of America A - Optics Image Science and Vision* 54: 950-955.

Nakayama K, and Tyler C W (1981) Psychophysical isolation of movement sensitivity by removal of familiar position cues. *Vision Research* 21: 427-433.

Nasanen R (1989) Effects of halftoning and noise on visual perception of spatial signals. PhD, Helsinki University of Technology.

Nasanen R, Kukkonen H, and Rovamo J (1993) Spatial integration of band-pass filtered patterns in noise. *Vision Research* 33: 903-911.

Naskar R, Vorwerk C, and Dreyer E (2000) Concurrent downregulation of a glutamate transporter and receptor in glaucoma. *Investigative Ophthalmology and Visual Science* 41: 1940-1944.

Nemesure B, Honkanen R, Hennis A, Wu S Y, and Leske M C (2007) Incident open-angle glaucoma and intraocular pressure. *Ophthalmology* 114: 1810-1815.

Neoh C, Kaye S B, Brown M, Ansons A M, and Wishart P (1994) Pattern electroretinogram and automated perimetry in patients with glaucoma and ocular hypertension. *British Journal of Ophthalmology* 78: 359 - 362.

Newsome W, Wurtz R, Dursteler M, and Mikami A (1985) Deficits in visual motion processing following ibotenic acid lesions of the middle temporal visual area of the macaque monkey. *Journal of Neuroscience* 5: 825-840.

Newsome W T, Britten K H, and Movshon J A (1989) Neuronal correlates of a perceptual decision. *Nature* 341: 52-54.

Newsome W T, and Pare E B (1988) A selective impairment of motion perception following lesions of the middle temporal visual area (MT). *Journal of Neuroscience* 8: 2201-2211.

Ng W S, Agarwal P K, Sidiki S, McKay L, Townend J, and Azuara-Blanco A (2010) The effect of socio-economic deprivation on severity of glaucoma at presentation. *British Journal of Ophthalmology* 94: 85-87.

Nickells R W (1999) Apoptosis of retinal ganglion cells in glaucoma: An update of the molecular pathways involved in cell death. *Survey of Ophthalmology* 43: S151-S161.

Nicolela M T, Walman B E, Buckley A R, and Drance S M (1996) Ocular hypertension and primary open-angle glaucoma: A comparative study of their retrobulbar blood flow velocity. *Journal of Glaucoma* 5: 308-310.

Nolan W P, See J L, Chew P T K, Friedman D S, Smith S D, Radhakrishnan S, Zheng C et al. (2007) Detection of primary angle closure using anterior segment optical coherence tomography in Asian eyes. *Ophthalmology* 114: 33-39.

Nomoto H, Matsumoto C, Takada S, Hashimoto S, Arimura E, Okuyama S, and Shimomura Y (2009) Detectability of glaucomatous changes using SAP, FDT, flicker perimetry, and OCT. *Journal of Glaucoma* 18: 165-171.

North R V, Jones A, Drasdo N, Wild J M, and Morgan J E (2009) Electrophysiological evidence for early functional damage in glaucoma and ocular hypertension. *Investigative Ophthalmology and Visual Science* 22: 22.

Odom J V, Leys M J, Charlton J, Manihilov V, and Green M (2006) Detecting glaucomatous damage: evaluation with contrast independent tasks. *Journal of Modern Optics* 53: 1371-1383.

Ogden T E (1983) Nerve fiber layer of the macaque retina: Retinotopic organisation. *Investigative Ophthalmology and Visual Science* 24: 85-98.

Ogden T E (1984) Nerve fiber layer of the primate retina: Morphometric analysis. *Investigative Ophthalmology and Visual Science* 25: 19-29.

Olds E S, Cowan W B, and Jolicoeur P (1999) Effective color CRT calibration techniques for perception research. *Journal of the Optical Society of America A - Optics Image Science and Vision* 16: 1501-1505.

Oppenheim R (1991) Cell death during development of the nervous system. *Annual Review of Neuroscience* 14: 453-501.

Osborne N, Chidlow G, Layton C, Wood J, Casson R, and Melena J (2004) Optic nerve and neuroprotection strategies. *Eye* 18: 1075-1084.

Osborne N, Ugarte M, Chao M, Bae J, Wood J, and Nash M (1999) Neuroprotection in relation to retinal ischemia and relevance to glaucoma. *Survey of Ophthalmology* 43: S102-S128.

Osbourne N N, Casson R J, Wood J P M, Chidlow G, Graham M, and Melena J (2004) Retinal ischaemia: Mechanisms of damage and potential therapeutic strategies. *Progress in Retinal Eye Research* 23: 91-147.

Papst N, Bopp M, and Schnaudigel O (1984) Pattern electroretinogram and visually evoked cortical potentials in glaucoma. *Graefe's Archive for Clinical and Experimental Ophthalmology* 222: 29-33.

Pardhan S (2004) Contrast sensitivity loss with aging: Sampling efficiency and equivalent noise at different spatial frequencies. *Journal of the Optical Society of America A - Optics Image Science and Vision* 21: 169-175.

Pardhan S, Gilchrist J, and Beh G K (1993) Contrast detection in noise: A new method for assessing the visual function in cataract. *Optometry and Vision Science* 70: 914-922.

Pardhan S, Gilchrist J, Elliott D B, and Beh G K (1996) A comparison of sampling efficiency and internal noise level in young and old subjects. *Vision Research* 36: 1641-1648.

Park S B, Sung K R, Kang S Y, Kim K R, and Kook M S (2009) Comparison of glaucoma diagnostic Capabilities of Cirrus HD and Stratus optical coherence tomography. *Archives of Ophthalmology* 127: 1603-1609.

Pasternak T, and Leinen L J (1986) Pattern and motion vision in cats with selective loss of cortical directional selectivity. *Journal of Neuroscience* 6: 938-945.

Paulsson L E, and Sjostrand J (1980) Contrast sensitivity in the presence of a glare light. Theoretical concepts and preliminary clinical studies. *Investigative Ophthalmology and Visual Science* 19: 401-406.

Pederson J, and Anderson D (1980) The mode of progressive disc cupping in ocular hypertension and glaucoma. *Archives of Ophthalmology* 98: 490-495.

Pederson J E, and Gaasterland D E (1984) Laser-induced primate glaucoma. I. Progression of cupping. *Archives of Ophthalmology* 102: 1689-1692.

Pelli D G (1981) Effects of visual noise. PhD, Cambridge University.

Pelli D G (1990) The quantum efficiency of vision. In: Blakemore, C [ed.] *Vision: Coding and Efficiency*. Cambridge: Cambridge University Press.

Pelli D G, and Farell B (1999) Why use noise? *Journal of the Optical Society of America A - Optics Image Science and Vision* 16: 647-653.

Pelli D G, Levi D M, and Chung S T L (2004) Using visual noise to characterize amblyopic letter identification. *Journal of Vision* 4: 904-920.

- Pelli D G, and Zhang L (1991) Accurate control of contrast on microcomputer displays. *Vision Research* 31: 1337-1350.
- Perry V H, Oehler R, and Cowey A (1984) Retinal ganglion cells that project to the dorsal lateral geniculate nucleus in the macaque monkey. *Neuroscience* 12: 1101-1123.
- Pesudovs K, Hazel C A, Doran R M L, and Elliott D B (2004) The usefulness of Vistech and FACT contrast sensitivity charts for cataract and refractive surgery outcomes research. *British Journal of Ophthalmology* 88: 11-16.
- Peterson B B, and Dacey D M (1998) Morphology of human retinal ganglion cells with intraretinal axon collaterals. *Visual Neuroscience* 15: 377-387.
- Petri D (1996) Dither signals and quantization. *Measurement* 19: 147-157.
- Phelps C, and Corbett J (1985) Migraine and low-tension glaucoma. A case-control study. *Investigative Ophthalmology and Visual Science* 26: 1105-1108.
- Plange N, Remky A, and Arend O (2003a) Colour doppler imaging and fluorescein filling defects of the optic disc in normal tension glaucoma. *British Journal of Ophthalmology* 87: 731-736.
- Plange N H, Kaup M, Remky A, Harris A, and Arend O (2003b) Hypercapnia and retrobulbar blood flow velocities in normal tension glaucoma and healthy controls. *Investigative Ophthalmology and Visual Science* 44: 142.
- Porciatti V, di Bartolo E, Nardi M M, and Fiorentini A (1997) Responses to chromatic and luminance contrast in glaucoma: a psychophysical and electrophysiological study. *Vision Research* 37: 1975-1987.
- Porciatti V, Falsini B, Brunori S, Colotto A, and Moretti G (1987) Pattern electroretinogram as a function of spatial frequency in ocular hypertension and early glaucoma. *Documenta Ophthalmologica* 65: 349-355.
- Porciatti V, and von Berger G (1984) Pattern electroretinogram and visual evoked potential in optic nerve disease: Early diagnosis and prognosis. *Documenta Ophthalmologica Proceedings Series* 40: 117-126.
- Pournaras C J, Riva C E, Bresson-Dumont H, De Gottrau P, and Bechetoille A (2004) Regulation of optic nerve head blood flow in normal tension glaucoma patients. *European Journal of Ophthalmology* 14: 226-235.
- Powers M (2009) Paper tools for assessing visual function. *Optometry and Vision Science* 86: 613-618.
- Prata T S, De Moraes C G, Teng C C, Tello C, Ritch R, and Liebmann J M (2009) Factors affecting rates of visual field progression in glaucoma patients with optic disc hemorrhage. *Ophthalmology* 4: 4.

- Punjabi O S, Stamper R L, Bostrom A G, Han Y, and Lin S C (2008) Topographic comparison of the visual function on multifocal visual evoked potentials with optic nerve structure on Heidelberg Retinal Tomography. *Ophthalmology* 115: 440-446.
- Quaid P, Simpson T, and Flanagan J (2005) Frequency doubling illusion: Detection vs. form resolution. *Optometry and Vision Science* 82: 36-42.
- Quigley H (1996) Number of people with glaucoma worldwide. *British Journal of Ophthalmology* 80: 389-393.
- Quigley H, Sanchez R, Dunkelberger G, L'Hernault N, and Baginski T (1987) Chronic glaucoma selectively damages large optic nerve fibers. *Investigative Ophthalmology and Visual Science* 28: 913-920.
- Quigley H A, and Addicks E M (1981) Regional differences in the structure of the lamina cribrosa and their relation to glaucomatous optic nerve damage. *Archives of Ophthalmology* 99: 137-143.
- Quigley H A, Addicks E M, and Green W R (1982) Optic nerve damage in human glaucoma. III. Quantitative correlation of nerve fiber loss and visual field defect in glaucoma, ischemic neuropathy, papilledema, and toxic neuropathy. *Archives of Ophthalmology* 100: 135-146.
- Quigley H A, and Broman A T (2006) The number of people with glaucoma worldwide in 2010 and 2020. *British Journal of Ophthalmology* 90: 262-267.
- Quigley H A, Brown A E, and Dormanpease M E (1991) Alterations in elastin of the optic nerve head in human and experimental glaucoma. *British Journal of Ophthalmology* 75: 552-557.
- Quigley H A, Dunkelberger G, and Green W R (1988) Chronic human glaucoma causing selectively greater loss of large optic nerve fibres. *Ophthalmology* 95: 357 - 363.
- Quigley H A, Dunkelberger G, and Green W R (1989) Retinal ganglion cell atrophy correlated with automated perimetry in human eyes with glaucoma. *American Journal of Ophthalmology* 107: 453.
- Quigley H A, Enger C, Katz J, Sommer A S, R., and Gilbert D (1994a) Risk factors for the development of glaucomatous visual field loss in ocular hypertension. *Archives of Ophthalmology* 112: 644-649.
- Quigley H A, and Green W R (1979) The histology of human glaucoma cupping and optic-nerve damage - clinicopathologic correlation in twenty one eyes. *Ophthalmology* 86: 1803-1830.
- Quigley H A, Hohman R M, Addicks E M, Massof R W, and Green W R (1983) Morphologic changes in the lamina cribrosa correlated with neural loss in open-angle glaucoma. *American Journal of Ophthalmology* 95: 673-691.

Quigley H A, Nickells R W, Zack D J, Kerrigan L A, Thibault D J, and Pease M E (1994b) Ganglion cell death in glaucoma occurs by apoptosis. *Investigative Ophthalmology and Visual Science* 35: S2083.

Quigley H A, Varma R, Tielsch J M, Katz J, Sommer A, and Gilbert D L (1999) The relationship between optic disc area and open-angle glaucoma: The Baltimore eye survey. *Journal of Glaucoma* 8: 347-352.

Racette L, Medeiros F A, Zangwill L M, Ng D, Weinreb R N, and Sample P A (2008) Diagnostic accuracy of the Matrix 24-2 and original N-30 Frequency-Doubling Technology tests compared with standard automated perimetry. *Investigative Ophthalmology and Visual Science* 49: 954-960.

Radhakrishnan H, and Pardhan S (2006) Contrast detection in noise with positive and negative defocus in myopes. *Vision Research* 46: 2949-2955.

Radius R L (1980) Thickness of the retinal nerve fibre layer in primate eyes. *Archives of Ophthalmology* 98: 1625-1629.

Radius R L (1987) Anatomy of the optic nerve head and glaucomatous optic neuropathy. *Survey of Ophthalmology* 32: 35.

Radius R L, and Bade B (1981) Pressure-induced optic nerve axonal transport interruption in cat eyes. *Archives of Ophthalmology* 99: 2163-2165.

Radius R L, and Pederson J E (1984) Laser-induced primate glaucoma. II. Histopathology. *Archives of Ophthalmology* 102: 1693-1698.

Ramrattan R S, Wolfs R C W, Jonas J B, Hofman A, and De Jong P T V M (1999) Determinants of optic disc characteristics in a general population: The Rotterdam study: Historical image. *Ophthalmology* 106: 1588-1596.

Rankin S J A, Drance S M, Buckley A R, and Walman B E (1996) Visual field correlations with colour doppler studies in open angle glaucoma. *Journal of Glaucoma* 5: 15-21.

Reibaldi A, and Uva M G (1992) Surgical management of closed angle glaucoma: Our experience. *International Ophthalmology* 16: 4-5.

Reus N J, and Lemij H G (2004a) Diagnostic accuracy of the GDx VCC for glaucoma. *Ophthalmology* 111: 1860-1865.

Reus N J, and Lemij H G (2004b) Scanning laser polarimetry of the retinal nerve fiber layer in perimetrically unaffected eyes of glaucoma patients. *Ophthalmology* 111: 2199-2203.

Richards W, and Felton T (1973) Spatial frequency doubling: Retinal or central. *Vision Research* 13: 2129-2137.

Riva C E, Salgarello T, Logean E, Colotto A, Galan E M, and Falsini B (2004) Flicker-evoked response measured at the optic disc rim is reduced in ocular hypertension and early glaucoma. *Investigative Ophthalmology and Visual Science* 45: 3662-3668.

Robinson F, Riva C E, Grunwald J E, Petrig B L, and Sinclair S H (1986) Retinal blood flow autoregulation in response to acute increase of blood pressure. *Investigative Ophthalmology and Visual Science* 27: 1706-1712.

Rodieck R W (1998) *The first step in seeing*. Sunderland, MA: Sinauer Associates.

Ross J E, Clarke D D, and Bron A J (1985) Effect of age on contrast sensitivity function: unocular and binocular findings. *British Journal of Ophthalmology* 69: 51-56.

Rossetti L, Fogagnolo P, Miglior S, Centofanti M, Vetrugno M, and Orzalesi N (2006) Learning effect of short-wavelength automated perimetry in patients with ocular hypertension. *Journal of Glaucoma* 15: 399-404.

Rossi E A, and Roorda A (2009) The relationship between visual resolution and cone spacing in the human fovea. *Nature Neuroscience* 13: 156-157.

Rovamo J, Donner K, Nasanen R, and Raninen A (2000) Flicker sensitivity as a function of target area with and without temporal noise. *Vision Research* 40: 3841-3851.

Rovamo J, Franssila R, and Nasanen R (1992) Contrast sensitivity as a function of spatial-frequency, viewing distance and eccentricity with and without spatial noise. *Vision Research* 32: 631-637.

Rovamo J, and Kukkonen H (1996) The effect of noise check size and shape on grating detectability. *Vision Research* 36: 271-279.

Rovamo J, Kukkonen H, Raninen A, and Donner K (2003) Efficiency of temporal integration of sinusoidal flicker. *Investigative Ophthalmology and Visual Science* 44: 5049-5055.

Rovamo J, Kukkonen H, Tiippana K, and Nasanen R (1993a) Effects of luminance and exposure time on contrast sensitivity in spatial noise. *Vision Research* 33: 1123-1129.

Rovamo J, Luntinen O, and Nasanen R (1993b) Modelling the dependence of contrast sensitivity on grating area and spatial-frequency. *Vision Research* 33: 2773-2788.

Rovamo J, Raninen A, and Donner K (1999) The effects of temporal noise and retinal illuminance on foveal flicker sensitivity. *Vision Research* 39: 533-550.

Rovamo J, Raninen A, Lukkarinen S, and Donner K (1996) Flicker sensitivity as a function of spectral density of external white temporal noise. *Vision Research* 36: 3767-3774.

Rovamo J, and Virsu V (1979) An estimation and application of the human cortical magnification factor. *Experimental Brain Research* 37: 495-510.

Rovamo J M, Kankaanpaa M I, and Hallikainen J (2001) Spatial neural modulation transfer function of human foveal visual system for equiluminous chromatic gratings. *Vision Research* 41: 1659-1667.

Rovamo J M, Mustonen J K, and Nasanen R (1993c) Grating contrast sensitivity as a function of exposure time and retinal illuminance. *Investigative Ophthalmology and Visual Science* 34: 780-780.

Rudnicka A R, Frost C, Owen C G, and Edgar D F (2001) Nonlinear behavior of certain optic nerve head parameters and their determinants in normal subjects. *Ophthalmology* 108: 2358-2368.

Ruppertsberg A I, Wuerger S M, and Bertamini M (2003) The chromatic input to global motion perception. *Visual Neuroscience* 20: 421-428.

Sacca S C, and Izzotti A (2008) Oxidative stress and glaucoma: injury in the anterior segment of the eye. *Progress in Brain Research* 173: 385-407.

Saccà S C, Rolando M, Marletta A, Macrì A, Cerqueti P, and Ciurlo G (1998) Fluctuations of intraocular pressure during the day in open-angle glaucoma, normal-tension glaucoma and normal subjects. *Ophthalmologica* 212: 115-119.

Saeed M U, Chang B Y P, Khandwala M, Shivane A G, and Chakrabarty A (2006) Twenty year review of histopathological findings in enucleated/eviscerated eyes. *Journal of Clinical Pathology* 59: 153-155.

Samdani A F, Dawson T M, and Dawson V L (1997a) Nitric oxide synthase in models of focal ischaemia. *Stroke* 28: 1283-1288.

Samdani A F, Newcamp C, Resink A, Facchinetti F, Hoffman B E, Dawson V L, and Dawson T M (1997b) Differential susceptibility to neurotoxicity mediated by neurotrophins and neuronal nitric oxide synthase. *Journal of Neuroscience* 17: 4633-4641.

Sample P, Boynton R, and Weinreb R (1988) Isolating the color vision loss in primary open-angle glaucoma. *American Journal of Ophthalmology* 106: 686-691.

Sample P, and Weinreb R (1990) Color perimetry for assessment of primary open-angle glaucoma. *Investigative Ophthalmology and Visual Science* 31: 1869-1875.

Sample P A, Bosworth C F, Blumenthal E Z, Girkin C, and Weinreb R N (2000) Visual function-specific perimetry for indirect comparison of different ganglion cell populations in glaucoma. *Investigative Ophthalmology and Visual Science* 41: 1783-1790.

Sample P A, Medeiros F A, Racette L, Pascual J P, Boden C, Zangwill L M, Bowd C et al. (2006a) Identifying Glaucomatous Vision Loss with Visual-Function-Specific Perimetry in the Diagnostic Innovations in Glaucoma Study. *Invest. Ophthalmol. Vis. Sci.* 47: 3381-3389.

Sample P A, Medeiros F A, Racette L, Pascual J P, Boden C, Zangwill L M, Bowd C et al. (2006b) Identifying glaucomatous vision loss with visual-function-specific perimetry in

the diagnostic innovations in glaucoma study. *Investigative Ophthalmology and Visual Science* 47: 3381-3389.

Sanchez R, Dunkelberger G, and Quigley H A (1986) The number and diameter distribution of axons in the monkey optic nerve. *Investigative Ophthalmology and Visual Science* 27: 1342-1350.

Saragovi H U, Hamel E, and Di Polo A (2009) A neurotrophic rationale for the therapy of neurodegenerative disorders. *Current Alzheimer Research* 6: 419-423.

Satilmis M, Orgul S, Doubler B, and Flammer J (2003) Rate of progression of glaucoma correlates with retrobulbar circulation and intraocular pressure. *American Journal of Ophthalmology* 124: 46-52.

Saunders D C (1990) Acute closed-angle glaucoma and Nd-YAG laser iridotomy. *British Journal of Ophthalmology* 74: 523-525.

Savoy R L, and McCann J J (1975) Visibility of low-spatial-frequency sine-wave targets: Dependence on number of cycles. *Journal of the Optical Society of America A - Optics Image Science and Vision* 65: 343-350.

Schade O H (1956) Optical and photoelectric analog of the eye. *Journal of the Optical Society of America A - Optics Image Science and Vision* 46: 721-739.

Schiller P H (1986) The central visual system. *Vision Research* 26: 1351-1386.

Schmeisser E T, and Smith T J (1989) High-frequency flicker visual-evoked potential losses in glaucoma. *Ophthalmology* 96: 620.

Sehi M, Guaqueta D C, Feuer W J, and Greenfield D S (2007) A comparison of structural measurements using 2 Stratus optical coherence tomography instruments. *Journal of Glaucoma* 16: 287-292.

Sehi M, Pinzon-Plazas M, Feuer W J, and Greenfield D S (2009) Relationship between pattern electroretinogram, standard automated perimetry, and optic nerve structural assessments. *Journal of Glaucoma* 18: 608-617.

Seider M I, Pekmezci M, Han Y, Sandhu S, Kwok S Y, Lee R Y, and Lin S C (2009) High prevalence of narrow angles among Chinese-American glaucoma and glaucoma suspect patients. *Journal of Glaucoma* 18: 578-581.

Sekeroglu M A, Irkec M, Mocan M C, Ileri E, Dikmenoglu N, Seringec N, Karaosmanoglu D et al. (2009) The association of ocular blood flow with haemorheological parameters in primary open-angle and exfoliative glaucoma. *Acta Ophthalmologica* 23: 23.

Shapley R (1990) Visual sensitivity and parallel retinocortical channels. *Annual Review of Psychology* 41: 635-658.

Sigal L H (1999) Molecular biology and immunology for clinicians, and pathogenesis of autoimmunity-apoptosis. *Journal of Clinical Rheumatology* 5: 239-242.

Silverman S, Trick G, and Hart W, Jr (1990) Motion perception is abnormal in primary open-angle glaucoma and ocular hypertension. *Investigative Ophthalmology and Visual Science* 31: 722-729.

Simpson W A, Falkenberg H K, and Manahilov V (2003a) Sampling efficiency and internal noise for motion detection, discrimination, and summation. *Vision Research* 43: 2125-2132.

Simpson W A, Findlay K, and Manahilov V (2003b) Efficiency and internal noise for detection of suprathreshold patterns measured using simple reaction time. *Vision Research* 43: 1103-1109.

Sloane M E, Owsley C, and Alvarez S L (1988) Aging, senile miosis and spatial contrast sensitivity at low luminance. *Vision Research* 28: 1235-1246.

Smith P, and Ratcliff R (2009) An integrated theory of attention and decision making in visual signal detection. *Psychological Review* 116: 283-317.

Soares A S, Artes P H, Andreou P, Leblanc R P, Chauhan B C, and Nicolela M T (2004) Factors associated with optic disc hemorrhages in glaucoma. *Ophthalmology* 111: 1653-1657.

Sommer A, Katz J, Quigley H A, Miller N R, Robin A L, Richter R C, and Witt K A (1991a) Clinically detectable nerve fiber atrophy precedes the onset of glaucomatous field loss. *Archives of Ophthalmology* 109: 77-83.

Sommer A, Tielsch J M, Katz J, Quigley H A, Gottsch J D, Javitt J, and Singh K (1991b) Relationship between intraocular-pressure and primary open angle glaucoma among white and black-Americans - the Baltimore Eye Survey. *Archives of Ophthalmology* 109: 1090-1095.

Sonnsjo B, and Krakau C E T (1993) Arguments for a Vascular Glaucoma Etiology. *Acta Ophthalmologica* 71: 433-444.

Sorensen T L, and Kemp H (2010) Ranibizumab treatment in patients with neovascular age-related macular degeneration and very low vision. *Acta Ophthalmologica* 2010: 6.

Sponsel W E, Arango S, Trigo Y, and Mensah J (1998) Clinical classification of glaucomatous visual field loss by frequency doubling perimetry. *American Journal of Ophthalmology* 125: 830-836.

Spraul C W, Lang G E, Lang G K, and Grossniklaus H E (2002) Morphometric changes of the choriocapillaris and the choroidal vasculature in eyes with advanced glaucomatous changes. *Vision Research* 42: 923-932.

Spry P G D, Johnson C A, McKendrick A M, and Turpin A (2001) Variability components of standard automated perimetry and frequency-doubling technology perimetry. *Investigative Ophthalmology and Visual Science* 42: 1404-1410.

- Stalmans I, Harris A, Vanbellinghen V, Zeyen T, and Siesky B (2008) Ocular pulse amplitude in normal tension and primary open angle glaucoma. *Journal of Glaucoma* 17: 403-407.
- Stanislaw H, and Olzak L A (1990) Parametric methods for gamma and inverse gamma correction, with extensions to halftoning. *Behavior Research Methods, Instruments and Computers* 22: 402-408.
- Stone J, and Johnston E (1981) The topography of primate retina: A study of the human, bushbaby, and New- and Old-world monkeys. *Journal of Comparative Neurology* 196: 205-224.
- Stromeyer C F, and Julesz B (1972) Spatial-frequency masking in vision: critical bands and spread of masking. *Journal of the Optical Society of America A - Optics Image Science and Vision* 62: 1221-1232.
- Strouthidis N G, Demirel S, Asaoka R, Cossio-Zuniga C, and Garway-Heath D F (2010) The Heidelberg Retina Tomograph Glaucoma Probability Score: reproducibility and measurement of progression. *Ophthalmology* 117: 724-729.
- Strouthidis N G, Gardiner S K, Owen V M, Zuniga C, and Garway-Heath D F (2009) Predicting progression to glaucoma in ocular hypertensive patients. *Journal of Glaucoma* 2: 2.
- Stys P, and Lesiuk H (1996) Correlation between electrophysiological effects of mexiletine and ischaemic protection in central nervous system white matter. *Neuroscience* 71: 27-36.
- Sullivan-Mee M, Gentry J M, and Qualls C (2006) Relationship between asymmetric central corneal thickness and glaucomatous visual field loss within the same patient. *Optometry and Vision Science* 83: 516-519.
- Sung K R, Wollstein G, Bilonick R A, Townsend K A, Ishikawa H, Kagemann L, Noecker R J et al. (2009a) Effects of age on optical coherence tomography measurements of healthy retinal nerve fiber layer, macula, and optic nerve head. *Ophthalmology* 116: 1119-1124.
- Sung K R, Wollstein G, Schuman J S, Bilonick R A, Ishikawa H, Townsend K A, Kagemann L et al. (2009b) Scan quality effect on glaucoma discrimination by glaucoma imaging devices. *British Journal of Ophthalmology* 93: 1580-1584.
- Swanson W H, Dul M W, and Fischer S E (2005) Quantifying effects of retinal illuminance on frequency doubling perimetry. *Investigative Ophthalmology and Visual Science* 46: 235-240.
- Szmajda B, Grünert U, and Martin P (2008) Retinal ganglion cell inputs to the koniocellular pathway. *Journal of Comparative Neurology* 20: 251-268.
- Tafreshi A, Sample P A, Liebmann J M, Girkin C A, Zangwill L M, Weinreb R N, Lalezary M et al. (2009) Visual function-specific perimetry to identify glaucomatous

visual loss using three different definitions of visual field abnormality. *Investigative Ophthalmology and Visual Science* 50: 1234-1240.

Takeuchi T, De Valois K K, and Hardy J L (2003) The influence of color on the perception of luminance motion. *Vision Research* 43: 1159-1175.

Tan J C H, and Hitchings R A (2004) Reversal of disc cupping after intraocular pressure reduction in topographic image series. *Journal of Glaucoma* 13: 351-355.

Tannenbaum D P, Hoffman D, Lemij H G, Garway-Heath D F, Greenfield D S, and Caprioli J (2004) Variable corneal compensation improves discrimination between normal and glaucomatous eyes with the scanning laser polarimeter. *Ophthalmology* 111: 259-264.

Thayaparan K, Crossland M D, and Rubin G S (2007) Clinical assessment of two new contrast sensitivity charts. *British Journal of Ophthalmology* 91: 749-752.

Tielsch J M, Katz J, Quigley H A, Miller N R, and Sommer A (1988) Intraobserver and interobserver agreement in measurement of optic disc characteristics. *Ophthalmology* 95: 350-356.

Tielsch J M, Sommer A, Katz J, Royall R M, Quigley H A, and Javitt J (1991) Racial variations in the prevalence of primary open-angle glaucoma. The Baltimore Eye Survey. *Journal of the American Medical Association* 266: 369-374.

Tootell R B H, Reppas J B, Kwong K K, and al. e (1995) Functional analysis of human MT and related visual cortical areas using magnetic-resonance imaging. *Journal of Neuroscience* 15: 3215-3230.

Traverso C E, Walt J G, Kelly S P, Hommer A H, Bron A M, Denis P, Nordmann J P et al. (2005) Direct costs of glaucoma and severity of the disease: a multinational long term study of resource utilisation in Europe. *British Journal of Ophthalmology* 89: 1245-1249.

Travis D (1991) *Effective colour displays theory and practice*. London: Academic Press.

Trew D R, and Smith S E (1991) Postural studies in pulsatile ocular blood flow: II. Chronic open angle glaucoma. *British Journal of Ophthalmology* 75: 71-75.

Trick G L, Steinman S B, and Amyot M (1995) Motion perception deficits in glaucomatous optic neuropathy. *Vision Research* 35: 2225-2233.

Tuulonen A, and Airaksinen P J (1991) Initial glaucomatous optic disc and retinal nerve-fibre layer abnormalities and their progression. *American Journal of Ophthalmology* 111: 485-490.

Tyler C (1981) Specific deficits of flicker sensitivity in glaucoma and ocular hypertension. *Investigative Ophthalmology and Visual Science* 20: 204-212.

Vallam K, and Metha A (2007) Spatial structure of the frequency doubling illusion. *Vision Research* 47: 1732-1744.

- Van Buren A (1963) *The retinal ganglion cell layer*. Springfield: Thomas.
- Varma D, Baylis O, Wride N, Phelan P S, and Fraser S G (2006) Viscogonioplasty: an effective procedure for lowering intraocular pressure in primary angle closure glaucoma. *Eye* 21: 472-475.
- Varma R, Skaf M, and Barron E (1996) Retinal nerve fiber layer thickness in normal human eyes. *Ophthalmology* 103: 2114-2119.
- Varma R, Steinmann W, and Scott I (1992) Expert agreement in evaluating the optic disc for glaucoma. *Ophthalmology* 99: 215-221.
- Varma R, Tielsch J M, Quigley H A, Hilton S C, Katz J, Spaeth G L, and Sommer A (1994) Race-related, age-related, gender-related, and refractive error-related differences in the normal optic disc. *Archives of Ophthalmology* 112: 1068-1076.
- Varma R, Ying-Lai M, Francis B A, Nguyen B B-T, Deneen J, Wilson M R, and Azen S P (2004) Prevalence of open-angle glaucoma and ocular hypertension in Latinos: The Los Angeles Latino Eye Study. *Ophthalmology* 111: 1439-1448.
- Ventura L M, and Porciatti V (2005) Restoration of retinal ganglion cell function in early glaucoma after intraocular pressure reduction: A pilot study. *Ophthalmology* 112: 20-27.
- Ventura L M, Porciatti V, Ishida K, Feuer W J, and Parrish Ii R K (2005) Pattern electroretinogram abnormality and glaucoma. *Ophthalmology* 112: 10-19.
- Vernon S A (1991) Screening siblings for glaucoma in the UK. *Journal of the Royal Society of Medicine* 84: 545-546.
- Vickers J C, Hof P R, Schumer R A, Wang R F, Podos S M, and Morrison J H (1997) Magnocellular and parvocellular visual pathways are both affected in a macaque monkey model of glaucoma. *Australian and New Zealand Journal of Ophthalmology* 25: 239-243.
- Vickers J C, Schumer R A, Podos S M, Wang R F, Riederer B M, and Morrison J H (1995) Differential vulnerability of neurochemically identified subpopulations of retinal neurons in a monkey model of glaucoma. *Brain Research* 680: 23-35.
- Virsu V, and Rovamo J (1979) Visual resolution, contrast sensitivity, and the cortical magnification factor. *Experimental Brain Research* 37: 475-494.
- Visontai Z, Mersich B, and Hollo G (2005) Carotid artery elasticity and baroreflex sensitivity in patients with glaucoma. *Journal of Glaucoma* 14: 30-35.
- Vorwerk C, Gorla M, and Dreyer E (1999a) An experimental basis for implicating exotoxicity in glaucomatous optic neuropathy. *Survey of Ophthalmology* 43: S142-S150.
- Vorwerk C, Naskar R, and Dreyer E (1999b) Excitotoxicity and glaucoma. *Klinische Monatsblätter für Augenheilkunde* 214: 2-11.

- Wall M, Chauhan B, FrisÅ©n L, House P H, and Brito C (2004a) Visual Field of High-Pass Resolution Perimetry in Normal Subjects. *Journal of Glaucoma* 13.
- Wall M, Chauhan B, Frisen L, House P H, and Brito C (2004b) Visual field of high-pass resolution perimetry in normal subjects. *Journal of Glaucoma* 13: 15-21.
- Wall M, Jennisch C S, and Munden P M (1997) Motion perimetry identifies nerve fiber bundlelike defects in ocular hypertension. *Archives of Ophthalmology* 115: 26-33.
- Wall M, and Ketoff K M (1995) Random dot motion perimetry in patients with glaucoma and in normal subjects. *American Journal of Ophthalmology* 120: 587.
- Wall M, Woodward K R, Doyle C K, and Artes P H (2009) Repeatability of automated perimetry: A comparison between standard automated perimetry with stimulus size III and V, matrix, and motion perimetry. *Investigative Ophthalmology and Visual Science* 50: 974-979.
- Wanger P, and Persson H (1983) Pattern-reversal electroretinograms in unilateral glaucoma. *Investigative Ophthalmology and Visual Science* 24: 749-753.
- Watanabe M, and Rodieck R W (1989) Parasol and midget ganglion cells of the primate retina. *Journal of Comparative Neurology* 289: 434 - 454.
- Wax M B, Barrett D A, and Pestronk A (1994) Increased incidence of paraproteinemia and autoantibodies in patients with normal-pressure glaucoma. *American Journal of Ophthalmology* 117: 561-568.
- Weber A, Kaufman P, and Hubbard W (1998) Morphology of single ganglion cells in the glaucomatous primate retina. *Investigative Ophthalmology and Visual Science* 39: 2304-2320.
- Weber A J, Chen H, Hubbard W C, and Kaufman P L (2000) Experimental glaucoma and cell size, density, and number in the primate lateral geniculate nucleus. *Investigative Ophthalmology and Visual Science* 41: 1370-1379.
- Weber A J, and Harman C D (2005) Structure-function relations of parasol cells in the normal and glaucomatous primate retina. *Investigative Ophthalmology and Visual Science* 46: 3197-3207.
- Weber A J, Harman C D, and Viswanathan S (2008) Effects of optic nerve injury, glaucoma, and neuroprotection on the survival, structure, and function of ganglion cells in the mammalian retina. *The Journal of Physiology* 586: 4393-4400.
- Weih L M, Mukesh B N, McCarty C A, and Taylor H R (2001a) Association of demographic, familial, medical, and ocular factors with intraocular pressure. *Archives of Ophthalmology* 119: 875-880.
- Weih L M, Mukesh B N, McCarty C A, and Taylor H R (2001b) Prevalence and predictors of open-angle glaucoma: Results from The Visual Impairment Project. *Ophthalmology* 108: 1966-1972.

Weinreb R N, Bowd C, and Zangwill L M (2003) Glaucoma detection using scanning laser polarimetry with Variable Corneal Polarization Compensation. *Archives of Ophthalmology* 121: 218-224.

Weinreb R N, Dreher A W, Coleman A, Quigley H, Shaw B, and Reiter K (1990) Histopathologic Validation of Fourier-Ellipsometry Measurements of Retinal Nerve Fiber Layer Thickness. *Archives of Ophthalmology* 108: 557-560.

Weinreb R N, and Levin L A (1999) Is neuroprotection a viable therapy for glaucoma? *Archives of Ophthalmology* 117: 1540-1544.

Weinreb R N, Shakiba S, and Zangwill L (1995) Scanning laser polarimetry to measure the nerve fibre layer of normal and glaucomatous eyes. *American Journal of Ophthalmology* 119: 627-636.

Werner E, and Drance S (1977) Early visual field disturbances in glaucoma. *Archives of Ophthalmology* 95: 1173-1175.

Westcott M C, Garway-Heath D F, Fitzke F W, Kamal D, and Hitchings R A (2002) Use of high spatial resolution perimetry to identify scotomata not apparent with conventional perimetry in the nasal field of glaucomatous subjects. *British Journal of Ophthalmology* 86: 761-766.

Wetherill G B, and Levitt H (1965) Sequential estimation of points on a psychometric function. *The British Journal of Mathematical and Statistical Psychology* 18: 1-10.

White A J R, Sun H, Swanson W H, and Lee B B (2002) An examination of physiological mechanisms underlying the frequency-doubling illusion. *Investigative Ophthalmology and Visual Science* 43: 3590-3599.

Wild J M (2001) Short wavelength automated perimetry. *Acta Ophthalmologica Scandinavica* 79: 546-559.

Wild J M (2010) Cardiff School of Optometry and Vision Sciences. *Personal communication*.

Wild J M, Bourtsoukli I, Cunliffe I A, Ansari E A, Rajkumar K, North R V, and Morgan J E (2005) Patterns of normal neuroretinal rim configuration: The reliability of the ISNT rule in clinical decisions for glaucoma. *Investigative Ophthalmology and Visual Science* 46: 2494-.

Wild J M, Cubbidge R P, Pacey I E, and Robinson R (1998) Statistical aspects of the normal visual field in short-wavelength automated perimetry. *Investigative Ophthalmology and Visual Science* 39: 54-63.

Wild J M, Kim L S, Pacey I E, and Cunliffe I A (2006) Evidence for a learning effect in short-wavelength automated perimetry. *Ophthalmology* 113: 206-215.

Wild J M, Moss I D, Whitaker D, and O'Neill E C (1995) The statistical interpretation of blue-on-yellow visual field loss. *Investigative Ophthalmology and Visual Science* 36: 1398-1410.

Wild J M, Pacey I E, O'Neill E C, and Cunliffe I A (1999) The SITA perimetric threshold algorithms in glaucoma. *Investigative Ophthalmology and Visual Science* 40: 1998-2009.

Williams Z Y, Schuman J S, Gamell L, Nemi A, Hertzmark E, Fujimoto J G, Mattox C et al. (2002) Optical coherence tomography measurement of nerve fiber layer thickness and the likelihood of a visual field defect. *American Journal of Ophthalmology* 134: 538-546.

Willis A, and Anderson S J (2000) Effects of glaucoma and aging on photopic and scotopic motion perception. *Investigative Ophthalmology and Visual Science* 41: 325-335.

Wilson H R (1985) A model for direction selectivity in threshold motion perception. *Biological Cybernetics* 51: 213-222.

Wojtkowski M, Srinivasan V, Fujimoto J G, Ko T, Schuman J S, Kowalczyk A, and Duker J S (2005) Three-dimensional retinal imaging with high-speed ultra high-resolution optical coherence tomography. *Ophthalmology* 112: 1734-1746.

Wollstein G, Schuman J S, Price L L, Aydin A, Beaton S A, Stark P C, Fujimoto J G et al. (2004) Optical coherence tomography (OCT) macular and peripapillary retinal nerve fiber layer measurements and automated visual fields. *American Journal of Ophthalmology* 138: 218-225.

Wollstein G, Schuman J S, Price L L, Aydin A, Stark P C, Hertzmark E, Lai E et al. (2005) Optical coherence tomography longitudinal evaluation of retinal nerve fiber layer thickness in glaucoma. *Archives of Ophthalmology* 123: 464-470.

Wright C, and Drasdo N (1985) The influence of age on the spatial and temporal contrast sensitivity function. *Documenta Ophthalmologica* 59: 385-395.

Wyllie A (1992) Apoptosis and the regulation of cell numbers in normal and neoplastic tissues: An overview. *Cancer Metastasis Review* 11: 95-103.

Wyllie A, Kerr J, and Currie A (1980) Cell death: The significance of apoptosis. *International Review of Cytology* 68: 251-306.

Yablonski M E, and Asamoto A (1993) Hypothesis concerning the pathophysiology of optic nerve damage in open angle glaucoma. *Journal of Glaucoma* 2: 119-127.

Yamada E S, Silveira L C, and Perry V H (1996) Morphology, dendritic field size, somal size, density and coverage of M and P retinal ganglion cells of dichromatic Cebus monkeys. *Visual Neuroscience* 13: 1011-1029.

Yamazaki Y, and Drance S M (1997) The relationship between progression of visual field defects and retrobulbar circulation in patients with glaucoma. *American Journal of Ophthalmology* 124: 287-295.

Yates J T, Monique J L, Marc G, Wei H, Judie C, Janis R, Bao-Zhong D et al. (1998) Parallel pathways, noise masking and glaucoma detection: behavioral and electrophysiological measures. *Documenta Ophthalmologica* V95: 283-299.

Yoshiyama K, and Johnson C (1997) Which method of flicker perimetry is most effective for detection of glaucomatous visual field loss? *Investigative Ophthalmology and Visual Science* 38: 2270-2277.

Yucel Y H, Zhang Q, Gupta N, Kaufman P L, and Weinreb R N (2000) Loss of neurons in magnocellular and parvocellular layers of the lateral geniculate nucleus in glaucoma. *Archives of Ophthalmology* 118: 378-384.

Yucel Y H, Zhang Q, Weinreb R N, Kaufman P L, and Gupta N (2001) Atrophy of relay neurons in magno- and parvocellular layers in the lateral geniculate nucleus in experimental glaucoma. *Investigative Ophthalmology and Visual Science* 42: 3216-3222.

Yucel Y H, Zhang Q A, Weinreb R N, Kaufman P L, and Gupta N (2003) Effects of retinal ganglion cell loss on magno-, parvo-, koniocellular pathways in the lateral geniculate nucleus and visual cortex in glaucoma. *Progress in Retinal and Eye Research* 22: 465-481.

Zangwill L, Medeiros F, Bowd C, and Weinreb R (2004a) Optic nerve imaging: Recent advances. In: Grehn, F, and Stamper, R [eds.] *Glaucoma*. Berlin: Springer, pp. 63-91.

Zangwill L M, Bowd C, Berry C C, Williams J, Blumenthal E Z, Sanchez-Galeana C A, Vasile C et al. (2001) Discriminating between normal and glaucomatous eyes using the Heidelberg Retina Tomograph, GDx Nerve Fiber Analyzer, and Optical Coherence Tomograph. *Archives of Ophthalmology* 119: 985-993.

Zangwill L M, Weinreb R N, Beiser J A, Berry C C, Cioffi G A, Coleman A L, Trick G et al. (2005) Baseline topographic optic disc measurements are associated with the development of primary open-angle glaucoma: the Confocal Scanning Laser Ophthalmoscopy Ancillary Study to the Ocular Hypertension Treatment Study. *Archives of Ophthalmology* 123: 1188-1197.

Zangwill L M, Weinreb R N, Berry C C, Smith A R, Dirkes K A, Liebmann J M, Brandt J D et al. (2004b) The confocal scanning laser ophthalmoscopy ancillary study to the ocular hypertension treatment study: study design and baseline factors. *American Journal of Ophthalmology* 137: 219-227.

Zangwill L M, Weinreb R N, Berry C C, Smith A R, Dirkes K A, Liebmann J M, Brandt J D et al. (2004c) Racial differences in optic disc topography. *Archives of Ophthalmology* 122: 22-28.

Zeiter J H, Shin D H, Juzych M S, Jarvi T S, Spoor T C, and Zwas F (1992) Visual field defects in patients with normal-tension glaucoma and patients with high-tension glaucoma. *American Journal of Ophthalmology* 114: 758.

Zeitz O, Matthiessen E T, Wiermann A, Reuss J, Richard G, and Klemm M (2004) Ocular hemodynamics in normal tension glaucoma: Effect of bimatoprost. *Klinische Monatsblätter für Augenheilkunde* 221: 550-554.

Zeile A J, Pokorny J, Lee D Y, and Ireland D (2007) Anisometropic amblyopia: Spatial contrast sensitivity deficits in inferred magnocellular and parvocellular vision. *Investigative Ophthalmology and Visual Science* 48: 3622-3631.

Appendix

Summary of patents pending

Country/Region	No:	Filing Date	Title
United Kingdom	GB0606680.7	03/04/2006	Method of and Apparatus for Detecting Degradation of Visual Performance
USA	11/729,287	28/03/2007	Method of and Apparatus for Detecting Degradation of Visual Performance
PCT	PCT/GB2007/001093	27/03/2007	Method of and Apparatus for Detecting Degradation of Visual Performance
Australia	2007232371	03/10/2008	Method of and Apparatus for Detecting Degradation of Visual Performance
Canada	2,647,696	03/10/2008	Method of and Apparatus for Detecting Degradation of Visual Performance
China	tbc	tbc	Method of and Apparatus for Detecting Degradation of Visual Performance
Europe	07732154.5	07/10/2008	Method of and Apparatus for Detecting Degradation of Visual Performance
Japan	2009-503636	03/10/2008	Method of and Apparatus for Detecting Degradation of Visual Performance
Mexico	MX/a/2008/012782	03/10/2008	Method of and Apparatus for Detecting Degradation of Visual Performance
Norway	tbc	tbc	Method of and Apparatus for Detecting Degradation of Visual Performance
South Africa	2008/08290	03/10/2008	Method of and Apparatus for Detecting Degradation of Visual Performance
Malaysia	tbc	tbc	Method of and Apparatus for Detecting Degradation of Visual Performance
Brazil	PI0709725-5	03/10/2008	Method of and Apparatus for Detecting Degradation of Visual Performance

India	tbc	tbc	Method of and Apparatus for Detecting Degradation of Visual Performance
Russia	2008143400	03/10/2008	Method of and Apparatus for Detecting Degradation of Visual Performance

Patent filed under the Patent Cooperation Treaty (PCT)

		European Patent Office 80298 MUNICH GERMANY Tel. +49 (0)89 2399 - 0 Fax +49 (0)89 2399 - 4465	
 RATTAN, Rishi		For any questions about this communication: Tel. +31 (0)70 340 45 00	
		Date 07.11.08	
Reference	Application No / Patent No 07732154.5 - 2305 PCT/GB2007001093		
Applicant/Proprietor University College Cardiff Consultants, Ltd.			
Notification of the data mentioned in Rule 19(3) EPC In the above-identified patent application you are designated as inventor/co-inventor. Pursuant to Rule 19(3) EPC the following data are notified herewith:			
DATE OF FILING	:	27.03.07	
PRIORITY	:	GB/03.04.06/ GBA 0606680	
TITLE	:	METHOD OF AND APPARATUS FOR DETECTING DEGRADATION OF VISUAL PERFORMANCE	
DESIGNATED STATES	:	AT BE BG CH CY CZ DE DK EE ES FI FR GB GR HU IE IS IT LI LT LU LV MC MT NL PL PT RO SE SI SK TR	
Receiving Section 			
EPO Form 1204 12.07			

Abstract for ARVO



Control/Tracking Number: 06-A-6089-ARVO

Activity: Abstract

Current Date/Time: 12/2/2005 4:16:33 PM

Masking Effects and Spatial Limitations of White Pixelated Noise

Author Block: *R.Rattan, J.Rovamo, J.M. Wild.* School of Optometry & Vision Sciences, Cardiff University, Cardiff, United Kingdom.

Purpose: The spectral density of spatio-temporal noise can be modified by changing the root-mean-square (rms) contrast, the noise check size and the duration of the noise check. The latter two parameters can be increased to strengthen a noise mask up to a point, beyond which it can no longer be considered to mimic 'white' noise. We compared the spatial cut-off, in terms of noise checks per cycle, when masking stationary and drifting cosine gratings. **Methods:** The authors measured contrast energy thresholds, E , for stationary and drifting (16 Hz) vertical cosine gratings, at spatial frequencies of 1 and 8 cycles per degree. The gratings were embedded in spatio-temporal noise and contrast energy thresholds were determined against a range of noise check sizes. The noise spectral density of spatio-temporal noise was calculated by multiplying the duration of the noise frame, the area of the noise check, and the noise rms contrast squared.

Results: With fewer noise checks per grating cycle, the contrast energy thresholds increased as the spectral density of noise strengthened. The signal-to-noise (SNR) ratio remained constant, until the grating contrast threshold started to decrease, indicating that the noise was no longer effective as a mask. The stationary gratings of 1 and 8 cycles per degree were masked down to 3.6 and 3.5 noise checks per cycle, respectively. The drifting gratings of 1 and 8 cycles per degree were masked down to 2.4 and 2.0 checks per cycle, respectively. **Conclusions:** The spatial cut-off for a two-dimensional, spatio-temporal mask is dependent on the temporal parameters of the signal. The critical numbers of checks per cycle that will mimic 'white' noise are shown to be smaller for drifting gratings than for stationary gratings.

Author Disclosure Block: **R. Rattan**, None; **J. Rovamo**, None; **J.M. Wild**, None.

Reviewing Codes (Complete): 271 psychophysical methods – VI

Presentation Preference (Complete): Poster Only

Keyword (Complete): 473 contrast sensitivity ; 626 perception

